U.PORTO
FEUP FACULDADE DE ENGENHARIA
UNIVERSIDADE DO PORTO

# The NETmix® Technology, Applied to Gas Hydrates Production: A Potential Solution to CCS

*Ph.D Dissertation*
*in*
*Chemical and Biological Engineering*
*By*

**Marcelo Filipe dos Santos Costa**

*Supervisors:*
*Prof. Dr. José Carlos Brito Lopes*
*Prof. Dr. Joaquim Luís Bernardes Martins de Faria*




*Laboratory of Separation and Reaction Engineering – Laboratory of Catalysis and Materials*
*Associate Laboratory LSRE – LCM*
***Faculdade de Engenharia***
***Universidade do Porto***

*November 2017*

*To my family and friends*

*"The greatest challenge to any thinker*
*is stating the problem in a way*
*that will allow a solution"*
**Bertrand Russell**

This work was partly financed by Project POCI-01-0145-FEDER-006984 – Associate Laboratory LSRE – LCM – funded by FEDER – Fundo Europeu de Desenvolvimento Regional – through COMPETE2020 – Programa Operacional Competitividade e Internacionalização (POCI) and by national funds through FCT – Fundação para a Ciência e Tecnologia; and by – European Institute of Innovation & Technology (EIT), through the KIC InnoEnergy Program in the project HydraGtS, in cooperation with Galp Energia.


















# Agradecimentos

Gostaria de agradecer a ajuda e apoio dados pelos meus orientadores durante a realização deste trabalho, Prof. José Carlos Lopes e Prof. Joaquim Faria. Gostaria também de agradecer todo o apoio dado pela Profª. Madalena Dias.

A toda a equipa do *mixing group* do LSRE-LCM, gostaria de agradecer pelo incansável apoio que me deram durante estes últimos anos, por não desistirem de me aturar nos dias menos bons (e foram tantos...) e por toda a ajuda a que se prestaram durantes estes últimos 4 anos e meio. Em particular, gostaria de destacar a ajuda dada pelo Carlos e Rómulo, que em muito contribuíram para o avanço do projeto, bem como do Luís Moura, Luís Esteves, José Pedro e o Dr. Ricardo Santos. Gostaria também de agradecer a todos os colegas de gabinete E-417 que por lá passaram durante estes últimos anos, partilhando o espaço comigo e resultando em discussões de ideias, amenas cavaqueiras e por vezes enormes gargalhadas: sobretudo à Gabriela, à Catarina e à Margarida, mas também ao Enis e à Marina. A todos eles, o meu muito obrigado. Gostaria também de agradecer aos restantes membros do *mixing group*, aos que já saíram, como é o caso do Carlos e Cláudio Fonte, Anna, Nuno, Franziska, Tobias, Joana e Mariana, bem como os que cá continuam, tal como Nélson, Carla, Andreia e Yaidelin. Finalmente, gostaria de agradecer a todos os restantes elementos do LSRE-LCM, em especial a Ariana, a Maria João, a Carina, a Márcia e a Catarina (a Costa).

Gostaria também de agradecer aos Drs. João Pedro Araújo e Armandina Lopes, da FCUP, pelo apoio na caracterização dos materiais; à Maria João Lima pela disponibilidade de fornecimento de azoto; aos Engs. Luís Carlos, Nuno Guerreiro e José Luís Moreira pela pronta ajuda no que fosse necessário.

À Fundação para a Ciência e Tecnologia (FCT) pelo apoio financeiro através da bolsa de Doutoramento com a referência SFRH/BD/87817/2012.

À GALP por ter possibilitado a realização deste trabalhado nas instalações do LSRE-LCM, num projeto conjunto com a KIC InnoEnergy através do projeto HydraGtS. Gostaria também de agradecer ao INEGI, em particular ao Eng. Joaquim Santos, bem como à Paralab, em particular aos Engs. Rui Soares e Miguel Mota, por todo o apoio e disponibilidade na construção da instalação experimental.

Gostaria também de agradecer a todos os meus amigos, pois não teria conseguido ultrapassar esta etapa sem o apoio deles, em especial ao Gil, pela ajuda na tradução para Francês.

Por fim, gostaria de agradecer a toda a minha família, em particular aos meus pais e irmão, espero que este novo passo na minha vida seja um orgulho para eles.

# Statement

This thesis is performed within the scope of a collaborative project between Faculdade de Engenharia da Universidade do Porto (FEUP), Instituto Superior Técnico (IST), AGH University of Science and Technology, Fluidinova S.A. and Galp Energia S.A., partially funded by the European Institute of Innovation & Technology (EIT), through the program KIC InnoEnergy.

The experimental setup designed for the development of the present work is owned by Galp Energia S.A.

All results from this work were obtained at the installations of LSRE-LCM, unless when stated otherwise

Marcelo Filipe dos Santos Costa

# Abstract

The present work concerns the study of the capacity of the NETmix technology to solve one of the major problems in today's society: the global warming caused by the emission of pollutant gases, such as carbon dioxide. This work suggests the use of the NETmix technology for the precipitation of gas hydrates as means to capture and store carbon dioxide, and includes heat transfer studies and experimental analysis of a continuous process to do so.

A 3D CFD model based on previous works is used to investigate the capacity of the NETmix technology to remove heat from or to its medium. NETmix has shown to possess up to 5 times larger capacity to remove heat than the most typical devices industrially used, such as stirred tanks or tubular reactors. It has shown that it can remove up to 10 times more heat than microfluidic devices.

An experimental setup was designed and built based on the NETmix technology, and experimentally applied for the continuous production of carbon dioxide hydrates, which can be used as CCS applications. The setup is capable to treat approximately $1\,\mathrm{kg}\cdot\mathrm{h}^{-1}$, using a device with a residence time of 1 second, resulting in a successful production of carbon dioxide hydrates. If the conditions of the process are carefully chosen, thermodynamic equilibrium is achieved in a single stage. However, if the conditions are not properly chosen, mass transfer limitations to gas dissolution may be detected. Dissociation showed that about 18% in weight of the hydrate is composed by carbon dioxide, being lower than the theoretical value due to gas release during depressurization. The use of a process based on NETmix to continuously produce and transport carbon dioxide hydrates has shown to be competitive when compared to supercritical carbon dioxide $\left(18.5\,\mathrm{USD}\cdot\mathrm{ton}_{\mathrm{CO_2}}^{-1}\ \text{vs.}\ 19.3\,\mathrm{USD}\cdot\mathrm{ton}_{\mathrm{CO_2}}^{-1}\right)$.

The NETmix technology can also be used as equilibrium units in a multi-stage counter-current process for the separation of nitrogen from carbon dioxide, the main

constituents of flue gas exhausted as the result of fuel combustion. The concept has been presented, and the preliminary analysis shows that about 85% of the carbon dioxide can be removed from the gas stream for a 5-stage process, reducing the carbon dioxide concentration by 4 times.

This work shows that NETmix is a promising technology for the continuous production of gas hydrates at large throughputs. It has the capacity to absorb most of the heat released during hydration on a small-scaled device.

**Keywords:** Clathrates;
Hydrates;
NETmix;
Heat transfer;
Mass transfer;
Hydrate dissociation;
Carbon dioxide;
Flue gas.

# Resumo

A presente dissertação foca-se no estudo da capacidade da tecnologia de mistura NETmix para a resolução de um dos grandes problemas da sociedade atual: o aquecimento global, causado pela emissão e acumulação de gases poluentes, tal como o dióxido de carbono, na atmosfera. Este trabalho sugere a aplicação da tecnologia NETmix para a precipitação de hidratos (ou clatratos) de gás de forma a promover a captura e armazenamento de dióxido de carbono, e inclui estudos de transferência de calor e análise experimental do processo em contínuo.

Foi utilizado um modelo CFD tridimensional, usado em trabalhos anteriores, para investigar a capacidade da tecnologia NETmix de remover ou absorver calor. Os resultados demonstraram que a tecnologia consegue apresentar até 5 vezes mais capacidade de remover calor do que outras tecnologias que são aplicadas industrialmente, tais como tanques agitados ou reatores tubulares. A tecnologia também demonstrou possuir 10 vezes mais capacidade de remover calor do que microdispositivos.

Foi desenhada e construída uma instalação experimental ao longo deste trabalho, com o objetivo de aplicar a tecnologia NETmix num processo para a produção em contínuo de hidratos de dióxido de carbono, com potencial interesse para a captura e armazenamento de dióxido de carbono. A instalação, com capacidade para tratar cerca de $1\,\mathrm{kg}\cdot\mathrm{h}^{-1}$ de dióxido de carbono numa unidade com um tempo de residência de apenas 1 segundo, provou ser capaz de produzir hidratos de dióxido de carbono com sucesso. As condições de operação têm relevância na eficiência do processo. Se forem bem escolhidas, o equilíbrio termodinâmico é alcançado, verificando-se a ausência de gás. Se as condições não forem ideais, é verificado que existem limitações à transferência de massa na dissolução do gás. Testes de dissociação ao sólido mostraram que cerca de 18% do hidrato, em massa, corresponde a dióxido de carbono. Este valor é menor do que o teórico devido à gaseificação que ocorre durante

a despressurização da amostra. A aplicação da tecnologia NETmix num processo para a produção em contínuo e transporte de hidratos de dióxido de carbono demonstrou ser economicamente competitivo, quando comparado com o transporte através de dióxido de carbono supercrítico $\left(18.5\ \mathrm{USD}\cdot\mathrm{ton}_{\mathrm{CO_2}}^{-1}\ \text{vs.}\ 19.3\ \mathrm{USD}\cdot\mathrm{ton}_{\mathrm{CO_2}}^{-1}\right)$.

A tecnologia NETmix pode também ser utilizada enquanto unidades de equilíbrio num processo multi-estágios em contra-corrente, para a separação de nitrogénio do dióxido de carbono, que são os principiais constituintes do gás de exaustão que é libertado devido à combustão de combustíveis. O conceito foi apresentado, e os resultados preliminares mostram que cerca de 85% do dióxido de carbono é removido da corrente de gás num processo com 5 estágios de equilíbrio, reduzindo a sua concentração para 4 vezes menos.

Esta dissertação mostra que a tecnologia NETmix é promissora para a produção em contínuo de hidratos de gás com elevadas produtividades. Demonstrou ser capaz de absorver uma grande quantidade do calor libertado durante o processo num dispositivo de pequena escala.

**Palavras-chave:** Clatratos;
Hidratos;
NETmix;
Transferência de calor;
Transferência de massa;
Dissociação de hidratos;
Dióxido de carbono;
Gás de exaustão.

# Résumé

Cette dissertation se focalise sur l'étude de la capacité de la technologie de mélange NETmix pour la résolution d'un des plus grands problèmes de la société actuelle: le réchauffement climatique, causé par l'émission et accumulation de polluants gazeux comme le dioxyde de carbone dans l'atmosphère. Ce travail suggère l'application de la technologie NETmix pour la précipitation d'hydrates (ou clathrates) de gaz afin de promouvoir la capture et stockage de dioxyde de carbone, et comprend des études de transfert de chaleur et analyse expérimentale en un processus en continu.

Un modèle MFN (ou CFD, en anglais) tridimensionnel a été utilisé, comme dans des travaux précédents, pour examiner la capacité de la technologie NETmix pour retirer ou absorber de la chaleur. Les résultats ont démontré que la technologie peut présenter jusqu'à 5 fois plus de capacité de retirer de la chaleur que d'autres technologies qui sont appliquées industriellement, comme les réservoirs agités ou les réacteurs tubulaires. La technologie a également démontré qu'elle a 10 fois plus de capacité de retirer de la chaleur que les microdispositifs.

Une installation expérimentale a été dessinée et construite tout au long de ce travail, afin d'appliquer la technologie NETmix dans un processus pour la production en continu d'hydrates de dioxyde de carbone, avec l'intérêt de capturer e stocker le dioxyde de carbone. L'installation, avec une capacité pour traiter environ $1\,\mathrm{kg}\cdot\mathrm{h}^{-1}$ de dioxyde de carbone dans une unité avec un temps de séjour de seulement 1 seconde, a prouvé être capable de produire des hydrates de dioxyde de carbone avec succès. Les conditions d'opération sont importantes pour l'efficience du processus. Si elles sont correctement choisies, l'équilibre thermodynamique est atteint, sans gaz. Si les conditions ne sont pas idéales, il est possible de vérifier qu'il y a des limitations au transfert de masse dans la dissolution du gaz. Des tests de dissociation au solide ont démontré qu'environ 18% de l'hydrate, en masse, correspond au dioxyde de carbone. Cette valeur est inférieure par rapport au théorique à cause de la gazéification

pendant la dépressurisation de l'échantillon. L'application de la technologie NETmix dans un processus pour la production en continu et transport d'hydrates de dioxyde de carbone a démontré être économiquement compétitif, par rapport au transport à travers le dioxyde de carbone supercritique $\left(18.5\ \mathrm{USD}\cdot\mathrm{ton}_{\mathrm{CO_2}}^{-1}\ \text{vs.}\ 19.3\ \mathrm{USD}\cdot\mathrm{ton}_{\mathrm{CO_2}}^{-1}\right)$.

La technologie NETmix peut être également utilisée comme unité d'équilibre dans un processus multi-étages en contre-courant pour la séparation de nitrogène du dioxyde de carbone, qui sont les principaux constituants du gaz d'échappement qui est libéré dû à la combustion de carburants. Le concept a été présenté et les résultats préliminaires démontrent qu'environ 90% du dioxyde de carbone est retiré du courant de gaz dans un processus avec 5 étages d'équilibre, réduisant sa concentration en 4 fois.

Cette dissertation démontre que la technologie NETmix est prometteuse pour la production en continu d'hydrates de gaz avec des productivités élevées. Elle a également démontré être capable d'absorber une grande quantité de chaleur pendant le processus dans un dispositif à petite échelle.

**Mots clés:** Clathrates;
Hydrates;
NETmix;
Transfert de chaleur;
Transfert de masse;
Dissociation d'hydrates;
Dioxyde de carbone;
Gaz d'échappement.

# Table of Contents

**List of Figures** ..... vii

**List of Tables** ..... xvii

**Notation** ..... xix

**1 Introduction** ..... 1

1.1 Motivation and Relevance ..... 4

1.1.1 Gas Hydrates ..... 5

1.1.2 NETmix Technology ..... 6

1.2 Thesis Objectives and Layout ..... 7

1.3 References ..... 9

**2 State of the Art** ..... 13

2.1 Climate Changes ..... 13

2.2 Overview on Carbon Capture & Storage (CCS) ..... 17

2.2.1 Carbon Dioxide Capture Technologies ..... 19

2.2.2 Carbon Dioxide Transport ..... 31

2.2.3 Carbon Dioxide Storage ..... 31

2.3 Gas Hydrates ..... 33

2.3.1 Hydrates Structures and Properties ..... 34

2.3.2 Hydrates Formation ..... 41

2.3.3 Inhibitors and Promoters ..... 52

2.3.4 Applications ..... 56

2.3.5 Continuous Production ..... 63

2.4 Static Mixers ..... 66

2.4.1 Commercial Static Mixers ..... 66

2.4.2 The NETmix Technology ..... 67

2.5 References ..... 77

**3 HEAT TRANSFER PERFORMANCE OF NETMIX ..... 89**

3.1 Introduction ..... 89

3.2 3D CFD Modelling ..... 92

3.2.1 Governing Equations and Boundary Conditions ..... 94

3.2.2 Numerical Simulation Strategy ..... 95

3.2.3 Numerical Discretization and Solution Methods ..... 96

3.3 Heat Transfer Performance ..... 97

3.4 Heat Transfer Validation and Comparison ..... 106

3.5 Nusselt Number Correlations ..... 111

3.6 NETmix Heat Transfer Benchmarking ..... 118

3.7 Conclusions ..... 125

3.8 References ..... 126

**4 $CO_2$ HYDRATES – EXPERIMENTAL SETUP ..... 129**

4.1 Introduction ..... 129

4.2 Setup Requirements ..... 130

4.3 Process Design ..... 135

4.3.1 Process Flow Diagram ..... 135

4.3.2 Equipment Design and Selection ..... 141

4.3.3 3D Setup Layout ..... 154

4.4 Heat Transfer Analysis ..... 159

4.4.1 Heat Transfer Resistances ..... 159

4.4.2 Global Heat Transfer Coefficient Estimation ..... 171

4.5 Conclusions ..... 174

4.6 References ..... 175

**5 $CO_2$ HYDRATES – EXPERIMENTAL PRODUCTION ..... 179**

5.1 Introduction ..... 179

5.2 Hydrates Thermodynamics ..... 180

5.2.1 CSMGem ..... 180

5.2.2 Phase Equilibrium and Enthalpy ..... 185
5.2.3 Flash Calculation Model ..... 193
5.3 Energy Balance to a Crystallization Unit ..... 198
5.3.1 Case 1: Liquid – Liquid ..... 203
5.3.2 Case 4: Liquid – Gas ..... 206
5.3.3 Case 7: Gas – Liquid ..... 207
5.3.4 Case 10: Gas – Gas ..... 207
5.3.5 Other Considerations ..... 207
5.4 Experimental Description ..... 208
5.4.1 Materials ..... 208
5.4.2 Set of Experiments ..... 208
5.4.3 Experimental Procedure ..... 211
5.5 Results and Discussion ..... 214
5.5.1 Process Analysis ..... 214
5.5.2 Global Heat Transfer Coefficient ..... 239
5.5.3 Solid Material Properties ..... 241
5.6 Conclusions ..... 249
5.7 References ..... 251
**6 $CO_2$ Hydrates – Cost Analysis ..... 255**
6.1 Introduction ..... 255
6.2 Strategy ..... 256
6.3 Process Description ..... 257
6.4 Cost Estimation ..... 260
6.5 Benchmarking ..... 262
6.6 Conclusions ..... 265
6.7 References ..... 266
**7 $N_2/CO_2$ Hydrate-Based Separation Concept ..... 269**
7.1 Introduction ..... 269
7.2 Separation Concept ..... 270

7.3 Physical Model ..... 272
7.3.1 Model and Considerations ..... 272
7.3.2 Model Equations ..... 274
7.3.3 Thermodynamic Modelling ..... 278
7.4 Algorithm ..... 282
7.4.1 Initial Estimates ..... 284
7.5 Results and Discussion ..... 286
7.6 Final Considerations ..... 293
7.7 Conclusions ..... 295
7.8 References ..... 296

**8 Final Remarks ..... 299**

8.1 Conclusions ..... 299
8.2 Future Work ..... 304
8.3 References ..... 305

**Appendix A Physical Properties ..... 307**

A.1 Water Properties ..... 307
A.2 Ethanol – Water Mixture Properties ..... 307
A.3 Carbon Dioxide Properties ..... 308
A.4 Steel Properties ..... 309
A.5 References ..... 310

**Appendix B CSMGem Fugacity Models ..... 311**

B.1 Aqueous Phase ..... 312
B.2 Vapour Phase ..... 316
B.3 Hydrate Phase ..... 317
B.4 References ..... 320

**Appendix C Calcium Carbonate Equilibrium ..... 321**

C.1 Equilibrium Modelling ..... 321
C.2 Equilibrium Constants ..... 325

C.3 Procedure Considerations ..... 325

C.4 References ..... 326

**APPENDIX D THF EXPERIMENTAL P-T PROFILES ..... 327**

**APPENDIX E $N_2/CO_2$ HYDRATE EQUILIBRIUM FITTINGS ..... 329**

E.1 Equilibrium Pressure ..... 329

E.2 Components Equilibrium Fractions ..... 332

# List of Figures

**Figure 1.1** – World population and growth rate evolution. Shadowed area represents the world population. Data prior to 1960 from UN (2014) and data after 1960 from WorldBank (2016).....2

**Figure 1.2** – Typical gas hydrate structure with water molecules forming a cage trapping gas molecules (Maslin et al. 2010).....5

**Figure 2.1** – Global $CO_2$ emissions from fossil fuel use and cement industries (Olivier et al. 2015).....16

**Figure 2.2** – Example of $CO_2$ capture and storage technology from source to storage. Adapted from Smit et al. (2014).....18

**Figure 2.3** – Carbon dioxide capture systems (Holloway et al. 2006).....19

**Figure 2.4** – Process flow diagram of a generic IGCC plant showing retrofit modifications for $CO_2$ capture (from EPRI (2012)).....23

**Figure 2.5** – Process flow diagram for $CO_2$ recovery from flue gas by chemical absorption (adapted from Metz et al. (2005)).....25

**Figure 2.6** – Oxyfuel process schematic of a pulverized coal fired power plant (Metz et al. 2005).....29

**Figure 2.7** – Storage security as a function of the storage mechanism (Metz et al. 2005).....32

**Figure 2.8** – Hydrate cavities of structures I, II and H.....35

**Figure 2.9** – Gas hydrates structures from cavity entities (Adapted from HWIPE (2016))...36

**Figure 2.10** – Solid $CO_2$ hydrate: (a) using a thermodynamic cell (BGS 2016); (b) wet obtained in continuous process (Groen 2012).....37

**Figure 2.11** – $CO_2 - H_2O$ phase diagram.....43

**Figure 2.12** – (a) Hydrate phase equilibria for $N_2/CO_2$ system, for different compositions; (b) Phase-composition diagram at three different temperatures. The curves represent trendlines (Kang and Lee 2000).....44

**Figure 2.13** – Comparison between experimental data and thermodynamic model based on the van der Waals and Platteeuw model developed by Sfaxi et al. (2012) for $CO_2$ hydrates. .....45

**Figure 2.14** – Gas consumption vs. time for hydrate formation. Adapted from Sloan and Koh (2007). .....46

**Figure 2.15** – Schematic of radial dissociation (Sloan and Koh 2007). .....49

**Figure 2.16** – Hydrate dissociation lines for mixtures of methane with ethane, propane, butane and isobutane (Sloan and Koh 2007). .....51

**Figure 2.17** – Influence of THF on the dissociation enthalpy of $CO_2$ hydrates (data from Delahaye et al. (2006)). .....55

**Figure 2.18** – Phase equilibrium data for the system $N_2/CO_2$ and the influence of THF and TBAB (data extracted from Ma et al. (2016)) .....56

**Figure 2.19** – Plug formation via aggregation (Sloan and Koh 2007). .....57

**Figure 2.20** – Clathrate hydrate slurry (Ogoshi and Takao 2004). .....59

**Figure 2.21** – Process flow diagram of a hydrate-based $CO_2$ recovery process (Kang and Lee 2000). .....61

**Figure 2.22** – Simplified process flow diagram of the experimental setup by Gudmundsson et al. (2000). .....64

**Figure 2.23** – (a) Block flow diagram of the SIMTECHE capture process (Yang et al. 2011); (b) Schematic of the experimental setup using a tail-tube reactor (Yang et al. 2008).....65

**Figure 2.24** – Examples of commercially available static mixers: a) Kenics mixer from Chemineer Inc. (Chemineer 2016b); b) KMX mixer from Sulzer (Sulzer 2016); c) HEV mixer from Chemineer Inc. (Chemineer 2016a); d) ISG mixer from Ross Mixers (Ross 2016). .....67

**Figure 2.25** – (a) NETmix network; (b) network of 2D unit cells; (c) network of 3D unit cells. .....68

**Figure 2.26** – Velocity magnitude contour maps of NETmix chambers at: a) $Re = 50$ (below critical Reynolds number); b) $Re = 500$ (above critical Reynolds number). Adapted from Laranjeira (2005).....69

**Figure 2.27** – NETmix prototypes: a) NETmix 3D; b) Multi-Inlet NETmix 2D; c) Lab-Scale NETmix 2D. ..... 69

**Figure 2.28** – nanoXIM industrial production site at Fluidinova: a) NETmix industrial reactor; b) Centrifuge; c) Spray-dry unit (adapted from Faria (2008)). ..... 71

**Figure 2.29** – Comparison between experimental unit cell pressure drop and model from Equation 2.11 for different NETmix devices (adapted from Fonte et al. (2013)). ..... 73

**Figure 2.30** – Energy performance of NETmix mixer: (a) Z-number; (b) power number and (c) mixing power per volume (Fonte et al. 2013). Red regions represent the conditions at which flow patterns present an oscillatory and chaotic behaviour..... 73

**Figure 3.1** – NETmix Unit Block (NUB) CFD model and surfaces identification. ..... 93

**Figure 3.2** – Temperature contour maps at the middle plane of the domain of the chamber at the fourth row of NUB, for $\mathrm{Re}_{in} = 300$ and constant wall heat flux as a function of time. The red circles identify the hot spots..... 98

**Figure 3.3** – Unit cell Nusselt number as a function of the inlet Reynolds number for both wall boundary conditions: constant temperature and constant heat flux. Dashed lines represent the boundaries of the different identified flow regimes..... 103

**Figure 3.4** – $z$-vorticity contour maps at the middle plane of the unit cell at the fourth row as a function of the inlet Reynolds number, and trajectories for simulations with constant wall temperature. ..... 105

**Figure 3.5** – Heat transfer in laminar flow between parallel plates schematic and development of thermal boundary layer with length. ..... 107

**Figure 3.6** – Nusselt number as a function of the dimensionless thermal entrance length for constant wall temperature boundary condition. The points represent the NUB unit cell values evaluated for the cell at the fourth row; the solid line represents the analogue values for laminar flow between parallel plates; the dashed line represents the new asymptotic value for NETmix..... 110

**Figure 3.7** – Nusselt number as a function of the dimensionless thermal entrance length for constant wall heat flux boundary condition. The points represent the NUB unit cell values evaluated for the cell at the fourth row; the solid line represents the analogue values for laminar flow between parallel plates; the dashed line represents the new asymptotic value for NETmix. ..... 111

**Figure 3.8** – Enhancement factor for Nusselt number as a function of the Reynolds number, as defined by Equation 3.29, for both boundary conditions: filled circles – constant wall temperature; empty circles – constant wall heat flux. The dashed lines represent the fitting curves. ....112

**Figure 3.9** – Nusselt number comparison between parallel plates, tubes and NETmix for two different $\omega_n/d_c$ ratios, as a function of the dimensionless thermal entrance length for constant wall temperature. The dashed lines represent the NETmix analogue curve, obtained using Equations 3.21 and 3.28, while the dotted lines represent the NETmix curves when heat transfer enhancement due to oscillations is observed, obtained using Equation 3.30....115

**Figure 3.10** – Temperature contour maps in NUB for $\mathrm{Re}_{in} = 50$ and constant wall temperature, at the middle plane, for $\omega_n/d_c = 3$ and $\omega_n/d_c = 1$ ....118

**Figure 3.11** – Comparison of the Nusselt number as a function of Reynolds number of fully developed laminar flow in pipes and between parallel plates, turbulent flow in pipes and between parallel plates, and for NETmix device with $\omega_n/d_c = 3$, for constant wall temperature and $\mathrm{Pr} \approx 7$. ....119

**Figure 3.12** – Specific surface area comparison for different heat exchange devices. ....122

**Figure 3.13** – Specific heat transfer capacity comparison between typical heat exchange devices and NETmix. ....124

**Figure 4.1** – Sandwich-type layer-by-layer microNETmix unit scheme with two cooling plates configurations: (a) in parallel; (b) in series. ....132

**Figure 4.2** – (a) Ice slurry velocity working conditions and working regimes (SlurryICE); (b) Effect of particle size and solids loading on pressure drop increase (Liu et al. 1988)....134

**Figure 4.3** – Process flow diagram (PFD) for the lab-scale continuous hydrates production process using the microNETmix unit. Black diamond symbols with white borders are numbering the flow lines, while the full back diamond symbols are numbering the pneumatic lines, used for in the pneumatic valves actuators.....136

**Figure 4.4** – microNETmix unit parts: (a) Network plate; (b) Cooling plate; (c) Distributor plate; (d) Inlet closing plate with fluid distribution in reactants side; (e) Outlet closing plate; (f) Shim plate and support body; (g) Closing body. ....142

**Figure 4.5** – Schematic of the microNETmix network plate. ....142

**Figure 4.6** – Schematic of the microNETmix cooling plate. ..... 143

**Figure 4.7** – microNETmix unit pre-mixed injection scheme. ..... 144

**Figure 4.8** – (a) microNETmix assembly; (b) microNETmix assembly drawings: Orange lines represent the flow of one of the reactants through the inlet A; red lines represent the flow of the other reactants through inlet B; green lines represent the flow of the medium mixture in the network plates, leaving the system through outlet C; blue and red arrows represent the flow of the cooling fluid, entering through inlet D and exiting through outlet E. ..... 146

**Figure 4.9** – Pumps in the experimental setup: (a) Dosing Mono LTM pump for water; (b) HPLC Knauer Azura P 4.1S pump for liquid $CO_2$; (c) Peristaltic Watson Marlow 323 pump for cooling fluid. ..... 148

**Figure 4.10** – (a) Installed filter column; (b) Microscope imaging of the different meshes used to filter (obtained using a SEM Phenom Pro X microscope – see Section 5.4.3.3). ..... 149

**Figure 4.11** – (a) Visualizer schematic and main dimensions; (b) Real visualizer. ..... 152

**Figure 4.12** – Gas line jacketed tube schematic. ..... 153

**Figure 4.13** – (a) Real experimental setup; (b) 3D model of experimental setup. ..... 154

**Figure 4.14** – Front and top views of the water circuit from experimental setup. ..... 155

**Figure 4.15** – Front and top views of the guest compound circuit from experimental setup: (a) gas carbon dioxide (or nitrogen – carbon dioxide mixture); (b) liquid carbon dioxide. .. 156

**Figure 4.16** – Front and lateral views of the recirculation circuit of the product stream from experimental setup. ..... 157

**Figure 4.17** – Front and lateral views of the pressure circuit that includes relief valve V-21. ..... 158

**Figure 4.18** – Front and top views of part of the cooling circuit from experimental setup. . 158

**Figure 4.19** – (a) Heat transfer coefficient and (b) resistance in the NETmix side as a function of the mass flowrate (assuming water as the working fluid). ..... 161

**Figure 4.20** – Different regions in the cooling plates: red regions are the channels in contact with the NETmix network; blue regions are the flow collectors/distributors; green regions are the inlet and outlet regions; grey regions present solid. ..... 162

**Figure 4.21** – Part of the cooling plate simulated by CFD and respective boundary conditions. The numbers identify each of the section's channels. ..... 163

**Figure 4.22** – Flow distribution in the cooling plate channels for each of the sections. .....165

**Figure 4.23** – Cooling plates channel's Nusselt number as a function of the dimensionless entrance length (circles) and comparison with laminar flow in tubes for constant wall heat flux (line). .....168

**Figure 4.24** – Cooling plates channel's Nusselt number comparison. The dashed line represents the Nusselt number obtained if the flowrate was equally distributed in all channels.....169

**Figure 4.25** – (a) Heat transfer coefficient and (b) resistance on the cooling plate side as a function of the mass flowrate (assuming ethanol – water mixture as the working fluid).....170

**Figure 4.26** – Global heat transfer coefficient for the microNETmix unit as a function of the NETmix channel's Reynolds number, for several values of cooling plates channels Reynolds number. .....172

**Figure 4.27** – microNETmix unit plates overlap. The red regions represent the regions of the NETmix network that are in laid in the cooling fluid channels, while the blue regions represent regions where the NETmix network is laid in the cooling plates baffles (baffles are represented by the dashed lines). .....173

**Figure 5.1** – Carbon dioxide – water system's phase diagram. The lines represent: red – $CO_2$ hydrates equilibrium curve, obtained from CSMGem; blue – $CO_2$ liquid-vapour and supercritical equilibrium curves; black – solid-liquid equilibrium curve of water. The points represent experimental data compiled by (Sloan and Koh 2007): ○ Larson (1955); □ Takenouchi and Kennedy (1965); ◆ Robinson and Metha (1971); • Ng and Robinson (1985). .....186

**Figure 5.2** – Comparison of carbon dioxide solubility between CSMGem (lines) and experimental data (points): (a) as a function of temperature for atmospheric pressure (Carroll et al. 1991) and at hydrate equilibrium pressure (Diamond and Akinfiev 2003); (b) as a function of the pressure for different temperatures (Anderson 2002).....189

**Figure 5.3** – Enthalpy of dissociation of carbon dioxide hydrates. The line represents the enthalpy determined from Equations 5.22 through 5.28. The points represent experimental data from Lirio and Pessoa (2013), Udachin et al. (2001) and Delahaye et al. (2006). .....193

**Figure 5.4** – Schematic of the microNETmix unit and stream representation. .....199

**Figure 5.5** – Flow diagram of algorithm used to estimate the amount of produced hydrates. ..... 202

**Figure 5.6** – Temperature and pressure profiles for experiment E-001. ..... 215

**Figure 5.7** – Different regimes at different instants for experiment E-001 at different instants: (a) thermal stabilization; (b) after carbon dioxide injection at working pressure; (c) beginning of precipitation; (d) production of hydrates; (e) filling of visualization window with hydrates. ..... 217

**Figure 5.8** – Pressure-temperature paths of experiment E-001. ..... 218

**Figure 5.9** – Temperature and pressure profiles for experiment E-002. ..... 221

**Figure 5.10** – Temperature and pressure profiles for experiment E-003. ..... 222

**Figure 5.11** – Different regimes at different instants for experiments: (a) E-002; (b) E-003. 223

**Figure 5.12** – Temperature and pressure profiles for experiment E-004. ..... 225

**Figure 5.13** – Temperature and pressure profiles for experiment E-005. ..... 226

**Figure 5.14** – Different regimes at different instants for experiments: (a) E-004; (b) E-005. 227

**Figure 5.15** – Temperature and pressure profiles for experiment E-006. ..... 229

**Figure 5.16** – Temperature and pressure profiles for experiment E-007. ..... 230

**Figure 5.17** – Different regimes at different instants for experiments: (a) E-006; (b) E-007. 231

**Figure 5.18** – Temperature and pressure profiles for experiment E-008. ..... 232

**Figure 5.19** – Temperature and pressure profiles for experiment E-009. ..... 233

**Figure 5.20** – Different regimes at different instants for experiments (a) E-008; (b) E-009. 234

**Figure 5.21** – Temperature and pressure profiles for experiment E-010. ..... 235

**Figure 5.22** – Different regimes at different instants for experiment E-010 at different times: (a) beginning of precipitation; (b) a few seconds after beginning; (c) constant production.. 236

**Figure 5.23** – Temperature and pressure profiles for experiment E-011. ..... 237

**Figure 5.24** – Different regimes at different instants for experiments: (a) E-011; (b) E-012; (c) E-013. ..... 239

**Figure 5.25** – Average global heat transfer coefficient for the different experiments. ..... 240

**Figure 5.26** – Gasification due to depressurization. ..... 242

**Figure 5.27** – Gas hydrate obtained from filtration column E-11 after depressurization in cold conditions. ....242

**Figure 5.28** – Dissociation tests for different amounts of cooling time. ....243

**Figure 5.29** – Dissociation progress with time. ....244

**Figure 5.30** – Effect of radiation on the hydrate dissociation for samples cooled for 2 days. 245

**Figure 5.31** – SEM imaging for (a) carbon dioxide hydrate; (b) typical ice. ....246

**Figure 5.32** – XRD pattern for carbon dioxide hydrate sample cooled for two hours. Upper and lower ticks correspond to structure sI hydrate and hexagonal ice, respectively. ....247

**Figure 6.1** – Process diagram for production of a slurry of carbon dioxide hydrates. ....258

**Figure 6.2** – Different steps for transportation of hydrate slurry via pipeline. ....260

**Figure 6.3** – Process diagram for supercritical carbon dioxide preparation and transport. ....263

**Figure 7.1** – Counter-current process schematic. ....273

**Figure 7.2** – Detailed stage model. ....274

**Figure 7.3** – Algorithm for the solution of the physical model. ....282

**Figure 7.4** – Carbon dioxide recovery and nitrogen loss from the gas stream. ....288

**Figure 7.5** – Carbon dioxide concentration in the outlet gas stream. ....289

**Figure 7.6** – Stage pressure and equilibrium pressure for the 5-stage simulation. ....290

**Figure 7.7** – Influence of the solids content $X^{w}_{hyd}$ in the process: (a) effect on the carbon dioxide recovery and nitrogen loss; (b) effect on the final carbon dioxide concentration at the outlet. ....291

**Figure 7.8** – Influence of the concentration of solids after separation $\phi_{slurry}$ in the process: (a) effect on the carbon dioxide recovery and nitrogen loss; (b) effect on the final carbon dioxide concentration at the outlet. ....292

**Figure 7.9** – Influence of the solids separation ratio in the separation nodes $\varsigma_{hyd}$ in the process: (a) effect on the carbon dioxide recovery and nitrogen loss; (b) effect on the final carbon dioxide concentration at the outlet. ....293

**Figure D.1** – Temperature and pressure profiles for experiment E-012. ....327

**Figure D.2** – Temperature and pressure profiles for experiment E-013. ....328

**Figure E.1** – CSMGem data (symbols) and fitting curve (dashed line) using values from Table E.1 for the parameter $\varpi$ for the determination of the equilibrium pressure..... 330

**Figure E.2** – CSMGem data (symbols) and fitting curve (dashed line) using values from Table E.1 for the parameter $k^*$ for the determination of the equilibrium pressure..... 330

**Figure E.3** – CSMGem data (symbols) and fitting curve (dashed line) using values from Table E.1 for the parameter $\lambda$ for the determination of the equilibrium pressure..... 331

**Figure E.4** – CSMGem data (symbols) and fitting curve (dashed line) using values from Table E.1 for the parameter $n$ for the determination of the equilibrium pressure..... 331

**Figure E.5** – Equilibrium pressure from CSMGem (symbols) and from the fitting curves (dashed lines) using the values from Table E.1 and Equation 7.17 and 7.18..... 332

**Figure E.6** – Carbon dioxide (full circles) and nitrogen (open circles) and fitting curves (dashed lines) for different phases in equilibrium: (a) vapour phase; (b) liquid phase; (c) hydrate phase..... 333

# List of Tables

**Table 2.1** – $CO_2$ emissions from different technologies (Narula et al. 2002). ..... 15

**Table 2.2** – Gas hydrates structural properties (Sloan and Koh 2007). ..... 35

**Table 2.3** – Hydration number of carbon dioxide hydrates from literature. ..... 39

**Table 2.4** – Mixed $N_2/CO_2$ hydrates ratio for sI structure (Anderson 2003). ..... 40

**Table 2.5** – Molecules identified as hydrate formers (Gao 2006). ..... 41

**Table 2.6** – Comparison between experimental enthalpies of dissociation with values obtained from Clapeyron equation (Kang et al. 2001, Yoon et al. 2003, Sloan and Koh 2007, Sabil et al. 2010). ..... 52

**Table 2.7** – NETmix reactor prototypes geometrical characteristics. ..... 71

**Table 2.8** – List of academic thesis (Masters and PhD's) using the NETmix technology. ..... 75

**Table 2.9** – List of NETmix-related patents. ..... 75

**Table 2.10** – List of publications in international research journals of works using the NETmix technology. ..... 76

**Table 3.1** – Equation 3.30 fitting parameters. ..... 113

**Table 4.1** – Process variables requirements. ..... 133

**Table 4.2** – Characteristic dimensions of the network and cooling plates. ..... 143

**Table 4.3** – Knauer Azura P 4.1S main specifications. ..... 147

**Table 4.4** – Air cooled chillers main specifications (Julabo). ..... 151

**Table 4.5** – Other equipment list. ..... 154

**Table 5.1** – Fitting parameters for Equation 5.16. ..... 187

**Table 5.2** – Constants used in Equation 5.25 (Duan et al. 2008). ..... 191

**Table 5.3** – Set of experiments and experimental conditions. ..... 209

**Table 5.4** – Process variables for experiments from Table 5.3. ..... 210

**Table 5.5** – Solutions conditions and amount of precipitated calcium carbonate for the sample cooled for two days. ..... 248

**Table 6.1** – Equipment costs and energy consumption for the process of Figure 6.1. ..... 261

**Table 6.2** – Equipment costs and energy consumption for the process of Figure 6.3. ..... 263

**Table 6.3** – Comparison of different methods of transporting carbon dioxide: supercritical versus hydrates ..... 265

**Table A.1** – Stainless steel 316 physical properties (AZoM 2017) ..... 310

**Table C.1** – Equilibrium constant values. ..... 325

**Table E.1** – Fitting parameters for Equations 7.17 and 7.18. ..... 329

**Table E.2** – Fitting parameters for the determination of equilibrium component fractions using Equation 7.20. ..... 332

# Notation

*Nomenclature*

Note: The units represented are represented only for dimensional analysis. Multiples or equivalent units may be used throughout this work.

| | |
|---|---|
| $[i]$ | Molar concentration of species $i$, [M] |
| $a$ | Activity |
| $A$ | Area, [$m^2$] |
| $A_{DH}$ | Debye-Hückel constant, [$kg^{1/2} \cdot mol^{-1/2}$] |
| $C$ | Number of components |
| $C'$ | Configurational flow constant |
| $C_{i,m}$ | Langmuir constant for guest $i$ in type $m$ cages, [$bar^{-1}$] |
| $C_{equip}$ | Cost of equipment, [US $] |
| $c_P$ | Specific heat capacity at constant pressure, [$J \cdot mol^{-1} \cdot K^{-1}$ or $J \cdot kg^{-1} \cdot K^{-1}$] |
| $C_{\mu ch}$ | Empirical constant for Equation 3.40 |
| $d$ | Width, [m] |
| $D$ | Diameter, [m] |
| $d_h$ | Hydraulic diameter, [m] |
| $e$ | Electronic charge, [C] |
| $E_{Nu}$ | Nusselt number enhancement factor |
| $f$ | Fugacity, [Pa] |
| $F$ | Degrees of freedom |
| $\tilde{g}$ | Specific Gibbs energy, [$J \cdot kg^{-1}$ or $J \cdot mol^{-1}$] |
| $\overline{g}$ | Specific partial Gibbs energy, [$J \cdot kg^{-1}$ or $J \cdot mol^{-1}$] |
| $\vec{g}$ | Gravitacional acceleration vector, [$m \cdot s^{-2}$] |
| Gz | Graetz number |
| $h$ | Convective heat transfer coefficient, [$W \cdot m^{-2} \cdot K^{-1}$] |
| $\tilde{h}$ | Specific enthalpy, [$J \cdot kg^{-1}$ or $J \cdot mol^{-1}$] |

| | |
|---|---|
| $\overline{h}$ | Specific partial enthalpy, [J·kg$^{-1}$ or J·mol$^{-1}$] |
| $\hat{h}$ | Specific heat transfer capacity, [W·m$^{-3}$·K$^{-1}$] |
| $H$ | Equilibrium constant |
| $I$ | Ionic strength |
| $IP$ | Ionic product, [M$^2$] |
| $K$ | NETmix equivalent loss coefficient for pressure drop (for Equation 2.11) |
| $k_{a_1}$ | First acid dissociation constant, [M] |
| $k_{a_2}$ | Second acid dissociation constant, [M] |
| $K_{i,k}$ | Ratio between the fugacity coefficients for component $i$ between phase $k$ and the reference phase |
| $K_H$ | Henry's constant, [Pa·m$^3$·mol$^{-1}$] |
| $K_H^*$ | Modified Henry's constant, [Pa] |
| $k_L a$ | Volumetric mass transfer coefficient, [s$^{-1}$] |
| $k_{sp}$ | Solubility constant, [M$^2$] |
| $k_w$ | Water auto dissociation constant, [M$^2$] |
| $L$ | Length, [m] |
| $\text{Loss}_i$ | Loss of component $i$, [%] |
| $m$ | Mass, [kg] |
| $\dot{m}$ | Mass flow rate, [kg·s$^{-1}$] |
| $\tilde{m}$ | Molality, [mol·kg$^{-1}$] |
| $M_w$ | Molecular weight, [kg·mol$^{-1}$] |
| $n$ | Number of moles, [mol] |
| $\vec{n}$ | Normal vector pointing outwards the control surface |
| $n_{cc}$ | Number of cooling channels |
| $n_h$ | Hydration number, [mol·mol$^{-1}$] or [kg·kg$^{-1}$] |
| $n_{np}$ | Number of network plates |
| $n_s$ | Number of stages |
| $n_x$ | Number of rows |

| | |
|---|---|
| $n_y$ | Number of columns |
| $N_{\mathrm{A}}$ | Avogadro's number, [$\mathrm{mol^{-1}}$] |
| $N_{\mathrm{hours/year}}$ | Number of hours per year [$\mathrm{h \cdot yr^{-1}}$] |
| $N_{\mathrm{years}}$ | Economical lifespan, [yr] |
| Nu | Nusselt number |
| $p$ | Pressure, [bar] |
| $p_0$ | Pressure at stage number 0, [bar] |
| $\dot{P}_{\mathrm{CO_2}}$ | Productivity of carbon dioxide, [$\mathrm{kg \cdot s^{-1}}$] |
| $p_{\mathrm{vap}}$ | Vapour-pressure, [bar] |
| Pr | Prandtl number |
| $\tilde{q}$ | Specific heat, [$\mathrm{J \cdot kg^{-1}}$ or $\mathrm{J \cdot mol^{-1}}$] |
| $\dot{q}$ | Heat flux, [W] |
| $\hat{q}$ | Specific heat flux, [$\mathrm{W \cdot m^{-1}}$] |
| $r$ | Interest rate, [%] |
| $R$ | Thermal resistance, [$\mathrm{m^2 \cdot K \cdot W^{-1}}$] |
| $R_{\mathrm{gas}}$ | Gas constant, [$\mathrm{J \cdot K^{-1} \cdot mol^{-1}}$] |
| $R_m$ | Radius of cages of type $m$, [Å] |
| Re | Reynolds number |
| $\overline{\mathrm{Re}}$ | Average Reynolds number |
| $\mathrm{Rec}_i$ | Recovery of component $i$, [%] |
| $s$ | Hydrate lattice dimension or specific entropy, [Å] |
| $S$ | Cross-sectional area, [$\mathrm{m^2}$] |
| $T$ | Temperature, [K] |
| $t_{\mathrm{exper}}$ | Experiment time, [s] |
| $\tilde{u}$ | Specific internal energy, [$\mathrm{J \cdot kg^{-1}}$ or $\mathrm{J \cdot mol^{-1}}$] |
| $U$ | Global heat transfer coefficient, [$\mathrm{W \cdot m^{-2} \cdot K^{-1}}$] |
| $V$ | Volume, [$\mathrm{m^3}$] |
| $\tilde{w}$ | Specific work, [$\mathrm{J \cdot kg^{-1}}$ or $\mathrm{J \cdot mol^{-1}}$] |
| $W$ | Width, [m] |

| | |
|---|---|
| $w_i$ | Fraction of component $i$ in hydrate phase |
| $x$ | Distance from the inlet in the flow direction, [m] |
| $x^*$ | Dimensionless thermal entrance length |
| $x_i$ | Fraction of component $i$ in liquid/aqueous phase |
| $X_{\text{hyd}}$ | Hydrates content in the liquid phase (neglecting vapour) |
| $y_i$ | Fraction of component $i$ in vapour phase |
| $Z$ | Compressibility Factor |
| $z_i$ | Global fraction of component $i$ in the system |
| $z_j$ | Charge of ion $j$ |

*Greek Letters*

| | |
|---|---|
| $\alpha_k$ | Fraction of phase $k$ |
| $\gamma$ | Activity coefficient |
| $\delta$ | Thickness, [m] |
| $\Delta\overline{\nu}$ | Specific partial molar volume change, [$m^3 \cdot kg^{-1}$ or $m^3 \cdot mol^{-1}$] |
| $\Delta\tilde{h}$ | Specific enthalpy change, [$J \cdot kg^{-1}$ or $J \cdot mol^{-1}$] |
| $\Delta H$ | Enthalpy change, [$J \cdot kg^{-1}$ or $J \cdot mol^{-1}$] |
| $\Delta H^{\infty}_{CO_2 \rightarrow H_2O}$ | Enthalpy change due to carbon dioxide dissolution in water at infinite dilution, [$J \cdot kg^{-1}$ or $J \cdot mol^{-1}$] |
| $\Delta p$ | Pressure change (pressure drop or pressure increase), [bar] |
| $\Delta T$ | Temperature difference, [K] |
| $\Delta x$ | Fluid element size, [m] |
| $\varepsilon_1, \varepsilon_2$ | Error for system 1 or 2 |
| $\varepsilon_0$ | Vacuum permittivity, [$C^2 \cdot N^{-1} \cdot m^{-2}$] |
| $\varepsilon_{\text{elec}}$ | Dielectric constant |
| $\varepsilon_{\text{p}}$ | Potential well depth, [J] |
| $\theta$ | Stability variable |
| $\theta_{i,m}$ | Fractional occupancy of guest $i$ in type $m$ cages |
| $\kappa$ | Thermal conductivity, [$W \cdot m^{-1} \cdot K^{-1}$] |

| | |
|---|---|
| $\overline{\kappa}$ | Average thermal conductivity, [W·m$^{-1}$·K$^{-1}$] |
| $\lambda$ | Wavelength, [Å] |
| $\mu$ | Viscosity, [Pa·s] |
| $\hat{\mu}_{i,k}$ | Chemical potential of component $i$ in the phase $k$, [J·mol$^{-1}$] |
| $\tilde{\nu}$ | Specific molar volume, [m$^3$·kg$^{-1}$ or m$^3$·mol$^{-1}$] |
| $\overline{\nu}$ | Specific partial molar volume, [m$^3$·kg$^{-1}$ or m$^3$·mol$^{-1}$] |
| $\xi$ | Flow-related constant in Equation 3.8 |
| $\xi^*$ | Modified flow-related constant in Equation 3.9 |
| $\rho$ | Density, [kg·m$^{-3}$] |
| $\varsigma_k$ | Separation efficiency of phase $k$, [%] |
| $\sigma$ | Soft core radius, [Å] |
| $\tau$ | Residence time, [s] |
| $\upsilon$ | Velocity, [m·s$^{-1}$] |
| $\overline{\upsilon}$ | Average velocity, [m·s$^{-1}$] |
| $\vec{\upsilon}$ | Velocity field, [m·s$^{-1}$] |
| $\varphi$ | Number of phases |
| $\phi$ | Fugacity coefficient |
| $\phi_{\text{slurry}}$ | Hydrate slurry concentration after separation, [wt.%] |
| $\chi$ | Potential function, [J] |
| $\omega$ | Depth, [m] |
| $\vec{\omega}$ | Vorticity field, [s$^{-1}$] |
| $\omega_{\text{ac}}$ | Acentric factor |
| $\omega_{\text{Born}}$ | Born coefficient, [J·mol$^{-1}$] |

*Indices*

| | |
|---|---|
| $\beta$ | Hypothetical empty hydrate lattice |
| * | Hypothetical 1 molal solution |
| anion | Anion |
| aq | Aqueous |
| BL | Boundary layer |
| bulk | Bulk |

| | |
|---|---|
| c | Channel |
| $Ca^{2+}$ | Calcium cation |
| $CaCO_3$ | Calcium carbonate |
| $Ca(OH)_2$ | Calcium hydroxide |
| cation | Cation |
| cc | Cooling channel |
| cf | Cooling fluid |
| ch | Chamber |
| chic | Chicane |
| cp | Cooling plates |
| cs | Cooling spacers |
| $CO_2$ | Carbon dioxide |
| $CO_3$ or $CO_3^{2-}$ | Carbonate anion |
| cond | Conduction |
| conv | Convection |
| crit | Critical |
| DH | Debye-Hückel |
| diss | Dissociation |
| enh | Enhanced |
| eq | Equilibrium |
| exp | Expected |
| EtOH | Ethanol |
| f | Formation |
| fin | Final |
| flask | Flask |
| fus | Fusion |
| $H^+$ | Hydron cation or proton |
| $HCO_3^-$ | Bicarbonate anion |
| $H_2CO_3$ | Carbonic acid |
| $H_2O$ | Water |

| | |
|---|---|
| $H_3O^+$ | Hydronium cation |
| hyd | Hydrate phase |
| ig | Ideal gas |
| in | Inlet |
| in-out | From inlet to outlet |
| ini | Initial |
| int | Integration |
| lm | Logarithmic mean |
| loc | Local |
| LR | Long range |
| max | Maximum |
| mix | Mixture |
| mol | Molar |
| n | Network |
| $N_2$ | Nitrogen |
| nom | Nominal |
| np | Network plates |
| o | Standard conditions<br>Initial estimate (Chapter 7) |
| $OH^-$ | Hydroxide anion |
| out | Outlet |
| PP | Parallel plates |
| $r$ | Reference phase |
| red | Reduced |
| salt | Salt |
| sol | Solution |
| solids | Solids |
| SR | Short range |
| steel | Steel |
| step | Time-step |
| $t$ | Time |
| tot | Total |

| | |
|---|---|
| transf | Of transfer |
| tube | Tube |
| uc | Unit cell |
| vap | Vapour |
| w | Weight |
| wall | Wall |
| $\mu$ch | Microchannel |

*Acronyms and Abbreviations*

| | |
|---|---|
| AACE | Association for the Advancement of Cost Engineering |
| ACCE | Aspen Capital Cost Estimator |
| AdP | Águas do Porto |
| AISI | American Iron and Steel Institute |
| ASME | The American Society of Mechanical Engineers |
| ATR | Auto Thermal Reforming |
| BGS | British Geological Survey |
| BPR | Back Pressure Regulator |
| CAPEX | Capital Expenditure |
| CCS | Carbon Capture and Storage |
| CFC | Chlorofluorocarbons |
| CFD | Computational Fluid Dynamics |
| COP | Coefficient of Performance |
| CSMGem | Colorado School of Mines – Gibbs Energy Minimization |
| DDB | Dortmund Data Bank |
| DSC | Differential Scanning Calorimetry |
| DTAC | Dodecyl-Trimethyl-Ammonium Chloride |
| EBTP | European Biofuels Technology Platform |
| EIA | US Energy Information Administration |
| EOR | Enhanced Oil Recovery |
| EoS | Equation of State |
| EPA | Environmental Protection Agency |
| EPRI | Electric Power Research Institute |

| | |
|---|---|
| EU | European Union |
| FPSO | Floating Production Storage and Offloading |
| GHG | Greenhouse Gas |
| HBCC | Hydrate-Based Carbon Capture |
| HCFC | Hydrochlorofluorocarbons |
| HEV | High Efficiency Vortex |
| HFC | Hydrofluorocarbons |
| HDPE | High Density Polyethylene |
| HPLC | High-Performance Liquid Chromatography |
| HRSG | Heat Recovery Steam Generator |
| HWIPE | Heriot-Watt Institute of Petroleum Engineering |
| ID | Inner Diameter |
| IEA | International Energy Agency |
| IEAGHG | International Energy Agency – Greenhouse Gases |
| IGCC | Integrated Gasification Combined Cycle |
| IN | Institute of Nanoscience and Nanotechnology |
| INEGI | Instituto de Ciência e Inovação em Engenharia Mecânica e Engenharia Industrial |
| IPCC | Intergovernmental Panel on Climate Change |
| IR | Infrared |
| ISG | Interfacial Surface Generator |
| ITM | Ion Transport Membranes |
| KEPCO | Kansai Electric Power Co. |
| LSRE-LCM | Laboratory of Separation and Reaction Engineering - Laboratory of Catalysis and Materials |
| LT | Level Transducer |
| MEA | Mono-Ethanolamine |
| MFC | Mass Flow Controller |
| MFM | Mass Flow Meter |
| MHI | Mitsubishi Heavy Industries |
| MOF | Metal-Organic Framework |
| MUSCL | Monotonic Upstream-Centered Scheme for Conservation Laws |
| NG | Natural Gas |

| | |
|---|---|
| NGCC | Natural-Gas-Fired Combined Cycle |
| NETL | US National Energy Technology Laboratory |
| NIST | US National Institute of Standards and Technology |
| NUB | NETmix Unit Block |
| OD | Outer Diameter |
| OECD | Organization of Economic Cooperation and Development |
| OPEX | Operational Expenditure |
| PFC | Perfluorocarbons |
| PFD | Process Flow Diagram |
| PI | Pressure Indicator |
| POX | Partial Oxidation |
| ppm | Parts Per Million |
| PT | Pressure Transducer |
| PSA | Pressure Swing Adsorber/Adsorption |
| PVCap | Poly-N-Vinylcaprolactam |
| PVP | Poly-N-Vinylpyrrolidone |
| RAM | Random Access Memory |
| RTD | Resistance Temperature Detector |
| SDS | Sodium Dodecyl Sulfate |
| SEM | Scanning Electron Microscopy |
| SIMPLEC | Semi-Implicit Method for Pressure-Linked Equations Consistent |
| SLM | Salt Lake Metals |
| SRK | Soave-Redlich-Kwong |
| Stabil | Stabilization |
| STP | Standard Temperature and Pressure |
| TBAB | Tetra N-Butylammonium Bromide |
| TEG | Triethylene Glycol |
| THF | Tetrahydrofuran |
| TSA | Temperature Swing Adsorber/Adsorption |
| TT | Temperature Transducer |
| UN | United Nations Organization |
| UNFCCC | United Nations Framework Convention on Climate Changes |

| | |
|---|---|
| UPS | United Pipeline Systems |
| USA | United States of America |
| UV | Ultra-Violet |
| VOF | Volume of Fluid |
| VR | Vibration Reduction |
| WGSR | Water-Gas Shift Reaction |
| XRD | X-Ray Diffraction |
| ZEP | Zero Emissions Platform |

# 1 Introduction

Energy has been identified as an indispensable driving-force for most economic activities around the world, and as a consequence of the continuous growth in the world population, an increase in the energy consumption worldwide has been observed. However, the world population growth rate has been decreasing in the last few years, but the global energy consumption does not seem to follow the same trend. This indicates that other factors than world population increasing is responsible for the observed increase in the world energy consumption and the continuously increasing forecasts from different sources. Factors such as the urbanisation process as well as growing industrialization worldwide are seen as responsible for the latest increase in world energy consumption (Kofi Adom et al. 2012).

After the increase in more than 400% of the world population over the 20$^{th}$ century, the annual growth rate has decreased considerably (Ortiz-Ospina and Roser 2016). It is expected that a population growth of 50% is reached in the 21$^{st}$ century, resulting in a world population of about 11 billion by 2100, as opposed to the 7.5 billion observed in 2016 (worldometers.info 2016). The evolution of the growth rate in the 20$^{th}$ century and forecasts until 2100 is shown in Figure 1.1.

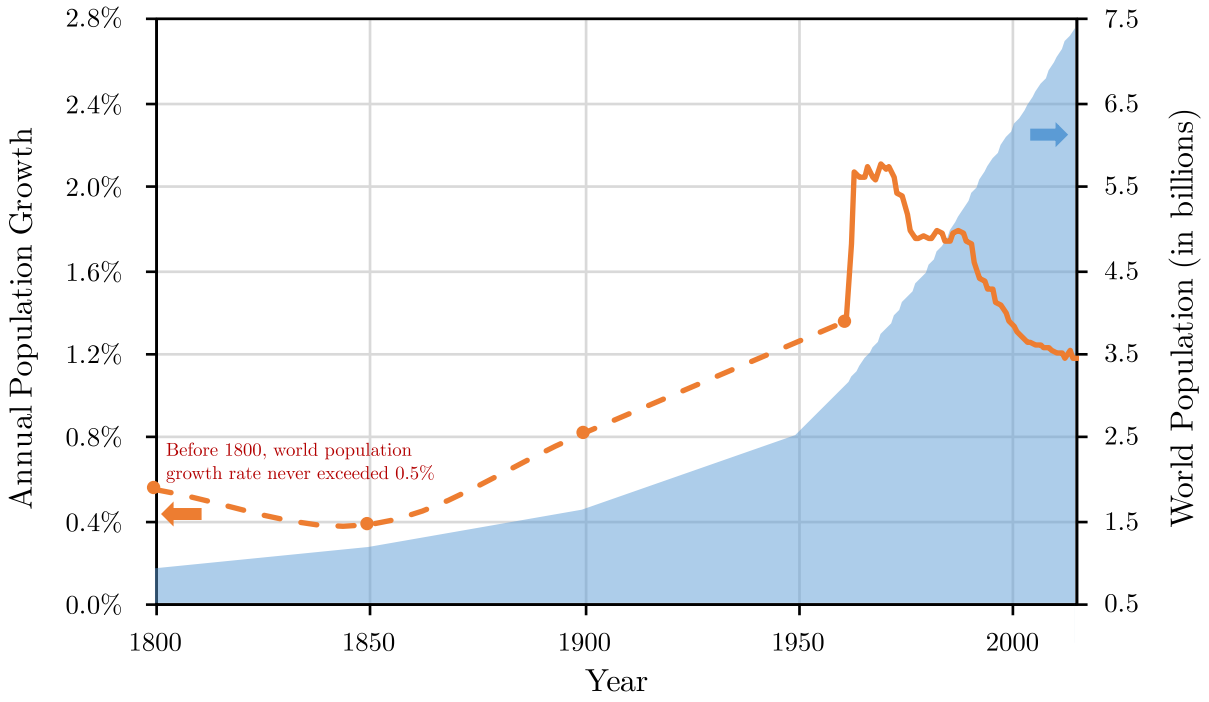



Figure 1.1 – World population and growth rate evolution. Shadowed area represents the world population. Data prior to 1960 from UN (2014) and data after 1960 from WorldBank (2016).

It is accepted worldwide that climate changes are occurring, and many associate these changes to the human use of fossil fuels. Emissions of carbon dioxide $\left(CO_2\right)$, one of the most important greenhouse gases, are a serious problem in present electricity, oil refinery and steel industries.

As a consequence of the increase in energy consumption, the emission of pollutant gases to the atmosphere also increases. Greenhouse gases (GHGs) are of particular interest, since their emissions highly contribute for the enhancement of the greenhouse effect. The greenhouse effect is the process by which radiation from the atmosphere warms the planet's surface, to a higher temperature as if no atmosphere was present. Greenhouse gases, usually emitted in several industrial processes, in particular, in power generation industries, are radiatively active gases that absorb radiation and radiate it in all directions, including in the surface direction. The increase of these gases in the atmosphere means that more radiation is absorbed and radiated to the surface. As a consequence, an increase of the planet's temperature is being observed. This phenomenon is called global warming. The main gaseous components that contribute for the greenhouse effect are: water vapour (contributing

36-70%); carbon dioxide (produced as a result of fuel combustion, with a contribution of 9-26%); methane (the major component of natural gas, contributing 4-9%); and ozone (that contributes 3-7%) (Kiehl and Trenberth 1997, RealClimate 2005). Carbon dioxide is the most relevant greenhouse gas in the atmosphere, although many others exist. Water vapour is the major contributor for the greenhouse effect, but it is not usually considered a relevant greenhouse gas, due to its different contribution, when compared to carbon dioxide (RealClimate 2005). GHGs can have two types of contributions: a forcing contribution or a feedback contribution. Forcing contribution has to do with the direct contribution from the gas, regarding the amount of energy received from the sun and the amount that is sent back to space. Forcing contributors, such as carbon dioxide, or methane, are the major contributors for climate change, and originate from outside the climate system itself. On the other hand, feedback contributions are an indirect or a secondary change, which occurs as a response or a consequence of a forcing contribution. Water vapour fits in this last group. As an example, if a forcing contribution leads to a global temperature increase, more water could evaporate from the oceans, increasing its concentration in the atmosphere. This leads to a higher absorbance capacity from the atmosphere, thus enhancing the original forcing contribution. On the other hand, more water vapour results in more clouds, which increase the amount of radiation that is reflected back to space, balancing the first effect. This capacity to balance its positive and negative effects as a result of a feedback response to a change is what makes water non-relevant for the global greenhouse effect.

The growth of carbon dioxide concentration in the air that has been happening since the industrial era is worrisome. Since this gas is the major contributor for greenhouse effect from forcing contributions, anthropogenic carbon dioxide emissions results in an increase of the greenhouse effect and in an increase of global temperature. Therefore, the resolution of carbon dioxide emissions problem has gained an increasing interest from the scientific community, highly focused and motivated to find a sustainable solution.

## 1.1 Motivation and Relevance

One of the most interesting strategies to solve this environmental problem caused by the carbon dioxide emissions resultant from direct human action, is by capturing the carbon dioxide from the emission site, transporting it to a storage site and depositing it far enough from the atmosphere, to avoid contamination. This is the definition of Carbon Capture & Storage (CCS) that aims to prevent the release of large quantities of carbon dioxide into the atmosphere.

Three main types of technologies are used nowadays by $CO_2$ emitting industries:

- Pre-combustion capture;
- Post-combustion capture;
- Oxyfuel combustion capture.

Within the main three technology groups, several chemical and physical processes are employed, such as absorption, adsorption, membrane separations and others. Pre-combustion capture consists in the separation and capture of carbon dioxide from syngas, a mixture of hydrogen and carbon dioxide, resultant from steam reforming processes. It is called pre-combustion capture since it occurs prior to the fuel combustion (in this case, hydrogen) (Metz et al. 2005). Post-combustion capture consists in the capture of carbon dioxide from flue gas (a mixture of nitrogen and carbon dioxide) produced after the combustion of hydrocarbons for power generation (Metz et al. 2005). Amines scrubbing is the most widely process as a post-combustion system, at a competitive cost that has been decreasing over the years (Rochelle 2009). Oxyfuel combustion consists in the purification of oxygen from air, to use as the oxidizing agent in the combustion process. The use of pure oxygen instead of air results in a flue gas rich in carbon dioxide, instead of a flue gas rich in nitrogen. This leads to a easier carbon dioxide capture (Metz et al. 2005).

Current CCS processes are costly, contributing by 70-90% of the total operating cost. This means that cheaper and more efficient alternative solutions are necessary, in

order to reduce operational costs. Several alternative solutions have been proposed over the years. One particular solution, the use of gas hydrates for carbon dioxide capture, has gained special attention in the last few years.

### 1.1.1 Gas Hydrates

Hydrate-based $CO_2$ capture (HBCC) technology is a novel process that has gained large interest by the scientific community. It consists on the precipitation of $CO_2$ hydrates, concentrating large amounts of gas in solid crystals (Kang and Lee 2000). The process requires mild pressures and temperatures, through a unique separation mechanism that is easy to regenerate and capable of separating gas mixtures, which might not be achievable via conventional technologies

Gas hydrates, or clathrates, consist of two (or more) dissimilar molecules (a gas guest molecule and water) mechanically intermingled but not truly chemically bonded, instead one molecule forms a framework (water) that traps the other molecule (gas guest) (Figure 1.2). Gas hydrates can be considered modified ice structures enclosing hydrocarbons and other gases, but they can melt at temperatures well above normal ice (Sloan and Koh 2007).

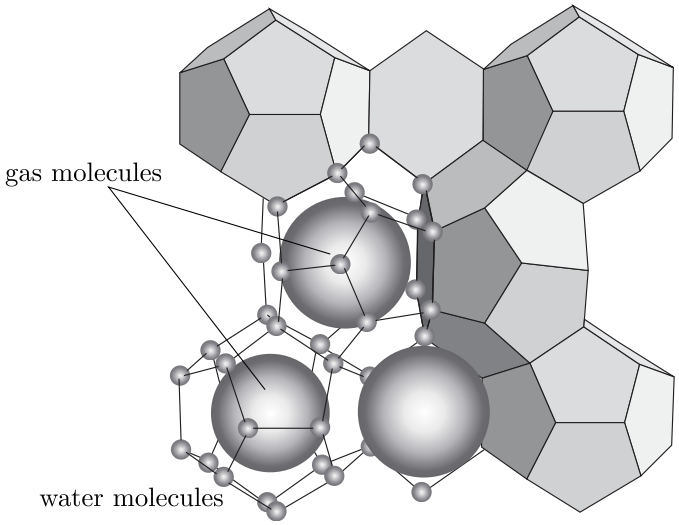



Figure 1.2 – Typical gas hydrate structure with water molecules forming a cage trapping gas molecules (Maslin et al. 2010).

Gas hydrates are formed under favorable thermodynamic conditions of low temperature and high pressure, exhibiting various structures that depend on the size and chemical properties of the guest molecules (Sloan and Koh 2007).

Carbon dioxide capture using gas hydrates is based on the different thermodynamic affinities for different gases in a mixture to precipitate in the form of hydrates. Carbon dioxide forms hydrates at lower pressure in comparison with other components in flue gas, nitrogen in particular. Separating carbon dioxide from flue gas can be achieved by first forming a solid hydrate phase that is enriched with $CO_2$. Dissociating the hydrates (transformation from solid to gas and water), after separating the hydrate phase from the gaseous phase, leads to the recovery of $CO_2$ that is much higher in concentration than the initial feed (can be four times higher). The process sequence starts with the gas mixture being sent to a hydrate formation unit, in which $CO_2$ hydrates form. The hydrate slurry is then separated from the $CO_2$-lean gas in a separator and sent to a hydrates dissociation reactor, from which purified $CO_2$ is collected, and the $CO_2$-rich gas is recycled for further processing.

The main problem of hydrates production resides on its slow kinetics, due to the large amount of heat that the process releases, and that needs to be removed in order to avoid precipitation hindering. Thus the need of equipment capable to effectively dissolve the gas into the aqueous phase, while at the same time removing all crystallization heat at large rates. Furthermore, in order to increase the process efficiency and reduce the costs, a continuous process should be used rather than a batch process. In order to achieve these goals, a hydrate-based capture process using the NETmix technology is here proposed.

### 1.1.2 NETmix Technology

The NETmix technology, developed at and patented by Universidade do Porto (Lopes et al. 2005), has been applied for the precipitation of nanoparticles of several

materials (Silva et al. 2008, Gomes et al. 2009, Leblebici et al. 2013), due to its unique mixing properties.

NETmix is a novel micro-meso structured reactor and mixer consisting of a network of static mixing chambers interconnected by transport channels. Networks are generated by the repetition of unit cells, where each unit cell consists of one chamber and two inlet and two outlet half-channels (Laranjeira 2005).

Mixing in the NETmix reactor can only be achieved above a critical channel's Reynolds number, where the flow inside the mixing chambers evolves to a self-sustained oscillatory laminar flow regime inducing strong local laminar mixing (Laranjeira et al. 2009). This occurs due to the geometric characteristics of the NETmix network and the local hydrodynamic instabilities induced by the immerging jets interactions at the chambers and therefore, no mechanical mixing equipment is present.

NETmix allows the careful distribution of reactants and flow rate control at the inlet, according to the reaction stoichiometry, and product extraction with different properties at different outlets. The network can be easily scaled-up or numbered-up depending on the process and production objectives.

NETmix has already proven being capable to handle multiphase and fast reactions (Silva et al. 2008, Fonte 2013), having unique capabilities to transport both mass and heat to and from the system (Gomes 2011, Fonte 2013), very useful characteristics for the production of gas hydrates, where mass and transport are the limiting steps.

## 1.2 Thesis Objectives and Layout

The main objective of this work is to evaluate the capacity of NETmix and also the development of a process for the continuous production of gas hydrate slurry, for $CO_2$ capture and storage. For this purpose, both simulation and experimental work has been performed. The NETmix intrinsic mixing capacities have been evaluated regarding heat transfer, following the work developed by Fonte (2013). Heat and

mass transfer in the hydration reactor has a crucial importance, since it is known that the process kinetics are usually limited due to deficient heat and mass transfer.

The NETmix capacities will be assessed for the production of $CO_2$ and mixtures of $N_2/CO_2$ hydrates, in the presence or not of thermodynamic promoters. This system is particularly difficult since it is a multiphase system comprising gas, liquid and solid phases, as well as rapid interfacial mass and heat transfer.

Finally, industrial processes are proposed and evaluated using simulation software, to assess it viability, both technically and economically.

The present thesis is divided as follows:

- This chapter, **Chapter 1**, is where the motivation and relevance of the present work are described, as well as the main objectives.
- In **Chapter 2** a global overview of the main problems involved is presented. Initially, the problematic of climate changes due to the consumption of energy and thus, emission of greenhouse gases, mainly $CO_2$, is discussed. The state-of-the-art regarding carbon capture and storage technologies is presented, with special focus on pre-combustion, post-combustion and oxyfuel combustion technologies. As a potential CCS solution, precipitation of gas hydrates is proposed. The characteristics, properties and mechanisms of production are also briefly described in **Chapter 2**, as well as the state-of-the-art regarding gas hydrates production technologies or processes. Finally, a description of the importance of static mixers, more specifically regarding the NETmix technology, is presented.
- In **Chapter 3**, the evaluation of the NETmix's heat transfer capacity is performed. The heat transfer coefficients for the NETmix are determined using CFD and presented in this chapter. The main objective is to use the knowledge obtained from simulations in order to more accurately design a

NETmix device, capable of handling multiphase reactions, such as gas hydrates precipitation, while simultaneously removing heat.

- The design and description of the experimental apparatus, built specifically for the continuous production and post-treatment of gas hydrates, is described in **Chapter 4**. The process flow diagram, which is based on a microNETmix unit as the core piece of equipment, is presented and thoroughly described. Finally, an evaluation of the heat transfer capacity of the device is presented.
- **Chapter 5** focuses on the continuous production of $CO_2$ hydrates in aqueous slurry. The objectives of the experiments were to determine whether gas hydrates were produced, and quantify the amount of carbon dioxide enclatherated in the solids. Parametric studies were performed, evaluating the influence of temperature, pressure, flow rates and the presence or not of THF, a thermodynamic promoter widely used for hydrates precipitation.
- An industrial process for $CO_2$ hydrates production is designed and presented in **Chapter 6**, together with its economical viability for $CO_2$ transport, which is determined using process engineering simulation software.
- The separation of flue gas (a mixture of $N_2/CO_2$) using a hydrate-based process is discussed in **Chapter 7**. In this chapter, a potential process concept based on counter-current equilibrium stages with the formation of mixed gas hydrates is proposed and simulated. The performance of the process regarding the separation efficiency is evaluated.
- **Chapter 8** presents the main conclusions of the present work, as well as suggestions for future work for a deeper understanding on this topic.

## 1.3 References

Fonte, C.M. **2013**. "The NETmix Reactor: Application to High Added-Value Products" [*Ph.D Thesis*]. Porto, Portugal: Departamento de Engenharia Química, Universidade do Porto.

Gomes, P.J. **2011**. "The NETmix® Reactor - Strategies for Optimizing Mixing and Development of New Reactor Designs" [*Ph.D Thesis*]. Porto, Portugal: Departamento de Engenharia Química, Universidade do Porto.

Gomes, P.J., Silva, V.M., Quadros, P.A., Dias, M.M., Lopes, J.C., **2009**. "A Highly Reproducible Continuous Process for Hydroxyapatite Nanoparticles Synthesis". *Journal of Nanoscience and Nanotechnology* 9, 3387-3395.

Kang, S.-P., Lee, H., **2000**. "Recovery of $CO_2$ from Flue Gas Using Gas Hydrate: Thermodynamic Verification through Phase Equilibrium Measurements". *Environmental Science & Technology* 34, 4397-4400.

Kiehl, J.T., Trenberth, K.E., **1997**. "Earth's Annual Global Mean Energy Budget". *Bulletin of the American Meteorological Society* 78, 197-208.

Kofi Adom, P., Bekoe, W., Amuakwa-Mensah, F., Mensah, J.T., Botchway, E., **2012**. "Carbon Dioxide Emissions, Economic Growth, Industrial Structure, and Technical Efficiency: Empirical Evidence from Ghana, Senegal, and Morocco on the Causal Dynamics". *Energy* 47, 314-325.

Laranjeira, P.E. **2005**. "NETmix Static Mixer - Modelling, CFD Simulation and Experimental Characterisation" [*Ph.D Thesis*]. Porto, Portugal: Departamento de Engenharia Química, Universidade do Porto.

Laranjeira, P.E., Martins, A.A., Lopes, J.C.B., Dias, M.M., **2009**. "NETmix®, a New Type of Static Mixer: Modeling, Simulation, Macromixing, and Micromixing Characterization". *AIChE Journal* 55, 2226-2243.

Leblebici, M.E., Fonte, C.M., Costa, M.F., Ataíde, F., Garcia, M.P., Silva, V.M., Devic, T., Horcajada, P., Tavares, P., Araújo, J.P., Oliveira, R., Dias, M.M., Lopes, J.C., **2013**. "Continuous Production of Magnetic and Metal-Organic Nanoparticles With NETmix Reactor". Paper presented at: 2013 AIChE Annual Meeting; San Francisco, CA, USA.

Lopes, J.C., Laranjeira, P.E., Dias, M.M., Martins, A.A., Assigned to Faculdade de Engenharia da Universidade do Porto, **2005**. "Network Mixer and Related Mixing Process". Patent No. PCT/IB2005/000647.

Maslin, M., Owen, M., Betts, R., Day, S., Dunkley Jones, T., Ridgwell, A., **2010**. "Gas Hydrates: Past and Future Geohazard?". *Philosophical Transactions A, Mathematical, Physical, and Engineering Sciences* 368, 2369-2393.

Metz, B., Davidson, O., De Coninck, H., Loos, M., Meyer, L., Intergovernmental Panel on Climate Change, **2005**. "IPCC Special Report on Carbon Dioxide Capture and Storage.". New York, NY, USA.

Ortiz-Ospina, E., Roser, M., **2016**. "World Population Growth". *Published online at Our World In Data*. Retrieved from: https://ourworldindata.org/world-population-growth/ [Online Resource]

RealClimate, "Water Vapour: Feedback or Forcing?". *Published online at RealClimate.org*. Available at: http://www.realclimate.org/index.php?p=142.

Rochelle, G.T., **2009**. "Amine Scrubbing for $CO_2$ Capture". *Science* 325, 1652-1654.

Silva, V.M., Quadros, P.A., Laranjeira, P.E., Dias, M.M., Lopes, J.C., **2008**. "A Novel Continuous Industrial Process for Producing Hydroxyapatite Nanoparticles". *Journal of Dispersion Science and Technology* 29, 542-547.

Sloan, E.D., Koh, C., **2007**. "Clathrate Hydrates of Natural Gases", 3rd ed. CRC Press, Boca Raton, FL, USA.

UN, United Nations, Department of Economic and Social Affairs, Population Division, **2014**. "World Population Prospects: The 2012 Revision, Methodology of the United Nations Population Estimates and Projections". New York, NY, USA, Doc. No ESA/P/WP.235.

WorldBank, "Population Growth (Annual %)". *Published online at data.worldbank.org.* Available at: http://data.worldbank.org/indicator/SP.POP.GROW?end=2015&start=1960&view=chart.

worldometers.info, "Current World Population". *Published online at worldometers.info.* Available at: http://www.worldometers.info/world-population/.

# 2 State of the Art

## 2.1 Climate Changes

It is worldwide accepted that climate changes are occurring, and many associate these changes to the human use of fossil fuels. The increase of the emissions of pollutants due to the use of fossil fuels is usually associated to the increase of the world's energy consumption, which in turn is intimately related to the increase of the world's population (see Figure 1.1).

The world population growth rate has been increasing since 1850, with its peak in 1962, when it reached a growth rate of 2.1%. Since then, the growth rate has been decreasing and is expected to decrease even further until 2100, to a value of about 0.06% (Ortiz-Ospina and Roser 2016). Furthermore, this growth in world's population, as well as the potential continuous industrialization and development of some regions, such as Africa or Asia, pushes the energy consumption to even higher levels than the ones observed nowadays. A recently released study (EIA 2016) projects that the world energy consumption should grow by 48% between 2012 and

2040, adding that most of this growth will come from countries that are not in the Organization of Economic Cooperation and Development (OECD), including China and India, where demand is driven by strong economic growth and where the population growth rate is higher.

The expected growth in both industrialization and energy demand/consumption has significantly worsen the ecological environment, being particularly relevant in the case of fossil fuels and other non-renewable energy sources, thereby increasing the rate of global warming (Kofi Adom et al. 2012, EIA 2016). As a consequence of the continuous increase of the energy consumption over the years, global warming rate caused by the emission of greenhouse gases (GHGs) resulting from the refining and burning of fossil fuels, seems to be increasing as well. Gases such as carbon dioxide $\left(CO_2\right)$, methane $\left(CH_4\right)$, nitrous oxide $\left(N_2O\right)$, and fluorinated compounds (CFCs, HFCs, HCFCs, PFCs, and others) are the main substances that contribute for the increase of the earth global temperature by absorbing significant amounts of radiative energy.

Carbon dioxide is, by far, the most relevant greenhouse gas emitted in 2014 to the atmosphere in United States, according to EPA (2016). About 37% of emitted carbon dioxide in the United States is produced from combustion of different sources of fossil fuels to produce electricity to power homes, business and industries. Coal, oil and natural gas are the main fossil fuels used in power generation. A special attention is given to coal-fired power plants, since these plants generate a significant amount of electricity, and produce the highest rate of $CO_2$ waste per kilowatt hour of produced energy (see Table 2.1, from Narula et al. (2002)). It is estimated that coal combustion for power generation will be responsible for about 41% of the world's $CO_2$ emissions by 2025 (Parker et al. 2008). The second most important sector for carbon dioxide emissions is also related with combustion of fossil fuels such as gasoline or diesel, for people or goods transportation, accounting for about 31% of total $CO_2$ emissions. Non-energy related industries are responsible for about 15% of

total emissions. These emissions are associated to industries in which chemical reactions, other than combustion, may or may not be involved, such as mining and steel industries, cement or chemical industries. Combustion for buildings heating and/or cooking represents about 10% of total carbon dioxide emissions.

Table 2.1 – $CO_2$ emissions from different technologies (Narula et al. 2002).

| TECHNOLOGY | $CO_2$ EMISSIONS $\left(kg \cdot MWh^{-1}\right)$ |
|---|---|
| Pulverised Coal (subcritical) | 850 |
| Pulverised Coal (supercritical) | 800 |
| IGCC | 670 |
| NGCC | 370 |
| Nuclear | 0 |

China is in the lead regarding $CO_2$ emissions, representing about 30% of worldwide emissions, according to 2014 data from Olivier et al. (2015), while U.S. and EU represent about 15% and 10% of total emissions, respectively. Interestingly, this takeover of the lead by China only happened in 2000s. As it can be seen from Figure 2.1, where carbon dioxide emissions during the past 35 years are represented, the emissions of U.S. and EU28 represented about 50% of the global emissions in 1970, keeping the amount of $CO_2$ emitted nearly constant through the years. It is even possible to detect a slight decrease of emissions due to the late efforts to reduce and regulate the emission of greenhouse gases. On the other hand, while developing regions like China and India had a residual weight in the global emissions in 1970, their contribution largely increased in recent years, being the main responsible for the global increase of emitted $CO_2$ in the atmosphere (Olivier et al. 2015). A 126% increase of $CO_2$ emissions from 1970 to 2014 was observed, resultant from direct human interference. However, in the past couple of years, the global $CO_2$ emission rate almost stalled (Olivier et al. 2015).

Solving the greenhouse gas emissions problem is a huge international challenge. Governments, policy makers and businessmen are being pushed to establish policies and rules that allow the mitigation of global warming, which is related with climate

changes. For the past few decades, policies and regulations from different governmental entities have been created, in order to control the observed growth pattern of $CO_2$ emissions. These regulations aim to cover different sectors such as the industrial sectors, by limiting the emissions of carbon dioxide to the atmosphere, as well as the transportation sectors, encouraging manufacturers to developed cleaner technologies for their vehicles. This obviously means that a very strong commitment from these sectors is crucial, and only possible if legal constraints are created and properly supervised by regulatory entities. Kyoto protocol and Paris agreement are examples of worldwide agreements to reduce the emissions of several pollutants to the atmosphere (UNFCCC 2016).

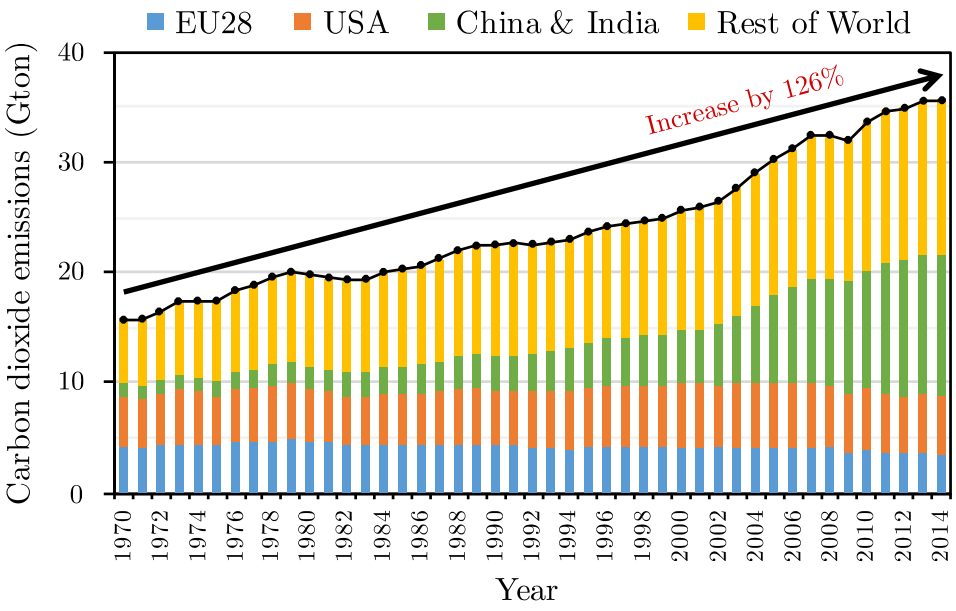



Figure 2.1 – Global $CO_2$ emissions from fossil fuel use and cement industries (Olivier et al. 2015).

Whether the seriousness of this commitment is driven by regulatory sanctions or simply on a peer pressure basis, the urgent need of efficient technologies capable to reduce the footprint of industrial activities is undeniable. In a simplistic overlook, one can say that four possible strategies can be used in order to control and/or reduce the amount of emitted $CO_2$ (and other GHG) to the atmosphere: increase of the energetic efficiency, by creating better insulation for housing, or creating more efficient electrical devices, with particular attention to vehicle's motors; energy conservation, by minimizing the amount of wasted energy (electricity or petroleum);

switching fuels to cleaner sources of energy such as renewable sources (solar, wind or wave energy) or nuclear energy; and carbon capture and storage (CCS), by going to the emission source, capture the $CO_2$ and store it in natural reservoirs, avoiding that this $CO_2$ is emitted to the atmosphere. From these strategies, CCS is the only one with the potential to significantly reduce $CO_2$ emissions from the use of fossil fuels (IEA 2015).

## 2.2 Overview on Carbon Capture & Storage (CCS)

Carbon dioxide capture and storage/sequestration (or CCS) is a set of technologies that can greatly reduce $CO_2$ emissions from coal and/or gas-fired power plants (new or existing) and large industrial sources. As mentioned before, CCS is the most important technology capable to significantly reduce the amount of emitted $CO_2$ to the atmosphere, from the use of fossil fuels, without changing industrial processes neither their efficiency that could arise from the change of the energy source. CCS can reduce the amount of $CO_2$ emissions not only from power generation, but also from industrial sectors, such as iron and steel, refining, petrochemical or cement manufacturing, and is estimated to be able to provide almost 20% of global emission cuts required by 2050 (IEA 2013). On the other hand, IEA (2013) estimates that the costs of achieving global climate objectives without CCS could be 70% higher.

Although it is not very common, CCS can also be applied to the combustion of biomass-based fuels. Some studies even consider that the use of CCS in biotechnology, considering on projected biomass available in Europe, has potential to remove 800 million tonnes of carbon dioxide from the atmosphere every year by 2050, which represents more than 50% of today's EU emissions from the energy sector (EBTP/ZEP 2012). Regardless of the source of burned fuel that originates large amounts of carbon dioxide, CCS has the potential to be used in all of these sectors to reduce $CO_2$ emissions.

The first concept of separating and storing carbon dioxide was first proposed by Marchetti (1977), by proposing a series of steps $CO_2$ capture (Figure 2.2).

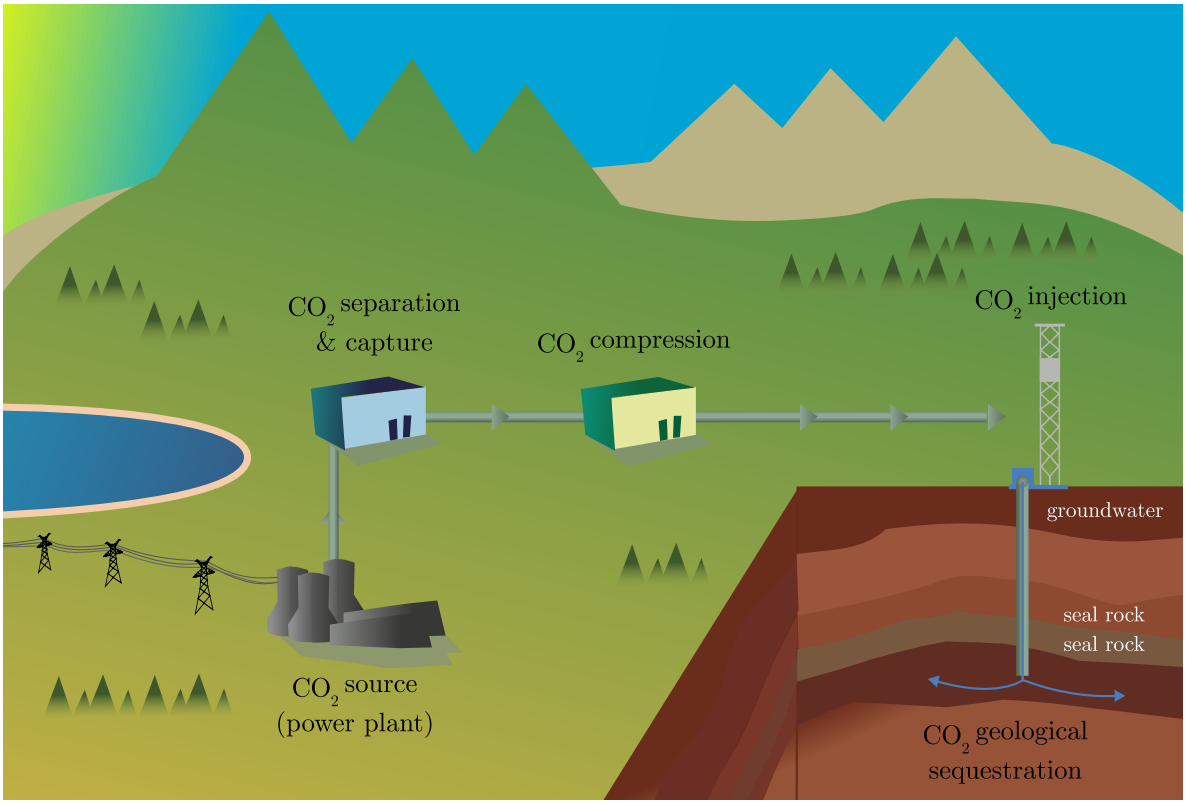



Figure 2.2 – Example of $CO_2$ capture and storage technology from source to storage. Adapted from Smit et al. (2014).

Carbon capture and storage is a three-step process that comprises (Smit et al. 2014):

- Capture of $CO_2$ from power plants or any other industrial processes where large amounts of $CO_2$ are produced. This stage involves separating $CO_2$ from other gases.
- Transport of the captured and compressed $CO_2$, using not only, but mostly pipelines.
- $CO_2$ injection underground and/or geologic sequestration into deep underground rock formations. These formations are usually porous rock layers that hold the carbon dioxide, being trapped by the existence of impermeable non-porous rock layers, preventing it from migrating upward.

### 2.2.1 Carbon Dioxide Capture Technologies

Several types of technologies for $CO_2$ capture are currently available. Some of them are already available commercially, while others are still under development. There are mainly three possible pathways to reduce emissions of $CO_2$ from power plants or other industrial processes: pre-combustion technology, where $CO_2$ and other pollutants are removed through gasification before fuel combustion (Jansen et al. 2015); post-combustion technology, as represented in Figure 2.2, where $CO_2$ is removed after combustion (Herzog et al. 2009); and oxy-fuel combustion technology, where $CO_2$ is separated during combustion, generating a flue gas stream containing mostly carbon dioxide and water vapour (Buhre et al. 2005, Metz et al. 2005, Stanger et al. 2015). All technologies have the potential to capture up to 90% of the $CO_2$ emitted (ZEP 2016). A 100% $CO_2$ capture is technically possible but still economically unviable. The general process for $CO_2$ capture using different technologies is summarized in Figure 2.3. An overview on the different technologies is made on the next sections.

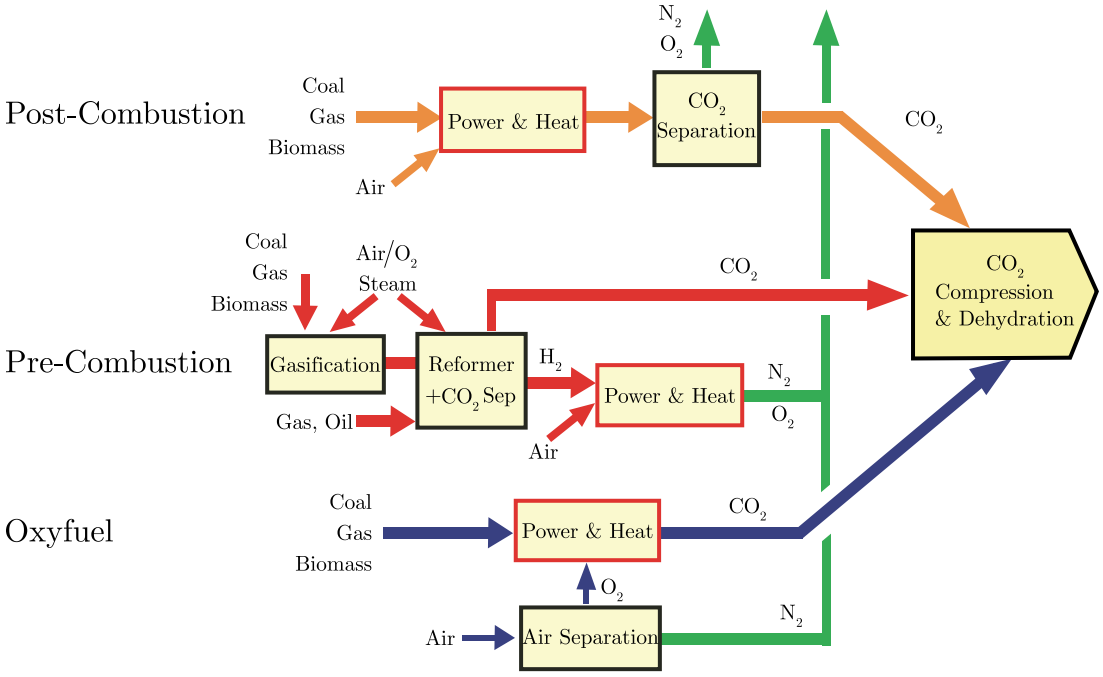



Figure 2.3 – Carbon dioxide capture systems (Holloway et al. 2006).

#### *2.2.1.1 Pre-Combustion Capture*

A pre-combustion capture process usually comprises an initial reaction stage, where a mixture of hydrogen and carbon monoxide (also called syngas) from a primary fuel is produced, via both steam reforming (by adding steam, Equation 2.1) or partial oxidation (by adding oxygen, Equation 2.2) reactions. Typically, a water gas shift reaction (WGSR, Equation 2.3) follows the first reaction, by adding more steam, converting CO to $CO_2$.

$$C_xH_y + xH_2O \rightleftharpoons xCO + \left(x + y/2\right)H_2 \quad (2.1)$$

$$C_xH_y + x/2O_2 \rightleftharpoons xCO + \left(y/2\right)H_2 \quad (2.2)$$

$$CO + H_2O \rightleftharpoons CO_2 + H_2 \quad (2.3)$$

The carbon dioxide resulting from the WGSR is removed from the syngas, by separating it from the $H_2$ and can be stored afterwards.

This pre-combustion technology can be particularly interesting for two potential applications. The first is for the production of pure hydrogen fuel, where $CO_2$ removal is of great importance. Secondly, this approach can also be used to reduce carbon content in fuels, being the removed $CO_2$ (since the largest portion of the removed carbon is in the $CO_2$ form) stored. This is usually done by converting the produced carbon-rich syngas to liquid using a Fischer-Tropsch reaction, converting it to fuels or chemicals with lower carbon content.

Regarding already existing technologies, steam reforming is the dominant technology for hydrogen production. Methane steam reforming, where the burned fuel is natural gas, is of particular interest. The process begins with the removal of sulphur in order to avoid nickel-based catalyst poisoning. Steam is added afterwards, occurring reaction 2.1 over a catalyst at temperatures in the range of 800-900 °C. Reaction 2.1 is endothermic, and therefore heat is supplied to the reactor by burning part of the fuel (called secondary fuel). The resulting gas is cooled down, generating the required steam for the reactions and passed into the CO shift system. After that, CO is

converted in $CO_2$ in accordance with the exothermic reaction 2.3, thus reducing the carbon dioxide concentration in the reformed gas/syngas, down to 0.2-0.3%. Shift reactors typically operate at temperatures of 400-500 °C, using a catalyst (both iron-chromium and copper are amongst the most used, the latter allows the operation at lower temperatures – 350 °C). The shifted gas is cooled and $CO_2$ is separated from $H_2$ using absorption processes with amines or hot potassium (explained in further detail in Section 2.2.1.2).

Newer technologies to separate $CO_2$ from $H_2$ are emerging and their industrial application is growing. Amongst these technologies is Pressure Swing Adsorption (PSA), where the gases are separated by adsorbing in solid porous particles, such as activated carbon (Plaza et al. 2010, García et al. 2011, Silvestre-Albero et al. 2011), zeolites (Cavenati et al. 2006) or MOFs (Mason et al. 2011, Simmons et al. 2011), within switching particle beds. This technology is based on two basic steps: adsorption, in which the species with more affinity with the adsorbent, due to Van der Waals interactions, are selectively removed; and regeneration (desorption), where the adsorbed species are removed from the adsorbent, regenerating it. In both stages, it is possible to obtain desirable products, depending on the different interaction between the products and the solid/stationary phase. The PSA process is based on the pressure decrease (or the use of a less adsorbable gas purge) to clean the adsorbent bed. The number of stages in PSA can be increased, by comprising a pressurization step, and a depressurization/blowdown step (Skarstrom 1960). $CO_2$ is obtained on a stream from the regeneration cycle, containing still small amounts of methane and hydrogen. $H_2$ is obtained in the pressurization step, exiting the PSA with a purity up to 99.999%. Usually, the $CO_2$-rich stream is fed to the reformer to act as a fuel, being vented to the atmosphere as flue gas (mixture of $CO_2$ and $N_2$), requiring a post-combustion process for this last stage (detailed in Section 2.2.1.2).

Regarding partial oxidation processes (POX, Equation 2.2), fuel reacts with oxygen at high pressure, in an exothermic reaction that occurs at high temperatures (of the order of 1200-1400 °C). The required heat is supplied by the partial combustion of the fuel, and there is no need of external heat supply. The syngas is cooled afterwards, shifted and $CO_2$ is removed from the stream. As in the case of steam reforming, the same technologies to separate $CO_2$ from the syngas can be applied for POX processes. POX technology is very similar to steam reforming, presenting lower efficiency, but wider fuel range. It is important to highlight another type of POX process called gasification. The reaction is the same as POX, however the fuel source is a solid (coal as being the best example). This process contrasts from typical POX processes in the equipment design, specially regarding reactors, where fixed bed, fluidized bed or entrained flow gasifiers are common types of reactors. In gasification, it is usual to clean the exiting syngas (prior to the shift reaction), removing sulphur compounds and particles. Afterwards, the clean syngas is burnt to produce electricity via a gas turbine/steam turbine combined cycle (IGCC). Usually both stages (syngas generation/cleaning and electricity production) occur at the same site, avoiding the costs of pipeline transportation. A similar process to IGCC named NGCC is also common and the differences between both lies on the use of natural gas (NGCC) instead of a solid fuel (IGCC). IGCC or NGCC do not usually comprise a $CO_2$ capture step. However, the integration of $CO_2$ capture with IGCC process has been already suggested, by integrating a WGSR stage in IGCC, and producing electricity from highly pure and high pressure (60 bar) $H_2$ stream (Figure 2.4).

Capture of $CO_2$ from IGCC plants can be regarded as a commercially available technology, which has already undergone pilot demonstrations: Vattenfall project in Buggenum (Netherlands, Damen et al. (2011)); ELCOGAS in Puertollano (Spain, Casero et al. (2014)); and Eagle Project (Japan, Nagasaki et al. (2013)).

A third technology, autothermal reforming (ATR) can also be considered, as a combination of steam reforming and POX. In this process, the heat required in steam

reforming is supplied from the heat generated in POX. Operating temperatures of ATR are typically 950-1050 °C, depending on the design of the process. $CO_2$ capture can be done using absorption with chemical solvents or cyclic adsorption processes (as described above).

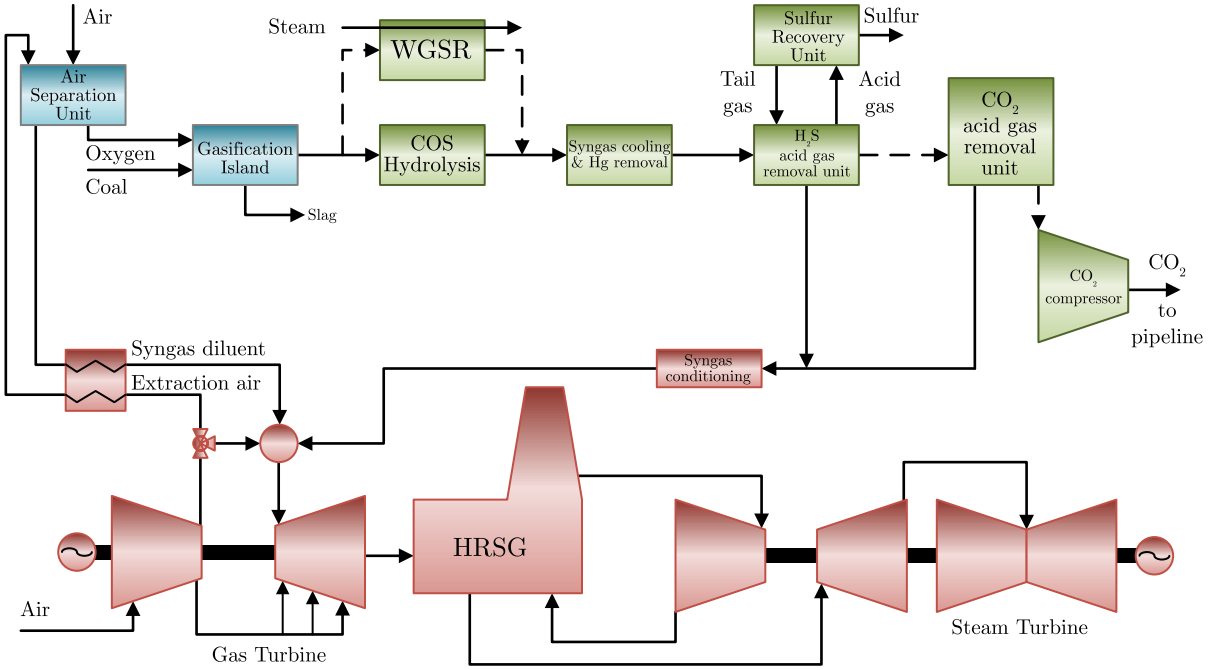



Figure 2.4 – Process flow diagram of a generic IGCC plant showing retrofit modifications for $CO_2$ capture (from EPRI (2012)).

In conclusion, all pre-combustion systems from hydrogen production are extremely similar in their conversion routes. The differences arise from the initial method and fuel employed for syngas production, as well as from the subsequent need to remove impurities that originate from fuel feed to the plant. The syngas reacts with steam to produce more hydrogen and carbon dioxide, which can be separated using typical technologies also used in post-combustion processes, as it will be explained in the next section. The produced hydrogen can be used afterwards to produce electricity (by turbines in IGCC or by fuel cells), or to produce chemicals and/or Fischer-Tropsch fuels.

#### *2.2.1.2 Post-Combustion Capture*

Post-combustion capture technologies are the most widely used technologies, due to its easy implementation and wide range of applications for different industries, in particular, in industries non-related to power generation, where $CO_2$ is produced by the combustion of fuels. In this section, the addressed key subject is the separation of $CO_2$ from the flue gas resulting from the combustion of hydrocarbons (Metz et al. 2005, Herzog et al. 2009).

Flue gas (a mixture of mostly nitrogen and carbon dioxide, with traces of water vapour and other compounds, resultant from the combustion with air) is usually exhausted at atmospheric pressure, resulting in large volumetric flow rates. Flue gas $CO_2$ content vary with the fuel source, with approximately 3% for natural gas and less than 15% for a coal-fired combustion plant. $CO_2$-capture for post-combustion technologies are, in theory, applicable to any fuel source, varying the capture efficiency and process design with the concentration of $CO_2$ in the flue gas.

There are several commercially available technologies, which can be used for $CO_2$ capture from flue gas. However, absorption processes based on chemical solvents are currently the preferred option for post-combustion capture, offering high capture efficiency and selectivity, and the lowest energy use and costs (Metz et al. 2005). Absorption processes for post-combustion capture takes advantage of the reversible nature of complex chemical reactions that occur between an alkaline solvent (usually an amine) and an acid or sour gas. An example of an absorption process with chemical solvents is illustrated in Figure 2.5. The flue gas is cooled and fed to the absorber, where it is put in contact with the solvent, at temperatures typically between 40 and 60 °C. At these conditions, $CO_2$ bonds with the solvent. The flue gas then undergoes a water wash section to balance water in the system and to remove any solvent droplets. The $CO_2$-rich solvent is then pumped to the top of a stripper,

regenerating the solvent and removing the carbon dioxide. This regeneration step is carried out at relatively high temperatures (100-140 °C) and pressures slightly higher than atmospheric pressure, requiring heat that is supplied to the reboiler. Steam, which acts as stripping gas, is recovered in the condenser and fed back to the stripper, whereas the $CO_2$ product gas leaves the stripper. The clean solvent is then pumped back to the absorber.

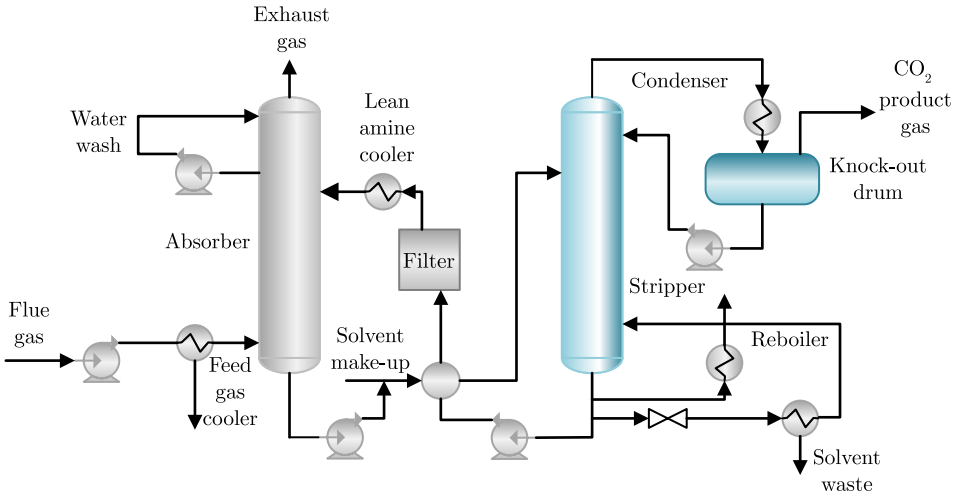



Figure 2.5 – Process flow diagram for $CO_2$ recovery from flue gas by chemical absorption (adapted from Metz et al. (2005)).

The key parameters to determine the technical and economic viability of $CO_2$ capture based on the absorption process are: flue gas flow rate, which determines the size of the absorber; $CO_2$ content in the flue gas, since the partial pressure of $CO_2$ determines which solvent is better; solvent flow rate and energy requirements, since they determine not only the size of the used equipment, but also represent a cost increase.

Several processes based on chemical-solvent absorption for post-combustion $CO_2$ capture are commercially available: the Kerr-McGee/ABB Lummus Crest process (Barchas and Davis 1992), which recovers $CO_2$ from coke and coal-fired boilers, using a 15-20% weight aqueous MEA (mono-ethanolamine) solution; the Fluor Daniel ECONAMINE™ process (Sander and Mariz 1992), also a MEA-based absorption process (in a 30% in weight aqueous solution), tailored for oxygen-containing gas

streams, since it uses a corrosion inhibitor; the KEPCO/MHI process (Mimura et al. 1997), based on sterically-hindered amines; HTC Purenergy, based on research done at the International Test Centre from the University of Regina, which developed a mixed amine solvent, inclusively offering modular units to reduce costs (Cohen et al. 2009); Aker Clean Carbon, a company that is proprietary of a process that uses a mixture of water and amine solvents for carbon dioxide scrubbing (Norway, Sanden et al. (2006)); and Cansolv, a recently developed amine system using a solvent named Absorbent DC101™, based on tertiary amines (Singh and Stéphenne 2014). It is important to highlight that usually some pre-treatment of the flue gas is required. Gas needs to be cooled, since it exits the combustion unit at approximately 100 °C. In addition, other acids, as well as sulphur compounds along with $NO_x$ need to be removed prior to $CO_2$ capture, since they also possess chemical interactions with the solvents, thus resulting in a loss of the absorption capacity, due to the potential formation of stable salts, which is highly undesirable. Therefore, the pre-removal of $NO_x$ and $SO_x$ becomes essential. Another important issue regarding amine-based absorption is the effluents that are created as a result of the decomposition of the solvent, which can require special handling and treatment, meaning higher costs.

Physical absorption process can also be used, and is carried out by the weak binding of $CO_2$ and the solvent at high pressures. Therefore, this is only an option for high $CO_2$ concentration flue gas, where the partial pressure of $CO_2$ is high. Rectisol, Purisol and Selexol solvents are used for physical adsorption (Metz et al. 2005).

Some other technologies are emerging for post-combustion $CO_2$ capture. One that has already been covered, is the used of adsorption technologies (that are also used to separate $CO_2$ resultant from the WGSR of syngas in pre-combustion systems), in particular PSA. It has not yet reached a commercial stage for post-combustion processes. However, some research groups have been giving special attention to the topic (Webley 2014).

Another potential technology for $CO_2$ separation from flue gas is through membranes. The use of typical polymeric membranes has the disadvantage of the low driving force across the membrane resulting from the $CO_2$ low partial pressure on the flue gas. However, the use of hybrid membrane-absorbent system has gained special attention. These systems use membranes to provide a very high surface area to volume ratio for mass transfer between the gas and the liquid solvent. The advantages of these systems over conventional absorption processes are the avoidance of operational problems, such as foaming, flooding entrainment and channelling (Metz et al. 2005).

Finally, recent studies have shown the potential of the use of clathrate hydrates to selectively separate $CO_2$ from flue gas, which can be used for $CO_2$ capture. Hydrates (explained in further detail in Section 2.3) are solid compounds that are formed from gas molecules and water, at given thermodynamic conditions. This concept was initially proposed by Spencer (1999) to solve the problem of sequestration. But several studies have shown the promising potential for $CO_2$ capture. It is estimated that compression costs can be reduced from 75% to 53% of the power produced for a typical 500 MW plant.

#### *2.2.1.3 Oxyfuel Combustion*

The oxyfuel combustion process eliminates nitrogen from flue gas by combusting a hydrocarbon fuel (including biomass) in either pure oxygen or a mixture of pure oxygen and a $CO_2$-rich recycled flue gas stream. The combustion temperature in such system is approximately 3500 $^{o}$C, which is far too high for most common power plants, meaning that changes to the plant would be required. The resulting flue gas consists of mainly carbon dioxide, water vapour together with excess oxygen that is required to ensure complete combustion of the fuel. The 'dried' flue gas (after condensation of the water vapour) contains about 80-98% of carbon dioxide depending on the fuel source and on the process itself. This $CO_2$-rich stream can be

compressed, dried and purified for pipeline transportation. Elements of oxyfuel combustion technologies are already present in aluminium, iron/steel and glass melting industries, however, $CO_2$ capture using oxyfuel technologies have yet to be deployed on a commercial scale. The key factor on oxyfuel combustion is the separation of nitrogen from the oxygen/air stream, using technologies that already exist. Current methods for oxygen production by air separation comprise cryogenic distillation, adsorption using multi-bed PSA and/or polymeric membranes. The $CO_2$ capture efficiency is close to 100% using the oxyfuel combustion approach. In this section, several oxyfuel combustion systems will be addressed, and classified according to how the heat of combustion is supplied, and whether the flue gas is used as a working fluid.

In oxyfuel systems with indirect heating, the released heat from combustion of any hydrocarbon fuel is transferred to a separate fluid. The heat can be used for either process heating, or in a boiler with a steam cycle for power generation. This is a way of using released energy to compensate the large amounts of energy that are necessary to separate oxygen from air. Several studies comprising this technology at pilot scale are described in literature, using both natural gas and coal as fuels. In all studies, researchers gave special attention on the heat exchange to the fluid, as well as to contaminant concentration, and concluded that the amount of produced $NO_x$ can be reduced up to 75% (for coal) if highly pure oxygen is used, when compared to air combustion (Châtel-Pélage et al. 2003). The same observation was made when natural gas was used instead of coal (Tan et al. 2002). Also, studies seem to indicate that oxyfuel combustion using altered nitrogen-free boilers benefits from higher heat exchange rates, reducing size and volume flows (McDonald and Palkes 1999). Regarding industrial plants using this technology, Dillon et al. (2005) presents data from an oxyfuel system using pulverized coal as a fuel and a supercritical steam cycle (Figure 2.6). In the system described by Dillon et al. (2005), the burner and the gas recycle ratio were designed to achieve the same temperatures as in air combustion. The heat transfer was improved due to the higher emissivity of $CO_2/H_2O$ mixture

when compared to nitrogen, leading to a boiler efficiency increase up to 5%, when combined with the recycle of hot flue gas. Regarding retrofitting, Wilkinson et al. (2003) have reported that the application of oxyfuel combustion technologies for the retrofit of power plant boilers in a refinery complex is technically feasible, at a competitive cost. The existing boiler is modified to allow combustion using highly concentrated oxygen and partial flue gas recycling for temperature control. There is also described in literature an indirect heating system that incorporates a high-temperature oxygen transport membrane (Griffin et al. 2003).

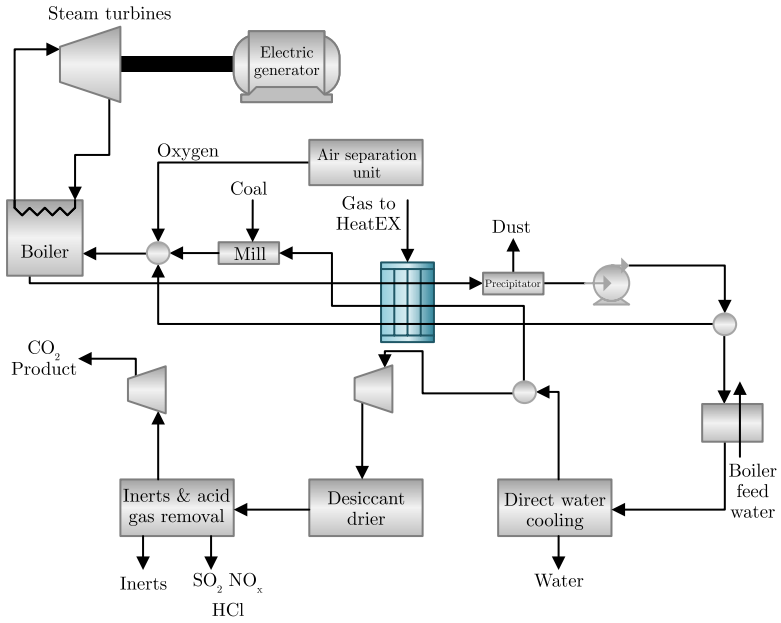



Figure 2.6 – Oxyfuel process schematic of a pulverized coal fired power plant (Metz et al. 2005).

A second type of oxyfuel technology consists in the direct heating of the gas. In this system, combustion takes place at a pressurized $CO_2$-rich recirculating stream in a modified gas turbine. The pressurized hot gas is expanded, producing power. The turbine exhaust is cooled in order to provide heat for a steam cycle, while water is condensed. The $CO_2$-rich gas is compressed, and removed from the system. This technology has the disadvantage of working only in a limited range of fuels (natural gas, light hydrocarbons or syngas). There is also the possibility of using a direct heating technology in a steam turbine cycle. In this case, water is pressurized and then is evaporated, heated by direct injection and combustion of a fuel with pure oxygen, and expanded in a turbine. Most of the water of the low-pressure turbine

exhaust is cooled and condensed, while the produced $CO_2$ is removed and compressed for transport.

As mentioned before, the critical factor in each of the presented oxyfuel types of processes lies on the separation of oxygen from air, which is a very complex separation. One of the most used techniques to do so is cryogenic distillation. In a typical cryogenic air separation plant, air is compressed to a pressure of 5 to 6 bar and purified to remove water, $CO_2$, $N_2O$ and trace hydrocarbons, using two (or more) fixed bed adsorber. These adsorbers can be regenerated by temperature (TSA) or pressure swing adsorption (PSA), using a low-pressure waste nitrogen steam. The air is then cooled and separated into pure oxygen and nitrogen fractions in a double distillation column.

There is also the possibility of separating oxygen from air using ion transport membranes (ITM). Due to the very high selectivity for oxygen that some ceramic mixed metal oxide materials are exhibiting at high temperatures (in the range of 500-700 $^{o}$C), a selective separation is possible. Oxygen permeability in membranes made out of these materials is primarily controlled by the oxygen ion vacancies in the crystalline structures lattices. A difference in the partial pressure of oxygen in the membrane results in the ionization of the ceramic surface, passing to the crystal surface and to the permeate side.

Oxyfuel combustion, which can be applied to furnaces, process heaters, boilers and power generation systems, is feasible, both technically and economically. Early use of this technology is likely to address applications involving indirect heating for power generation, since the required modifications are small, and retrofitting is a possibility. Direct heating technologies, for both gas and steam turbine cycles, still require the development of new components and further efficiency increase. Chemical looping technology is extremely promising, however, it is still in a very early stage of development. To date, the only two examples of oxyfuel combustion are the Swedish

utility Vattenfall's 30 MW pilot plant in Schwarze Pumpe, Germany, and the energy company TOTAL's Lacq project in south-western France (ZEP 2016).

### 2.2.2 Carbon Dioxide Transport

After the capture of $CO_2$, it is necessary to transport it to the site where the carbon dioxide is going to be deposited. There are two main ways of transporting $CO_2$: through pipeline and by ship. There is also the possibility of truck or rail transport for small amounts of $CO_2$ (Holloway et al. 2006).

Through pipeline, carbon dioxide is usually transported in its supercritical state (critical point is 31.1 $^{o}$C and 73.9 bar) at a initial boost pressure of 150 bar (Metz et al. 2005). The idea of transporting $CO_2$ in the form of hydrates is being also addressed by several research groups, studying the flow assurance of hydrates slurries (Hu et al. 2010, Prah and Yun 2016). This last approach has the advantage of requiring much lower pressures for transport, and can be directly used for EOR (enhanced oil recovery), taking advantage of the harsh conditions at which EOR is performed, and also of the presence of water already during transportation. A problem often described in literature regarding $CO_2$ transportation through pipeline, is the high rate of corrosion that may exist if water is still present, due to the acidic nature of carbon dioxide (Sari et al. 2008, Choi and Nešić 2011, Zhang et al. 2013). A drying process, where the remaining water is removed, is usually required to reduce pipeline corrosion rate. Also, the presence of small amounts of acids, such as $H_2S$, can increase corrosion rate, leading to the rupture of pipelines and to dangerous leaking problems.

### 2.2.3 Carbon Dioxide Storage

To present itself as a viable climate change mitigation option, sequestration of $CO_2$ must be safe and secure. Well-selected, designed and managed geological

sequestration sites provide a safe way to permanently sequester $CO_2$ (Marchetti 1977).

Engineered injection of $CO_2$ into subsurface geological formations was first undertaken in the early 1970s, as part of EOR projects and has been on-going at many locations.

Geological formations are composed of transported and deposited rock grains, organic material and minerals that form after the rocks are deposited. The pores (between grains or minerals) are usually occupied by fluid (mostly water). Injection of $CO_2$ in both rock formation pores and fractures, can either displace water or dissolve the oil (since supercritical $CO_2$ is known for being an oil solvent) and thus extracting oil from the pores. Geological storage effectiveness depends on a combination of physical and geochemical trapping mechanisms. The most effective storage sites are those where $CO_2$ is immobile because: it is permanently trapped under a thick, low-permeability seal; is converted to solid minerals; is adsorbed on the surfaces of coal micropores; or through a combination of physical and chemical trapping mechanisms (Figure 2.7, Metz et al. (2005)).

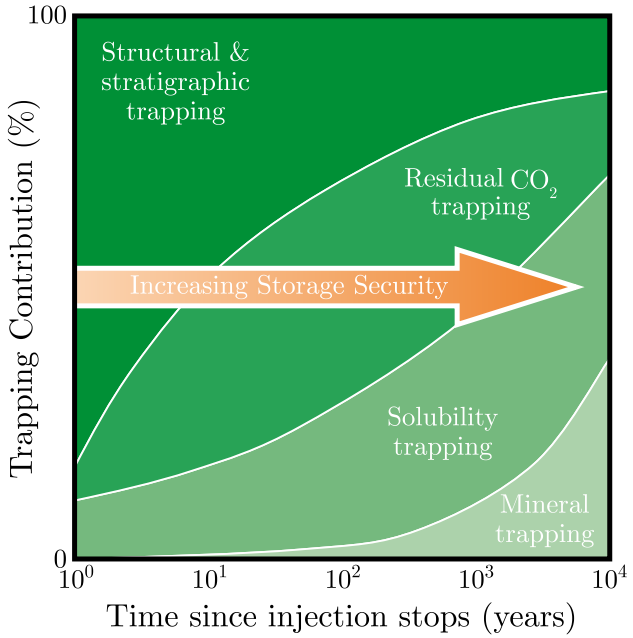



Figure 2.7 – Storage security as a function of the storage mechanism (Metz et al. 2005).

It is important to highlight the fact that for $CO_2$ storage, another option is available, taking advantage of the particular characteristics of $CO_2$ hydrates (Spencer 1999). Due to the pressure and temperature conditions that are observed in deep sea, in the same range at which hydrates are thermodynamically stable, it is possible to store $CO_2$ by depositing hydrates in the bottom of the ocean, since they will remain stable (IEA 2004).

## 2.3 Gas Hydrates

The use of gas hydrates for carbon capture and storage is useful in every stage of CCS: capture, transport and geological storage. In this section, the particular properties of gas hydrates are scrutinized to assess its importance as a CCS alternative solution.

The first significant contact with gas hydrates is credited to Davy (1811) who studied several forms of production of chlorine gas (or oxymuratic gas as it was called back then) from hydrochloric acid. Davy (1811) contradicted the generalized idea that chlorine crystallized at low temperatures, by observing that dried chlorine did not suffered a phase change, observed when water was in contact with the gas. However, the major breakthrough regarding gas hydrates understanding started when Hammerschmidt (1934) reviewed previous works and recognized that natural gas pipelines were being blocked by the presence of methane hydrates, and not by ice, as initially thought, since the operation temperatures were above the ice point of water. From that point, research on thermodynamics and properties of gas hydrates has been intensified, as well as the discovery of ways of avoiding their precipitation. Even nowadays, gas hydrates are a problem for natural gas flow assurance engineers, since they can present a serious threat to normal pipeline operation (Sloan and Koh 2007, Carroll 2014).

### 2.3.1 Hydrates Structures and Properties

Hydrates (or aqueous clathrates) are non-stoichiometric crystalline solid compounds, consisting in water molecules enclosing a guest molecule. The concept of clathrates hydrates distinguishes from organic or inorganic hydrated compounds from the fact that no chemical bonding is observed in the first ones, hence they present themselves as non-stoichiometric compounds. Nonetheless, the hydrate structure is held by hydrogen bonds between water molecules and strong van der Waals forces between the water molecules and the enclatherated guest molecules, resulting in a polyhedral crystalline structure, forming cages. Typically, one cage contains one guest molecule. However, in extraordinary situations, two guest molecules may enter the same cage (Sloan and Koh 2007).

Depending on the sizes of the guest(s) molecules included in the hydrate, three hydrate structures are known: cubic structure I (sI); cubic structure II (sII); and hexahedral structure H (sH). Each of these structures own different arrangements and number of the water molecules, resulting in different number and size of cavities available to host the guest gas molecules (Sloan and Koh 2007). Udachin and Ripmeester (1999) have described a new and complex hydrate structure made out of choline (a water-soluble vitamin), consisting of alternating stacks of sII and sH structures.

The basic repeating unit of cubic structure I is a primitive lattice consisting of two small cages and six large cages. The small cages, pentagonal dodecahedron labeled $5^{12}$, have 12 pentagonal faces with equal edge lengths and angles. The large cages, tetrakaidecahedron labeled $5^{12}6^2$, have 12 pentagonal and 2 hexagonal faces. One sI unit cell can hold 46 water molecules in its structure and fits in a cube with edge length of 12 Å. The repeating unit from the sII structure contains also two types of cavities, the small ones comprising 16 pentagonal dodecahedron $5^{12}$, while the large cages, 8 hexakaidecahedron, have 12 pentagonal faces and 4 hexagonal faces, labeled as $5^{12}6^4$. This type II hydrate can hold 136 water molecules in its structure, fitting in a cube with edge length of 17.3 Å. Finally, in hydrate type H, a layer of $5^{12}$ connects

with a layer of $5^{12}6^8$ and $4^35^66^3$ cavities (Sloan and Koh 2007). Crystallographic properties and structure are summarized in Table 2.2, and represented in Figure 2.8 and Figure 2.9.

Table 2.2 – Gas hydrates structural properties (Sloan and Koh 2007).

| **Structure** | **sI** | | **sII** | | **sH** | | |
|---|---|---|---|---|---|---|---|
| **Cavity type** | Small | Large | Small | Large | Small | Medium | Large |
| **Label** | $5^{12}$ | $5^{12}6^2$ | $5^{12}$ | $5^{12}6^4$ | $5^{12}$ | $4^35^66^3$ | $5^{12}6^8$ |
| **Num. Cavities** | 2 | 6 | 16 | 8 | 3 | 2 | 1 |
| **Average cage radius (Å)** | 3.95 | 4.33 | 3.91 | 4.73 | 3.94 | 4.04 | 5.79 |
| **Coordination number** | 20 | 24 | 20 | 28 | 20 | 20 | 36 |
| **Lattice size (Å)** | 12 | | 17.3 | | 12.2 | | |
| **Num. water molecules** | 46 | | 136 | | 34 | | |

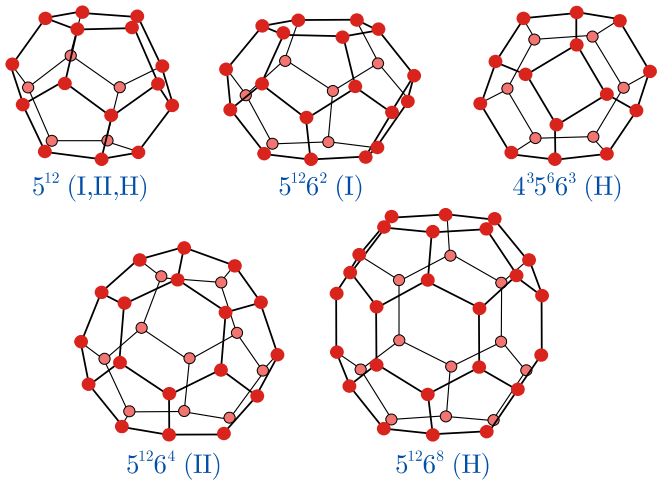



Figure 2.8 – Hydrate cavities of structures I, II and H.

Which type of hydrate structure is crystallized depends on the thermodynamic conditions, but most importantly, on the guest molecule, or the composition of the gas. Generally, guest molecules in the size range of 3.8-6.5 Å of diameter, can form sI and sII hydrates, if they cannot form hydrogen bonds. Depending on the size of the guest molecule, it can fill both small and large cavities or only the larger cavities. However, the filling of the small cages only is not possible, since that would raise thermodynamic stability issues. Therefore, if a molecule is capable to penetrate into the small cages, it means it will also be filling the larger cages, to stabilise the

structure (Sloan and Koh 2007). On the contrary, it is possible to stabilise sI and sII structures by filling only the larger cavities.

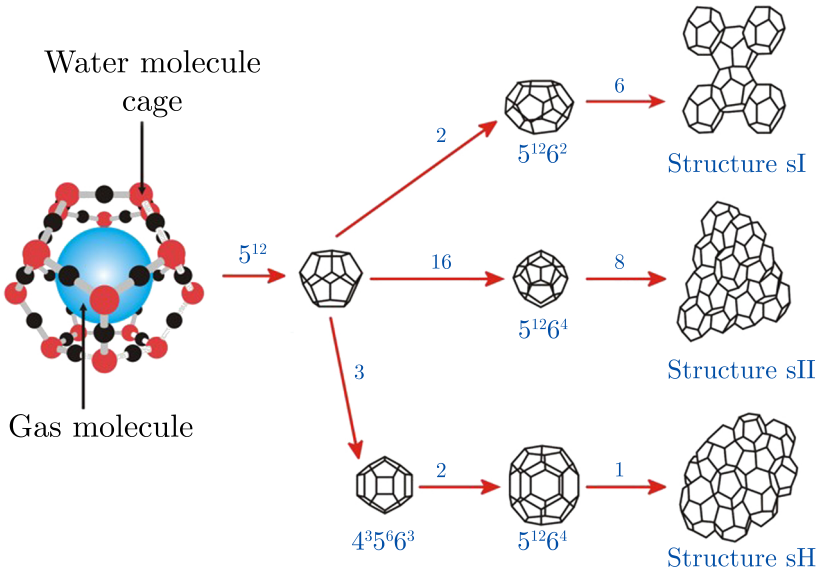



Figure 2.9 – Gas hydrates structures from cavity entities (Adapted from HWIPE (2016)).

Methane, ethane, $CO_2$ or Xe typically form type sI hydrates. Methane, $CO_2$ and Xe are small enough to penetrate into smaller cavities of the sI structure, while ethane can only fill the larger cavities. Tetrahydrofuran (THF), propane and iso-butane fit in larger cavities of type II hydrates structure, while $O_2$ and $N_2$ (also forming sII structures) can be enclatherated in both small and large cages. Type sH structure has unique features, since it requires both small and large sizes of molecules to stabilize the structure (neohexane and cycloheptane cannot form hydrates alone but only with the help of methane for example, to form a sH hydrate). Flue gas is, for the most part, a $N_2/CO_2$ mixture with a lower percentage of water and oxygen (a similar molecule to $N_2$). If $CO_2$ is present with mole concentration higher than 15%, hydrates form sI structures (Kang and Lee 2000). However, if $CO_2$ molar concentration is lower than 15%, then structure II hydrates are formed. The addition of THF (which naturally forms sII hydrates) in these mixtures results in the change from sI to sII hydrates, increasing the amount of caged molecules and enhancing the hydrate stability.

Hydrates are commonly mistaken with regular ice, due to their macroscopic similarities, as can be seen in Figure 2.10, but ice and hydrates present different crystal structures. However, the most important difference is that hydrates are not formed if no guest hydrate-forming molecule of a proper size is present, while ice forms as a pure component. Mechanical properties of hydrates however, are very similar to the properties of ice, since water represents a large portion of the hydrate composition. The amount of water in a hydrate per molecule of guest is named the hydration number $n_h$, and depends on the type of hydrate and on the guest molecule.



(a) (b)

Figure 2.10 – Solid $CO_2$ hydrate: (a) using a thermodynamic cell (BGS 2016); (b) wet obtained in continuous process (Groen 2012).

The process of transforming water and a guest gas molecule to a solid hydrate can be conceptualized in the form of a chemical reaction.

$$G + n_h H_2O \rightleftharpoons G \cdot n_h H_2O \downarrow \tag{2.4}$$

Phase state of the reactants on Equation 2.4 were intentionally not written, since both water and ice, as well as gas or liquid guest molecules are able to form solid hydrates. It is important to highlight though, that Equation 2.4 does not represent a real chemical reaction, since no chemical bonding is created/destroyed in the process. The structure is held based on relatively strong physical bonds. Also, in chemical reactions, $n_h$ would have to be an integer number due to stoichiometry, however,

from crystal information, the ideal theoretical $n_h$ value is not integer. The nature of the process is still controversial, and it is also possible to consider this precipitation process as a typical phase change process.

The ideal hydration number $n_h$ can be determined using the information available in Table 2.2. For instance, considering $CH_4$ as guest molecule, which forms sI hydrates, 46 molecules of water create the network, comprising 2 small cavities and 6 large cavities. Since it is known that methane molecules can fill both cavities, the maximum possible number of $CH_4$ molecules in a sI structure is 8. Therefore, for this structure the ideal hydration number can be determined by

$$n_h = n_{H_2O} / n_{CH_4} = 46/8 = 5.75 \quad (2.5)$$

On the other hand, in the case of $CO_2$, in the formed type I hydrate only the large cavities are filled, since the guest molecule is too large to fit in the smaller cages. Therefore, in theory, only 6 molecules of carbon dioxide are enclatherated in the hydrate, leading to an ideal hydration number of 7.66.

As already mentioned, gas hydrates possess very similar mechanical properties to ice. Hydrates present a higher density than hydrocarbons, but most importantly, they can enclose large amounts of gas, if all the cages are fully occupied. In this case, one volume of gas hydrates can contain up to 180 volumes STP of gas (Sloan and Koh 2007). Considering methane, the concentration in hydrates is comparable to compressed gas at 25 °C and 210 bar.

Carbon dioxide for example, as already mentioned, has a theoretical molar ratio $H_2O/CO_2$ of 7.66, as a result of a partial filling of the sI hydrates cages. However, several authors experimentally observed that this value is not exactly 7.66, but varying within the range of 6.07 to 7.8 (Yamamuro and Suga 1989, Sloan and Koh 2007). Bozzo et al. (1975) obtained a value of 7.3, very close to the 7.23 observed by Kang et al. (2001). Aya et al. (1997), which also studied $CO_2$ solubility in both non-

forming and forming hydrates regions, obtained a relationship between the hydrate crystal density as a function of the hydration number, while Anderson (2003) developed a simple equation to estimate the hydration number as a function of the temperature, based on the $CO_2 - H_2O -$ hydrate equilibrium data. Table 2.3 presents a review of some of the works referring to the determination, both directly or indirectly, of the hydration number of $CO_2$ hydrates.

Table 2.3 – Hydration number of carbon dioxide hydrates from literature.

| $T(K)$ | $n_h$ | Method | Reference |
|---|---|---|---|
| | | **Direct** | |
| n.a. | 7.24 – 7.68 | Raman | Uchida et al. (1995) |
| n.a. | 6.0 – 7.8 | Pressure Drop | Aya et al. (1997) |
| n.a. | $> 7$ | NMR | Ripmeester and Ratcliffe (1998) |
| 278.1 | 7.23 | Calorimetry | Kang et al. (2001) |
| 276.0 | 6.2 | XRD | Udachin et al. (2001) |
| | | **Indirect** | |
| 273.2 | 7.3 | Clapeyron equation | Bozzo et al. (1975) |
| 273.2 – 273.6 | 6.21 – 8.25 | | Yoon et al. (2003) |
| 274.15 – 282.15 | 5.7 – 6.4 | | Anderson (2003) |
| 281.4 | 5.98 | | Sabil et al. (2010) |
| 275.3 – 279.9 | 6.6 – 7.9 | | Lirio and Pessoa (2013) |

Sloan and Koh (2007) describe two methodologies that can be used to indirectly determine the hydration number. These methods emerged due to the difficulties verified using direct methods. The first method applies the Clapeyron equation to the equilibrium data to estimate the heat of hydration, and from there, determine the hydration number. The second method, called Miller and Strong method, considers the hydration process as an equilibrium chemical reaction, characterized by an equilibrium constant, that can be used to determine both fugacity and activity of water, the guest molecule and the hydrate. This last approach is, however, more commonly used when inhibitors (molecules that hinder the formation of hydrate – see Section 2.3.3) are present (Sloan and Koh 2007).

Other studies have focused on the determination of the hydration number for mixed hydrates (hydrates formed from mixtures of guest molecules), in particular the $N_2/CO_2$ mixture. In this case, not only the temperature is an important factor, but also the $N_2/CO_2$ ratio. Two different hydration numbers are required for each guest molecules

$$n_{CO_2}CO_2 \cdot n_{N_2}N_2 \cdot 46H_2O \quad (2.6)$$

$$n_{CO_2}CO_2 \cdot n_{N_2}N_2 \cdot 136H_2O \quad (2.7)$$

where $n_{CO_2}$ represents the number of carbon dioxide molecules, while $n_{N_2}$ represents the number of molecular nitrogen in the hydrate. Two formulas are given due to the fact that, depending on the composition of the mixture, sI (Equation 2.6) or sII (Equation 2.7) hydrates can be formed. Again, the hydration number of each of the components represents the ratio between the number of water molecules and the guest molecules. Nevertheless, since this hydration number is constrained by the crystal structure, the values (for the sum of both molecules) should lay in the range of 5-8. Anderson (2003) estimated these values for both low $CO_2$ concentration and high $CO_2$ concentration in the gas, but still in the range of sI hydrate crystallization (Table 2.4).

Table 2.4 – Mixed $N_2/CO_2$ hydrates ratio for sI structure (Anderson 2003).

| **$CO_2$ Emissions (% mol)** | $n_{CO_2}$ | $n_{N_2}$ |
|---|---|---|
| **17%** | 5.43 | 1.89 |
| **70%** | 7.08 | 0.25 |

Because of these properties, in particular, the large capacity of holding a significant amount of gas in a concentrated manner, gas hydrates are of great importance for several applications or fields, as described in Section 2.3.4.

Table 2.5 lists molecules identified as hydrate formers, present in different industrial processes (Gao 2006).

Table 2.5 – Molecules identified as hydrate formers (Gao 2006).

| Natural Gas | Oils | Process Industry | Other |
|---|---|---|---|
| Nitrogen | Benzene[1] | Ethylene | Inert gases |
| Carbon Dioxide | Cyclopentane[1] | Propylene | Oxygen |
| Hydrogen Sulphide | Cyclohexane[1] | Other olefins | Hexafluorosulphide |
| Methane | Methylcyclopentane[1] | | Cyclopropane |
| Ethane | Cycloheptane[1] | | |
| Propane | Methylcyclohexane[1] | | |
| Buthane[1] | Ethylcyclopentane[1] | | |
| Isobuthane | Cyclo-octane[1] | | |
| Neopentane[1] | 1,1-dimethylcyclohexane[1] | | |
| | cis 1,2-dimethylcyclohexane[1] | | |
| | 2-methyl-butane[1] | | |
| | 2,2-dimethyl-butane[1] | | |
| | 2,3-dimethyl-butane[1] | | |
| | 2,2,3-trimethyl-butane[1] | | |
| | 3,3-dimethyl-pentane[1] | | |
| | 2,2-dimethyl-pentane[1] | | |
| | 2,3-dimethyl-1-butene[1] | | |
| | 3,3-dimethyl-1-butene[1] | | |
| | 3,3-dimethyl-1-butyne[1] | | |
| | cis cyclo-octene[1] | | |
| | Bicyclo[2.2.2]oct-2-ene[1] | | |
| | Adamantene[1] | | |

[1] Requires presence of smaller molecule to stabilise the structure, originating hexagonal structure (sH) hydrates.

### 2.3.2 Hydrates Formation

Clathrate hydrates are formed when free water is in contact with a hydrate-forming guest molecule, in temperature and pressure conditions that are thermodynamically favourable. Hydrate formation is a phase change process that can be treated as a crystallization process, requiring supersaturating conditions. This means that the concentration of the guest compound has to be larger than its solubility in water.

The process of formation of hydrates depends not only on the thermodynamic conditions (described on Section 2.3.2.1), but also on the kinetics inherent to the

nucleation and growth process (a simple description of these processes are presented in Section 2.3.2.2).

#### *2.3.2.1 Equilibrium Conditions*

At equilibrium conditions, solid hydrates coexist in equilibrium with liquid water (or ice), gas and/or another phase. In this situation, the species chemical potential is equal in all equilibrium phases. The equilibrium temperature and pressure are defined by the equilibrium curves that are a function of the gas composition. The equilibrium line can be seen as the condition at which the first nucleation sites for hydrates are formed. This means that hydrates are only macroscopically formed/visible within the region of hydrates stability that is delimited by the equilibrium curve. Hydrates can only form at temperatures lower than the equilibrium temperature at a given pressure, or at pressures higher than the equilibrium pressure, at a given temperature. Figure 2.11 shows the phase diagram curve for the $CO_2 - H_2O -$ hydrate system.

Several different regions are identified in Figure 2.11. The four red regions, delimited by the red curve, are the regions with favourable thermodynamic conditions for the production of $CO_2$ hydrates, if water and $CO_2$ are in contact, and if supersaturation conditions are present. The different red regions represent different physical states of both water and carbon dioxide: regions at the left of the dashed blue water solid-liquid line contain water in the form of ice, while the regions at the right of that line contain water in liquid state; regions above the black $CO_2$ saturation line contain $CO_2$ in its liquid state, while regions below the line contains vapour $CO_2$. Figure 2.11 also shows the $CO_2$ critical point, the point at which $CO_2$ liquid-vapour equilibrium curve ends, reaching a new phase called supercritical state.

When a gas mixture is present, the partial pressure of a component in the mixture is of high importance. If a mixture comprises two hydrate-forming compounds, the mixture equilibrium curve shifts to a region between the equilibrium curves of the

pure components. For instance, nitrogen forms hydrates at very harsh pressure and temperature conditions, while, on the other hand, carbon dioxide does not require such severe conditions. For a given temperature, the equilibrium pressure can be 3-5 larger in nitrogen than in carbon dioxide. However, if the gas is a mixture of both, the equilibrium pressure should be within the range of the equilibrium pressure of the pure components (Figure 2.12).

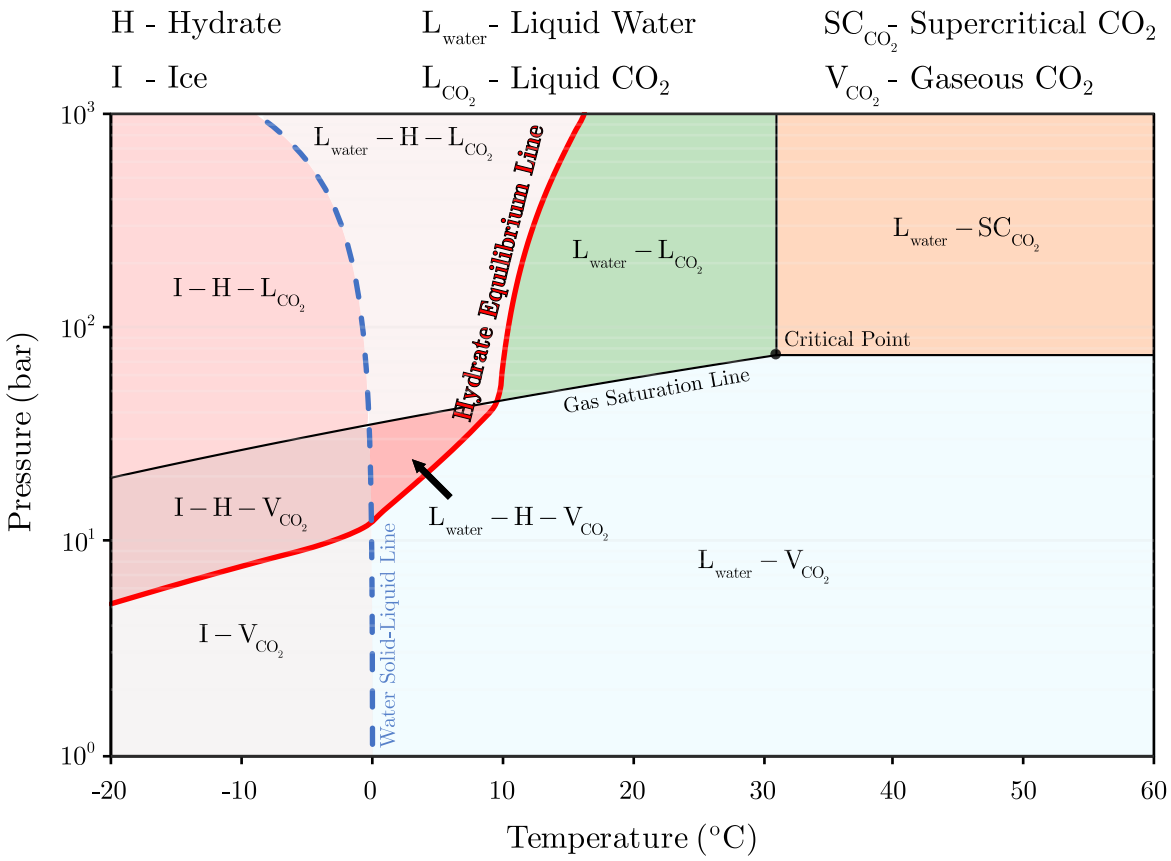



Figure 2.11 – $CO_2 - H_2O$ phase diagram.

Equilibrium curves can be determined either experimentally or by thermodynamic modelling (Sloan and Koh 2007). Thermodynamic models are based on the van der Waals and Platteeuw model, derived from statistical thermodynamic considerations (van der Waals and Platteeuw 1958). Usually, thermodynamic modelling described in literature refers to modifications to the van der Waals and Platteeuw model, or an optimization of the thermodynamic parameters. The equilibrium curve is usually calculated starting from the thermodynamic equilibrium condition:

$$\hat{\mu}_{H_2O,\,aq} - \hat{\mu}_{H_2O,\,hyd} = 0 \tag{2.8}$$

where $\hat{\mu}_{H_2O,\,aq}$ is the chemical potential of water in the liquid aqueous phase, and $\hat{\mu}_{H_2O,\,hyd}$ is the chemical potential of water in the hydrate phase.

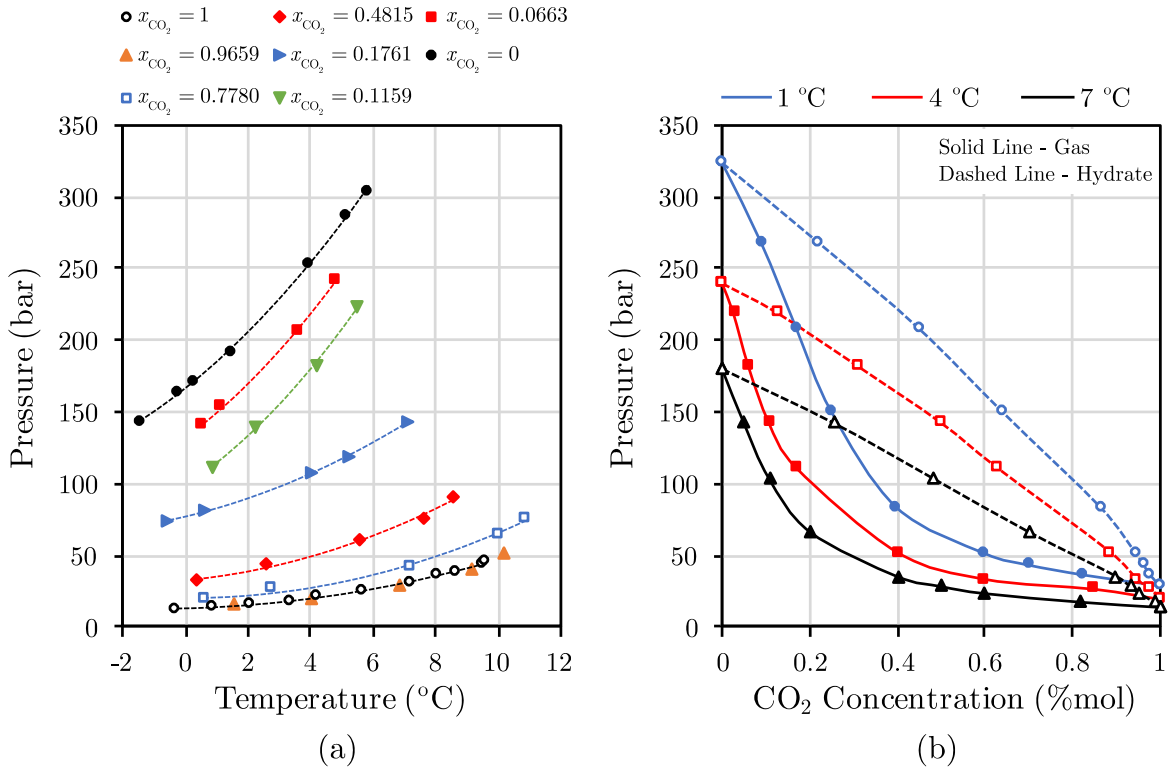



Figure 2.12 – (a) Hydrate phase equilibria for $N_2/CO_2$ system, for different compositions; (b) Phase-composition diagram at three different temperatures. The curves represent trendlines (Kang and Lee 2000).

The chemical potential of water in the liquid phase is usually expressed in terms of its activity. However, the potential in the hydrate phase is not straightforward, and it is necessary to compute the potential of water in a hypothetical empty lattice hydrate phase. The difference of the chemical potential of water in the hydrated hydrate and in the empty hydrate is determined using the van der Waals and Platteeuw model, which relates the fugacity of the guest components in the gas phase with the fractional filling of the cavities, using a Langmuir type equation. This means that accurate modelling of the gas phase (whether using a typical equation of state or virial equation) and of the aqueous phase is essential for accurate results. In general, these models are able to estimate the equilibrium curve for pure gas hydrates, with good agreement when compared with experimental results. However, some models seem to deviate when it comes to the determination of the equilibrium phase

compositions. Equilibrium data obtained experimentally, and comparison using a thermodynamic model for hydrates of carbon dioxide is shown in Figure 2.13 (Sfaxi et al. 2012).

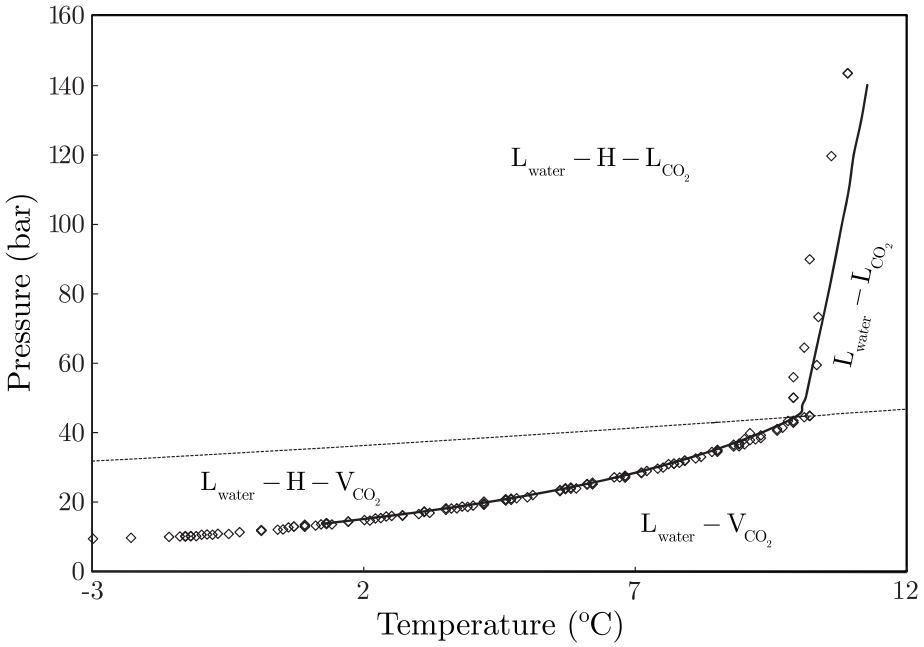



Figure 2.13 – Comparison between experimental data and thermodynamic model based on the van der Waals and Platteeuw model developed by Sfaxi et al. (2012) for $CO_2$ hydrates.

There are several software models available for hydrate equilibrium determination. One of the most important is CSMGem, developed at the Colorado School of Mines, based on the minimization of the Gibbs Energy of the system (Ballard 2002). There are also some simple methods that can be used based on hand calculations (Sloan and Koh 2007).

Experimentally, hydrate equilibrium is determined using thermodynamic cells with controlled temperature (Sloan and Koh 2007). In these measurements, equilibrium is achieved when no significant change on the system's thermodynamic properties (temperature and pressure the most important, but also concentration) with time is observed. How much time it takes to reach equilibrium is determined solely by the process kinetics. Typically, hydration processes require large periods of time (it can take days to reach thermodynamic equilibrium in poorly mixed systems). The experiments are performed in closed vessels with gas entering the cell that already

contains water. The cell often has some kind of mixing device, however, the mixing quality is never evaluated. The gas is in contact to water, leading to a primary dissolution process in water until saturation conditions are achieved. During this process, gas is injected to keep the pressure of the system constant, while a bath removes the gas dissolution heat, keeping the temperature constant. Gas is dissolved until the concentration of gas in water is lower than the saturation concentration. If the amount of gas is higher than the saturation concentration, a supersaturation condition is obtained in a second phase called induction (or nucleation), which is the phase where the nuclei hydrates are being formed, but are still not visible. After the formation of these microscopic nuclei's, a growing process occurs, leading to a higher consumption of the guest gas. When equilibrium is reached, the pressure is kept constant with no need of further gas injection. This behaviour is observed in Figure 2.14.

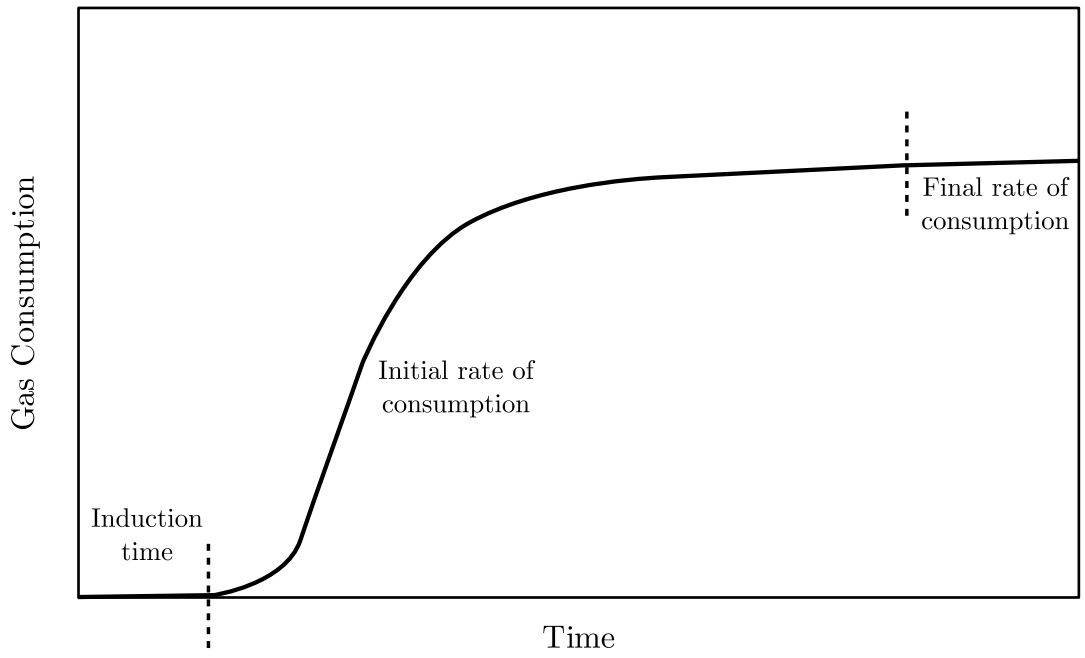



Figure 2.14 – Gas consumption vs. time for hydrate formation. Adapted from Sloan and Koh (2007).

#### *2.3.2.2 Nucleation and Growth*

Hydrate nucleation is the process during which small clusters of water and gas grow and disperse until some nuclei have grown to a critical size (Sloan and Koh 2007). Nucleation may occur spontaneously (homogeneous nucleation), or it may be induced

around impurities (heterogeneous nucleation). In contrast to primary nucleation, where nucleation commences without crystals present, secondary nucleation occurs in the vicinity of already growing crystals in the system (Mullin 2001).

Nucleation is a process based on its driving force or supersaturation. Several authors have identified this supersaturation as the chemical potential difference between the old (water in liquid) and the new (water in the hydrate) phase (Sloan and Koh 2007).

The time from the first gas-liquid contact to the first detection of a hydrate phase is called the induction time. Usually, the induction time is used as a measure of the nucleation period (Sloan and Koh 2007). Several nucleation mechanisms have been proposed over time. Some of them assume that nucleation occurs in the water/ice phase (Sloan and Fleyfel 1991), while others state that it should occur at the gas-liquid interface (either on the gas or liquid side) (Rodger 1990, Christiansen and Sloan 1994, Kvamme 1994).

An interesting phenomenon usually observed is related to the so called hydrate "memory effect" (Sloan and Koh 2007). Hydrates form more easily from gas and water obtained by melting hydrate, than from fresh water with no previous hydrate history. This effect can be explained in two ways: remaining hydrate structures in water that are not visible to the naked eye, eliminating the induction period (secondary nucleation); remaining dissolved gas in solution, reducing the induction time. Which one of the hypothesis is accurate is still unclear.

Hydrate growth, on the other hand, is a more complicated subject. During the growth process, heat and mass transfer become of major importance. This is the stage where most of the gas is consumed, therefore limited heat and mass transfer limits the hydrates growth rate. A very significant amount of gas is required to stabilize the hydrate structure. Therefore, interphase mass transfer from the gas phase to the liquid phase is of high importance. Also, both gas dissolution and hydrate formation (nucleation and growth) processes are highly exothermal processes. This means that the process is heat transfer limited, which is usually observed experimentally, and

heat removal controls the growth kinetics. This is somehow corroborated by Morgan et al. (1999), that observed that under vigorous mixing, by reducing the interphase mass and heat resistances, hydrates were rapidly formed. If nucleation and growth occurs at a system unable to remove the released heat from the hydration process, then the heat is absorbed by the system and the temperature increases up to values where hydrates are not thermodynamically stable (see Figure 2.11).

At the molecular level, hydrate growth can be considered to be a combination of three factors: the kinetics of crystal growth at the hydrate surface; mass transfer of components to the growing crystal surface; heat transfer of the exothermic heat of hydrate formation away from the growing crystal surface. Taking into consideration these three steps, several models were created to estimate the rate of formations of hydrates (Sloan and Koh 2007). However, these models are usually valid only in specific conditions, being either controlled by growth kinetics, mass transfer rate or heat transfer rate.

#### *2.3.2.3 Dissociation and Dissociation Enthalpy*

Hydrate decomposition or dissociation is driven by the difference between the equilibrium fugacity and the vapour fugacity of the gas phase.

The modern conceptual picture of dissociation of a hydrate core typically involves radial dissociation (Figure 2.15), where the hydrate plug remains at the center and is surrounded by a stationary water phase (Sloan and Koh 2007).

A quite interesting dissociation phenomenon occurs and is called hydrate self-preservation. Self-preservation is the phenomenon where hydrates can remain stable for extended periods outside the hydrate stable region (Sloan and Koh 2007). This phenomenon is usually observed when hydrates are able to maintain its structure at low temperatures and low pressure. This behavior is important, since for pipeline transportation, pressure drop due to fiction occurs, thus reducing the system's pressure. This phenomenon allows the hydrates to preserve in a metastable state

(they are not stable, they just dissociate at a very low rate), as long as the temperature is low enough.

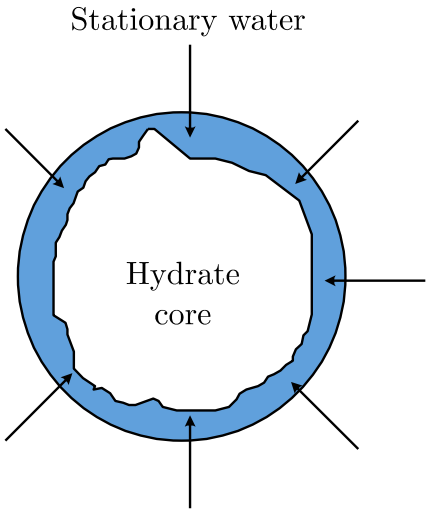



Figure 2.15 – Schematic of radial dissociation (Sloan and Koh 2007).

Dissociation process is the opposite to hydrate crystallization. Dissociation is endothermic (absorbs energy), while hydrate formation is exothermic (releases energy). This means that, in order to dissociate hydrates, a supply of energy to the system, in the form of heat, is required. If heat is not available, the system may use its sensible heat to dissociate, leading to a decrease on the system's temperature.

About 80% of the enthalpy of dissociation is due to strong crystal hydrogen bonds, which require energy to be destroyed. This means that the enthalpy depends on the cavity occupations. Also, it is expected that an increase of the number guest molecules trapped in the cages of the hydrate structure results in a decrease of the dissociation enthalpy (Kang et al. 2001).

As with the hydration number, dissociation enthalpy can be determined both experimentally and theoretically (using also experimental data) (Sloan and Koh 2007).

The heat of dissociation is usually experimentally determined using calorimetry (Handa 1986, Kang et al. 2001). Udachin et al. (2001) used X-Ray diffraction for the

determination of heat of dissociation, while Delahaye et al. (2006) used differential scanning DSC.

Kang et al. (2001) made a comparison between enthalpies of dissociation of methane hydrates. The differences were relatively small (less than 10%), varying from 53 to 57 $kJ \cdot mol^{-1}$, agreeing within the experimental uncertainty. In the same study, pure $CO_2$ and $N_2$ hydrate dissociation enthalpy were determined, with values of 65.2 and 65.8 $kJ \cdot mol^{-1}$, respectively. Kang et al. (2001) also determined the enthalpy of mixed $N_2/CO_2$ hydrates for two different compositions, observing that the enthalpy of formation was higher when the $N_2$ concentration on the feed gas is larger. However, this difference is less than 2%, and a direct correlation cannot be made.

The main problem of using an experimental method to determine the heat of dissociation is that these methods are usually not very reliable, due to problems of metastability and occlusion (Sloan and Koh 2007). For this reason, the need of determining the heat of dissociation in a more rigorous way using a theoretical approach has emerged.

Regarding theoretical dissociation enthalpy, the use of the Clapeyron equation can present itself as an extremely useful tool to determine the energy required to dissociate hydrates, using equilibrium data,

$$\frac{d\left(\ln p\right)}{d\left(1/T\right)} = -\frac{\Delta H_{\text{hyd}}^{\text{mol, diss}}}{ZR_{\text{gas}}} \tag{2.9}$$

$p$ is the pressure, $T$ is the absolute temperature, $\Delta H_{\text{hyd}}^{\text{mol, diss}}$ is the molar hydrate dissociation enthalpy, $Z$ is the gas compressibility factor and $R_{\text{gas}}$ is the gas constant. Since dissociation is endothermic, $\Delta H_{\text{hyd}}^{\text{mol, diss}}$ is larger than zero. This method for the enthalpy estimation is completely based on modelling if the equilibrium curve is estimated (and not measured), using thermodynamic models.

Sloan and Koh (2007) represented the enthalpies obtained using the Clapeyron equation for methane hydrates mixed with ethane and propane (Figure 2.16), and observed that the curves for different compositions were parallel, meaning that the enthalpy of dissociation was fairly constant (74 $kJ \cdot mol^{-1}$ for the methane-ethane mixture and 79.2 $kJ \cdot mol^{-1}$ for the methane-propane mixture). This means that the composition is not as important as the guest molecule sizes. But again, this difference may be within the experimental uncertainty. Another important aspect to be highlighted is that pure methane and propane hydrates form sI structures, while the mixed hydrates, for high concentration of methane, form sII structures.

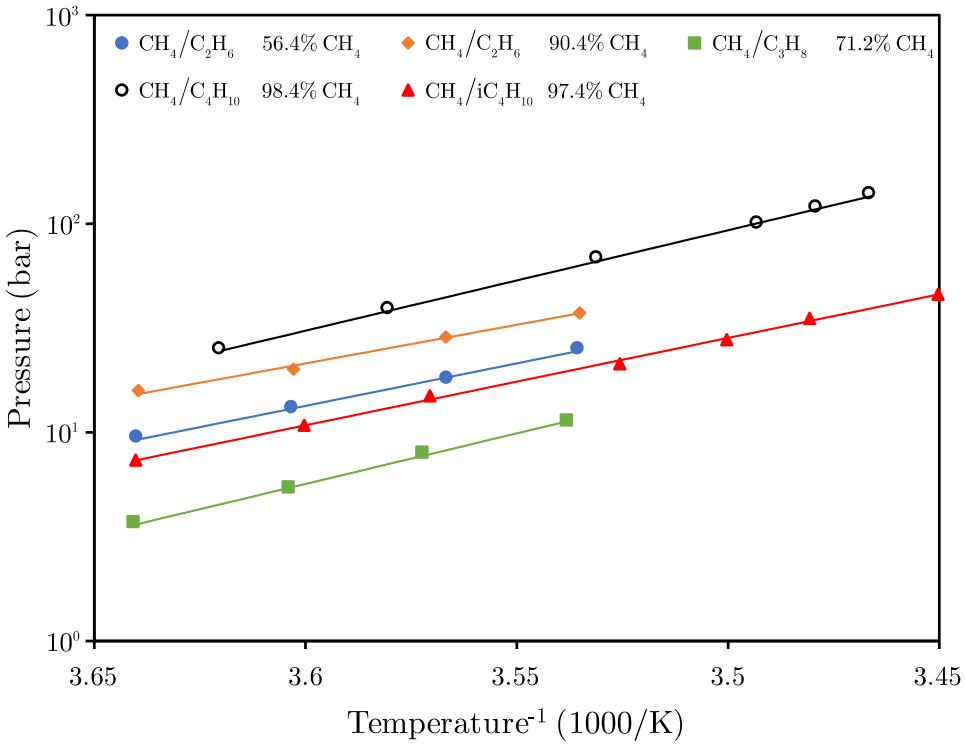



Figure 2.16 – Hydrate dissociation lines for mixtures of methane with ethane, propane, butane and isobutane (Sloan and Koh 2007).

In general, dissociation enthalpies obtained using the Clapeyron equation are in good agreement with obtained experimental values. Dissociation enthalpies obtained both experimentally and using the Clapeyron method for different hydrates are compared in Table 2.6.

Table 2.6 – Comparison between experimental enthalpies of dissociation with values obtained from Clapeyron equation (Kang et al. 2001, Yoon et al. 2003, Sloan and Koh 2007, Sabil et al. 2010).

| COMPONENT | $\Delta H_{hyd}^{mol,\,diss}\left(kJ \cdot mol^{-1}\right)$ | |
|---|---|---|
| | EXPERIMENTAL | CLAPEYRON |
| Nitrogen | 49.5 | 65.2 |
| Carbon Dioxide | 59.1 | 65.8 |
| Methane | 54.2 | 56.9 |
| Ethane | 71.8 | 71.1 |
| Propane | 129.2 | 126.0 |

The values represented in Table 2.6 are in agreement with the observations made by Sloan and Koh (2007) that the size of the guest molecule fixes the dissociation enthalpy.

### 2.3.3 Inhibitors and Promoters

It is known that some compounds display the capability to either inhibit or to stimulate the production of hydrates (Sloan and Koh 2007). The first group of compounds are called inhibitors, while the second are called promoters.

There are two types of inhibitors: thermodynamic and kinetic inhibitors. Thermodynamic inhibitors are species that either lower the $L_W - H - V$ temperature or increase the $L_W - H - V$ pressure. Substances that have considerable solubility in the aqueous phase, such as alcohols, glycols and salts, normally act as inhibitors to hydrate formation, possibly due to the increased competition for water molecules by the dissolved inhibitor molecule or ion through hydrogen bonding for alcohols or glycols, or via Coulombic forces (for salt ions) (Sloan and Koh 2007). As a first try, it was speculated that the temperature depression would be equal to the depression observed in the ice freezing point temperature in the presence of the inhibitor. However, it was shown that for the hydrates temperature, the depression is lower by a factor of

$$\Delta H_{ice}^{mol,\,fus} \Big/ \Delta H_{hyd}^{mol,\,diss} \tag{2.10}$$

where $\Delta H_{\text{ice}}^{\text{mol, fus}}$ represents the enthalpy of phase change of ice from the solid state to liquid state.

It has been observed that the energy effects on the inhibition phenomenon are not significant, i.e., inhibitors do not increase nor decrease the dissociation enthalpy. Therefore, from Clapeyron equation, it is possible to conclude that the equilibrium curve has a shift in its position, being parallel to the original non-inhibited hydrate equilibrium curve.

Alcohols (such as methanol, ethanol and glycols), present at least one hydroxyl group that is capable to form hydrogen bonds with water. On the other hand, the hydrocarbon end of the alcohol causes a clustering effect, as observed in hydrates. Therefore, these components act as inhibitors by competing with the original guest molecules by both hydrogen bonding with water and clustering. This last effect can act as a promoting effect, since it can induce the formation of hydrate to stabilize the original guest molecule. However, this is only observed at very low concentrations of the inhibitor. At larger concentrations, the effect of the hydrogen bonding is enhanced and inhibition occurs. When compared to typical alcohols, glycols have an enhanced inhibition effect due to the presence of more hydroxyl groups, capable to compete for water to bond.

Salts can also act as inhibition agents. However, the mechanism through which it inhibits hydrates formation is different than what is observed in alcohols (Sloan and Koh 2007). The salt ionizes in solution and interacts with the dipoles of the water molecules with a much stronger Coulombic bond than either the hydrogen bond or the van der Waals forces (that cause clustering around the non-polar solute molecule). The stronger bonds of water with salt ions inhibit hydrate formation, since water is more attracted to ions more than to the hydrate structure. Also, a decrease on the guest molecule solubility is usually verified.

Kinetic inhibitors are low molecular weight polymers dissolved in a carrier solvent and injected into the water phase. These inhibitors bond to the hydrate surface and

prevent plug formation for a long period of time. The use of these inhibitors is widely used in pipelines, to prevent plugging, since it prevents the plug formation for a longer period than the pipeline residence time (Sloan and Koh 2007). The mechanism of inhibition is not yet fully understood. However, it appears that these molecules work by preventing, or slowing down, the hydrates growth rate. Polymers such as PVP, PVCap, Polyalkylacrylamides and amino acids are known for being kinetic inhibitors.

On the opposite side of the equation, promoters facilitate the production of hydrates. As inhibitors, there are two types of promoters: thermodynamic and kinetic.

Thermodynamic promotion of gas hydrates is a consequence of the active formation of mixed promoter/gas hydrates at moderate conditions of temperature and pressure. The hydrates formed in this way serve as storage medium for gas-like components but may also contain significant amounts of the added promoter.

Kang et al. (2001) studied the influence of THF (tetrahydrofuran) in the $N_2/CO_2$ mixed system, determining the hydration number and the dissociation enthalpy. It was observed that the dissociation enthalpy increases in the presence of THF. The addition of THF (that forms hydrates at 1 bar and 4 °C, according to Delahaye et al. (2006) and Strobel et al. (2009)) to the $N_2/CO_2$ system changed the hydrate structure I to II and increased the total amount of entrapped guest species, thus leading to an enhanced hydrate stability. As a result, the enthalpy of dissociation increased up to a factor of 2. This was also observed by Delahaye et al. (2006) or Lirio and Pessoa (2013). Furthermore, it was observed that the enthalpy increases with the increase of the THF concentration (Figure 2.17).

The addition of THF in the $N_2/CO_2$ system has a very significant impact on the equilibrium conditions, shifting down the equilibrium curve. Various other compounds present the same effect as THF, such as TBAB, cyclopentane or propane, usually large molecules that crystallize hydrates easily (Dashti et al. 2015). It is

however, claimed that $CO_2$ gas uptake in hydrates is larger when using THF than TBAB or others (Figure 2.18).

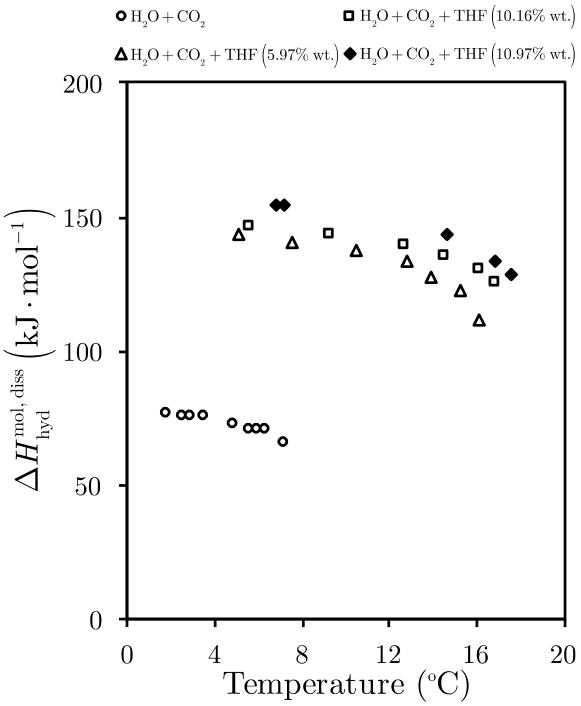



Figure 2.17 – Influence of THF on the dissociation enthalpy of $CO_2$ hydrates (data from Delahaye et al. (2006)).

Recently, a process for the $CO_2$ sequestration as hydrate using 30 ppm of nanographene oxide-based nanofluid is described, recovering approximately 95% of the gaseous $CO_2$ (ZareNezhad and Montazeri 2016).

Regarding kinetic promoters, Zhang et al. (2014) have tested the surfactant SDS (sodium dodecyl sulphate) in the $N_2/CO_2$ system, together with the thermodynamic promoter THF. Kinetic promoters only function is to increase hydration kinetics, without altering its thermodynamic equilibrium. The mechanism through which kinetic promoters operate is still unclear. However, it is speculated that these surfactants have the capacity to increase the gas dissolution rate. These molecules, containing a hydrophilic and hydrophobic end, interact with the gas molecule through strong hydrophobic interactions. Migration of the formed surfactant-gas associates to water molecules and/or structured water molecules is much easier than for pure gas molecules, due to stronger affinity between water molecules and the

hydrophilic end of the surfactant, thus reducing induction time (Zhang et al. 2007). In this sense, kinetic promoters operate as common catalysts, since they accelerate the reaction by create an intermediary complex molecule, but do not enter in the reaction, nor alter the system's thermodynamics.

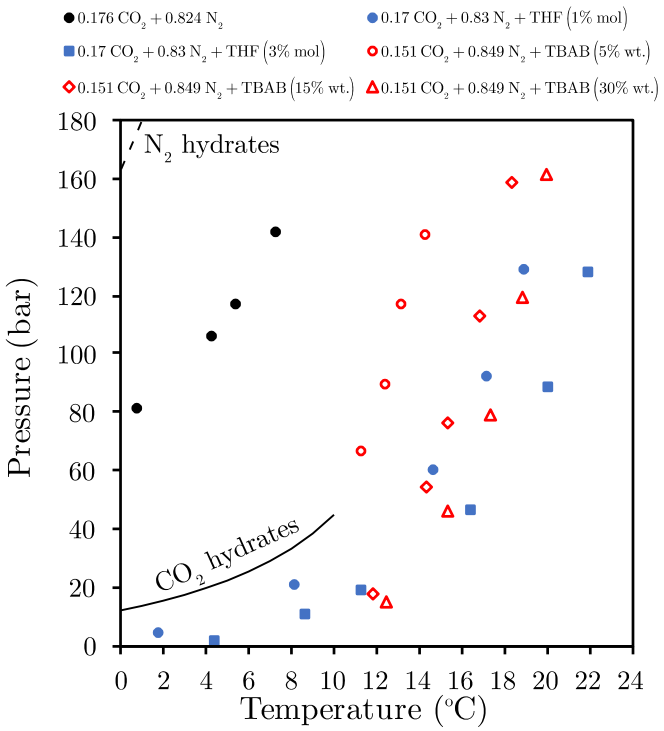



Figure 2.18 – Phase equilibrium data for the system $N_2/CO_2$ and the influence of THF and TBAB (data extracted from Ma et al. (2016)).

Many surfactants have been investigated for hydrate-based $CO_2$ separation. Tween-80 (T-80), dodecyl-trimethyl-ammonium chloride (DTAC) and SDS are the most widely used. Amongst these three surfactants, SDS shows the greatest effect on hydrate promotion (Dashti et al. 2015).

### 2.3.4 Applications

#### *2.3.4.1 Pipeline Flow Assurance*

Although the discovery of hydrates was made long before, research only started to focus on hydrates when Hammerschmidt (1934) concluded that natural gas pipeline plugging was due to hydrates formation and not to ice.

The coexistence of free water and light hydrocarbons, such as methane, is very common. In particular, during deep-water operations in oil and gas production, where thermodynamic conditions are ideal for the formation of hydrates in pipelines, the presence of water is extremely common. This can pose a serious problem if the concentration of hydrates is large enough, so that the transported fluid does not possess enough momentum to drag the solids. This originates an increase of the pressure drop, and thus a decrease of the velocity, which often results in the deposition of the solids at the bottom of the pipelines, and eventually leading to complete blockage of the pipeline. Hydrate plugs interrupt normal operation and can take days or months to dissociate, posing great economic loss and hazardous conditions. Hydrate plugging in long (and often sub-seafloor) flow lines is even more problematical, since it can present itself as a challenge just to accurately locate the blockage site. A possible hydrate formation in pipeline mechanism is presented by Turner (2005) and represented in Figure 2.19.

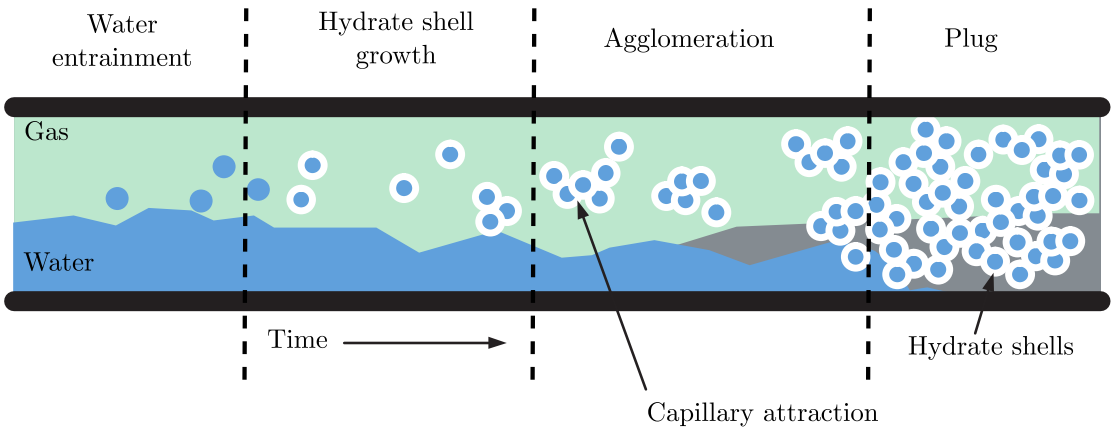



Figure 2.19 – Plug formation via aggregation (Sloan and Koh 2007).

Because of this serious risk of pipeline plugging, typical operations prior to pipeline transportation comprise one or more units with the purpose of removing any other undesirable hydrate-former compounds (such as sulphurs) and water. However, there is still the possibility of some water transport along with the hydrocarbons, posing a severe risk of pipeline blockage. The avoidance of the plugging during operations is difficult, since temperature and pressure are not easily controlled along the pipeline.

Therefore, the use of inhibitors, such as methanol, is required and often used. Also, pipeline insulation is required to minimize de risk of hydrate formation.

Hydrate prevention is usually expensive in both capital and operational expenditure, with an estimation of approximately 1 million US dollars per day being used on the injection of inhibitors (Gao 2006).

This risk is particularly relevant in gas transportation, since it does not possess enough inertia to drag the solids, due to the large differences of density between the hydrates and the gas. If the continuous phase is a liquid with density very close to the hydrate density, then that problem should not be an issue, as long as the solids concentration is not large. This is due to the fact that hydrates possess mechanical properties that are very similar to the properties presented by ice, which is known to flow in slurries with no efforts (Liu et al. 1988). The critical variable is the gas/water ratio. For large gas/water ratio, it is expected serious pipeline plugging, while for low gas/water ratio, the excess water has capacity to drag the particles at a cost of a slight increase in the pressure drop. Andersson and Gudmundsson (2000) studied the pressure drop on hydrate slurries, leading to the conclusion that if the velocities are large enough, so that turbulent eddies are formed, then the presence of hydrates does not lead to a significant pressure increase. On the other hand, on laminar regime, that pressure drop increase is observed.

#### *2.3.4.2 Hydrates as an Energy Resource*

Recently, hydrates of predominantly methane have been found in sediments below the seafloor and in permafrost regions (Haq 1999). Because of hydrates capacity to enclose large amounts of gas in a small volume (it can reduce the volume up to 180 when compared to STP gas), it is estimated that the amount of light hydrocarbons of interest, in particular methane, is up to one order of magnitude larger than in all known reservoirs in the world (Collett 2003). Therefore, these hydrates represent a very significant source of clean energy, if an economically feasible extraction process is developed.

#### *2.3.4.3 Hydrates as Cooling Fluid*

Recently, some research groups have studied the use of hydrates (in the form of slurries) in refrigeration systems, acting as secondary fluid. As an initial response to the need of reducing the energy expenditure of air conditioning systems, water and/or ice was used as a cooling storage medium. This way, the refrigerator can be operated at high coefficient of performance (COP). The problem is that a system like this requires a volume of ice larger than the system itself, making it impracticable. However, the use of gas hydrates can solve this problem, since they present a higher thermal density than ice.

Ogoshi and Takao (2004) tested this application using an aqueous slurry of hydrates using TBAB as the guest molecule. This particular hydrate can be crystallized at relatively mild conditions (it can be formed at atmospheric pressure, and at temperatures near 5 °C). It is claimed that TBAB hydrates can present 2-3 times larger cooling storage capacity than conventional chilled water or ice. Also, the slurry has the consistency of soft ice cream, since it presented particles in size range of 10-100 μm (Figure 2.20). This means that the flow is stable and that it does not adhere or block pipes/valves nor heat exchangers.



Figure 2.20 – Clathrate hydrate slurry (Ogoshi and Takao 2004).

The same observation regarding slurry flowability is made by Hu et al. (2010). Hu et al. (2010) also measured the pressure drop for different solids concentration in the slurry, and also analysed the slurry stability, displaying a very good stability for 11.5 hours.

#### *2.3.4.4 Hydrates as CCS Solution*

A potential alternative to the methods described in Section 2.2.1 is by using gas hydrates to capture and store $CO_2$. Hydrates can be useful in this field in all three CCS stages (capture, transportation and sequestration/storage).

Regarding capture, it has been widely documented the potential of hydrates for gas separation. As any other separation methods, this separation is based on the different behaviour of different compounds in a physical or chemical process. For example, separation through distillation is based on different volatilities of components; membrane separation through molecular sieve or filtration is based on different molecule/particle sizes; sedimentation, elutriation or cyclone-based separation is based on different densities; gas absorption using solvents is based on the different solubility or reactivity between the solute and the solvent; adsorption is based on different affinity to physically bond to the adsorbent; and hydrates-based separation is based on the different affinities for the guest molecules to crystallize hydrates.

The use of hydrates for gas separation has been studied for $CO_2$ from flue gas (Kang and Lee 2000, Tajima et al. 2004, Linga et al. 2008), methane from nitrogen (Dabrowski et al. 2009, Zhao et al. 2013), hydrogen sulphide and sulfur hexafluoride on gas streams (Vorotyntsev et al. 2001, Cha et al. 2010), hydrogen purification (Rice 2006), and many others (Ballard 2002).

For $CO_2$ separation from flue gas in a post-combustion process, Kang and Lee (2000) studied the temperature and pressure conditions for different $CO_2$ concentrations in the flue gas, using a thermodynamic promoter (THF). It is claimed that about 99% mol of $CO_2$ from the original flue gas can be recovered, using a process based on hydrate crystallization and dissociation, similarly to the amine absorption and desorption process (Figure 2.21).

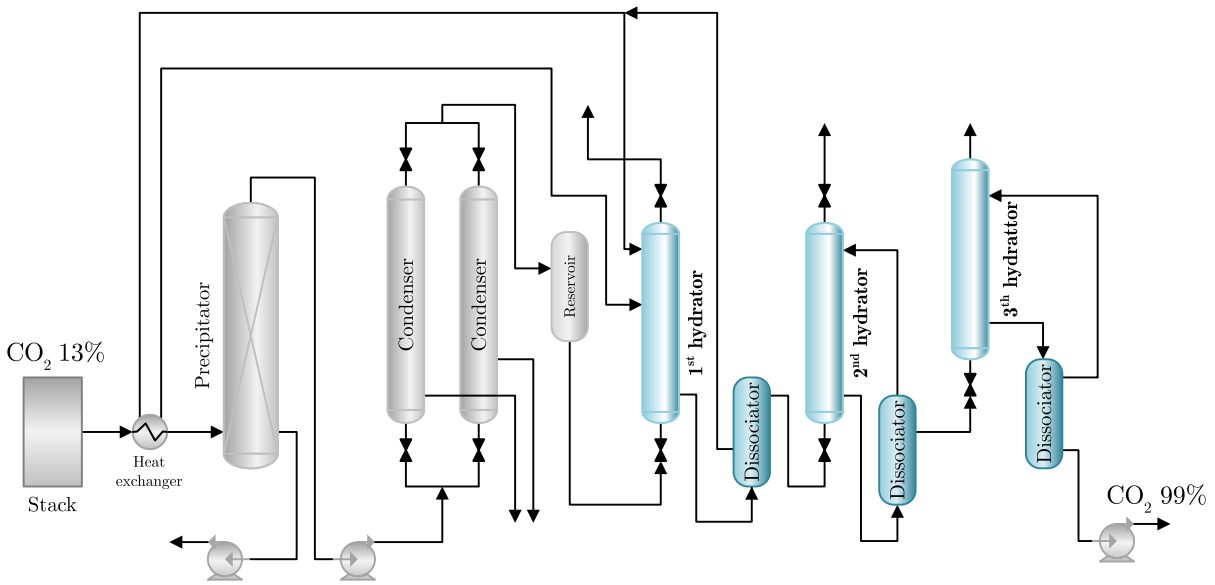



Figure 2.21 – Process flow diagram of a hydrate-based $CO_2$ recovery process (Kang and Lee 2000).

Both nitrogen and carbon dioxide are able to produce hydrates at different conditions (Sloan and Koh 2007). However, mixtures of nitrogen and carbon dioxide form hydrates at conditions between the pure gas conditions. Since $CO_2$ forms hydrates at lower pressures than $N_2$, it is expected that the formed hydrates from the mixture is $CO_2$-rich, thus resulting in a $N_2$-rich gas phase.

If the product of the process is liquid carbon dioxide (as in the amine scrubbing process), the hydrate-based separation contains two different sections, one for capture and one for release. In the capture section, the flue gas is compressed, cooled and mixed with water, forming hydrates. The produced slurry is then transferred to the release section of the process, where the solids are dissociated by heating or by lowering the pressure. The captured gas is released at conditions of moderate to high pressure, and low temperature.

Zhang et al. (2014) studied the influence of the combined use of a thermodynamic promoter (THF) and a kinetic promoter (SDS) for the $N_2/CO_2$ system, and developed a model to predict the equilibrium curve using these promoters. These promoters lower the pressure (or increase the temperature) of equilibrium, which was initially seen as one of the main disadvantages of a hydrate-based capture process.

The use of different promoting agents for the separation of $CO_2$ is reviewed by Dashti et al. (2015) and Ma et al. (2016).

Leppin and Sivaraman (2005) proposed a method of separating carbon dioxide from methane taking advantage of the capacity of $CO_2$ to displace methane molecules in the hydrate. This means that the induction of a driving force into the system could make the methane molecules to leave the hydrate structure and be replaced by carbon dioxide molecules, capturing $CO_2$ and cleaning methane.

Regarding transportation, the possibility of transporting $CO_2$ is still open to discussion, although there are some groups addressing the potential of this idea. The fact that there is a reduction in volume of the gas when using hydrates (even if the transportation is made using a 30% in weight slurry, there is a reduction in volume in 60 times when compared to STP gas) makes it potentially interesting for an economically competitive transport. Also, there is a significant reduction in compression costs of $CO_2$ if using hydrates, when compared to supercritical $CO_2$.

Finally, for $CO_2$ hydrates sequestration, deep-ocean deposition (IEA 2004) or natural gas reservoirs storage (Kvamme et al. 2007) have been proposed. The second option has the advantage of the possibility of using the hydrates to release the hydrocarbon gas, in a process similar to EOR.

#### *2.3.4.5 Other Applications*

Several research groups have studied other potential applications of hydrates in different fields. These works comprise areas such as in water desalination (Javanmardi and Moshfeghian 2003), recovery of contaminants from groundwater (Bontha and Kaplan 1999), biotechnology (Nguyen et al. 1991) or for separation of ionic liquids (Mohammadi et al. 2012).

### 2.3.5 Continuous Production

Not many works have addressed the subject of continuous production of gas hydrates. In a continuous production process, both gas and water streams are continuously fed, keeping the system at constant pressure (there is a reduction mostly due to friction).

Gudmundsson et al. (2000) developed a continuous process consisting in a stirred tank for natural gas hydrates production. The experimental setup (illustrated in Figure 2.22) is capable to operate at pressures up to 120 bar and temperatures in the range of 0-20 °C, and can produce up to 1 $kg \cdot h^{-1}$ of NG hydrates. Mixing in tank, essential for hydrates production, was achieved using a variable speed magnetically driven straight blade impeller. The gas is injected to the 9 litres reactor through a sparger at the bottom. The setup comprises a separator to separate the slurry from the gas, and a shell-and-tube heat exchanger to remove the reaction heat. The work showed a higher consumption rate of gas during hydrate formation with increasing gas injection rate at a given temperature. Also, a decreasing temperature at a given gas injection rate resulted in a higher gas consumption. Both situations increase supersaturation conditions, thus increasing kinetics.

Tam et al. (2001) presented a project for carbon dioxide capture for IGCC power plants using the proprietary SIMTECHE process, developed at the Los Alamos National Laboratory. Within the scope of the SIMTECHE project, Yang et al. (2008) studied the heat exchange capacity of multi-section tubular reactor with a jacket that was fed with clean coolant in each section (the process is represented in Figure 2.23). Results from the study show that the global heat transfer coefficient decreases with the increase of the solids content.

Yang et al. (2011) studied the kinetics of the process and tried to correlate the process kinetics with the multiphase flow observed patterns.

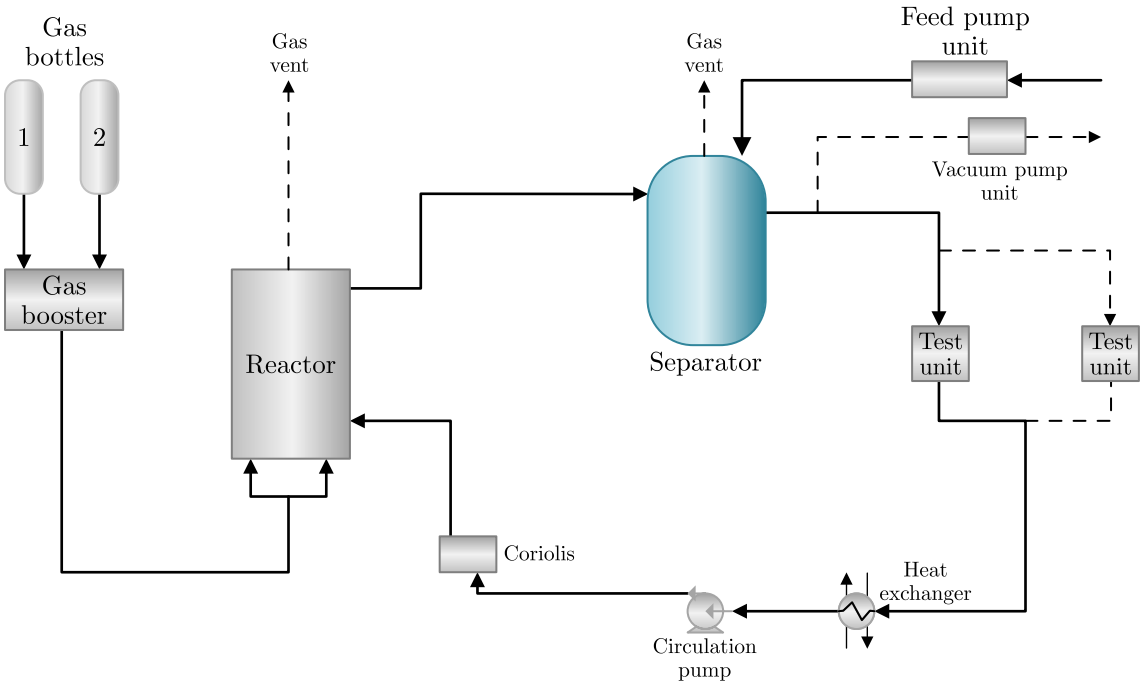



Figure 2.22 – Simplified process flow diagram of the experimental setup by Gudmundsson et al. (2000).

Groen (2012) described a system, consisting of two thermostatic baths and two coil heat exchangers, a gear pump and two buffer vessels. A saturated mixture of water and $CO_2$ is cooled at temperatures between 4 and 8 °C under hydrate forming conditions. The density was measured to estimate the solids content of the slurry.

Lobregt et al. (2016) proposed the use of a 1.9 meters in height fluidized bed heat exchanger for continuous production of $CO_2$ hydrates, for the application in fresh products rapid chilling. The setup operates at pressures in the range of 25-35 bar, achieving solid concentration of 40% in weight.

Tajima et al. (2005) studied the influence of static mixers using different elements, for the production of $CO_2$ hydrates from liquid carbon dioxide and water. Depending on the different elements and on the different velocities, Tajima et al. (2005) was able to identify and classify 6 different hydrate formation patterns. The temperature of the apparatus was controlled by the brine-circulation system (water and ethylene glycol mixture) covering the supply lines of liquid $CO_2$ and water, the mixer unit, and the post-mixing observation unit. The most important conclusion from this work

is that the increase of the velocity (of both water and liquid $CO_2$) resulted in a better-dispersed phase, while low velocities resulted in agglomeration that could lead to plugging.

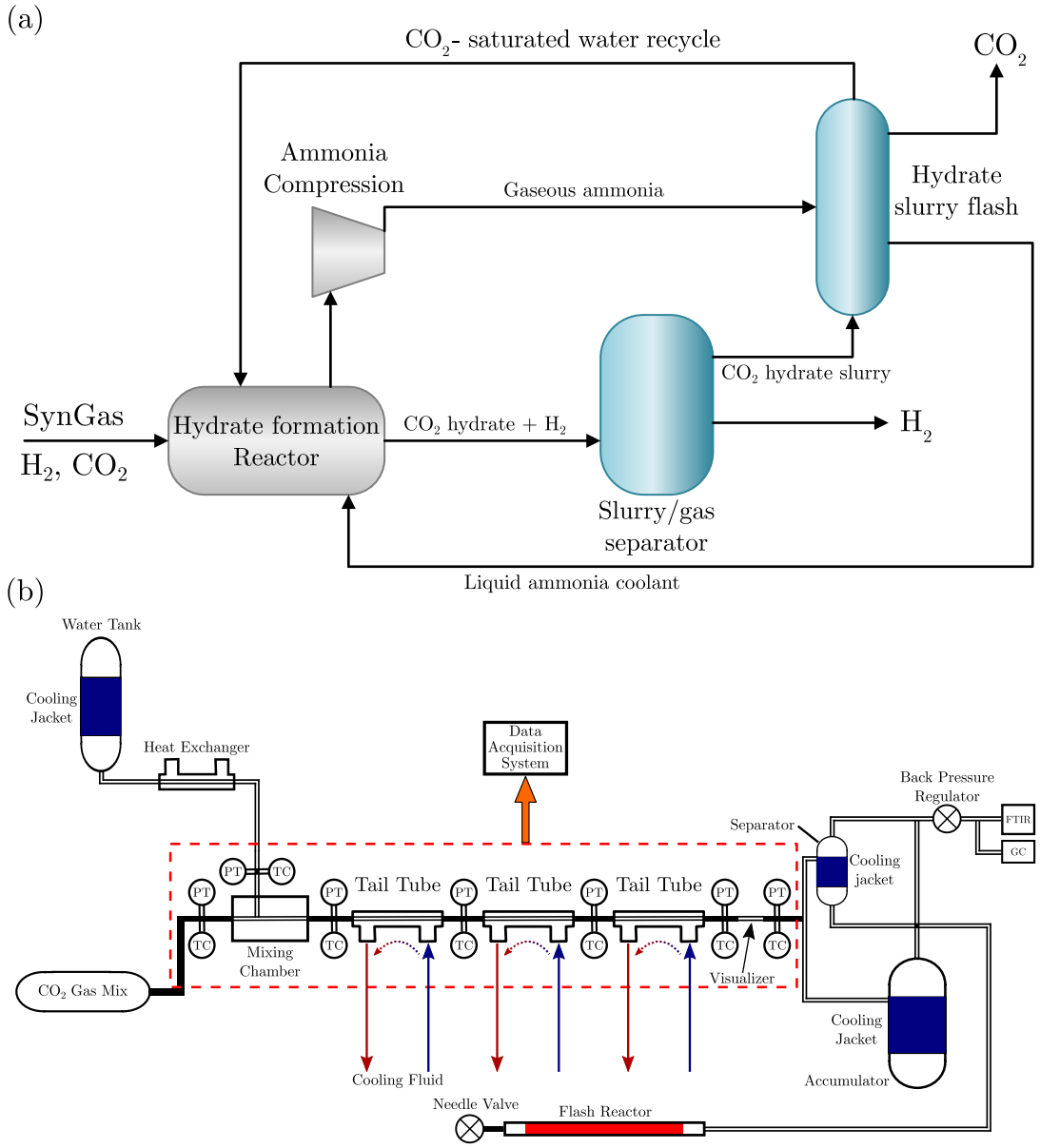



Figure 2.23 – (a) Block flow diagram of the SIMTECHE capture process (Yang et al. 2011); (b) Schematic of the experimental setup using a tail-tube reactor (Yang et al. 2008).

Regarding hydrate production using microfluidics technologies, not much has been described to this date, however, some works in that field start to appear, taking advantage of the mass and heat exchange capacities of such devices (Flowers and Hartman 2013).

## 2.4 Static Mixers

### 2.4.1 Commercial Static Mixers

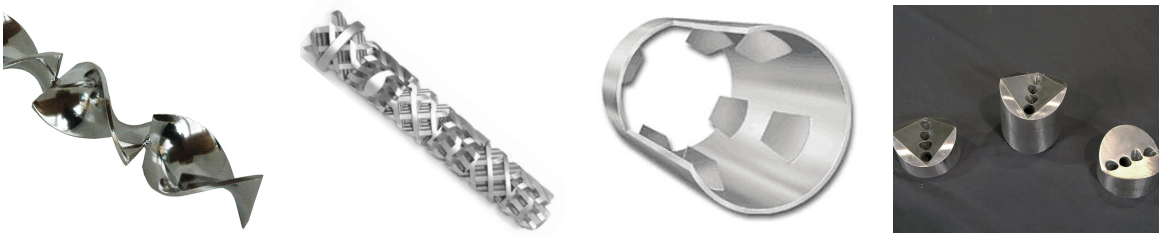
Static mixers have been used in industrial applications to perform continuous operations, becoming standard equipment since the 1970s, as an alternative to mechanical mixers, for mixing of miscible or immiscible fluids, homogenization of solid particles, and for heat and mass transfer enhancement (Szalai and Muzzio 2003, Thakur et al. 2003). This type of mixers is applied in a wide range of different industrial processes in the pharmaceutical, petrochemical, food, cosmetics, biotechnology, water/wastewater, paper or polymer industries (Thakur et al. 2003, Meijer et al. 2012).

The effectiveness of static mixers to deliver good mixing of miscible fluids or to enhance heat and mass transfer rates comes from their capacity to induce transverse mixing and to bring fluid elements into close proximity (Thakur et al. 2003). The most interesting characteristic of static mixers is that the fluids are mixed by flow energy alone, thus they do not require external power except the required power for pumping the fluids through the mixer; furthermore, static mixers usually require small space, low equipment cost and no moving parts (Thakur et al. 2003). However, an overall system pressure drop is usually observed in static mixers, as well as a greater potential for fouling, and greater cost (Thakur et al. 2003).

Several static mixers have become commercially available (Figure 2.24) and can be of different types:

- Twisted static mixers constructed of right and left twisted plates such as Kenics mixer, or the combination of individual segments positioned to divide and rotate the flow alternately such as the Statiflo static mixer series (Figure 2.24a).

- Structured static mixers made of stacked lamella elements positioned to create intricate network of flow channels such as the SMV, SMX, SMXL static mixers, the KMX static mixer or the Konax static mixer (Figure 2.24b).
- Vortex generating static mixers, where mixing is accomplished by controlled vortex structures generated by elements that suddenly change the cross section of the tubing, such as the High Efficiency Vortex Mixer (HEV) and the compacX (Figure 2.24c).
- Interfacial surface generator (ISG) static mixer consisting of individual mixing elements that are stacked in a tubular housing (Figure 2.24d).



(a) (b) (c) (d)

Figure 2.24 – Examples of commercially available static mixers: a) Kenics mixer from Chemineer Inc. (Chemineer 2016b); b) KMX mixer from Sulzer (Sulzer 2016); c) HEV mixer from Chemineer Inc. (Chemineer 2016a); d) ISG mixer from Ross Mixers (Ross 2016).

The use of static mixers is of great importance in processes where heat or mass transfer is of crucial importance for the success or failure of the system. Hence, in the following section, the NETmix mixer/reactor, a specific type of static mixer, is carefully described.

### 2.4.2 The NETmix Technology

NETmix is a novel mixing technology (Lopes et al. 2005) that consists on a network of mixing chambers interconnected by transport channels (Figure 2.25a). The NETmix network is built from the repetition of unit cells, organized into consecutive pairs of $n_x$ rows, with $n_y$ and $n_y - 1$ number of cells, and the NETmix device is open to flow through equal number, $n_x$, of inlets and outlets. Each unit cell consists of one chamber and two channels (two inlet and two outlet half channels) oriented at a 45° angle from the main flow direction and can be built out of either cylindrical chambers

and rectangular channels (2D unit cell, Figure 2.25b), or spherical chambers and cylindrical channels (3D unit cell, Figure 2.25c).

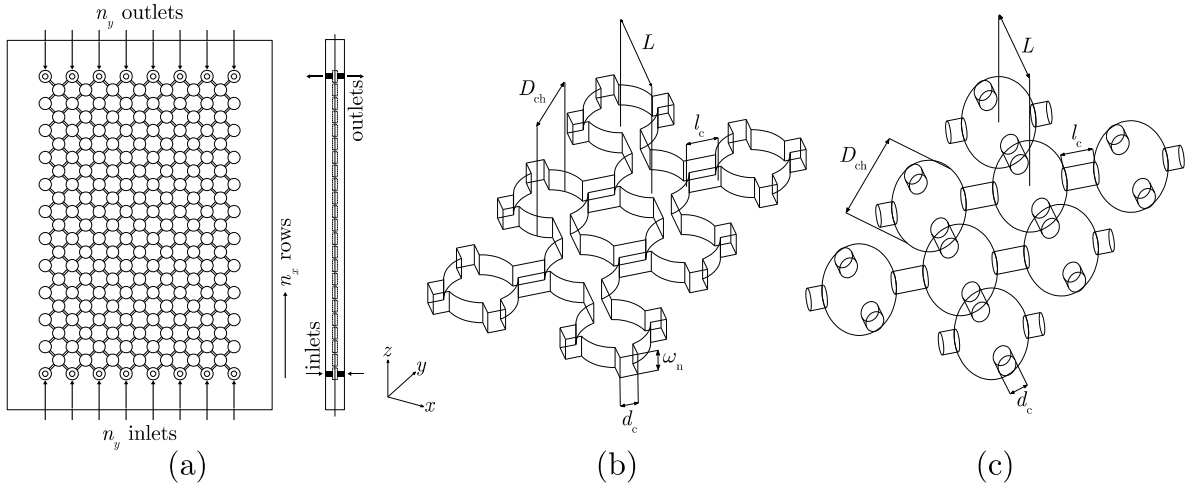



Figure 2.25 – (a) NETmix network; (b) network of 2D unit cells; (c) network of 3D unit cells.

The characteristic dimensions of each unit cell are the chamber diameter, $D_{ch}$, the channel width or diameter, $d_c$, and for the 2D unit cell, the network depth, $\omega_n$. $L$ is the distance that separates the centers of two adjacent chambers and $l_c$ is the length of each channel. The network size is given by the number of rows, $n_x$, and the number of columns, $n_y$.

Proper mixing in NETmix can only be achieved above the critical channel's Reynolds number, where the flow inside the chambers evolves from a fully developed laminar flow to a self-sustained dynamic and chaotic oscillatory flow regime inducing strong laminar mixing (Laranjeira et al. 2009). This occurs due to the geometric characteristics of the NETmix network and the local hydrodynamic instabilities induced by the immerging jets interactions at the chambers. This behavior is clearly visible in Figure 2.26.

Mixing in a NETmix reactor has been measured experimentally, and characterized through intensity of segregation from CFD simulations (Laranjeira et al. 2009, Gomes et al. 2011), proving that mixing can be effectively and efficiently controlled, making

this reactor particularly suited for complex and fast kinetics reactions where mixing quality and intensity are critical.

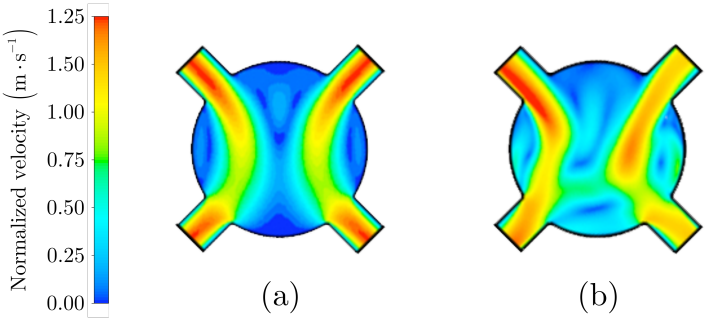



Figure 2.26 – Velocity magnitude contour maps of NETmix chambers at: a) $\mathrm{Re} = 50$ (below critical Reynolds number); b) $\mathrm{Re} = 500$ (above critical Reynolds number). Adapted from Laranjeira (2005).

NETmix allows the careful distribution of reactants and flow rate control at the inlet, in accordance to the intended reaction stoichiometry, and product extraction with different properties at different outlets (Laranjeira et al. 2011). The network can be easily scaled-up or numbered-up depending on the process and production objectives.

Three different NETmix prototypes currently exist for research and development of new products. The reactors, shown in Figure 2.27, were built for different purposes.

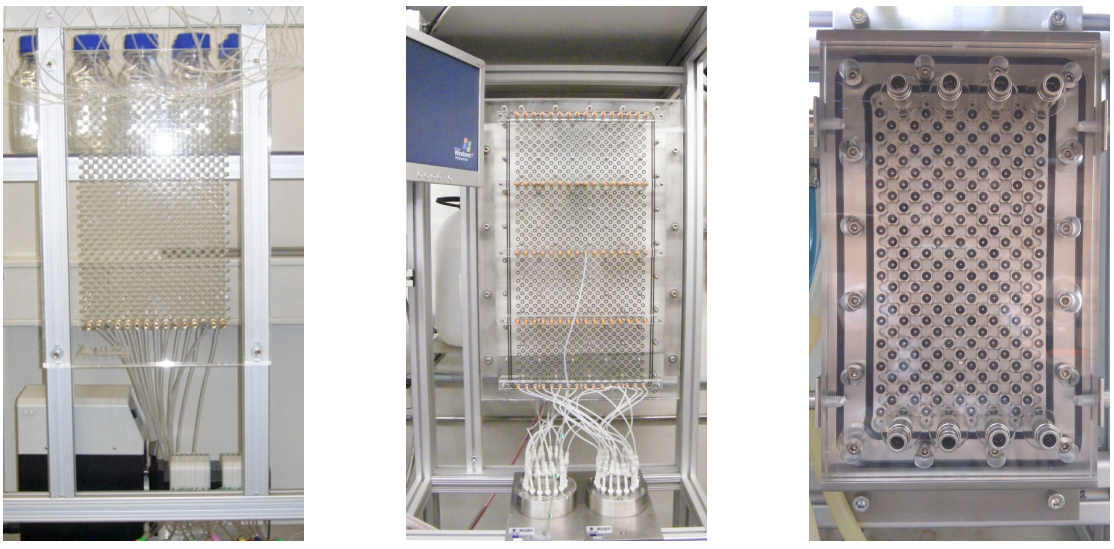



Figure 2.27 – NETmix prototypes: a) NETmix 3D; b) Multi-Inlet NETmix 2D; c) Lab-Scale NETmix 2D.

NETmix 3D was the first ever built prototype (Laranjeira 2005) and has spherical chambers and cylindrical channels. NETmix 3D was built from two acrylic slabs

where half chambers and channels were imprinted and then glued together. The work developed by Gomes (2011) allowed the configurational transition from 3D to 2D, representing a considerable decrease on the construction complexity since the chambers and channels are imprinted on only one slab. The two slabs are no longer glued together allowing the fast disassembling and easy cleaning of the reactor, and mechanical sealing is realized by mechanical compression and o-rings.

The Lab-scale NETmix 2D is a small lab-scale unit that was built for research projects with small throughputs. The Lab-scale NETmix 2D is composed of a stainless steel plate where the chambers and channels are imprinted and a front cover that can either be made of acrylic (for flow visualization) or stainless steel (for fluids that can chemically attack acrylic or for reactions at high temperatures/pressures).

For larger throughputs, the Multi-Inlet NETmix 2D, built entirely out of acrylic, can be used. The Multi-Inlet NETmix 2D has the particularity of incorporating multiple inlet injection points along the reactor. The geometrical characteristics of the two 2D NETmix reactors are summarized in Table 2.7.

The NETmix technology has been applied for the production of several products and/or processes. An industrial site using NETmix as the heart of the process (Figure 2.28), was built and is located at TECMAIA – Parque de Ciência e Tecnologia da Maia, in Portugal, for the production of high quality synthetic nanocrystalline hydroxyapatite, under the brand name of nanoXIM (Fluidinova), commercialized by the Portuguese company Fluidinova S.A., a spin-off company from LSRE (Laboratory of Separation and Reaction Engineering) at FEUP (Faculdade de Engenharia da Universidade do Porto).

Production of nanocrystalline hydroxyapatite using NETmix started before Fluidinova was created (Silva et al. 2008, Gomes et al. 2009). Several other products were produced at laboratorial scale using the Lab-scale NETmix 2D, such as metal-organic hybrid materials (MOFs) (Costa 2012, Fonte 2013) production in a continuous process, and nanoparticles of magnetic iron oxides (Leblebici et al. 2013,

Lima et al. 2014). The technology has also been employed as a photoreactor for the photo-Fenton process (Lima et al. 2016, Lima et al. 2017) and for photocatalysis using $TiO_2$ for $Cr(VI)$ reduction (Marinho et al. 2017) or n-decane oxidation (Filho et al. 2017).

Table 2.7 – NETmix reactor prototypes geometrical characteristics.

| **Device** | **NETmix 3D** | **Lab-scale NETmix 2D** | **Multi-Inlet NETmix 2D** |
|---|---|---|---|
| Number of Rows, $n_x$ | 49 | 29 | 65 |
| Number of Columns, $n_y$ | 15 | 8 | 16 |
| Chamber Diameter, $D_{ch}\,(\mathrm{mm})$ | 7 | 6.5 | 8.75 |
| Channel Width, $d_c\,(\mathrm{mm})$ | 1.5 | 1 | 1.5 |
| Network Depth, $\omega_n\,(\mathrm{mm})$ | – | 3 | 5.9 |
| Distance Between Centre of Two Adjacent Chambers, $L\,(\mathrm{mm})$ | 10 | 8.5 | 14 |
| Channel Length, $l_c\,(\mathrm{mm})$ | 3.2 | 2.1 | 5.4 |
| Network Volume, $V_n\,(\mathrm{mL})$ | 140 | 23 | 1500 |




(a) (b) (c)

Figure 2.28 – nanoXIM industrial production site at Fluidinova: a) NETmix industrial reactor; b) Centrifuge; c) Spray-dry unit (adapted from Faria (2008)).

### *2.4.2.1 Energy Performance*

The use of static mixers has attracted a lot of interest by the scientific community, since it constitutes an alternative to mechanical stirrers (such as blades) without the

inclusion of moving parts, and taking advantage of their particular geometry that uses solely the flow energy to bring the fluid elements together and thus, enabling mixing. This means that the energy is more efficiently used in static mixers, when compared to typical mechanical stirrers.

Fonte et al. (2013) studied the NETmix energy efficiency and compared its performance with the performance shown by other mixing devices (static mixers or not). The pressure drop in NETmix 3D, Lab-Scale NETmix 2D and Multi-Inlet NETmix 2D were experimentally determined, using water and aqueous glycerol solutions, using a Validyne DP 215 differential pressure sensor to measure the pressure differential between the inlet and the outlet of the reactor. A mechanistic model, based on a network model for flow in packed beds proposed by Martins et al. (2007), was developed. The pressure drop for a NETmix network is given by

$$\Delta p_{\mathrm{NETmix}} = \frac{n_x}{8}\frac{\mu^2}{\rho}\frac{\left(\omega_{\mathrm{n}}+d_{\mathrm{c}}\right)^2}{\omega_{\mathrm{n}}^2 d_{\mathrm{c}}^2}\mathrm{Re}_{\mathrm{c}}\left[\frac{32\left(\omega_{\mathrm{n}}+d_{\mathrm{c}}\right)}{\omega_{\mathrm{n}} d_{\mathrm{c}}}\left(l_{\mathrm{c}}+\frac{4\omega_{\mathrm{n}} d_{\mathrm{c}}}{\pi\left(\omega_{\mathrm{n}}+d_{\mathrm{c}}\right)}\right)K\,\mathrm{Re}_{\mathrm{c}}\right] \qquad (2.11)$$

where $\Delta p_{\mathrm{NETmix}}$ is pressure drop through the NETmix reactor, $\mathrm{Re}_{\mathrm{c}}$ is channel's Reynolds number, $\rho$ and $\mu$ are the fluid's density and viscosity, respectively. $K$ is a coefficient equivalent to the loss coefficients for sudden contractions and expansions systems, dependent on the geometrical characteristics of NETmix. The value of $K$, obtained by the minimization of least squares from the experimental data and the model, is 0.94 for NETmix 3D, 1.2 for the Lab-scale NETmix 2D and 1.3 for the Multi-Inlet NETmix 2D (Fonte et al. 2013). Comparison between the model and experimental data are illustrated in Figure 2.29.

In terms of its energy performance, the power number and the Z factor of NETmix were determined based on experimental measurements of the pressure drop, as well as CFD simulations (previously validated from pressure drop measurements), and proved to be competitive with existing mixers (Fonte et al. 2013), as illustrated in Figure 2.30.

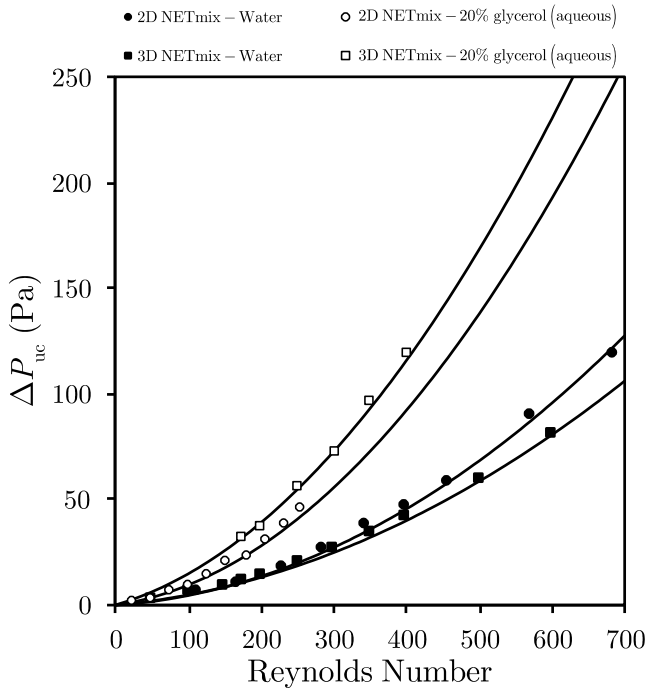



Figure 2.29 – Comparison between experimental unit cell pressure drop and model from Equation 2.11 for different NETmix devices (adapted from Fonte et al. (2013)).

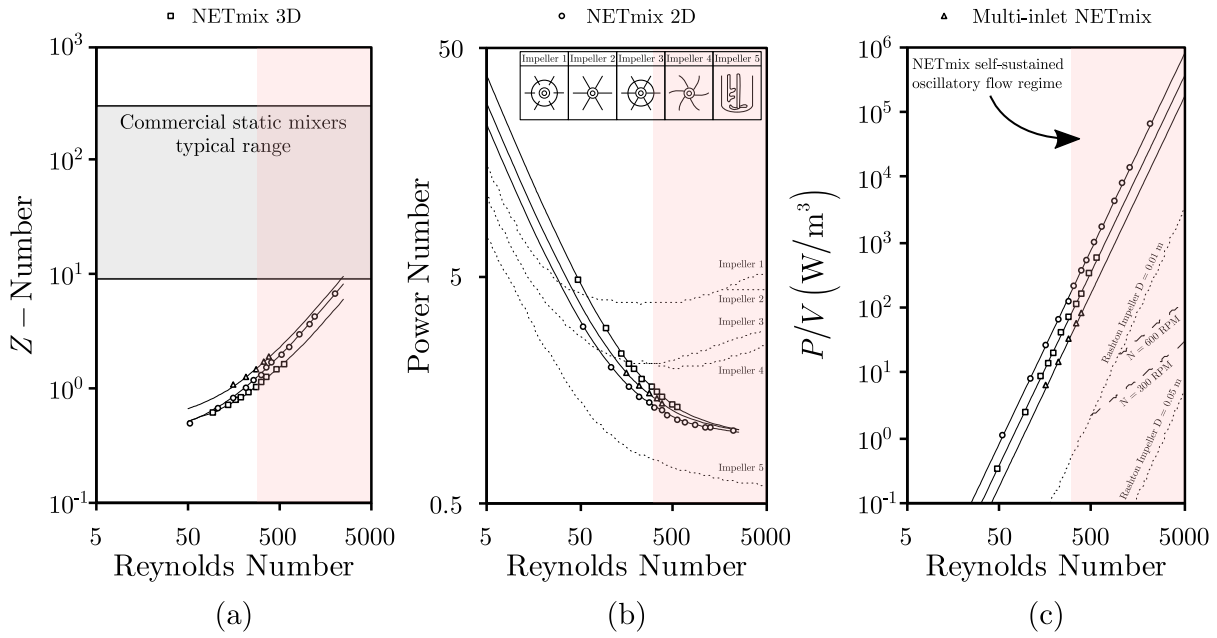



Figure 2.30 – Energy performance of NETmix mixer: (a) Z-number; (b) power number and (c) mixing power per volume (Fonte et al. 2013). Red regions represent the conditions at which flow patterns present an oscillatory and chaotic behaviour.

The Z-factor (Figure 2.30a) is one order of magnitude lower than the corresponding values for other commercially available static mixers, and the power number shows that NETmix is energetically more efficient than typical industrial impellers, when the flow is completely chaotic (Figure 2.30b). Also, the mixing power range delivered

by the NETmix is considerable larger than in stirred tanks using impellers (Figure 2.30c).

#### *2.4.2.2 Previous Works*

Since the filling of the patent by Lopes et al. (2005) and the first studies made by Laranjeira (2005), several other academic and research works have been done using the NETmix technology, to either evaluate and quantify the mixing quality and/or flow characteristics, or to perform chemical reactions, taking advantage of the outstanding enhanced mixing capacity of the device.

The most relevant academic works done to date, both master's or PhD's thesis are presented in Table 2.8. A list of all patents related to the NETmix technology is presented in Table 2.9. Table 2.10 lists all publications to data that directly or indirectly use the NETmix technology, whether it is to assess its properties or to produce products

The wide range of applications presented in Table 2.8 to Table 2.10 shows the large versatility of NETmix, as a mixer and a chemical reactor. Therefore, it is expected that the vast areas of applications of the reactor can grow.

#### *2.4.2.3 The Use of NETmix for Hydrates Production*

The use of the NETmix technology for the production of gas hydrates is the main objective of this work.

NETmix presents mixing capacity that is undeniably superior to other commercially available mixing technologies (either mechanical stirrers or static mixers).

The use of NETmix for the production of gas hydrates relies on the fact that the unique NETmix properties enhances mixing in such a way that typical difficulties usually observed in multiphase reactions, as the case of gas hydrates precipitation, regarding mixing and crystallization can be effectively overcome.

Table 2.8 – List of academic thesis (Masters and PhD's) using the NETmix technology.

| Description | Type | Reference |
|---|---|---|
| – Developing of the concept of NETmix, modelling, CFD simulation and experimental characterization. | PhD Thesis | Laranjeira (2005) |
| – Use of test reactions for micromixing assessment studies in NETmix. | PhD Thesis | Nunes (2007) |
| – Study of the maturation steps involved on the hydroxyapatite production by wet chemical reaction using the NETmix reactor. | MSc Thesis | Correia (2008) |
| – Study of the inclusion of iron to confer magnetic properties to nano-sized hydroxyapatite, using NETmix. | MSc Thesis | Rodrigues (2008) |
| – Optimization of the operational conditions for the production of nanoXIM (at Fluidinova). | MSc Thesis | Faria (2008) |
| – Study of the synthesis of zinc-doped hydroxyapatite for the application in transesterfication reactions, using NETmix. | MSc Thesis | Constantino (2009) |
| – Assessment of mixing mechanisms in NETmix, in both qualitative and quantitative terms, using CFD and experimental flow field characterization. | PhD Thesis | Gomes (2011) |
| – Experimental work to measure pressure drop in two different static mixers, including NETmix. | MSc Thesis | Leblebici (2011) |
| – Continuous production of high quality nanoparticles of hybrid Metal-Organic Frameworks using NETmix. | MSc Thesis | Costa (2012) |
| – Further investigation of the capabilities of the NETmix reactor, including numerical modeling, characterization and product development of high added-value products (Nitrobenzene and MOFs). | PhD Thesis | Fonte (2013) |

Table 2.9 – List of NETmix-related patents.

| Description | Type | Reference |
|---|---|---|
| – European patent of the NETmix concept. | European | Lopes et al. (2005) |
| – International patent of the process of wet precipitation of calcium phosphates (hydroxyapatite) using the NETmix technology. | International | Lopes et al. (2008a) |
| – International patent of the NETmix concept. | International | Lopes et al. (2008b) |
| – International patent of a device for heat transfer based on the NETmix concept. | International | (Lopes et al. 2017) |

Table 2.10 – List of publications in international research journals of works using the NETmix technology.

| Description | Type | Reference |
|---|---|---|
| – Study of the use of NETmix for production of high quality and reproducible hydroxyapatite and particle characterization. | Research Article | Silva et al. (2008) |
| – Characterization of hydroxyapatite nanoparticles produced using NETmix in a continuous process. | Research Article | Gomes et al. (2009) |
| – Description of the network model for the assessment of macro and micromixing in NETmix. | Research Article | Laranjeira et al. (2009) |
| – Experimental validation of the network model. Characterization of the mixing mechanisms at the local scale. | Research Article | Laranjeira et al. (2011) |
| – Network modelling for estimation of pressure drop in NETmix. Assessment of energetic performance and 3D CFD modelling. | Research Article | Fonte et al. (2013) |
| – Degradation of ciprofloxacin on a photo-Fenton process, using magnetic nanoparticles produced using NETmix. | Research Article | Lima et al. (2014) |
| – Validation of the application of NETmix reactor on homogeneous photo-Fenton treatment of natural waters contaminated with organic pollutants using solar light. | Research Article | Lima et al. (2016) |
| – Process intensification of heterogeneous $TiO_2$ photocatalysis using NETmix, to promote the hexavalent chromium reduction to its trivalent state. | Research Article | Marinho et al. (2017) |
| – Comparison of NETmix performance against conventional compound parabolic collector under homogeneous photo-Fenton treatment. | Research Article | Lima et al. (2017) |
| – Process intensification of heterogeneous $TiO_2$ photocatalysis using a UV transparent NETmix. | Research Article | Filho et al. (2017) |

It is expected that hydrates nucleation and growth occurs at larger rates using the NETmix technology, when compared to stirred tanks, since mixing and both heat and mass transfer is enhanced, thus reducing or eliminating transport resistances that limit crystallization kinetics. The first step of the process consists in the interfacial mass transfer of gas to the aqueous phase. Interphase mass transfer is always a challenge, but the work developed by Gomes (2011) shows that small fluid elements are created when a phase is dispersed in a second continuous phase, due to stretching that occurs in chambers, and shearing that occurs in channels. These small fluid elements promote mass transfer due to the increase of the gas-liquid interfacial area. On a second phase, the excess of gas (required in supersaturation conditions)

nucleates and growth occurs. The NETmix proven capacity to produce nanoparticles without the need of thermal or mechanical treatments allows presuming that relatively small particles will be created, as a result of the chaotic and oscillatory flow regime that is observed. This means that the produced slurry should not have significant problems of flow assurance in the reactor. At the same time, heat has to be removed fast enough. If not, the temperature of the system increases, thus reducing the supersaturation conditions, until a point where the hydrates are not thermodynamically stable, and dissociation occurs.

In all of the previously described stages, NETmix can present itself as a competitive advantage to both batch processes and other heat transfer-limited continuous processes.

## 2.5 References

Anderson, G.K., **2003**. "Enthalpy of Dissociation and Hydration Number of Carbon Dioxide Hydrate From the Clapeyron Equation". *The Journal of Chemical Thermodynamics* 35, 1171-1183.

Andersson, V., Gudmundsson, J.S., **2000**. "Flow Properties of Hydrate-in-Water Slurries". *Annals of the New York Academy of Sciences* 912, 322-329.

Aya, I., Yamane, K., Nariai, H., **1997**. "Solubility of $CO_2$ and Density of $CO_2$ Hydrate at 30 MPa". *Energy* 22, 263-271.

Ballard, A.L. **2002**. "A Non-Ideal Hydrate Solid Solution Model For a Multi-Phase Equilibria Program" [*Ph.D Thesis*]. Golden, CO, USA: Department of Chemical and Petroleum-Refining Engineering, Colorado School Of Mines.

Barchas, R., Davis, R., **1992**. "The Kerr-McGee/ABB Lummus Crest Technology For the Recovery of $CO_2$ From Stack Gases". *Energy Conversion and Management* 33, 333-340.

BGS, "Hydrates and Ices Laboratory". *Published online at British Geological Survey - Natural Environment Research Council*. Available at: http://www.bgs.ac.uk/scienceFacilities/laboratories/research/hydrates.html.

Bontha, J.R., Kaplan, D.I., **1999**. "Immobilization or Recovery of Chlorinated Hydrocarbons From Contaminated Groundwater Using Clathrate Hydrates: A Proof-of-Concept". *Environmental Science & Technology* 33, 1051-1055.

Bozzo, A.T., Hsiao-Sheng, C., Kass, J.R., Barduhn, A.J., **1975**. "The Properties of the Hydrates of Chlorine and Carbon Dioxide". *Desalination* 16, 303-320.

Buhre, B.J.P., Elliott, L.K., Sheng, C.D., Gupta, R.P., Wall, T.F., **2005**. "Oxy-Fuel Combustion Technology for Coal-Fired Power Generation". *Progress in Energy and Combustion Science* 31, 283-307.

Carroll, J., **2014**. "Natural Gas Hydrates", 3rd ed. Gulf Professional Publishing, Boston, MA, USA.

Casero, P., Peña, F.G., Coca, P., Trujillo, J., **2014**. "ELCOGAS 14MWth Pre-Combustion Carbon Dioxide Capture Pilot. Technical & Economical Achievements". *Fuel* 116, 804-811.

Cavenati, S., Grande, C.A., Rodrigues, A.E., **2006**. "Separation of Mixtures by Layered Pressure Swing Adsorption for Upgrade of Natural Gas". *Chemical Engineering Science* 61, 3893-3906.

Cha, I., Lee, S., Lee, J.D., Lee, G.-w., Seo, Y., **2010**. "Separation of SF6 From Gas Mixtures Using Gas Hydrate Formation". *Environmental Science & Technology* 44, 6117-6122.

Châtel-Pélage, F., Carty, R., Philo, G.R., Farzan, H., Vecci, S.J., **2003**. "A Pilot-Scale Demonstration of Oxy-Combustion With Flue Gas Recirculation in a Pulverized Coal-Fired Boiler". Paper presented at: The 28th International Technical Conference on Coal Utilization & Fuel Systems; Clearwater, FL, USA.

Chemineer, "HEV Mixers". *Published online at Chemineer Inc.* Available at: http://www.chemineer.com/products/kenics/hev-mixers.html.

Chemineer, "KM Mixers". *Published online at Chemineer Inc.* Available at: http://www.chemineer.com/products/kenics/km-mixers.html.

Choi, Y.-S., Nešić, S., **2011**. "Determining the Corrosive Potential of $CO_2$ Transport Pipeline in High $pCO_2$–Water Environments". *International Journal of Greenhouse Gas Control* 5, 788-797.

Christiansen, R.L., Sloan, E.D., **1994**. "Mechanisms and Kinetics of Hydrate Formation". *Annals of the New York Academy of Sciences* 715, 283-305.

Cohen, A., Fowler, M., Waltzer, K., **2009**. "“NowGen”: Getting Real About Coal Carbon Capture and Sequestration". *The Electricity Journal* 22, 25-42.

Collett, T.S., **2003**. Natural Gas Hydrate as a Potential Energy Resource, in: Max, M.D. (Ed.), Natural Gas Hydrate: In Oceanic and Permafrost Environments, 1st ed. Springer Netherlands, Dordrecht, Netherlands, pp. 123-136.

Constantino, D.S. **2009**. "Produção de Hidroxiapatite Funcionalizada com Propriedades Catalíticas" [*MSc Thesis*]. Porto, Portugal: Departamento de Engenharia Química, Universidade do Porto.

Correia, D.F. **2008**. "Production of Hydroxyapatite Nanoparticles for Cosmetic and Orthopaedic Applications: Effect of Chelants and Dispersants" [*MSc Thesis*]. Porto, Portugal: Departamento de Engenharia Química, Universidade do Porto.

Costa, M.F. **2012**. "Development of Nanomaterials Using the NETmix® Technology: Application to Production of MOFs" [*MSc Thesis*]. Porto, Portugal: Departamento de Engenharia Química, Universidade do Porto.

Dabrowski, N., Windmeier, C., Oellrich, L.R., **2009**. "Purification of Natural Gases With High $CO_2$ Content Using Gas Hydrates". *Energy & Fuels* 23, 5603-5610.

Damen, K., Gnutek, R., Kaptein, J., Ryan Nannan, N., Oyarzun, B., Trapp, C., Colonna, P., van Dijk, E., Gross, J., Bardow, A., **2011**. "Developments in the Pre-Combustion $CO_2$ Capture Pilot Plant at the Buggenum IGCC". *Energy Procedia* 4, 1214-1221.

Dashti, H., Zhehao Yew, L., Lou, X., **2015**. "Recent Advances in Gas Hydrate-Based $CO_2$ Capture". *Journal of Natural Gas Science and Engineering* 23, 195-207.

Davy, H., **1811**. "On a Combination of Oxymuriatic Gas and Oxygene Gas". *Philosophical Transactions of the Royal Society of London* 101, 155-162.

Delahaye, A., Fournaison, L., Marinhas, S., Chatti, I., Petitet, J.-P., Dalmazzone, D., Fürst, W., **2006**. "Effect of THF on Equilibrium Pressure and Dissociation Enthalpy of $CO_2$ Hydrates Applied to Secondary Refrigeration". *Industrial & Engineering Chemistry Research* 45, 391-397.

Dillon, D., Panesar, R., Wall, R., Allam, R., White, V., Gibbins, J., Haines, M., **2005**. "Oxy-Combustion Processes for $CO_2$ Capture From Advanced Supercritical PF and NGCC Power Plant". 1, 211-220.

EBTP/ZEP, European Technology Platform for Zero Emission Fossil Fuel Power Plants, **2012**. "Biomass With $CO_2$ Capture and Storage (Bio-CCS)".

EIA, U.S. Energy Information Administration, **2016**. "International Energy Outlook 2016". Washington D.C., WA, USA, Doc. No ESA/P/WP.235.

EPA, U.S. Environmental Protection Agency, **2016**. "Inventory of U.S. Greenhouse Gas Emissions and Sinks: 1990-2014". Washington D.C., WA, USA, Doc. No EPA 430-R-16-002.

EPRI, Global CCS Institute, **2012**. "$CO_2$ Capture Technologies - Pre Combustion Capture". Canberra, Australia.

Faria, R.P. **2008**. "Estudo e Optimização do Processo Industrial de Produção de Hidroxiapatite Recorrendo à Tecnologia NETmix" [*MSc Thesis*]. Porto, Portugal: Departamento de Engenharia Química, Universidade do Porto.

Filho, B.M., Araujo, A.L., Silva, G.V., Boaventura, R.A., Dias, M.M., Lopes, J.C., Vilar, V.J., **2017**. "Intensification of Heterogeneous $TiO_2$ photocatalysis Using an Innovative Micro-Meso-Structured-Photoreactor for N-Decane Oxidation at Gas Phase". *Chemical Engineering Journal* 310, 331-341.

Flowers, B., Hartman, R.L., **2013**. "Microfluidic Synthesis of Methane (sI) and Propane (sII) Hydrates". Paper presented at: 2013 AIChE Annual Meeting; San Francisco, CA, USA.

Fluidinova, "FLUIDINOVA - The Nano-Hydroxyapatite Specialist". *Published online at Fluidinova*. Available at: http://www.fluidinova.pt.

Fonte, C.M. **2013**. "The NETmix Reactor: Application to High Added-Value Products" [*Ph.D Thesis*]. Porto, Portugal: Departamento de Engenharia Química, Universidade do Porto.

Fonte, C.M., Leblebici, M.E., Dias, M.M., Lopes, J.C., **2013**. "The NETmix Reactor: Pressure Drop Measurements and 3D CFD Modeling". *Chemical Engineering Research and Design* 91, 2250-2258.

Gao, S. **2006**. "Formation and Dissociation Mechanisms of Clathrates Hydrates" [*Ph.D Thesis*]. Houston, TX, USA: Department of Chemical and Biomolecular Engineering, Rice University.

García, S., Gil, M.V., Martín, C.F., Pis, J.J., Rubiera, F., Pevida, C., **2011**. "Breakthrough Adsorption Study of a Commercial Activated Carbon for Pre-Combustion $CO_2$ Capture". *Chemical Engineering Journal* 171, 549-556.

Gomes, P.J. **2011**. "The NETmix® Reactor - Strategies for Optimizing Mixing and Development of New Reactor Designs" [*Ph.D Thesis*]. Porto, Portugal: Departamento de Engenharia Química, Universidade do Porto.

Gomes, P.J., Fonte, C.M., Dias, M.M., Lopes, J.C., **2011**. "The NETmix® Reactor: Characterization and Quantification of Mixing". Paper presented at: ChemPor 2011 - 11th International Chemical and Biological Engineering Conference; Lisbon, Portugal.

Gomes, P.J., Silva, V.M., Quadros, P.A., Dias, M.M., Lopes, J.C., **2009**. "A Highly Reproducible Continuous Process for Hydroxyapatite Nanoparticles Synthesis". *Journal of Nanoscience and Nanotechnology* 9, 3387-3395.

Griffin, T., Sundkvist, S.G., Asen, K., Bruun, T., **2003**. "Advanced Zero Emissions Gas Turbine Power Plant". Paper presented at: ASME Turbo Expo 2003 (2003 International Joint Power Generation Conference); Atlanta, GA, USA.

Groen, C.B. **2012**. "$CO_2$ Hydrate Formation in Coil Heat Exchangers - An Experimental and Theoretical Study" [*MSc Thesis*]. Delft, Netherlands: Department of Sustainable Processes and Energy Technologies, TU Delft.

Gudmundsson, J.S., Parlaktuna, M., Levik, O.I., Andersson, V., **2000**. "Laboratory for Continuous Production of Natural Gas Hydrates". *Annals of the New York Academy of Sciences* 912, 851-858.

Hammerschmidt, E.G., **1934**. "Formation of Gas Hydrates in Natural Gas Transmission Lines". *Industrial & Engineering Chemistry* 26, 851-855.

Handa, Y.P., **1986**. "Calorimetric Determinations of the Compositions, Enthalpies of Dissociation, and Heat Capacities in the Range 85 to 270 K for Clathrate Hydrates of Xenon and Krypton". *The Journal of Chemical Thermodynamics* 18, 891-902.

Haq, B.U., **1999**. "Methane in the Deep Blue Sea". *Science* 285, 543-544.

Herzog, H., Meldon, J., Hatton, A., Clean Air Task Force, **2009**. "Advanced Post-Combustion $CO_2$ Capture".

Holloway, S., Karimjee, A., Akai, M., Pipatti, R., Rypdal, K., **2006**. Carbon Dioxide Transport, Injection and Geological Storage, in: Eggleston, S., Buendia, L., Miwa, K., Ngara, T., Tanabe, K. (Eds.), 2006 IPCC Guidelines for National Greenhouse Inventories, 1st ed. Institute for Global Environmental Strategies (IGES), Hayama, Japan.

Hu, J., Sari, O., Mahmed, C., Cereghetti, R., Homsy, P., **2010**. "$CO_2$ Hydrate Slurry". Yverdon-les-Bains, Switzerland, Doc. No GRS 032/08.

HWIPE, "What Are Gas Hydrates?". *Published online at Heriot-Watt Institute of Petroleum Engineering - Centre For Gas Hydrate Research*. Available at: http://www.pet.hw.ac.uk/research/hydrate/hydrates_what.cfm.

IEA, IEA Greenhouse Gas R&D Programme, **2004**. "Gas Hydrates For Deep Ocean Storage Of $CO_2$". Doc. No PH4-26.

IEA, International Energy Agency, **2013**. "Technology Roadmap - Carbon Capture and Storage". Paris, France.

IEA, International Energy Agency, **2015**. "Carbon Capture and Storage: The Solution for Deep Emissions Reductions". Paris, France.

Jansen, D., Gazzani, M., Manzolini, G., Dijk, E.v., Carbo, M., **2015**. "Pre-Combustion $CO_2$ Capture". *International Journal of Greenhouse Gas Control* 40, 167-187.

Javanmardi, J., Moshfeghian, M., **2003**. "Energy Consumption and Economic Evaluation of Water Desalination by Hydrate Phenomenon". *Applied Thermal Engineering* 23, 845-857.

Kang, S.-P., Lee, H., **2000**. "Recovery of $CO_2$ from Flue Gas Using Gas Hydrate: Thermodynamic Verification through Phase Equilibrium Measurements". *Environmental Science & Technology* 34, 4397-4400.

Kang, S.P., Lee, H., Ryu, B.J., **2001**. "Enthalpies of Dissociation of Clathrate Hydrates of Carbon Dioxide, Nitrogen, (Carbon Dioxide + Nitrogen), and (Carbon Dioxide + Nitrogen+ Tetrahydrofuran)". *The Journal of Chemical Thermodynamics* 33, 513-521.

Kofi Adom, P., Bekoe, W., Amuakwa-Mensah, F., Mensah, J.T., Botchway, E., **2012**. "Carbon Dioxide Emissions, Economic Growth, Industrial Structure, and Technical Efficiency: Empirical Evidence from Ghana, Senegal, and Morocco on the Causal Dynamics". *Energy* 47, 314-325.

Kvamme, B., **1994**. "Mechanisms for Initiation of Hydrate from Liquid Water Liquid Phase Clustering, Surface Adsorbtion, or What?". *Annals of the New York Academy of Sciences* 715, 306-310.

Kvamme, B., Graue, A., Buanes, T., Kuznetsova, T., Ersland, G., **2007**. "Storage of $CO_2$ in Natural Gas Hydrate Reservoirs and the Effect of Hydrate as an Extra Sealing in Cold Aquifers". *International Journal of Greenhouse Gas Control* 1, 236-246.

Laranjeira, P.E. **2005**. "NETmix Static Mixer - Modelling, CFD Simulation and Experimental Characterisation" [*Ph.D Thesis*]. Porto, Portugal: Departamento de Engenharia Química, Universidade do Porto.

Laranjeira, P.E., Martins, A.A., Lopes, J.C.B., Dias, M.M., **2009**. "NETmix®, a New Type of Static Mixer: Modeling, Simulation, Macromixing, and Micromixing Characterization". *AIChE Journal* 55, 2226-2243.

Laranjeira, P.E., Martins, A.A., Nunes, M.I., Lopes, J.C.B., Dias, M.M., **2011**. "NETmix®, a New Type of Static Mixer: Experimental Characterization and Model Validation". *AIChE Journal* 57, 1020-1032.

Leblebici, M.E. **2011**. "Comparative Study of NETmix® and T-Jets Reactors Based on Pressure Dynamics" [*MSc Thesis*]. Porto, Portugal: Departamento de Engenharia Química, Universidade do Porto.

Leblebici, M.E., Fonte, C.M., Costa, M.F., Ataíde, F., Garcia, M.P., Silva, V.M., Devic, T., Horcajada, P., Tavares, P., Araújo, J.P., Oliveira, R., Dias, M.M., Lopes, J.C., **2013**. "Continuous Production of Magnetic and Metal-Organic Nanoparticles With NETmix Reactor". Paper presented at: 2013 AIChE Annual Meeting; San Francisco, CA, USA.

Leppin, D., Sivaraman, A., Assigned to Gas Technology Institute, **2005**. "Process For Separating Carbon Dioxide And Methane". Patent No. US 6946017.

Lima, M.J., Leblebici, M.E., Dias, M.M., Lopes, J.C., Silva, C.G., Silva, A.M., Faria, J.L., **2014**. "Continuous Flow Photo-Fenton Treatment of Ciprofloxacin in Aqueous Solutions Using Homogeneous and Magnetically Recoverable Catalysts". *Environmental Science and Pollution Research (International)* 21, 11116-11125.

Lima, M.J., Silva, A.M., Silva, C.G., Faria, J.L., Lopes, J.C., Dias, M.M., **2016**. "An Innovative Static Mixer Photoreactor: Proof of Concept". *Chemical Engineering Journal* 287, 419-424.

Lima, M.J., Silva, C.G., Silva, A.M., Lopes, J.C., Dias, M.M., Faria, J.L., **2017**. "Homogeneous and Heterogeneous Photo-Fenton Degradation of Antibiotics Using an Innovative Static Mixer Photoreactor". *Chemical Engineering Journal* 310, 342-351.

Linga, P., Adeyemo, A., Englezos, P., **2008**. "Medium-Pressure Clathrate Hydrate/Membrane Hybrid Process for Postcombustion Capture of Carbon Dioxide". *Environmental Science & Technology* 42, 315-320.

Lirio, C.F.S., Pessoa, F.L.P., **2013**. "Enthalpy of Dissociation of Simple and Mixed Carbon Dioxide Clathrate Hydrate". *Chemical Engineering Transactions* 32, 577-582.

Liu, K.V., Choi, U.S., Kasza, K.E., Argonne National Laboratory, **1988**. "Measurements Of Pressure Drop And Heat Transfer In Turbulent Pipe Flows Of Particulate Slurries". Lemont, IL, USA, Doc. No ANL-85-15.

Lobregt, S., Broeze, J., Ferreira, C.I., **2016**. "$CO_2$ Hydrate Slurries for Rapid Chilling of Fresh Food Products". Paper presented at: 16th International Refrigeration and Air Conditioning Conference; Purdue, IN, USA.

Lopes, J.C., Dias, M.M., Costa, M.F., Teixeira, C.M., Santos, R.J., Assigned to Petróleos de Portugal - Petrogal, S.A., **2017**. "Network Heat Exchanger Device and Method for Heat Transfer" (European Patent Provisional Application, PTA 110119).

Lopes, J.C., Dias, M.M., Silva, V.M.M.d., Quadros, P.A., Monteiro, F.J., Gomes, P.J., Mateus, A.Y., Assigned to Fluidinova Engenharia de Fluidos, S.A., Instituto Nacional de Engenharia Biomédica, **2008a**. "Production Method for Calcium Phosphate Nano-Particles With High Purity and Their Use". Patent No. EP 2041025.

Lopes, J.C., Laranjeira, P.E., Dias, M.M., Martins, A.A., Assigned to Faculdade de Engenharia da Universidade do Porto, **2005**. "Network Mixer and Related Mixing Process". Patent No. PCT/IB2005/000647.

Lopes, J.C., Laranjeira, P.E., Dias, M.M., Martins, A.A., Assigned to Faculdade de Engenharia da Universidade do Porto, **2008b**. "Network Mixer and Related Mixing Process". Patent No. EP 1720643.

Ma, Z.W., Zhang, P., Bao, H.S., Deng, S., **2016**. "Review of Fundamental Properties of $CO_2$ Hydrates and $CO_2$ Capture and Separation Using Hydration Method". *Renewable and Sustainable Energy Reviews* 53, 1273-1302.

Marchetti, C., **1977**. "On Geoengineering and the $CO_2$ Problem". *Climatic Change* 1, 59-68.

Marinho, B.A., Djellabi, R., Cristóvão, R.O., Loureiro, J.M., Boaventura, R.A., Dias, M.M., Lopes, J.C., Vilar, V.J., **2017**. "Intensification of Heterogeneous $TiO_2$ Photocatalysis Using an Innovative Micro–Meso-Structured-Reactor for Cr(VI) Reduction Under Simulated Solar Light". *Chemical Engineering Journal* 318, 76-88.

Martins, A.A., Laranjeira, P.E., Lopes, J.C., Dias, M.M., **2007**. "Network Modeling of Flow in a Packed Bed". *AIChE Journal* 53, 91-107.

Mason, J.A., Sumida, K., Herm, Z.R., Krishna, R., Long, J.R., **2011**. "Evaluating Metal–Organic Frameworks for Post-Combustion Carbon Dioxide Capture Via Temperature Swing Adsorption". *Energy & Environmental Science* 4, 3030.

McDonald, M., Palkes, M., **1999**. "A Design Study for the Application of $CO_2/O_2$ Combustion to an Existing 300 MW Coal-Red Boiler". Paper presented at: Combustion Canada 99 Conference - Combustion and Global Climate Change; Calgary, AB, Canada.

Meijer, H.E.H., Singh, M.K., Anderson, P.D., **2012**. "On the Performance of Satic Mixers: A Quantitative Comparison". *Progress in Polymer Science* 37, 1333-1349.

Metz, B., Davidson, O., De Coninck, H., Loos, M., Meyer, L., Intergovernmental Panel on Climate Change, **2005**. "IPCC Special Report on Carbon Dioxide Capture and Storage.". New York, NY, USA.

Mimura, T., Simayoshi, H., Suda, T., Iijima, M., Mituoka, S., **1997**. "Development of Energy Saving Technology for Flue Gas Carbon Dioxide Recovery in Power Plant by Chemical Absorption Method and Steam System". *Energy Conversion and Management* 38, S57-S62.

Mohammadi, A.H., Eslamimanesh, A., Belandria, V., Richon, D., Naidoo, P., Ramjugernath, D., **2012**. "Phase Equilibrium Measurements for Semi-Clathrate Hydrates of the ($CO_2$ + $N_2$ + Tetra-N-Butylammonium Bromide) Aqueous Solution System". *The Journal of Chemical Thermodynamics* 46, 57-61.

Morgan, J.J., Blackwell, V.R., Johnson, D.E., Spencer, D.F., North, W.J., **1999**. "Hydrate Formation from Gaseous $CO_2$ and Water". *Environmental Science & Technology* 33, 1448-1452.

Mullin, J.W., **2001**. "Crystallization", 4th ed. Butterworth-Heinemann, Oxford, UK.

Nagasaki, N., Sasaki, K., Suzuki, T., Dodo, S., Nagaremori, F., **2013**. "Near-Zero-Emission IGCC Power Plant Technology". *Hitachi Review* 62, 39-47.

Narula, R.G., Wen, H., Himes, K., **2002**. "Incremental Cost of $CO_2$ Reduction in Power Plants". Paper presented at: IGTI ASME Turbo Expo; Amsterdam, Netherlands.

Nguyen, H., Rao, A.M., Phillips, J.B., John, V.T., Reed, W.F., **1991**. "Gas Hydrate Formation in Reversed Micelles". *Applied Biochemistry and Biotechnology* 28, 843.

Nunes, M.I. **2007**. "Micromixing In Chemical Reactors - Test Reactions" [*Ph.D Thesis*]. Porto, Portugal: Departamento de Engenharia Química, Universidade do Porto.

Ogoshi, H., Takao, S., **2004**. "Air-Conditioning System Using Clathrate Hydrate Slurry". *JFE Technical Report* 3, 1-5.

Olivier, J.G.J., Janssens-Maenhout, G., Muntean, M., Peters, J.H.A.W., PBL Netherlands Environmental Assessment Agency, **2015**. "Trends in Global $CO_2$ Emissions - 2015 Report". The Hague, Netherlands, Doc. No JRC98184.

Ortiz-Ospina, E., Roser, M., **2016**. "World Population Growth". *Published online at Our World In Data*. Retrieved from: https://ourworldindata.org/world-population-growth/ [Online Resource]

Parker, L., Folger, P., Stine, D.D., Congressional Research Service, **2008**. "Capturing $CO_2$ from Coal-Fired Power Plants: Challenges for a Comprehensive Strategy". Doc. No RL34621.

Plaza, M.G., García, S., Rubiera, F., Pis, J.J., Pevida, C., **2010**. "Post-Combustion $CO_2$ Capture With a Commercial Aactivated Carbon: Comparison of Different Regeneration Strategies". *Chemical Engineering Journal* 163, 41-47.

Prah, B., Yun, R., **2016**. "Heat Transfer and Pressure Drop of $CO_2$ Hydrate Mixture in Pipeline". *International Journal of Heat and Mass Transfer* 102, 341-347.

Rice, W., **2006**. "Hydrogen Production From Methane Hydrate With Sequestering of Carbon Dioxide". *International Journal of Hydrogen Energy* 31, 1955-1963.

Ripmeester, J.A., Ratcliffe, C.I., **1998**. "The Diverse Nature of Dodecahedral Cages in Clathrate Hydrates As Revealed by $^{129}Xe$ and $^{13}C$ NMR Spectroscopy: $CO_2$ as a Small-Cage Guest". *Energy & Fuels* 12, 197-200.

Rodger, P.M., **1990**. "Stability of Gas Hydrates". *The Journal of Physical Chemistry* 94, 6080-6089.

Rodrigues, M.F. **2008**. "Doping of Hydroxyapatite Nanoparticles with Metal Ions for Biomedical, Orthopedic and Dentistry Applications" [*MSc Thesis*]. Porto, Portugal: Departamento de Engenharia Química, Universidade do Porto.

Ross, "ISG Motionless Mixer". *Published online at Ross Mixers*. Available at: http://www.mixers.com/products/isg-motionless-mixer/.

Sabil, K.M., Witkamp, G.-J., Peters, C.J., **2010**. "Estimations of Enthalpies of Dissociation of Simple and Mixed Carbon Dioxide Hydrates From Phase Equilibrium Data". *Fluid Phase Equilibria* 290, 109-114.

Sanden, K., Ursin, T., Haaland, A.-H., Haugen, H.A., **2006**. "$CO_2$ Capture From Gas Power Plants – Just Catch™ Potential Cost Reductions". Paper presented at: 8th International Conference on Greenhouse Gas Control Technologies; Trondheim, Norway.

Sander, M.T., Mariz, C.L., **1992**. "The Fluor Daniel® EconamineTM FG Process: Past Experience and Present Day Focus". *Energy Conversion and Management* 33, 341-348.

Sari, O., Hu, J., Eicher, S., Egolf, P.W., Homsy, P., **2008**. "Thermo-Physical and Flow Properties of $CO_2$ Hydrate Slurry". Paper presented at: 2008 International Refrigeration and Air Conditioning Conference; Purdue, IN, USA.

Sfaxi, I.B., Belandria, V., Mohammadi, A.H., Lugo, R., Richon, D., **2012**. "Phase Equilibria of $CO_2$ + $N_2$ and $CO_2$ + $CH_4$ Clathrate Hydrates: Experimental Measurements and Thermodynamic Modelling". *Chemical Engineering Science* 84, 602-611.

Silva, V.M., Quadros, P.A., Laranjeira, P.E., Dias, M.M., Lopes, J.C., **2008**. "A Novel Continuous Industrial Process for Producing Hydroxyapatite Nanoparticles". *Journal of Dispersion Science and Technology* 29, 542-547.

Silvestre-Albero, J., Wahby, A., Sepulveda-Escribano, A., Martinez-Escandell, M., Kaneko, K., Rodriguez-Reinoso, F., **2011**. "Ultrahigh $CO_2$ Adsorption Capacity on Carbon Molecular Sieves at Room Temperature". *Chemical Communications (Camb)* 47, 6840-6842.

Simmons, J.M., Wu, H., Zhou, W., Yildirim, T., **2011**. "Carbon Capture in Metal–Organic Frameworks - A Comparative Study". *Energy & Environmental Science* 4, 2177.

Singh, A., Stéphenne, K., **2014**. "Shell Cansolv $CO_2$ Capture Technology: Achievement From First Commercial Plant". *Energy Procedia* 63, 1678-1685.

Skarstrom, C.W., Assigned to Google Patents, **1960**. "Method and Apparatus for Fractionating Gaseous Mixtures by Adsorption". Patent No. US 2944627.

Sloan, E.D., Fleyfel, F., **1991**. "A Molecular Mechanism for Gas Hydrate Nucleation From Ice". *AIChE Journal* 37, 1281-1292.

Sloan, E.D., Koh, C., **2007**. "Clathrate Hydrates of Natural Gases", 3rd ed. CRC Press, Boca Raton, FL, USA.

Smit, B., Reimer, J.A., Oldenburg, C.M., Bourg, I.C., **2014**. "Introduction to Carbon Capture and Sequestration", 1st ed. Imperial College Press, London, UK.

Spencer, D.F., **1999**. Integration of an Advanced $CO_2$ Separation Process With Methods for Disposing of $CO_2$ in Oceans and Terrestrial Deep Aquifers, in: Elisasson, B., Riemer, P., Wokaun, A. (Eds.), Greenhouse Gas Control Technologies, 1st ed. Elsevier, Oxford, UK.

Stanger, R., Wall, T., Spörl, R., Paneru, M., Grathwohl, S., Weidmann, M., Scheffknecht, G., McDonald, D., Myöhänen, K., Ritvanen, J., Rahiala, S., Hyppänen, T., Mletzko, J., Kather, A., Santos, S., **2015**. "Oxyfuel Combustion for $CO_2$ Capture in Power Plants". *International Journal of Greenhouse Gas Control* 40, 55-125.

Strobel, T.A., Koh, C.A., Sloan, E.D., **2009**. "Thermodynamic Predictions of Various Tetrahydrofuran and Hydrogen Clathrate Hydrates". *Fluid Phase Equilibria* 280, 61-67.

Sulzer, "Static Mixers". *Published online at Sulzer*. Available at: https://www.sulzer.com/en/Products-and-Services/Mixpac-Cartridges-Applications-Static-Mixers/Static-Mixers.

Szalai, E.S., Muzzio, F.J., **2003**. "Fundamental Approach to the Design and Optimization of Static Mixers". *AIChE Journal* 49, 2687-2699.

Tajima, H., Yamasaki, A., Kiyono, F., **2004**. "Energy Consumption Estimation for Greenhouse Gas Separation Processes by Clathrate Hydrate Formation". *Energy* 29, 1713-1729.

Tajima, H., Yamasaki, A., Kiyono, F., **2005**. "Effects of Mixing Functions of Static Mixers on the Formation of $CO_2$ Hydrate from the Two-Phase Flow of Liquid $CO_2$ and Water". *Energy & Fuels* 19, 2364-2370.

Tam, S., Stanton, M., Ghose, S., Deppe, G., Spencer, D., Currier, R., Young, J., Anderson, G., Le, L., Devlin, D., **2001**. "A High Pressure Carbon Dioxide Separation Process for IGCC Plants". Paper presented at: First National Conference on Carbon Sequestration; Washington D.C., WA, USA.

Tan, Y., Douglas, M.A., Thambimuthu, K.V., **2002**. "$CO_2$ Capture Using Oxygen Enhanced Combustion Strategies for Natural Gas Power Plants". *Fuel* 81, 1007-1016.

Thakur, R.K., Vial, C., Nigam, K.D.P., Nauman, E.B., Djelveh, G., **2003**. "Static Mixers in the Process Industries—A Review". *Chemical Engineering Research and Design* 81, 787-826.

Turner, D.J. **2005**. "Clathrate Hydrate Formation in Water-in-Oil Dispersions" [*Ph.D Thesis*]. Golden, CO, USA: Department of Chemical and Petroleum Refining Engineering, Colorado School Of Mines.

Uchida, T., Takagi, A., Kawabata, J., Mae, S., Hondoh, T., **1995**. "Raman Spectroscopic Analyses of the Growth Process of $CO_2$ Hydrates". *Energy Conversion and Management* 36, 547-550.

Udachin, K.A., Ratcliffe, C.I., Ripmeester, J.A., **2001**. "Structure, Composition, and Thermal Expansion of $CO_2$ Hydrate from Single Crystal X-ray Diffraction Measurements". *The Journal of Physical Chemistry B* 105, 4200-4204.

Udachin, K.A., Ripmeester, J.A., **1999**. "A Complex Clathrate Hydrate Structure Showing Bimodal Guest Hydration". *Nature* 397, 420-423.

UNFCCC, "UN Climate Change". *Published online at UNFCCC*. Available at: http://newsroom.unfccc.int.

van der Waals, J.H., Platteeuw, J.C., **1958**. Clathrate Solutions, in: Prigogine, I. (Ed.), Advances in Chemical Physics, 2007 Digital ed. John Wiley & Sons, Inc., Hoboken, NJ, USA, pp. 1-57.

Vorotyntsev, V., Malyshev, V., Taraburov, P., Mochalov, G., **2001**. "Separation of Gas Mixtures by Continuous Gas Hydrate Crystallization". *Theoretical Foundations of Chemical Engineering* 35, 513-515.

Webley, P.A., **2014**. "Adsorption Technology for $CO_2$ Separation and Capture: A Perspective". *Adsorption* 20, 225-231.

Wilkinson, M.B., Simmonds, M., Allam, R.J., White, V., **2003**. "Oxyfuel Conversion of Heaters and Boilers for $CO_2$ Capture". Paper presented at: 2nd National Conference on Carbon Sequestration; Washington D.C., WA, USA.

Yamamuro, O., Suga, H., **1989**. "Thermodynamic Studies of Clathrate Hydrates". *Journal of thermal analysis* 35, 2025-2064.

Yang, D., Le, L., Martinez, R., Currier, R., Spencer, D., Deppe, G., **2008**. "Heat Transfer During $CO_2$ Hydrate Formation in a Continuous Flow Reactor". *Energy & Fuels* 22, 2649-2659.

Yang, D., Le, L.A., Martinez, R.J., Currier, R.P., Spencer, D.F., **2011**. "Kinetics of $CO_2$ Hydrate Formation in a Continuous Flow Reactor". *Chemical Engineering Journal* 172, 144-157.

Yoon, J.-H., Yamamoto, Y., Komai, T., Haneda, H., Kawamura, T., **2003**. "Rigorous Approach to the Prediction of the Heat of Dissociation of Gas Hydrates". *Industrial & Engineering Chemistry Research* 42, 1111-1114.

ZareNezhad, B., Montazeri, V., **2016**. "Nanofluid-Assisted Gas to Hydrate (GTH) Energy Conversion for Promoting $CO_2$ Recovery and Sequestration Processes in the Petroleum Industry". *Petroleum Science and Technology* 34, 37-43.

ZEP, "Carbon Dioxide Capture & Storage". *Published online at Zero Emissions Platform.* Available at: http://www.zeroemissionsplatform.eu.

Zhang, J.S., Lee, S., Lee, J.W., **2007**. "Kinetics of Methane Hydrate Formation From SDS Solution". *Industrial & Engineering Chemistry Research* 46, 6353-6359.

Zhang, Y., Gao, K., Schmitt, G., Hausler, R.H., **2013**. "Modeling Steel Corrosion Under Supercritical $CO_2$ Conditions". *Materials and Corrosion* 64, 478-485.

Zhang, Y., Yang, M., Song, Y., Jiang, L., Li, Y., Cheng, C., **2014**. "Hydrate Phase Equilibrium Measurements for (THF + SDS + $CO_2$ + $N_2$) Aqueous Solution Systems in Porous Media". *Fluid Phase Equilibria* 370, 12-18.

Zhao, J., Tian, Y., Zhao, Y., **2013**. "Separation of Methane From Coal Bed Gas Via Hydrate Formation in the Presence of Tetrahydrofuran and Sodium Dodecyl Sulfate". *Chemistry and Technology of Fuels and Oils* 49, 251-258.

# 3 Heat Transfer Performance of NETmix

## 3.1 Introduction

One of the major problems of the continuous production of gas hydrates is the large amount of energy that is released during the process. Insufficient removal of this hydration heat causes an increase in the medium temperature, which may result in the inhibition of the production of the hydrates, since the operational thermodynamic conditions may lay outside the hydrate stability region (see phase equilibrium diagram for $CO_2$ hydrates in Figure 2.11), and thus reducing the process productivity. In order to successfully transpose the process of the production of hydrates to a continuous and industrial environment using the NETmix technology, evaluation of the heat transfer capacity of the mixer is crucial.

Transport phenomena enhancement using static mixers is not a new topic for researchers in the area. Many works have discussed the beneficial effect on heat (and mass) transfer on several static mixers, trying also to quantify it for a better understanding of the behaviour behind it. Several researchers have tried to find the dimensionless heat transfer coefficient, the Nusselt number, in the form of correlations, for different static mixers or static mixing elements used in heat

exchangers. The objective is to more accurately design heat exchangers containing commercial static mixers. Grace (1971) and Nauman (1979) were the very first presenting studies on the enhancement of heat transfer and thermal homogeneity using static mixers. Lammers and Beenackers (1994) and Joshi et al. (1995) proposed Nusselt number correlations for Kenics static mixers, for flow in laminar regime, while Myers et al. (1997) determined correlations for the operation in turbulent flow regime. Li et al. (1996) studied heat transfer in the Sulzer SMX static mixer. Thakur et al. (2003) compiled correlations for different static mixing elements obtained experimentally in tubes containing these elements.

Most heat exchanger devices operate in the turbulent regime, since there is a generalized idea that the laminar regime is not efficient for heat transfer purposes (Rohsenow et al. 1998). Chaotic advection has been proposed by several authors as means to enhance heat transfer in laminar flows, as in static mixers (Mokrani et al. 1997, Kumar et al. 2006). Static mixers enhance heat transfer due to the presented improved radial mixing and flow division, resulting in the elimination of the boundary layers that form the major resistance to heat transfer in laminar flow (Thakur et al. 2003).

As a static mixing device, NETmix has proven to be extremely valuable for heat (as well as for mass) transfer, as already demonstrated by Gomes (2011) and Fonte (2013). Gomes (2011) studied mixing in NETmix using a multiphase CFD model, observing that a significant amount of interfacial surface area is generated in the mixing chambers, when the flow is fully chaotic and oscillatory, observed when the channel's Reynolds number is larger than the critical Reynolds number, of about 150 (Laranjeira 2005). The channel's Reynolds number is defined by

$$\mathrm{Re}_{\mathrm{c}} = \frac{\rho \overline{v}_{\mathrm{c}} d_{\mathrm{h}}}{\mu} \tag{3.1}$$

where $\rho$ and $\mu$ are the fluid's density and viscosity, respectively, $\overline{v}_{\mathrm{c}}$ is the mean channel's velocity and $d_{\mathrm{h}}$ is the channel's hydraulic diameter. Fonte (2013) estimated the Sherwood numbers (mass transfer equivalent to Nusselt number) for

homogeneous mass transfer from surface to the bulk, and verified that a mass transfer rate enhancement is observed above the critical Reynolds number. The same observation was made regarding heat transfer, when Fonte (2013) determined the Nusselt numbers for NETmix, providing a significant advance in the study of heat transfer in NETmix device.

The potential use of the NETmix technology as a heat exchange device is evaluated in this chapter, which is a follow-up of the work developed by Fonte (2013). The main objective is to assess NETmix's heat transfer capacity, in terms of the flow regime impact in the heat transfer resistances, at the fluid level, by estimation and analysis of Nusselt numbers. This estimation is done using a CFD tool, by simulating the flow and heat transfer inside a NETmix network. Finally, a comparison between NETmix and other technologies used for heat transfer is made. In Section 3.2, the three-dimensional CFD model is presented and discussed. The conservation equations, as well as the simulation strategy and numerical discretization are also presented in Section 3.2. The main results of the analysis, such as the dimensionless Nusselt numbers for the NETmix unit cell are presented in Section 3.3. A comparison between laminar flow between parallel plates and NETmix is made in Section 3.4, to both validate the obtained results, a strategy already used by Fonte (2013), and to highlight the enhancement that is shown by NETmix as a result of the oscillatory behaviour observed when the Reynolds number is higher than the critical Reynolds number. In Section 3.5, correlations for the determination of the Nusselt number as a function of the Reynolds number in NETmix are proposed, based on the analogue geometries between the NETmix channels and parallel plates. In Section 3.6, the specific heat transfer capacity of NETmix is determined, using the Nusselt numbers previously determined, and on the effective heat transfer area. A comparison between NETmix and other technologies that are commonly used for heat transfer is also made in Section 3.6. Brief conclusions are presented in Section 3.7, while the references are disclosed in Section 3.8.

## 3.2 3D CFD Modelling

The three-dimensional nature of the flow inside the mixing chambers and channels of a NETmix network hinders a potential geometrical simplification of the model. Furthermore, the non-stationary nature of the flow regime, for certain ranges of the domain of interest, requires the characterization of the heat transfer properties in terms of spatial and time averaging, as discussed later in Section 3.3.

The influence of the hydrodynamics within NETmix is of great importance to determine the NETmix's heat transfer performance, since it has already been observed that hydrodynamic changes occur when a critical channel's Reynolds number of 150 is achieved, the flow evolves from a fully developed laminar regime to a dynamic oscillatory flow regime, where mixing is enhanced due to chaotic advection.

For the analysis of the heat transfer performance of NETmix, the strategy already applied by Fonte (2013), comprising the NUB model, is used in the present work to further validate, understand and refine the previous results. The NUB model, which is based on the Lab-Scale NETmix 2D (shown in Figure 2.27c and Table 2.7), emerged from natural computational limitations, due to the impracticability of simulating the whole control volume of NETmix. Since both the geometry and expected flow patterns have a periodically repetitive nature (Laranjeira et al. 2009), it is conceivable to simplify the simulation of a larger system by modelling only a small representative part of its flow domain, thus reducing the computational effort. The NUB model, illustrated in Figure 3.1, comprises a network of five rows and three columns, where only two complete central chambers and six lateral half-chambers are represented. Transversal symmetry surfaces normal to the $xy$ plane, delimit the half-chambers by crossing the complete lateral chambers at the centre. A translational periodic boundary condition is applied to the resulting symmetry surfaces. The NUB transport model was validated using experimental data (Fonte et al. 2013), enabling

the computation of transport properties without the need for extra experimental data.

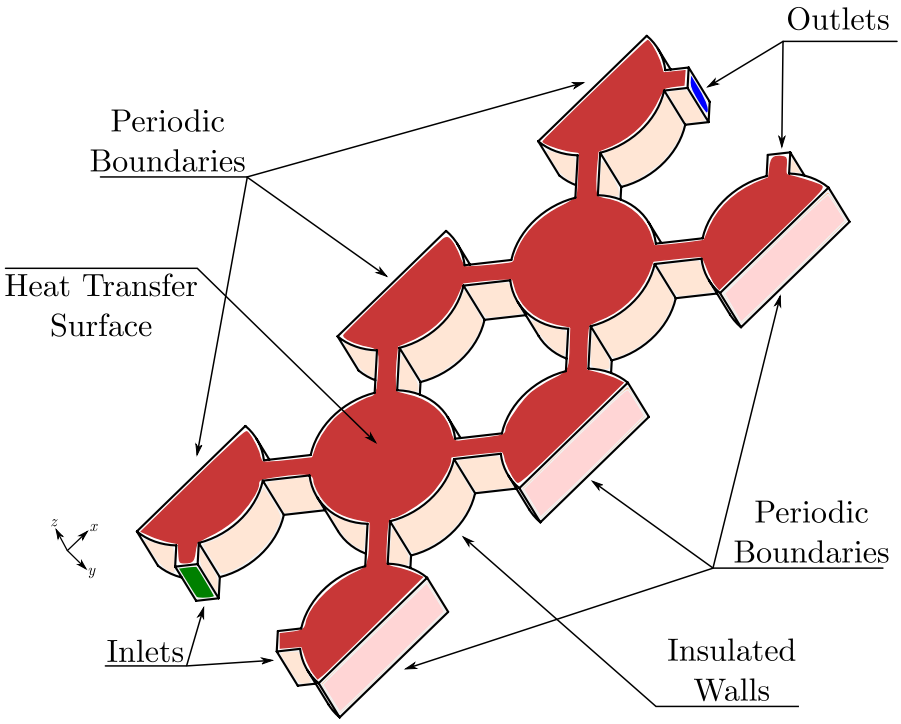



Figure 3.1 – NETmix Unit Block (NUB) CFD model and surfaces identification.

In the current model, it is assumed that heat transfer to the flowing fluid results mainly from conduction through the top and bottom solid wall surfaces (identified as *Heat Transfer Surface* in Figure 3.1), neglecting any potential heat conduction through the curved surfaces of the chambers and the lateral side surfaces of the channels (identified as *Insulated Walls* in Figure 3.1), which are driven by lesser thermal gradients between adjacent chambers and channels. Heat transfer by conduction through the solid walls of NETmix, in the same direction of the flow, can be important, in particular when large temperature differences between two fluids (as it occurs in systems with controlled temperature in the presence of highly exo/endothermic processes) are expected. However, in this work, this mechanism is not considered, since the work is focused on the performance of the NETmix at the inside liquid level only, meaning that the effect of temperature differences between different fluids is not relevant.

### 3.2.1 Governing Equations and Boundary Conditions

The flow field simulation is achieved by integration of the three-dimensional forms of the continuity and motion equations (the Navier-Stokes equations, Bird et al. (2002)), while the temperature field is obtained by solving the energy equation. The continuity equation (mathematical representation of the conservation of mass) and motion equation (mathematical representation of the conservation of momentum) assume the form

$$\frac{\partial \rho}{\partial t} + \nabla\left(\rho\vec{v}\right) = 0 \tag{3.2}$$

$$\frac{\partial\left(\rho\vec{v}\right)}{\partial t} + \vec{v}\cdot\nabla\left(\rho\vec{v}\right) = -\nabla p - \nabla\cdot\left(-\mu\left(\nabla\vec{v} + \left(\nabla\vec{v}\right)^{\mathrm{T}}\right)\right) + \rho\vec{g} \tag{3.3}$$

where $\vec{v}$ is the velocity field, $t$ is the time, $p$ is the fluid pressure, $\rho$ and $\mu$ are the local values of the fluid's density and viscosity, respectively. The energy equation, neglecting viscous dissipation, is given by

$$\frac{\partial\left(\rho c_{\mathrm{P}} T\right)}{\partial t} + \nabla\left(\rho c_{\mathrm{P}}\vec{v}T\right) = \nabla\cdot\left(\kappa\nabla T\right) \tag{3.4}$$

where $T$ is the temperature, $c_{\mathrm{P}}$ is the local fluid specific heat capacity and $\kappa$ is the local fluid thermal conductivity. Viscous dissipation is neglected in Equation 3.4 due to NETmix's high energy efficiency, as previously shown by Fonte et al. (2013). In the present operational simulation range, a maximum energy dissipation of less than $1\,\mathrm{mW}$ is expected, and can be considered negligible when compared to the amount of heat transferred from the outside.

Equations 3.2 to 3.4 are solved for the following boundary conditions: no-slip condition is assumed at the walls of the domain, $\vec{v}_{\mathrm{wall}} = 0$; simplified uniform velocity profile is applied to the inlet channels; parallel flow condition is applied at the outlet channels, by imposing a simplified constant and uniform pressure profile, $p_{\mathrm{out}} = p_0$; periodic boundary conditions are imposed at the symmetry surfaces of the half-chambers of the NUB model; either constant wall temperature, $T_{\mathrm{wall}} = T_0$ or constant

wall heat flux $\dot{q}_{\text{wall}} = \dot{q}_0$, is imposed at both top and bottom walls. These two last boundary conditions are the two limiting cases, consistent with the condition of no conduction at the wall. The flow is incompressible, and the working fluid is water with variable local physical properties with temperature, in the range of 273-373 K (Appendix A).

### 3.2.2 Numerical Simulation Strategy

The strategy used is very similar to the one used by Fonte (2013). Due to the non-stationary behaviour observed in NETmix for certain hydrodynamic conditions, it is necessary to adopt a strategy that takes into consideration the presence (or not) of oscillations inside the mixing chambers. When the Reynolds number is below the critical Reynolds number, no oscillation patterns are observed and therefore only a steady-state simulation is performed, applying the boundary conditions described in Section 3.2.1. On the contrary, when the Reynolds number reaches a value large enough so that oscillations are observed, a two-step simulation procedure is required. First, in order to obtain an initial and symmetrical solution, steady-state simulations are performed where symmetry conditions are applied by imposing shear-free surface conditions to both the symmetry surfaces of the half-chambers of the NUB model, and to the surfaces that split the two complete central chambers in the middle. Afterwards, shear-free surfaces at the complete chambers are removed, while the shear-free surface condition from the half-chambers is switched to periodic boundary conditions. With these conditions, a transient simulation is performed, for a total flow time large enough so that oscillation patterns inside the NUB chambers are fully developed. A total flow time of $15\tau_{\text{uc}}$ (where $\tau_{\text{uc}}$ is the unit cell residence time) is considered, and the Nusselt number is computed in each simulation time step. The time step size $t_{\text{step}}$ is determined by

$$t_{\text{step}} = \frac{\Delta x}{v_{\text{c, max}}} \tag{3.5}$$

where $\Delta x$ is the minimum dimension of a fluid element in the flow direction in the channel, where the highest velocities occur, and $v_{\mathrm{c,\,max}}$ is the maximum velocity in the channels, determined by

$$v_{\mathrm{c,\,max}} = \frac{3}{2}\overline{v}_{\mathrm{c}} \tag{3.6}$$

A uniform temperature of 293 K is imposed at the network inlet channels. For constant wall temperature simulations, a uniform temperature of 373 K is imposed to both the top and bottom surfaces. For simulations with constant wall heat flux condition, a constant average heat flux is imposed. The wall heat flux is estimated by imposing a maximum value to the temperature difference between the NUB inlet and outlet $\Delta T_{\mathrm{in\text{-}out}}$, and is given by (Fonte 2013)

$$\dot{q}_{\mathrm{wall}} = \frac{2\dot{m}_{\mathrm{c}} c_{\mathrm{P}} \Delta T_{\mathrm{in\text{-}out}}}{A_{\mathrm{transf}}} \tag{3.7}$$

where $\dot{q}_{\mathrm{wall}}$ is the heat flux through the walls, $\dot{m}_{\mathrm{c}}$ is the channel's mass flow rate, and $A_{\mathrm{transf}}$ is the total area available for heat transfer in the NUB. A thermal gradient of $\Delta T_{\mathrm{in\text{-}out}} = 60\ \mathrm{K}$ is chosen in order to ensure that all local temperature are within the validity range of the water's physical properties relationships (see Appendix A).

### 3.2.3 Numerical Discretization and Solution Methods

The computation tool ANSYS® 13 (ANSYS), an engineering simulation technology suite, is used for the geometrical design of the NUB model (using *Design Modeler*) and for the simulation grid generation (using *Meshing*). Grid dependency tests were performed by sequentially increasing the grid refinement in different directions. In each grid, both the heat flux and the average temperature at the middle of the channels were monitored and compared with the correspondent values obtained for the previous grid refinement. The process stopped when the relative variation between meshes with consecutive refinement levels was lower than 1%. This analysis was performed for different low Reynolds numbers. From this test, it was observed

that the grid discretization in the flow direction used by Fonte et al. (2013) was not sufficiently refined to accurately simulate the temperature field in the NUB domain. A grid with hexahedral finite volumes with maximum volume edge length of $\Delta x = 0.05$ mm in the flow direction is used. Successively refined discretizations in the $z$ direction were also performed. It was observed that applying a size growth algorithm in this direction, so that the size of the elements grew from 0.05 mm near the walls to 0.1 mm in the centre position of the NUB model, resulted in a sufficiently refined grid. This resulted in a computation grid with a total number of 2.5 million volume elements.

The flow equations solutions were obtained using the finite-volume commercial CFD software *Fluent* 13.0 (also from ANSYS). For steady-state simulations (to obtain symmetrical flow solutions), the SIMPLEC scheme was used for the pressure-velocity coupling, the Standard and Third-Order MUSCL schemes were used for the pressure and momentum discretization, respectively, and Third-Order MUSCL scheme was used for the discretization of the convective term of the energy conservation equation. For transient simulations, a second-order implicit scheme was used for time discretization. The simulation was considered to have converged when no significant variation of the outlet temperature and velocity values, averaged by the mass flow rate, was lower than 1% relatively to the previous iteration, and when the normalized residues of the governing equations were lower than $10^{-6}$ for steady-state simulations, or $10^{-4}$ for transient simulations, in each time step.

These simulations were run on an Intel® Xeon® 3GHz 8-core machine with 24 gigabytes of installed RAM memory, resulting in simulation times of approximately 30 minutes and 60 hours, for the steady and transient simulations, respectively.

## 3.3 Heat Transfer Performance

Two distinct sets of simulations, using different wall boundary conditions, were implemented: constant wall temperature and constant wall heat flux. Both sets of

simulations were performed at different Reynolds numbers (evaluated at the NUB inlet channels), varying from 5 to 600, in order to completely observe the transition in the hydrodynamic regime while maintaining a dynamic laminar flow regime.

CFD simulations have shown that with the increase of the Reynolds number, the characteristics of the flow patterns inside the unit cell changes, as already observed in previous works (Laranjeira et al. 2009, Laranjeira et al. 2011). These changes have an effect on the temperature maps in NETmix. Above the critical Reynolds number, due to the enhanced mixing quality, uniformization of the temperature distribution is observed, when compared with the temperature distribution obtained at a Reynolds number below the critical, where the flow is essentially parallel. When local mixing is poor, at low Reynolds number, permanent local hot spots are observed, resulting in a heterogeneous temperature field. When the Reynolds is above the critical Reynolds number, the non-stationarity nature of the flow reduces not only the number of the hot stops, but also their size. In this situation, the remaining hot spots are non-stationary as the flow, therefore, their position in the chamber is not always the same, but is rather changing with time. This reduces the global heterogeneities of the temperature field. This phenomenon is observed in Figure 3.2, where temperature contour maps of the central chamber of the fourth row is represented at different flow times, for $\mathrm{Re}_{in} = 300$.

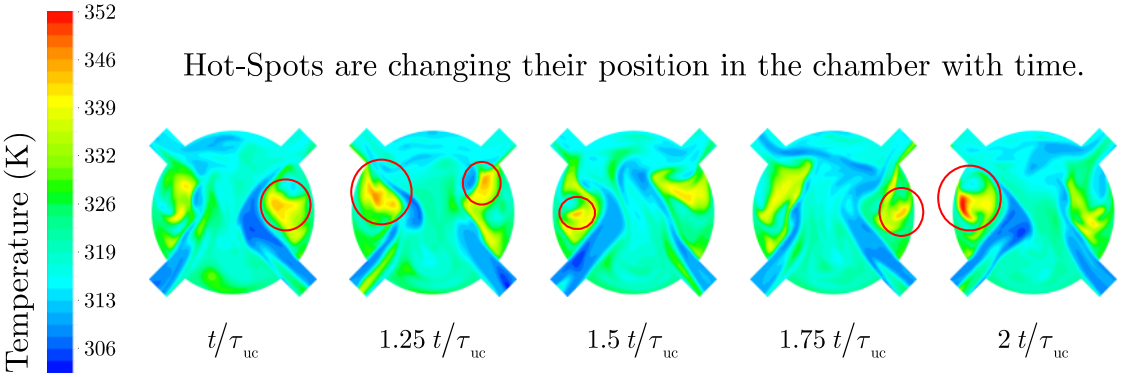



Figure 3.2 – Temperature contour maps at the middle plane of the domain of the chamber at the fourth row of NUB, for $\mathrm{Re}_{in} = 300$ and constant wall heat flux as a function of time. The red circles identify the hot spots.

A proper way to assess the heat transfer capacity of NETmix in the dynamic flow regime is by determining the time-average unit cell Nusselt number $\mathrm{Nu}_{\mathrm{uc}}$, defined by

$$\mathrm{Nu}_{\mathrm{uc}} = \left\langle \mathrm{Nu} \right\rangle_t = \frac{\int_0^{t_{\mathrm{int}}} \mathrm{Nu}_{\mathrm{uc}}\left(t\right) dt}{\int_0^{t_{\mathrm{int}}} dt} = \frac{d_{\mathrm{h}}}{t_{\mathrm{int}}} \int_0^{t_{\mathrm{int}}} \frac{h_{\mathrm{uc}}\left(t\right)}{\overline{\kappa}\left(t\right)} dt = d_{\mathrm{h}} \left\langle \frac{h_{\mathrm{uc}}}{\overline{\kappa}} \right\rangle_t \tag{3.8}$$

where $d_{\mathrm{h}}$ is the NETmix channel's hydraulic diameter, $h_{\mathrm{uc}}$ is the instantaneous unit cell heat transfer coefficient (evaluated at each instant), $\overline{\kappa}$ is the thermal conductivity evaluated at the unit cell average temperature, $t_{\mathrm{int}}$ is the total dynamic simulation integration time, and the operator $\left\langle \ \right\rangle_t$ represents the time-average mathematical operation. The channel's hydraulic diameter is calculated from

$$d_{\mathrm{h}} = \frac{2\omega_{\mathrm{n}} d_{\mathrm{c}}}{\omega_{\mathrm{n}} + d_{\mathrm{c}}} \tag{3.9}$$

where $d_{\mathrm{c}}$ and $\omega_{\mathrm{n}}$ are the NETmix channel's width and network depth, respectively, as defined in Section 2.4.2.

Defining $\mathrm{Nu}_{\mathrm{uc}}$ as the time-average unit cell Nusselt number is helpful since it can be applied for both hydrodynamic patterns (above and below critical Reynolds number). When the flow inside the chambers is chaotic, no steady-state solution is found and therefore, a time-dependent solution is required. This issue is solved if the Nusselt number is an average of the values at each instant, since both the heat transfer coefficient and the thermal conductivity are varying with time.

The values of $\mathrm{Nu}_{\mathrm{uc}}$ were not obtained using Equation 3.8, but rather a shortcut of it, by computing the time-average of $h_{\mathrm{uc}}$ and $\overline{\kappa}$ separately, that is

$$\mathrm{Nu}_{\mathrm{uc}} \approx d_{\mathrm{h}} \frac{\left\langle h_{\mathrm{uc}} \right\rangle_t}{\left\langle \overline{\kappa} \right\rangle_t} \tag{3.10}$$

Finally, to determine $\mathrm{Nu}_{\mathrm{uc}}$, it is necessary to independently determine the time-averaged $h_{\mathrm{uc}}$ and $\overline{\kappa}$

$$\left\langle h_{\mathrm{uc}} \right\rangle_t = \frac{1}{A_{\mathrm{transf,\,uc}} t_{\mathrm{int}}} \int_0^{t_{\mathrm{int}}} \frac{\dot{q}_{\mathrm{uc}}\left(t\right)}{\Delta T_{\mathrm{lm,\,uc}}\left(t\right)} dt \tag{3.11}$$

$$\left\langle \overline{\kappa} \right\rangle_t = \frac{1}{t_{\mathrm{int}}} \int_0^{t_{\mathrm{int}}} \overline{\kappa}\left(t\right) dt \tag{3.12}$$

where $\dot{q}_{\mathrm{uc}}$ is the instantaneous heat flux through the unit cell, $\Delta T_{\mathrm{lm,\,uc}}$ is a characteristic temperature difference, and $A_{\mathrm{transf,\,uc}}$ is the active heat transfer area of the unit cell, estimated by

$$A_{\mathrm{transf,\,uc}} = \frac{\pi D_{\mathrm{ch}}^2}{2} + 4 d_{\mathrm{c}} \left( L - \sqrt{D_{\mathrm{ch}}^2 - d_{\mathrm{c}}^2} \right) \tag{3.13}$$

where $D_{\mathrm{ch}}$ is the is the chamber's diameter, and $L$ is the distance between the centres of two adjacent chambers, as defined in Section 2.4.2. The total transferred heat flux $\dot{q}_{\mathrm{uc}}$ is determined by the energy balance to the unit cell, and given by the sum of the enthalpy fluxes at the two inlets and outlets (Fonte 2013)

$$\dot{q}_{\mathrm{uc}} = \sum_{\mathrm{in}} \int_{S_i} T \rho c_{\mathrm{P}} \left( \vec{v} \cdot \vec{n} \right) dS + \sum_{\mathrm{out}} \int_{S_j} T \rho c_{\mathrm{P}} \left( \vec{v} \cdot \vec{n} \right) dS \tag{3.14}$$

where $i$ stands for each of the two inlet channels, $j$ stands for each of the outlet channels, $\vec{n}$ represents the normal unitary vector pointing outwards the control surface that delimits the boundaries of the domain, and $S$ represents the respective cross-sectional flow area.

The characteristic temperature difference is determined by using an appropriate logarithmic mean temperature difference as the driving force (Bird et al. 2002)

$$\Delta T_{\mathrm{lm,\,uc}} = \frac{\left( T_{\mathrm{wall,\,in}} - T_{\mathrm{bulk,\,in}} \right) - \left( T_{\mathrm{wall,\,out}} - T_{\mathrm{bulk,\,out}} \right)}{\ln\left[ \left( T_{\mathrm{wall,\,in}} - T_{\mathrm{bulk,\,in}} \right) / \left( T_{\mathrm{wall,\,out}} - T_{\mathrm{bulk,\,out}} \right) \right]} \tag{3.15}$$

where $T_{\text{wall, in}}$ and $T_{\text{wall, out}}$ are the wall temperatures, at the inlet and outlet of the unit cell, respectively, and $T_{\text{bulk, in}}$ and $T_{\text{bulk, out}}$ are the bulk temperatures, estimated from the average temperature weighted by the mass flow rate of the fluid in the channel (Fonte 2013)

$$T_{\text{bulk, in/out}} = \frac{\iint_{A_{\text{in/out}}} \rho\left(\vec{v}\cdot\vec{n}\right) T \, dA}{\iint_{A_{\text{in/out}}} \rho\left(\vec{v}\cdot\vec{n}\right) dA} \tag{3.16}$$

The use of a logarithmic mean difference is usually preferred, because it is less dependent on the geometrical properties of the system, when compared with other characteristic temperature differences (Bird et al. 2002). Also, the Nusselt numbers determined from Equation 3.10 are surface average values rather than local values, hence the use of a mean temperature difference.

In order to determine the importance of the entry length effect along the NUB cells, a dimensionless thermal entrance variable $x^*$ is introduced as (Shah and London 1978)

$$x^* = \frac{1}{\text{Re}\,\text{Pr}} \frac{x}{\omega_{\text{n}}} \tag{3.17}$$

where $x$ is the distance from the inlet measured along the flow direction axis, and the Reynolds Number $\text{Re}$ and Prandtl number $\text{Pr}$ are evaluated at the local conditions. The Prandtl number is defined as

$$\text{Pr} = \frac{c_{\text{P}}\mu}{\kappa} \tag{3.18}$$

The variable $x^*$, which is the inverse of the Graetz number $\text{Gz}$, is normally used in studies of entry length effects on laminar flow heat transfer problems (Shah and London 1978).

Fonte (2013) demonstrated previously that the use of the convective heat transfer coefficient averaged between the dimensionless thermal entrance points $x^*_{\text{in}}$ (at the centre of the inlet channel), and $x^*_{\text{out}}$ (at the centre of the outlet channel), does not

result in a large deviation when compared to the local value. This deviation is determined from (Fonte 2013)

$$\left.\frac{h_{\mathrm{uc}}}{h_{\mathrm{loc}}}\right|_{x^*=x^*_{\mathrm{uc}}} = \frac{3}{2}\frac{\left(\frac{n_x}{n_x-1/2}\right)^{2/3}-\left(\frac{n_x-1}{n_x-1/2}\right)^{2/3}}{\left(\frac{1}{n_x-1/2}\right)} \tag{3.19}$$

where $h_{\mathrm{loc}}$ is the local convective heat transfer coefficient and $x^*_{\mathrm{uc}}$ is the dimensionless entrance length of the unit cell, determined using Equation 3.17, evaluated at $x_{\mathrm{uc}}$, which is the distance from the inlet to the centre of the unit cell in the flow direction. The ratio determined by Equation 3.19 quickly tends to one when $n_x$ increases along the NUB. Taking into account the dimensions of the Lab-Scale NETmix 2D used as the geometrical model basis, relatively small differences are obtained between the local and averaged heat transfer coefficient (e.g. 0.86% and 0.15% for unit cells of row two and four, respectively). Therefore, the Nusselt numbers can be considered as effectively constant after a few cells, and thus all the reported heat transfer coefficients were determined at the fourth cell of the NUB.

The Nusselt number values, for both sets of boundary conditions, are reported as a function of the inlet Reynolds number $\mathrm{Re}_{\mathrm{in}}$ (evaluated at the inlet channel's conditions), in Figure 3.3. The Nusselt number is constant for low Reynolds numbers $(<20)$, converging to an asymptotic lower constant value, where the thermal boundary layer is completely developed, resulting in a constant heat transfer coefficient along the device, regardless of the Reynolds number. For larger Reynolds numbers $(>20)$, a gradual increase of the Nusselt number is observed, being particularly evident in the range between $\mathrm{Re}_{\mathrm{in}}=50$ and $\mathrm{Re}_{\mathrm{in}}=150$, the regions at which instabilities, such as oscillations and small-scale vortices start to appear. Flow dynamics change at $\mathrm{Re}_{\mathrm{in}}=50$ with a strong impact in the increase of the Nusselt number. For $\mathrm{Re}_{\mathrm{in}}\geq 150$, the oscillatory flow patterns are completely developed, thus

inducing strong chaotic laminar mixing that greatly increases the heat transfer coefficient with increasing the Reynolds number.

The analysis of Figure 3.3 is more interestingly made if combined with Figure 3.4, which identifies different flow regimes at different Reynolds numbers. The increase of the Nusselt number with the Reynolds number is explained by the flow regime transitions that occur inside the mixing chambers. The contour maps of the sign (positive or negative, i.e., the direction of the flow) of the $z$ component of the vorticity field $\vec{\omega}$, at the middle plane of the unit cell at the fourth row for simulations with constant wall temperature boundary condition, for different Reynolds numbers is shown in Figure 3.4.

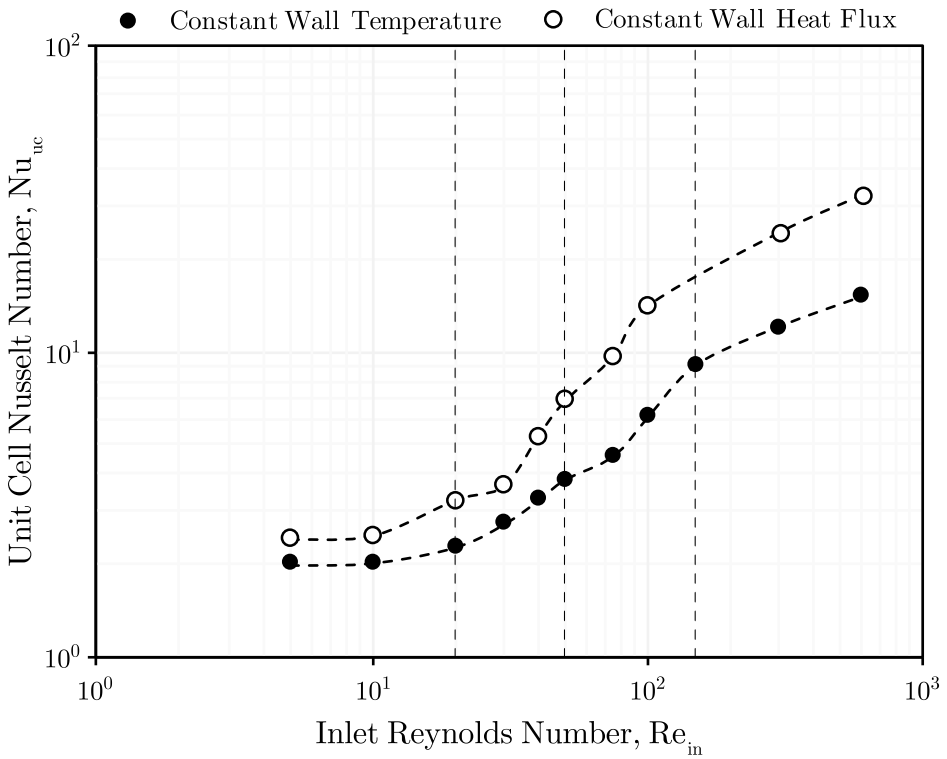



Figure 3.3 – Unit cell Nusselt number as a function of the inlet Reynolds number for both wall boundary conditions: constant temperature and constant heat flux. Dashed lines represent the boundaries of the different identified flow regimes.

From Figure 3.4, it is possible to distinguish different operational regimes from the vorticity map analysis. For very low Reynolds number $\left(\leq 10\right)$, the flow is mostly segregated and steady parallel flow is observed. For $\mathrm{Re}_{in} = 5$, the impinging jets present opposite sign vorticity due to the symmetry of the expansion that occurs at

the chamber. Small recirculation zones are only observed in the lower region of the chamber. The same behaviour is observed at $\mathrm{Re}_{in} = 10$, however, the increase of inertial forces translates the point of velocity curling to a point above the centre of the chamber. This turnover point moves up towards the wall of the chamber as Reynolds number increases. At $\mathrm{Re}_{in} = 20$, a flow regime transition occurs, which results in the appearance of strong dynamic vortices near the walls in the lateral regions of the chambers, and in the loss of the symmetry within the $z$ direction. This represents the start of the appearance of instabilities in the chambers, although there is no significant influence of these on the overall hydrodynamics. Nonetheless, this transition results in a Nusselt number increase. At this point, the flow is no long fully parallel. The vortices intensity, area and asymmetry increase with the increase of the Reynolds number, resulting in deformations, such as stretching and folding, and in an increase of the fluid volume interfacial area (Ottino 1989), thus enhancing heat transfer. This phenomenon should be also beneficial for interphase mass transfer.

A second flow regime transition is observed at $\mathrm{Re}_{in} \geq 50$, where vortices start to appear in the upper region of the chamber, near the walls. The slopes of the curves from Figure 3.3 in the region where $\mathrm{Re}_{in} \geq 50$ increases when compared to the region $20 < \mathrm{Re}_{in} < 50$, indicating that the appearance of these secondary vortices enhance mixing and heat transfer even further. When the Reynolds number reaches the critical value, at $\mathrm{Re}_{in} \geq 150$, the system evolves to a self-sustained chaotic dynamic laminar flow regime, characterized by its dynamic asymmetric flow patterns. This behaviour induces strong dynamic oscillations, which results in the formation of the vortices observed in Figure 3.4. These vortices have the capacity to interact with each other, deforming the fluid elements even further (Amon et al. 1996). This results in an increase of the heat transfer rates through the walls.

Figure 3.4 shows results for constant wall temperature simulations, but the same behaviour is observed for constant wall heat flux simulations, which is also evident from the shape of the two curves in Figure 3.3.

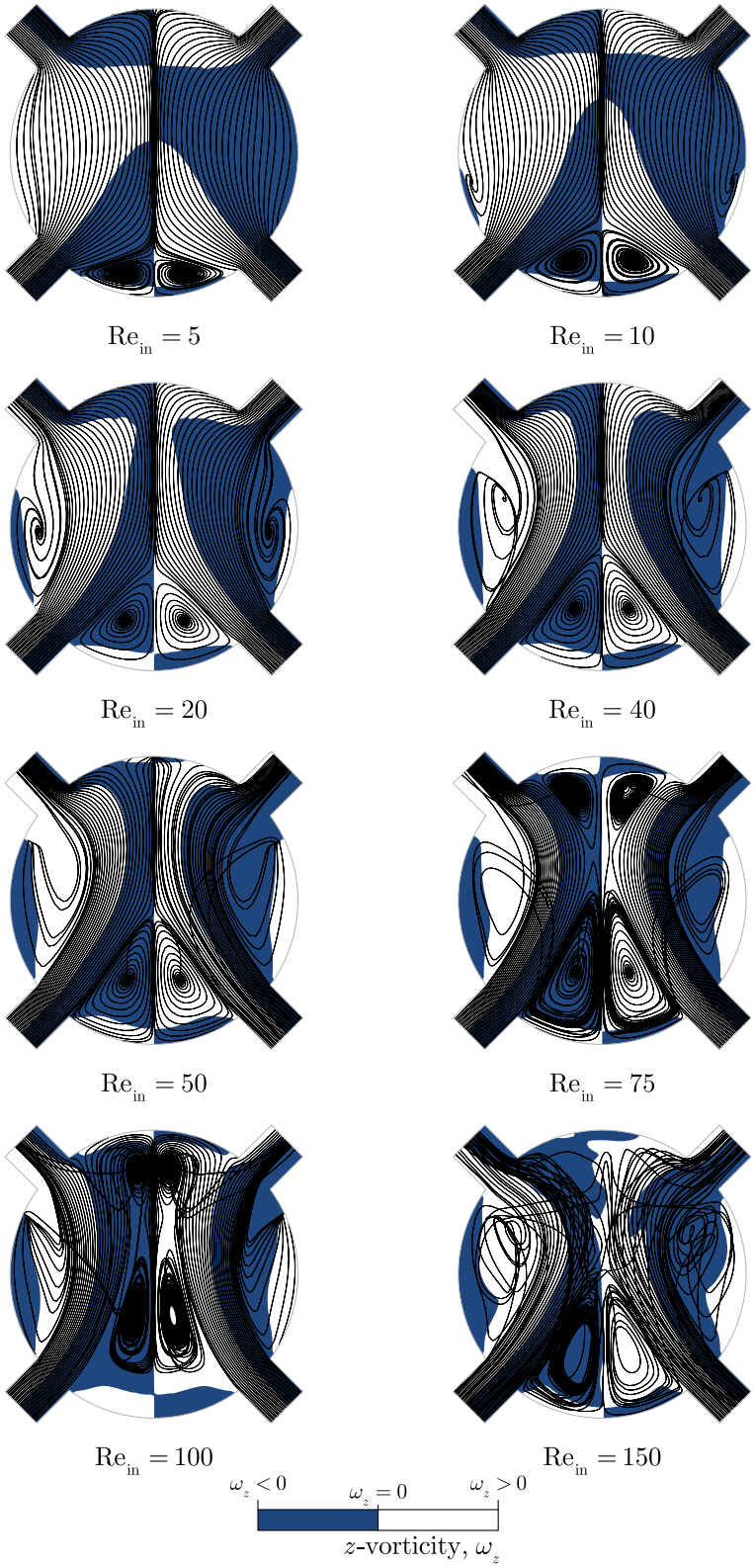



Figure 3.4 – $z$-vorticity contour maps at the middle plane of the unit cell at the fourth row as a function of the inlet Reynolds number, and trajectories for simulations with constant wall temperature.

## 3.4 Heat Transfer Validation and Comparison

To ascertain the impact of the previous results, a comparison of the NUB model with other similar heat transfer situations is required. Since the flow in NETmix for low Reynolds numbers is fully parallel and segregated, a comparison with laminar flow between parallel plates seems to be the most appropriate. Also, NETmix and parallel plates possess geometrical similarities, since heat transfer is done through both bottom and top walls, if neglecting conduction through lateral walls in NETmix. Additionally, the case for laminar flow between parallel plates presents analytical solutions for asymptotic regimes, derived for Newtonian fluids with constant physical properties and fully developed laminar velocity profiles (Bird et al. 2002), making it directly comparable.

Two asymptotic values are analysed in laminar flow between parallel plates, as clearly demonstrated in Figure 3.5. In a first region, the thermal boundary layer is still being developed with the distance, while in the second region the thermal boundary layer achieves its maximum thickness of $\omega_{PP}/2$ (half of the plates gap size), where the maximum heat transfer resistance is observed. The use of the dimensionless thermal entrance length $x^*$ is useful to determine in which regime the system is: for low thermal entrance lengths, the thermal boundary layer is still under development; for high thermal entrance lengths, the boundary layer is fully developed.

For flow between parallel plates, the local Nusselt number $\mathrm{Nu}_{PP}$ is defined as

$$\mathrm{Nu}_{PP} = \frac{2h_{PP}\omega_{PP}}{\kappa} \tag{3.20}$$

where $h_{PP}$ is the parallel plates local convective heat transfer coefficient.

For constant wall temperature, in the flow region where the thermal boundary layer is still under development, the local Nusselt number $\mathrm{Nu}_{PP}$ is a function of the dimensionless thermal entrance length, and is given by (Bird et al. 2002)

$$\mathrm{Nu}_{\mathrm{PP}} = \frac{2}{3^{1/3}\Gamma\left(4/3\right)}\left(x^{*}_{\mathrm{PP}}\right)^{-1/3} \tag{3.21}$$

where $\Gamma$ is the gamma function and $x^{*}_{\mathrm{PP}}$ is the dimensionless thermal entrance length and is estimated by

$$x^{*}_{\mathrm{PP}} = \frac{1}{\mathrm{Re}_{\mathrm{PP}}\,\mathrm{Pr}}\left(\frac{x_{\mathrm{PP}}}{\omega_{\mathrm{PP}}}\right) \tag{3.22}$$

where $x_{\mathrm{PP}}$ is the distance from the inlet and $\mathrm{Re}_{\mathrm{PP}}$ is the parallel plates Reynolds number, determined by

$$\mathrm{Re}_{\mathrm{PP}} = \frac{2\omega_{\mathrm{PP}}\rho\overline{v}_{\mathrm{PP}}}{\mu} \tag{3.23}$$

where $\overline{v}_{\mathrm{PP}}$ is the average velocity between parallel plates. For the thermally fully developed region, the Nusselt number for constant wall heat flux is constant and equal to $\mathrm{Nu}_{\mathrm{PP}} = 7.54$ (Bird et al. 2002).

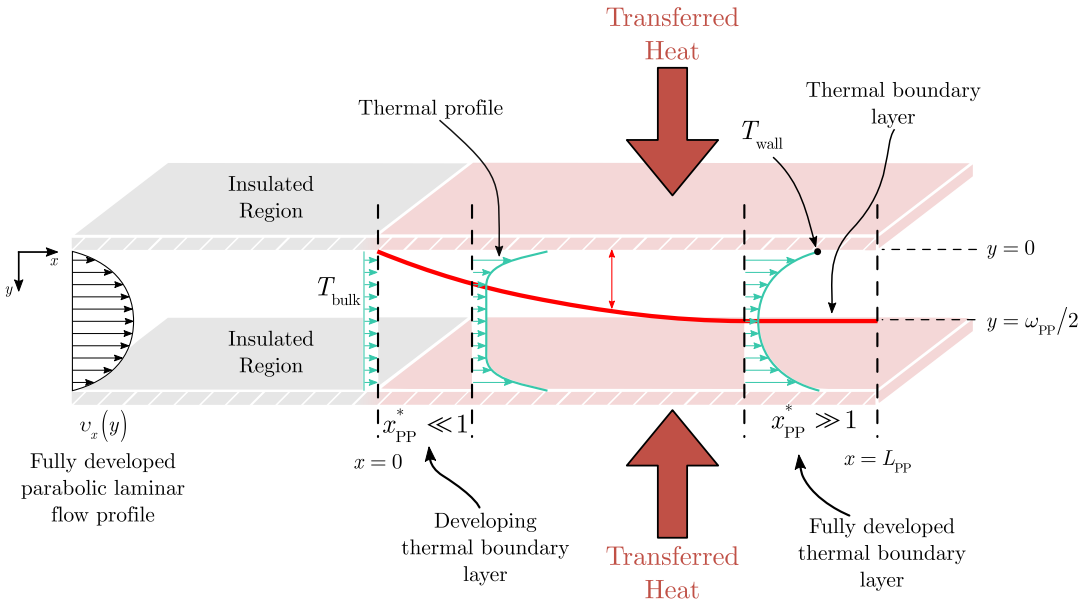



Figure 3.5 – Heat transfer in laminar flow between parallel plates schematic and development of thermal boundary layer with length.

For constant wall heat flux, in the region where the thermal boundary layer is still being developed, the Nusselt number $\mathrm{Nu}_{\mathrm{PP}}$ is given by (Bird et al. 2002)

$$\mathrm{Nu}_{\mathrm{PP}} = \frac{2\Gamma\left(2/3\right)}{3^{1/3}}\left(x^{*}_{\mathrm{PP}}\right)^{-1/3} \tag{3.24}$$

and for the thermally fully developed boundary layer, the Nusselt number is found to be $\mathrm{Nu}_{\mathrm{PP}} = 8.24$ (Bird et al. 2002). Equations 3.21 and 3.24 were obtained by analytically solving the energy equation, assuming that the laminar parabolic velocity profile is fully developed and constant fluid properties, as already mentioned.

As defined by Fonte (2013), prior to a direct comparison between Nusselt numbers for NUB and parallel plates, it is necessary to take into consideration the geometrical and Reynolds/Nusselt numbers definitions differences. The following analogy for the thermal entrance length is used

$$x^{*}_{\mathrm{uc}} = \frac{2\omega_{\mathrm{PP}}}{d_{\mathrm{h}}} x^{*}_{\mathrm{PP}} \tag{3.25}$$

where $x^{*}_{\mathrm{uc}}$ is the dimensionless thermal entrance length for the NETmix unit cell, and is defined as

$$x^{*}_{\mathrm{uc}} = \frac{1}{\mathrm{Re}_{\mathrm{c}}\,\mathrm{Pr}}\left(\frac{x_{\mathrm{uc}}}{\omega_{n}}\right) \tag{3.26}$$

where $x_{\mathrm{uc}}$ is determined from

$$x_{\mathrm{uc}} = \left(n_{x} - \frac{1}{2}\right)\frac{L}{\sqrt{2}} \tag{3.27}$$

For the Nusselt number, a similar strategy is used

$$\mathrm{Nu}_{\mathrm{uc}} = \frac{d_{\mathrm{h}}}{2\omega_{\mathrm{PP}}}\mathrm{Nu}_{\mathrm{PP}} \tag{3.28}$$

By using these analogies, the direct comparison of the Nusselt numbers computed for the unit cell at the fourth row of the NUB model, with the analogue value obtained for laminar flow between parallel plates is now possible. This direct comparison between NETmix and parallel plates is only meaningful if the NUB values can be validated in a region where the flow patterns for both cases are similar. From Figure 3.4, it is possible to observe that parallel and segregated flow in NETmix occurs only

at very low Reynolds numbers $\left(<10\right)$ and Fonte (2013) have shown that the Nusselt numbers obtained from simulations for the NUB model is in agreement with the analytical solutions for laminar flow between parallel plates, in the whole range of the working regimes, at $\mathrm{Re}_{\mathrm{in}}=10$. Fonte (2013) varied the dimensionless thermal entrance length by changing not the Reynolds number, but the Prandtl number, and verified that the NETmix behaves as parallel plates, even for very low values of $x_{\mathrm{uc}}^{*}$, thus validating the heat transfer model. A potential heat transfer enhancement could arise due to the hydrodynamic changes that occur with the increase of the Reynolds number. This means that the boundary layer profile is different than for parallel plates when instabilities start to appear, otherwise, it would increase at the same rate as in parallel plates.

The dependence of the unit cell Nusselt number on the dimensionless thermal entrance length is shown in Figure 3.6 and Figure 3.7, for both sets of simulations using different wall boundary conditions. With the increase of the Reynolds number, the Nusselt number values starts to deviate from the expected value for flow between parallel plates, tending to a considerably higher asymptotic value (represented by the dashed line in Figure 3.6). This is an already expected behaviour from the observed evolution of the flow patterns from Figure 3.4. This augmented heat transfer capability demonstrates the critical impact of the vortices generation on the Nusselt number, since this increase is not only due to the fact that the boundary layer is still not fully developed. In fact, these vortices have an important impact on the reduction of the boundary layer's thickness, thus enhancing the heat transfer rates. When the critical Reynolds number is achieved, the effect of the existence of three-dimensional flow in the mixing chambers due to the dynamic oscillatory flow regime, is responsible for the observed heat transfer rate enhancement when compared to the rate obtained for laminar flow between parallel plates. In the low Reynolds number region, NETmix presents the same behaviour as parallel plates, in agreement with the previous results. This behaviour is clearly observed in both wall boundary conditions (Figure 3.6 and Figure 3.7).

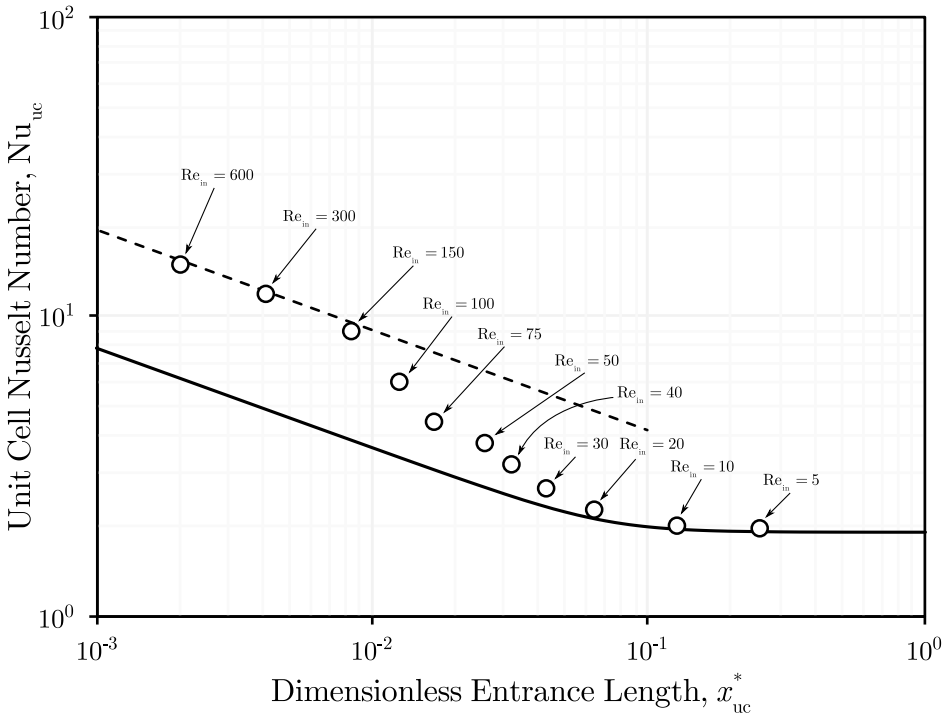



Figure 3.6 – Nusselt number as a function of the dimensionless thermal entrance length for constant wall temperature boundary condition. The points represent the NUB unit cell values evaluated for the cell at the fourth row; the solid line represents the analogue values for laminar flow between parallel plates; the dashed line represents the new asymptotic value for NETmix.

It was also observed that, for large Reynolds numbers $\left(\mathrm{Re}_{in} > 150\right)$, where the flow oscillations are fully developed, the Nusselt number values become independent of the distance from the inlet. This means that for large Reynolds numbers, the average NETmix unit cell Nusselt number is constant and equal for all chambers, whereas for low Reynolds numbers, the Nusselt number gradually decreases within the reactor. The flow disturbances that occur in the chambers due to the impinging jet interactions result in flow instabilities and oscillations, resulting in a constant boundary layer's thickness along the reactor, even in the very first rows of cells. This observation is particularly important, since it guarantees that the whole reactor is operating with the same heat transfer efficiency and homogenization, also due to the very small volume of dead zones (Laranjeira et al. 2009). This means that the heat transfer rate is varying along the reactor only due to different thermal gradients (the driving force for heat transfer).

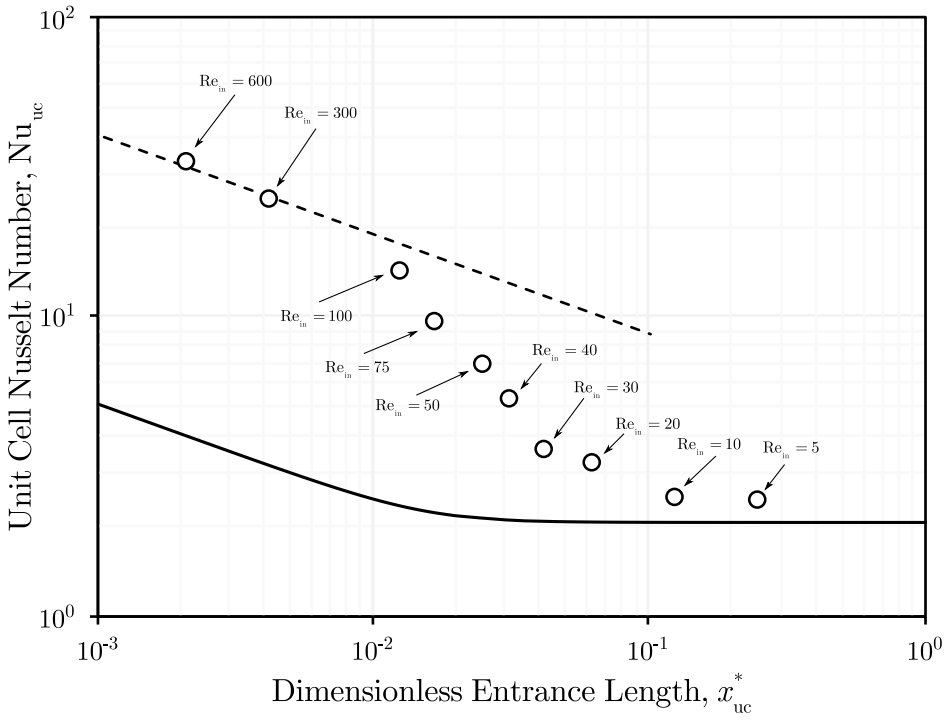



Figure 3.7 – Nusselt number as a function of the dimensionless thermal entrance length for constant wall heat flux boundary condition. The points represent the NUB unit cell values evaluated for the cell at the fourth row; the solid line represents the analogue values for laminar flow between parallel plates; the dashed line represents the new asymptotic value for NETmix.

## 3.5 Nusselt Number Correlations

Taking into consideration the relationships that can be made between the NUB and parallel plates, shown in Equations 3.25 and 3.28, the most suitable way to determine the Nusselt number for NETmix is by using the solution for laminar flow between parallel plates as a basis.

As also shown by Fonte (2013), the enhancement factor $E_{\mathrm{Nu}}$ of the Nusselt number for NUB when compared with parallel flow between plates can be determined by

$$E_{\mathrm{Nu}} = \frac{\mathrm{Nu}_{\mathrm{uc}}}{\mathrm{Nu}_{\mathrm{PP}}} \tag{3.29}$$

If no heat transfer rate enhancement was observed in the NETmix, the enhancement factor would be equal to one, regardless of the operational Reynolds number. For low Reynolds number $\left(<10\right)$, NETmix essentially behaves as parallel plates, and therefore $E_{\mathrm{Nu}} \to 1$. However, with the increase of the Reynolds number and the

deviation observed when compared the parallel plates, the enhancement factor also increases. The enhancement factor of NETmix for both sets of simulations is presented in Figure 3.8.

The fitting curves represented in Figure 3.8 can be fitted to a purely empirical mathematical expression with the following form

$$E_{\mathrm{Nu}} = E_0 + \frac{E_\infty - E_0}{1 + \exp\left(-k\left(\log_{10}\left(\mathrm{Re}\right) - \log_{10}\left(\mathrm{Re}_0\right)\right)\left|\log_{10}\left(\mathrm{Re}\right) - \log_{10}\left(\mathrm{Re}_0\right)\right|^{n-1}\right)} \tag{3.30}$$

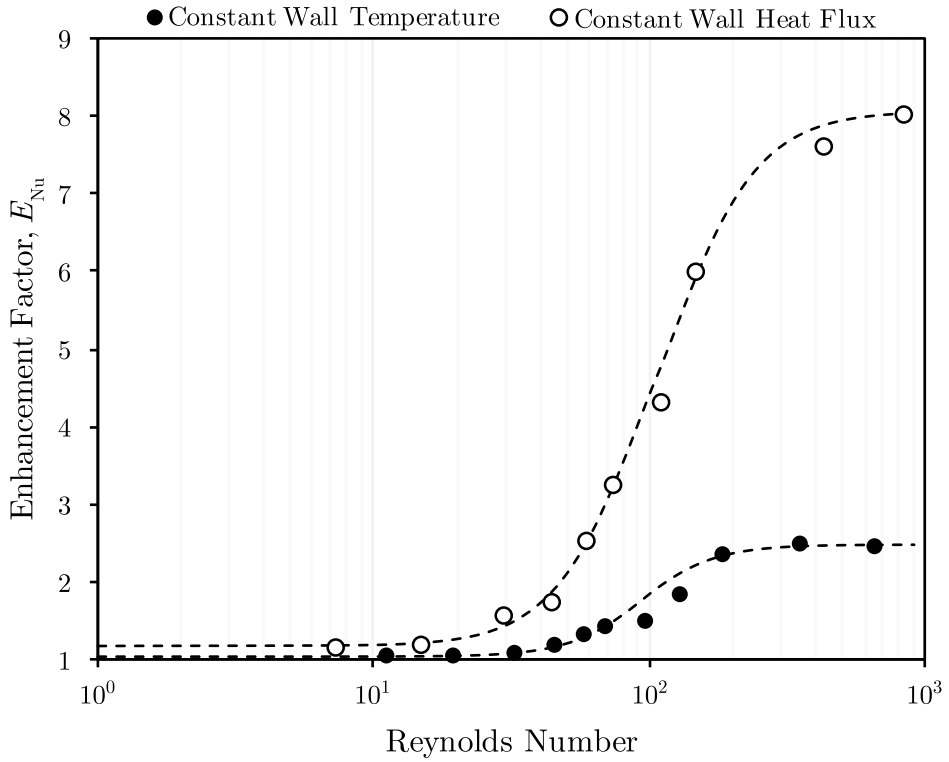



Figure 3.8 – Enhancement factor for Nusselt number as a function of the Reynolds number, as defined by Equation 3.29, for both boundary conditions: filled circles – constant wall temperature; empty circles – constant wall heat flux. The dashed lines represent the fitting curves.

The variables $E_0$, $E_\infty$, $\mathrm{Re}_0$, $k$ and $n$ are fitting parameters, obtained by minimization of the least squares method. The value of the parameters, together with the coefficient of determination $r^2$ of the fittings, is presented in Table 3.1. The term $\left|\log_{10}\left(\mathrm{Re}\right) - \log_{10}\left(\mathrm{Re}_0\right)\right|$ is only present due to mathematical domain limitations for certain values of $n$. In this way, $n$ can have any value.

Table 3.1 – Equation 3.30 fitting parameters.

| Parameter | Constant Wall Temperature | Constant Wall Heat Flux |
|---|---|---|
| $E_0$ | 1.05 | 1.17 |
| $E_\infty$ | 2.49 | 8.05 |
| $\mathrm{Re}_0$ | 92.6 | 104.7 |
| $k$ | 7.26 | 6.12 |
| $n$ | 0.97 | 1.05 |
| $r^2$ | 0.94 | 0.99 |

The fitting equation containing five parameters is capable to fit reasonably well the enhancement factor of the Nusselt number in NETmix when compared to parallel plates as a function of the local Reynolds number (evaluated at the local average conditions of temperature of the unit cell), within the range of the study. A maximum deviation of 25% between the fitting curve when compared to the result obtained from simulation is observed for the constant wall temperature simulation. Interestingly, deviations are larger when the Reynolds number is close to 100, probably due to the appearance of oscillations. As expected, the parameter $E_0$, which represents the value of the enhancement factor for low Reynolds numbers, is close to one, meaning that no significant enhancement when compared to parallel plates is observed in this region. The parameter $E_\infty$ represents the maximum enhancement obtained for large Reynolds numbers. This value triples for constant wall heat flux simulations when compared with constant wall temperature simulations. The parameter $\mathrm{Re}_0$ represents the inflection point of the regression, and its value is similar for both boundary conditions, and it may indicate the point at which the oscillations represent an important role for heat transfer. The parameter $k$ is related to the slope of the function near the inflection point $\mathrm{Re}_0$. Again, the values of $k$ are very similar in both sets of boundary conditions, which means that the heat transfer enhancement increases at the same rate, consistent with similar flow behaviours induced by the appearance of vortices and oscillations.

Knowing the enhancement factor, and determining the analogue Nusselt number for laminar flow between parallel plates, using Equations 3.21 through 3.28, it is possible to determine the effective NETmix unit cell Nusselt number, which can be used for the design of a NETmix device with heat transfer capabilities.

A topic that requires to be discussed is related with the geometrical relationships in the NUB model. The analogy between NETmix and laminar flow between parallel plates is a function of $d_h/\omega_{PP}$, as previously observed. If one assumes that $\omega_{PP} = \omega_n$, then

$$\frac{d_h}{\omega_n} = 2\left(\frac{\omega_n}{d_c} + 1\right)^{-1} \tag{3.31}$$

Which means that Equation 3.28 can be rewritten as

$$\mathrm{Nu}_{uc} = \left(\frac{\omega_n}{d_c} + 1\right)^{-1} \mathrm{Nu}_{PP} \tag{3.32}$$

This means that the Nusselt number decreases with the increase of the ratio $\omega_n/d_c$, which is the NETmix channel's aspect ratio, and increases with the decrease of $\omega_n/d_c$. When $\omega_n/d_c \to 0$, it means that $d_c \gg \omega_n$, and the unit cell Nusselt number tends to approach to the solution of the Nusselt number for laminar flow between parallel plates. On the contrary, when $\omega_n/d_c \to 1$, the Nusselt number tends to approach to the Nusselt number for laminar flow in tubes. This behaviour is shown in Figure 3.9, where it is represented the Nusselt number for laminar flow between parallel plates and in tubes for constant wall temperature condition, as a function of the thermal entrance length, as well as the curves for NETmix with two different $\omega_n/d_c$ ratios using Equation 3.30 as well as the parallel plates analogy. It is also represented the points obtained in this study by simulation for $\omega_n/d_c = 3$ (the original NUB model), and for $\omega_n/d_c = 1$ in the region where no oscillations are observed, just to verify the influence of the NETmix geometry in the parallel flow regime.

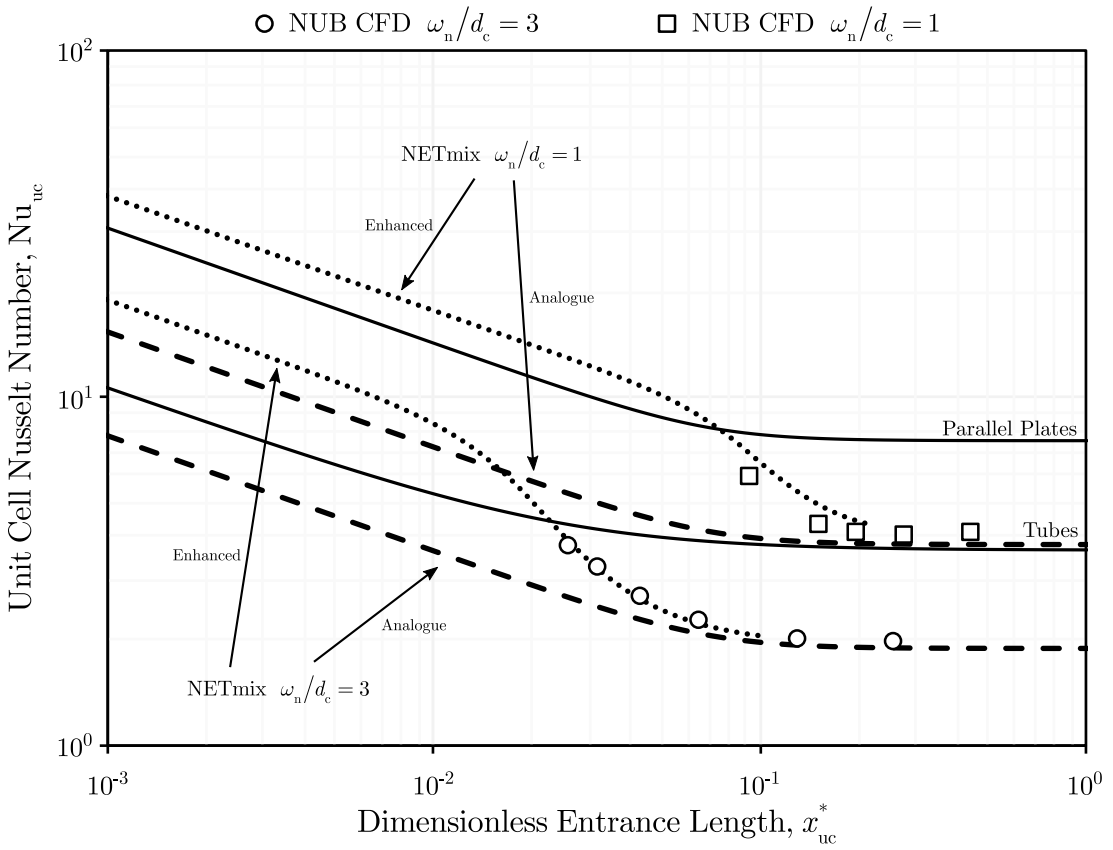



Figure 3.9 – Nusselt number comparison between parallel plates, tubes and NETmix for two different $\omega_n/d_c$ ratios, as a function of the dimensionless thermal entrance length for constant wall temperature. The dashed lines represent the NETmix analogue curve, obtained using Equations 3.21 and 3.28, while the dotted lines represent the NETmix curves when heat transfer enhancement due to oscillations is observed, obtained using Equation 3.30.

Similarly to parallel plates, laminar flow in tubes in the region where the thermal boundary layer is under development, assuming constant wall temperature, is represented by (Bird et al. 2002)

$$\mathrm{Nu}_{\mathrm{tube}} = \frac{2}{9^{1/3}\Gamma\left(4/3\right)}\left(x^*_{\mathrm{tube}}\right)^{-1/3} \tag{3.33}$$

where $\mathrm{Nu}_{\mathrm{tube}}$ is the local tube Nusselt number and defined as

$$\mathrm{Nu}_{\mathrm{tube}} = \frac{h_{\mathrm{tube}} D_{\mathrm{tube}}}{\kappa} \tag{3.34}$$

where $h_{\mathrm{tube}}$ is the tube local convective heat transfer coefficient and $D_{\mathrm{tube}}$ is the tube's diameter. The $x^*_{\mathrm{tube}}$ is the dimensionless thermal entrance length for tube and is estimated from

$$x_{\text{tube}}^{*} = \frac{1}{\text{Re}_{\text{tube}}\,\text{Pr}}\left(\frac{x_{\text{tube}}}{D_{\text{tube}}}\right) \tag{3.35}$$

where $x_{\text{tube}}$ is the distance from the inlet and $\text{Re}_{\text{tube}}$ is the Reynolds number for the tube, defined as

$$\text{Re}_{\text{tube}} = \frac{\rho \overline{v}_{\text{tube}} D_{\text{tube}}}{\mu} \tag{3.36}$$

where $\overline{v}_{\text{tube}}$ is the average fluid velocity in the tube. For the region where the thermal boundary layer is fully developed, the Nusselt number for laminar flow in tubes is constant and equal to $\text{Nu}_{\text{tube}} = 3.66$ (Bird et al. 2002).

In Figure 3.9, two different curves are represented for NETmix, for each $\omega_{\text{n}}/d_{\text{c}}$ ratio. The dashed lines represent the curves analogue to parallel plates for NETmix, as described in the beginning of Section 3.4 The dotted lines represent the curves for NETmix considering the enhanced Nusselt number for different Reynolds numbers, $\text{Nu}_{\text{uc}}^{\text{enh}}$. This is determined by considering that in the range of $x_{\text{uc}}^{*}$ presented in Figure 3.9, its variation is only due to variation in the Reynolds number. The following equation is used to determine the dotted curves:

$$\text{Nu}_{\text{uc}}^{\text{enh}} = E_{\text{Nu}}\left(\text{Re}\right)\text{Nu}_{\text{uc}}\left(\text{Re}\right) \tag{3.37}$$

where $E_{\text{Nu}}$ is determined for a given Reynolds number through Equation 3.30, and $\text{Nu}_{\text{uc}}$ is the unit cell Nusselt number analogue to parallel plate, and is determined for a given Reynolds, and thus a given $x_{\text{uc}}^{*}$, using Equation 3.21 and Equation 3.28.

The points represented in Figure 3.9 are the NETmix unit cell Nusselt numbers obtained from CFD simulation for $\omega_{\text{n}}/d_{\text{c}} = 3$, as previously discussed, and for $\omega_{\text{n}}/d_{\text{c}} = 1$, for constant wall temperature. These last values were obtained using the same strategy described in Section 3.2. The $\omega_{\text{n}}/d_{\text{c}}$ ratio is altered by reducing the network depth $\omega_{\text{n}}$ from $3\,\text{mm}$ to $1\,\text{mm}$. The numerical grid maintained the number

of elements, since the discretization in the $z$ direction was kept constant, by reducing the element size (but not the number) in this direction.

The Nusselt numbers obtained from CFD simulation for $\omega_n/d_c = 1$ are in good agreement with what is expected from the fitting Equation 3.30, meaning that the enhancement factor is only dependent on the Reynolds number, and not on the $\omega_n/d_c$. On the contrary, the NETmix Nusselt number tends to increase with the reduction of the $\omega_n/d_c$ ratio. Temperature contour maps in the middle plane of the NUB for $\omega_n/d_c = 3$ and $\omega_n/d_c = 1$ are shown in Figure 3.10.

The temperature contour maps for different $\omega_n/d_c$ ratios possess very similar temperature patterns. At $\mathrm{Re}_{in} = 50$, a few vortices are disclosed but still no fully chaotic flow patterns are observed, and thus mixing is poor, resulting in the dead zones observed in Figure 3.10, mainly in the lateral regions of the chambers. In the channels and in the central zone of the chambers, convection is relatively large, and the temperatures are lower than in the remaining regions. This behaviour is observed for both $\omega_n/d_c$ ratios. The increase of the temperature in the lateral regions is due to the fact that in the steady state, no significant flow is occurring in those regions, and the temperature increase mainly due to conduction. A significant difference however is verified if the magnitude of the temperatures is compared. The temperatures for $\omega_n/d_c = 1$ are globally higher than for $\omega_n/d_c = 3$, due to the smaller depth of the NETmix network, thus reducing the heat transfer resistance in the direction normal to the flow direction.

The previous results show that the NETmix unit cell Nusselt number can be estimated for the Lab-Scale NETmix 2D, at least in the range of $\omega_n/d_c \geq 1$. More studies are required to evaluate if for smaller aspect ratios $\left(\omega_n/d_c < 1\right)$, the presented models are still accurate.

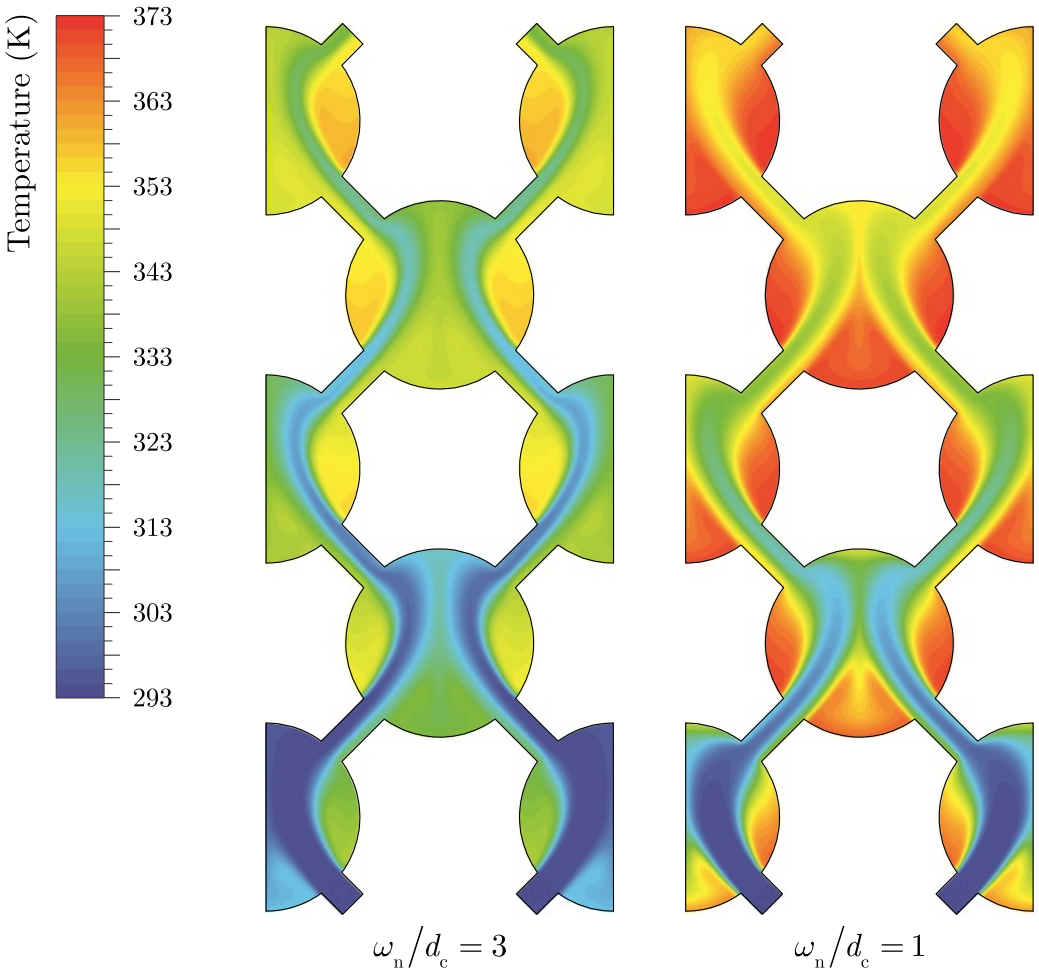



Figure 3.10 – Temperature contour maps in NUB for $Re_{in} = 50$ and constant wall temperature, at the middle plane, for $\omega_n/d_c = 3$ and $\omega_n/d_c = 1$.

## 3.6 NETmix Heat Transfer Benchmarking

The prediction of Nusselt numbers in the NUB model are crucial for the determination of the specific heat transfer capacity of NETmix, and for its comparison with the most common technologies at laboratorial and/or industrial scales, used for heat transfer, such as shell and tube or plates heat exchangers. The NETmix Nusselt numbers for constant wall temperature are compared in Figure 3.11 with the Nusselt numbers for fully developed flow in tubes and between parallel plates, for both laminar and turbulent regimes, also for constant wall temperature. For the comparison, only the heat transfer resistance for the inner side of the system was considered, i.e. the heat transfer by conduction through the lateral solid surfaces and the external heat transfer resistance are not considered.

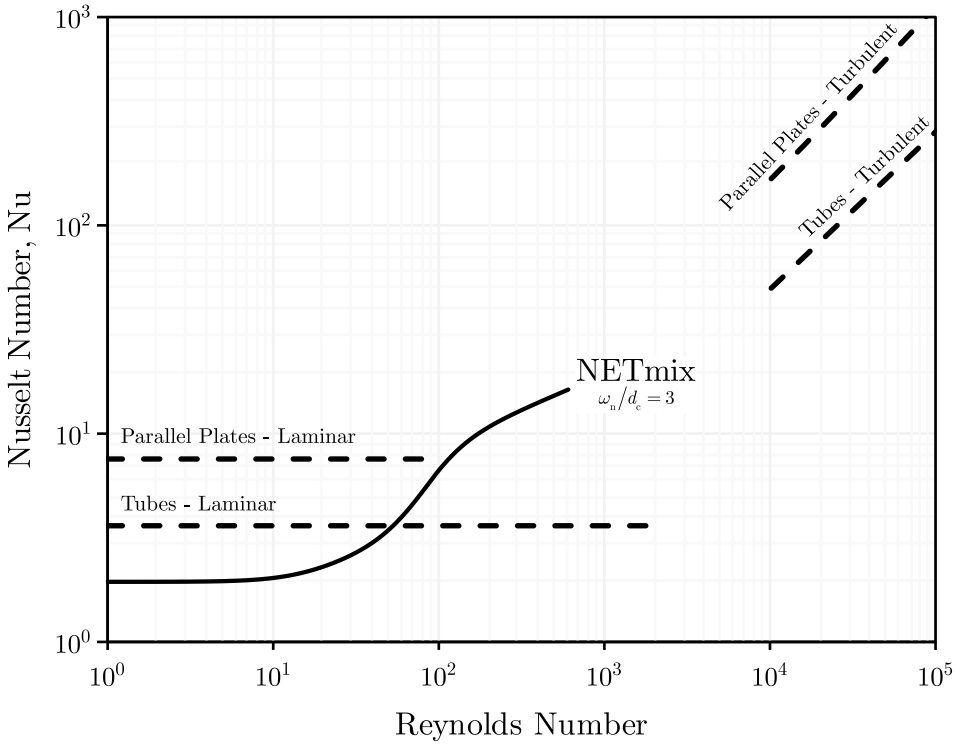



Figure 3.11 – Comparison of the Nusselt number as a function of Reynolds number of fully developed laminar flow in pipes and between parallel plates, turbulent flow in pipes and between parallel plates, and for NETmix device with $\omega_n/d_c = 3$, for constant wall temperature and $\mathrm{Pr} \approx 7$.

Nusselt numbers for the NETmix unit cell are determined using Equation 3.30, and the analogies with laminar flow between parallel plates, as explained in Section 3.4, for a NETmix network with the same characteristic dimensions as the Lab-Scale NETmix 2D and the NUB model. Nusselt numbers for fully developed laminar flow in tubes and between parallel plates for constant wall temperature, represented in Figure 3.11, are constant and independent of the Reynolds number (Shah and London 1978, Bird et al. 2002), as observed in Figure 3.9 for large dimensionless thermal length (the condition for fully developed thermal boundary layer). Nusselt number for fully developed turbulent flows in pipes and between parallel plates are also represented in Figure 3.11, and present a strong dependence on the Reynolds and Prandtl numbers, being possible to estimate from correlations existing in literature. The Dittus-Boelter correlation (Dittus and Boelter 1985) is widely used for the determination of the Nusselt number for turbulent flow in pipes, and can be adapted for the determination of the Nusselt number for turbulent flow between parallel plates (Shibani and Özisik 1977). In each of the cases, the Prandtl number, $\mathrm{Pr} \approx 7$,

used for comparison is that of the water at a temperature of about 25 °C (EngineeringToolBox).

Figure 3.11 shows that within the range of the present study, for the typical NETmix operation Reynolds numbers range between 150-600, NETmix presents Nusselt numbers up to 2-3 times larger than those of laminar flow in tubes or between parallel plates for constant wall temperature. As observed from Figure 3.8 can be 8 if the constant wall heat flux is compared. For low Reynolds numbers, the absence of flow oscillations and vortices in NETmix results in a constant fully developed Nusselt number, similar to what happens in laminar flow between parallel plates and in tubes. This is due to the formation of the thermal boundary layer that grows along the mixer. However, the presence of flow disturbances causes a significant increase in the Nusselt numbers, and at or above the critical Reynolds number, the Nusselt number is larger for the NETmix than for tubes or plates.

The overall heat transfer performance for different devices cannot be compared solely based on the Nusselt numbers (and hence, heat transfer coefficients). The heat transfer capacity of a heat exchange equipment is also determined by the availability of direct contact area for heat transfer. Therefore, a comparison of the active specific surface area for heat transfer between different heat exchange equipment has to be made. For that, the most commonly used equipment for heat transfer coupled with chemical reaction is considered for comparison purposes, namely: stirred tanks with external jack or serpentines; jacketed tubular reactors; stirred tanks with external heat exchanger; and microreactors.

The specific area of NETmix is determined from geometrical considerations, using the unit cell dimensions. NETmix has a similar geometry when compared to parallel plates. However, a reduction of the effective heat transfer area occurs for NETmix when compared with parallel plates with the same plate clearance as NETmix, i.e., $\omega_{n} = \omega_{PP}$. For the specific case of the NUB model (unit cell with the dimensions of the Lab-Scale NETmix 2D), an area reduction of 27% relatively to parallel plates is

obtained, even if the lateral areas of the NETmix chambers and channels are considered.

The specific surface area of a NETmix unit cell $A_{\text{transf, uc}}/V_{\text{uc}}$, considering the lateral areas is estimated from

$$\frac{A_{\text{transf, uc}}}{V_{\text{uc}}} \approx \left(\frac{1}{\omega_{\text{n}}}\right) \frac{1+2\left(\frac{\omega_{\text{n}}}{D_{\text{ch}}}\right)+\frac{8}{\pi}\left(\frac{L-\sqrt{D_{\text{ch}}^2-d_{\text{c}}^2}}{D_{\text{ch}}}\frac{d_{\text{c}}}{D_{\text{ch}}}+\frac{\omega_{\text{n}}}{D_{\text{ch}}}\frac{d_{\text{c}}}{D_{\text{ch}}}\right)}{\frac{1}{2}+\frac{4}{\pi}\left(\frac{L-\sqrt{D_{\text{ch}}^2-d_{\text{c}}^2}}{D_{\text{ch}}}\frac{d_{\text{c}}}{D_{\text{ch}}}\right)} \tag{3.38}$$

For stirred tanks with cooling jackets, serpentines or external heat exchangers, specific surface areas are presented in literature (Trambouze et al. 1984, Villermaux 1993). The specific surface area for tubular reactors and microreactors can be estimated from geometrical considerations, using typical values of characteristic dimensions (diameter for tubular reactors and channel's size for microreactors), since they can be conceptualized as cylinders/tubes that are in direct contact with the cooling fluid. In this analysis, it is ignored the fact that the area of heat transfer in a tube varies along the thickness of the tube, and therefore, only the inner diameter of the tubes are considered (since they represented that highest specific surface area).

Since reactors/heat exchangers are available with different dimensions, the specific surface areas of the equipment are determined within a specific range of characteristic dimensions, considering a minimum and a maximum value for this dimension, in agreement with typical values used in these technologies.

Specific surface areas for different heat exchange equipment are available in Figure 3.12, as well as the characteristic dimensions considered in the analysis, for each type of equipment, when applicable. Figure 3.12 shows that NETmix presents 2-3 orders of magnitude larger specific surface area for heat transfer than the most commonly used technologies, such as stirred tanks or tubular reactors. The specific surface area of NETmix is comparable with that of microreactors, which are devices known for having an extremely large specific surface area (Kiwi-Minsker and Renken 2005,

Kashid and Kiwi-Minsker 2009). This is possibly due to the small dimensions that a NETmix network can present, without losing its mixing capacities, showing that NETmix has the potential to remove large amounts of heat.

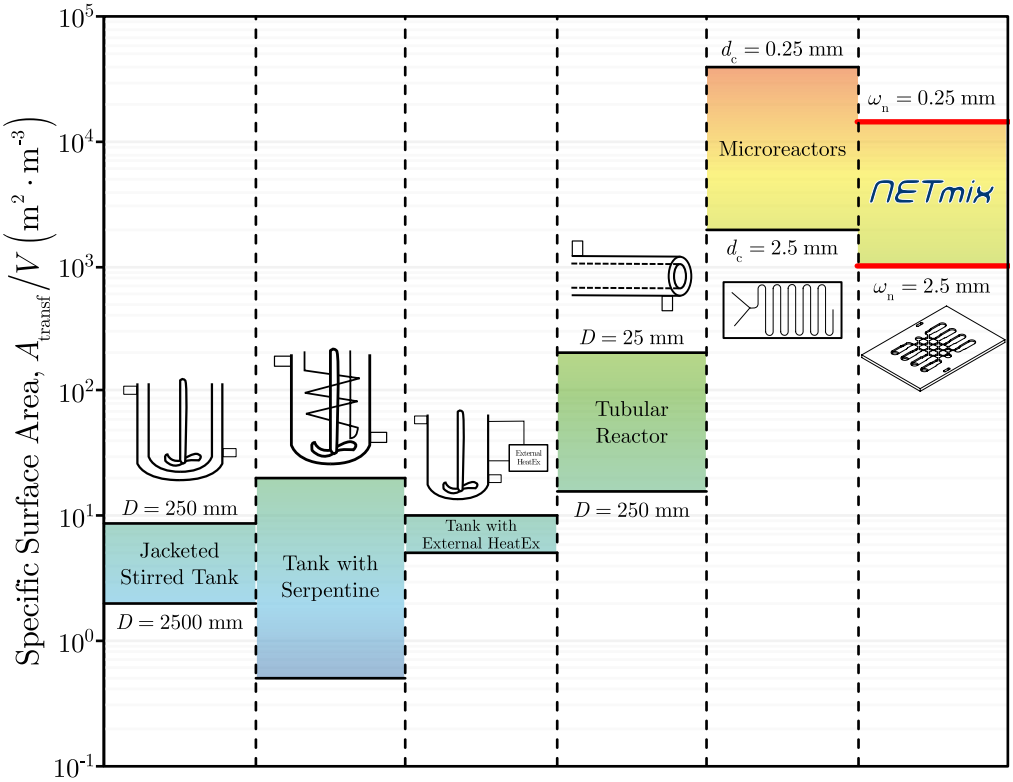



Figure 3.12 – Specific surface area comparison for different heat exchange devices.

Knowing both Nusselt numbers and specific surface area, it is now possible to combine both variables in a single variable, named here as the specific heat transfer capacity of a device, $\hat{h}$, obtained from

$$\hat{h} = \left\langle h \right\rangle_t \frac{A_{transf}}{V} \tag{3.39}$$

where $\left\langle h \right\rangle_t$ is the time-average (if applicable) heat transfer coefficient in the inner side, and $A_{transf}/V$ is the specific surface area for heat transfer.

The specific heat transfer capacity range for each equipment is computed using the lower and upper bound values of the specific surface area illustrated in Figure 3.12. The corresponding typical characteristic dimensions (also presented in Figure 3.12) are used for the determination of the heat transfer coefficient from Nusselt number.

For the specific case of stirred tanks, heat transfer coefficient range boundaries are obtained from literature (Trambouze et al. 1984, Ferrouillat et al. 2006). No information regarding hydrodynamic conditions is presented though, namely the Reynolds number. However, these devices usually operate in turbulent regime, in order to maximize heat fluxes. In this case, the lower bound of the specific heat transfer capacity is determined using the lower bound value of the specific surface area and the smaller value of the heat transfer coefficient, while the upper bound value is computed using the larger values of the specific surface area and heat transfer coefficients.

For tubular reactors, the Nusselt number is determined using the correlation for turbulent flow in tubes (Dittus and Boelter 1985), represented in Figure 3.11, assuming a Reynolds number of $10^4$ for the lower bound value of specific heat transfer capacity, and $10^5$ for the upper bound value, since this is the typical range of operation of tubular reactors in liquid phase.

For microfluidic devices, due to its small characteristic sizes, operation Reynolds number is very small, typically in the order of one (Tabeling and Chen 2005, Janasek et al. 2006), in conditions where the flow is laminar and fully developed. Microfluidic devices are usually built from channels, which can be either circular, as in tubes, or rectangular, as in rectangular ducts, having micrometric dimensions. The aspect ratio of the rectangular channel is typically close to one. One could use the Nusselt number for fully developed thermal boundary layer for laminar flow in tubes, as presented in Figure 3.11. However, when the channel's dimensions are within the micrometer range, usually lower Nusselt numbers than the ones obtained for laminar flow in pipes or between parallel plates are obtained (Rebrov et al. 2011). Peng et al. (1994) determined the Nusselt numbers for several microchannel geometries $\mathrm{Nu}_{\mu\mathrm{ch}}$, and proposed a correlation, which is similar to the Dittus-Boelter correlation for turbulent flow (Dittus and Boelter 1985), by changing the empirical constant for laminar flow in microchannels, which is a function of the channel aspect ratio:

$$\mathrm{Nu}_{\mu\mathrm{ch}} = C_{\mu\mathrm{ch}}\,\mathrm{Re}_{\mu\mathrm{ch}}^{0.62}\,\mathrm{Pr}^{1/3} \tag{3.40}$$

where $\mathrm{Re}_{\mu\mathrm{ch}}$ is the microchannels Reynolds number, and $C_{\mu\mathrm{ch}}$ is the empirical constant for laminar flow in microchannels, and is equal to 0.0384 for microchannels with aspect ratio close to the unity. Microchannels Reynolds number in the range of 1-50 is used in this analysis. Larger Reynolds numbers can be used, but due to the increase of the channel's pressure drop, this is not often the case (Sen et al. 2016). For NETmix, for the lower bound value of the specific heat transfer capacity, an operation Reynolds number of 150 is used (which is the minimum Reynolds number to obtain a fully chaotic flow regime), while for the upper bound, a Reynolds number of 600 is considered (the upper value of analysis in the present study).

The specific heat transfer capacity of each of the considered equipment is shown in Figure 3.13, where the great potential of the use of NETmix as a reactor with an outstanding heat transfer rate is highlighted, when compared with the most commonly used technologies for the coupling of reaction and heat transfer.

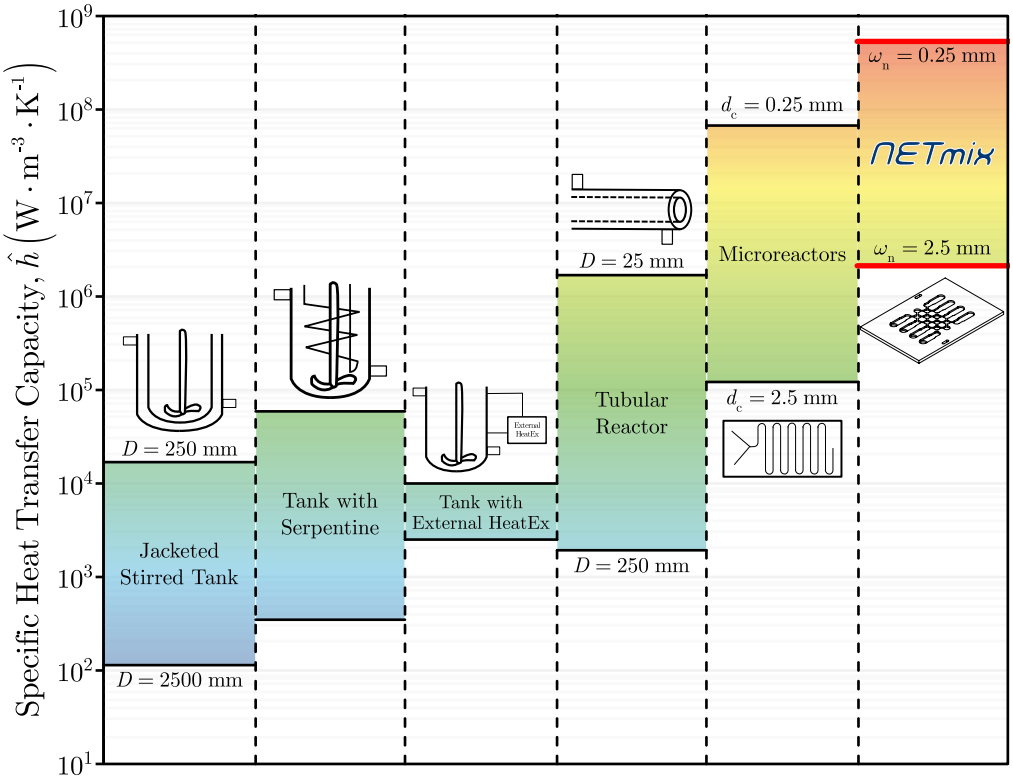



Figure 3.13 – Specific heat transfer capacity comparison between typical heat exchange devices and NETmix.

The difference from stirred tanks and NETmix is further accentuated when coupling the specific surface area and the heat transfer coefficient, resulting in about five orders of magnitude larger in some conditions. It is also possible to verify that NETmix is capable to remove heat at a rate that is almost one order of magnitude larger than microreactors, due to laminar mixing induced by oscillations. In microreactors, the flow is parallel and mixing is mostly achieved by molecular diffusion, because of the low convection rates that are observed, which leads to small heat transfer coefficients.

## 3.7 Conclusions

The results presented in this chapter show the capacity of the NETmix to outperform the most common reaction devices with heat transfer coupling, being a device with low power requirements, high mixing intensity, high throughput potential and enhance heat transfer capacity, which is essential for highly exothermic and endothermic processes (either reactions or not).

The heat transfer performance of NETmix was assessed and quantified using a CFD model, which was originally developed by Fonte (2013). The NETmix average unit cell Nusselt number was determined for different Reynolds numbers and it was observed that the existence of hot-spots is reduced when the flow patterns present an oscillatory behaviour, and the remaining are renewed with time, leading to a more efficient mixing and heat transfer.

For large Reynolds numbers, 3-8 times higher heat transfer rates can be achieved when compared to laminar flow between parallel plates. Maximum convective heat transfer coefficients are achieved when the flow inside the mixing chambers evolves to a self-sustained oscillatory laminar flow regime. An important result obtained from these simulations is that, above the critical Reynolds number, the thermal boundary layer is renewed along the network of chambers, enhancing the global specific heat transfer capacity of NETmix.

The specific heat transfer capacity of NETmix was compared with other technologies widely available commercially. It is observed that NETmix presents 2-5 orders of magnitude higher specific heat transfer capacity when compared to other technologies, such as stirred tanks, and nearly one order of magnitude larger specific heat transfer capacity than microfluidic devices.

These results are quite promising, since they indicate that NETmix is the most suited device for the production of gas hydrates slurries, if compared with most typical technologies used in industry, since it has a specific heat transfer capacity that outperforms the remaining devices. Also, the mixing capacity of NETmix has the potential to enhance not only heat transfer, but also mass transfer, specifically mass transfer between different phases due to the increase of interfacial surface are induced by the presence of vortices the causes deformations to the flow pattern.

The main results from the present chapter are published by (Costa et al. 2017) in the form of a scientific article in an international maganize (with a 2016 2-year impact factor of 2.836).

## 3.8 References

Amon, C.H., Guzmán, A.M., Morel, B., **1996**. "Lagrangian Chaos, Eulerian Chaos, and Mixing Enhancement in Converging–Diverging Channel Flows". *Physics of Fluids* 8, 1192-1206.

ANSYS, "Simulation Driven Product Development". *Published online at Ansys*. Available at: http://www.ansys.com/.

Bird, R.B., Stewart, W.E., Lightfoot, E.N., **2002**. "Transport Phenomena", 2nd ed. John Wiley & Sons, Inc., New York, NY, USA.

Costa, M.F., Fonte, C.M., Dias, M.M., Lopes, J.C.B., **2017**. "Heat Transfer Performance of NETmix - A Novel Micro-Meso Structured Mixer and Reactor". *AIChE Journal* 63, 2496-2508.

Dittus, F.W., Boelter, L.M.K., **1985**. "Heat Transfer in Automobile Radiators of the Tubular Type". *International Communications in Heat and Mass Transfer* 12, 3-22.

EngineeringToolBox, "Water - Thermodynamic Properties". *Published online at The Engineering ToolBox*. Available at: http://www.engineeringtoolbox.com/water-thermal-properties-d_162.html.

Ferrouillat, S., Tochon, P., Della Valle, D., Peerhossaini, H., **2006**. "Open Loop Thermal Control of Exothermal Chemical Reactions in Multifunctional Heat Exchangers". *International Journal of Heat and Mass Transfer* 49, 2479-2490.

Fonte, C.M. **2013**. "The NETmix Reactor: Application to High Added-Value Products" [*Ph.D Thesis*]. Porto, Portugal: Departamento de Engenharia Química, Universidade do Porto.

Fonte, C.M., Leblebici, M.E., Dias, M.M., Lopes, J.C., **2013**. "The NETmix Reactor: Pressure Drop Measurements and 3D CFD Modeling". *Chemical Engineering Research and Design* 91, 2250-2258.

Gomes, P.J. **2011**. "The NETmix® Reactor - Strategies for Optimizing Mixing and Development of New Reactor Designs" [*Ph.D Thesis*]. Porto, Portugal: Departamento de Engenharia Química, Universidade do Porto.

Grace, C.D., **1971**. "Static Mixing and Heat Transfer". *Chemical Processing & Engineering* 52, 57-59.

Janasek, D., Franzke, J., Manz, A., **2006**. "Scaling and the Design of Miniaturized Chemical-Analysis Systems". *Nature* 442, 374-380.

Joshi, P., Nigam, K.D.P., Nauman, E.B., **1995**. "The Kenics Static Mixer: New Data and Proposed Correlations". *The Chemical Engineering Journal* 59, 265-271.

Kashid, M.N., Kiwi-Minsker, L., **2009**. "Microstructured Reactors for Multiphase Reactions: State of the Art". *Industrial & Engineering Chemistry Research* 48, 6465-6485.

Kiwi-Minsker, L., Renken, A., **2005**. "Microstructured Reactors for Catalytic Reactions". *Catalysis Today* 110, 2-14.

Kumar, V., Saini, S., Sharma, M., Nigam, K.D.P., **2006**. "Pressure Drop and Heat Transfer Study in Tube-In-Tube Helical Heat Exchanger". *Chemical Engineering Science* 61, 4403-4416.

Lammers, G., Beenackers, A.A.C.M., **1994**. "Heat Transfer and the Continuous Production of Hydroxypropyl Starch in a Static Mixer Reactor". *Chemical Engineering Science* 49, 5097-5107.

Laranjeira, P.E. **2005**. "NETmix Static Mixer - Modelling, CFD Simulation and Experimental Characterisation" [*Ph.D Thesis*]. Porto, Portugal: Departamento de Engenharia Química, Universidade do Porto.

Laranjeira, P.E., Martins, A.A., Lopes, J.C.B., Dias, M.M., **2009**. "NETmix®, a New Type of Static Mixer: Modeling, Simulation, Macromixing, and Micromixing Characterization". *AIChE Journal* 55, 2226-2243.

Laranjeira, P.E., Martins, A.A., Nunes, M.I., Lopes, J.C.B., Dias, M.M., **2011**. "NETmix®, a New Type of Static Mixer: Experimental Characterization and Model Validation". *AIChE Journal* 57, 1020-1032.

Li, H.Z., Fasol, C., Choplin, L., **1996**. "Hydrodynamics and Heat Transfer of Rheologically Complex Fluids in a Sulzer SMX Static Mixer". *Chemical Engineering Science* 51, 1947-1955.

Mokrani, A., Castelain, C., Peerhossaini, H., **1997**. "The Effects of Chaotic Advection on Heat Transfer". *International Journal of Heat and Mass Transfer* 40, 3089-3104.

Myers, K.J., Bakker, A., D., R., **1997**. "Avoid Agitation by Selecting Static Mixers". *Chemical Engineering Progress* 93, 28-38.

Nauman, E.B., **1979**. "Enhancement of Heat Transfer and Thermal Homogenity with Motionless Mixers". *AIChE Journal* 25, 246-258.

Ottino, J.M., **1989**. "The Kinematics of Mixing: Stretching, Chaos, and Transport", 1st ed. Cambridge University Press, Cambridge, UK.

Peng, X.F., Peterson, G.P., Wang, B.X., **1994**. "Heat Transfer Characteristic of Water Flowing Through Microchannels". *Experimental Heat Transfer* 7, 265-283.

Rebrov, E.V., Schouten, J.C., de Croon, M.H.J.M., **2011**. "Single-Phase Fluid Flow Distribution and Heat Transfer in Microstructured Reactors". *Chemical Engineering Science* 66, 1374-1393.

Rohsenow, W.M., Hartnett, J.P., Cho, Y.I., **1998**. "Handbook of Heat Transfer", 3rd ed. McGraw-Hill, Boston, MA, USA.

Sen, N., Singh, K.K., Mukhopadhyay, S., Shenoy, K.T., **2016**. "Comparison of Different Microreactors for Solvent-Free, Continuous Synthesis of [EMIM][$EtSO_4$] Ionic Liquid: An Axperimental and CFD Study". *Journal of Molecular Liquids* 222, 622-631.

Shah, R.K., London, A.L., **1978**. "Laminar Flow Forced Convection in Ducts: A Source Book for Compact Heat Exchanger Analytical Data", 1st ed. Academic Press, New York, NY, USA.

Shibani, A.A., Özisik, M.N., **1977**. "A Solution to Heat Transfer in Turbulent Flow Between Parallel Plates". *International Journal of Heat and Mass Transfer* 20, 565-573.

Tabeling, P., Chen, S., **2005**. "Introduction to Microfluidics", 1st ed. Oxford University Press, Oxford, UK.

Thakur, R.K., Vial, C., Nigam, K.D.P., Nauman, E.B., Djelveh, G., **2003**. "Static Mixers in the Process Industries—A Review". *Chemical Engineering Research and Design* 81, 787-826.

Trambouze, P., van Landeghem, H., Wauquier, J.P., **1984**. "Les Réacteurs Chimiques: Conception, Calcul, Mise en Oeuvre", 1st ed. Editions Technip, Paris, France.

Villermaux, J., **1993**. "Génie de la Réaction Chimique: Conception et Fonctionnement des Réacteurs", 2nd ed. Tec & Doc, Paris, France.

# 4 $CO_2$ Hydrates – Experimental Setup

## 4.1 Introduction

Hydrate-based processes for CCS applications are widely studied and described in the literature. Most of these processes use large stirred batch tanks, but since hydrates precipitation releases large amounts of energy that may inhibit the production of hydrates if not removed, batch production results in long reaction times, due to the relatively small capacity of stirred tanks to remove heat (Sloan and Koh 2007, Yang et al. 2011).

Processes using continuous reactors (either tubular reactors or fluidized bed reactors) have also been developed. Patents for the continuous production of gas hydrates have been filled, using continuous stirred tanks (Kanda et al. 2012), multi-pipe or double-wall-pipe heat exchanger (Ohya et al. 2017), tubular reactors with dispersive nozzles (Iijima et al. 1994), or atomizers within spraying devices (Li et al. 2015).

The use of gas hydrates as a way of sequestering $CO_2$ or separating it from flue gas, which could be used near industrial compounds or FPSO units, is only feasible if a continuous and efficient process is developed. The objective of this work is to design a

process that takes advantage of the exceptional mixing capacities of the NETmix technology (Laranjeira et al. 2009), which can be industrially applied for the continuous and mass production of gas hydrates.

In this chapter, the experimental setup is presented and described. In Section 4.2, the setup requirements are carefully described. The continuous production of gas hydrates requires process specifications that need to be fulfilled, for their successful production and potential application at an industrial level. The developed process is presented and described in Section 4.3, including the design and/or selection of the equipment. In Section 4.3 is also presented the three-dimensional layout of the experimental setup. In Section 4.4, the heat transfer performance of the microNETmix unit is evaluated and predicted based on the results obtained in Chapter 3, as well as from modelling of the heat transfer in the cooling unit. The main of conclusions of this chapter are presented in Section 4.5, and in Section 4.6 the respective bibliography.

## 4.2 Setup Requirements

The experimental setup for the continuous production of gas hydrates must meet specific design requirements. These requirements emerge essentially from two distinct factors. The first is related to the hydrates process intrinsic requirements. As referred in Chapter 2, gas hydrates are very sensitive to the mixing conditions between water and the guest gas/compound. If mixing is not properly achieved, low reaction rates are obtained, and thus productivity decreases. Considering that the objective is to continuously produce gas hydrates, inefficient mixing originates low mass transfer rates from gas to liquid, leading to large equipment and reaction times. Furthermore heat transfer rates are also of high importance; if the rates are low, the process becomes heat transfer limited, and the productivity decreases. This means that the process and equipment should be designed to obtain efficient mixing, high interfacial mass transfer rates and high heat transfer rates. The second factor is related to the transition from a lab-scale process to industrial level. This means that the process

and process equipment units must be designed so that the scale-up is possible and it does not pose any additional difficulties.

The NETmix technology is particularly suited to meet the above requirements, due its mixing characteristics and its high heat transfer rates. In particular the NETmix unit must be capable to remove the hydration heat, which is, as mentioned in Chapter 2, approximately $60\,\mathrm{kJ}\cdot\mathrm{mol}^{-1}$ for the production of $CO_2$ hydrates without the presence of any promoters. This means that the unit must be designed in a way that the heat transfer rate is sufficient to remove the released heat. If not, the heat is absorbed by the reaction medium, leading to a temperature increase that could either inhibits or slows down the hydrates precipitation process.

The scale-up requirement implies that the NETmix unit (where the hydrates precipitation will take place by contacting high pressure and low temperature water and guest gas) must be assembled as a modular unit. This assembly has the advantage of being extremely easy to increase the productive capacity, by simply increasing the number of modules. The intrinsic design of NETmix eases the use of modular units.

To reduce both water and gas flow rates, a smaller NETmix unit with characteristic dimensions below 1 mm, hereafter called microNETmix, was designed and used in this work. The use of such small device decreases the overall production capacity but enhances the heat transfer capacity, since it results in an increase of the specific surface area of the reactor, as observed in Chapter 3.

To meet these requirements, a sandwich-type structure for the microNETmix unit, based on two types of plates is considered. Similarly to previous NETmix units based on the 2D unit cell (Fonte 2013), the network of chambers and channels is carved on the network plate. A second type of plate, called the cooling plate, is in contact with the network plate, allowing heat transfer from the network plate to the cooling plate. The cooling fluid flows through the cooling plate, to absorb the heat that is released

from the network plate. Multiple sets of this two-plate structure can be assembled on top of each other, forming a modular structure, as illustrated in Figure 4.1.

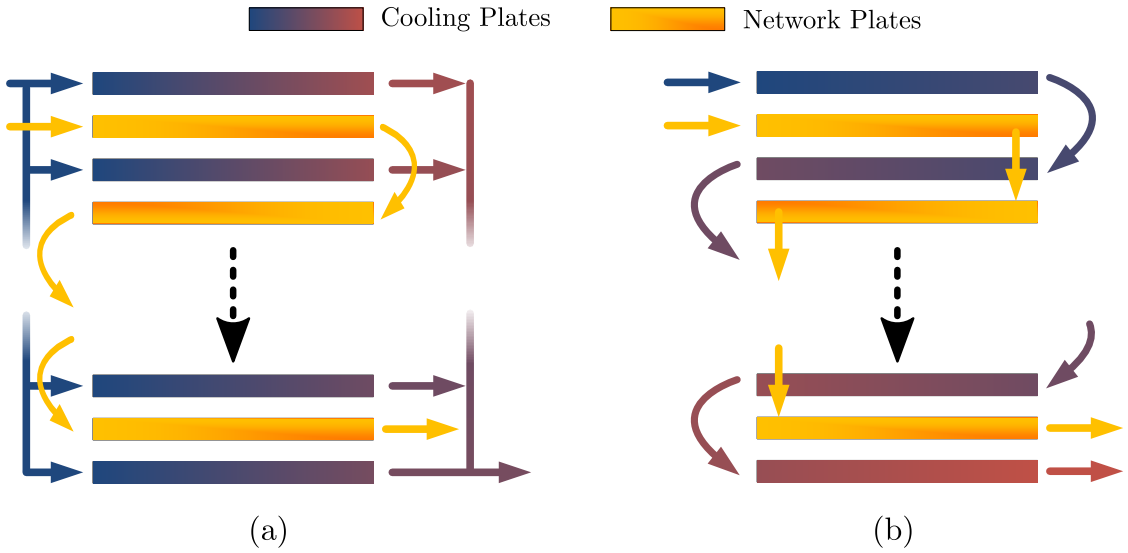



Figure 4.1 – Sandwich-type layer-by-layer microNETmix unit scheme with two cooling plates configurations: (a) in parallel; (b) in series.

Figure 4.1 shows two possible assemblies of a microNETmix unit, comprising network and cooling plates. The assembly of network and cooling plates must be designed so that the outlet stream of one network plate is the feed stream of the following network plate, thus increasing residence time. In the scheme shown in Figure 4.1a, the cooling fluid is fed through a single line, which is distributed to all cooling plates independently. In this way, the temperature gradient between the network and cooling plates is increased. Similarly, the cooling fluid exits each cooling plate independently, being collected at the outlet. Figure 4.1b illustrates a second assembly, where the cooling fluid is fed in the first plate and is series with the remaining cooling plates. Even though both assembly designs provide compact units, which are essential both in laboratorial and industrial environments, the assembly of Figure 4.1a is used in the present work.

Since gas hydrates are usually produced at high pressures (from 15 bar to 100 bar, or higher, depending on the guest molecule) and low temperatures (near 0 °C), the experimental setup must be capable to endure high pressures and low temperatures.

Refrigeration units such as chillers are required to cool both water and gas streams from ambient temperature to operating temperature. Moreover, the heat released due to hydration has to be removed; therefore these refrigeration units must have the capacity to remove the hydration heat.

It is an objective of the present work to assess the influence of the guest molecule source type. Therefore, for the case of pure carbon dioxide hydrates, the experimental setup must have the capacity to feed either gas or liquid carbon dioxide to the system.

Extra equipment is required for solid concentration and gas-liquid separation, thus allowing the evaluation of the process regarding productivity and separation efficiency.

Due to the inherent danger of operating gas streams at relatively high pressure, safety procedures need to be adopted including safety valves and other mechanisms.

The requirements regarding process variables are presented in Table 4.1. The selection of equipment to monitor and control flow rates, pressure and/or temperature are selected so that the requirements from Table 4.1 are fulfilled.

Table 4.1 – Process variables requirements.

| Process Variable | | Value |
|---|---|---|
| $CO_2$ Production Capacity | $\dot{m}_{CO_2}$ | $\sim 1\,\mathrm{kg \cdot h^{-1}}$ |
| Working Temperature | $T$ | $0 - 10\,^{\circ}\mathrm{C}$ |
| Maximum Working Pressure | $p_{max}$ | 60 bar |
| microNETmix Channel's Reynolds Number | $\mathrm{Re}_c$ | $200 - 300$ |
| Slurry Solids Content | $X^{w}_{hyd}$ | $20 - 30\%$ |

The productivity requirement is based on previous works on continuous production of hydrates, such as Gudmundsson et al. (2000), Yang et al. (2008) or Groen (2012). The temperature and pressure requirements result from the low temperatures and high pressures required to produce hydrates, in particular using from liquid $CO_2$ as

the carbon dioxide source. As previously observed (Laranjeira et al. 2009, Fonte et al. 2013) a critical channel's Reynolds number of 150 is required to promote mixing, and the range 200-300 is preferred as observed from the results presented in Chapter 3. Finally, to avoid plugging in the system, a maximum slurry concentration of 30% in solids is desired.

Regarding this last requirement, it was observed by several authors, that at relatively low concentration of solids, no solids agglomeration occurs, and no plugging is expected (Andersson and Gudmundsson 2000, Hu et al. 2010). This is particularly true in turbulent flows, where the turbulence hinders agglomeration. A similar behaviour is expected when the flow inside the mixing chambers in the microNETmix unit is fully chaotic and oscillatory. Although the number of rheological studies of hydrate slurries is scarce, several works focusing on the flow of ice slurries are described in literature (Liu et al. 1988, SlurryICE) and shown in Figure 4.2.

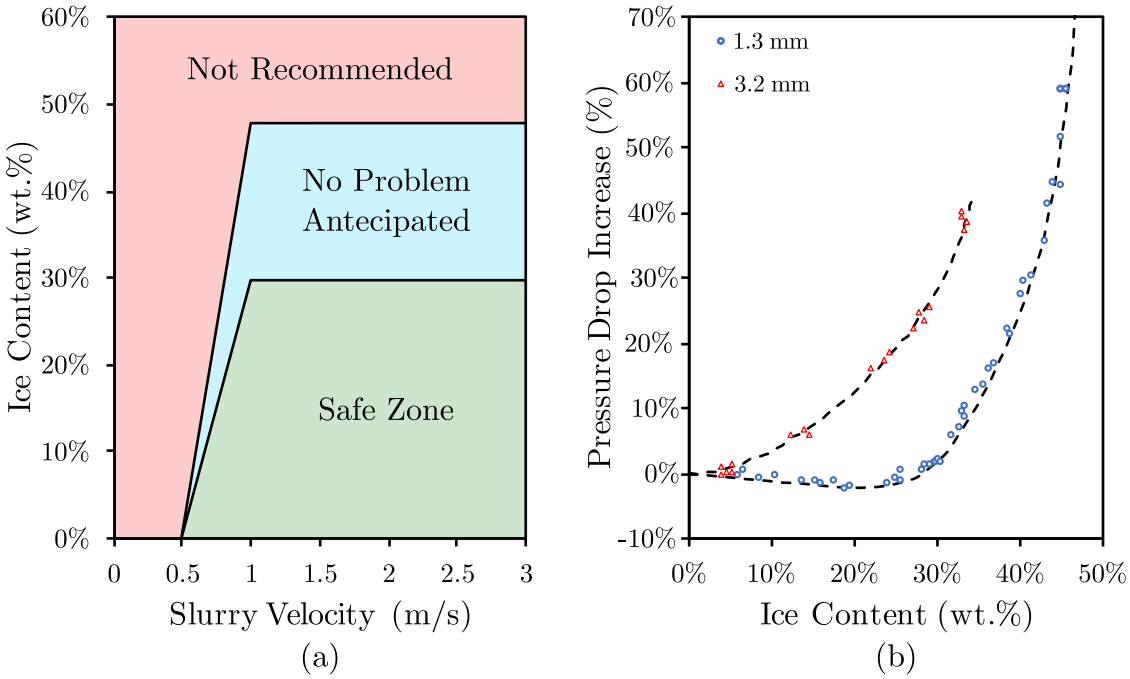



Figure 4.2 – (a) Ice slurry velocity working conditions and working regimes (SlurryICE); (b) Effect of particle size and solids loading on pressure drop increase (Liu et al. 1988).

As described in Chapter 2, ice and hydrates have very similar physical properties, so it is safe to assume that they present similar rheological behaviours. In the report produced by SlurryICE (n.a.), where the use of ice slurries as a refrigeration fluid is

studied, no plugging is detected. The report also evaluates the flow regimes as a function of the velocity and ice concentration (Figure 4.2a). A similar conclusion is made by Liu et al. (1988), who claim that when the particles are small enough, a 30% in volume of solids does not result in an increase of the pressure drop (Figure 4.2b). Taking this into account, a maximum of 30% concentration of solids is set, with a preferred operational value of 20%.

## 4.3 Process Design

The development of a lab-scale process for the continuous production of gas hydrates using a microNETmix unit is a joint effort from the Associate Laboratory LSRE-LCM (Laboratory of Separation and Reaction Engineering – Laboratory of Catalysis and Materials), INEGI (Instituto de Ciência e Inovação em Engenharia Mecânica e Engenharia Industrial, an institute that focuses on applied research and development, innovation and technology transfer activities for the industry) and Paralab (a company specialized in the design and assembly of experimental apparatus, as well as an equipment supplier).

A detailed description of the process is shown in Section 4.3.1. In Section 4.3.2, equipment design and selection for the process is presented. Three-dimensional drawings of the layout, as well as images of the experimental setup are presented in Section 4.3.3.

### 4.3.1 Process Flow Diagram

The experimental setup must be capable to continuously produce hydrates from water and pure $CO_2$ (in either gas or liquid phase). The flow diagram of the proposed process is presented in Figure 4.3.

Water is introduced to the system through a 20 litres vessel (E-1), which is filled with fresh water (through line 1). This vessel is at atmospheric pressure, since it is open. Temperature control in the vessel is done using a coil placed inside the vessel

(E-16), where cooling fluid is flowing inside. No mixing devices are installed in this tank, meaning that thermal stabilization requires some time.

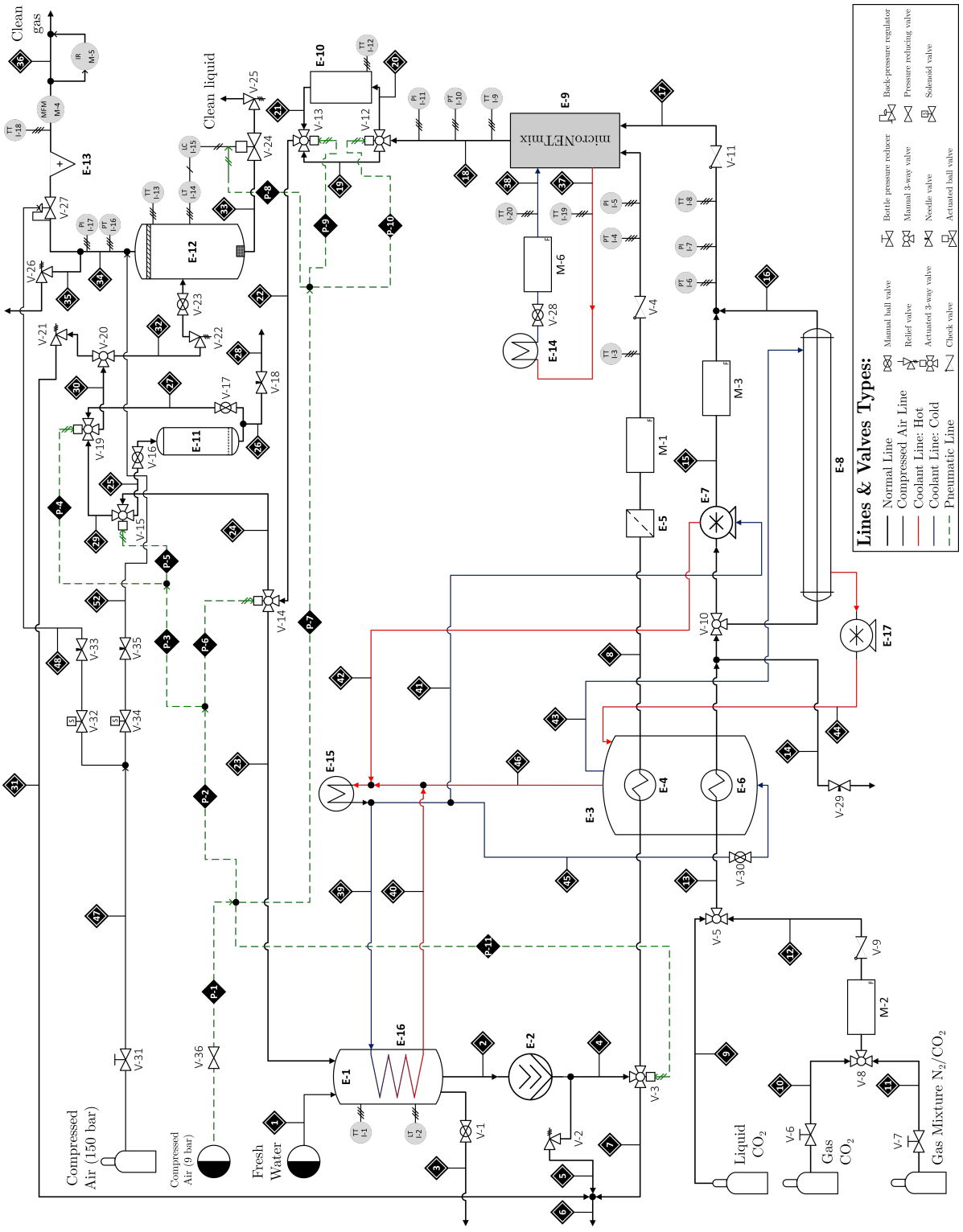



Figure 4.3 – Process flow diagram (PFD) for the lab-scale continuous hydrates production process using the microNETmix unit. Black diamond symbols with white borders are numbering the flow lines, while the full back diamond symbols are numbering the pneumatic lines, used for in the pneumatic valves actuators.

A thermocouple is placed inside the vessel (TT I-1) to monitor the water's temperature, as well as water's level indicator (LT I-2), that stops the pump once the water's amount is low, avoiding damaging the pump. Valve V-1 is installed at bottom of the vessel, allowing its purge by gravity.

A screw pump (E-2) pumps the water from the vessel to the system's lines. Downstream the pump, a relief valve (V-2) is installed. This valve is installed for safety concerns, and it guarantees that if the pressure upstream the pump is large, the fluid is routed to line 5, avoiding the damage of the pump. An actuated three-way valve (V-3) is installed downstream to switch from a waste line 6 or to the system. The presence of this valve is helpful to purge the vessel E-1 faster, since the purge through valve V-1 is made by gravity only. Water is fed to a serpentine (E-4), which is placed inside a container filled with cooling fluid (E-3) continuously fed. The temperature of water is reduced in serpentine E-4, to set the line temperature to the reaction's temperature. An inline filter (E-5) is installed in the water line, to prevent the entry of solid impurities in the system. Water flow rate is controlled using a Coriolis flow meter (M-1), and the temperature is monitored using a thermocouple (TT I-3). A check-valve (V-4) is installed upstream the microNETmix unit to avoid backflow. Pressure is measured through pressure transducers and manometers (PT I-4 and PI I-5), prior to entering the microNETmix unit (E-9).

Gas carbon dioxide is fed from a pressurized cylinder, and enters in the system through line 10. The setup also allows the feeding of a mixture of $N_2/CO_2$ through line 11 from a pressurized cylinder, but this gas will not be used in this work. The bottles contain pressure reducers (V-6 and V-7). Manual three-way valve V-8 is used to select which gas (carbon dioxide or $N_2/CO_2$ mixture) is fed to the system. The flow rate is controlled using a mass flow controller (MFC, M-2). A check-valve V-9 is installed downstream the MFC, to avoid the backflow of liquid that could damage the controller. Liquid carbon dioxide can also be fed to the system from a pressurized cylinder through line 9, and can be chosen by switching the position of the manual three-way valve V-5. The guest component (either gas or liquid) is then cooled in a

serpentine (E-6) that is installed in container E-3. A needle valve (V-29) is installed downstream the serpentine E-6 for safety purposes, allowing the depressurization of the line in case of abrupt pressure increase. When liquid $CO_2$ is the source, then carbon dioxide is fed to a dosing HPLC pump (E-7) that contains a cooled head (to avoid vaporization), where the flow rate is controlled, and measured through a Coriolis flow meter (M-3). When gas $CO_2$ (or $N_2/CO_2$ mixture), then the material bypasses the HPLC pump and enters in a jacketed tube (E-8 in line 16) where the temperature is reduced to the working temperature. Afterwards, the temperature and pressure of carbon dioxide are measured (PT I-6, PI I-7 and TT I-8), and a second check-valve is installed (V-11) upstream the microNETmix unit.

In the microNETmix unit (E-9), both water and the guest component (in either gas or liquid phase) come in contact with each other. At the same time, the cooling fluid is fed to the cooling plates of the microNETmix unit to remove heat that is released from gas dissolution in water and hydrates crystallization. The cooling fluid is in a closed loop between a chiller (E-14) and the microNETmix unit. The cooling fluid flow rate is controlled through valve V-28 and is measured through a flow meter (M-6). To perform the energy balance, as part of the process performance analysis, the cooling fluid's temperatures at the microNETmix inlet and outlet are measured through thermocouples (TT I-19 and TT I-20). The temperature and pressure at the outlet of the microNETmix unit are measured using a thermocouple and pressure transducers (TT I-9, PT I-10 and PI I-11).

Downstream the microNETmix, manual three-way valves (V-12 and V-13) are installed, allowing to choose to either enter a visualizing sampler window (E-10), where the temperature is monitored using a thermocouple (TT I-12), or bypass it. Afterwards, the stream enters to an actuated three-way valve (V-14), in which the stream can either be routed to the water vessel E-1 through line 23 in a recirculation loop, or it can be routed to line 24, where the pressure is controlled by a relief valve (V-21). If the stream is recirculating, the pressure of the system is the atmospheric pressure, and the only pressure increase is due to the pressure drop existing in the

system due to friction. However, if V-14 is set to relief V-21, the pressure of the system is increased according to the defined downstream pressure.

When V-14 is set in the direction of V-21, the stream can feed a HPLC column (E-11), or can bypass it, through the actuated three-way valves V-15 and V-19. The HPLC column operates as a filtration device, having filters at the bottom, while it is being fed at top. A needle purge valve (V-18) is installed to decrease the pressure in the column, allowing the operators to obtain samples of the solids for further characterization. Two manual ball valves (V-16 and V-17) are installed upstream and downstream the column, allowing its disassembly while keeping it pressurized. This is useful if the depressurization must be done in a cooled environment.

The manual three-way valve V-20 defines whether the stream goes to the relief valve V-21, which is a purge exit, or feeds the separator tank (E-12). A relief valve (V-22) is installed upstream the separator tank E-12 to create a pressure drop in the line. The manual on-off valve (V-23) installed at the feed stream of the tank E-12 allows the tank upstream isolation. Separator E-12 is a vessel that separates gas from heavy phases (liquid and solid) by gravity. This was designed to evaluate the efficiency of separation of nitrogen from carbon dioxide, a topic that will not be discussed in this study. Therefore, only a brief description of the process lines is made.

The pressure inside the vessel is controlled through the relief valves V-25 and V-26, as well as through the BPR (back pressure regulator) installed at the top outlet (V-27). Valve V-24 controls the level of liquid (indicated by the level indicator LT I-14) inside the tank. Temperature and pressure in the tank are monitored using a thermocouple (TT I-13) and a pressure transducer (PT I-16 and PI I-17).

The composition of the exhaust gas is analysed by measuring the temperature using a thermocouple (TT I-18), and the mass flow rate using a mass flow meter (MFM M-4). A water trap (E-13) is installed upstream to eliminate any potential liquid droplets that may be dragged by the vapour, avoiding the damage of the mass flow meter, and also for more accurate analysis. Finally, a $CO_2$ concentration detector is

installed (IR M-5), allowing the monitoring of the concentration of carbon dioxide in the remaining gas stream.

Some of the previously described valves are automatically controlled using a pneumatic system. This system requires pressurized air (of approximately 7-9 bar) that is supplied through the inline compressed air available at the laboratory. A pressure reducer (V-36) is installed to lower the pressure from the line. The air is then fed to the valves actuated through pneumatic actuators (dashed lines from Figure 4.3 to valves V-3, V-12, V-13, V-14, V-15, V-19 and V-24). The setup also requires a source of high-pressure compressed air, which is used to both control the pressure of the BPR valve (V-27) and pressurize the flash separator (E-12) at the start of the process. Since the pressure at which it is required to control both valve V-27 and tank E-12 must be larger than equilibrium pressure for hydrates production (that can range from 15 to 30 bar), a bottle of compressed air is installed, since the inline compressed air available does not have enough pressure to satisfy the needs. The air from the bottle (which is at a pressure of approximately 150 bar) suffers a pressure reduction through the pressure reducer valve V-31 in line 47. Line 47 diverges into lines 48 and 52 to feed the BPR or the separator tank, respectively. In each of the lines, a solenoid valve (V-32 and V-34) and manual needle valves (V-33 and V-35) are installed the control the air flux.

Cooling fluids are fed to the system through two chillers. Chiller E-14 feeds cooling fluid to the microNETmix unit. A secondary chiller E-15 supplies cooling fluid to the tank water coil (E-16), to the HPLC cooling device (E-7), and to the container E-3, where the water and gas/liquid serpentines are submerged. Valve V-30 controls the flux of cooling fluid from the secondary chiller to the container E-3. Cooling fluid for the jacket E-8 is supplied from container E-3 using a peristaltic pump (E-17).

The designed process allows not only the production of hydrates slurry, but also allows the monitoring of several variables that allow the analysis of the system. In a system such as this, the possibility of performing the energy balance to the microNETmix unit is of high importance to carefully understand processes that occur

when the guest (either gas or liquid) is put in contact with water, at conditions where precipitation of hydrates is thermodynamically favourable.

### 4.3.2 Equipment Design and Selection

In this section, all equipment required for the process described in Section 4.3.1 is presented and described.

#### *4.3.2.1 The microNETmix Unit*

The microNETmix unit comprises the network plates and the cooling plates. The network plates are built from mixing chambers connected by channels, all carved in a plate, forming the network. These plates are in contact with the cooling plates, which contain channels in which cooling fluid flows to remove heat from the network plates. Due to the possibility of hydrates production inhibition, heat must be removed from the system at high rates. Therefore, the microNETmix unit must be designed in a way to promote high heat transfer rates.

The microNETmix unit, as well as the remaining experimental setup, was designed by the project group at LSRE-LCM, taking into account the requirements from Table 4.1. The mechanical design of the microNETmix unit was made by INEGI and the unit was built by Ricardo & Barbosa, Lda., a maker of mechanical tools and moulds (ricardo&barbosa). The microNETmix unit is built in stainless steel, and comprises three network plates, four cooling plates, one distributor plate, two closing blocks (where the lines are connected), and a closing body (that holds all other plates together, avoiding high-pressure leakages). Each of these elements is shown in Figure 4.4. To better understand the plates from Figure 4.4, drawings from the microNETmix unit network and cooling plates are presented in Figure 4.5 and Figure 4.6. The most relevant dimensions of each plate and network are represented in these drawings and also in Table 4.2.

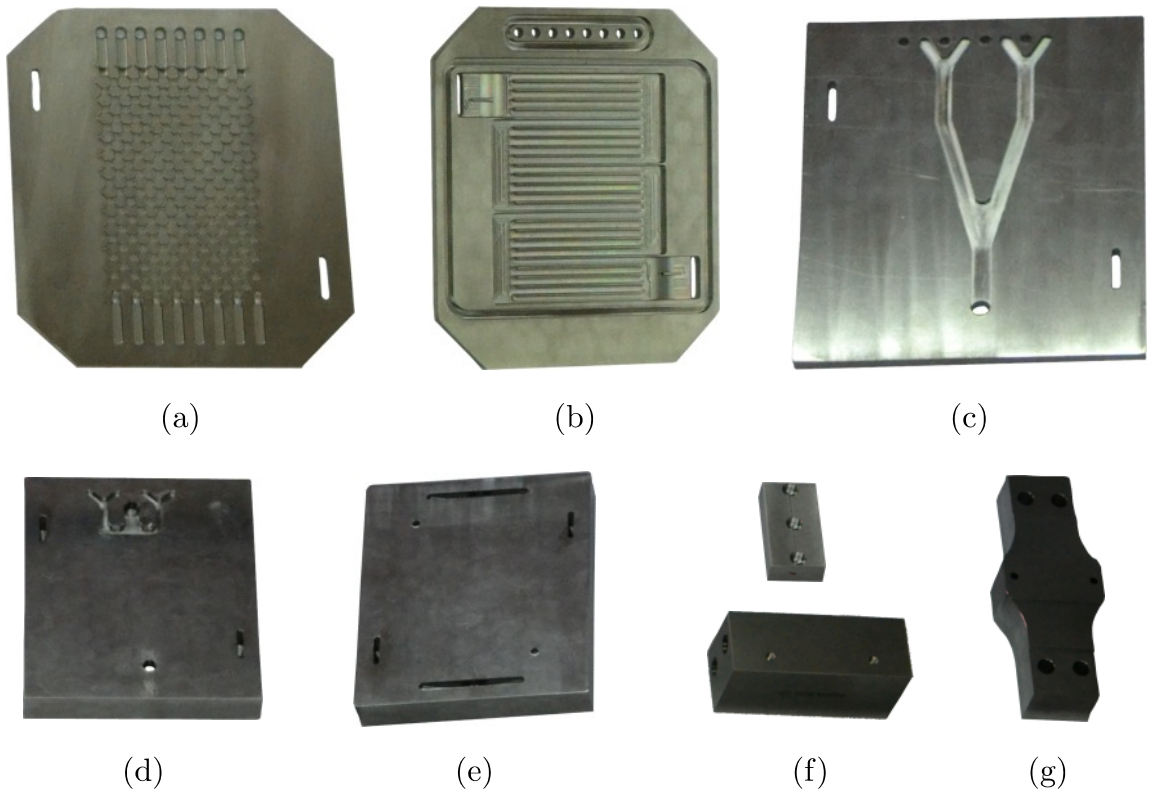



Figure 4.4 – microNETmix unit parts: (a) Network plate; (b) Cooling plate; (c) Distributor plate; (d) Inlet closing plate with fluid distribution in reactants side; (e) Outlet closing plate; (f) Shim plate and support body; (g) Closing body.

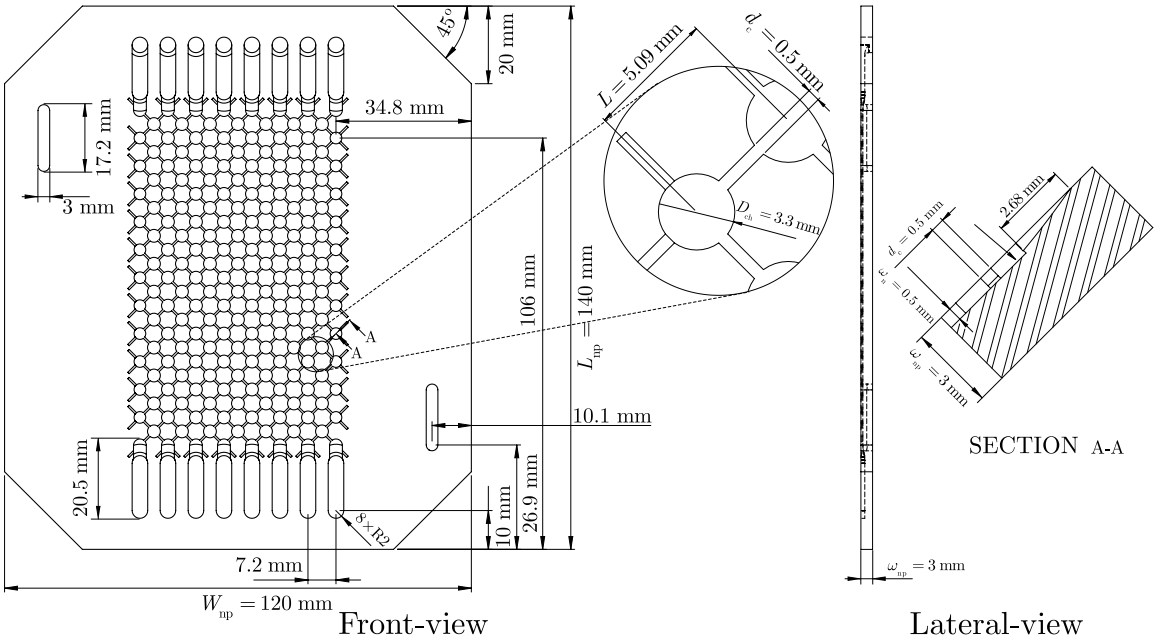



Figure 4.5 – Schematic of the microNETmix network plate.

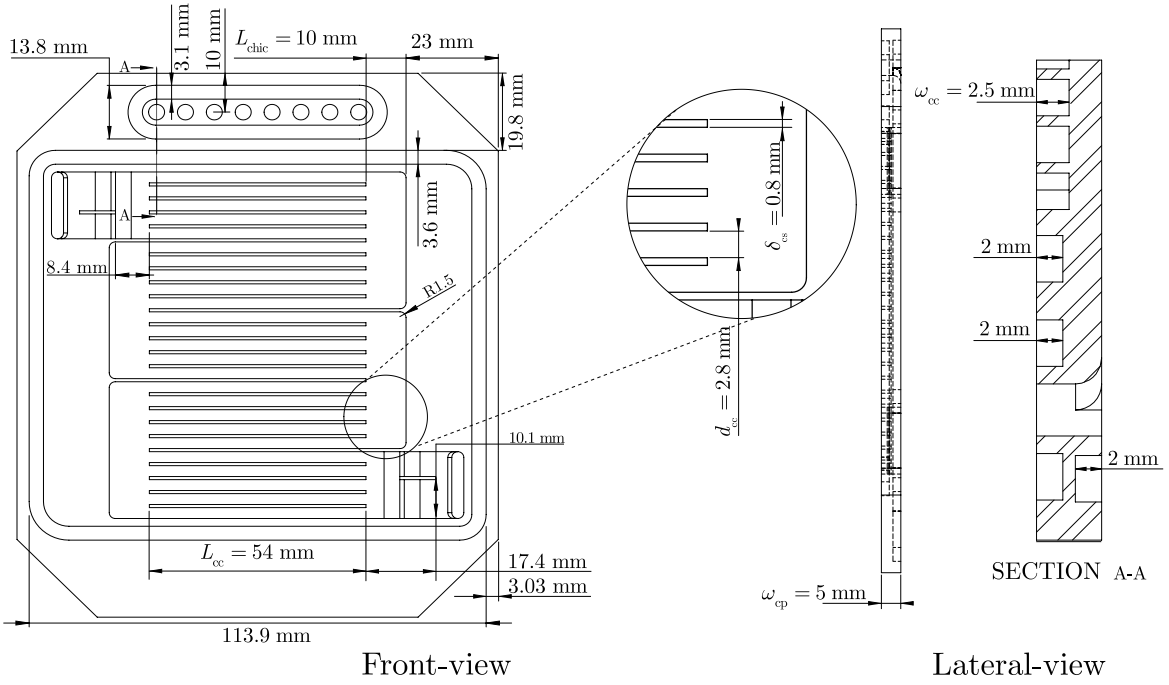



Figure 4.6 – Schematic of the microNETmix cooling plate.

Table 4.2 – Characteristic dimensions of the network and cooling plates.

| **Network Plates** | | **Cooling Plates** | |
|---|---|---|---|
| **Dimension** | **Value** | **Dimension** | **Value** |
| **Plate length,** $L_{np}$(mm) | 140 | **Channel's length,** $L_{cc}$(mm) | 54 |
| **Plate width,** $W_{np}$(mm) | 120 | **Channel's width,** $d_{cc}$(mm) | 2.8 |
| **Plate depth,** $\omega_{np}$(mm) | 3 | **Channel's depth,** $\omega_{cc}$(mm) | 2.5 |
| **Chamber's diameter,** $D_{ch}$(mm) | 3.3 | **Spacer's thickness,** $\delta_{cs}$(mm) | 0.8 |
| **Channel's width,** $d_{c}$(mm) | 0.5 | **Plate depth,** $\omega_{cp}$(mm) | 5 |
| **Channel's length,** $L$(mm) | 5.1 | **Chicane's length,** $L_{chic}$(mm) | 10 |
| **Network's depth,** $\omega_{n}$(mm) | 0.5 | | |

Due to mechanical design and constraints, the back walls of the network and cooling plates also present carved structures. These structures are not relevant for the analysis of the mixing unit, and therefore, no explanation of these details is

presented. The plates were designed to operate as described in Figure 4.1. The network and cooling plates can be repeatedly added to (or removed from) the unit to increase (decrease) both the residence time and the cooling capacity to the system, if required. The network plates comprise eight columns and twenty-five rows of chambers, where the bottom chambers are the inlet points, while the top chambers are the outlet points. The fluids are introduced in the pre-mixed scheme, as described previously by Laranjeira (2005), meaning that the reactants (water and gas) are fed to the system in alternate chambers, as illustrated in Figure 4.7.

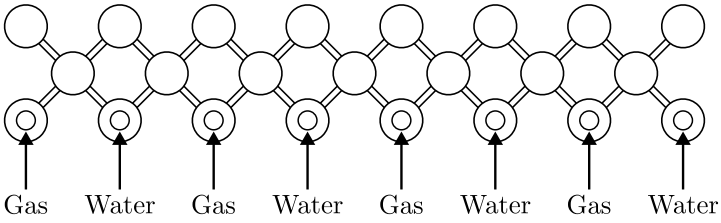



Figure 4.7 – microNETmix unit pre-mixed injection scheme.

The reactants are introduced to the system through two distribution plates (plate Figure 4.4c for one component and Figure 4.4d for the other component, embedded in the feed closing plate). With these distribution plates the component streams are fed to the microNETmix unit through a single connection for each component, and then distributed to the inlets of the network plate. Distribution channels are carved in the network plates, connecting the chambers inlets/outlets to the respective distribution plates. The use of these carved channels in the network plates is useful for assembly as a modular device. The two openings at the top-left and bottom-right of the network plates allow the distribution of the cooling fluids through the cooling plates. Cooling fluid is fed through a single connector, and is distributed through these openings.

The cooling fluid enters in one side of the plates, and is distributed to all cooling plates of the system, bypassing the network plates through the connection slots presented in Figure 4.5. Each cooling plate presents a series of five sections with five carved channels each. This allows an efficient cooling fluid distribution, maximizing the contact with the carved network from the adjacent network plate. At the end of

each section, a collection channel (a chicane or a collector) is designed to collect the cooling fluid from all five channels, before being distributed through to the next set of channels. Finally, the cooling fluid distributed to all cooling plates is collected at the outlet. The cooling plates are not perfectly symmetrical, since eight connection holes are installed, and visible at the bottom of the plate in Figure 4.6. These holes allow the bypassing through the cooling plates of the fluids (water and gas) that are fed in the network plates. The cooling fluid is introduced and removed to the microNETmix unit through single connectors placed in both closing plates (Figure 4.4d and Figure 4.4e).

The assembly of the microNETmix unit is shown in Figure 4.8. In this particular case, the unit is built from the repetition of three network and four cooling plates. At the inlet, two plates are added: the inlet closing plate, where both reactants streams are connected (through inlets A and B), and the distributor plate. The reactant fed through inlet B (red line) is distributed to four channels, which coincide with the inlets in the network plate, considering a pre-mixed injection scheme. The reactant fed through inlet A (orange line) bypasses the inlet closing plate and enters the distributor plate, where it is distributed to the remaining four channels. In the first network plate, both fluids mix in the mixing chambers and flow to the exit of said plate (represented by the green line in Figure 4.8). The mixture then flows in the normal direction of the flow in the network plate, bypassing the adjacent cooling plate through the connection holes, and feeding the following network plate, that operates counter-currently to the first. This sequence is repeated as many times as the number of installed network plates in the device. The mixture is then collected at the outlet closing plate, converging to a single exit C.

The cooling fluid is introduced through inlet D and is distributed to all cooling plates through the connection holes available in both network and cooling plates. The flow in the cooling plates is crossed with the flow in the network plates. The cooling fluid exits the cooling plate using the outlet at the bottom of the drawing in Figure 4.8b,

mixing with the fluid from all other cooling plate. The whole fluid exits the system through exit E, located at the outlet closing plate.

The whole unit is kept together by the action of the closing bodies represented in Figure 4.8b, support bodies and a single shim plate. These elements compress the remaining plates, to avoid inter-plate leakages that could lead to serious accidents, due to high-pressure operation. The unit is tightened by screws in one of the closing bodies, encompassing the whole unit.

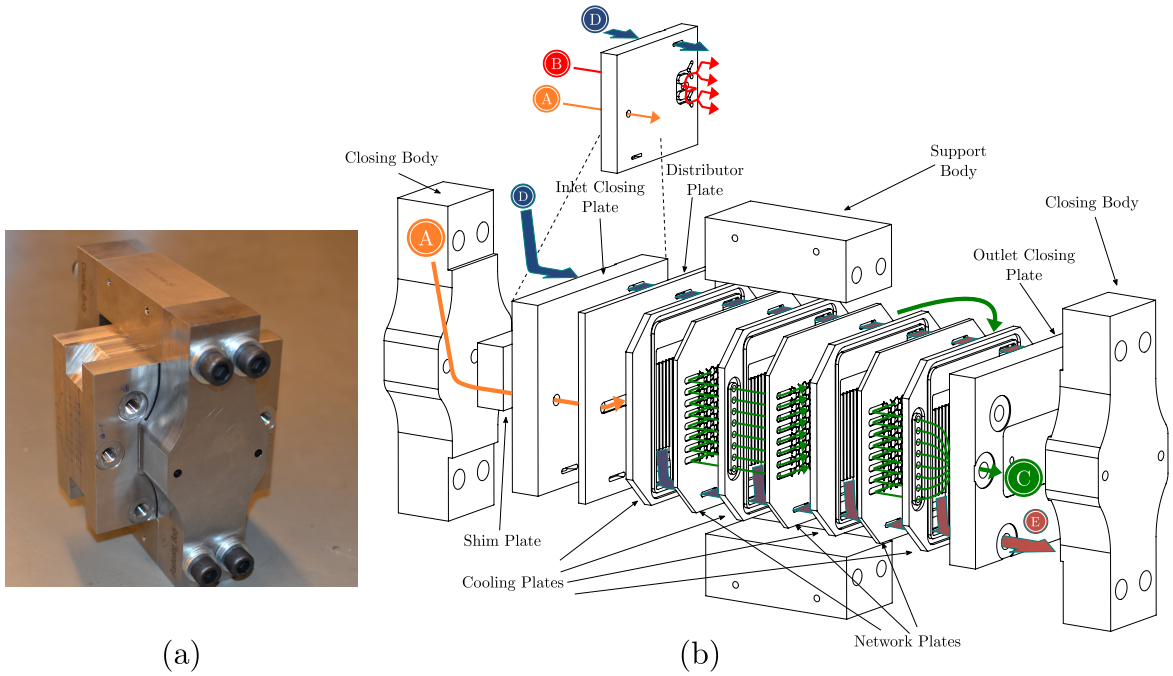



Figure 4.8 – (a) microNETmix assembly; (b) microNETmix assembly drawings: Orange lines represent the flow of one of the reactants through the inlet A; red lines represent the flow of the other reactants through inlet B; green lines represent the flow of the medium mixture in the network plates, leaving the system through outlet C; blue and red arrows represent the flow of the cooling fluid, entering through inlet D and exiting through outlet E.

#### *4.3.2.2 Pumps*

Two pumps are required for the experimental setup, which are represented by the units E-2 and E-7 in Figure 4.3. Water is fed to the system through pump E-2, while liquid $CO_2$ is pumped through pump E-7.

Due to the required operating pressure and flow rates ranges, a screw pump was found to be the most adequate choice to feed water to the system (Dosing by Mono (Mono$^{TM}$) LTM pump, Figure 4.9a). This pump is capable to flow up to $155\,L \cdot hr^{-1}$

and delivers a maximum pressure of 72 bar, which is enough to the maximum operation pressure (see Table 4.1). The relief valve V-2 is installed downstream the pump to avoid the damaging, due to the small difference between the working operation and the maximum pressure of the pump. The Mono LTM pump can be operated at temperatures up to 120 °C.

An HPLC pump was chosen to pump liquid $CO_2$ to the system, when required. The amount of $CO_2$ to be introduced to the system is much lower than the amount of water, thus, an alternative pump technology was required. HPLC pumps are commonly used to introduce relatively small amounts of liquid to a chromatography column filled with porous packing. This means that very high pressure-drops are common, and a high-pressure pump is required. The chosen pump is a dual-piston pump (Azura P 4.1S pump by Knauer (Knauer); Figure 4.9b). The pump is equipped with a stainless steel $50\,mL \cdot min^{-1}$ pump head that includes a cooling device. This system allows the flow of cooling fluid to the pump head, avoiding the undesired vaporization of the $CO_2$ due to temperature increase and pressure drop in the tubing. The main specifications of the pump are presented in Table 4.3.

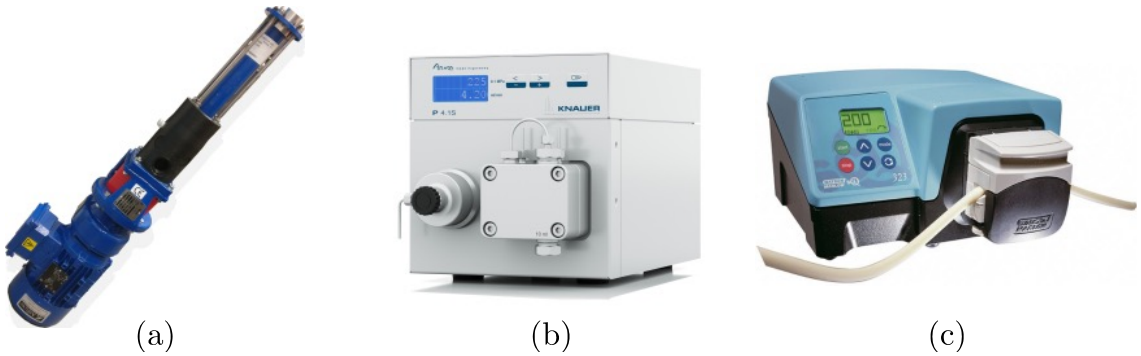
Table 4.3 – Knauer Azura P 4.1S main specifications.

| | **Specification** |
|---|---|
| **Flow Rate Range** | $0.01 - 50\,mL \cdot min^{-1}$ |
| **Maximum Pressure** | 150 bar |
| **Flow Rate Accuracy**[1] | ±1% |
| **Flow Rate Precision**[2] | $< 0.5\%$ |

[1]Measured at 5 – 50% of flow range using ethanol/water 10:90
[2]At $1\,mL \cdot min^{-1}$

A third pump, represented by unit E-17 in Figure 4.3 is required to pump the cooling fluid from the serpentines reservoir E-3 to the jacket E-8 that is placed in line 16, to cool the gas to the operation temperature. This pump works at atmospheric pressure (except for pressure drop due to friction) and a Watson Marlow (Watson-Marlow)

323 double-head peristaltic pump was chosen (Figure 4.9c). The 323 model pumps up to 2000 $mL \cdot min^{-1}$ and delivers pressures up to 2 bar.




(a) (b) (c)

Figure 4.9 – Pumps in the experimental setup: (a) Dosing Mono LTM pump for water; (b) HPLC Knauer Azura P 4.1S pump for liquid $CO_2$; (c) Peristaltic Watson Marlow 323 pump for cooling fluid.

Additional pumps to pump the cooling fluid to the system are embedded in the refrigeration units.

The gas is fed to the system from compressed bottles, which means that no extra devices to pump the gas are required.

#### *4.3.2.3 Filtration Column*

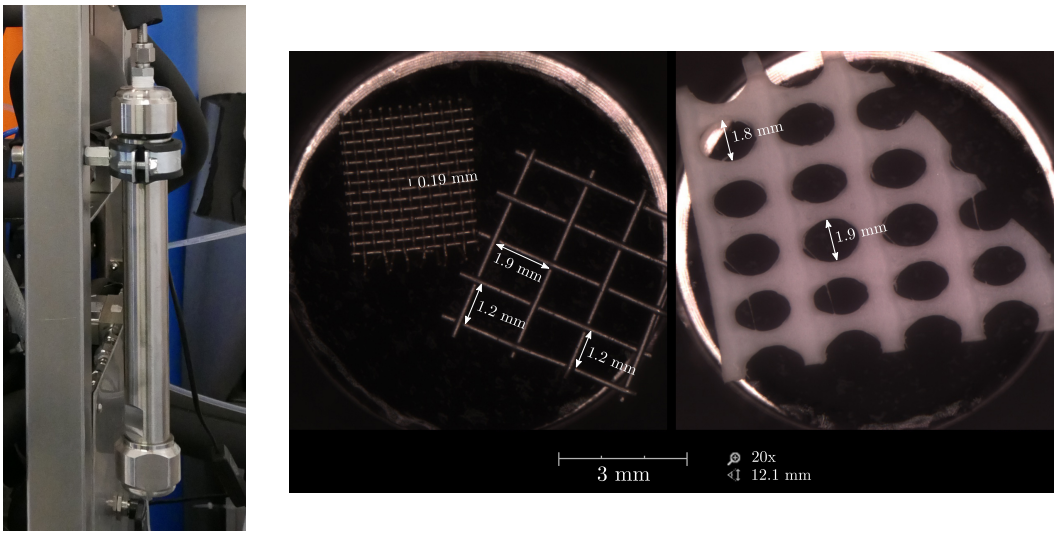
The unit E-11 is a filtration device that separates the solid hydrates from the slurry water. This filtration column is built from a typical HPLC column, designed to operate at very high pressures. The used HPLC column is manufactured by Phenomenex®, but it was altered to suite the process needs. To avoid plugging or large pressure drops due to expansions and/or reductions, the entrance was enlarged to fit 1/4" connections (Figure 4.10a). The outlet was kept unchanged, since only water leaves the column, and this area reduction is helpful to filter the solids. At the bottom of the column, three layers of meshes (two metallic and one made of a plastic material) with different mesh sizes are used (Figure 4.10b). The presence of these meshes eases the filtration of water.

This system allows the continuous processing of the hydrates slurry until the column is filled with solid. When the column is full, valves V-15 and V-19 are switched to

bypass the column. At this point, the column is under pressure, being required to reduce the pressure prior to its opening, which is done through valve V-18. This depressurization can be done *in situ*, or can be done with the column separated from the remaining setup, by closing the ball valves V-16 and V-17, keeping it under pressure. This layout allows the depressurization inside a cooling device, to stabilize the hydrate solid, and to take advantage of the metastability (or self-preservation) of the hydrates observed at low temperatures (see Section 2.3.2.3). After depressurization, the column is opened from the top and the solid material is removed.

The use of the filtration unit arises from the fact if the water surrounding the hydrate is not removed, the hydrate is not as stable as if it were "dry", at atmospheric pressure, for relatively large periods of time, since the heat transfer with the environment is easier, and dissociation is faster. In this way, the "dried" solid material can be further analysed regarding composition and crystal structure.

The filtration column has a useful volume of approximately $90\,\mathrm{mL}$, an inner diameter of $21.2\,\mathrm{mm}$ and a height of $250\,\mathrm{mm}$. The column can operate at pressures up to $400\,\mathrm{bar}$ and at temperatures in the range of $-60\,^{\circ}\mathrm{C}$ to $200\,^{\circ}\mathrm{C}$.




(a) (b)

Figure 4.10 – (a) Installed filter column; (b) Microscope imaging of the different meshes used to filter (obtained using a SEM Phenom Pro X microscope – see Section 5.4.3.3).

#### *4.3.2.4 Refrigeration Units*

Two refrigeration units are used in the process, represented by units E-14 and E-15 in Figure 4.3. Unit E-14 supplies cooling fluid solely to the microNETmix unit, removing the heat that is released due to gas hydrates crystallization. Unit E-15 supplies cooling fluid to every other part where it is necessary to remove heat, such as the serpentines tank E-3, the coil inside the water vessel E-16 and the HPLC pump E-7 head cooling device. Also, since the cooling fluid is removed from the tank E-3 to feed the jacketed tube E-8, the refrigeration unit must also remove the heat from this line.

Two chillers from Julabo are used in the setup. Unit E-14 is a JULABO FL1203 and unit E-15 is a JULABO FL601. These chillers are based on vapour-compression refrigeration cycles, using a single-stage compressor and R404A as refrigerant, which is an HFC blend from Linde. In a vapour-compression refrigeration cycle, the refrigerant undergoes phase changes (condensation and evaporation) (Smith et al. 2005). The refrigerant enters the compressor as saturated vapour, being compressed to a higher pressure, and increasing its temperature. The superheated vapour is condensed in the condenser, where it transfers heat to the air (in air cooled chillers) or with water (in water cooled chillers). The saturated liquid is then routed to a throttle valve, where it expands, resulting in the decrease of the pressure and temperature. Part of the liquid may undergo flash evaporation in the expansion valve. The resulting multiphase mixture is then fed to an evaporator, where the remaining liquid is evaporated. In the evaporator, the refrigerant absorbs heat from the cooling fluid, reducing the temperature of the second. The saturated vapour produced in the evaporator is again fed to the compressor, completing the cycle.

Lab-scale chillers usually contain a deposit, which can be filled with cooling fluid that is used to exchange heat with the refrigerant in the evaporator. A recirculation pump is used to pump the cooling fluid to an external circuit, if desired. The main specifications of the chillers are condensed in Table 4.4.

Table 4.4 – Air cooled chillers main specifications (Julabo).

| Model | FL601 | | | FL1203 | | |
|---|---|---|---|---|---|---|
| Temperature Range | $-20-+40$ °C | | | | | |
| Temperature Stability | $\pm 0.5$ °C | | | | | |
| Temp. Resolution | 0.1 °C | | | | | |
| Cooling Capacity[1] | 20 °C | 0 °C | −20 °C | 20 °C | 0 °C | −10 °C |
| | 0.6 kW | 0.4 kW | 0.2 kW | 1.2 kW | 0.8 kW | 0.5 kW |
| Pump Max. Flow Rate | $23\ \mathrm{L \cdot min^{-1}}$ | | | $40\ \mathrm{L \cdot min^{-1}}$ | | |
| Pump Max. Pressure | 1 bar | | | 3 bar | | |
| Coolant Volume | 8 L | | | 17 L | | |

[1]Using water-glycol mixture

#### *4.3.2.5 Slurry Visualizer*

A sampler visualizer, represented by unit E-10 in Figure 4.3, is installed downstream the microNETmix unit, to clearly identify the presence of hydrates slurry. The visualizer, designed by INEGI and made by Tecnogial, is built from two acrylic plates, a metallic support structure and two metallic plates (Figure 4.11). The metallic structures and plates are required to give mechanical stability to the visualizer due to high pressures. The acrylic plates allow the visual characterization of the slurry downstream the microNETmix. The whole structure is kept structurally compact using a set of sixteen screws, carefully screwed to avoid mechanical fractures in the acrylic.

The slurry flow enters the visualizer through an inlet located at the bottom. A thermocouple is also placed at the bottom, to monitor the temperature inside the visualizer. To reduce the effect of abrupt expansions and reductions, gradual expansions/reductions of the flow cross sectional area are designed near the inlet/outlet. The mixture exits the visualizer at the top outlet.

The main dimensions of the visualizer are illustrated in Figure 4.11. The visualizer block has a total volume of $420\ \mathrm{mL}$, where about $36\ \mathrm{mL}$ are useful for the flow of the slurry, with a visualizing area of $18\ \mathrm{cm^2}$.

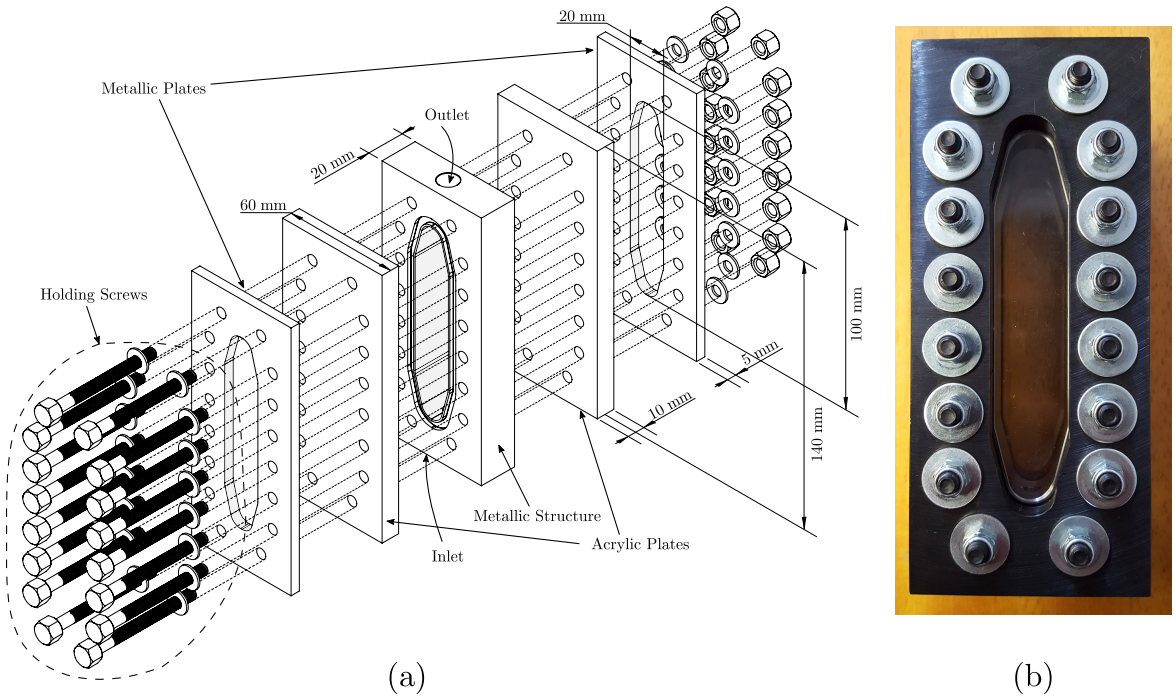



Figure 4.11 – (a) Visualizer schematic and main dimensions; (b) Real visualizer.

#### *4.3.2.6 Other Equipment*

Several other devices and equipment are installed in the experimental setup, including valves and piping. For simplicity, the specifications of the valves and piping are not described. The main remaining parts of the setup are:

- The water tank (E-1 in Figure 4.3), a 20 L HPDE (high density polyethylene) vessel. Inside, a 20 m coil made from polyurethane (8 mm of outer diameter OD and 5.5 mm of inner diameter ID) is coiled and kept together using plastic clamps. This coil is directly connected to chiller E-16 that pumps cooling fluid.
- The serpentines tank (E-3) is made of plastic, having an inlet at the bottom and an outlet at the top, connected to chiller E-15. The tank was designed to promote radial flow within, promoting mixing and reducing dead zones. Therefore, the inlet and outlet of this tank are tangential. A removable cover is installed at the top, where holes are drilled to allow the installation of the serpentines E-4 and E-6, which are made of stainless steel 316 tubing. Water serpentine E-4 is 5 m long, while E-6 is 10 m long. Jacketed tube E-8 is fed with cooling fluid from the serpentine tank through pump E-17. The jacketed

tube was handcrafted using a typical hose with outer diameter of 14.5 mm and a length of approximately 2 m. The gas tube (of outer diameter of 1/8 inches) is passing inside the hose concentrically. At both ends of the hose, stainless steel tee's are inserted. The tee outlet normal to the flow is connected to tubes that are recirculating the fluid from the serpentine tank to the jacket. The remaining outlets are closed using rubber stoppers and silicone, to minimize the leakage of the cooling fluid, while allowing the passage of the gas tube. A simple schematic of the apparatus is shown in Figure 4.12.

- A water-trap, represented by unit E-13, is required downstream the separation tank, to remove possible moisture that can be dragged by the gas, and not eliminated by the device installed at the top of tank E-12. This is done using a 1 L flask with an inlet and outlet at the top, carved in the lid. A tube is installed inside to route the feed of the flask to the bottom, thus facilitating the water removal. Again, this part of the setup was not used throughout this work.

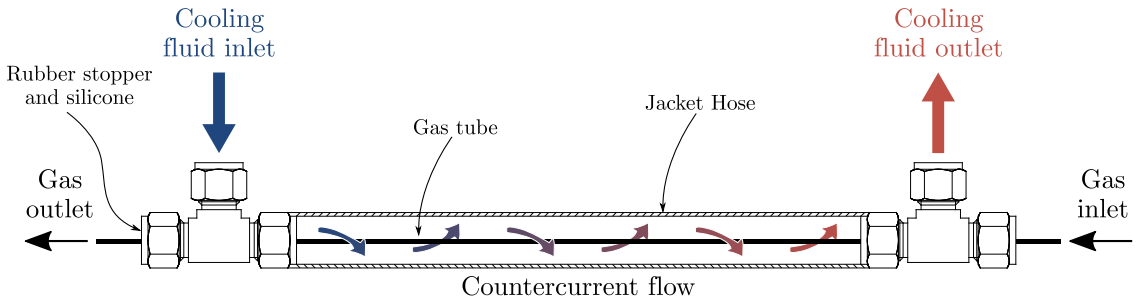



Figure 4.12 – Gas line jacketed tube schematic.

The remaining small-scale devices used in the experimental setup are presented in Table 4.5.

To minimize heat transfer with the environment, tubing and the microNETmix unit, as well as some other equipment, are covered with Armaflex (Armacell), a thermal insulation material.

Table 4.5 – Other equipment list.

| TYPE | MANUFACTURER | MODEL/REF. | UNIT[1] |
|---|---|---|---|
| Water coriolis | Bronkhorst | Mini Cori-FLOW | M-1 |
| Gas mass flow controller | Bronkhorst | EL-Flow | M-2 |
| Liquid $CO_2$ coriolis | Bronkhorst | Mini Cori-FLOW | M-3 |
| Gas mass flow meter | Bronkhorst | EL-Flow | M-5 |
| Liquid flow meter | Cynergy 3 | UF28B | M-7 |
| Filter | Hy-Lok | FTH-4T-WF | E-5 |
| Thermocouple | OMEGA | Type K | All TT |
| Pressure sensors | KELLER | PA-21Y | All PT |
| Pneumatic actuators | HOKE | 0713A4 | Actuated Valves |
| Solenoid valves | C.E.M.E. | 8615 | V-32/V-34 |

[1]Represented in Figure 4.3.

### 4.3.3 3D Setup Layout

The experimental setup from the process described in Section 4.3.1 is installed in a compact unit, shown in Figure 4.13.

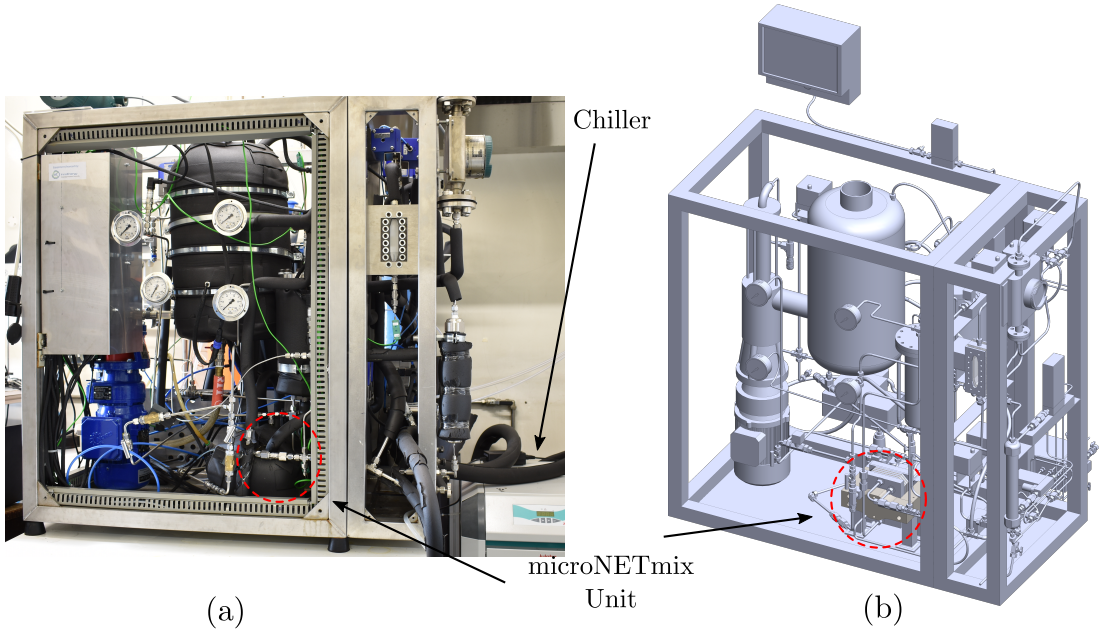



Figure 4.13 – (a) Real experimental setup; (b) 3D model of experimental setup.

This setup can be split in several sections. The first section comprises the water section from the tank to the microNETmix unit, shown in Figure 4.14.

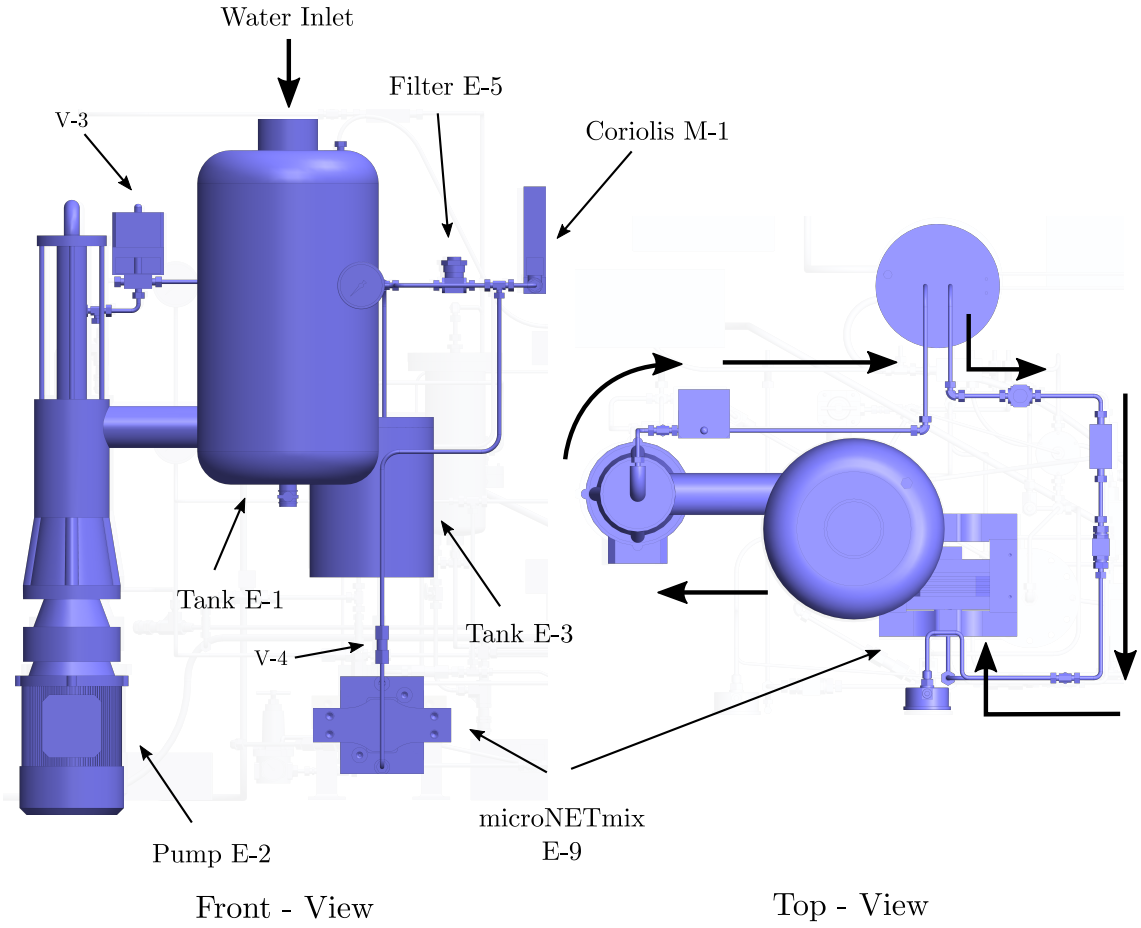



Figure 4.14 – Front and top views of the water circuit from experimental setup.

The circuits for carbon dioxide feeding to the system are shown in Figure 4.15.

The circuits downstream the microNETmix unit are represented in Figure 4.16 and Figure 4.17. In Figure 4.16, the fluid that exits the microNETmix device can bypass or not the visualizing sampler E-10 and recirculates to the water feed tank E-1. Since valve V-14 is not directed to any relief valve to control pressure, the line's pressure is atmospheric. This circuit was designed to help in the stabilization of the temperature in the system's lines and the microNETmix unit before production. Due to the low pressure of these lines, any addition of gas to the system results in the formation of bubbles but no hydrates crystallize.

When the system is ready to produce, the switch of valve V-14 allows the increase of the system's pressure defined by relief valves V-21 or V-25, depending on valve V-20 position. If valve V-20 is directing the fluid to valve V-21, then the circuit represented in Figure 4.17 is active. The operation in this circuit can occur with or without the addition of gas (or any other form of guest compound) into the system.

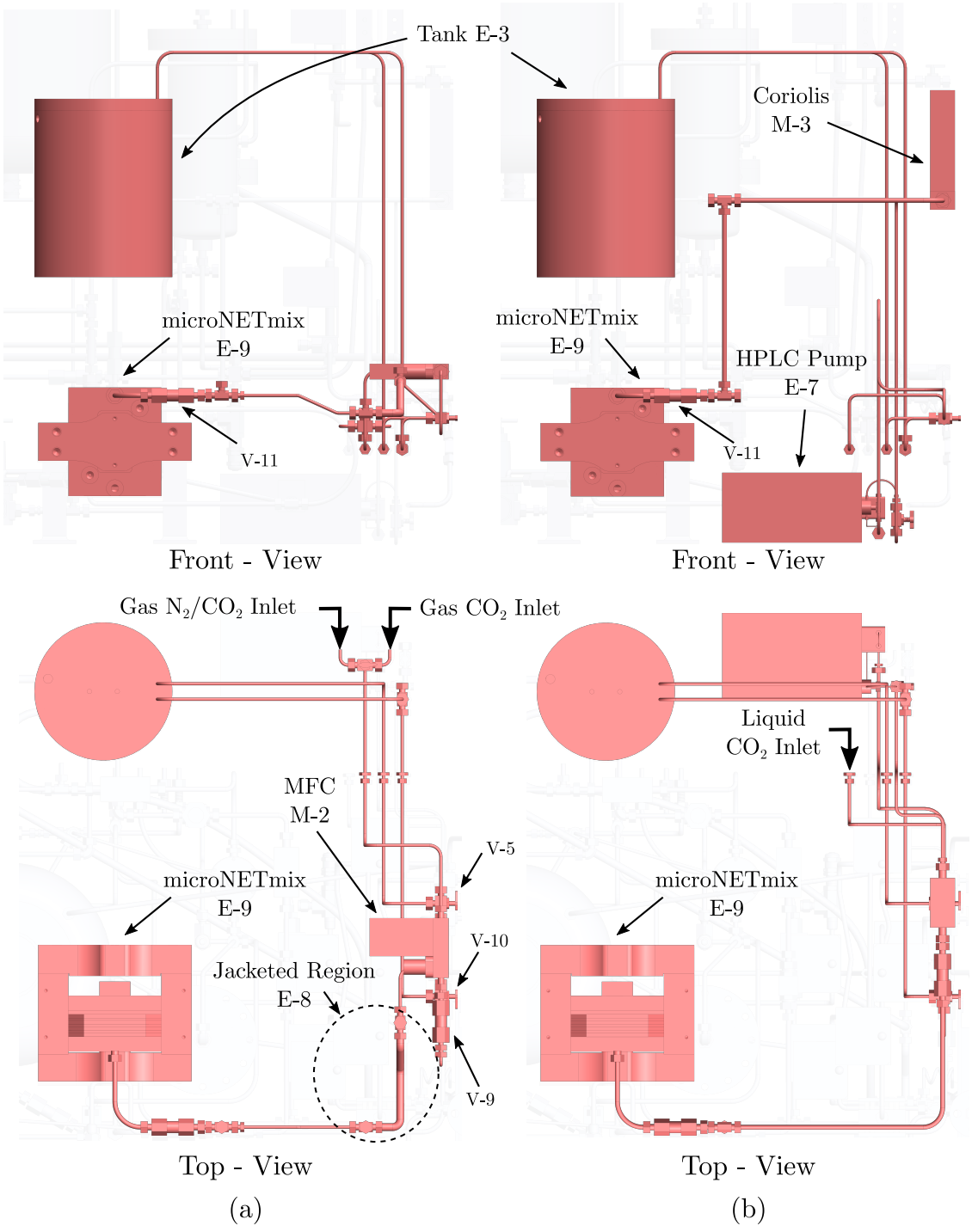



Figure 4.15 – Front and top views of the guest compound circuit from experimental setup: (a) gas carbon dioxide (or nitrogen – carbon dioxide mixture); (b) liquid carbon dioxide.

The pressurization of the system when switching valve V-14 takes only a few seconds. When gas is introduced in the system, the gas line is not pressurized, and an extra amount of time to increase the pressure of the gas is required. Once both water and gas lines are at the same pressure, hydrates are formed, if heat is removed at a rate fast enough to avoid a severe temperature increase. Again, in this circuit, the fluid can bypass or not the visualizing sampler E-10. It can also bypass or not the filtration column E-11.

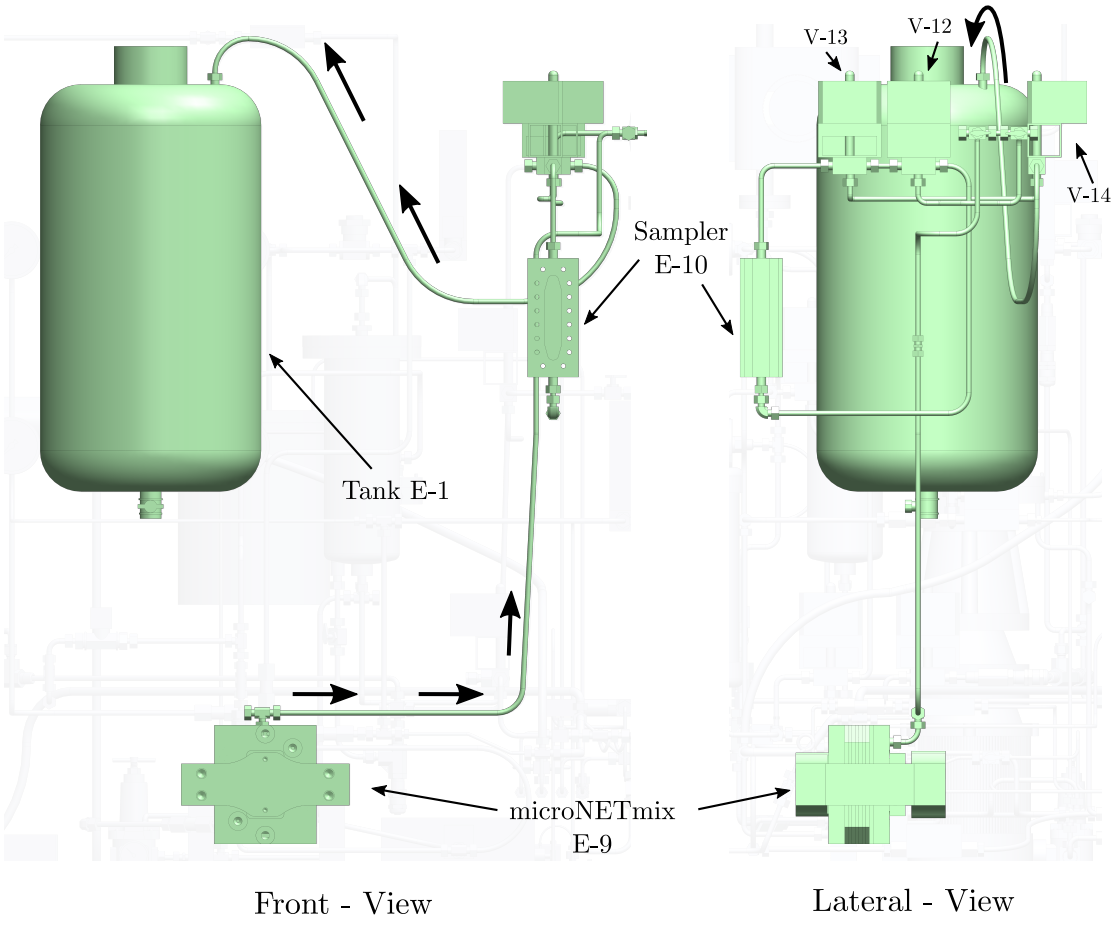



Figure 4.16 – Front and lateral views of the recirculation circuit of the product stream from experimental setup.

An extra circuit is required, which represents the cooling fluid circuit, as shown in Figure 4.18. The cooling fluid is fed to the microNETmix unit E-9 via chiller E-14, while is fed to the tank E-3 and to the coil E-16 via chiller E-15. The serpentines E-4 and E-6 that are inside tank E-3 are not visible in Figure 4.18, as well as the coil E-16 and the connections with the chiller E-15.

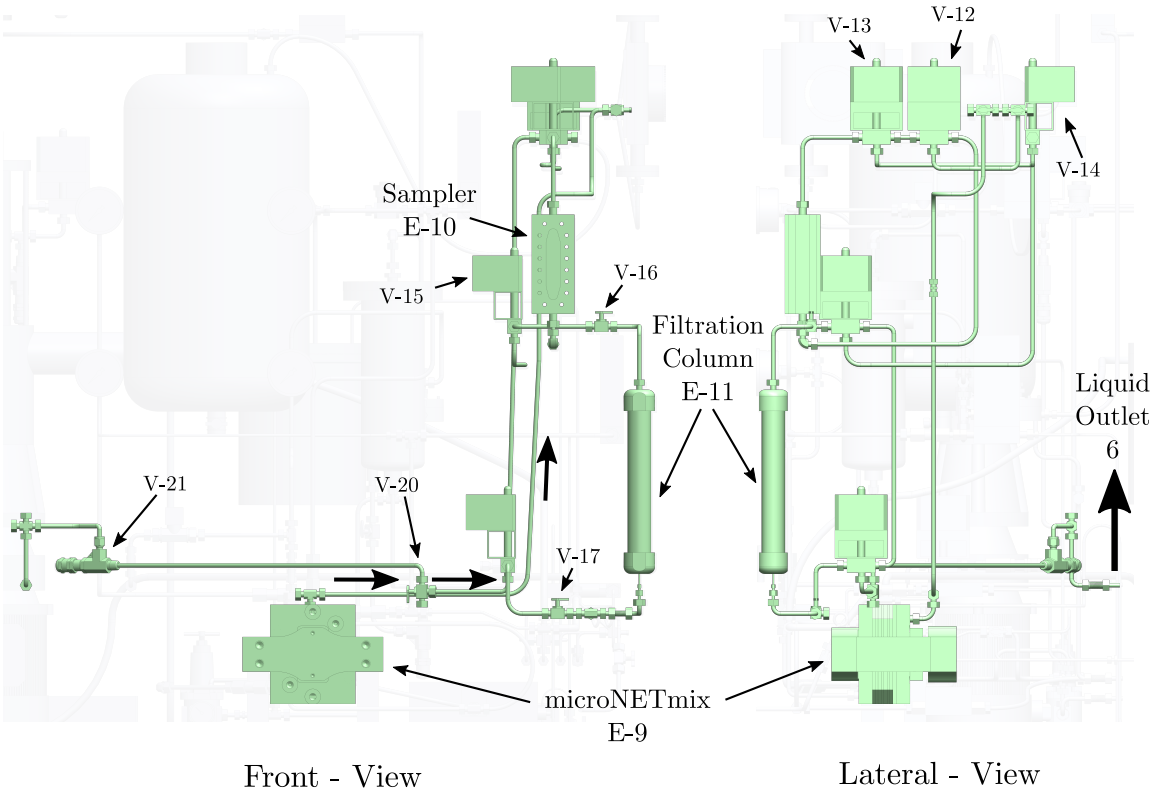



Figure 4.17 – Front and lateral views of the pressure circuit that includes relief valve V-21.

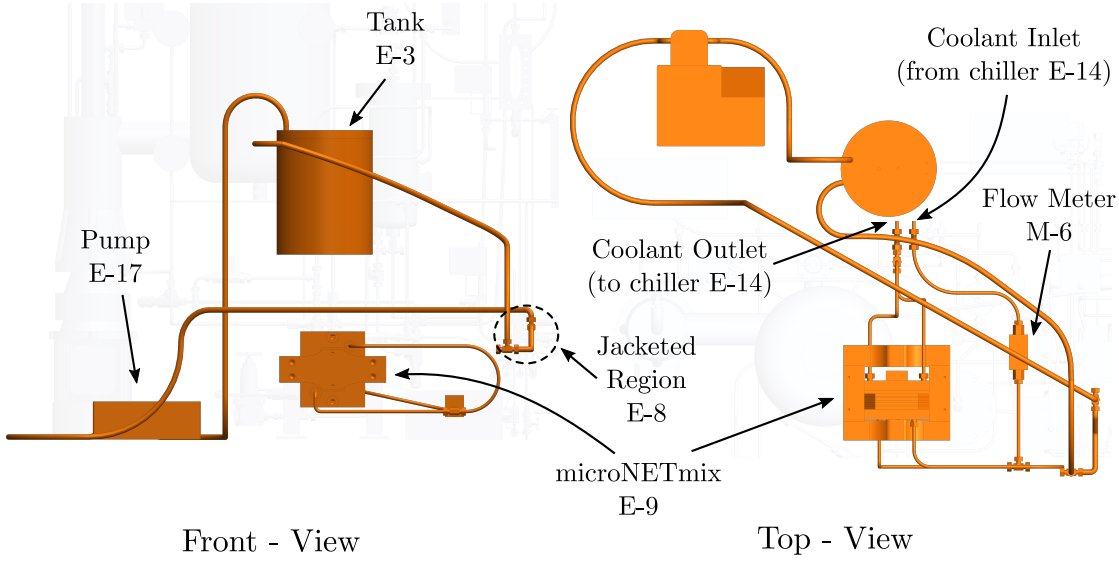



Figure 4.18 – Front and top views of part of the cooling circuit from experimental setup.

## 4.4 Heat Transfer Analysis

The experimental setup so that the expected released heat is removed from the system. To evaluate the microNETmix unit embedded in the experimental apparatus regarding heat transfer, evaluation of its performance is required. For this purpose, results obtained in Chapter 3 are of important to estimate the global heat transfer coefficient and to predict heat transfer rates in the process.

### 4.4.1 Heat Transfer Resistances

Heat transfer resistance in a convective heat transfer mechanism, $\mathrm{R}_{\mathrm{conv}}$, can be determined from

$$\mathrm{R}_{\mathrm{conv}} = \frac{1}{hA_{\mathrm{transf}}} \tag{4.1}$$

where $h$ is the convective heat transfer coefficient, either local and instantaneous or an average value, and $A_{\mathrm{transf}}$ is the active area for heat transfer . The heat transfer resistance is a measure of the difficulty of a medium to transport heat through a surface. The higher the resistance, the higher the difficulty of the medium to transport heat. In a case where the removal of heat has an important impact, low heat transfer resistance is desired.

Heat transfer resistance by conduction through a solid $\mathrm{R}_{\mathrm{cond}}$ can be determined from

$$\mathrm{R}_{\mathrm{cond}} = \frac{\delta}{\kappa A_{\mathrm{transf}}} \tag{4.2}$$

where $\delta$ is the solid thickness, and $\kappa$ is the solid thermal conductivity. Again, if large amounts of heat are released, small heat transfer resistances are of interest.

Resistance by conduction in solids for constant transfer area can only be altered by either changing the material (and thus changing $\kappa$) or by changing the thickness of the solid in the direction of the heat flow. Convective resistance on fluids, on the other hand, depends not only on the material medium (i.e. the fluid itself), but also

on the system hydrodynamic conditions. Usually these hydrodynamic conditions are highly dependent on the geometry of the flow system and on the capacity of generating flow disturbances that can enhance heat transfer, as observed in Chapter 3.

#### *4.4.1.1 NETmix Side*

The convective resistance on a NETmix plate can be determined using the results of Chapter 3. The microNETmix used in the experimental setup is different than the NETmix NUB model simulated in Chapter 3. In particular the ratio $\omega_n/d_c$ is equal to one in the microNETmix unit.

Heat transfer coefficient can be determined from the Nusselt number using Equation 3.10. The NETmix unit cell Nusselt number is determined using the correlation represented by Equation 3.30 that yields the enhancement factor for a given Reynolds number, and using Equation 3.37. The strategy applied in Section 3.5 regarding the effect of the $\omega_n/d_c$ ratio must be used for the determination of Nusselt numbers, since the original correlations were obtained for a NETmix with a $\omega_n/d_c$ ratio equal to three.

Convective heat transfer coefficient and heat transfer resistance in the microNETmix, as a function of the flow rate of water at a temperature of $2\,°C$ (which is the typical temperature for the production of gas hydrates) are represented in Figure 4.19.

As already mentioned in Section 3.6, the capacity of NETmix to transfer heat is comparable only to the capacity of microreactors, with large heat transfer fluxes due to their large specific heat transfer areas. The increase of the heat transfer coefficient (and thus the decrease of the resistance) with increasing flow rate is expected, and its behaviour is similar to the one presented in Figure 3.11, which is the result of the enhancement observed due to the appearance of flow disturbances at large Reynolds numbers.

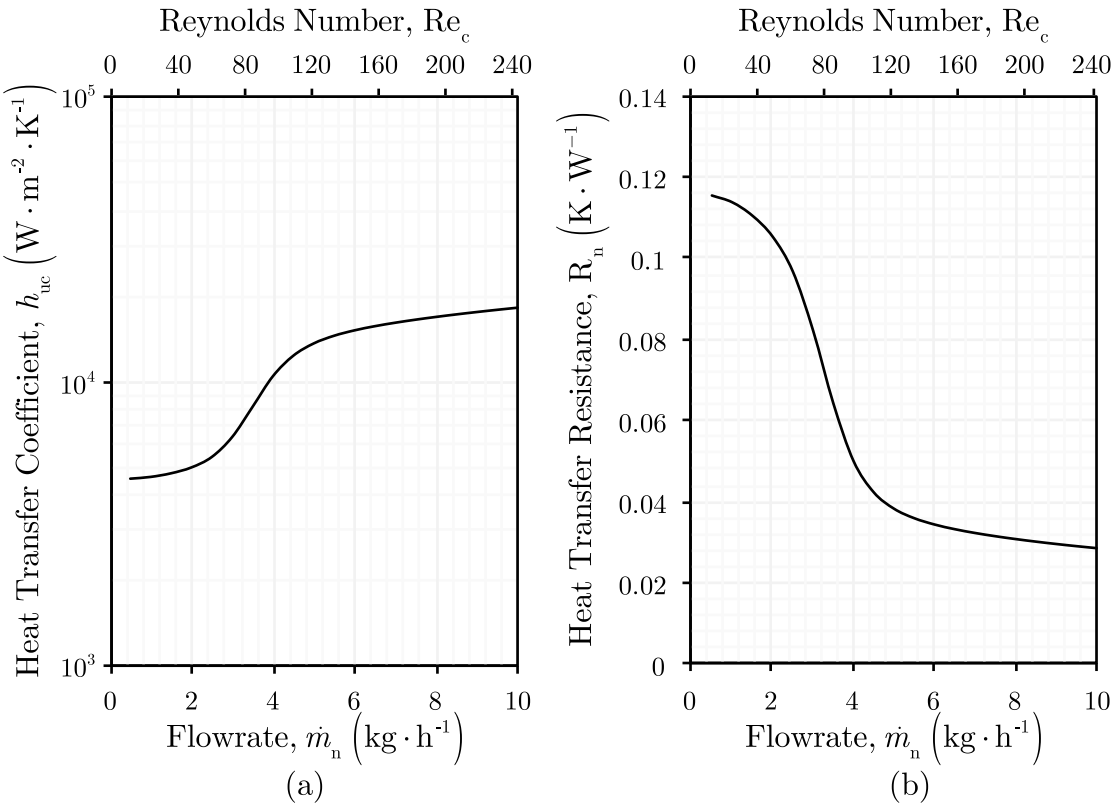



Figure 4.19 – (a) Heat transfer coefficient and (b) resistance in the NETmix side as a function of the mass flowrate (assuming water as the working fluid).

It is also important to emphasize that during operation, gas will be introduced into the system. It is unclear the effect of the presence of gas in the performance of the microNETmix unit regarding heat transfer. However, the potential addition of flow disturbances as a result of the presence of multiphase gas-liquid flow should lead to a further increase of the heat transfer coefficient.

#### *4.4.1.2 Cooling Plates Side*

For the determination of the heat transfer coefficient on the cooling plates side, it is necessary to identify the different flow regions of the plate. As can be seen in Figure 4.20, essentially two different flow regions exist, identified by the different colours. The regions marked in the red are the regions of the channels with length $L_{cc}$ and a cross-sectional area with width of $d_{cc}$ and width of $\omega_{cc}$ (see Table 4.2). These are regions where the velocities are higher, and thus the heat transfer coefficient should also be higher. Also, the network of channels and chambers from the NETmix plates are in contact with the areas in red, not being in contact with the areas in blue.

These latter regions are collectors, which have the objective of collecting the cooling fluid from the channels and to distribute it to the next channels. The objective of this design is to maximize the distribution along the cooling plates.

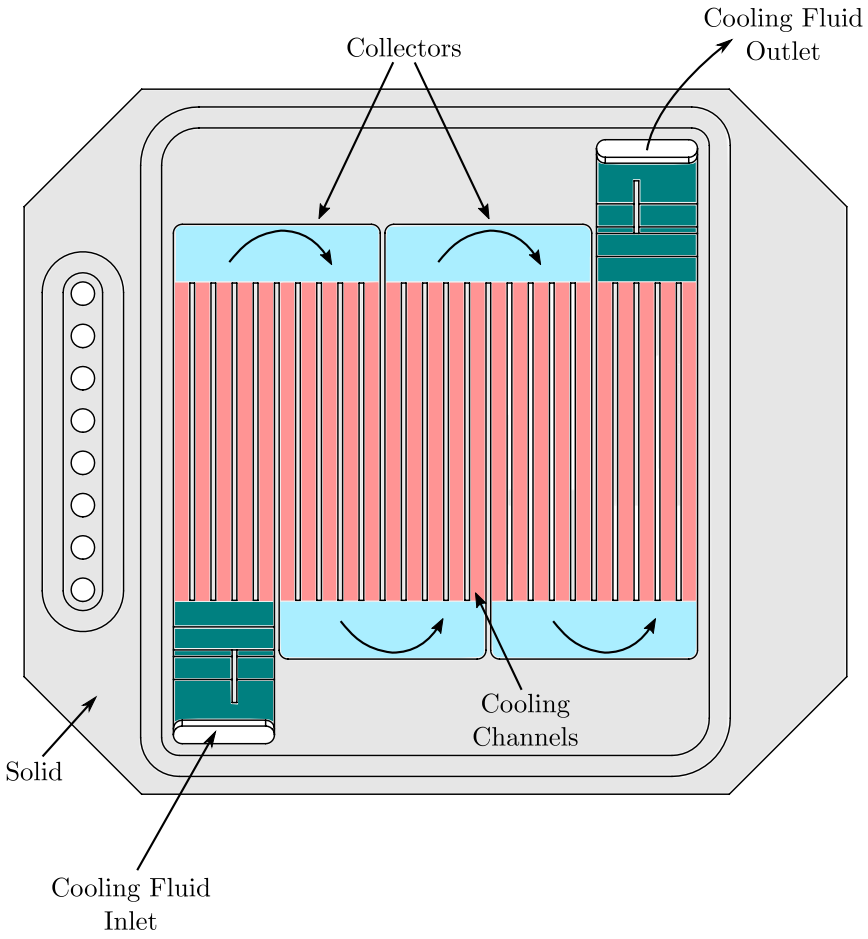



Figure 4.20 – Different regions in the cooling plates: red regions are the channels in contact with the NETmix network; blue regions are the flow collectors/distributors; green regions are the inlet and outlet regions; grey regions present solid.

Since the NETmix network is in contact only with the red regions, the blue regions will be ignored in the present analysis of heat transfer.

To assess the capability of the system to remove heat, CFD simulations were performed on a small, representative part of the cooling plate comprising two sections of channels and one collector, as shown in Figure 4.21. This representative part includes the cooling plate inlet, as well as the collector and distributor at the end of the first section, which routes the fluid to the second section, distributing it to five channels.

For a more accurate determination of the heat transfer coefficient in the cooling channels zones, which are the zones that are in contact with the NETmix network, the acknowledgment of the flow distribution along these channels is extremely important. Therefore, the simulation of the flow in the collections and distributors is required.

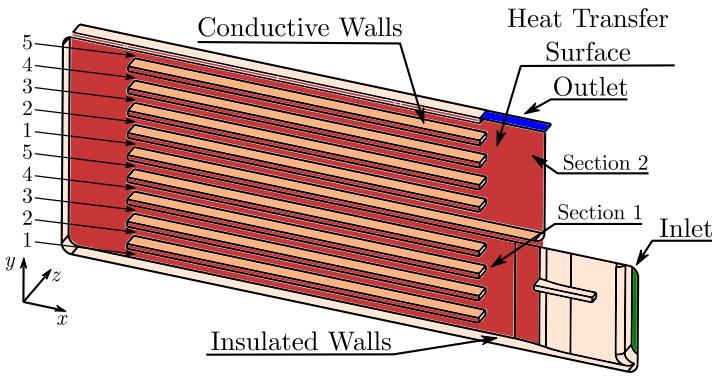



Figure 4.21 – Part of the cooling plate simulated by CFD and respective boundary conditions. The numbers identify each of the section's channels.

The equations presented in Section 3.2.1 are also applicable in the simulation of the cooling plates. The following boundary-conditions are applied in the simulation: no-slip condition is assumed at the walls of the domain, $\vec{v}_{\text{wall}} = 0$; simplified uniform velocity profile is applied to the inlet channels; parallel flow condition is applied at the outlet channels, by imposing a simplified constant and uniform pressure profile, $p_{\text{out}} = p_0$; constant wall heat flux $\dot{q}_{\text{wall}} = \dot{q}_0$, is imposed at all walls. The inlet temperature is $T_{\text{in}} = 261\,\text{K}$. This value was selected based on the minimum temperature gradient between the cooling fluid and the reaction fluid, which is approximately 15 K. Since the characteristic temperature for hydrates formation is 275-276 K, the coolant temperature should be close to 261 K. The total wall heat flux is $\dot{q}_{\text{wall}} = 100\,\text{W}$, which corresponds to approximately one third of the total released heat expected for the precipitation of hydrates for the production rate from Table 4.1 (see Section 5.2 for more information on how the dissociation enthalpy is determined). The velocity at the inlet is set so that the total flow rate of cooling fluid is approximately $50\,\text{kg}\cdot\text{h}^{-1}$, value chosen based on the capacity of the pump of the chiller E-14 to feed all four cooling plates. This results in a low Reynolds number on

the channels (in the range of 300-500), and thus a laminar model is applied. The flow is incompressible, and the working fluid is an ethanol-water mixture, containing 40% in volume of ethanol, with variable local physical properties with temperature (Appendix A). Conduction through the solid has a relevant impact on this system, mostly in the baffles that separate the channels from each other. Therefore, a proper choice of the solid is important. The simulated solid is stainless steel AISI 316, assuming constant thermal properties (see Appendix A)

The simulation was performed in steady state, using *Fluent* 15 from ANSYS®, while the geometry and mesh were created in *Design Modeler* and *Meshing*, respectively. The SIMPLEC scheme was used for the pressure-velocity coupling, the Standard and Second-Order MUSCL schemes were used for the pressure and momentum discretization, respectively, while the Second-Order MUSCL scheme was used for the discretization of the convective term of the energy conservation equation. The simulation was considered to have converged when no significant variation of the outlet channels temperature and velocity values, averaged by the mass flow rate, was lower than 1% relatively to the previous iteration, and when the normalized residues of the governing equations were lower than $10^{-6}$ for steady-state simulations.

The flow distribution in each channel, presented in terms of the channel Reynolds number is shown in Figure 4.22. The first section that comprises the first five channels is the region where the cooling fluid enters the plate. The flow distribution is far from optimal, since a gradual flow rate increase is observed from the channel near the bottom wall (channel 1) to the top channel in the first section. The fluid is then collected in the collector and distributed to the five channels of the second section. The collector design greatly affects the flow in the first channel of the second section, since the flow rate in this channel is lower than 10% of the total flow rate. This is due to the acceleration that the fluid suffers in the collector, increasing its inertia and its resistance for proper distribution.

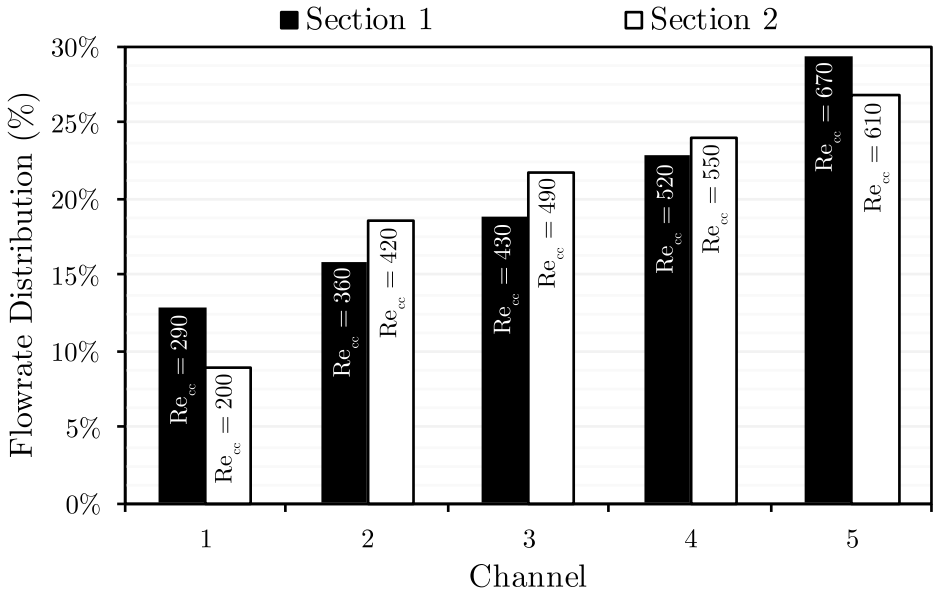



Figure 4.22 – Flow distribution in the cooling plate channels for each of the sections.

The Nusselt number in the cooling plate, namely in the channels, can be estimated using a strategy similar to the one used in Section 3.4. However, the geometrical considerations from Equations 3.25 and 3.28 are not applicable in this case. Equations 3.25 and 3.28 allow a direct comparison between flow in parallel plates and in rectangular channels. However, in both cases, heat transfer occurred only through two of the four walls. In this case, heat transfer occurs from the four walls, and thus it becomes more accurate to compare the Nusselt numbers with the ones obtained for laminar flow in tubes for constant wall heat flux. In the regions where the thermal boundary layer is still in development, the Nusselt number in a tube is given by (Bird et al. 2002)

$$\mathrm{Nu}_{\mathrm{tube}} = \frac{2\Gamma\left(2/3\right)}{9^{1/3}}\left(x^{*}_{\mathrm{tube}}\right)^{-1/3} \tag{4.3}$$

where $x^{*}_{\mathrm{tube}}$ is determined from Equation 3.35. To apply Equation 4.3 to a rectangular duct, the tube diameter must be replaced by the channel hydraulic diameter $d_{\mathrm{h,\,cc}}$ determined from

$$d_{\mathrm{h,\,cc}} = \frac{2\omega_{\mathrm{cc}} d_{\mathrm{cc}}}{\omega_{\mathrm{cc}} + d_{\mathrm{cc}}} \tag{4.4}$$

In the region where the thermal boundary layer is completely developed, $\mathrm{Nu}_{\mathrm{tube}} = 4.364$ (Bird et al. 2002). The Nusselt number obtained for each of the cooling channels is a spatial average value, and is computed from

$$\mathrm{Nu}_{\mathrm{cc}} = \frac{h_{\mathrm{cc}}}{\overline{\kappa}} d_{\mathrm{h,\,cc}} \tag{4.5}$$

where $h_{\mathrm{cc}}$ is the cooling plates channel's average heat transfer coefficient and $\overline{\kappa}$ is the average thermal coefficient for the mixture water-ethanol. The heat transfer coefficient $h_{\mathrm{cc}}$ is determined from

$$h_{\mathrm{cc}} = \frac{\dot{q}_{\mathrm{cc}}}{A_{\mathrm{transf,\,cc}} \Delta T_{\mathrm{lm,\,cc}}} \tag{4.6}$$

where $\dot{q}_{\mathrm{cc}}$ is the heat flux that is transferred from the channel walls to the fluid, $A_{\mathrm{transf,\,cc}}$ is the area of transfer of the channels and $\Delta T_{\mathrm{lm,\,cc}}$ is a characteristic temperature gradient. Equation 3.14 can be used to determine $\dot{q}_{\mathrm{cc}}$, while Equation 3.15 can be used to determine $\Delta T_{\mathrm{cc}}$. The transfer area $A_{\mathrm{transf,\,cc}}$ of a single channel is determined from

$$A_{\mathrm{transf,\,cc}} = 2L_{\mathrm{cc}}\left(d_{\mathrm{cc}} + \omega_{\mathrm{cc}}\right) \tag{4.7}$$

The average Nusselt numbers determined from Equation 4.5 cannot be directly compared with the local numbers obtained from Equations 3.21 to 3.28 and 3.32. The local Nusselt number for the cooling plates channels $\mathrm{Nu}_{\mathrm{cc,\,loc}}$ has the following form

$$\mathrm{Nu}_{\mathrm{cc,\,loc}} = \xi\left(x^{*}_{\mathrm{cc}}\right)^{-1/3} \tag{4.8}$$

where $\xi$ is a constant related to the flow characteristics, and $x^{*}_{\mathrm{cc}}$ is the dimensionless entrance length in the channels, and can be calculated using Equation 3.17 evaluated at the distance from the channel's inlet $x_{\mathrm{cc}}$. Results from simulations demonstrated that a maximum temperature increase of $3\,\mathrm{K}$ from the inlet to the outlet of the channel is observed, so both the Reynolds and Prandtl number can be assumed to be constant throughout the channel. If that is the case, Equation 4.8 can be replaced by

$$\mathrm{Nu}_{\mathrm{cc,\,loc}} = \xi^{*}\left(x_{\mathrm{cc}}\right)^{-1/3} \tag{4.9}$$

where $\xi^{*}$ is a modified constant given by

$$\xi^{*} = \xi\left(\mathrm{Re}\,\mathrm{Pr}\,\omega_{\mathrm{cc}}\right)^{-1/3} \tag{4.10}$$

The average Nusselt number $\mathrm{Nu}_{\mathrm{cc}}$ can be calculated from the local Nusselt number using

$$\mathrm{Nu}_{\mathrm{cc}} = \frac{\int_{0}^{L_{\mathrm{cc}}} \mathrm{Nu}_{\mathrm{cc,\,loc}}\left(x_{\mathrm{cc}}\right) dx_{\mathrm{cc}}}{L_{\mathrm{cc}}} = \frac{3}{2}\xi^{*}\left(L_{\mathrm{cc}}\right)^{-1/3} \tag{4.11}$$

Equation 4.11 yields the following relationship

$$\frac{\mathrm{Nu}_{\mathrm{cc}}}{\mathrm{Nu}_{\mathrm{cc,\,loc}}} = \frac{3}{2}\left(\frac{L_{\mathrm{cc}}}{x_{\mathrm{cc}}}\right)^{-1/3} \tag{4.12}$$

and this means that Nusselt number equivalence is obtained when

$$x_{\mathrm{cc}} = \left(\frac{2}{3}\right)^{3} L_{\mathrm{cc}} \tag{4.13}$$

The comparison between the local Nusselt number for laminar flow in tubes for constant wall heat flux and the average Nusselt number for the channels as a function of the thermal entrance length is represented in Figure 4.23.

The average Nusselt numbers obtained through CFD simulations agree with the theoretical values for laminar flow in tubes, meaning that these correlations can be used for the determination of the average Nusselt number. It is important to highlight the fact that all values of $x_{\mathrm{cc}}^{*}$ for the CFD simulated values are computed using the relation obtained from Equation 4.13. The variations are due to the different flow rates that are observed in each of the channels, which have a significant impact on the channel's Reynolds number. Also, the slight deviation of the CFD values from the theoretical values may be due to the assumption of a not completely developed hydrodynamic boundary layer at the inlet of the channels, a condition assumed in Equation 4.3.

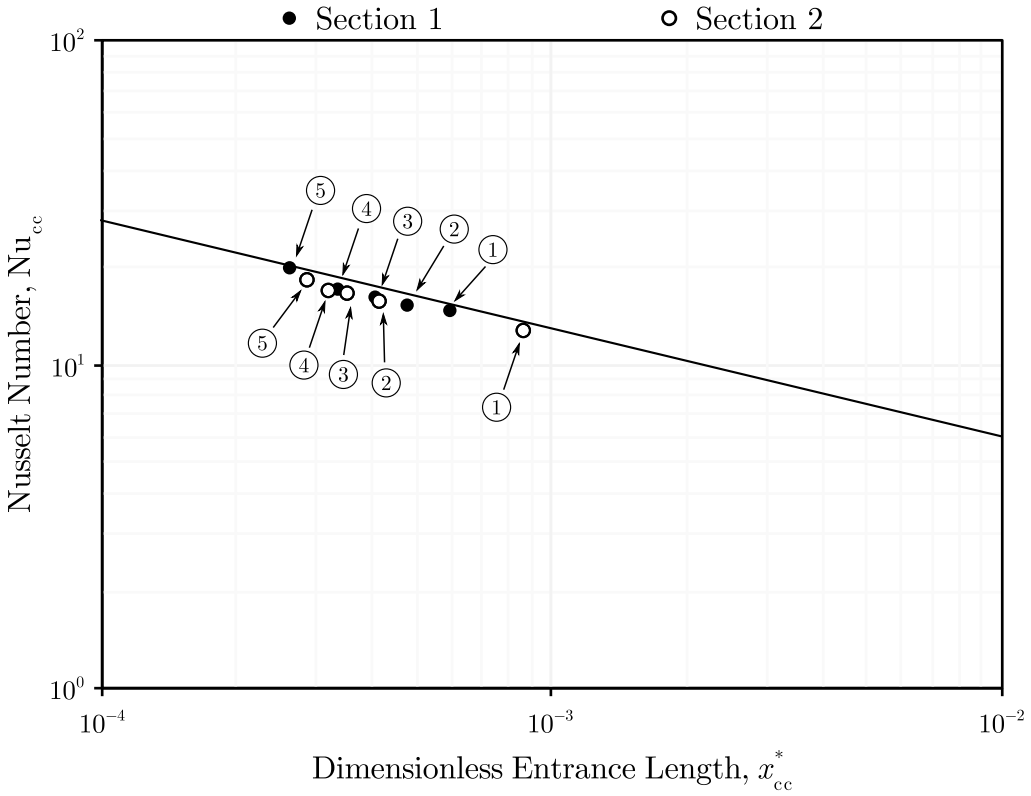



Figure 4.23 – Cooling plates channel's Nusselt number as a function of the dimensionless entrance length (circles) and comparison with laminar flow in tubes for constant wall heat flux (line).

The average Nusselt number in each of the channels is represented in Figure 4.24. The horizontal line represents the average Nusselt number evaluated at the average Reynolds number $\overline{\mathrm{Re}_{cc}}$, assuming a uniform flow distribution through the channels, and determined from

$$\overline{\mathrm{Re}_{cc}} = \frac{\sum_i \mathrm{Re}_{cc,\,i}}{n_{cc}} \tag{4.14}$$

where $i$ is the channel number and $n_{cc}$ is the total number of channel in each section.

Figure 4.24 shows that the channels where the flow is higher present a larger Nusselt number than the Nusselt number obtained at the average Reynolds number, while the channels with lower flow rates present even smaller Nusselt numbers.

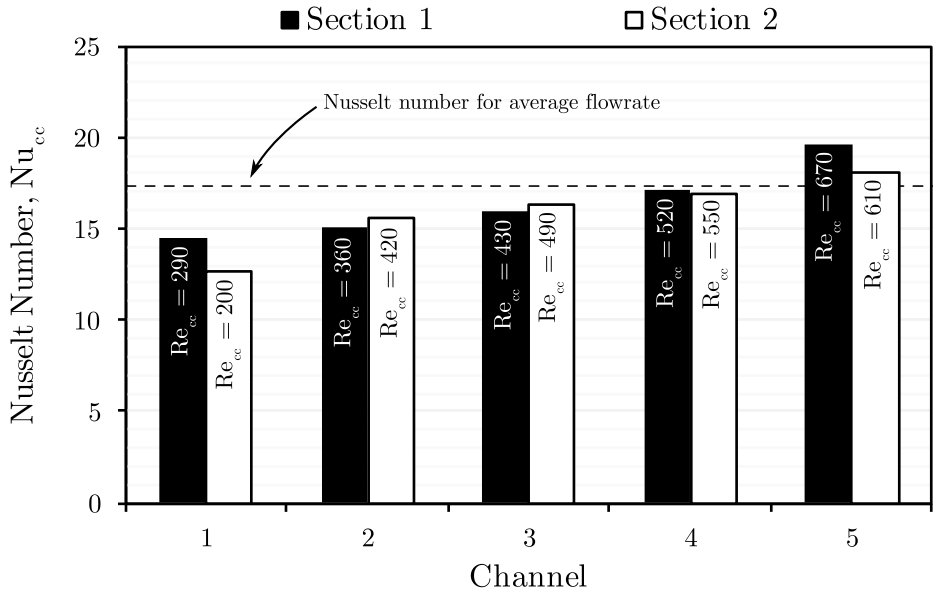



Figure 4.24 – Cooling plates channel's Nusselt number comparison. The dashed line represents the Nusselt number obtained if the flowrate was equally distributed in all channels.

Similarly to what was done for NETmix in Chapter 3, an effective specific heat transfer capacity for each of the cooling plate's sections can be determined by

$$\hat{q}_{\text{cc, eff}} = \frac{A_{\text{transf, cc}}}{V_{\text{cc}}} \sum_{i} h_{\text{cc},i} \tag{4.15}$$

where $A_{\text{transf, cc}} / V_{\text{cc}}$ is the specific heat transfer area of a single channel, determined from

$$\frac{A_{\text{transf, cc}}}{V_{\text{cc}}} = \frac{2\left(\omega_{\text{cc}} + d_{\text{cc}}\right)}{\omega_{\text{cc}} d_{\text{cc}}} \tag{4.16}$$

Similarly, a specific heat transfer capacity based on the average channel's Reynolds number $\hat{q}_{\text{cc, }\overline{\text{Re}_{\text{cc}}}}$ can be determined using

$$\hat{q}_{\text{cc, }\overline{\text{Re}_{\text{cc}}}} = \frac{A_{\text{transf, cc}}}{V_{\text{cc}}} n_{\text{cc}} h_{\text{cc, }\overline{\text{Re}_{\text{cc}}}} \tag{4.17}$$

In general, the effective specific heat transfer capacity is higher than the specific heat transfer capacity based on the average channels Reynolds number. However, due to the difficulty to determine the flow distribution in all sections of the cooling plates, assuming a uniform distribution is the best possible estimate. In the first section (accounting the first five channels), the specific heat capacity determined using the

average Reynolds number deviates 4.18% from its effective specific heat transfer capacity, while the number increases to 7.60% in the second section. This agrees with Figure 4.22, which shows that the distribution is less uniform along the plate. If both sections are combined, the global deviation is 5.87%. Therefore, the use of the Reynolds number assuming a perfect and equal distribution through the channels is a good approach for the estimate of the heat transfer capacity of the cooling plates.

The average channel's heat transfer coefficient as a function of the Reynolds number, as well as the heat transfer resistance for the cooling plate is represented in Figure 4.25.

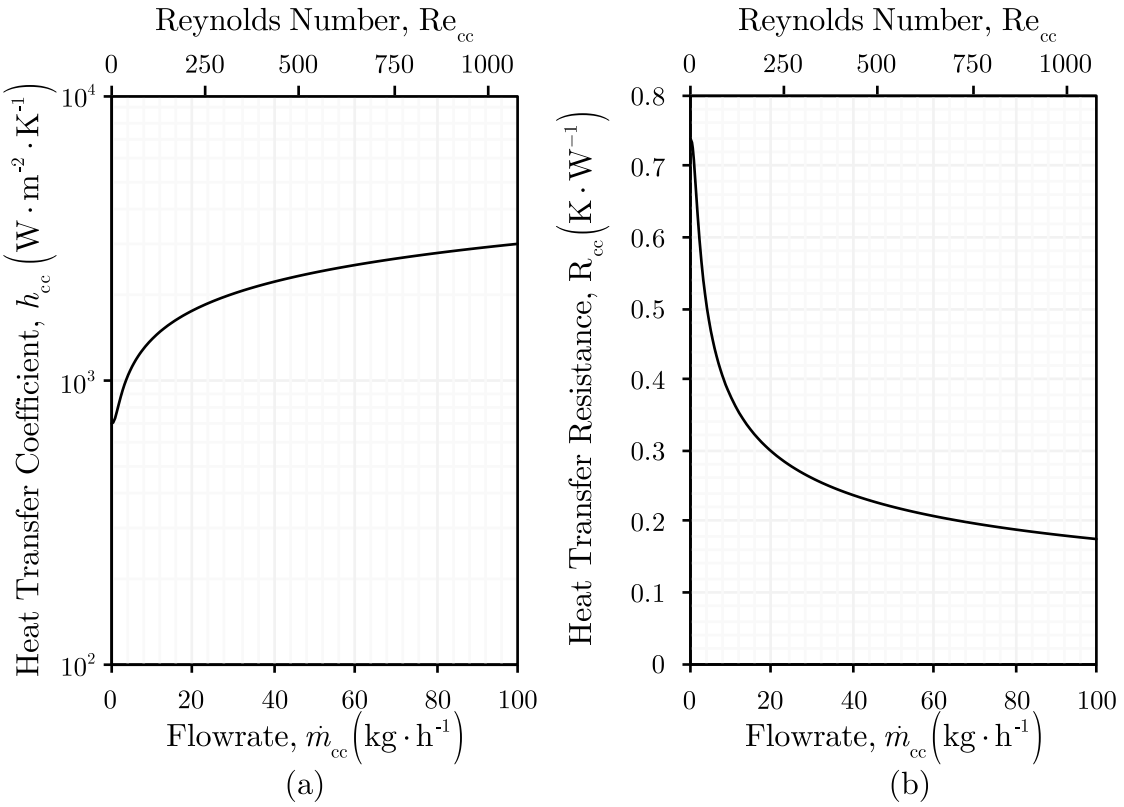



Figure 4.25 – (a) Heat transfer coefficient and (b) resistance on the cooling plate side as a function of the mass flowrate (assuming ethanol – water mixture as the working fluid).

Figure 4.25 shows that the increase of the cooling fluid's flow rate results in an increase of the heat transfer coefficient, and thus in a reduction of the heat transfer resistance.

### 4.4.2 Global Heat Transfer Coefficient Estimation

The global heat transfer coefficient in the direction normal to the NETmix plate flow direction can be determined by the association in series of the resistances of both NETmix and cooling plates, at the liquid level through convection, and of the solid that separates both plates, through conduction. Assuming equal area for heat transfer in each resistance, the global heat transfer coefficient can be determined from

$$U = \left( \frac{1}{h_{\text{uc}}} + \frac{\omega_{\text{cp}} - \omega_{\text{cc}}}{\kappa_{\text{steel}}} + \frac{1}{h_{\text{cc}}} \right)^{-1} \tag{4.18}$$

where $\kappa_{\text{steel}}$ is the conductivity of the solid material, which is stainless steel AISI 316 (see Appendix A) and $\omega_{\text{cp}} - \omega_{\text{cc}}$ represents the thickness of the steel thin plate that separates the fluids from NETmix and cooling plate (see Figure 4.6). The global heat transfer coefficient for the microNETmix unit is represented in Figure 4.26 as a function of the Reynolds number both in the NETmix channels and in the cooling channels.

From the analysis of Figure 4.19b and Figure 4.25b, it is possible to observe that the resistance on the NETmix side is much lower than in the cooling plates as expected from Figure 3.13. This resistance decreases with the Reynolds number. The shape of the curves is not the same, and a more accentuated decrease in the case of NETmix near the critical Reynolds number is observed. As discussed in Chapter 3, this is related to the appearance of oscillations that enhance heat transfer rates.

Figure 4.26 shows an abrupt increase of the global heat transfer coefficient in the region near the critical channel's Reynolds number. The amplitude of this increase also increases with the Reynolds number of the cooling plates channels. This means that for low cooling channels Reynolds number, the heat transfer mechanism is controlled by convection in the cooling plates. When the resistance in this side decreases, even small variations of the NETmix Reynolds number has a significant impact on the global heat transfer coefficient. Also, the fact that above the critical

Reynolds number the heat transfer coefficient remains constant indicates that, as expected, the major resistances are on either the solid, through conduction, or on the cooling plate, through convection.

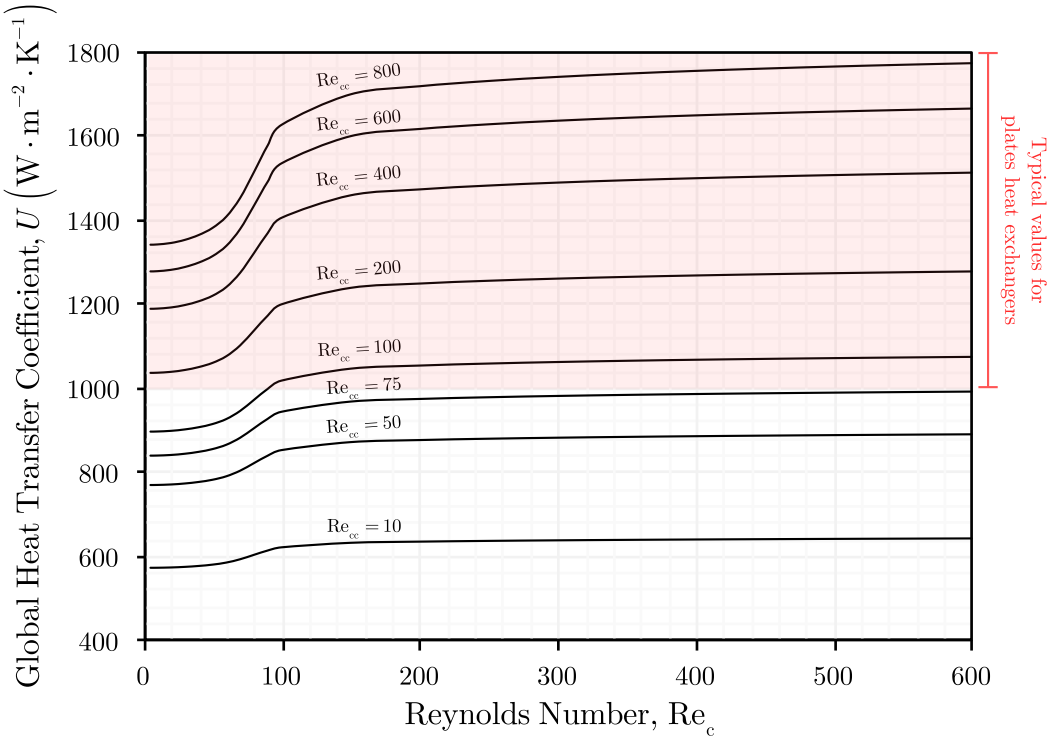



Figure 4.26 – Global heat transfer coefficient for the microNETmix unit as a function of the NETmix channel's Reynolds number, for several values of cooling plates channels Reynolds number.

The typical range of global heat transfer coefficients for plate heat exchangers is also represented in Figure 4.26 by the red region. Plate heat exchangers typically feature global heat transfer coefficients for liquid-liquid systems in the range of 1000-4000 $\mathrm{W\cdot m^{-2}\cdot K^{-1}}$ (EngineeringToolBox). It is expected that the microNETmix unit present values within this range, in particular for large (above 100) Reynolds numbers in the cooling channels. This observation is extremely relevant since this device can achieve the same heat transfer coefficients than plate heat exchangers in the laminar regime. From Figure 4.26 shows that the resistance in the cooling side has a significant impact on the global heat transfer coefficient, and a better heat transfer performance is expected if the Reynolds number in the cooling channels increases even further.

The area of transfer can be coupled to the global heat transfer coefficient. However, it is important to note that part of the area of the network is perfectly laid on the

channels of the cooling plate, while the remaining is laid on the solid that constitutes the baffles that separate the cooling channels (see Figure 4.27). Figure 4.27 shows that most of the area occupied by the network chambers are laid on the cooling channels, while the network channels are laid on the cooling baffles. The chambers represent about 78% of the total area of a NETmix network (for the dimensions from Table 4.2), meaning most of the total area is represented by the global heat coefficient determined from Equation 4.18.

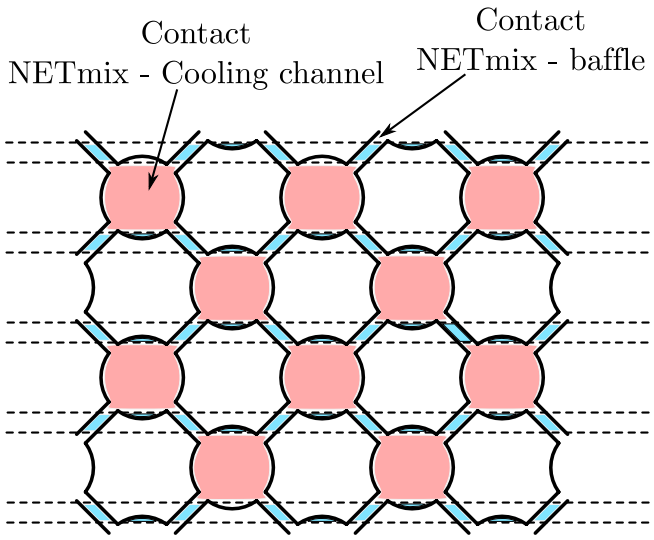



Figure 4.27 – microNETmix unit plates overlap. The red regions represent the regions of the NETmix network that are in laid in the cooling fluid channels, while the blue regions represent regions where the NETmix network is laid in the cooling plates baffles (baffles are represented by the dashed lines).

For the microNETmix unit, the total area of exchange can be obtained by multiplying the area of heat transfer for the NETmix network by $2n_{\text{np}}$, where $n_{\text{np}}$ is the number of network plates, since each NETmix plate features two possible areas for heat transfer with the cooling plates. The total heat flux absorbed by the cooling plates of the microNETmix unit is given by

$$\hat{q}_{\text{cc, tot}} = 0.78 \times 2n_{\text{np}} \hat{q}_{\text{cc, } \overline{\text{Re}_{\text{cc}}}} \tag{4.19}$$

Finally, in real operation, it is expected that the heat removed in the microNETmix unit can be slightly larger since in this analysis, it is assumed that no heat transfer through conduction occurs through the solid in the normal direction to the flow, which is not the reality, although it is expected the amount of heat removed by

conduction to be much smaller when compared to the amount of heat removed by convection.

## 4.5 Conclusions

This chapter focused on the description of the experimental setup for the continuous production of gas hydrates. The setup was designed in such a way that hydrates could be produced at a gas rate of approximately $1\,\mathrm{kg}\cdot\mathrm{h}^{-1}$, at pressures near 60 bar, and producing solid slurries at a weight concentration of 20% wt. The Reynolds number is kept above the critical Reynolds number, to both enhance mixing and heat transfer, following the results of Chapter 3.

The process comprises several devices that enable both monitoring and control of the process, namely temperature and pressure. The core of the process is the microNETmix unit, comprising three NETmix plates with dimensions within the micrometric range, and four cooling plates, designed to remove the heat released from the crystallization of solid hydrates. The setup also comprises a visualizing sampler downstream the microNETmix unit, enabling a direct observation of the slurries, a filtration column designed to obtained concentrated hydrates, and a flash drum to separate gas from liquid and solids. The setup is flexible and versatile, with different modes of operation, using pure carbon dioxide in either gas or liquid state. Although not used in the present work, the setup is designed to support the feeding of a mixture of $\mathrm{N_2}/\mathrm{CO_2}$ to produce hydrates.

Finally, the designed microNETmix unit was evaluated regarding heat transfer. Transposing the results at the NETmix level from Chapter 3, and analysing the performance of the cooling plates, it was possible to conclude that the microNETmix unit presents a global heat transfer coefficient of the same order of magnitude as plate heat exchangers for liquid-liquid heat transfer. The heat transfer process is controlled by conduction through the solid that separates both NETmix and cooling plates, or by convection in the cooling plate side. The expected global heat transfer

coefficients obtained within the laminar flow regime presents promising values for the application of this process in the production of gas hydrates.

## 4.6 References

Andersson, V., Gudmundsson, J.S., **2000**. "Flow Properties of Hydrate-in-Water Slurries". *Annals of the New York Academy of Sciences* 912, 322-329.

Armacell, "Armacell - Making a Difference Around the World". *Published online at armacell.com*. Available at: corporate.armacell.com/.

Bird, R.B., Stewart, W.E., Lightfoot, E.N., **2002**. "Transport Phenomena", 2nd ed. John Wiley & Sons, Inc., New York, NY, USA.

EngineeringToolBox, "Heat Exchanger Heat Transfer Coefficients". *Published online at The Engineering ToolBox*. Available at: http://www.engineeringtoolbox.com/heat-transfer-coefficients-exchangers-d_450.html.

Fonte, C.M. **2013**. "The NETmix Reactor: Application to High Added-Value Products" [*Ph.D Thesis*]. Porto, Portugal: Departamento de Engenharia Química, Universidade do Porto.

Fonte, C.M., Leblebici, M.E., Dias, M.M., Lopes, J.C., **2013**. "The NETmix Reactor: Pressure Drop Measurements and 3D CFD Modeling". *Chemical Engineering Research and Design* 91, 2250-2258.

Groen, C.B. **2012**. "$CO_2$ Hydrate Formation in Coil Heat Exchangers - An Experimental and Theoretical Study" [*MSc Thesis*]. Delft, Netherlands: Department of Sustainable Processes and Energy Technologies, TU Delft.

Gudmundsson, J.S., Parlaktuna, M., Levik, O.I., Andersson, V., **2000**. "Laboratory for Continuous Production of Natural Gas Hydrates". *Annals of the New York Academy of Sciences* 912, 851-858.

Hu, J., Sari, O., Mahmed, C., Cereghetti, R., Homsy, P., **2010**. "$CO_2$ Hydrate Slurry". Yverdon-les-Bains, Switzerland, Doc. No GRS 032/08.

Iijima, M., Yamada, M., Tomikawa, F., Negoro, M., Minemoto, M., Haneda, H., Assigned to Mitsubishi Jukogyo Kabushiki Kaisha, **1994**. "Method for the Fixation of Carbon Dioxide, Apparatus for Fixing and Disposing Carbon Dioxide, and Apparatus for the Treatment of Carbon Dioxide". Patent No. US 5364611.

INEGI, "INEGI - Driving Science & Innovation". *Published online at INEGI - Instituto de Ciência e Inovação em Engenharia Mecânica e Engenharia Industrial*. Available at: http://www.inegi.up.pt/.

Julabo, "Julabo". *Published online at julabo.com*. Available at: http://www.julabo.com/.

Kanda, N., Takahashi, M., Iwasaki, T., Assigned to Mitsui Engineering & Shipbuilding Co., Ltd., **2012**. "Process for Producing Mixed Gas Hydrate". Patent No. US 8138382.

Knauer, "KNAUER: Your Expert for HPLC, SMB and Osmometry". *Published online at knauer.net*. Available at: http://www.knauer.net/.

Laranjeira, P.E. **2005**. "NETmix Static Mixer - Modelling, CFD Simulation and Experimental Characterisation" [*Ph.D Thesis*]. Porto, Portugal: Departamento de Engenharia Química, Universidade do Porto.

Laranjeira, P.E., Martins, A.A., Lopes, J.C.B., Dias, M.M., **2009**. "NETmix®, a New Type of Static Mixer: Modeling, Simulation, Macromixing, and Micromixing Characterization". *AIChE Journal* 55, 2226-2243.

Li, X., Xu, C., Chen, Z., Li, G., Zhang, Y., Assigned to Guangzhou Institute Of Energy Conversion, Chinese Academy Of Sciences, **2015**. "Spraying Device for Quickly Forming Gas Hydrates". Patent No. CN 103623766.

Linde, "Linde - Industrial Gases". *Published online at linde-gas.com*. Available at: http://www.linde-gas.com/en/products_and_supply/refrigerants/hfc_refrigerants/r404a/index.html.

Liu, K.V., Choi, U.S., Kasza, K.E., Argonne National Laboratory, **1988**. "Measurements Of Pressure Drop And Heat Transfer In Turbulent Pipe Flows Of Particulate Slurries". Lemont, IL, USA, Doc. No ANL-85-15.

LSRE-LCM, "Laboratory of Separation and Reaction Engineering - Laboratory of Catalysis and Materials". *Published online at Associated Laboratory LSRE-LCM*. Available at: http://lsre.fe.up.pt/.

Mono™, "Mono Pumps | Pump Manufacturer". *Published online at mono-pumps.com*. Available at: http://www.mono-pumps.com/.

Ohya, N., Tokunaga, N., Hayase, T., Takahashi, M., Assigned to Mitsui Engineering & Shipbuilding Co., Ltd., **2017**. "Device for Producing Gas Hydrate". Patent No. US 9533277.

Paralab, "Paralab". *Published online at Paralab*. Available at: http://www.paralab.pt/.

Phenomenex®, "Phenomenex – Global Technology Leader in Analytical Chemistry Solutions". *Published online at phenomenex.com*. Available at: http://www.phenomenex.com/.

ricardo&barbosa, "Ricardo & Barbosa - Mechanical Mold and Tool Maker". *Published online at ricardo-barbosa.com*. Available at: http://www.ricardo-barbosa.com/.

Sloan, E.D., Koh, C., **2007**. "Clathrate Hydrates of Natural Gases", 3rd ed. CRC Press, Boca Raton, FL, USA.

SlurryICE, **n.a.** "Thermal Energy Storage: Design Guide".

Smith, J.M., Van Ness, H., Abbott, M., **2005**. "Introduction to Chemical Engineering Thermodynamics", 7th ed. McGraw-Hill, New York, NY, USA.

Tecnogial, "Tecnogial". *Published online at tecnogial.pt*. Available at: http://www.tecnogial.pt/.

Watson-Marlow, "Watson-Marlow". *Published online at watson-marlow.com*. Available at: http://www.watson-marlow.com/.

Yang, D., Le, L., Martinez, R., Currier, R., Spencer, D., Deppe, G., **2008**. "Heat Transfer During $CO_2$ Hydrate Formation in a Continuous Flow Reactor". *Energy & Fuels* 22, 2649-2659.

Yang, D., Le, L.A., Martinez, R.J., Currier, R.P., Spencer, D.F., **2011**. "Kinetics of $CO_2$ Hydrate Formation in a Continuous Flow Reactor". *Chemical Engineering Journal* 172, 144-157.

# 5 $CO_2$ Hydrates – Experimental Production

## 5.1 Introduction

The main purpose of this chapter is to understand the dynamics inherent to a continuous process for the production of pure $CO_2$ hydrates using the NETmix technology, embedded in the experimental apparatus described in Chapter 4, to prove the process concept. The main objective is to verify if the designed microNETmix unit is capable to remove the heat released from mixing carbon dioxide and water in conditions of low temperature and high pressure. The influence of the use of liquid or gas $CO_2$ as the source feedstock, as well as the use of the thermodynamic promoter THF is also evaluated.

Firstly, the thermodynamics involved in the process of precipitating hydrates is described in Section 5.2. This section includes a short description of a software package, CSMGem, capable to predict the phase equilibrium in the hydrates stability region, as well as validation of the predicted equilibrium curves and the development of a simplified model, which can be used to easily determine the amount of hydrates expected as a function of the operational conditions of the process. In Section 5.3, an

energy balance to a crystallization unit is conceptualized and described. The set of experiments, experimental procedure and used materials are presented in Section 5.4, including the description of all the stages required from the start-up of the installation until it reaches the steady state. The main experimental results are presented in Section 5.5. These include the study of the effect of the presence of THF and of the feed of liquid or gaseous carbon dioxide. The main conclusions from this chapter are presented in Section 5.6. The references for the current section are presented in Section 5.7.

## 5.2 Hydrates Thermodynamics

As mentioned in Section 2.3.2.1, several authors have proposed thermodynamic models to predict the phase equilibrium of clathrate hydrates, in the presence of hydrate-forming guest molecules in water, in conditions at which precipitation can occur. These models are based on the behaviour of each of the phases in equilibrium. At the equilibrium, the chemical potential of any component is equal in all phases, thus enabling the computation of the thermodynamic properties. Therefore, an accurate modelling of each phase is of high importance.

One of the most interesting models was developed by Ballard (2002) from Colorado School of Mines, resulting in the development of a software package called CSMGem, which will be described next.

### 5.2.1 CSMGem

CSMGem (CSM stands for Colorado School of Mines while Gem stands for Gibbs Energy Minimization) is a software package developed by the Colorado School of Mines for hydrates formation prediction, written in Visual Fortran and linked to Visual Basic (Ballard 2002). CSMGem allows the prediction of thermodynamically stable structures and cage occupancy at a given pressure, temperature and composition.

This software allows not only the determination of the equilibrium pressure/temperature at given temperature, pressure and composition, thus determining the minimum pressure or the maximum temperature at which hydrates are stable, but also performs flash calculations using the minimization of the Gibbs energy method. It can also predict the influence of the presence of inhibitors in a system, such as alcohols and/or salts. Another advantage is that it is one of the few models capable to determine the hydrates cage occupancy However, one of the main disadvantages of this software is its inability to model the influence of the presence of promoters, such as THF or TBAB in the equilibrium.

#### *5.2.1.1 Gibbs Energy Minimization*

Most models capable to accurately estimate the hydrate dissociation curve are based on the van der Waals and Platteuw model (van der Waals and Platteeuw 1958) or its modifications. However, to perform flash calculations, a good hydrate phase model is not sufficient, since it is also required to accurately model all the remaining phases present in the equilibrium. CSMGem does it by considering all the possible phases that may be present in the system, and then, by minimizing the Gibbs energy, to determine the amount of each of the phases.

When in thermodynamic equilibrium, the Gibbs energy is minimum, which is a statement of the 2$^{nd}$ law of thermodynamics (that states that the total entropy of an isolated system can only increase over time). This means that minimizing the Gibbs energy at a given temperature and pressure guarantees that the system is at equilibrium, and that three conditions must be observed: temperature is equal in all equilibrium phases; pressure is equal in all equilibrium phases; and chemical potential of a component is equal in all equilibrium phases. When the number of phases at equilibrium is known *a priori*, these three conditions are necessary and sufficient. However, when the number of phases is unknown, these conditions are necessary but not sufficient, guaranteeing only that the Gibbs energy is at a minimum, but not necessarily the global minimum (Ballard 2002). Therefore, in cases where the number

of phases is unknown, Ballard (2002) imposed a fourth condition, that is the minimization of the Gibbs energy.

Multi-flash calculations using CSMGem are done by mathematically representing the three conditions of thermodynamic equilibrium, plus the Gibbs energy minimum condition. The mass balance for a system with $C$ components and $\varphi$ phases is represented by

$$\sum_{k=1}^{\varphi} \alpha_k x_{i,k}^{\text{mol}} = z_i^{\text{mol}} \qquad \left(i = 1,...,C\right) \tag{5.1}$$

where $\alpha_k$ is the normalized fraction of the $k$, $x_{i,k}^{\text{mol}}$ is the mole fraction of component $i$ (from 1 to $C$) in phase $k$ and $z_i^{\text{mol}}$ is the overall mole fraction of component $i$ in the system. Assuming a hypothetical reference phase $r$, with the requirement that it must be present at equilibrium, then Equation 5.1 can be re-written as

$$\alpha_r x_{i,r}^{\text{mol}} + \sum_{\substack{k=1 \\ k \neq r}}^{\varphi} \alpha_k x_{i,k}^{\text{mol}} = z_i^{\text{mol}} \qquad \left(i = 1,...,C\right) \tag{5.2}$$

Two constraints are imposed to Equation 5.2 to guarantee mass conservation

$$\alpha_r = 1 - \sum_{\substack{k=1 \\ k \neq r}}^{\varphi} \alpha_k \tag{5.3}$$

$$\sum_{i=1}^{C} x_{i,k}^{\text{mol}} = 1 \qquad \left(k = 1,...,\varphi\right) \tag{5.4}$$

The equilibrium conditions of equal temperature, pressure and chemical potential in all phases are set in terms of fugacity

$$f_{i,k} = x_{i,k}^{\text{mol}} \phi_{i,k} p \tag{5.5}$$

where $f_{i,k}$ is the fugacity of component $i$ in phase $k$, $\phi_{i,k}$ is respective the fugacity coefficient, and $p$ is the pressure.

The fugacities of all components and phases present at equilibrium must equal, and thus the fugacity ratio, defined as

$$\frac{f_{i,r}}{f_{i,k}} = \frac{x_{i,r}^{\text{mol}}\phi_{i,r}}{x_{i,k}^{\text{mol}}\phi_{i,k}} \tag{5.6}$$

must be equal to unit. However, if phase $k$ is not present in the equilibrium, the conditions from Equation 5.6 is not satisfied. The following condition is always observed, whether phase $k$ is or is not present.

$$\frac{f_{i,r}}{f_{i,k}} \begin{cases} = 1 & \text{if phase } k \text{ is present} \\ < 1 & \text{if phase } k \text{ is not present} \end{cases} \tag{5.7}$$

Equation 5.6 may be written as

$$K_{i,k} = \frac{x_{i,k}^{\text{mol}}}{x_{i,r}^{\text{mol}}} e^{-\ln\left(\frac{f_{i,k}}{f_{i,r}}\right)} \tag{5.8}$$

where $K_{i,k}$ is the ratio between the fugacity coefficients between phase $k$ and the reference phase $r$, of component $i$

$$K_{i,k} = \frac{\phi_{i,r}}{\phi_{i,k}} \tag{5.9}$$

Ballard (2002) simplified Equation 5.9 as

$$\frac{x_{i,k}^{\text{mol}}}{x_{i,r}^{\text{mol}}} = K_{i,k} e^{\theta_k} \tag{5.10}$$

where $\theta_k$ is defined as the stability variable. This equation is valid for all phases, regardless of the respective presence at equilibrium.

The minimum Gibbs energy is obtained using the condition

$$\frac{\alpha_k \theta_k}{\alpha_k + \theta_k} = 0 \tag{5.11}$$

which is applied to and valid for all $\varphi$ phases. If phase $k$ is present, then $\alpha_k > 1$ and $\theta_k = 0$, whereas if the phase is not present, then $\theta_k \neq 0$ but $\alpha_k = 0$.

Replacing Equation 5.10 into Equation 5.2

$$\left(\alpha_r + \sum_{\substack{k=1 \\ k\neq r}}^{\varphi} \alpha_k K_{i,k} e^{\theta_k}\right) x_{i,r}^{\text{mol}} = z_i^{\text{mol}} \tag{5.12}$$

and taking into consideration the constraint given by Equation 5.3

$$x_{i,r}^{\text{mol}} = \frac{z_i^{\text{mol}}}{1 + \sum_{\substack{k=1 \\ k\neq r}}^{\varphi} \alpha_k \left(K_{i,k} e^{\theta_k} - 1\right)} \tag{5.13}$$

Considering that the reference phase must be present at equilibrium, $\theta_r = 0$ and $K_{i,r} = 1$ and thus

$$x_{i,k}^{\text{mol}} = \frac{z_i^{\text{mol}} K_{i,k} e^{\theta_k}}{1 + \sum_{\substack{j=1 \\ j\neq r}}^{\varphi} \alpha_j \left(K_{i,j} e^{\theta_j} - 1\right)} \tag{5.14}$$

Imposing the constraint given by Equation 5.4, the objective function is obtained as

$$\sum_{i=1}^{C} \frac{z_i^{\text{mol}} K_{i,k} e^{\theta_k}}{1 + \sum_{\substack{j=1 \\ j\neq r}}^{\varphi} \alpha_j \left(K_{i,j} e^{\theta_j} - 1\right)} - 1 = 0 \qquad \left(k = 1,\ldots,\varphi; k \neq r\right) \tag{5.15}$$

which is applied to all $\varphi$ phases, except the reference phase. Equation 5.15 must be verified for all phases, whether a given phase is present or not, ensuring that the Gibbs energy is minimum. The number of equations of the same type of Equation 5.15 in the flash calculation is as many as the phases considered.

CSMGem has an algorithm that reduces the number of considered phases in the calculation, based on the values of temperature, pressure and feed composition of the system. Also, it allows manually turning on or off phases for the calculation, which is helpful if convergence problems are being detected.

The phases considered by the software are the following: aqueous, ice, vapour, liquid hydrocarbon, sI hydrate, sII hydrate, sH hydrate, solid NaCl, solid KCl and solid $CaCl_2$ (Ballard 2002). To solve the set of equations represented in Equation 5.15,

fugacity models, for each of possible phase, are required. Ballard (2002) used in CSMGem the following models: the Shock and Helgeson model with Bromley activity model to describe the aqueous phase; vapour and liquid hydrocarbon phases are described by Soave-Redlich-Kwong (SRK) equation of state (EoS); solid salt phases and ice are modelled using the solid freeze-out model; the hydrate phases (sI, sII or sH) are described using a version of the van der Waals and Platteeuw model, modified by Ballard (2002) and with optimized parameters. Although one of the best thermodynamic models to describe the water-carbon dioxide mixture is the Peng-Robinson EoS, CSMGem uses the SRK EoS since it represents relatively well the behaviour of this specific mixture, and it is also a more general EoS, and it can be accurately applied to a larger range of guest gas molecules. A more detailed description on the used models, as described by Ballard (2002), is presented in Appendix B.

The software CSMGem will be the base of the present work regarding thermodynamic modelling.

### 5.2.2 Phase Equilibrium and Enthalpy

For a successful hydrates precipitation, there are two conditions that must be met. The first is the requirement of a supersaturated environment, common to many crystallization processes (Mullin 2001, Sloan and Koh 2007), which imposes that the amount of gas fed to the system must be larger than the water's capacity to dissolve it. The second requirement is that the system's temperature and pressure must lay within the region of stability of hydrates. As referred in Chapter 2, hydrates are only formed if the temperature is lower than the equilibrium temperature, or if the pressure is larger than the equilibrium pressure.

For a binary mixture, for a typical three-phase system (gas, aqueous and solid hydrate), the Gibbs' phase rule allows to conclude that only one freedom degree is obtained $\left(F = C - \varphi + 2 = 1\right)$. This means that one thermodynamic condition, either temperature or pressure, must be known to define the system. Although hydrates

precipitation could be conceptualized as a chemical reaction, with hydrates as a reaction product, this approach is not thermodynamically accurate, since there is no formation or destruction of chemical bonds. Therefore, for thermodynamic purposes, hydrates are modelled as a solid phase and not as a component.

The water-carbon dioxide phase equilibrium diagram is represented in Figure 5.1. Blue lines represent the phase changes of pure carbon dioxide, while black line represents the solid to liquid phase transition of water (water freezing). The red line represents the hydrates dissociation curve, below which hydrates dissociate, and above which hydrates precipitate, which was determined using CSMGem. The circles represent equilibrium points obtained experimentally by the methods briefly described in Section 2.3.2.1, and compiled by Sloan and Koh (2007).

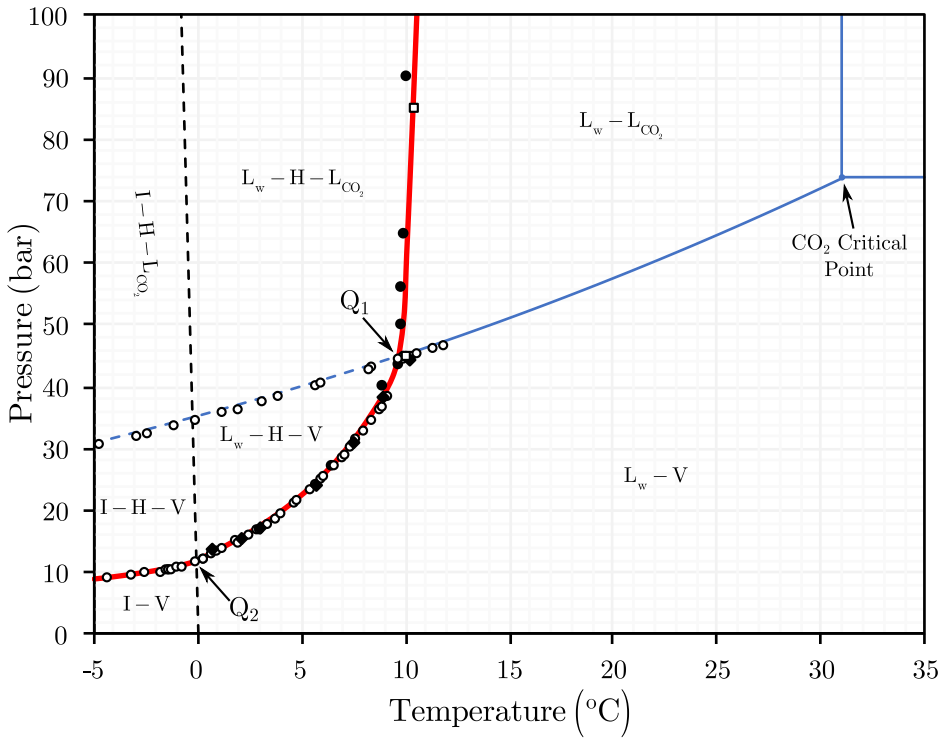



Figure 5.1 – Carbon dioxide – water system's phase diagram. The lines represent: red – $CO_2$ hydrates equilibrium curve, obtained from CSMGem; blue – $CO_2$ liquid-vapour and supercritical equilibrium curves; black – solid-liquid equilibrium curve of water. The points represent experimental data compiled by (Sloan and Koh 2007): ○ Larson (1955); □ Takenouchi and Kennedy (1965); ◆ Robinson and Metha (1971); • Ng and Robinson (1985).

Figure 5.1 shows that the three-phase equilibrium experimental points are well represented by the curves. $Q_1$ and $Q_2$ are quadruple points that represent the

equilibrium between ice-water-hydrate-vapour $CO_2$, and between water-hydrate-vapour $CO_2$-liquid $CO_2$, respectively.

To avoid the use of CSMGem in the calculations in the remainder of this work, the $CO_2$ hydrates equilibrium curve was fitted to the following polynomial approximations

$$p_{eq} = \begin{cases} a_1 T^2 + b_1 T + c_1 & T_0 \leq T < T_1 \\ a_2 T^2 + b_2 T + c_2 & T_1 \leq T < T_2 \\ b_3 T + c_3 & T_2 \leq T < T_3 \end{cases} \tag{5.16}$$

where $p_{eq}$ is the equilibrium pressure for $CO_2$ hydrates (in bar), $T$ is the system's temperature (in °C), and $a_1$, $b_1$, $c_1$, $a_2$, $b_2$, $c_2$, $b_3$, $c_3$, $T_0$, $T_1$, $T_2$ and $T_3$ are fitting parameters, whose values were obtained by the least squares method. The values of the parameters are presented in Table 5.1.

Table 5.1 – Fitting parameters for Equation 5.16.

| **Branch $i$** | $i = 0$ | $i = 1$ | $i = 2$ | $i = 3$ |
|---|---|---|---|---|
| $a_i \left(\mathbf{bar \cdot K^{-2}}\right)$ | – | $3.01 \times 10^{-3}$ | 0.269 | – |
| $b_i \left(\mathbf{bar \cdot K^{-1}}\right)$ | – | 0.343 | 0.592 | 83.0 |
| $c_i \left(\mathbf{bar}\right)$ | – | 10.8 | 12.9 | −770 |
| $T_i \left(\mathbf{°C}\right)$ | −53.9 | −0.89 | 9.8 | 11.0 |

The blue line, which represents the liquid-vapour saturation curve for pure $CO_2$ up to the critical point, $T_{crit} = 31.1\,°C$ and $p_{crit} = 73.9$ bar (NIST), can be represented by an Antoine-type equation for $CO_2$ vapour-pressure determination (DDBST):

$$p_{vap,\,CO_2} = 10^{4.935 - \frac{987.44}{290.9 + T}} \tag{5.17}$$

where $p_{\text{vap, CO}_2}$ is the vapour-pressure (in bar) and $T$ is the system's temperature (in °C). This relationship is valid from -57 °C up to the critical temperature of carbon dioxide.

To produce hydrates, it is necessary to create a supersaturated environment, i.e., the total amount of carbon dioxide introduced in the system must be larger than the amount of carbon dioxide that water is capable to dissolve in its bulk. Therefore, it is of high importance to know *a priori*, the $CO_2$ solubility, in water, as a function of temperature. Carroll et al. (1991) and Diamond and Akinfiev (2003) compiled $CO_2$ solubility in water data for several temperature and pressure ranges, and developed thermodynamic models for solubility estimation. Carroll et al. (1991) give an empirical correlation that allows the determination of the Henry constant as a function of temperature, at atmospheric pressure.

$$p_{CO_2} = K^{\text{mol}}_{\text{H,CO}_2} x^{\text{mol}}_{CO_2} \tag{5.18}$$

where $p_{CO_2}$ is the carbon dioxide's partial pressure, $x^{\text{mol}}_{CO_2}$ is the molar carbon dioxide solubility in water, represented as mole fraction, and $K^{\text{mol}}_{\text{H,CO}_2}$ is the Henry constant, usually a function of temperature, in mole fraction basis. The value of $K^{\text{mol}}_{\text{H,CO}_2}$ as a function of temperature, at atmospheric pressure can be estimated from (Carroll et al. 1991):

$$K^{\text{mol}}_{\text{H,CO}_2} = 10\exp\left(-6.836 + \frac{1.2817\times10^4}{T} - \frac{3.7668\times10^6}{T^2} + \frac{2.997\times10^8}{T^3}\right) \tag{5.19}$$

where $K^{\text{mol}}_{\text{H,CO}_2}$ is in bar and $T$ in K. Diamond and Akinfiev (2003) present empirical equations to determine the solubility of carbon dioxide in water in the three-phase hydrates, liquid water and $CO_2$ vapour coexistence curve (red curve in Figure 5.1 from $Q_1$ to $Q_2$, Equation 5.20) and in the three-phase hydrates, liquid water and liquid $CO_2$ coexistence curve (red curve in Figure 5.1, above $Q_1$, Equation 5.21):

$$x^{\text{mol}}_{CO_2} = 1.57\times10^{-2} + 7.89\times10^{-4}T + 4.73\times10^{-5}T^2 + 4.56\times10^{-6}T^3 - 3.80\times10^{-7}T^4 \tag{5.20}$$

$$x_{CO_2}^{mol} = 8.91\times10^{-2} - 1.96\times10^{-2}T + 2.22\times10^{-3}T^2 - 1.05\times10^{-4}T^3 + 1.92\times10^{-6}T^4 \quad (5.21)$$

where $T$ is in °C. Anderson (2002) focused his study on the temperature and pressure regions below the region of formation of hydrates, and experimentally determined the $CO_2$ solubility. These values are compared with results obtained from CSMGem in Figure 5.2.

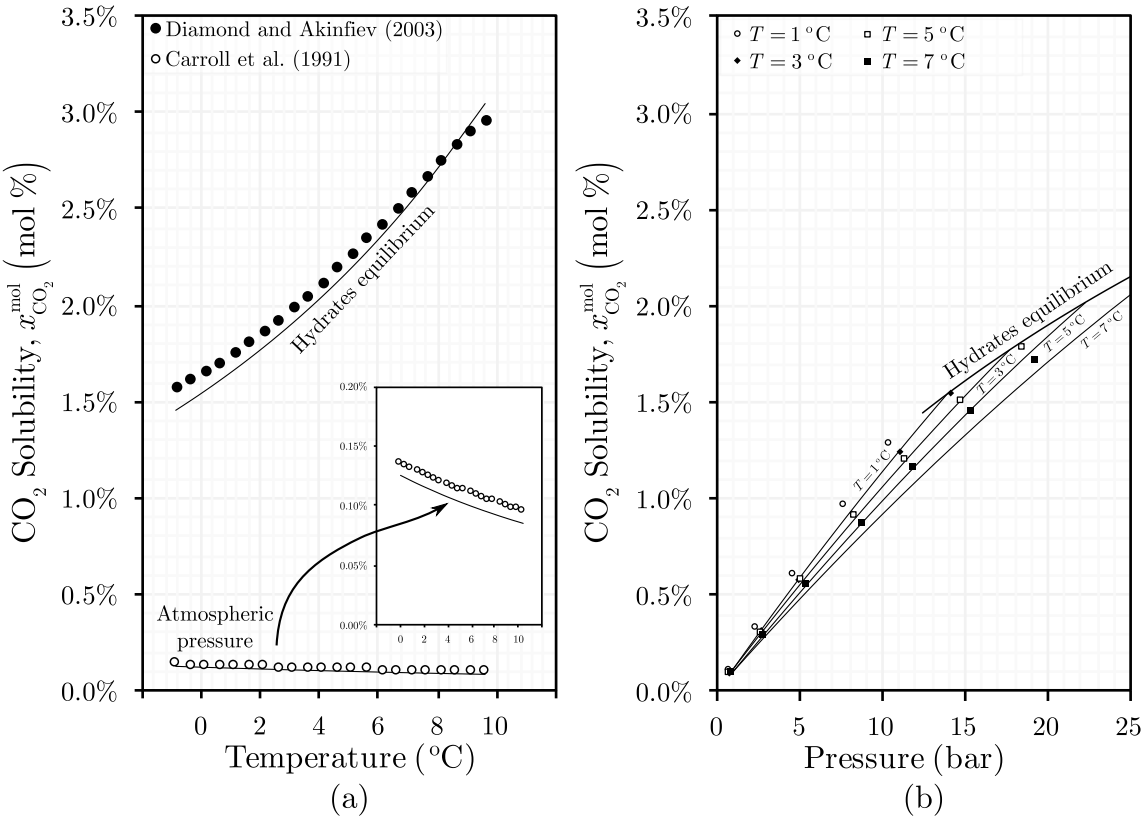



Figure 5.2 – Comparison of carbon dioxide solubility between CSMGem (lines) and experimental data (points): (a) as a function of temperature for atmospheric pressure (Carroll et al. 1991) and at hydrate equilibrium pressure (Diamond and Akinfiev 2003); (b) as a function of the pressure for different temperatures (Anderson 2002).

Figure 5.2 shows that CSMGem predicts the carbon dioxide solubility in water with a small deviation. In general, CSMGem underestimates the solubility of $CO_2$ when compared with the experimental data. One of the reasons for this, is that the modelling approach from Ballard (2002) does not take into consideration the chemical equilibrium of species resultant from the dissociation of carbon dioxide, such as carbonic acid $H_2CO_3$. Diamond and Akinfiev (2003) state that at relatively mild pressures and low temperatures, the impact of these species is negligible. Figure 5.2b shows that in the range of pressures and temperatures of interest, the solubility of

carbon dioxide for a given temperature, increases almost linearly with pressure, meaning that the Henry constant $K^{\text{mol}}_{\text{H,CO}_2}$ does not significantly change with pressure.

Other important aspect obtained from CSMGem, is that, for a given temperature, the amount of carbon dioxide dissolved in the water in equilibrium with the solid hydrate, is constant. Therefore, this means that for a given temperature, the amount of dissolved $CO_2$ in water increases approximately linearly with pressure, until hydrate equilibrium pressure is achieved. At this point, the amount of $CO_2$ dissolved will remain constant, and the excess (the supersaturated amount) is precipitated in the form of hydrates, and the vapour phase disappears, if conversion is complete. It is important to highlight though, that this is only valid when the amount of water fed to the system is much larger than the amount of carbon dioxide $\left(z^{\text{w}}_{\text{CO}_2} < 20\% - 30\%\right)$. These conditions are observed in the present study, since the objective is to form a slurry of hydrates particles, which means that the continuum phase (water) is in large excess.

The enthalpy of dissociation can be obtained as a function of temperature, using the Clapeyron equation (Equation 2.9), which can be rewritten in the following form (Anderson 2003)

$$\Delta H^{\text{mol, diss}}_{\text{hyd}} = \frac{dp}{dT}\Delta\tilde{\nu}^{\text{mol}} \tag{5.22}$$

where $\Delta\tilde{\nu}^{\text{mol}}$ is the specific molar volume change due to the hydration process. The derivative $dp/dT$ is easily determined when using Equation 5.16, but $\Delta\tilde{\nu}^{\text{mol}}$ needs to be estimated. In his analysis, Anderson (2003) takes into consideration that the process represented by Equation 2.4 is based on a simplification. The dissociation of hydrate does not originate water and gas, but $CO_2$-saturated water and gas, and this is taken into account by Anderson (2003) for the determination of the hydration enthalpy. The volume change in the dissociation process is determined from

$$\Delta\tilde{\nu}^{\mathrm{mol}} = \left(1 - \frac{n_{\mathrm{h}} x_{\mathrm{CO_2}}^{\mathrm{mol}}}{1 - x_{\mathrm{CO_2}}^{\mathrm{mol}}}\right)\tilde{\nu}_{\mathrm{vap}}^{\mathrm{mol}} + n_{\mathrm{h}}\tilde{\nu}_{\mathrm{aq}}^{\mathrm{mol}} - \tilde{\nu}_{\mathrm{hyd}}^{\mathrm{mol}} \tag{5.23}$$

where $n_{\mathrm{h}}$ is the hydration number, $\tilde{\nu}_{\mathrm{vap}}^{\mathrm{mol}}$ is the molar volume of the gas phase, $\tilde{\nu}_{\mathrm{aq}}^{\mathrm{mol}}$ is the molar volume of the liquid aqueous phase and $\tilde{\nu}_{\mathrm{hyd}}^{\mathrm{mol}}$ is the molar volume of the gas phase. The gas molar volume $\tilde{\nu}_{\mathrm{vap}}^{\mathrm{mol}}$ can be determined as a function of pressure and temperature using any equation of state that represents the behaviour of carbon dioxide; in this work, similarly to CSMGem, the SRK equation of state is used. The molar volume of the liquid phase $\tilde{\nu}_{\mathrm{aq}}^{\mathrm{mol}}$ can be determined using the model proposed by Duan et al. (2008)

$$\tilde{\nu}_{\mathrm{aq}}^{\mathrm{mol}} = \frac{x_{\mathrm{CO_2}}^{\mathrm{mol}} M_{\mathrm{w,\,CO_2}} + \left(1 - x_{\mathrm{CO_2}}^{\mathrm{mol}}\right) M_{\mathrm{w,\,H_2O}}}{1000\rho_{\mathrm{H_2O}}}\left[1 + \left(A_1 + A_2 p\right) x_{\mathrm{CO_2}}^{\mathrm{mol}}\right] \tag{5.24}$$

where $p\left(\text{in bar}\right)$ is the system's pressure, $M_{\mathrm{w,\,CO_2}}$ and $M_{\mathrm{w,\,H_2O}}$ are the molecular weight of carbon dioxide and water, respectively, $\rho_{\mathrm{H_2O}}$ is the water density, and $A_1$ and $A_2$ are parameters determined from

$$A_i = \sum_{j=1}^{5} A_{ij}\left(T + 273.15\right)^{3-j} \tag{5.25}$$

where $T$ is in °C, and the $A_{ij}$ constants are given in Table 5.2.

Table 5.2 – Constants used in Equation 5.25 (Duan et al. 2008).

| $j$ | $A_{1j}$ | $A_{2j}$ |
|---|---|---|
| 1 | $3.84\times10^{-4}$ | $-5.77\times10^{-7}$ |
| 2 | $-5.60\times10^{-1}$ | $8.28\times10^{-4}$ |
| 3 | $3.04\times10^{2}$ | $-4.38\times10^{-1}$ |
| 4 | $-7.20\times10^{4}$ | $1.01\times10^{2}$ |
| 5 | $6.30\times10^{6}$ | $-8.68\times10^{3}$ |

The hydrate molar volume $\tilde{\nu}_{\mathrm{hyd}}^{\mathrm{mol}}$ is determined using the approach described by Teng et al. (1996).

$$\tilde{\nu}_{\text{hyd}}^{\text{mol}} = \frac{N_A s^3 M_{\text{w, hyd}} + \left(1 - x_{\text{CO}_2}^{\text{mol}}\right)}{46 M_{\text{w, CO}_2}} \left[0.409 + \frac{w_{\text{CO}_2}^{\text{mol}}}{1 - w_{\text{CO}_2}^{\text{mol}}}\right]^{-1} \tag{5.26}$$

where $N_A\left(\text{in mol}^{-1}\right)$ is the Avogadro number and is equal to $6.022\times10^{23}$, $s$ is the lattice dimension, which is equal to 12 Å for sI structure (see Table 2.2), $M_{\text{w, hyd}}$ is the hydrate average molecular weight, and is equal to $M_{\text{w, hyd}} = M_{\text{w, CO}_2} + n_{\text{h}} M_{\text{w, H}_2\text{O}}$, and $w_{\text{CO}_2}^{\text{mol}}$ is the mole fraction of carbon dioxide in the hydrate. The hydration number is related to the mole fraction of carbon dioxide by

$$n_{\text{h}} = \frac{1 - w_{\text{CO}_2}^{\text{mol}}}{w_{\text{CO}_2}^{\text{mol}}} \tag{5.27}$$

This approach followed by Anderson (2003) and based on the Clapeyron equation, takes into consideration that when dissociation occurs, it results in a aqueous solution saturated with $\text{CO}_2$, and therefore, in addition to the enthalpy determined by Equation 5.22, it is necessary to include the heat that is released due to dissolution. Anderson (2003) refers in his work that, since the amount of carbon dioxide in water is relatively small (lower than 3% molar), the enthalpy of solution at infinite dilution of $\text{CO}_2$ can be used as a basis. Using the value for the $\text{CO}_2$ dissolution enthalpy of $\Delta H_{\text{CO}_2\rightarrow\text{H}_2\text{O}}^{\text{mol},\infty} = -22.83\ \text{kJ}\cdot\text{mol}^{-1}$, the heat absorbed by the gasification of a solution resultant from hydrates dissociation is given by

$$\Delta H_{\text{CO}_2\rightarrow\text{H}_2\text{O}}^{\text{mol, sol}} = \frac{n_{\text{h}} x_{\text{CO}_2}^{\text{mol}}}{1 - x_{\text{CO}_2}^{\text{mol}}} \Delta H_{\text{CO}_2\rightarrow\text{H}_2\text{O}}^{\text{mol},\infty} \tag{5.28}$$

where $\Delta H_{\text{CO}_2\rightarrow\text{H}_2\text{O}}^{\text{mol, sol}}$ is the total dissolution enthalpy of carbon dioxide in water. The hydration number $n_{\text{h}}$ is obtained directly from CSMGem at any given temperature. The sum of the enthalpies $\Delta H_{\text{hyd}}^{\text{mol, diss, tot}} = \Delta H_{\text{hyd}}^{\text{mol, diss}} + \left(-\Delta H_{\text{CO}_2\rightarrow\text{H}_2\text{O}}^{\text{mol, sol}}\right)$, determined from Equations 5.22 and 5.28, is represented in Figure 5.3 as a function of temperature, in the range 0 °C - 9.5 °C (between the quadruple points $\text{Q}_1$ and $\text{Q}_2$), since this is the

region of interest for continuous production of hydrates. Figure 5.3 also represents the values of enthalpies determined experimentally, based on calorimetric measurements, showing that the enthalpy determined by Anderson (2003) method with the modifications described above for the determination of the molar volume change $\Delta\tilde{\nu}^{\mathrm{mol}}$, can well represent the experimental values obtained from different sources, using different techniques. The average value usually described in the literature of $60\ \mathrm{kJ \cdot mol^{-1}}$ is also in agreement with the model.

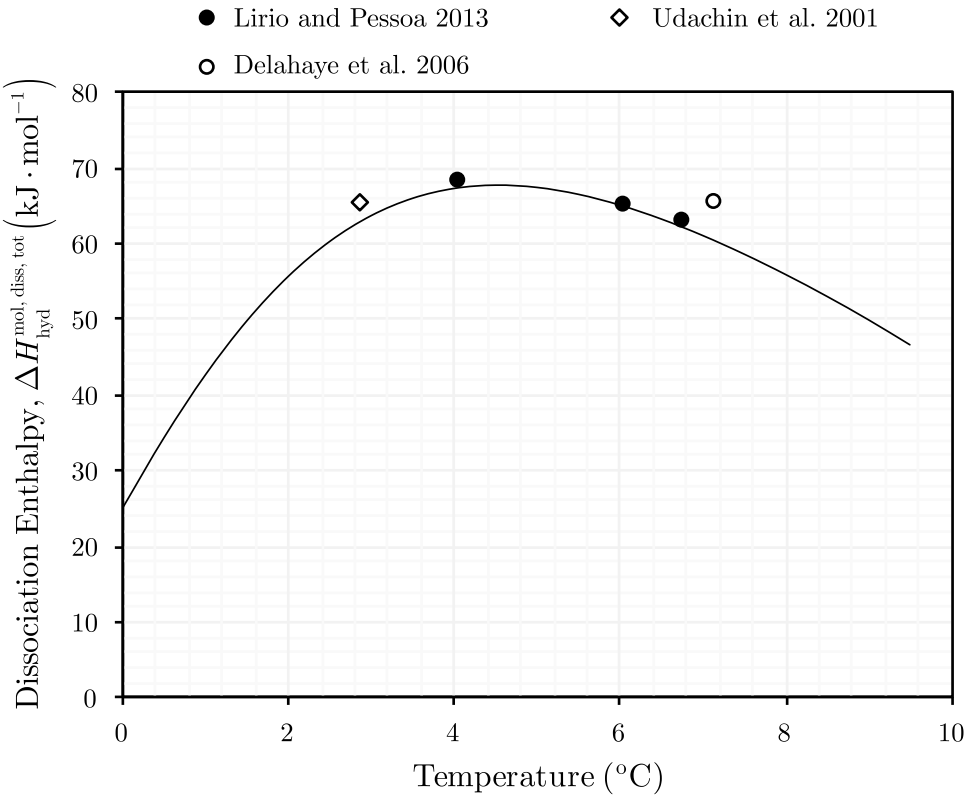



Figure 5.3 – Enthalpy of dissociation of carbon dioxide hydrates. The line represents the enthalpy determined from Equations 5.22 through 5.28. The points represent experimental data from Lirio and Pessoa (2013), Udachin et al. (2001) and Delahaye et al. (2006).

### 5.2.3 Flash Calculation Model

Flash calculation models allow the determination not only of the phase equilibrium compositions, but also of the fractions of each phase at the equilibrium, as referred in Section 5.2.1.1. CSMGem is capable to perform flash calculations based on the method of the minimization of the Gibbs energy. The information given by flash

calculations is particularly useful when process modelling and simulation is required, allowing performing mass and energy balances to the equilibrium units.

For the simulation of a process comprising a unit where gas hydrates are produced, it is impractical the use of CSMGem for the equilibrium flash calculation. Therefore, a simplified model based on mass and energy balances, using the information supplied in Section 5.2.2 was developed.

The analysis of the solubility of carbon dioxide in water from both experimental results and CSMGem, leads to the conclusion that if the weight ratio between carbon dioxide and water that is fed to an equilibrium unit is low (lower than 0.3 in weight), one of the following situations can occur at a given temperature and pressure:

- If the pressure is lower than the equilibrium pressure (or the temperature higher than the equilibrium temperature), and
    - if the amount of $CO_2$ is lower than its solubility in water, then all $CO_2$ is dissolved in water, resulting in an acidic aqueous solution;
    - if the amount of $CO_2$ is higher than its solubility in water, then a fraction of the $CO_2$ that corresponds to the solubility is dissolved in water, while the remaining $CO_2$ remains in the vapour phase, resulting in a two-phase system;
- If the pressure is higher than the equilibrium pressure (or the temperature lower than the equilibrium temperature), and
    - if the amount of $CO_2$ is lower than its solubility in water, then all $CO_2$ is dissolved in water, resulting in an acidic aqueous solution;
    - if the amount of $CO_2$ is higher than its solubility in water, then a fraction of the $CO_2$ that corresponds to the solubility is dissolved in water, while the remaining crystallizes in the form of hydrates, resulting in a two-phase system.

This last situation is the desired one. Under these conditions, no gas phase is expected if thermodynamic equilibrium is achieved. If a three-phase system is obtained (vapour – aqueous – hydrate), it means that the equilibrium is not achieved, and that the conversion of gas $CO_2$ to hydrates is not complete.

For a given water and carbon dioxide mass flow rate $\left(\dot{m}_{CO_2} / \dot{m}_{H_2O} < 0.3\right)$, temperature and pressure, the expected amount of hydrates can be calculated from a simple mass balance, taking into account the amount of carbon dioxide dissolved in water. At equilibrium, the amount of carbon dioxide dissolved in water $\dot{m}^{eq}_{CO_2,\,sol}$ is given by

$$\dot{m}^{eq}_{CO_2,\,sol} = \frac{x^{w}_{CO_2}}{1 - x^{w}_{CO_2}} \dot{m}^{eq}_{H_2O,\,aq} \tag{5.29}$$

where $\dot{m}^{eq}_{H_2O,\,aq}$ is the amount of free water in the aqueous phase at the equilibrium, estimated from

$$\dot{m}^{eq}_{H_2O,\,aq} = \dot{m}^{in}_{H_2O} - \dot{m}^{eq}_{H_2O,\,hyd} \tag{5.30}$$

where $\dot{m}^{in}_{H_2O}$ is the mass flow rate of water at the inlet and $\dot{m}^{eq}_{H_2O,\,hyd}$ is the flow rate of water that is converted into hydrates. $x^{w}_{CO_2}$ is the weight fraction of dissolved carbon dioxide, and can be determined from Equation 5.20 or 5.21, as a function of the temperature. Note that these are only valid if at a given temperature, the pressure of the system is higher than the equilibrium pressure for hydrates precipitation. The conversion from mole fraction to weight fraction in the binary carbon dioxide – water system is given by

$$x^{w}_{CO_2} = \frac{x^{mol}_{CO_2} M_{w,\,CO_2}}{x^{mol}_{CO_2} M_{w,\,CO_2} + \left(1 - x^{mol}_{CO_2}\right) M_{w,\,H_2O}} \tag{5.31}$$

A mass balance to the carbon dioxide allows the determination of the excess amount that is converted to hydrates

$$\dot{m}^{eq}_{CO_2,\,hyd} = \dot{m}^{in}_{CO_2} - \dot{m}^{eq}_{CO_2,\,sol} \tag{5.32}$$

where $\dot{m}^{\text{in}}_{\text{CO}_2}$ is the mass flow rate of carbon dioxide at the inlet. The total amount of water in the hydrate can be determined by

$$\dot{m}^{\text{eq}}_{\text{H}_2\text{O, hyd}} = n^{\text{w}}_{\text{h}} \dot{m}^{\text{eq}}_{\text{CO}_2\text{, hyd}} \tag{5.33}$$

where $n^{\text{w}}_{\text{h}}$ is the weight ratio between water and carbon dioxide in the hydrate, related to the molar based hydration number $n_{\text{h}}$ by

$$n^{\text{w}}_{\text{h}} = n_{\text{h}} \frac{M_{\text{w, H}_2\text{O}}}{M_{\text{w, CO}_2}} \tag{5.34}$$

The hydration number $n_{\text{h}}$ varies slightly with temperature. According to CSMGem, $n_{\text{h}}$ is equal to 6.77 at 0 °C and decreases to 6.33 at 10 °C (7.0% variation). Nevertheless, these values are larger than the theoretical value of 5.75 obtained if all cages of the sI structure are filled with carbon dioxide. The fact that this number is larger than 5.75 means that these cages are not completely filled. The hydration number can be determined as a function of temperature using the following expression

$$n_{\text{h}} = 6.15 \times 10^{-4} T^2 - 4.91 \times 10^{-6} T + 6.76 \tag{5.35}$$

which is valid in the temperature range of 0 to 10 °C, and where $T$ is in °C. The amount of produced hydrate is given by

$$\dot{m}^{\text{eq}}_{\text{hyd}} = \dot{m}^{\text{eq}}_{\text{CO}_2\text{, hyd}} + \dot{m}^{\text{eq}}_{\text{H}_2\text{O, hyd}} = \left(1 + n^{\text{w}}_{\text{h}}\right) \dot{m}^{\text{eq}}_{\text{CO}_2\text{, hyd}} \tag{5.36}$$

Rearranging Equations 5.29 to 5.36, the amount of hydrates formed is given by

$$\dot{m}^{\text{eq}}_{\text{hyd}} = \left(1 + n^{\text{w}}_{\text{h}}\right) \frac{\dot{m}^{\text{in}}_{\text{CO}_2} - \left(\dot{m}^{\text{in}}_{\text{CO}_2} + \dot{m}^{\text{in}}_{\text{H}_2\text{O}}\right) x^{\text{w}}_{\text{CO}_2}}{1 - \left(1 + n^{\text{w}}_{\text{h}}\right) x^{\text{w}}_{\text{CO}_2}} \tag{5.37}$$

and the amount of carbon dioxide in the hydrate is given by

$$\dot{m}^{\text{eq}}_{\text{CO}_2\text{, hyd}} = \frac{\dot{m}^{\text{in}}_{\text{CO}_2} - \left(\dot{m}^{\text{in}}_{\text{CO}_2} + \dot{m}^{\text{in}}_{\text{H}_2\text{O}}\right) x^{\text{w}}_{\text{CO}_2}}{1 - \left(1 + n^{\text{w}}_{\text{h}}\right) x^{\text{w}}_{\text{CO}_2}} \tag{5.38}$$

The remaining variables $\dot{m}^{eq}_{CO_2,\,sol}$, $\dot{m}^{eq}_{H_2O,\,aq}$ and $\dot{m}^{eq}_{H_2O,\,hyd}$ can be determined from the values of $\dot{m}^{eq}_{CO_2,\,hyd}$ and $\dot{m}^{eq}_{hyd}$, by performing mass balances to the system.

This simplified model allows to easily determine the amount of hydrates at equilibrium for a continuous unit that contains water in contact with carbon dioxide at temperatures and pressures adequate for the precipitation of hydrates. It should be once again emphasized that the amount of carbon dioxide must be enough to supersaturate the solution. For a temperature of 9.5 °C (below the $Q_1$ point), the solubility determined by Equation 5.21 is 6.64% in weight. This means that the supersaturation condition is achieved when

$$\dot{m}^{in}_{CO_2} > \frac{x^{w}_{CO_2}}{1 - x^{w}_{CO_2}} \dot{m}^{in}_{H_2O} > 7.11\% \dot{m}^{in}_{H_2O} \tag{5.39}$$

The total heat released during this process is obtained from: the heat of hydration of the excess $CO_2$ that is converted to hydrates, using the enthalpy of dissociation (plus dissolution) from Equation 5.28; the heat of dissolution to the dissolved $CO_2$, using a enthalpy of dissolution at infinite dilution. The total released heat $\dot{q}_{diss}$ is given by

$$\dot{q}_{diss} = \frac{\dot{m}^{eq}_{CO_2,\,hyd}}{M_{w,\,CO_2}} \Delta H^{mol,\,diss,\,tot}_{hyd} + \frac{\dot{m}^{eq}_{CO_2,\,sol}}{M_{w,\,CO_2}} \Delta H^{mol,\,\infty}_{CO_2 \rightarrow H_2O} \tag{5.40}$$

where $\Delta H^{mol,\,diss,\,tot}_{hyd}$ is determined from Equations 5.22 to 5.28 (converting it to weight).

If any of the other situations occur, the model presented in this section must suffer slight changes. In the first case, where the amount of carbon dioxide is lower than its solubility at a given temperature and pressure (which are outside the region of formation of hydrates), the pressure has a significant impact. Equation 5.29 is used to determine the amount of dissolved carbon dioxide. However, the solubility in this case, is not determined from Equation 5.20, but from Equations 5.18 and 5.19. Also, the amount of water in the liquid phase remains constant, i.e., $\dot{m}^{eq}_{H_2O,\,aq} = \dot{m}^{in}_{H_2O}$ and the

released heat is given only by the second term of the right side of Equation 5.40. In the second case, the amount of carbon dioxide is higher than its solubility in water, but the temperature and pressure are outside the range of precipitation of hydrates. In this case the amount of carbon dioxide dissolved is determined by Equation 5.29, with the solubility being determined from Equations 5.18 and 5.19. The excess carbon dioxide remains in the vapour phase. The amount of water in the liquid phase remains constant (some water is transferred to the vapour phase, but is negligible at low temperatures) and the released heat is given only by the second term of the right side of Equation 5.40. In the third case, the solution is undersaturated, but the temperature and pressure are inside the region of formation of hydrates. In this case, the maximum possible solubility is determined from Equation 5.20 or 5.21. Again, Equation 5.29 is used to determine the amount of carbon dioxide dissolved in water, and since no hydrates are formed, the amount of water in the liquid phase remains constant. The released heat is given only by the second term of the right side of Equation 5.40.

## 5.3 Energy Balance to a Crystallization Unit

One of difficulties in producing gas hydrates is the determination of the amount of consumed guest component. In batch (or semi-batch) processes, the amount of water placed in the thermodynamic cell is fixed and gas is being added to the cell, as described in Section 2.3.2 (Sloan and Koh 2007). The gas added to the system is used not only to precipitate in the form of hydrates, but also to keep the pressure in the cell constant, since precipitation results in a pressure decrease due to the volume change. In continuous systems, this procedure cannot be used. Therefore, an alternative way of determining the amount of produced hydrate (or consumed gas) is required. Due to the relatively high accuracy of the thermodynamic models regarding $CO_2$ hydrates, namely through the use of CSMGem and the approach described in Section 5.2.3, it is possible to estimate the amount of produced carbon dioxide by performing an energy balance to the unit of contact between the guest compound and

water. In the case of this work, the contact between water and carbon dioxide is made in the microNETmix unit (as described in Chapter 4).

The microNETmix unit, as a hydrate-crystallization unit, can be modelled as the equilibrium unit illustrated in Figure 5.4.

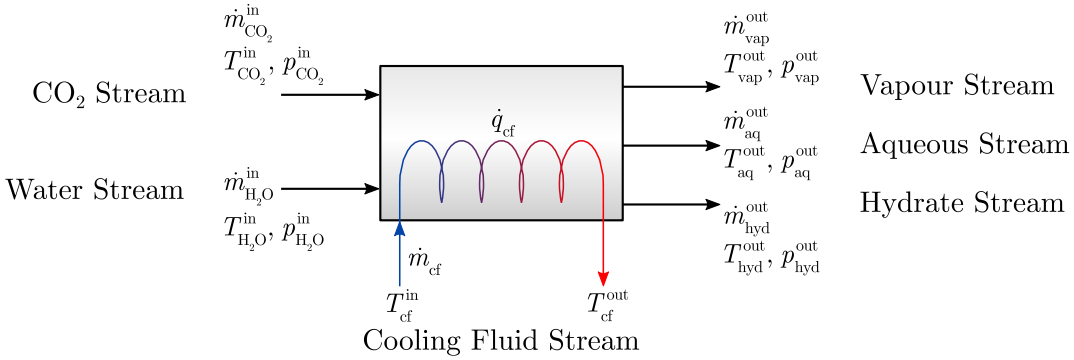



Figure 5.4 – Schematic of the microNETmix unit and stream representation.

To perform the energy balance, it is necessary to assume that all possible phases at the outlet of the unit (vapour, liquid and hydrate) are in a dynamic equilibrium, i.e., the temperature and pressure are equal in all phases. This assumption implies that the unit is conceptualized as a perfectly mixed unit. In this way, $T^{out}_{vap}$, $T^{out}_{aq}$ and $T^{out}_{hyd}$ can be replaced by $T^{out}$, while $p^{out}_{vap}$, $p^{out}_{aq}$ and $p^{out}_{hyd}$ are replaced by $p^{out}$.

The global energy balance is done by determining the energy change in the cooling fluid stream. From the first law of thermodynamics, the energy balance to a system is obtained from

$$d\tilde{u} = d\tilde{q} + d\tilde{w} \tag{5.41}$$

where $d\tilde{u}$ is the change of the specific internal energy of the streams, $d\tilde{q}$ is the specific heat transferred to or from the system, and $d\tilde{w}$ is the specific work. The specific heat is given by

$$d\tilde{q} = Td\tilde{s} \tag{5.42}$$

where $d\tilde{s}$ is the variation of the specific entropy of the system, and the specific work is given by

$$d\tilde{w} = -pd\tilde{\nu} \tag{5.43}$$

Therefore, Equation 5.41 can be written as

$$d\tilde{u} = Td\tilde{s} - pd\tilde{\nu} \tag{5.44}$$

The definition of enthalpy is

$$\tilde{h} = \tilde{u} + p\tilde{\nu} \tag{5.45}$$

Differentiating Equation 5.45, one gets

$$d\tilde{h} = d\tilde{u} + \tilde{\nu}dp + pd\tilde{\nu} \tag{5.46}$$

Replacing Equation 5.44 into Equation 5.46, we obtain

$$d\tilde{h} = Td\tilde{s} + \tilde{\nu}dp \tag{5.47}$$

The enthalpy change $d\tilde{h}$ from Equation 5.47 can be written as a function of the temperature and pressure only. The definition of heat capacity at constant pressure $c_{\mathrm{P}}$ is

$$c_{\mathrm{P}} = \left(\frac{\partial \tilde{h}}{\partial T}\right)_p \tag{5.48}$$

The enthalpy variation with the pressure is given by (Smith et al. 2005)

$$\left(\frac{\partial \tilde{h}}{\partial p}\right)_T = \tilde{\nu} - T\left(\frac{\partial \tilde{\nu}}{\partial T}\right)_p \tag{5.49}$$

Using the definitions from Equations 5.48 and 5.49, the enthalpy change can be determined by (Smith et al. 2005)

$$d\tilde{h} = c_{\mathrm{P}}dT + \left[\tilde{\nu} - T\left(\frac{\partial \tilde{\nu}}{\partial T}\right)_p\right]dp \tag{5.50}$$

The first term in Equation 5.50 is related to isobaric temperature variation while the second term represents isothermal expansion (or compression).

The enthalpy change due to heat transfer $\dot{q}_{\mathrm{cf}}$ from the microNETmix unit to the cooling fluid is determined using

$$\dot{q}_{\mathrm{cf}} = \dot{m}_{\mathrm{cf}}\Delta\tilde{h}^{\mathrm{w}}_{\mathrm{cf}} = \int_{T^{\mathrm{in}}_{\mathrm{cf}}}^{T^{\mathrm{out}}_{\mathrm{cf}}} c^{\mathrm{w}}_{\mathrm{P,\,cf}}\,dT + \int_{p^{\mathrm{o}}_{\mathrm{cf}}}^{p^{\mathrm{in}}_{\mathrm{cf}}}\left[\tilde{\nu}^{\mathrm{w}}_{\mathrm{cf}} - T^{\mathrm{in}}_{\mathrm{cf}}\left(\frac{\partial \tilde{\nu}^{\mathrm{w}}_{\mathrm{cf}}}{\partial T}\right)_{p,\,T^{\mathrm{in}}_{\mathrm{cf}}}\right]dp - \int_{p^{\mathrm{o}}_{\mathrm{cf}}}^{p^{\mathrm{out}}_{\mathrm{cf}}}\left[\tilde{\nu}^{\mathrm{w}}_{\mathrm{cf}} - T^{\mathrm{out}}_{\mathrm{cf}}\left(\frac{\partial \tilde{\nu}^{\mathrm{w}}_{\mathrm{cf}}}{\partial T}\right)_{p,\,T^{\mathrm{out}}_{\mathrm{cf}}}\right]dp \tag{5.51}$$

where $\Delta\tilde{h}_{\mathrm{cf}}^{\mathrm{w}}$ is the specific weight enthalpy change of the cooling fluid, $\dot{m}_{\mathrm{cf}}$ is the mass flow rate of the cooling fluid, $T_{\mathrm{cf}}^{\mathrm{in}}$ and $T_{\mathrm{cf}}^{\mathrm{out}}$ are the cooling fluid's streams temperature at the inlet and outlet of the system, respectively, $p_{\mathrm{cf}}^{\mathrm{in}}$ and $p_{\mathrm{cf}}^{\mathrm{out}}$ are the cooling fluid's streams pressure at the inlet and outlet, $c_{\mathrm{P,\,cf}}^{\mathrm{w}}$ is the specific weight heat capacity of the cooling fluid, $\tilde{\nu}_{\mathrm{cf}}^{\mathrm{w}}$ represents the specific weight volume of the cooling fluid, and $p_{\mathrm{cf}}^{\mathrm{o}}$ is the reference pressure for the cooling fluid. The two last two terms in Equation 5.51 are neglected. Assuming a reference pressure of $p_{\mathrm{cf}}^{\mathrm{o}} = 1\,\mathrm{bar}$ and since the pressure increase in these streams is only due to pressure drop in the tubing where cooling fluid is flowing, it is expected that both $p_{\mathrm{cf}}^{\mathrm{in}}$ and $p_{\mathrm{cf}}^{\mathrm{out}}$ are close to 1 bar, therefore these two terms are close to zero. Also, since this is a liquid, it can be assumed that in these conditions the fluid is incompressible and thus the pressure variation does not result in a significant volume change. Equation 5.51 is then simplified to

$$\dot{q}_{\mathrm{cf}} = \int_{T_{\mathrm{cf}}^{\mathrm{in}}}^{T_{\mathrm{cf}}^{\mathrm{out}}} c_{\mathrm{P,\,cf}}^{\mathrm{w}}\, dT \tag{5.52}$$

The global enthalpy balance to the unit illustrated in Figure 5.4 is expressed as

$$\dot{m}_{\mathrm{H_2O}}^{\mathrm{in}}\tilde{h}_{\mathrm{H_2O}}^{\mathrm{w,\,in}} + \dot{m}_{\mathrm{CO_2}}^{\mathrm{in}}\tilde{h}_{\mathrm{CO_2}}^{\mathrm{w,\,in}} = \dot{m}_{\mathrm{vap}}^{\mathrm{out}}\tilde{h}_{\mathrm{vap}}^{\mathrm{w,\,out}} + \dot{m}_{\mathrm{aq}}^{\mathrm{out}}\tilde{h}_{\mathrm{aq}}^{\mathrm{w,\,out}} + \dot{m}_{\mathrm{hyd}}^{\mathrm{out}}\tilde{h}_{\mathrm{hyd}}^{\mathrm{w,\,out}} + \dot{q}_{\mathrm{cf}} \tag{5.53}$$

where $\tilde{h}_{\mathrm{H_2O}}^{\mathrm{w,\,in}}$ and $\tilde{h}_{\mathrm{CO_2}}^{\mathrm{w,\,in}}$ are the specific weight enthalpies of water and carbon dioxide streams at the inlet, respectively, $\tilde{h}_{\mathrm{vap}}^{\mathrm{w,\,out}}$, $\tilde{h}_{\mathrm{aq}}^{\mathrm{w,\,out}}$ and $\tilde{h}_{\mathrm{hyd}}^{\mathrm{w,\,out}}$ are the specific weight enthalpies of the vapour, liquid aqueous and hydrate phases at the outlet, respectively, and $\dot{m}_{\mathrm{vap}}^{\mathrm{out}}$, $\dot{m}_{\mathrm{aq}}^{\mathrm{out}}$ and $\dot{m}_{\mathrm{hyd}}^{\mathrm{out}}$ are the mass flow rates at the outlet of the vapour, aqueous and hydrate phases, respectively.

Depending on the inlet an outlet conditions, one of twelve possible cases can occur, and in each case, the specific enthalpy of each of the stream/phase of Equation 5.53 is different. Figure 5.5 shows an algorithm flow diagram that allows the identification

of each case that may occur during the experiment. The cases that comprise the precipitation of gas hydrates are explained in further detail in the next sections, including the computation of the specific enthalpies of the streams in Figure 5.4.

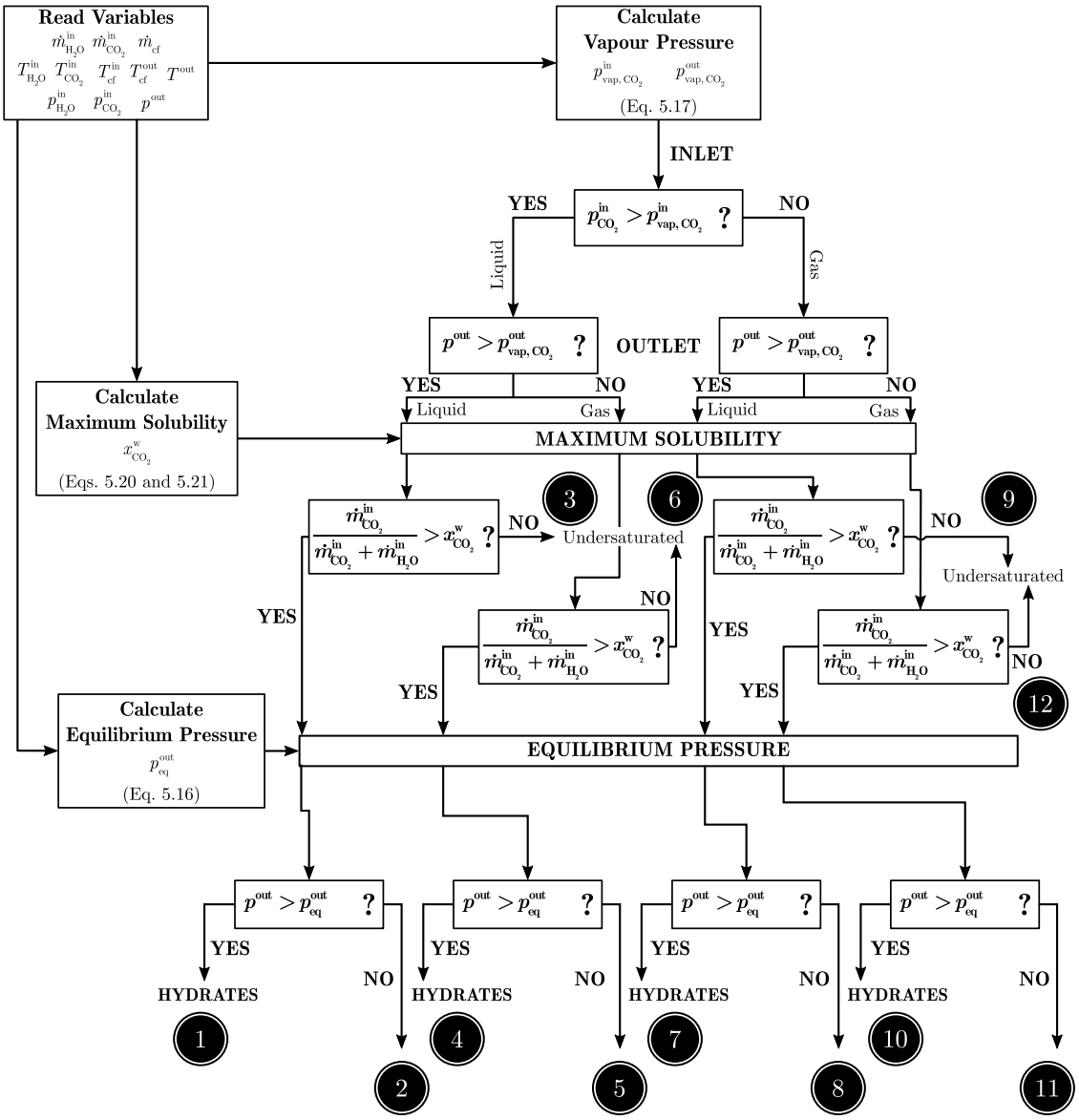



Figure 5.5 – Flow diagram of algorithm used to estimate the amount of produced hydrates.

Analysis of the flow diagram in Figure 5.5 shows that:

- For cases 3, 6, 9 and 12, the ratio at the inlet of the flow rates between carbon dioxide and water is lower than the minimum required to supersaturate the solution at the outlet conditions (in particular, $T^{out}$ )
- For cases 2, 5, 8 and 11, the amount of carbon dioxide inserted to the system is enough to supersaturate the solution. However, in these cases, the pressure

$p^{\text{out}}$ is lower than the equilibrium pressure evaluated at $T^{\text{out}}$, $p_{\text{eq}}^{\text{out}}$. Therefore, no hydrates are formed

- Only in cases 1, 4, 7 and 10 the system is in thermodynamic conditions to form hydrates. These are the four cases that are going to be thoroughly analysed in the next sections. The global energy balance is performed using Equation 5.53 in all cases. However, the specific enthalpies change depending on the case.

### 5.3.1 Case 1: Liquid – Liquid

In Case 1 shown in Figure 5.5, the pressure of the carbon dioxide at the inlet and the outlet pressure are above the vapour pressure of carbon dioxide at $T_{\text{CO}_2}^{\text{in}}$ and $T^{\text{out}}$ respectively. This means that carbon dioxide enters and exits the microNETmix unit in its liquid state, and its carbon dioxide solubility in water is given by Equation 5.21 (region above $\text{Q}_1$ in Figure 5.1). The vapour phase shown in Figure 5.4 is in this case replaced by a liquid carbon dioxide phase.

The specific enthalpies of each stream are calculated from the enthalpy of formation of the species and enthalpy changes. The enthalpy of the water stream at the inlet can be written as

$$\tilde{h}_{\text{H}_2\text{O}}^{\text{w, in}} = \tilde{h}_{\text{f, H}_2\text{O}}^{\text{w, o}} + \int_{T^{\text{o}}}^{T_{\text{H}_2\text{O}}^{\text{in}}} c_{\text{P, H}_2\text{O}}^{\text{w}}\, dT \tag{5.54}$$

where $\tilde{h}_{\text{f, H}_2\text{O}}^{\text{w, o}}$ is the specific weight formation enthalpy of water at the standard conditions $T^{\text{o}}$ and $p^{\text{o}}$. Typically, the standard conditions are 298 K and 1 atm. The terms related to the pressure changes can be neglected since the volume of water does not significantly change with pressure.

At the standard conditions, carbon dioxide is in its gaseous state, and behaves like an ideal gas. However, in this case, carbon dioxide enters the unit in its liquid phase.

Taking this into account, the specific enthalpy of the carbon dioxide stream at the inlet is given by

$$\tilde{h}_{\mathrm{CO_2}}^{\mathrm{w,\,in}} = \tilde{h}_{\mathrm{f,\,CO_2}}^{\mathrm{w,\,o}} + \int_{T^{\mathrm{o}}}^{T_{\mathrm{CO_2}}^{\mathrm{in}}} c_{\mathrm{P,\,CO_2}}^{\mathrm{w,\,ig}}\, dT + \int_{p^{\mathrm{o}}}^{p_{\mathrm{vap,\,CO_2}}^{\mathrm{in}}} \left[ \tilde{\nu}_{\mathrm{CO_2}}^{\mathrm{w}} - T_{\mathrm{CO_2}}^{\mathrm{in}} \left( \frac{\partial \tilde{\nu}_{\mathrm{CO_2}}^{\mathrm{w}}}{\partial T} \right)_{p,\, T_{\mathrm{CO_2}}^{\mathrm{in}}} \right] dp + \left( -\Delta H_{\mathrm{vap,\,CO_2}}^{\mathrm{w,\,in}} \right) \quad (5.55)$$

where $c_{\mathrm{P,\,CO_2}}^{\mathrm{w,\,ig}}$ is the ideal gas specific weight heat capacity for carbon dioxide, $\tilde{\nu}_{\mathrm{CO_2}}^{\mathrm{w}}$ is the carbon dioxide weight volume, and $\Delta H_{\mathrm{vap,\,CO_2}}^{\mathrm{w,\,in}}$ is the latent heat of vaporization of carbon dioxide, evaluated at the inlet conditions (see Appendix A). Again, the Redlich-Kwong-Soave EoS is used to determine $\tilde{\nu}_{\mathrm{CO_2}}^{\mathrm{w}}$ at any conditions. An extra term could be considered regarding the pressure increase of the liquid carbon dioxide up to $p_{\mathrm{CO_2}}^{\mathrm{in}}$. However, since it is liquid, this term is neglected. The first term of Equation 5.55 corresponds to the standard enthalpy of formation of $\mathrm{CO_2}$; the second term is related to the sensible heat at atmospheric pressure; the third term is related to the compression of the gas up to the vapour pressure relative to the standard pressure; and the last term corresponds to the latent heat of vaporization. Both Equations 5.54 and 5.55 assume that each of the streams is composed by a single component.

At the outlet, similar relationships can be found. In the case of the liquid carbon dioxide stream, it is assumed that it is composed by carbon dioxide only. The specific enthalpy can be expressed as

$$\tilde{h}_{\mathrm{vap}}^{\mathrm{w,\,out}} = \tilde{h}_{\mathrm{f,\,CO_2}}^{\mathrm{w,\,o}} + \int_{T^{\mathrm{o}}}^{T^{\mathrm{out}}} c_{\mathrm{P,\,CO_2}}^{\mathrm{w,\,ig}}\, dT + \int_{p^{\mathrm{o}}}^{p_{\mathrm{vap,\,CO_2}}^{\mathrm{out}}} \left[ \tilde{\nu}_{\mathrm{CO_2}}^{\mathrm{w}} - T^{\mathrm{out}} \left( \frac{\partial \tilde{\nu}_{\mathrm{CO_2}}^{\mathrm{w}}}{\partial T} \right)_{p,\, T^{\mathrm{out}}} \right] dp + \left( -\Delta H_{\mathrm{vap,\,CO_2}}^{\mathrm{w,\,out}} \right) \quad (5.56)$$

The aqueous stream is mostly water, but due to its supersaturated condition, this stream is saturated with carbon dioxide. The fraction of carbon dioxide dissolved in water is given by Equation 5.21 (converted to weight fraction). The specific enthalpy of this stream is given by

$$\tilde{h}_{\mathrm{aq}}^{\mathrm{w,\,out}} = \left(1 - x_{\mathrm{CO_2}}^{\mathrm{w,\,out}}\right)\left(\tilde{h}_{\mathrm{f,\,H_2O}}^{\mathrm{w,\,o}} + \int_{T^{\mathrm{o}}}^{T^{\mathrm{out}}} c_{\mathrm{P,\,H_2O}}^{\mathrm{w}}\, dT\right) + x_{\mathrm{CO_2}}^{\mathrm{w,\,out}}\left(\tilde{h}_{\mathrm{f,\,CO_2}}^{\mathrm{w,\,o}} + \int_{T^{\mathrm{o}}}^{T^{\mathrm{out}}} c_{\mathrm{P,\,CO_2}}^{\mathrm{w,\,ig}}\, dT + \int_{p^{\mathrm{o}}}^{p_{\mathrm{vap,\,CO_2}}^{\mathrm{out}}}\left[\tilde{\nu}_{\mathrm{CO_2}}^{\mathrm{w}} - T^{\mathrm{out}}\left(\frac{\partial \tilde{\nu}_{\mathrm{CO_2}}^{\mathrm{w}}}{\partial T}\right)_{p,\,T^{\mathrm{out}}}\right] dp + \left(-\Delta H_{\mathrm{vap,\,CO_2}}^{\mathrm{w,\,out}}\right) + \Delta H_{\mathrm{CO_2 \rightarrow H_2O}}^{\mathrm{w,\,sol}}\right) \tag{5.57}$$

The last term of Equation 5.57 corresponds to the heat that is released due to carbon dioxide dissolution in water (converted to weight basis). The specific enthalpy of the hydrates stream can be written in a similar way. However, two cases may occur in this situation. If the equilibrium pressure at which hydrates precipitate is lower than the vapour pressure of carbon dioxide at the outlet conditions, and assuming that the solid is incompressible, then the specific enthalpy of the hydrates stream is given by

$$\tilde{h}_{\mathrm{hyd}}^{\mathrm{w,\,out}} = \frac{n_{\mathrm{h}}^{\mathrm{w}}}{1 + n_{\mathrm{h}}^{\mathrm{w}}}\left(\tilde{h}_{\mathrm{f,\,H_2O}}^{\mathrm{w,\,o}} + \int_{T^{\mathrm{o}}}^{T^{\mathrm{out}}} c_{\mathrm{P,\,H_2O}}^{\mathrm{w}}\, dT\right) + \frac{1}{1 + n_{\mathrm{h}}^{\mathrm{w}}}\left(\tilde{h}_{\mathrm{f,\,CO_2}}^{\mathrm{w,\,o}} + \int_{T^{\mathrm{o}}}^{T^{\mathrm{out}}} c_{\mathrm{P,\,CO_2}}^{\mathrm{w,\,ig}}\, dT + \int_{p^{\mathrm{o}}}^{p_{\mathrm{eq}}^{\mathrm{out}}}\left[\tilde{\nu}_{\mathrm{CO_2}}^{\mathrm{w}} - T^{\mathrm{out}}\left(\frac{\partial \tilde{\nu}_{\mathrm{CO_2}}^{\mathrm{w}}}{\partial T}\right)_{p,\,T^{\mathrm{out}}}\right] dp + \left(-\Delta H_{\mathrm{vap,\,CO_2}}^{\mathrm{w,\,out}}\right) + \left(-\Delta H_{\mathrm{hyd}}^{\mathrm{w,\,diss,\,tot}}\right)\right) \tag{5.58}$$

If the equilibrium pressure is higher than the vapour pressure (it occurs after the $Q_1$ point from Figure 5.1), the enthalpy of the stream is given by

$$\tilde{h}_{\mathrm{hyd}}^{\mathrm{w,\,out}} = \frac{n_{\mathrm{h}}^{\mathrm{w}}}{1 + n_{\mathrm{h}}^{\mathrm{w}}}\left(\tilde{h}_{\mathrm{f,\,H_2O}}^{\mathrm{w,\,o}} + \int_{T^{\mathrm{o}}}^{T^{\mathrm{out}}} c_{\mathrm{P,\,H_2O}}^{\mathrm{w}}\, dT\right) + \frac{1}{1 + n_{\mathrm{h}}^{\mathrm{w}}}\left(\tilde{h}_{\mathrm{f,\,CO_2}}^{\mathrm{w,\,o}} + \int_{T^{\mathrm{o}}}^{T^{\mathrm{out}}} c_{\mathrm{P,\,CO_2}}^{\mathrm{w,\,ig}}\, dT + \int_{p^{\mathrm{o}}}^{p_{\mathrm{vap,\,CO_2}}^{\mathrm{out}}}\left[\tilde{\nu}_{\mathrm{CO_2}}^{\mathrm{w}} - T^{\mathrm{out}}\left(\frac{\partial \tilde{\nu}_{\mathrm{CO_2}}^{\mathrm{w}}}{\partial T}\right)_{p,\,T^{\mathrm{out}}}\right] dp + \left(-\Delta H_{\mathrm{vap,\,CO_2}}^{\mathrm{w,\,out}}\right) + \left(-\Delta H_{\mathrm{hyd}}^{\mathrm{w,\,diss,\,tot}}\right)\right) \tag{5.59}$$

The determination of the amount of gas hydrates produced via Equations 5.54 to 5.59 assumes that the aqueous phase is fully saturated with carbon dioxide to produce gas hydrates. In this case, a mass balance relates the outlet liquid carbon dioxide mass flow rate with the outlet mass flow rate of produced hydrates, and is expressed as

$$\dot{m}_{\mathrm{vap}}^{\mathrm{out}} = \dot{m}_{\mathrm{CO_2}}^{\mathrm{in}} - \frac{x_{\mathrm{CO_2}}^{\mathrm{w,\,out}}}{1 - x_{\mathrm{CO_2}}^{\mathrm{w,\,out}}}\dot{m}_{\mathrm{H_2O}}^{\mathrm{in}} + \left[\frac{x_{\mathrm{CO_2}}^{\mathrm{w,\,out}}}{1 - x_{\mathrm{CO_2}}^{\mathrm{w,\,out}}} n_{\mathrm{h}}^{\mathrm{w}} - 1\right]\frac{\dot{m}_{\mathrm{hyd}}^{\mathrm{out}}}{1 + n_{\mathrm{h}}^{\mathrm{w}}} \tag{5.60}$$

The aqueous phase mass flow rate can be similarly determined using the following relationship

$$\dot{m}_{\mathrm{aq}}^{\mathrm{out}} = \frac{\dot{m}_{\mathrm{H_2O}}^{\mathrm{in}}}{1 - x_{\mathrm{CO_2}}^{\mathrm{w,\,out}}} \frac{n_{\mathrm{h}}^{\mathrm{w}}}{1 + n_{\mathrm{h}}^{\mathrm{w}}} \dot{m}_{\mathrm{hyd}}^{\mathrm{out}} \tag{5.61}$$

Replacing Equations 5.60 and 5.61 into Equation 5.53, results in an equation that is only a function of the mass flow rate of hydrates. Rearranging Equation 5.53 and replacing the specific enthalpies of each stream represented by Equation 5.54 to 5.59, it is possible to eliminate both standard formation enthalpies $\tilde{h}_{\mathrm{f,\,H_2O}}^{\mathrm{w,\,o}}$ and $\tilde{h}_{\mathrm{f,\,CO_2}}^{\mathrm{w,\,o}}$ as well as the standard temperature $T^{\mathrm{o}}$.

### 5.3.2 Case 4: Liquid – Gas

In Case 4 of Figure 5.5, carbon dioxide enters the microNETmix unit in its liquid phase but exits in its vapour phase. Equation 5.54 is still valid in this case (it is valid in all cases). Equation 5.55 is also valid in this case, since the input assumptions are the same. Equation 5.56 is replaced by another equation that includes the formation of the vapour phase as illustrated in Figure 5.4

$$\tilde{h}_{\mathrm{vap}}^{\mathrm{w,\,out}} = \tilde{h}_{\mathrm{f,\,CO_2}}^{\mathrm{w,\,o}} + \int_{T^{\mathrm{o}}}^{T^{\mathrm{out}}} c_{\mathrm{P,\,CO_2}}^{\mathrm{w,\,ig}}\, dT + \int_{p^{\mathrm{o}}}^{p^{\mathrm{out}}} \left[ \tilde{\nu}_{\mathrm{CO_2}}^{\mathrm{w}} - T^{\mathrm{out}} \left( \frac{\partial \tilde{\nu}_{\mathrm{CO_2}}^{\mathrm{w}}}{\partial T} \right)_{p,\,T^{\mathrm{out}}} \right] dp \tag{5.62}$$

Equation 5.57 is now replaced by

$$\begin{aligned} \tilde{h}_{\mathrm{aq}}^{\mathrm{w,\,out}} = {} & \left(1 - x_{\mathrm{CO_2}}^{\mathrm{w,\,out}}\right) \left( \tilde{h}_{\mathrm{f,\,H_2O}}^{\mathrm{w,\,o}} + \int_{T^{\mathrm{o}}}^{T^{\mathrm{out}}} c_{\mathrm{P,\,H_2O}}^{\mathrm{w}}\, dT \right) + \\ & x_{\mathrm{CO_2}}^{\mathrm{w,\,out}} \left( \tilde{h}_{\mathrm{f,\,CO_2}}^{\mathrm{w,\,o}} + \int_{T^{\mathrm{o}}}^{T^{\mathrm{out}}} c_{\mathrm{P,\,CO_2}}^{\mathrm{w,\,ig}}\, dT + \int_{p^{\mathrm{o}}}^{p^{\mathrm{out}}} \left[ \tilde{\nu}_{\mathrm{CO_2}}^{\mathrm{w}} - T^{\mathrm{out}} \left( \frac{\partial \tilde{\nu}_{\mathrm{CO_2}}^{\mathrm{w}}}{\partial T} \right)_{p,\,T^{\mathrm{out}}} \right] dp + \Delta H_{\mathrm{CO_2 \rightarrow H_2O}}^{\mathrm{w,\,sol}} \right) \end{aligned} \tag{5.63}$$

The enthalpy of the hydrate stream is also modified and is given by

$$\begin{aligned} \tilde{h}_{\mathrm{hyd}}^{\mathrm{w,\,out}} = {} & \frac{n_{\mathrm{h}}^{\mathrm{w}}}{1 + n_{\mathrm{h}}^{\mathrm{w}}} \left( \tilde{h}_{\mathrm{f,\,H_2O}}^{\mathrm{w,\,o}} + \int_{T^{\mathrm{o}}}^{T^{\mathrm{out}}} c_{\mathrm{P,\,H_2O}}^{\mathrm{w}}\, dT \right) + \\ & \frac{1}{1 + n_{\mathrm{h}}^{\mathrm{w}}} \left( \tilde{h}_{\mathrm{f,\,CO_2}}^{\mathrm{w,\,o}} + \int_{T^{\mathrm{o}}}^{T^{\mathrm{out}}} c_{\mathrm{P,\,CO_2}}^{\mathrm{w,\,ig}}\, dT + \int_{p^{\mathrm{o}}}^{p_{\mathrm{eq}}^{\mathrm{out}}} \left[ \tilde{\nu}_{\mathrm{CO_2}}^{\mathrm{w}} - T^{\mathrm{out}} \left( \frac{\partial \tilde{\nu}_{\mathrm{CO_2}}^{\mathrm{w}}}{\partial T} \right)_{p,\,T^{\mathrm{out}}} \right] dp + \left( -\Delta H_{\mathrm{hyd}}^{\mathrm{w,\,diss,\,tot}} \right) \right) \end{aligned} \tag{5.64}$$

Equations 5.60 and 5.61 are still verified in this and in upcoming cases.

### 5.3.3 Case 7: Gas – Liquid

In Case 7, the inlet conditions of the carbon dioxide stream indicate that $CO_2$ is fed to the system in the gas phase. However, at the outlet, it is expected to have liquid carbon dioxide. The specific enthalpy of the inlet carbon dioxide stream is modified to

$$\tilde{h}^{\mathrm{w,\,in}}_{\mathrm{CO_2}} = \tilde{h}^{\mathrm{w,\,o}}_{\mathrm{f,\,CO_2}} + \int_{T^{\mathrm{o}}}^{T^{\mathrm{in}}_{\mathrm{CO_2}}} c^{\mathrm{w,\,ig}}_{\mathrm{P,\,CO_2}}\, dT + \int_{p^{\mathrm{o}}}^{p^{\mathrm{in}}_{\mathrm{CO_2}}} \left[ \tilde{\nu}^{\mathrm{w}}_{\mathrm{CO_2}} - T^{\mathrm{in}}_{\mathrm{CO_2}} \left( \frac{\partial \tilde{\nu}^{\mathrm{w}}_{\mathrm{CO_2}}}{\partial T} \right)_{p,\, T^{\mathrm{in}}_{\mathrm{CO_2}}} \right] dp \tag{5.65}$$

The specific enthalpies of the outlet streams can be calculated using Equations 5.56 to 5.59.

### 5.3.4 Case 10: Gas – Gas

Case 10 is the most common case at pressures of about 30 bar. Under these conditions, carbon dioxide is fed in its gas phase and exits the microNETmix unit in the gas phase as well.

The specific enthalpy of the inlet carbon dioxide stream is given by Equation 5.65 and the specific enthalpies of the outlet streams are determined through Equations 5.62 to 5.64.

### 5.3.5 Other Considerations

The previous equations are used to estimate the mass flow rate of hydrates based on the amount of heat that is removed through the cooling fluid, at any instant of the experiment, by introducing the known variables to an algorithm as represented in Figure 5.5. The fraction of solids $X^{\mathrm{w,\,out}}_{\mathrm{hyd}}$ can be easily estimated, once the amount of produced hydrates is known, through

$$X^{\mathrm{w,\,out}}_{\mathrm{hyd}} = \frac{\dot{m}^{\mathrm{out}}_{\mathrm{hyd}}}{\left( 1 + \dfrac{\dot{m}^{\mathrm{in}}_{\mathrm{H_2O}}}{1 - x^{\mathrm{w,\,out}}_{\mathrm{CO_2}}} \dfrac{n^{\mathrm{w}}_{\mathrm{h}}}{1 + n^{\mathrm{w}}_{\mathrm{h}}} \right) \dot{m}^{\mathrm{out}}_{\mathrm{hyd}}} \tag{5.66}$$

It is important to emphasize that the equations presented in Sections 5.2 and 5.3 are only valid when carbon dioxide is the only guest component present in the system. The addition of thermodynamic promoters, such as tetrahydrofuran, has an impact on the equilibrium, and thus the model may not be suitable.

## 5.4 Experimental Description

### 5.4.1 Materials

Gaseous and liquid carbon dioxide, with a purity of 99.995% and water concentration below 20 ppm were supplied by Air Liquide (Alphagaz™ $CO_2$). Gaseous $CO_2$ was supplied in bottles with pressure of approximately 60 bar and liquid $CO_2$ was supplied using a cylinder with dip tube, to guarantee that only liquid carbon dioxide is fed. Tap water was supplied by Águas do Porto, E.M., with pH ranging from 6.5 to 9 AdP (2017). Compressed air (Ar K) for system pressurization was supplied by Air Liquide (Alphagaz™ Ar), with a stated purity of $> 99.999\%$, and a pressure of approximately $200\,\text{bar}$. A thermodynamic promoter THF was used, supplied by Valente & Ribeiro, Lda. The cooling fluid is a mixture of ethanol and water, with a concentration of 40% in volume of ethanol. The ethanol was supplied by Aga, with concentration of 96% in volume, and then diluted in tap water to the desired concentration.

### 5.4.2 Set of Experiments

The set of experiments performed is presented in Table 5.3. The experiments were designed to study the influence of the most important parameters of process. In all experiments, mass flow rate of water was kept constant at $8\,\text{kg}\cdot\text{h}^{-1}$ to guarantee a minimum channel's Reynolds number of approximately 200 in the microNETmix unit, based on the flow rate of water at the inlet. Experiment E-001 is defined as the experiment with the standard experimental conditions. Experiments E-002 and E-003 have the objective of assessing the influence of the flow rate of the cooling fluid in the

cooling plates. In experiments E-004 and E-005, the pressure was gradually reduced to a pressure below the equilibrium curve. The effect of the temperature is assessed in experiments E-006 and E-007.

Table 5.3 – Set of experiments and experimental conditions. Shades represent the altered variable.

| EXP. | $T\left(°C\right)$ | $p\left(\text{bar}\right)$ | $\dot{m}_{H_2O}^{in}\left(\text{kg}\cdot\text{h}^{-1}\right)$ | $\dot{m}_{CO_2}^{in}/\dot{m}_{H_2O}^{in}$ | $x_{THF}^{mol}\left(\text{mol.\%}\right)$ | $\dot{m}_{cf}\left(\text{kg}\cdot\text{h}^{-1}\right)$ |
|---|---|---|---|---|---|---|
| **E-001**[1] | 2 | 30 | 8 | 0.1 | 0 | 40 |
| **E-002** | 2 | 30 | 8 | 0.1 | 0 | 100 |
| **E-003** | 2 | 30 | 8 | 0.1 | 0 | 200 |
| **E-004** | 2 | 20 | 8 | 0.1 | 0 | 40 |
| **E-005** | 2 | 10 | 8 | 0.1 | 0 | 40 |
| **E-006** | 5 | 30 | 8 | 0.1 | 0 | 40 |
| **E-007** | 10 | 30 | 8 | 0.1 | 0 | 40 |
| **E-008** | 2 | 30 | 8 | 0.05 | 0 | 40 |
| **E-009** | 2 | 30 | 8 | 0.01 | 0 | 40 |
| **E-010** | 2 | 50[2] | 8 | 0.1 | 0 | 40 |
| **E-011** | 2 | 30 | 8 | 0.1 | 1 | 40 |
| **E-012** | 2 | 20 | 8 | 0.1 | 1 | 40 |
| **E-013** | 2 | 10 | 8 | 0.1 | 1 | 40 |

[1]Standard conditions.
[2]Liquid carbon dioxide is the source.

The effect of the supersaturation condition is evaluated in experiments E-008 and E-009, where the amount of gas introduced to the system is reduced. In experiment E-008 the amount of produced hydrates should decrease, while in experiment E-009, since the amount of gas is lower than its solubility (see Equation 5.39), no hydrates are expected. Experiment E-010 was performed at a pressure of approximately 50 bar and the carbon dioxide source was liquid $CO_2$. In the last three experiments, THF was mixed in water in a concentration of 1% mol, and the pressure was reduced to the same values of experiments E-001, E-004 and E-005. The effect of the concentration of THF was not studied though, since it is widely described in literature that increasing the concentration of THF above 1% molar leads to a shift of the equilibrium curve downwards, but not at a rate that can be considered interesting from the process point of view (Ma et al. 2016).

Relevant process variables for each experiment are presented in Table 5.4.

Table 5.4 – Process variables for experiments from Table 5.3.

| EXP. | $\mathbf{Re}_{c,H_2O}$ | $\tau_{np}$ (s) | $x_{CO_2}^{w,exp}$ (wt. %) | VAPOUR PHASE? | $X_{hyd}^{w,exp}$ (wt. %) |
|---|---|---|---|---|---|
| **E-001** | 195 | 1.3 | 4.17% | No | 22.0% |
| **E-002** | 195 | 1.3 | 4.17% | No | 22.0% |
| **E-003** | 195 | 1.3 | 4.17% | No | 22.0% |
| **E-004** | 195 | 1.3 | 4.17% | No | 22.0% |
| **E-005** | 195 | 1.3 | 2.66% | Yes | 0.0% |
| **E-006** | 210 | 1.3 | 5.02% | No | 19.0% |
| **E-007** | 230 | 1.3 | 5.12% | Yes | 0.0% |
| **E-008** | 195 | 1.3 | 4.17% | No | 2.7% |
| **E-009** | 195 | 1.3 | 0.99% | Yes | 0.0% |
| **E-010** | 195 | 1.3 | 4.17% | No | 22.0% |
| **E-011** | 195 | 1.3 | 4.17% | ? | ? |
| **E-012** | 195 | 1.3 | 4.17% | ? | ? |
| **E-013** | 195 | 1.3 | 4.17% | ? | ? |

Residence time values are estimated based on the flow rate of water at the inlet, inside the microNETmix unit network plates only. It is estimated from

$$\tau_{np} = \frac{3V_{np}\rho_{H_2O}}{\dot{m}_{H_2O}^{in}} \tag{5.67}$$

The expected values of solubility and solids content is based on the equilibrium model described in Section 5.2.3. It is assumed that the $CO_2$ solubility in water is not affected by the presence of 1% molar of THF. However, it is not clear yet the influence of THF on the final production of hydrates, therefore, it is not clear if a vapour phase may or may not coexist under these conditions, and thus the simplified model from Section 5.2.3 cannot be applied. It is expected that no production of hydrates occurs in experiment E-005, since the operating pressure is below the equilibrium pressure at the operating temperature. The same is expected in experiment E-007, where the temperature increases up to a point where the operating regions lays outside the zone of stability of hydrates. In experiment E-009, the amount of carbon dioxide fed to the system is not large enough to guarantee the

supersaturation condition, i.e., the amount of $CO_2$ does not completely saturate the water.

### 5.4.3 Experimental Procedure

Tap water was added to tank E-1 (see Figure 4.3). For experiments E-011 to E-013, tetrahydrofuran was mixed with water in a concentration of 1% molar. Initially, the recirculation circuit (Figure 4.16) is active in order to thermally stabilize the system. Pump E-2 was set to the desired water flow rate, passing through the microNETmix unit and returning to tank E-1, being the line at the atmospheric pressure. Chiller E-14 and E-15 were turned on and their set point was adjusted in a way that conditions from Table 5.3 are met. During this time, cooling fluid from chiller E-14 is flowing into the cooling plates of the microNETmix unit, cooling not only the unit itself but also the water stream that is recirculating. Cooling fluid from chiller E-15 flows to coil E-16, reducing the temperature of the water in the tank, and also to serpentines tank E-3 where it cools the water that is flowing in the line, which can absorb heat from the outside and also due to heat dissipation of the screw pump. After about 60 minutes, steady state is achieved. At this point, valve V-14 position was switched on, activating the circuit shown in Figure 4.17. Water passes through filtration column E-11 in order to reduce its temperature before production. After a few seconds, the pressure increased. The relief valve V-21 was gradually opened, so that the pressure measured downstream the microNETmix unit (through pressure transducer I-10) was near the value defined by Table 5.3. After the system's pressure and temperature were stabilized, production started. If the source of carbon dioxide was gas carbon dioxide, the pressure downstream the bottle is set in valve V-6 (this pressure must be larger than the pressure defined in valve V-21). The mass flow rate of carbon dioxide was defined through MFC M-2. The pressure of the line gradually increased until it achieved steady state. After this point, the system was ready to produce. If liquid carbon dioxide was inserted, the position of valve V-5 was switched on, and the flow rate is set through the HPLC pump E-7. When solids are being produced, column E-11 is getting filled and the solids concentrated. This resulted in

an increase of the pressure in this line (identified by an increase of the pressure of transducer I-10). This increase, together with the residence time in the column and experiment time, indicated the point at which the column was completely filled. When this happened, the position of valves V-15 and V-19 were switched on so that the flow bypassed the filtration column.

In all experiments, a camera was installed in front of visualization window E-10 to record the flow of the hydrates slurry. This was carried out using a Canon D3400 with an AF-P DX Nikkor 18 – 55 mm VR lens, which was set to take photographs of the visualization window.

#### *5.4.3.1 Dissociation Tests*

Dissociation tests were performed using samples obtained from the conditions of experiment E-001. The objective is to study the kinetics of dissociation at normal conditions of pressure and temperature, at which carbon dioxide hydrates are thermodynamically unstable. The hydrate samples were obtained from the filtration column E-11. When this column was filled, valves V-15 and V-19 bypassed the column, isolating it. At this point, the pressure was still near the production pressure. Valve V-18 was slowly opened in order to decrease the pressure inside the column. After this depressurization, the column is disassembled and the hydrate sample is removed. This last procedure can be done at ambient temperature, or after immersing the column in a cold medium, so that depressurization occurs at low temperature. The sample is then cut and placed inside a $50\,\mathrm{mL}$ plastic container. A small orifice $\left(<5\,\mathrm{mm}\right)$ was drilled in the container's lid to allow the removal of the dissociation resultant gas. The container was placed in a weighing scale and the mass was measured with time. The weighing scale was an A&D HR-120 with a $0.1\,\mathrm{mg}$ resolution.

### *5.4.3.2 Gas Uptake Measurement*

An estimative of the amount of gas trapped in the hydrates cages is obtained from the dissociation tests described above. An alternative method can be used, which consists in the precipitation of calcium carbonate when carbon dioxide is introduced in a saturated aqueous solution of calcium hydroxide.

The saturated solution was obtained by mixing distilled water and calcium hydroxide (obtained from Fluka Analytical with a purity of $\geq 96\%$). A known amount of hydrate sample that was carefully retrieved from the sample of column E-11 was immersed in this solution. The saturated solution was initially cooled down to temperatures in the range of 1-3 °C, to avoid thermal shock with the hydrates sample during immersion. When the hydrate was immersed in the solution, the bottle was closed, containing the carbon dioxide that will be released due to dissociation. This released carbon dioxide reacts with the calcium hydroxide forming calcium carbonate according to the following chemical reaction

$$\mathrm{Ca(OH)_2(aq) + CO_2(g) \rightarrow CaCO_3(s) + H_2O(l)} \tag{5.68}$$

Calcium carbonate has a very low solubility in water, and thus precipitation will occur even if small amounts of carbon dioxide are added. This solid is obtained through filtration, and dried in the oven at approximately 100 °C for two hours. The dried solid is then cooled in a desiccator for 30 minutes, and the dried residue is weighed. The amount of obtained solid can be used to estimate the amount of $CO_2$ in the hydrate. A simplified description based on the chemical equilibrium between species is presented in Appendix C.

### *5.4.3.3 Characterization*

Further characterization of hydrates and respective properties was obtained with resource to techniques for commonly used in materials characterization.

SEM (scanning electron microscopy) was performed using a bench-scale SEM equipment from Phenom World model ProX. The equipment has a resolution of

nearly 10 nm and voltages ranging from 5 kV to 15 kV. Due to the nature of the sample, a temperature controlled sampler holder was used, to minimize the effect of the electron beam and vacuum damage of the sample. The sample obtained from the filtration column was divided in smaller parts of approximately 5-7 mm. The temperature-controlled holder was already at a temperature of 5 °C. Afterwards, the sample was placed in the sampler, which was placed in the holder. The holder was inserted in the SEM equipment, and vacuum is done. Once vacuum is done, the temperature in the sampler holder was decreased down to -20 °C. This procedure is important for the minimization of gasification due to dissociation, while avoiding the sublimation of water vapour near the sampler.

X-ray diffraction (XRD) analysis were performed at Institute of Nanoscience and Nanotechnology (IN), using a Rigaku SmartLab diffractometer. XRD patterns were obtained using a $Cu-K\alpha_1$ radiation source with $\lambda = 1.54056$ Å in the 2-theta range of $20-45°$. Samples preparation consists in the use of a press to make small pellets from the solid hydrate.

## 5.5 Results and Discussion

### 5.5.1 Process Analysis

Figure 5.6 shows the evolution of temperature and pressure of the water inlet line, gas inlet line and microNETmix outlet line with time, for experiment E-001 (conditions from Table 5.3).

Several steps prior to hydrate precipitation can be identified from Figure 5.6. These steps are identified in Figure 5.6. In a first step, only water is flowing at atmospheric pressure. Thermal stabilization of the system is done during this step. In a second step, valve V-14 is switched on and the pressure increased to the pressure set in relief valve V-21. This transient causes perturbations in the profiles, such as instantaneous flow rate oscillations and temperature changes. Nevertheless, the system quickly reaches steady state. In a third step, carbon dioxide is introduced. In this step, a

gradual increase of the pressure in the gas line is observed, due to the introduction of carbon dioxide to the system. No gas or hydrates are observed in the visualization window at this point, since no gas is yet entering in the microNETmix unit. At this point, the temperature of carbon dioxide tends to slowly decrease.

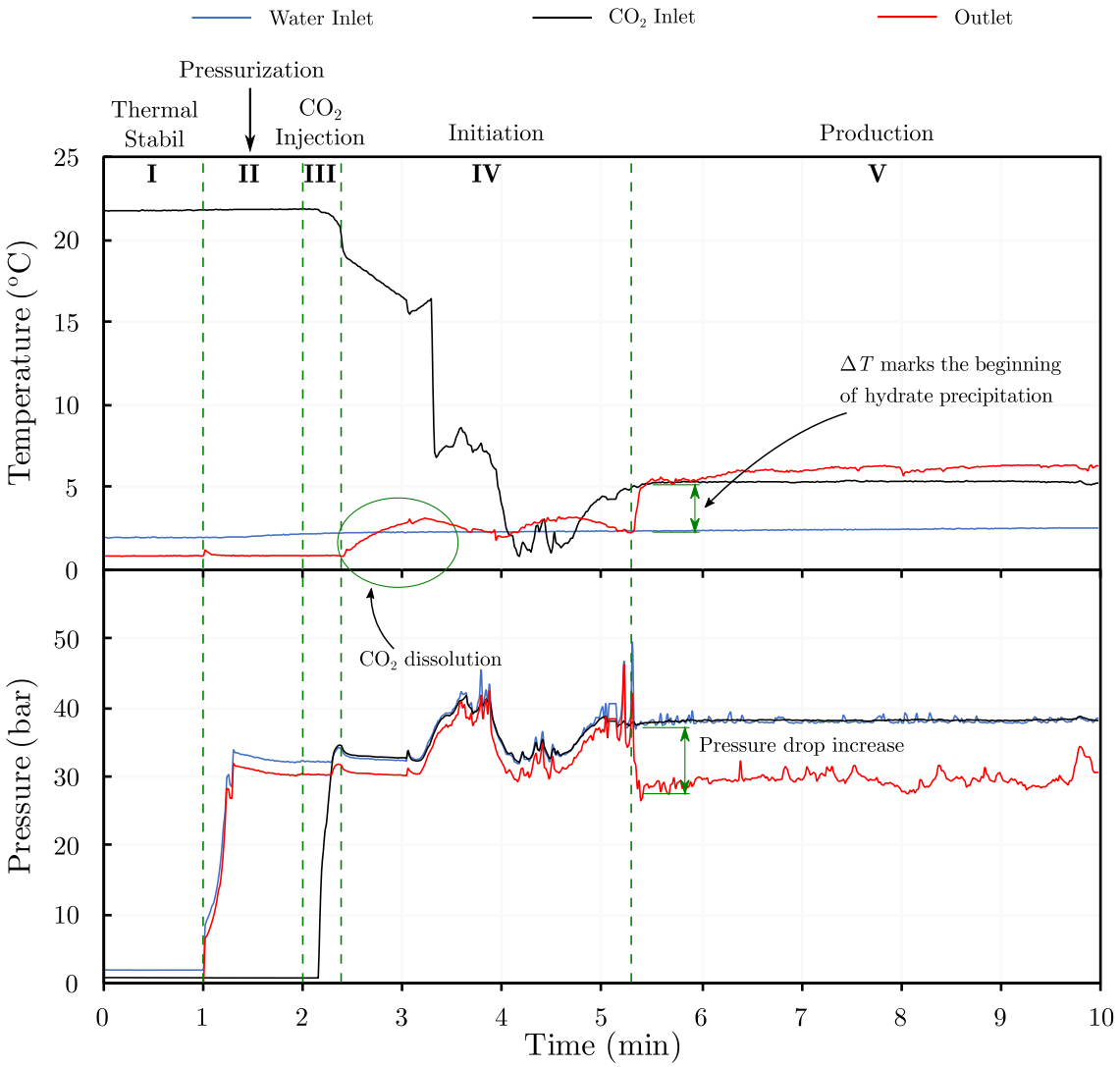



Figure 5.6 – Temperature and pressure profiles for experiment E-001.

The fourth step begins when the pressure of gas line equals the pressure of the water line, meaning the gas is already entering the microNETmix unit. The first contact between gas and water results in a relatively small increase of the temperature at the outlet of the microNETmix unit. This is attributed to heat that is released due to carbon dioxide dissolution. At this point however, no hydrates are formed yet. The beginning of precipitation of hydrates (and of the fifth step) is clearly identified by a second temperature increase and an increase of the pressure drop (difference between

red and blue/black lines from the bottom part of Figure 5.6). It should be highlighted that this is the pressure drop for all microNETmix plates (including distributors and collectors), as well as check-valves. The increase of the pressure drop may be attributed to some solid accumulation that can occur in some regions of the network plates where mixing is not so effective, such as in the lateral columns, as well as in the collector plate of the unit. Pressure drop due to friction may also occur and increases with the presence of gas, due to the increase of the velocity of the flow. However, the increase of the pressure drop in the region of formation of hydrates is probably due to the volume changes that occur inside the mixer due to carbon dioxide dissolution and hydrates precipitation. If the equilibrium is reached (according to the model from Section 5.2.3), a volume reduction of approximately 60% in the slurry is expected, resulting in an expansion, and thus, a larger pressure decrease. Although there is an increase of the pressure drop when hydrates start to form, since it does not increase along the experiment, this means that no blockage or plugging occurs in the system.

The temperature increase at the outlet of the unit means that the amount of heat released is higher than the amount of heat removed through the cooling plates. From the energy balance, it is determined that the difference in the heat released from the system and absorbed by the cooling plates is approximately 30 W.

It is interesting to analyse the path of the carbon dioxide temperature. Initially, the temperature is high (close to 22 °C). With the injection of the carbon dioxide, the temperature expectably starts to decrease. With the increase of the pressure of carbon dioxide, the temperature decreases even further, being cooled down to temperatures near the temperature of water. Pressure perturbations typical from gas-liquid systems, at 3.5 minutes, have an influence on the temperature of carbon dioxide. After the abrupt decrease and oscillations on the gas temperature, the temperature is kept constant during step five (production). Figure 5.6 clearly shows that a steady state is reached and that constant hydrates precipitation is obtained.

Different instants of the visualization window are shown in Figure 5.7.

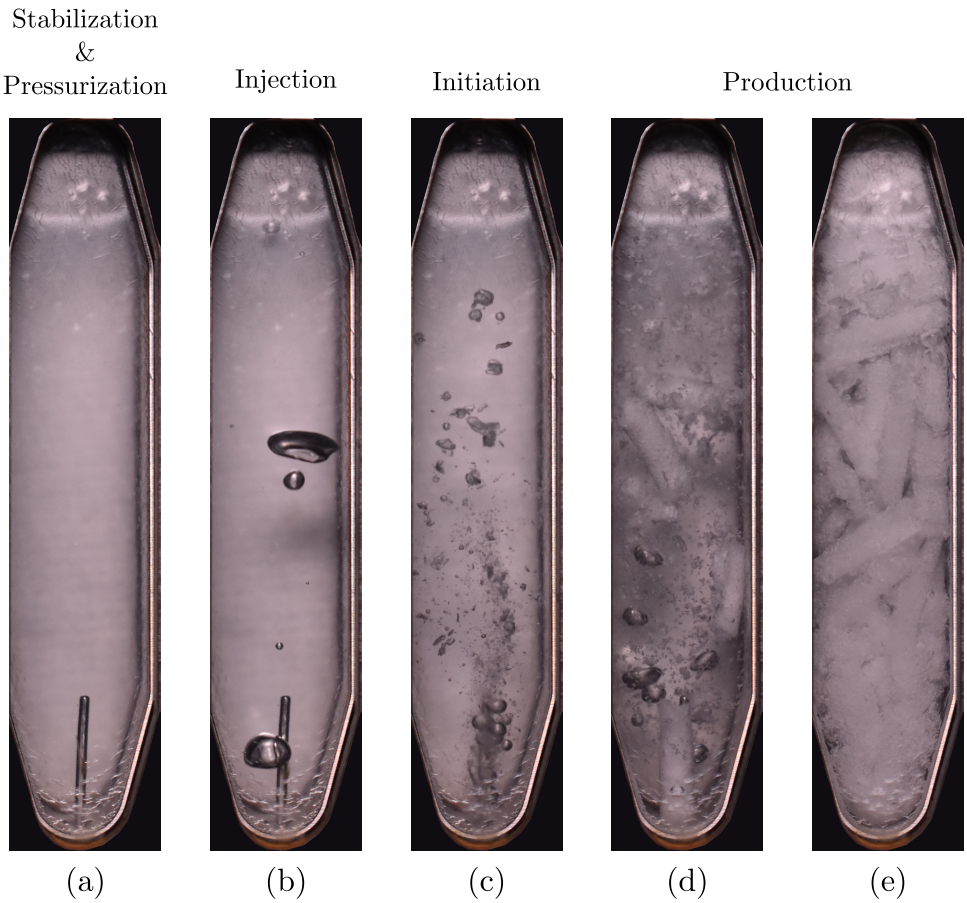



Figure 5.7 – Different regimes at different instants for experiment E-001 at different instants: (a) thermal stabilization; (b) after carbon dioxide injection at working pressure; (c) beginning of precipitation; (d) production of hydrates; (e) filling of visualization window with hydrates.

In Figure 5.7a, only water is flowing in the visualization window. When gas enters in the microNETmix and the pressure of the system is increased to the working pressure (30 bar for experiment E-001), some large bubbles start to appear, which are visible in Figure 5.7b. At this point, still no hydrates precipitate, because although the temperature at the outlet is low enough and the pressure is high enough to promote the precipitation of hydrates, this precipitation only occurs when the carbon dioxide temperature reduces to values within the region of stability of hydrates. This may indicate that the first contact between water and carbon dioxide is of high importance, requiring that the temperature of gas-liquid interface in the gas side is at the thermodynamic conditions that allow hydrates precipitation. The beginning of the precipitation is visible in Figure 5.7c. At this instant, a blur is visible due to the presence of small particles of hydrates dispersed in water. Consistent solids are visible immediately after this step, as shown in Figure 5.7d. These solids appear to be highly

concentrated. The expansion in the window promotes flow instability of the solids, which oscillate, leading to accumulation of the solids at the outlet, as shown in Figure 5.7e. The presence of gas is no longer observable from Figure 5.7e.

The solids produced are not ice, since the temperatures involved are larger than the freezing point of water. Also, solidification only occurs when the gas is introduced in the system, which is characteristic of the formation of hydrates.

It is interesting to analyse the transition from the step four and five. In Figure 5.8, the temperature-pressure path is represented, as well as the equilibrium lines.

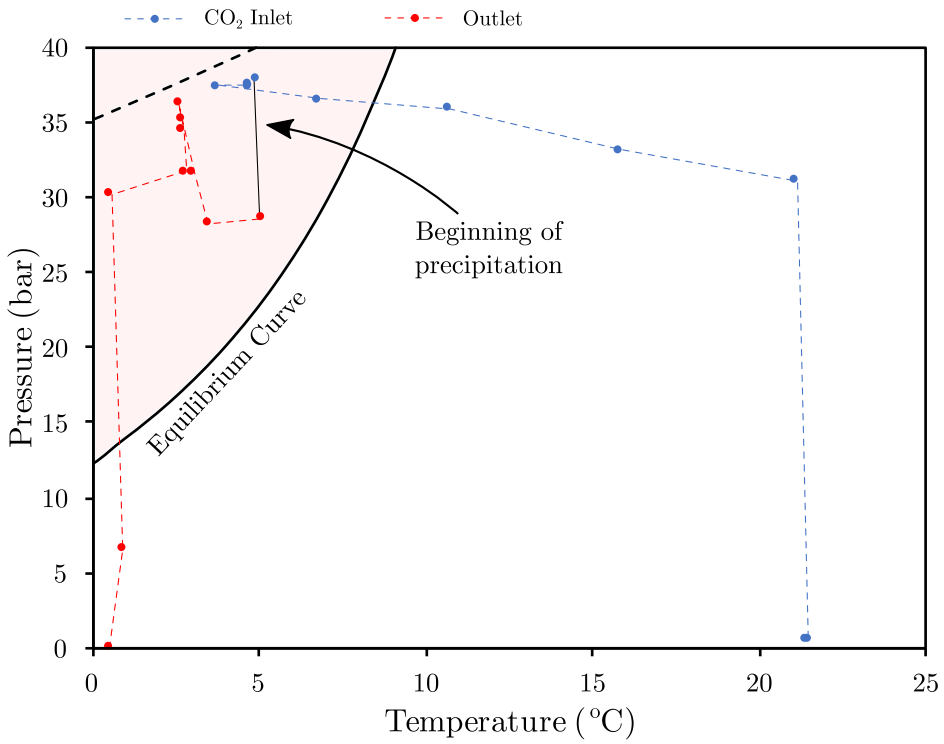



Figure 5.8 – Pressure-temperature paths of experiment E-001.

For simplicity, only a few points from Figure 5.6 are represented in Figure 5.8. The first points (at $p = 1$ bar) represent the initial conditions of the experiment. The pressure at the outlet increases isothermally up to the region of hydrates stability. At this point, the conditions of carbon dioxide are still not within the region of stability of hydrates. Although the cooling plates have the capacity to quickly reduce the temperature of the carbon dioxide at the inlet of the microNETmix unit, the first contact between water and carbon dioxide results only in dissolution. In this first

contact however, the temperature of carbon dioxide at the inlet is above 20 °C. This dissolution is detected by the small increase of temperature at the outlet to approximately 2 °C. The pressure at the outlet increases as a result of the perturbations already observed in Figure 5.6 at about 3-4 minutes. The precipitation of hydrates starts in the region identified. From the beginning of the first contact between gas and water until the beginning of the hydrates precipitation it takes approximately 3 minutes. Precipitation started only when carbon dioxide conditions at the inlet lay inside the region of precipitation of hydrates. This indicates that the conditions at the outlet are not, by themselves, sufficient to guarantee that precipitation will occur. On the contrary, the conditions of water and carbon dioxide at the inlet appear to have a significant impact.

As it can be seen from Figure 5.8, the pressure-temperature conditions at the outlet of the microNETmix unit is well within the region of hydrate stability through all the production step, resulting in a steady and continuous process of hydrates production. This results in the production of a slurry absent of gas phase, which holds $0.8\,\mathrm{kg}\cdot\mathrm{h}^{-1}$ of carbon dioxide, either in the aqueous phase or in the solid phase.

In the regions where hydrates are being formed (after 5 minutes in Figure 5.6), the energy balance equations presented in Section 5.3 are applied. The average amount of hydrates produced during the experiment is obtained by time-averaging the instantaneous mass flow rate of hydrates produced

$$\left\langle \dot{m}_{\mathrm{hyd}}^{\mathrm{out}} \right\rangle_t = \frac{\sum_{t=0}^{t_{\mathrm{exper}}} \dot{m}_{\mathrm{hyd}}^{\mathrm{out}}\left(t\right)}{t_{\mathrm{exper}}} \tag{5.69}$$

where $\left\langle \dot{m}_{\mathrm{hyd}}^{\mathrm{out}} \right\rangle_t$ is the time-average mass flow rate of hydrates, and $t_{\mathrm{exper}}$ is the experiment time. The average weight concentration of solids $X_{\mathrm{hyd}}^{\mathrm{w,\,out}}$ is obtained by time-averaging the instantaneous solids content

$$\left\langle X_{\text{hyd}}^{\text{w, out}} \right\rangle_t = \frac{\sum_{t=0}^{t_{\text{exper}}} X_{\text{hyd}}^{\text{w, out}}\left(t\right)}{t_{\text{exper}}} \tag{5.70}$$

The dynamic thermal data in Figure 5.6 are consistent with the production of a slurry of hydrates with a 14.1% weight concentration in solids by applying the energy balance, as opposed of the expected 22% from Table 5.4 for isothermal production at 2 °C. However, the use of the model from Section 5.2.3 at the outlet conditions results in an expected solids concentration of 17.4% in weight. This is the result of the observed temperature increase, and so the value of 14.1% obtained experimentally should be compared with 17.4% to evaluate the deviation from the equilibrium. The presence of macroscopic gas bubbles is not visible in Figure 5.7 during the instants where precipitation of carbon dioxide hydrates is observed. The deviation is significant, however it does not guarantee that equilibrium is not reached at the outlet of the microNETmix unit. The use of type-K thermocouples introduces significant errors in the temperature measurements (thermocouples have accuracy errors close to 2 °C), which have impact on the global energy balance from Section 5.3. The balance to the cooling fluid, where the flow rate is significantly larger than the water flow rate in the network plates, is particularly sensitive to small variations of temperature. Therefore, at this point, it is still unclear whether the deviation of the solids concentration is due to measurement and modelling errors, or if it means that no equilibrium is reached. This issue must be solved in the future to more accurately determine the amount of hydrates produced. This can be done by replacing the thermocouples by RTD's than can decrease the accuracy error to half.

#### *5.5.1.1 Influence of Cooling Fluid Rate*

In experiments E-002 and E-003, the mass flow rate of the cooling fluid was set to 100 and 200 $\text{kg} \cdot \text{h}^{-1}$. The increase of the cooling fluid flow rate should result in an increase of the heat transfer capacity of the microNETmix unit. Therefore, if experiment E-001 is controlled by the heat transfer rate, the amount of produced hydrates in experiments E-002 and E-003 should increase and should be detected by

the application of the energy balance to the dynamic data. On the other hand, by increasing the mass flow rate of the cooling fluid, the errors associated to temperature measurements are also enhanced.

The dynamic thermal data for experiments E-002 and E-003 are presented in Figure 5.9 and Figure 5.10.

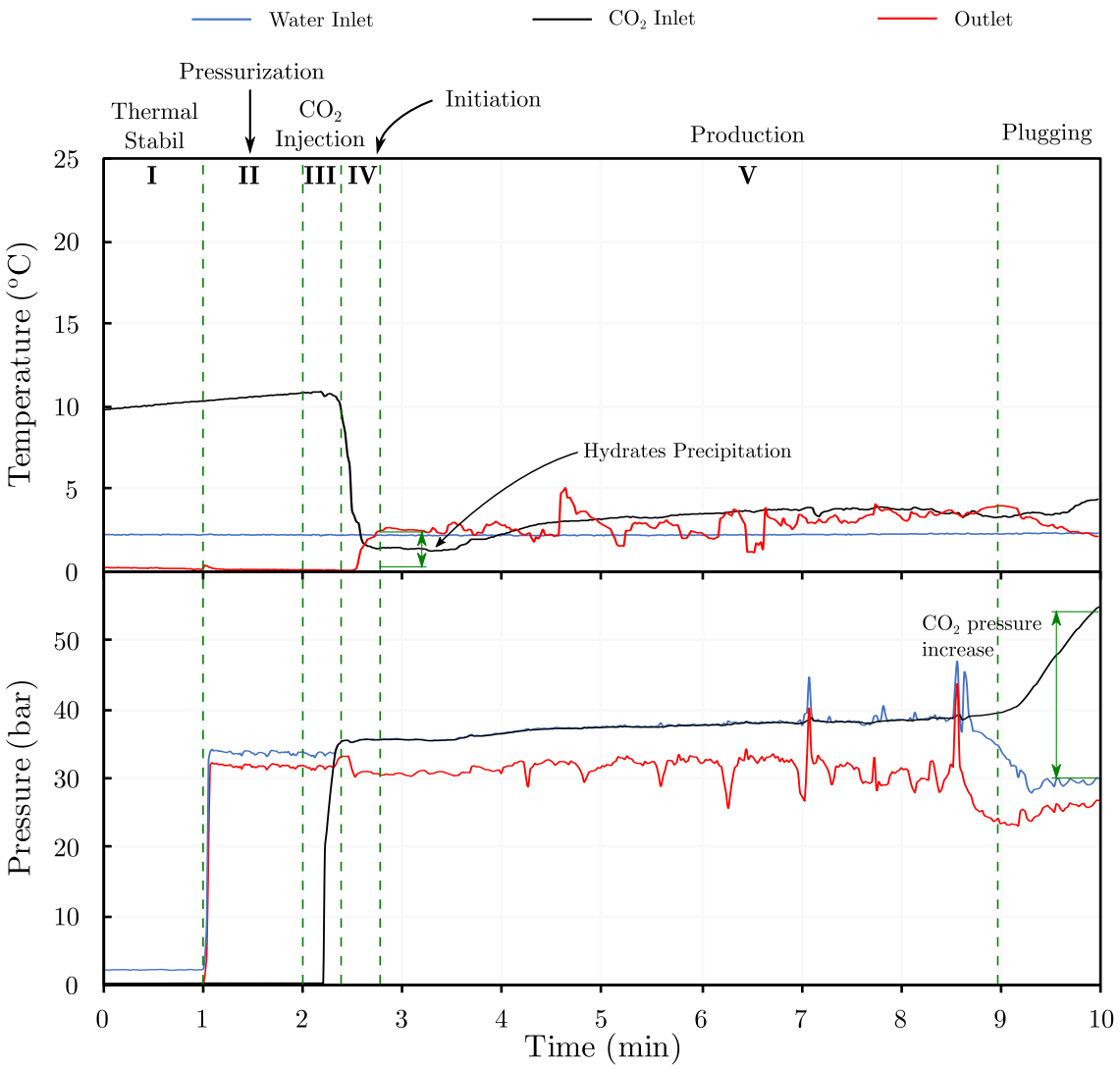



Figure 5.9 – Temperature and pressure profiles for experiment E-002.

The shape of the curves presented in Figure 5.9 and Figure 5.10 are very similar to the curves obtained in experiment E-001. The same five regions can be identified. As before, the beginning of the precipitation of the hydrates is identified by a positive jump of the temperature at the outlet of the microNETmix and by the increase of the pressure drop.

The temperature increase when hydrates start to precipitate is nearly the same in both experiments E-002 and E-003, as well as in experiment E-001.

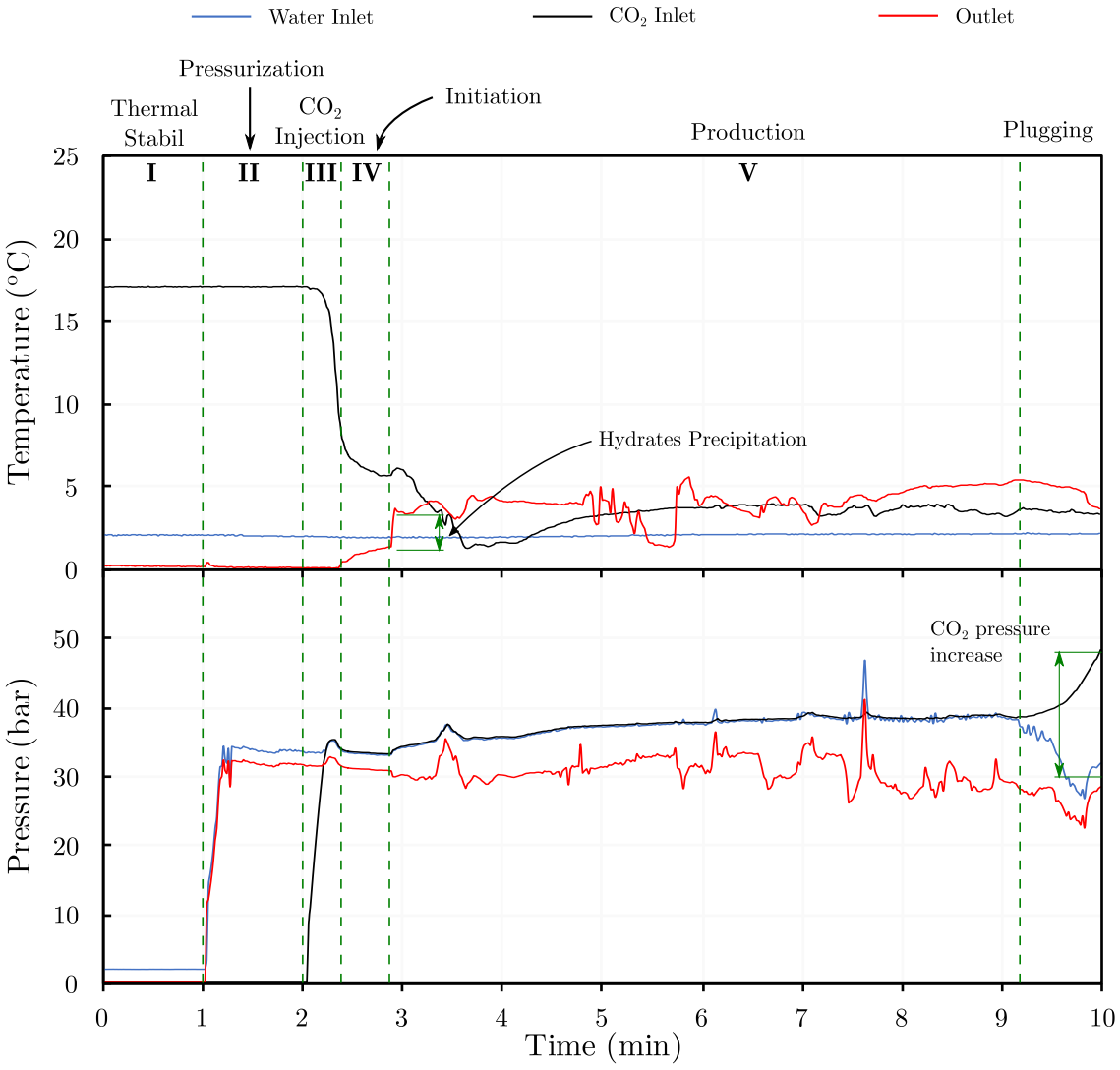



Figure 5.10 – Temperature and pressure profiles for experiment E-003.

At the end of these experiments, the pressure of the carbon dioxide line increases in both experiments while the pressure of the remaining lines slightly decreases. This behaviour was not observed in experiment E-001. This plugging of the carbon dioxide line may be caused by the presence of stagnated water that backflows from the microNETmix. This may originate annular flow in the carbon dioxide lines due to the large velocity differences of the liquid and the gas, resulting in the formation of a water film near the walls, that can freeze due to heat transfer by conduction in the pipes. The gradual increase of the film size may originate larger gas velocities that enhance the behaviour, ultimately resulting in the partial blockage of the line, and in

a pressure increase above the pressure of carbon dioxide supply. In the region identified as plugging, the carbon dioxide flow rate is reduced to zero. These results in the decrease of the pressure drop (regarding the water line) in the system, to values similar to the ones observed before gas is introduced. Most importantly, the pressure increase of the carbon dioxide line only indicates that plugging does not occur in the network plates of the microNETmix unit. If that were the case, the pressure of the water stream would increase as well to equilibrate the system. A second reason may be attributed to the potential formation of hydrates in these regions where liquid is stagnated, in a similar way as in gas pipelines, as described in Section 2.3.4.1. The reason why this behaviour is not observed in experiment E-001 may be explained by the fact that in experiments E-002 and E-003, the cooling capacity is higher due to the higher cooling fluid flow rate.

Images of the visualization window at different instants for both experiments are presented in Figure 5.11.




Figure 5.11 – Different regimes at different instants for experiments: (a) E-002; (b) E-003.

The analysis of Figure 5.9 to Figure 5.11 indicates that the change of the cooling fluid flow rate does not have an impact on the solids macroscopic morphology.

Expectably, the flow behaviour inside the visualization window in experiment E-001 is also observed in experiments E-002 and E-003, since the cooling fluid flow rate does not alter the flow patterns of the main streams of the system.

The energy balance allows determining that the solids content at the outlet of the microNETmix unit is 15.1% and 16.4% for experiments E-002 and E-003, respectively. Again, these values deviate from the expected values. However, these values are very similar to the value obtained in experiment E-001, although a slight increase is obtained with the increase of the coolant flow rate. However, the error associated with the temperature measurement can explain the deviation from the obtained values. These results seem to indicate that the process is still slightly controlled by heat transfer. This is in agreement with the conclusion from Section 4.4.1, which indicates that convection of the cooling plate side controls the heat transfer process.

#### *5.5.1.2 Influence of Pressure*

Experiments E-004 and E-005 aim to study the influence of pressure on the production rate. Dynamic thermal data for these two experiments are presented in Figure 5.12 and Figure 5.13.

Figure 5.12 shows that hydrates are formed in experiment E-004, which is ran at a pressure of 20 bar, well above the equilibrium pressure at 2 ºC (which is close to 15 bar). This is identified by the increase of the temperature at the outlet of the microNETmix unit, as well as by the increase of the pressure drop. The pressure drop increase in this experiment is much higher than observed in experiment E-001, which indicates that this is not a result of pressure drop due to friction or accumulation. If pressure drop was due to friction only, then it should be equal for experiment E-004, since the amount of solids should be the same. An interesting fact is that the inlet pressure increases to the same values of experiment E-001, while the outlet pressure is 10 bar lower. The reason for this behaviour is not fully understood, but may also be attributed to the volume reduction that exists in the system, which is larger in

this case, due to the lower density of carbon dioxide at the inlet conditions. Also, it is possible that since the system tends to achieve its thermodynamic condition of hydrates in equilibrium in a saturated water solution, a minimum amount of carbon dioxide to promote not only hydration but also carbon dioxide dissolution may be required. This could be the result of low interphase mass transfer rate at 20 bar. Therefore, it is expected that the amount of hydrates produced in this experiment is lower than the amount produced in experiment E-001. The low pressure may result in ice formation or hydrate accumulation in the carbon dioxide line as explained in Section 5.5.1.1, that originates the plugging observed at the end of the experiment.

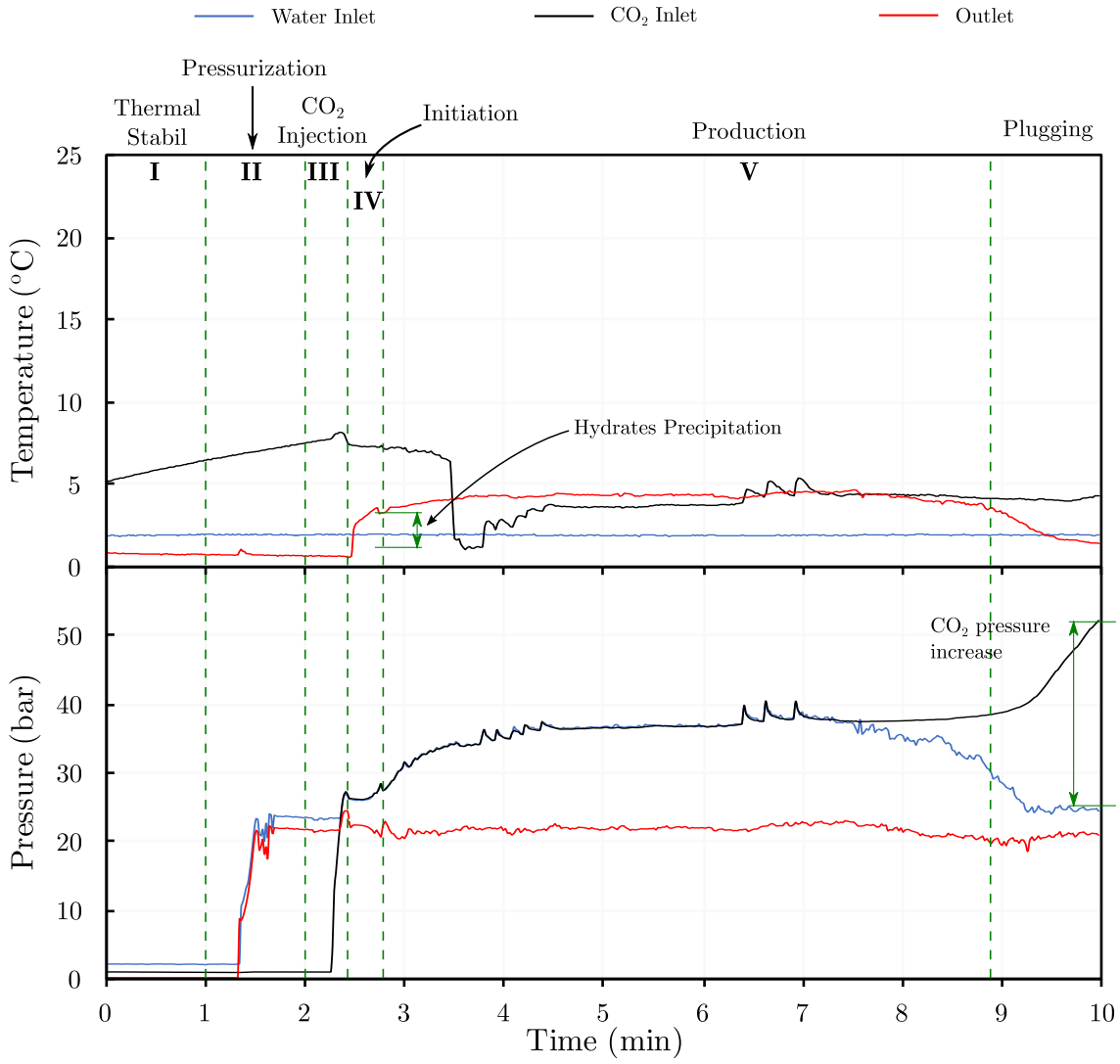



Figure 5.12 – Temperature and pressure profiles for experiment E-004.

In experiment E-005 no hydrates are visible, even though a slight temperature increase at the outlet of the microNETmix unit is verified. This is due to the dissolution of carbon dioxide in water, which is an exothermal process.

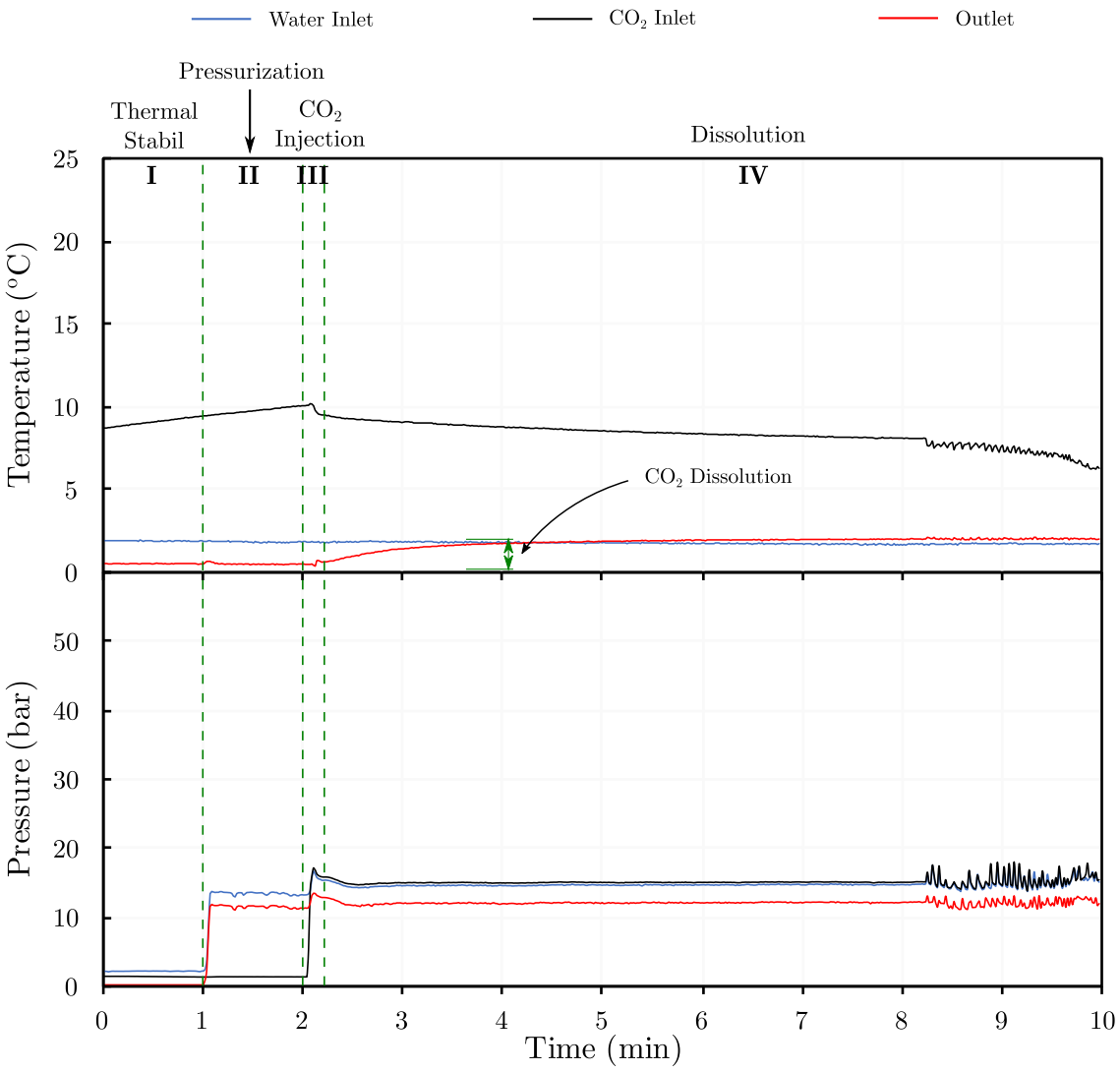



Figure 5.13 – Temperature and pressure profiles for experiment E-005.

Interestingly, due to the already relatively low temperature of carbon dioxide in experiment E-004, the duration of step four is reduced. This corroborates the observation made from Figure 5.8 that indicates that the temperature at the inlet of carbon dioxide is important to promote the precipitation of hydrates.

One observation made from Figure 5.12 and Figure 5.13 is that even though the cooling conditions are similar to experiment E-001, plugging of the carbon dioxide line only occurs in experiment E-004, where the pressure downstream the

microNETmix unit is set to approximately 20 bar. In experiment E-004, due to the volume change, a larger pressure drop than in experiments E-001 and E-005 is obtained, and that may contribute for the formation of ice that plugs the carbon dioxide line. The reason why is still unclear, but may be due to gas expansion in the carbon dioxide line that could result in the formation of ice in the water film that is formed. In experiment E-005, since the pressure decrease is not so large, the energy absorbed due to expansion is lower, disabling the formation of ice or delaying it. Even though the temperature at the outlet increases, local temperature decrease below the water freezing point may occur.

Images of the visualization window at different instants for the three experiments are presented in Figure 5.14. From Figure 5.14a, it is possible to see a different behaviour than in experiment E-001, since in this case not only hydrates are visible, but also gas bubbles are observed, resulting in the blurred region of the image. This is possibly the result of the lower pressure at the outlet the partially dissociates the solid, even though thermodynamic conditions are achieved. In Figure 5.14b, only gas bubbles are observed, as expected, since the working pressure is well below the equilibrium pressure.

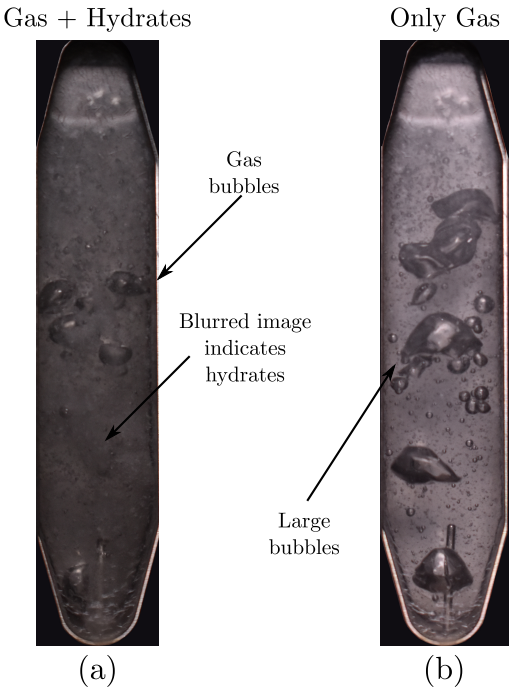



Figure 5.14 – Different regimes at different instants for experiments: (a) E-004; (b) E-005.

The energy balance allows determining that the solids content at the outlet of the microNETmix unit is 14.8% for experiment E-004, which is close to the value obtained in experiment E-001. This is an indication of the relevance of the errors associated to the experimental temperature measurements for the application of the model of Section 5.2.3. Figure 5.7d and Figure 5.14a clearly show different regimes, which is not reflected on the energy balance model. These deviations are systematic and occur in all experiments.

#### *5.5.1.3 Influence of Temperature*

The influence of temperature at constant pressure is assessed from experiments E-006 and E-007. The equilibrium pressure at 5 °C is about 22.5 bar, while at 10 °C is above 60 bar. At 30 bar, it is expected that at 5 °C, hydrates are formed, but not at 10 °C. Dynamic thermal data for experiments E-006 and E-007 are presented in Figure 5.15 and Figure 5.16.

Unexpectedly, Figure 5.15 does not indicate that hydrates are formed. Although a temperature increase is observed, this is associated to carbon dioxide dissolution, since no pressure drop increase is observed. The system is completely stable throughout the experiment, and no ice formation in the carbon dioxide line is detected.

The absence of hydrates in experiment E-006 can be explained with the reduction of the driving force, since the pressure difference to the equilibrium is reduced from experiment E-001 and E-006. The increase of temperature also results in an increase in 20% of the carbon dioxide solubility. Since more carbon dioxide needs to be dissolved, the driving force may not be sufficient to completely saturate the medium. This means that the supersaturation condition is not obtained even though the amount of introduced carbon dioxide is enough to supersaturate the medium. As a result, no hydrates formed, even though thermodynamic conditions are achieved. This may be due to the existence of mass transfer limitations in the system, which inhibits the precipitation of hydrates.

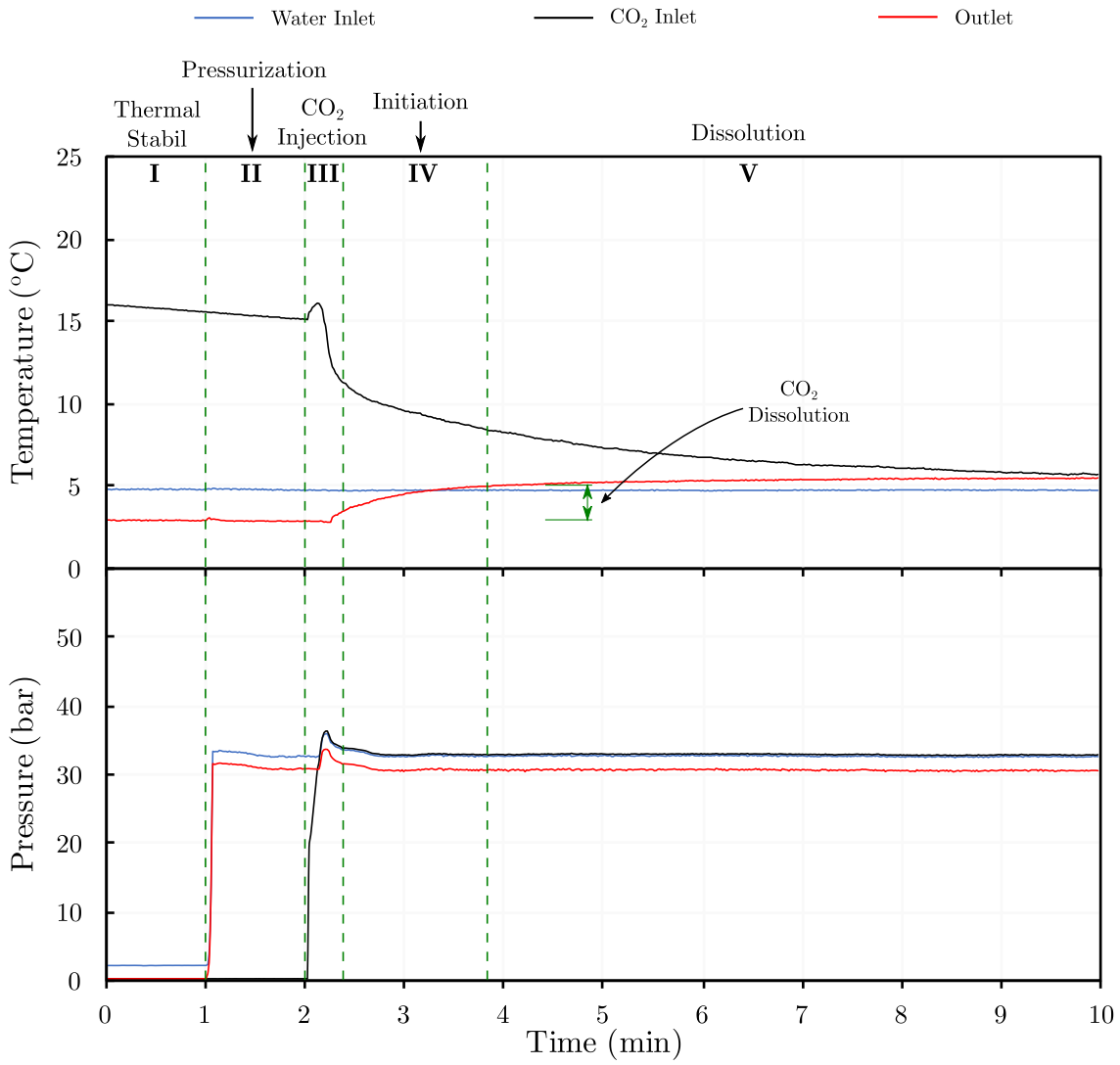



Figure 5.15 – Temperature and pressure profiles for experiment E-006.

A similar behaviour is observed in Figure 5.16. However, the temperature of experiment E-007 is outside the region of hydrates precipitation, therefore, no hydrates precipitation is expected. The temperature at the outlet is within the region of stability however. Thus, this indicates again that the conditions at the inlet have a more significant impact on the promotion of the crystallization of hydrates than the conditions inside or at the outlet of the microNETmix.

Images of the visualization window are presented in Figure 5.17.

Figure 5.17 shows that in both cases, gas is observed in the visualization sampler, indicating that no hydrates are formed, as observed from dynamic thermal data. In Figure 5.17a, the amount of gas is much lower, meaning that a significant part of the

carbon dioxide is dissolved in water, as indicated by the temperature increase in Figure 5.15 that is slightly larger than in Figure 5.16.

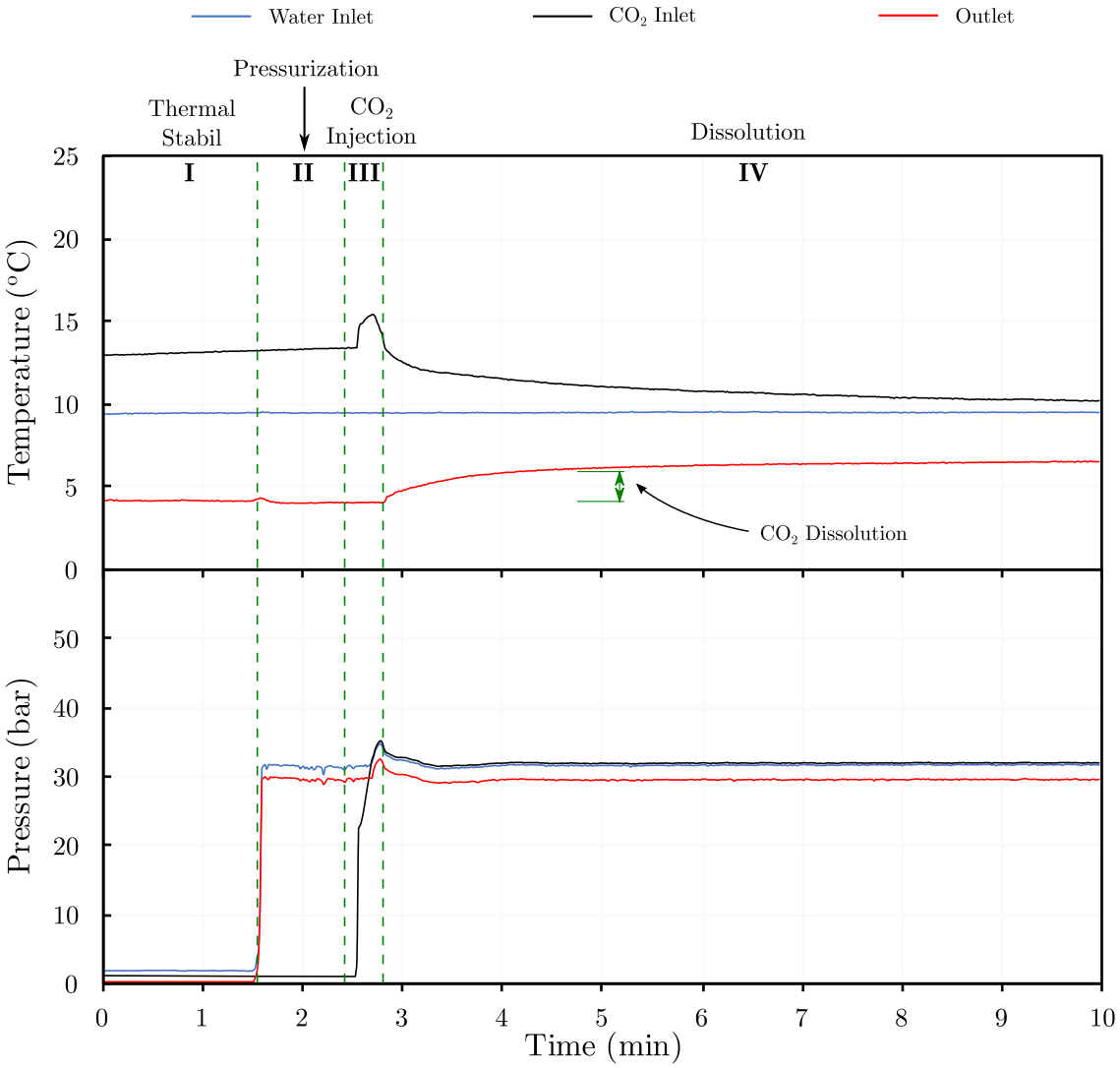



Figure 5.16 – Temperature and pressure profiles for experiment E-007.

#### *5.5.1.4 Influence of Gas/Water Ratio*

Experiments E-008 and E-009 aim to study the influence of the amount of gas introduced to the system. For a given pressure and temperature, there is a minimum amount of gas that is required to guarantee that the supersaturation condition is reached, and this amount can be determined using Equation 5.39. This condition is observed in the conditions of experiment E-008, but not in experiment E-009. As in the case of temperature, the supersaturation influences the amount of produced hydrates. From Table 5.4 it is possible to see that a slurry containing only 2.7% of

solids in weight is expected, which means that the supersaturation condition is barely reached. Dynamic thermal data from both experiments are presented in Figure 5.18 and Figure 5.19.

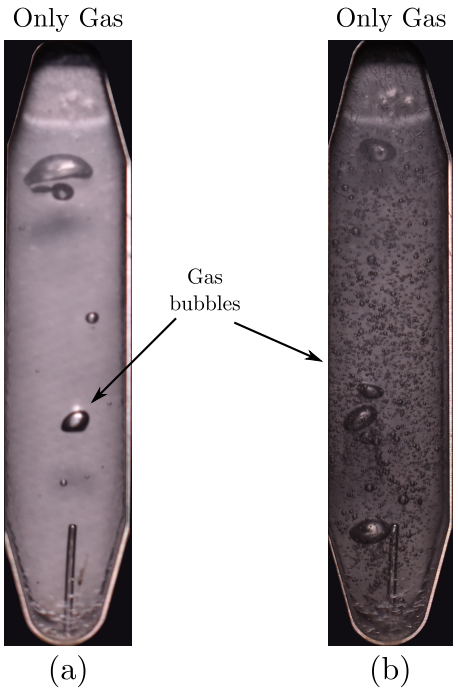



Figure 5.17 – Different regimes at different instants for experiments: (a) E-006; (b) E-007.

The behaviour of the system in experiments E-008 and E-009 is similar to what is observed in other experiments. Small temperature increases in both Figure 5.18 and Figure 5.19 are observed, and are a result of either gas hydration or simply gas dissolution in water. The temperature increase in experiment E-008 is larger than in experiment E-009, which again could be due to the increase of the amount of dissolved carbon dioxide, or due to hydration. The pressure increase in experiment E-008 is much lower than observed in experiment E-001, meaning that lower amounts of hydrates are being produced, and so the driving force for the precipitation can be reduced.

The question of whether the temperature increase is due to dissolution or hydration can be answered by analysing the different instants in the visualization window, as presented in Figure 5.20.

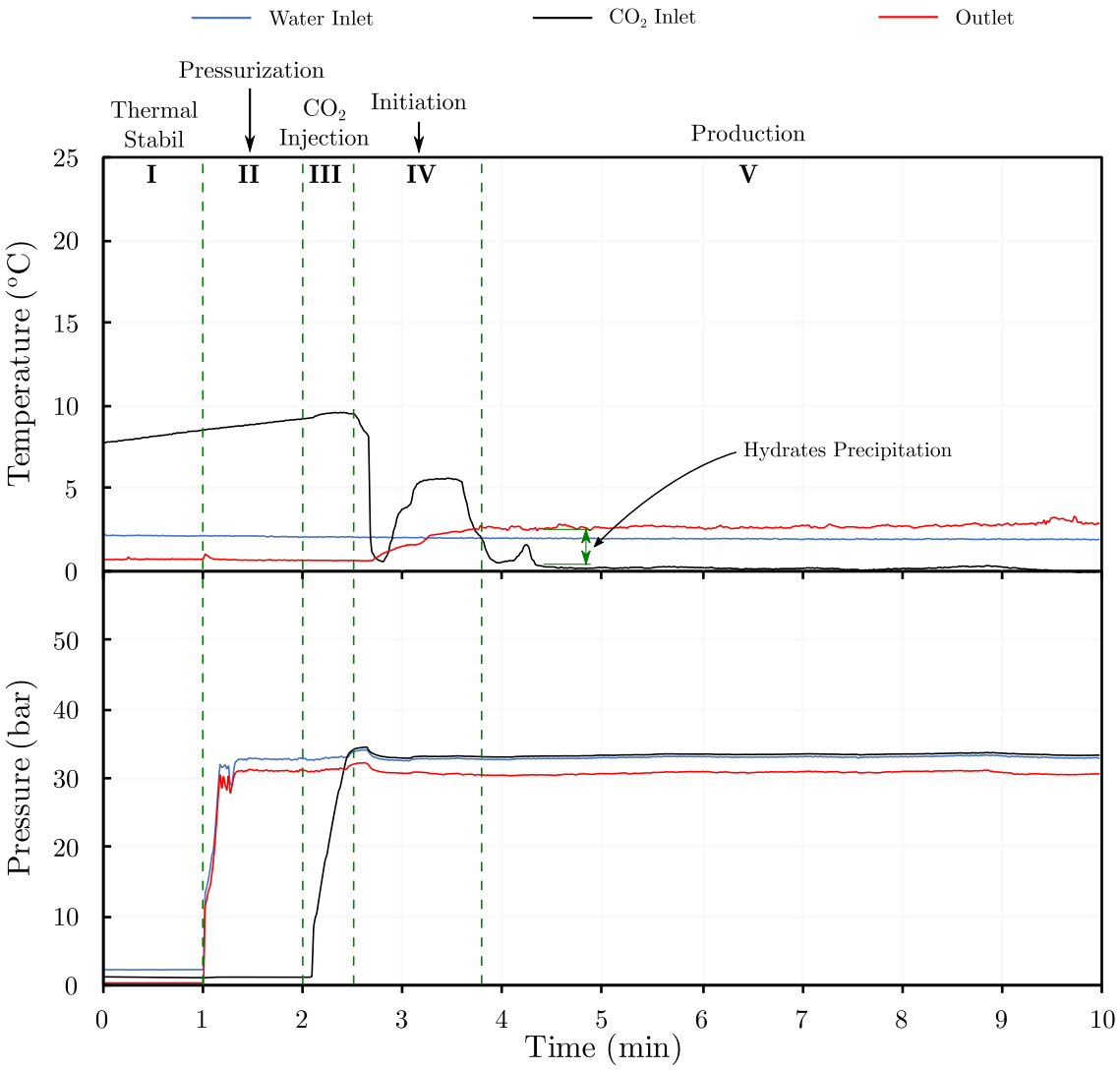



Figure 5.18 – Temperature and pressure profiles for experiment E-008.

Figure 5.20a shows that hydrates are formed in experiment E-008. However, the amount is significantly lower than in experiment E-001. In Figure 5.20b, no hydrates or gas are visible, as expected. The supersaturation condition is not reached, and thus, all the gas introduced to the system is dissolved.

The weight fraction of solids at the outlet determined from the energy balance is near 5.9%, which is lower than the value obtained for experiment E-001, as expected. Although the value still deviates from the theoretical one of 2.7%, the reduction of the concentration of hydrates predicted gives consistency to the model, which is capable to predict these variations, within the error associated to the temperature measurement.

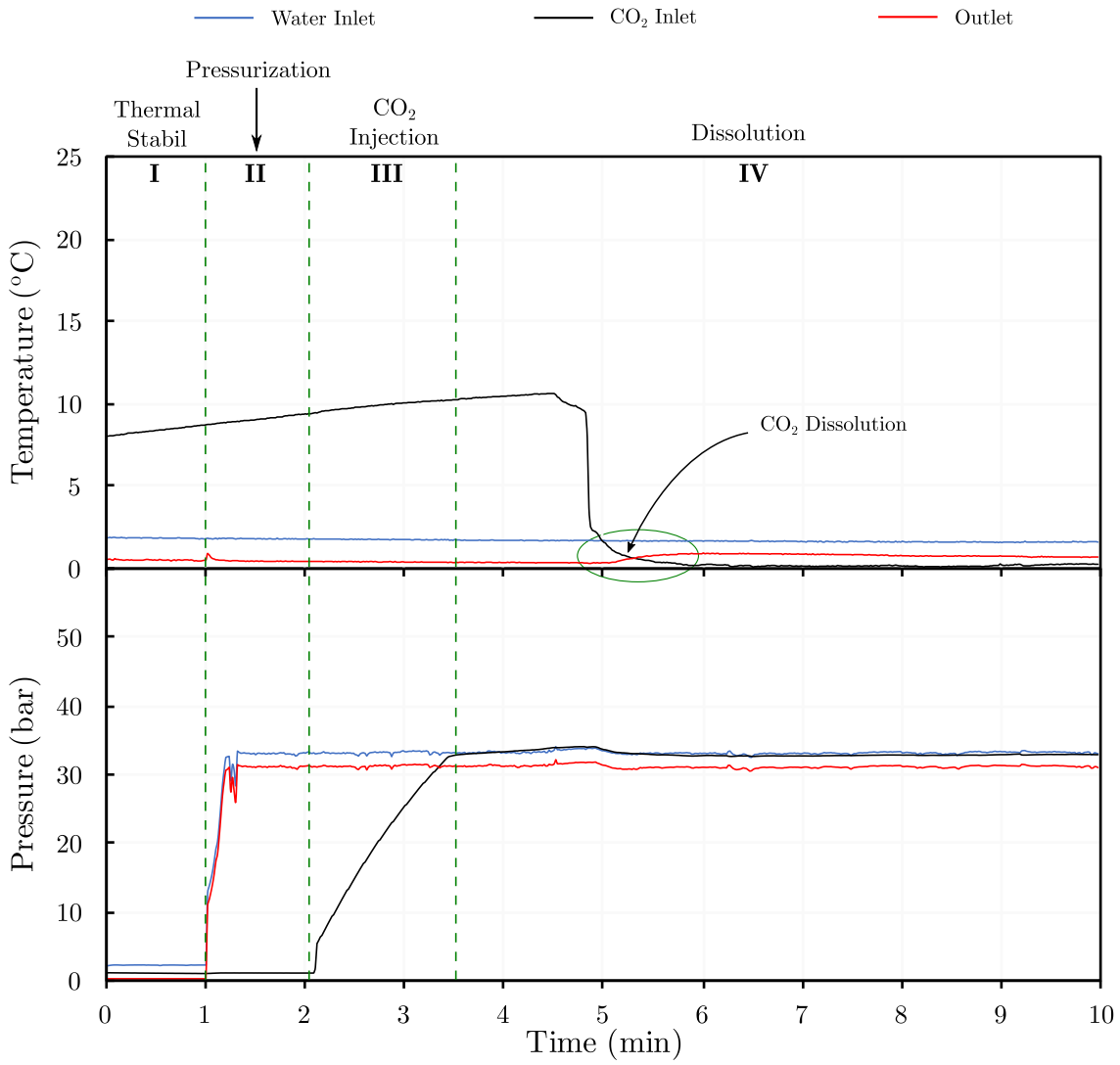



Figure 5.19 – Temperature and pressure profiles for experiment E-009.

#### *5.5.1.5 Influence of Carbon Dioxide Source*

Experiment E-010 allows evaluating the influence of the introduction of carbon dioxide in its liquid state, rather than in its gas state. To do so, the pressure of the system must be significantly increased to values in the range of 50 bar. The pressure increase should not have any other implication regarding the equilibrium, since the temperature is kept at 2 °C. Dynamic data for experiment E-010 is presented in Figure 5.21.

The dynamic behaviour observed in Figure 5.21 is similar to the other experiments. The procedure for pressurization is slightly different than in the experiments using

gas, due to the instability of system to keep the liquid carbon dioxide flow rate constant at operable pressures.




Figure 5.20 – Different regimes at different instants for experiments (a) E-008; (b) E-009.

The main conclusion from Figure 5.21 is that the beginning of precipitation occurs latter than when using gas. This may be due to the relatively poor mixing conditions when compared to the use of gas. The reduction of the density of the liquid (near 10 times less dense that gaseous carbon dioxide) results in lower velocities inside the mixing chambers. This is indicated by the lack of temperature increase when carbon dioxide is injected, which would be expected due to dissolution. However, the influence of the inlet temperature of carbon dioxide does not seem to have the same importance as when using gas. At 7.5 minutes, hydrates start to form, as indicated by the temperature and pressure drop increase.

Images from the visualization window are presented in Figure 5.22

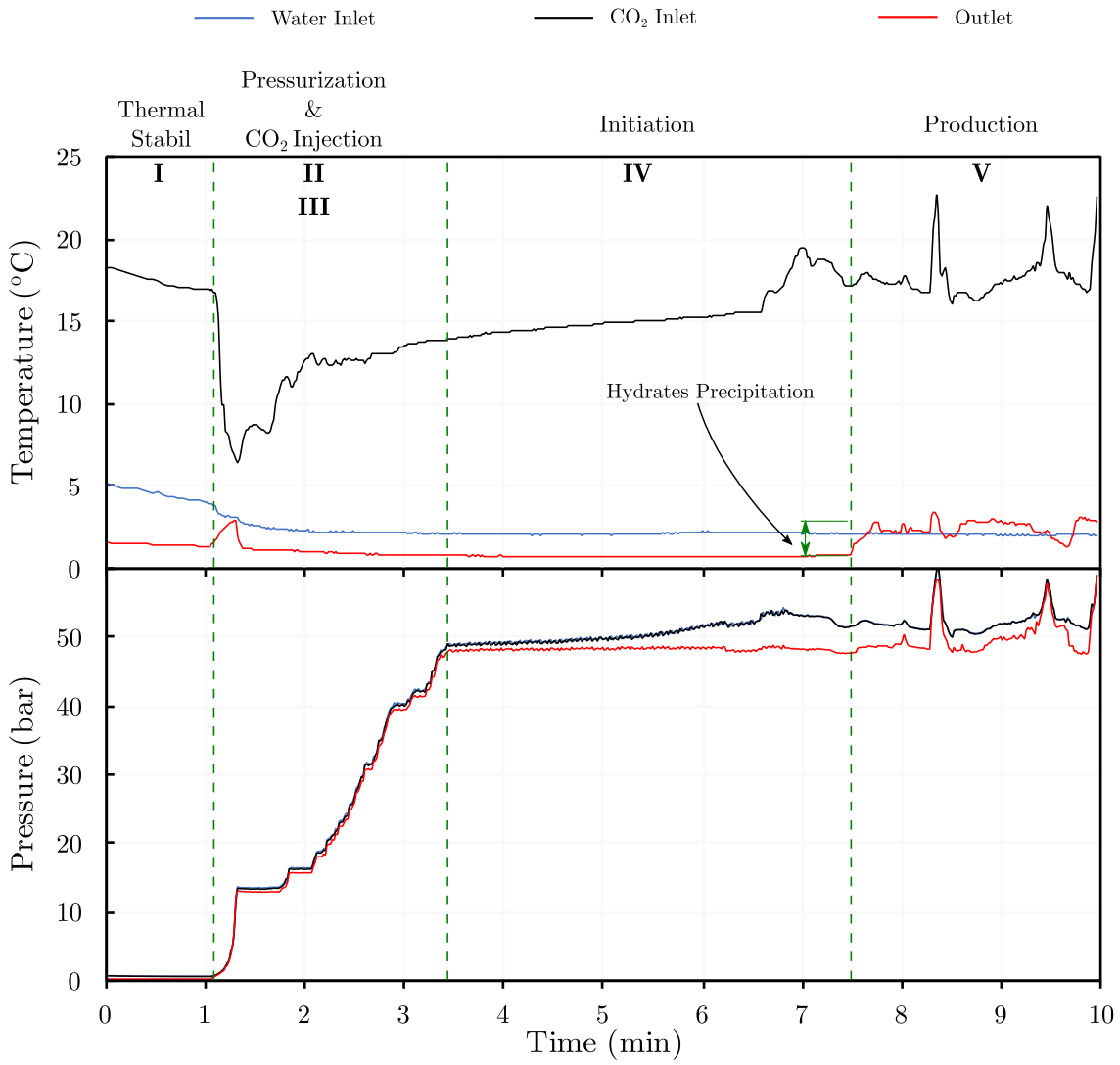



Figure 5.21 – Temperature and pressure profiles for experiment E-010.

Figure 5.22 shows that the behaviour of the hydrates produced are different than in experiment E-001. In this experiment, no rods due to the tubing are observed. On the contrary, the solids appear to be more dispersed in water, resulting in the structure observed in Figure 5.22c. With this structure, the slurry has lower tendency to clog the tubing. This is also observed from the pressure drop increase that is significantly lower than in other experiments. Also, the reduction of the pressure drop could be the result on the need of the system of lower driving force, since mixing two liquids is considerably easier than mixing gas and liquid.

The weight fraction of solids at the outlet determined from the energy balance is close to 17.8%, closer to the expected value of 22%.

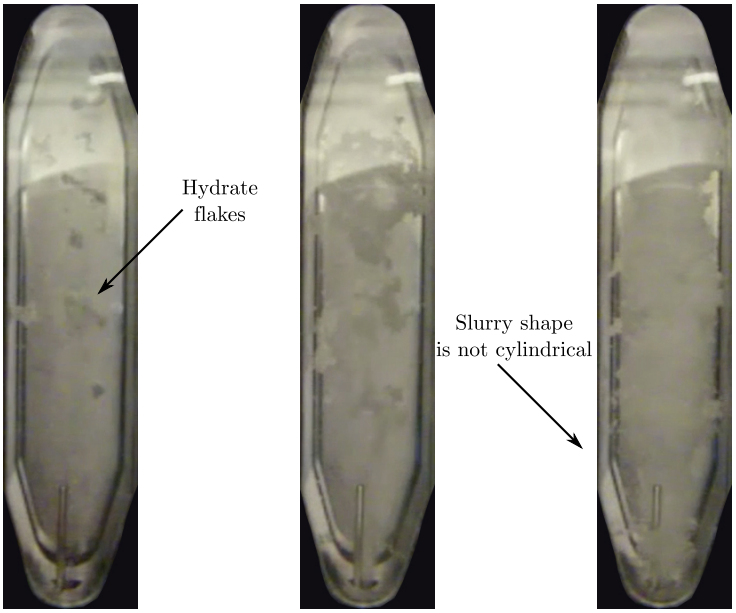



Figure 5.22 – Different regimes at different instants for experiment E-010 at different times: (a) beginning of precipitation; (b) a few seconds after beginning; (c) constant production.

#### *5.5.1.6 Influence of THF*

The addition of thermodynamic promoters such as tetrahydrofuran shifts the equilibrium curve to less harsh conditions. The effect of THF has been widely studied for pure carbon dioxide hydrates using thermodynamic cells (Delahaye et al. 2006, Lirio and Pessoa 2013). Delahaye et al. (2006) evaluated the influence of the concentration of THF and observed reductions of the equilibrium pressure of approximately ten times.

In experiments E-011 to E-013, 1% molar of THF was added to the water to decrease the equilibrium pressure. In these experiments, the pressure was decreased from 30 bar to 10 bar. The models from Section 5.2 and 5.3 are not valid for the conditions of these experiments.

The presence of THF alters the hydrate equilibrium by being incorporated in their structure. However, the amount of THF introduced in a system using carbon dioxide is still unclear, so no flash calculation is possible. Furthermore, the hydration heat released in the presence of THF almost doubles, according to some studies (Delahaye et al. 2006). Therefore, it is not possible to either estimate the amount of hydrates

produced in these experiments, and to perform the energy balance to the microNETmix unit.

For simplicity, and since the behaviour of the three experiments are quite similar, dynamic thermal data of experiment E-011 only is shown in Figure 5.23, being the remaining presented in Appendix D.

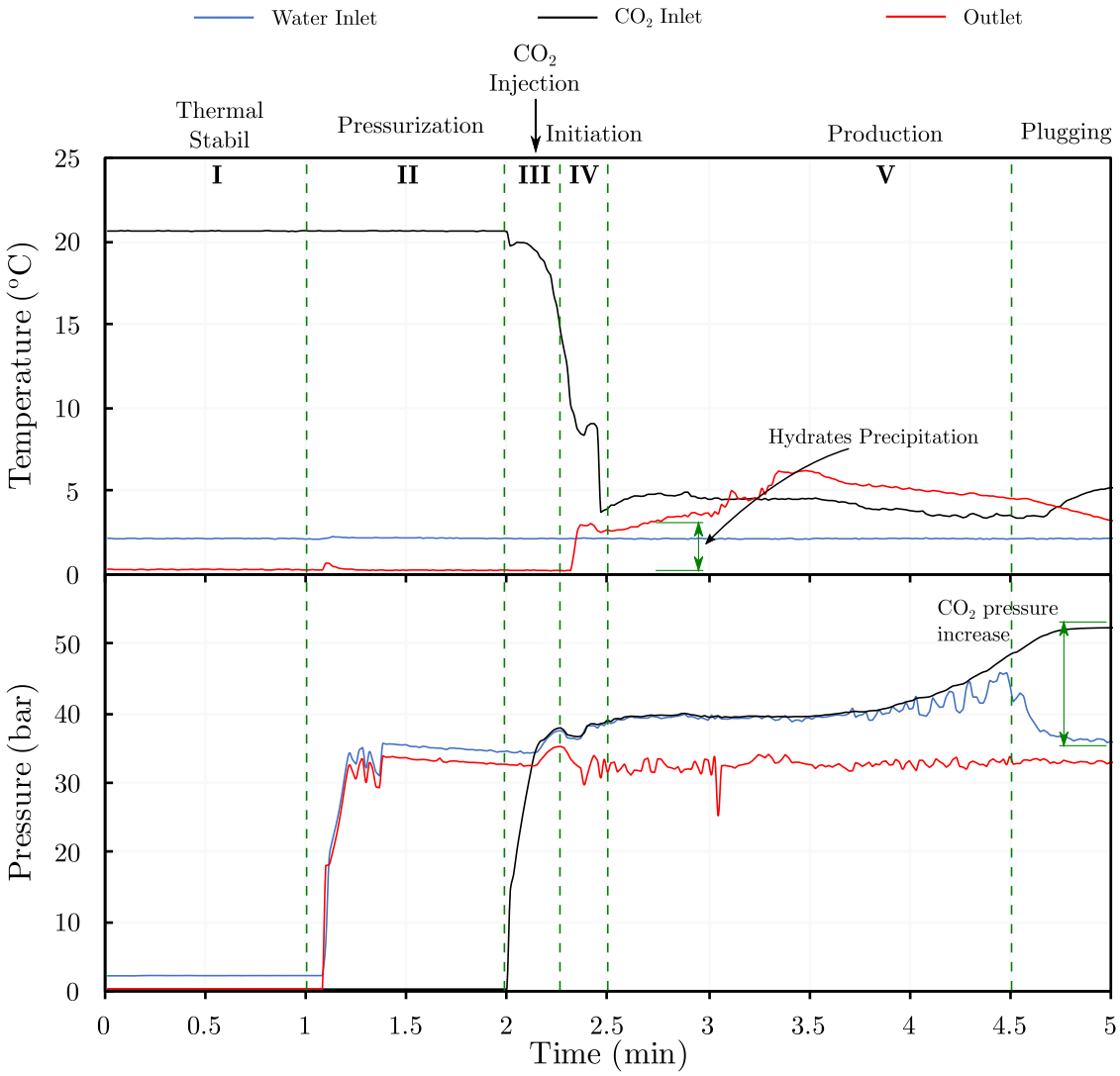



Figure 5.23 – Temperature and pressure profiles for experiment E-011.

Figure 5.23 shows a behaviour that is slightly different than previously observed. Firstly, the duration of the experiment is reduced to half due to the carbon dioxide line pressure increase. Again this may be the result of ice formation, since THF can increase the freezing point of water (DDBST), or due to the formation of hydrates in

the carbon dioxide line since THF significantly promotes the hydrates formation, or both effects combined.

The instant at which hydrates start to be produced is identified by the temperature increase at the outlet. The beginning of the hydrates precipitation is almost instantaneous after carbon dioxide is introduced in these experiments, thus confirming the promoting capacity of THF. The pressure drop in the microNETmix unit also increases.

The behaviour presented by experiments E-012 (Figure D.1) and E-013 (Figure D.2) is similar to the behaviour presented by experiment E-004, performed at lower pressure. A difference is that unlike in experiment E-004, addition of THF in an experiment at 10 bar results in the formation of hydrates, thus confirming that tetrahydrofuran can reduce the equilibrium pressure. The effect of the volume decrease may also explain why the pressure upstream the microNETmix unit is approximately 40 bar in these three experiments, while the pressure downstream is being decreased from experiment to experiment.

Images from the visualization window are presented in Figure 5.24. The appearance of the solids produced in experiments E-011 to E-013 is similar to the ones obtained in previous experiments. A jet of hydrates is formed with the shape of the tubing that is connected to the visualization window. The jet however does not keep its shape through the window, as it happened in other experiments. At the top, the slurry tends to disaggregate from the rod-shaped structure creating the blurred region observed in Figure 5.24. This difference may be caused by the potential change of the hydrate structure since THF may be part of the hydrate structure (Sloan and Koh 2007).

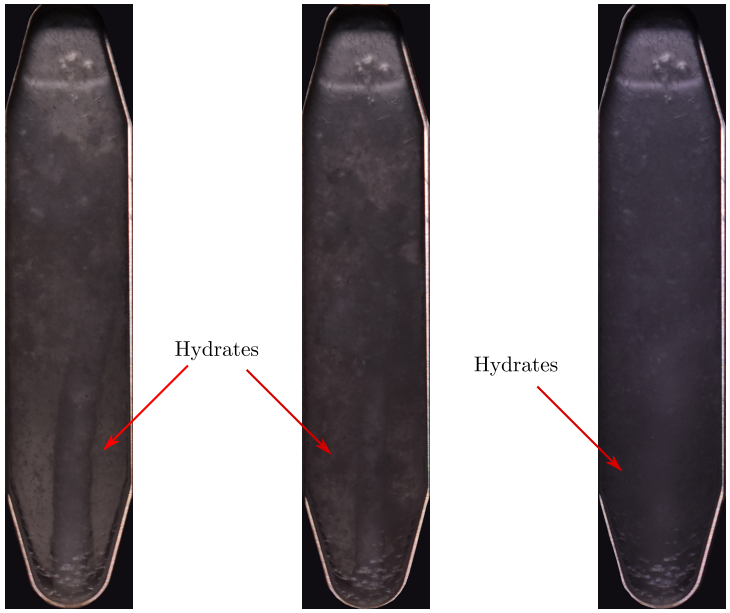



Figure 5.24 – Different regimes at different instants for experiments: (a) E-011; (b) E-012; (c) E-013.

### 5.5.2 Global Heat Transfer Coefficient

The energy balance to the cooling fluid allows the determination of an average global heat transfer coefficient, using the following equation

$$\left\langle U \right\rangle_t = \frac{1}{A_{\text{transf}} t_{\text{exper}}} \int_{t=0}^{t_{\text{exper}}} \frac{\dot{q}_{\text{cf}}\left(t\right)}{\Delta T_{\text{lm, NETmix}}} dt \tag{5.71}$$

where $A_{\text{transf}}$ is the area of heat transfer between the network plates and the cooling plates, and $\Delta T_{\text{lm, NETmix}}$ is an appropriate temperature difference, determined using an adapted version of Equation 3.15. The average global heat transfer coefficients for all experiments are compared in Figure 5.25. Two sets of values are presented in Figure 5.25. The global heat transfer coefficients determined when gas was introduced to the system (forming or not hydrates) are represented in black, while the global heat transfer coefficient for water only is represented in white. The global heat transfer coefficients obtained experimentally present deviations from the values expected from the resistance model in Section 4.4. It is important to note that the errors from temperature measurements also have an impact on these results, which may be the reason for this deviation. On the other hand, the fact that the values obtained

experimentally are larger than the theoretical indicates that significant amounts of heat are transferred through conduction in some regions that were not accounted for, such as the lateral areas of the network unit cells.

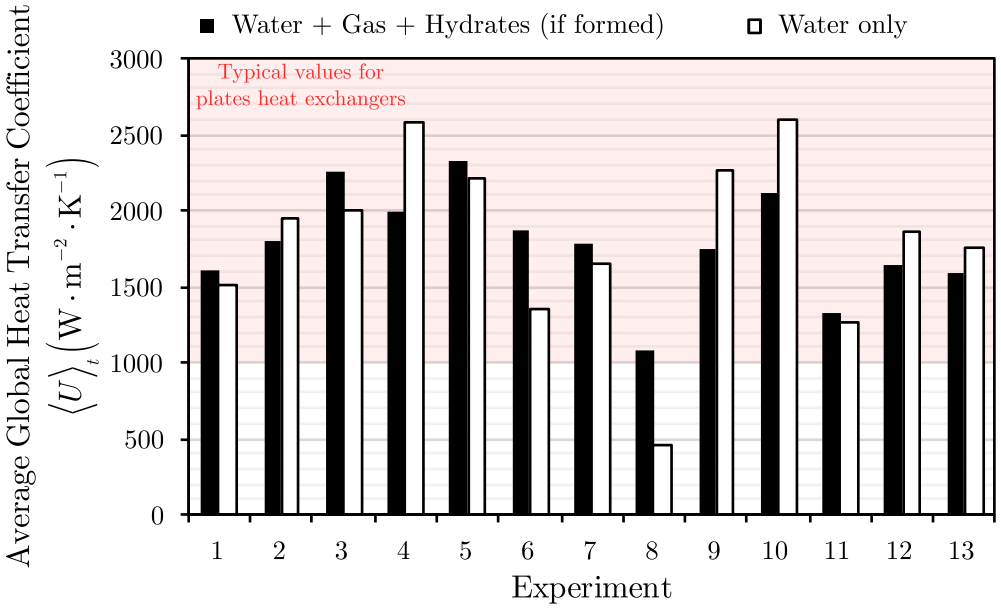



Figure 5.25 – Average global heat transfer coefficient for the different experiments.

The first three experiments result in an increase of the global heat transfer coefficient due to the increase of the coolant flow rate, and the respective increase of the convective rate at the cooling side. The amount of gas does not seem to have a significant impact on the global heat transfer coefficient, being expected that homogeneous liquid heat transfer presents similar values of heat transfer coefficient. Global heat transfer coefficients values from water only does not present a trend when compared with the values obtained in the presence of gas and hydrates. In general, the global heat transfer coefficients in the presence or not of hydrates present values of the same order of magnitude, thus allowing concluding that the major heat transfer resistances are in the cooling plates side or in the plate side through conduction. Again, this conclusion is based on the results obtained experimentally, that can be misleading and within the error of the temperature measurement.

An important result that Figure 5.25 brings to attention is that, as expected, the global heat transfer coefficients are within the range of the coefficients featured by plate heat exchangers.

### 5.5.3 Solid Material Properties

One problem regarding hydrates characterization is their instability at ambient conditions (Stern et al. 2001). Some authors have disclosed the existence of a phenomenon called hydrates self-preservation (Stern et al. 2001, Sloan and Koh 2007), at which hydrates reach a metastable phase at temperatures below ice point and atmospheric pressure and others (Kuhs et al. 2004) suggest that by depressurizing the hydrates at low temperatures, an ice coating layer is formed, controlling the release of the gas from the framework. This significantly reduces the kinetics of the dissociation, which allows the characterization of the materials.

Since no significant changes from different experiments were obtained regarding solids morphology, solid samples obtained at the same conditions of experiment E-001 are analysed.

#### *5.5.3.1 Stabilization of Hydrate Samples*

The first attempt to assess the capacity of the hydrates to keep their solid characteristics at low pressure was done by rapidly decrease the pressure of the visualization window while containing hydrates. The result from this attempt is registered in Figure 5.26.

By abruptly decreasing the pressure (which is done by shifting valve V-14 to recirculation mode), the hydrates have a thermodynamic tendency to dissociate into water and gas. However, this stage requires energy since the dissociation is endothermal. The fact that water is in contact with the hydrate, eases the heat transfer to dissociate the hydrate. The depressurization from Figure 5.26 is done at the working temperature, which is higher than the ice point of water. The fact that no ice layer can be formed, and that large amounts of water are in direct contact with the solid hydrate, results in a quick dissociation of the solid. In the last image of Figure 5.26, it is possible to see that 25 seconds after the pressure reduction, the solid is completely dissociated in water and gas.

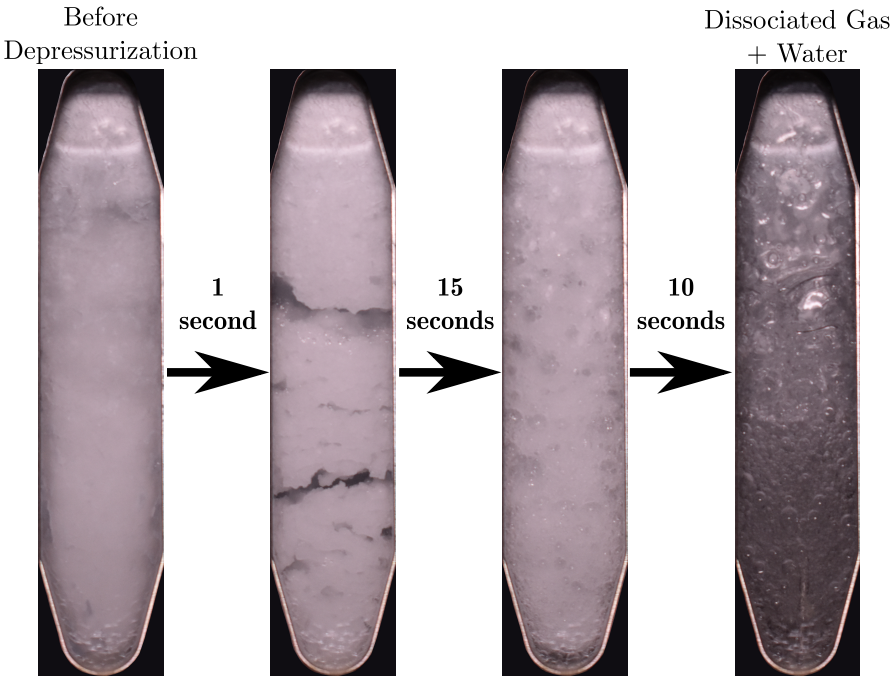



Figure 5.26 – Gasification due to depressurization.

A second attempt is done by using the filtration column E-11. This setup is designed in a way that it is possible to separate this column from the remaining setup, keeping unchanged the pressure inside. The filter inside the column allows the concentration of the solids in the column, eliminating most of the water. The solid obtained directly from depressurization of the column at ambient pressure has the shape of the column, as it is visible in Figure 5.27.



Figure 5.27 – Gas hydrate obtained from filtration column E-11 after depressurization in cold conditions.

A third attempt was done by storing the pressurized column at low temperature (in a refrigerator, at approximately -20 °C). After some time, the column is depressurized and the solid, also with the shape of the column, is obtained.

### *5.5.3.2 Hydrate Dissociation*

Dissociation tests as described in Section 5.4.3.1 are performed. The weight loss as a function of the time is represented in Figure 5.28 for different samples with different cooling times. The hydration number is represented in the secondary vertical axis. In one of the samples, the solid was obtained by depressurizing the column at ambient temperature, while the other samples were cooled for 2 hours and 2 days, respectively.

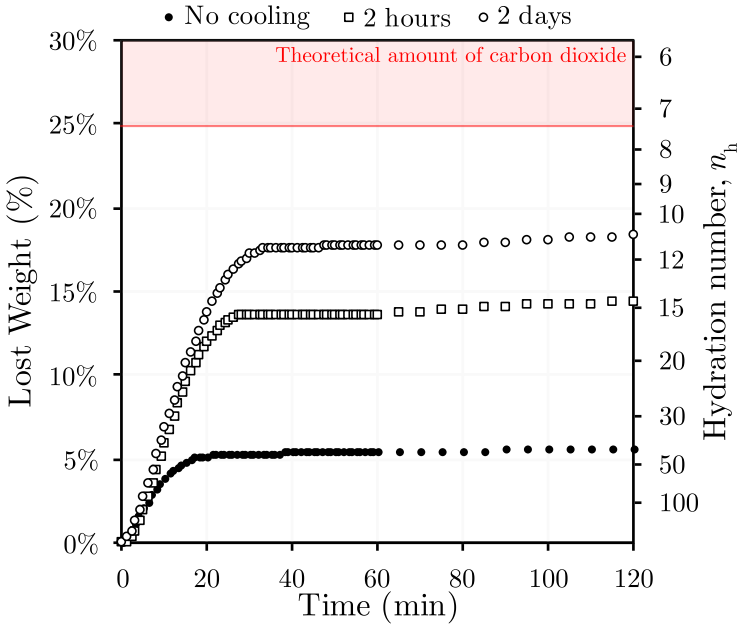



Figure 5.28 – Dissociation tests for different amounts of cooling time.

Figure 5.28 shows very interesting results. Samples produced at the same conditions, but depressurized at different conditions, result in different gas uptakes. In the first minutes, the weight reduction of the sample is very fast. Almost 80% of the total weight loss occurs in the first 5-10 minutes. The slope of the curves in these first minutes is very similar in all samples, meaning that the dissociation kinetics is not significantly changed, since it is controlled by heat transfer to the environment. A second stage is obtained when, after this large weight loss, the curve reaches a

constant value, which takes approximately 40 minutes in all samples. After 40 minutes, the weight reduces again at a much lower pace. Images of the sample holder for samples stored for 2 days are presented in Figure 5.29 for different time instants.

Figure 5.29 shows that dissociation is fast at the beginning, and occurs at the bottom of the sample holder, which is in contact with the sample and with the weighing scale. The solid's size is being gradually reduced in the first 40 minutes, resulting the small amounts of water at the bottom of the sample holder that is bubbling due to the release of carbon dioxide. Although most of the weight is lost in these first 40 minutes, that does not coincide in the complete dissociation of the hydrate into water and carbon dioxide. The reason for this may be due to the limited amount of heat that is transferred to the sample that may result in the formation of ice. Therefore, the solid sample that is being gradually reduced in size, may also be being transformed in ice, while carbon dioxide is released. The constant step after 40 minutes coincides with the melting of the solid into water. The fact that during this step, no mass changes occur, means that the process taking place at this stage is ice melting and no hydrate dissociation. Hydrate dissociation is limited to the first 30-40 minutes. At the end, more weight loss occurs, probably due to evaporation of water.

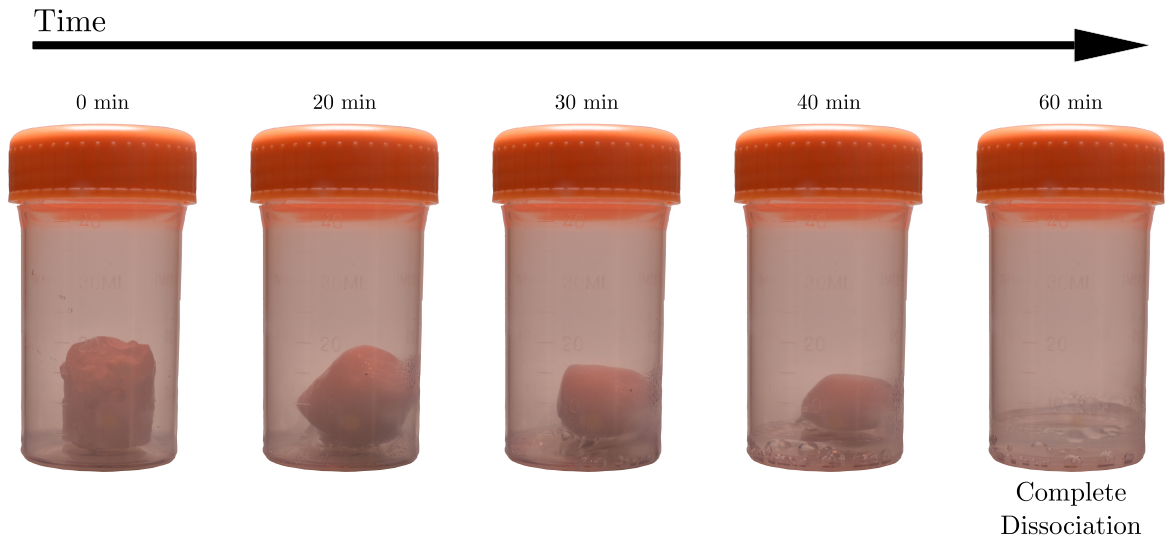



Figure 5.29 – Dissociation progress with time.

The effect of radiation is also assessed, by performing a dissociation test in conditions at which radiation is reduced, by covering the weighing scale with tin foil. The results are presented in Figure 5.30.

Figure 5.30 shows that the reduction of the radiation results in slower kinetics, as illustrated by the slope decrease in the first 40 minutes. This is in agreement with the fact that hydrates are very dependent on the heat transfer rate to either dissociate or precipitate.

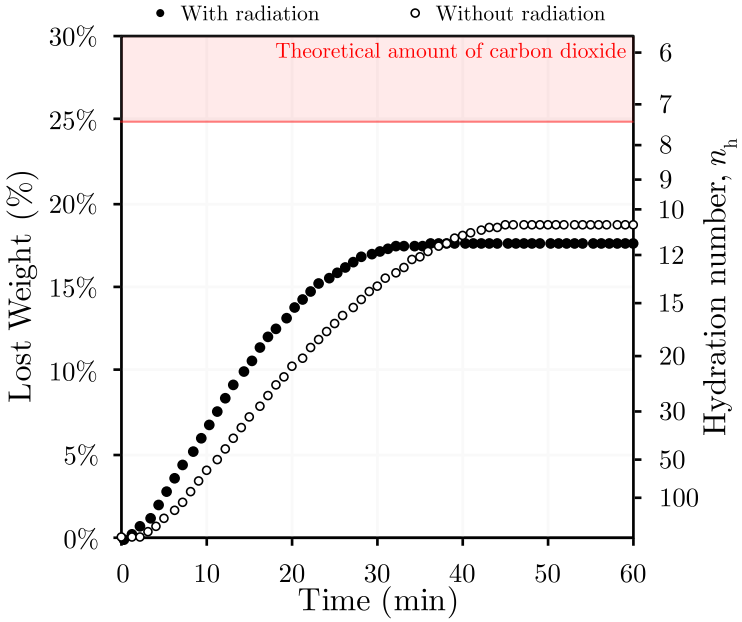



Figure 5.30 – Effect of radiation on the hydrate dissociation for samples cooled for 2 days.

These results are of high importance, because they indicate that the depressurization process is very important to determine the amount of gas that is stored. Depressurizing at ambient temperature results in a partial dissociation inside the column and results in the formation of large amounts of ice. If this depressurization is done at low temperatures, the amount of stored carbon dioxide is significantly enhanced, nearly three times. This results in a maximum hydration number of approximately 9.9. However, this is not the hydration number obtained locally during production, but after depressurization and after partial dissociation at the surface. The hypothesis of having a layer of ice that enables the gas to be trapped inside the framework seems to explain the behaviour observed in these tests.

The presence of ice can be detected from Figure 5.31 that shows the SEM imaging of the hydrate sample stored for two hours (Figure 5.31a) and common ice (Figure 5.31b).

As it can be seen, the surface of both samples has some similarities, indicating that ice is present at the surface of the two samples. Some white filaments are visible in both images, which can be the result of fracture sections of the solid. Also, the hydrate sample presents some holes in its structure that are not visible on the ice image. These structures may be formed due to the intense gasification that occurs during the handling of the sample. The gas has the thermodynamic tendency to escape from the solid, and the release produces these holes from which the solid molecules escape.

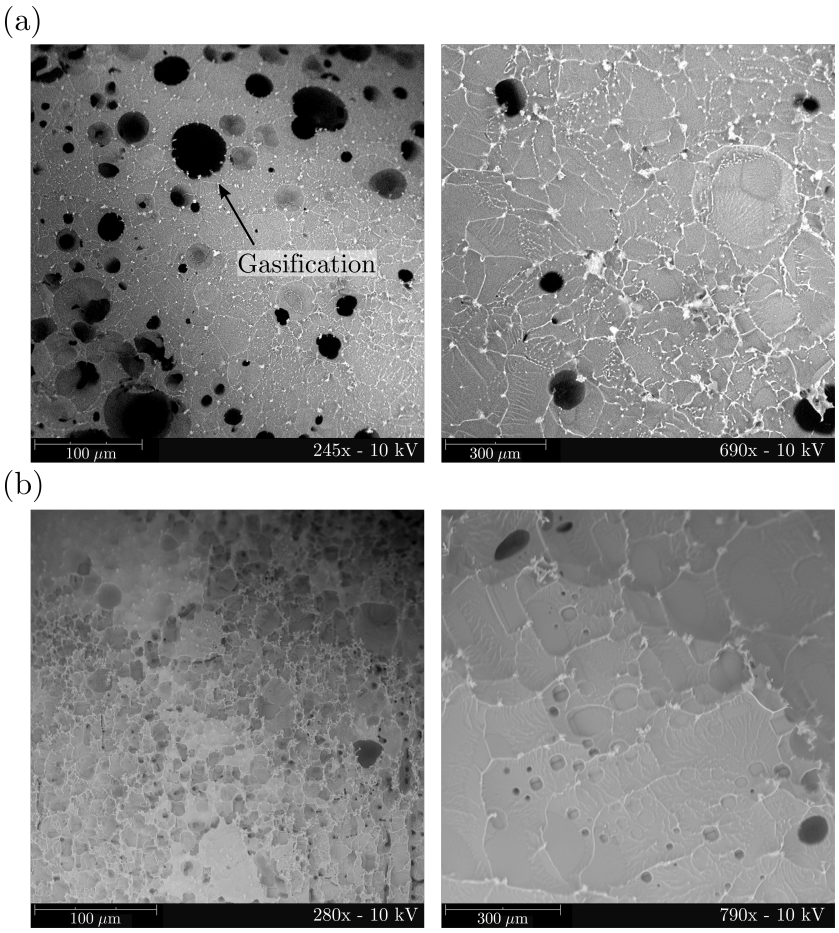



Figure 5.31 – SEM imaging for (a) carbon dioxide hydrate; (b) typical ice.

XRD patterns of two hydrates samples are presented in Figure 5.32. The pattern indicates that two different phases are present, and is in agreement with the pattern

observed by Makiya et al. (2010) for sI structure mixed carbon dioxide-ethanol hydrates. Typical hexagonal ice, together with sI structure hydrates can be detected from the pattern in Figure 5.32. Again, this confirms the theory that ice is formed during depressurization at low temperatures, but also that the hydrate structure is kept even though the thermodynamic conditions are not favourable.

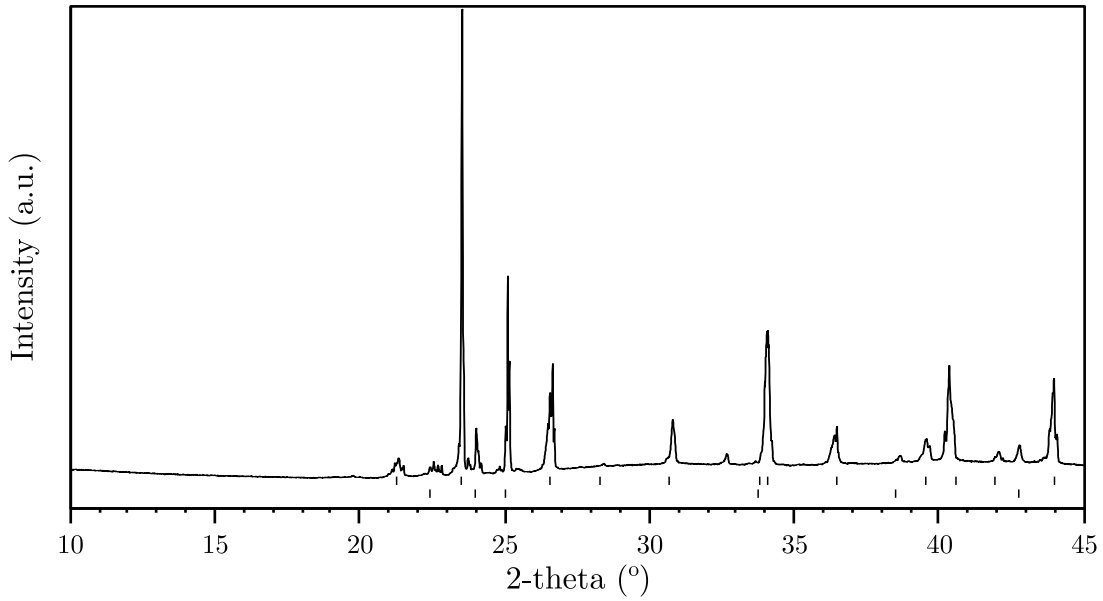



Figure 5.32 – XRD pattern for carbon dioxide hydrate sample cooled for two hours. Upper and lower ticks correspond to structure sI hydrate and hexagonal ice, respectively.

#### *5.5.3.3 Gas Uptake*

A first estimative of the gas uptake of the hydrate was done by determining the amount of weight that is lost during dissociation. However, this weight lost could be the result of water evaporation or gasification of the hydrate. By using a second method, it is possible to more accurately determine if the weight loss is due to carbon dioxide release or not.

The objective of this section is to verify if this methodology can be applied with success for the quantification of the carbon dioxide that is released from the hydrates. Therefore, this method was only applied for the sample stored for two days. The conditions and results of the technique are presented in Table 5.5.

The amount of calcium carbonate precipitated is about $2.18\,\mathrm{g}$. The amount of carbon dioxide is determined using

$$m_{CO_2} = m_{CaCO_3} \frac{M_{w,\,CO_2}}{M_{w,\,CaCO_3}} \tag{5.72}$$

where $m_{CO_2}$ and $m_{CaCO_3}$ are the mass of carbon dioxide and calcium carbonate respectively, while $M_{w,\,CO_2}$ and $M_{w,\,CaCO_3}$ are the molecular weight of carbon dioxide and calcium carbonate respectively, equal to 44.01 and 100.09 $\mathrm{g \cdot mol^{-1}}$.

Table 5.5 – Solutions conditions and amount of precipitated calcium carbonate for the sample cooled for two days.

| | |
|---|---|
| **Solution Volume (L)** | 2.25 |
| **$Ca(OH)_2$ Mass (g)** | 3.89 |
| **Hydrate Mass (g)** | 5.40 |
| **Precipitated $CaCO_3$ (g)** | 2.177 |

The amount of carbon dioxide determined from the data of Table 5.5 is $0.96\,\mathrm{g}$, which results in a weight fraction of 17.8%. This value is still far from the expected value from the hydration number (should be in the range of 25%-30% in weight of carbon dioxide). However, the value is quite similar to the values observed in the dissociation tests. From Figure 5.28, it is possible to observe that the amount of weight lost in the first 60 minutes, before complete ice melting occurs, is very similar to the value obtained from the precipitation of calcium carbonate, meaning that the amount of weight lost during dissociation is in fact due to carbon dioxide release. Also, this approach underestimates the amount of carbon dioxide, since some of the carbon dioxide is dissociated to ionic species, which are dissolved in water and do not precipitate in the form of calcium carbonate (as explained in Appendix C).

The handling problems observed in the dissociation tests are still present in this methodology. This methodology has proved to be interesting for the determination of carbon dioxide uptake in the hydrate. However, it has the major disadvantage of being extremely sensitive to the depressurization conditions.

## 5.6 Conclusions

The present chapter aims to prove that the NETmix technology is capable to produce carbon dioxide hydrates from water and carbon dioxide, at low temperature and high pressure. The high mixing intensity and high heat transfer rates presented by NETmix are used in favour of the production of hydrates, which are an extremely difficult process to execute, since it is a multiphase system that requires large heat transfer rates to avoid inhibition of the crystallization process. NETmix has been shown to present the capacity to produce large amounts of carbon dioxide hydrates in a continuous way.

A simplified thermodynamic model was created based on the solubility of carbon dioxide at low gas/water ratio. If the gas represents less than 30% in weight, then a two-phase system is obtained when thermodynamic equilibrium is reached. The amount of hydrates produced is directly related to the supersaturation level of the system, i.e., the amount of carbon dioxide in the system above its solubility in water. If heat is removed fast enough, then the extra amount of carbon dioxide precipitate in the form of gas hydrates, which, from the hydration number $n_h$, means that carbon dioxide's volume is reduced about 180 times when compared to carbon dioxide at 25 °C and 1 atm (STP). An energy balance model to a crystallization unit was developed, based on the unit streams enthalpies. The model allows the determination of the amount of produced carbon dioxide hydrates from the amount of heat that is absorbed by the cooling fluid in the unit.

In general, the results from experiments using the setup from Chapter 4 agree with those expected from the flash model:

- The cooling fluid rate does not have a significant influence on the amount of produced hydrates, meaning that the process is not strongly controlled by heat transfer in the NETmix device used in this thesis;
- The pressure has an important influence. At 20 bar, the driving force for gas dissolution and hydration is not enough to fully promote the nucleation and

crystallization of the hydrates, resulting in a mixture of hydrates and gas. Also, the increase of the pressure difference from the inlet and outlet of the microNETmix unit seems to indicate that a minimum driving force is required for the precipitation process at these conditions. This is also an indication that mass transfer has a significant impact on the kinetics of the process in the microNETmix unit, at Reynolds numbers near 200. The increase of the Reynolds number should be able to decrease mass transfer limitations, but decreases the residence time;

- The influence of the temperature is more relevant than the influence of pressure, since by increasing the temperature at constant pressure, the driving force for dissolution and hydration is reduced, and hydrates are not formed, even though the thermodynamic conditions are achieved;
- The reduction of the amount of carbon dioxide results in the expected behaviour. With the decrease of the gas, but still above supersaturation conditions, the amount of produced hydrates is significantly reduced. If the gas is below supersaturation conditions, then carbon dioxide is fully dissolved in water and no gas phase is obtained;
- The use of liquid carbon dioxide does not significantly alter the process, having only an influence on the rate that hydrates start to nucleate;
- The use of THF to decrease the equilibrium pressure results in an intense formation of gas hydrates with morphological characteristics slightly different than those produced in the absence of THF.

The obtained solids are capable to hold a significant part of the carbon dioxide in its structure if depressurization of the system is done at low temperatures. In general, hydrates held more carbon dioxide when the solid is stored for longer periods of time at low temperatures prior to depressurization. This is due to the self-preservation effect that occurs at low temperatures, probably due to the formation of a layer of ice at the surface of the solid, which represents a resistance to carbon dioxide release. The presence of ice was detected from XRD patterns and confirmed from SEM analysis of the surface of the solid material. Dissociation tests have shown that the

amount of gas is dependent on the depressurization conditions and have also shown that the limitation of heat transfer to the solid slows down the dissociation kinetics.

The use of a technique based on the precipitation of calcium carbonate to determine the amount of carbon dioxide in the hydrate proved to be promising for a more accurate measurement of the gas uptake. The use of this technique allowed the conclusion that the weight lost during dissociation is due to carbon dioxide release. However, the handling of the hydrate before introducing it in the calcium hydroxide solution, leads to partial gasification. The result from this technique agrees with the weight lost from dissociation.

The global heat transfer coefficients determined experimentally are in agreement with the values expected and presented in Chapter 4, in the range of $1000 - 2000\ \mathrm{W \cdot m^{-2} \cdot K^{-1}}$, the same range featured by plate heat exchangers. The presence of multi-phase flow does not seem to significantly enhance heat transfer in the microNETmix unit, although this conclusion may be misleading due to the errors associated with the temperature measurement.

## 5.7 References

AdP, "Águas do Porto". *Published online at aguasdoporto.pt.* Available at: http://www.aguasdoporto.pt/rede-publica - 39.

Anderson, G.K., **2002**. "Solubility of Carbon Dioxide in Water under Incipient Clathrate Formation Conditions". *Journal of Chemical & Engineering Data* 47, 219-222.

Anderson, G.K., **2003**. "Enthalpy of Dissociation and Hydration Number of Carbon Dioxide Hydrate From the Clapeyron Equation". *The Journal of Chemical Thermodynamics* 35, 1171-1183.

Ballard, A.L. **2002**. "A Non-Ideal Hydrate Solid Solution Model For a Multi-Phase Equilibria Program" [*Ph.D Thesis*]. Golden, CO, USA: Department of Chemical and Petroleum-Refining Engineering, Colorado School Of Mines.

Carroll, J.J., Slupsky, J.D., Mather, A.E., **1991**. "The Solubility of Carbon Dioxide in Water at Low Pressure". *Journal of Physical and Chemical Reference Data* 20, 1201-1209.

DDBST, "Saturated Vapor Pressure". *Published online at DDBST GmbH.* Available at:

http://ddbonline.ddbst.com/AntoineCalculation/AntoineCalculationCGI.exe?component=Carbon+dioxide.

DDBST, "Solid-Liquid Equilibrium Data". *Published online at DDBST GmbH.* Available at: http://www.ddbst.com/en/EED/SLE/SLE Tetrahydrofuran%3BWater.php.

Delahaye, A., Fournaison, L., Marinhas, S., Chatti, I., Petitet, J.-P., Dalmazzone, D., Fürst, W., **2006**. "Effect of THF on Equilibrium Pressure and Dissociation Enthalpy of $CO_2$ Hydrates Applied to Secondary Refrigeration". *Industrial & Engineering Chemistry Research* 45, 391-397.

Diamond, L.W., Akinfiev, N.N., **2003**. "Solubility of $CO_2$ in Water From −1.5 to 100 °C and From 0.1 to 100 MPa: Evaluation of Literature Data and Thermodynamic Modelling". *Fluid Phase Equilibria* 208, 265-290.

Duan, Z., Hu, J., Li, D., Mao, S., **2008**. "Densities of the $CO_2$–$H_2O$ and $CO_2$–$H_2O$–NaCl Systems Up to 647 K and 100 MPa". *Energy & Fuels* 22, 1666-1674.

IN, "IN - Institute of Nanoscience and Nanotechnology". *Published online at IN - Institute of Nanoscience and Nanotechnology.* Available at: http://www.in-nano.net/.

Kuhs, W.F., Genov, G., Staykova, D.K., Hansen, T., **2004**. "Ice Perfection and Onset of Anomalous Preservation of Gas Hydrates". *Physical Chemistry Chemical Physics* 6, 4917-4920.

Larson, S.D. **1955**. "Phase Studies of the Two Component Carbon Dioxide-water System Involving the Carbon Dioxide Hydrate" [*Ph.D Thesis*]. Urbana-Champaign, IL, USA, University of Illinois.

Lirio, C.F.S., Pessoa, F.L.P., **2013**. "Enthalpy of Dissociation of Simple and Mixed Carbon Dioxide Clathrate Hydrate". *Chemical Engineering Transactions* 32, 577-582.

Ma, Z.W., Zhang, P., Bao, H.S., Deng, S., **2016**. "Review of Fundamental Properties of $CO_2$ Hydrates and $CO_2$ Capture and Separation Using Hydration Method". *Renewable and Sustainable Energy Reviews* 53, 1273-1302.

Makiya, T., Murakami, T., Takeya, S., Sum, A.K., Alavi, S., Ohmura, R., **2010**. "Synthesis and Characterization of Clathrate Hydrates Containing Carbon Dioxide and Ethanol". *Physical Chemistry Chemical Physics* 12, 9927-9932.

Mullin, J.W., **2001**. "Crystallization", 4th ed. Butterworth-Heinemann, Oxford, UK.

Ng, H.-J., Robinson, D.B., **1985**. "Hydrate Formation in Systems Containing Methane, Ethane, Propane, Carbon Dioxide or Hydrogen Sulfide in the Presence of Methanol". *Fluid Phase Equilibria* 21, 145-155.

NIST, "Carbon Dioxide". *Published online at National Institute of Standards and Technology.* Available at: http://webbook.nist.gov/cgi/cbook.cgi?ID=C124389&Mask=4.

Robinson, D.B., Metha, B.R., **1971**. "Hydrates In the Propane-Carbon Dioxide-Water System". *Journal of Canadian Petroleum Technology* 10.

Sloan, E.D., Koh, C., **2007**. "Clathrate Hydrates of Natural Gases", 3rd ed. CRC Press, Boca Raton, FL, USA.

Smith, J.M., Van Ness, H., Abbott, M., **2005**. "Introduction to Chemical Engineering Thermodynamics", 7th ed. McGraw-Hill, New York, NY, USA.

Stern, L.A., Circone, S., Kirby, S.H., Durham, W.B., **2001**. "Anomalous Preservation of Pure Methane Hydrate at 1 atm". *The Journal of Physical Chemistry B* 105, 1756-1762.

Takenouchi, S., Kennedy, G.C., **1965**. "Dissociation Pressures of the Phase $CO_2 \cdot 5¾H_2O$". *The Journal of Geology* 73, 383-390.

Teng, H., Yamasaki, A., Shindo, Y., **1996**. "Stability of the Hydrate Layer Formed on the Surface of a $CO_2$ Droplet in High-Pressure, Low-Temperature Water". *Chemical Engineering Science* 51, 4979-4986.

Udachin, K.A., Ratcliffe, C.I., Ripmeester, J.A., **2001**. "Structure, Composition, and Thermal Expansion of $CO_2$ Hydrate from Single Crystal X-ray Diffraction Measurements". *The Journal of Physical Chemistry B* 105, 4200-4204.

van der Waals, J.H., Platteeuw, J.C., **1958**. Clathrate Solutions, in: Prigogine, I. (Ed.), Advances in Chemical Physics, 2007 Digital ed. John Wiley & Sons, Inc., Hoboken, NJ, USA, pp. 1-57.

# 6 $CO_2$ Hydrates – Cost Analysis

## 6.1 Introduction

CCS technologies applied in post-combustion power plants require the separation of carbon dioxide from flue gas. Transportation of carbon dioxide is often required to move it from the source site to the storage or injection site, depending on the final application (Figure 2.2). Prior to $CO_2$ transportation, it is necessary a preparation step for transport, where carbon dioxide is set to conditions that allow efficient transport.

The most efficient and common way of transporting $CO_2$ is by preparing it to supercritical conditions followed by transport through pipelines (Metz et al. 2005). Supercritical $CO_2$ has both the characteristics of gas and liquid phase. At high pressure, carbon dioxide presents large density (characteristic of liquids) and small viscosity (characteristic of gases), resulting in a high transportation efficiency, which leads to pipeline diameter reduction (as well as pipeline costs) and improving the throughput (Chen and Cao 2015). The transport of carbon dioxide under these conditions is preferred since it is safer (failure rate reduced from $0.0010\,\mathrm{km}^{-1}\cdot\mathrm{year}^{-1}$

in 1972 to $0.0002\,\mathrm{km}^{-1}\cdot\mathrm{year}^{-1}$ in 2002), than other alternative systems (Metz et al. 2005).

This work presents an alternative way of preparing carbon dioxide for pipeline transport, by producing an aqueous slurry of carbon dioxide hydrates, which results in a volume reduction, also leading to small pipeline diameter.

This chapter aims is to evaluate the costs of a process for the production of carbon dioxide hydrates in the form of a slurry, and its transportation through pipeline, and infer its potential application and economical feasibility. To better assess the impact of a hydrate-based technology for $CO_2$ transport, the costs for preparing $CO_2$ for transport are compared with the costs for preparing $CO_2$ to supercritical conditions, as well as the transportation costs in both methods. In both cases, a simplified cost analysis of a process at industrial scale is used.

Firstly, the strategy adopted for the cost analysis is described in Section 6.2. In Section 6.3, the process for the industrial production of carbon dioxide hydrates is presented and described. All considerations regarding the process are also presented in this section. The cost analysis of both production and transport of carbon dioxide hydrates are presented in Section 6.4. Cost comparison between the transport of carbon dioxide hydrates and transport of supercritical carbon dioxide is made in Section 6.5. This section also includes a few considerations regarding corrosion in the pipelines due to the presence of $CO_2$, as well as a comparison of the transport characteristics of both methods. The main conclusions from this chapter are presented in Section 6.6, while the references for the current section are presented in Section 6.7.

## 6.2 Strategy

The costs of the process can be divided in two types: CAPEX (or capital expenditure) that is related to the capital costs of a plant; and OPEX (or operational

expenditure), which is related to the on-going costs of the process. Both cost types will be estimated in the present analysis.

To reduce the influence of the plant productivity, the cost results are normalized by the amount of carbon dioxide treated (in $\text{ton} \cdot \text{h}^{-1}$). This way it ensures that OPEX is not influenced by the production scale. However, CAPEX usually depends on the scale. The calculation is done assuming a base of $100\ \text{ton} \cdot \text{h}^{-1}$ of treated $CO_2$

CAPEX costs were estimated considering only the direct costs related to equipment (not only the equipment cost, but also installation and logistics). The costs of buildings and other facilities are not accounted in the analysis. Direct equipment costs were estimated using the software Aspen Capital Cost Estimator (ACCE) from AspenTech™ (AspenTech), version v8.8. This cost estimation tool provides AACE Class IV through Class II capital costs for oil and gas, refining and chemical industries for the year of 2014 (AspenTech). NETmix unit costs were estimated based on the cost of the steel required for its construction.

OPEX costs were determined by considering only the energy requirements of the process. For that, Aspen Hysys (also from AspenTech™), version v8.8 is used. Aspen Hysys is a process simulation software that contains several standard unit operations that can be simulated. It also allows the customization of unit blocks, thus allowing the creation of new unit operations.

For an accurate determination of the energy requirements, an accurate thermodynamic model is required. To be coherent with the previous analysis, the thermodynamic package model SRK is used for the main streams of the process, while the thermodynamic package Glycol is used for the cooling fluid streams.

## 6.3 Process Description

The process simulated is illustrated in Figure 6.1.

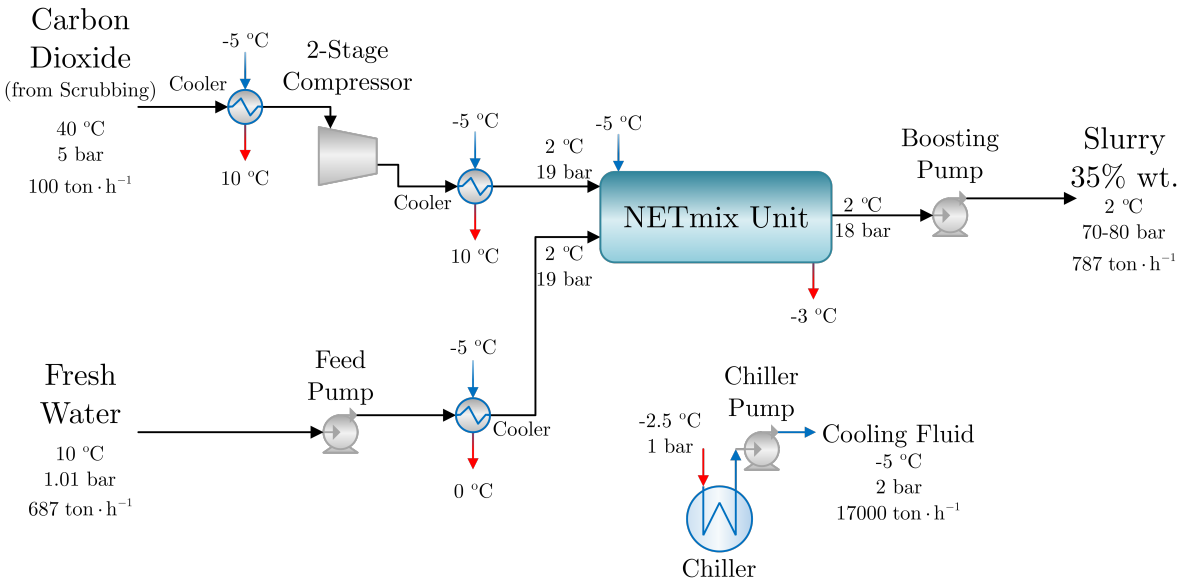



Figure 6.1 – Process diagram for production of a slurry of carbon dioxide hydrates.

The process has two inlet streams. The first stream is pure carbon dioxide fed at 40 °C and 5 bar, which are typical values for post-combustion power plants, one of the major applications of this technology, where flue gas is purified using scrubbers. The gas stream is then cooled to 2 °C in a shell-and-tube heat exchanger, prior to compression. The gas is compressed in a two-stage compressor up to 19 bar which is, as observed previously, inside the range of precipitation of hydrates. The number of stages of the compressor is defined by limiting the compression ratio of each stage to a maximum of 3, to avoid large temperature increase at the outlet of the compression stage (Hall 2012). Interstage and afterstage cooling are required, cooling the compressed gas to 2 °C.

Water is fed at 10 °C and 1 atm, and the flowrate set is enough to produce a slurry of 35% in weight. At these conditions, only liquid and solids are expected, and therefore, no vapour separator is required. The water stream is pressurized to 19 bar using a centrifugal pump, and is cooled to 2 °C using a shell-and-tube heat exchanger. No tetrahydrofuran is considered in the present analysis.

At this point, both streams are introduced in a NETmix unit to produce hydrates. In the present analysis, it is assumed that no heat and mass transfer limitations are verified. Flash models for the formation of hydrates are not available in Aspen Hysys,

and thus a custom block with the NETmix block using the hydrates flash model from Section 5.2.3 is used. The model assumes that equilibrium is obtained instantaneously and isothermal operation (i.e., the heat is completely removed from the unit).

A slurry containing 35% in weight of solids is obtained at the outlet. The pressure of the solids is raised to 70-80 bar using a pump. This is the pressure at which the hydrates are transported in pipelines.

All heat exchangers and the NETmix block require cool sources to decrease the temperature of the lines and to remove the hydration heat. This is done using an aqueous-based cooling fluid containing 25% in volume of ethylene glycol, which has an expected freezing point below -8 °C (EngineeringToolBox). The cooling fluid is typically fed to the heat exchangers at -5 °C, exiting with a temperature in the range of -3 to 10 °C. The cooling fluid is then fed to a vapour-compression refrigeration unit to cool the fluid back to -5 °C.

A pressure drop of 0.7 bar due to friction is considered in all heat exchangers (Edwards 2008), while a pressure drop of 1 bar is assumed in the NETmix block (Fonte et al. 2013). ASME method is used as the model for isentropic compressors with a global efficiency of 79.2%. Pump efficiency is assumed to be 81%. No pressure drop due to friction in piping was considered.

The process from Figure 6.1 requires: one NETmix unit with cooling capacity; one refrigeration unit (chiller); three centrifugal pumps; one two-stage compressor; and three shell-and-tube heat exchangers (plus a intercooler in the two-stage compressor).

The process from Figure 6.1 allows the treatment of $100\,\mathrm{ton}\cdot\mathrm{h}^{-1}$ of carbon dioxide. About 81% of the total fed carbon dioxide exits the process inside the hydrate framework, while the remaining is dissolved in water. This process allows the preparation of carbon dioxide for transportation at a distance of 100 km. After that, the slurry must be pressurized again using a pump, in a boosting station, up to 50 bar. These different steps are illustrated in Figure 6.2.

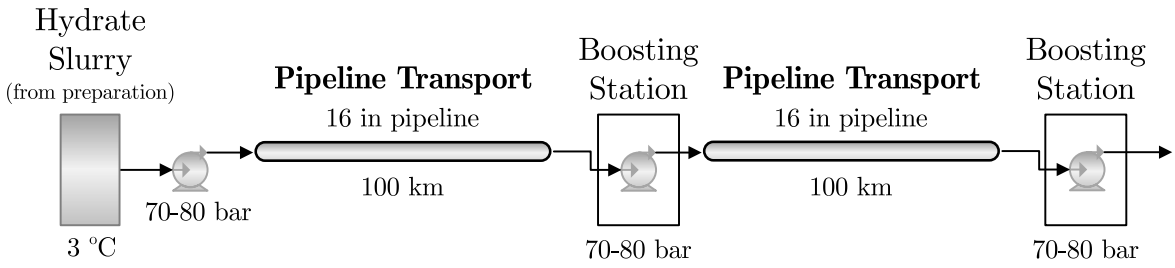



Figure 6.2 – Different steps for transportation of hydrate slurry via pipeline.

It is assumed that the slurry can operate at low pressure if the heat transfer rate from the environment is reduced. Therefore, high quality thermal insulation is required in the pipelines for transportation.

## 6.4 Cost Estimation

CAPEX costs were determined from the direct equipment costs of the plant. It is assumed that the plant has an economic lifespan of 30 years, and an interest rate of 4.5% is considered. The normalized CAPEX costs are determined using the following expression (Cussler and Moggridge 2011)

$$\text{CAPEX} = \frac{\sum_i C_{\text{equip},\,i}}{N_{\text{hours/years}} \dot{P}_{\text{CO}_2}} \frac{\left(1+r\right)^{N_{\text{years}}}}{N_{\text{years}}} \tag{6.1}$$

where $C_{\text{equip},\,i}$ is the direct cost of the equipment $i$, $r$ is the interest rate, $\dot{P}_{\text{CO}_2}$ is the productivity for carbon dioxide, expressed in tonnes per hour, $N_{\text{hours/years}}$ is the number of operating hours per years, considered to be 8760 hours per year in this analysis, and $N_{\text{years}}$ is the economical lifespan.

OPEX costs were determined based on the energy consumptions of all equipment. For the specific case of the refrigeration unit, a COP (coefficient of performance) of 6.5 is considered. COP is the ratio between of the useful cooling and the work provided by the compressor (Smith et al. 2005). The base price of electricity is $90\ \text{USD}\cdot\text{MWh}^{-1}$.

Equipment costs and energy requirements per type of operation units are presented in Table 6.1. Cost of the pipeline for the transportation of carbon dioxide as hydrates is not considered.

Table 6.1 – Equipment costs and energy consumption for the process of Figure 6.1.

| EQUIPMENT | DIRECT COSTS (MM USD) | ENERGY CONSUMPTION $\left(\mathbf{kWh \cdot ton_{CO_2}^{-1}}\right)$ |
|---|---|---|
| COMPRESSORS | 2.3 | 21.9 |
| PUMPS | 2.5 | 20.6 |
| HEAT EXCHANGERS | 1.6 | - |
| NETMIX | 0.5 | - |
| CHILLER | 1.5 | 61.8 |
| TOTAL | 8.4 | 104.3 |

From Table 6.1, a CAPEX and OPEX of $1.2\,\mathrm{USD \cdot ton_{CO_2}^{-1}}$ and $9.2\,\mathrm{USD \cdot ton_{CO_2}^{-1}}$, respectively, are obtained. The total value for the preparation of carbon dioxide for transportation through pipeline is $10.4\,\mathrm{USD \cdot ton_{CO_2}^{-1}}$.

For the determination of the transportation costs, the CAPEX of the pipeline is required. For a pressure of 70-80 bar at the preparation stage, for the transport at a distance of 100 km, a pipeline with a diameter of 16 inches (approximately 0.41 meters) is required. Pipeline diameter was estimated taking into account the desired pressure drop, as well as the thickness of the coating layers.

An anti-corrosive coating is used to avoid corrosion due to dissolved carbon dioxide in water. A HDPE liner is considered as internal coating for the pipeline. The cost used for the liner is $62\,\mathrm{USD \cdot m^{-2}}$, and was obtained by directly contacting the vendor United Pipeline Systems UPS (2016).

Aspen Capital Cost Estimator allows the estimation of pipeline costs. The pipelines have polyurethane insulation with almost 8 cm of thickness, together with fibreglass insulation. The pipe has a thickness circa 1 cm and is built from carbon steel. The thickness of the insulation layer was defined from analysis of the heat transfer from

the outside to the inside of the pipeline. To avoid dissociation, the pipeline must not present significant temperature increase. The methodology used for determination of the heat transfer coefficient of the pipeline (and insulation layers) is similar to the one used by Zhang et al. (2006). The heat transfer pipeline model was simulated in Aspen Hysys, and validated used data from Chaczykowski and Osiadacz (2012), leading to a temperature increase of less than 1 °C for a distance of 100 km, which could result in gasification of 1% of the carbon dioxide in the hydrate.

For the case in analysis, considering a pipeline of 16 inches, a total pipeline cost of 43.6 MM USD is obtained. Applying Equation 6.1, the CAPEX costs of the pipeline are $6.2\ \mathrm{USD}\cdot\mathrm{ton}_{\mathrm{CO_2}}^{-1}$. If the boosting pump (to raise the pressure again to 70-80 bar) is added to the previous value, the total CAPEX costs for transportation are $6.3\ \mathrm{USD}\cdot\mathrm{ton}_{\mathrm{CO_2}}^{-1}$. OPEX costs for transport are due to maintenance of the pipeline, whose value considered is given by NETL (2014), and energy consumption of the boosting pump, and is equal to $1.8\ \mathrm{USD}\cdot\mathrm{ton}_{\mathrm{CO_2}}^{-1}$. Therefore, the total transportation cost is $8.1\ \mathrm{USD}\cdot\mathrm{ton}_{\mathrm{CO_2}}^{-1}$.

The total cost for the preparation and transportation of a $CO_2$ hydrate slurry through pipeline is $18.5\ \mathrm{USD}\cdot\mathrm{ton}_{\mathrm{CO_2}}^{-1}$.

## 6.5 Benchmarking

The standard way to transport carbon dioxide through pipeline is by transporting it in its supercritical state. At supercritical conditions, the gas density increases, and thus the pipeline costs are reduced, since the diameter of the pipeline is smaller.

To have a directly comparable case, cost estimation of the process of transport of supercritical carbon dioxide, simulation of the process was done using Aspen Hysys, assuming the same considerations of Sections 6.2 to 6.4. The process diagram is presented in Figure 6.3.

In this process, it is assumed that the cooling fluid is water. In a first compression stage, a 3-stage compressor is required to raise the pressure from 5 to 150 bar. In the boosting stations, a single stage compressor is used to increase the pressure from 75 to 150 bar. Both equipment costs and energy consumptions for the preparation step are presented in Table 6.2.

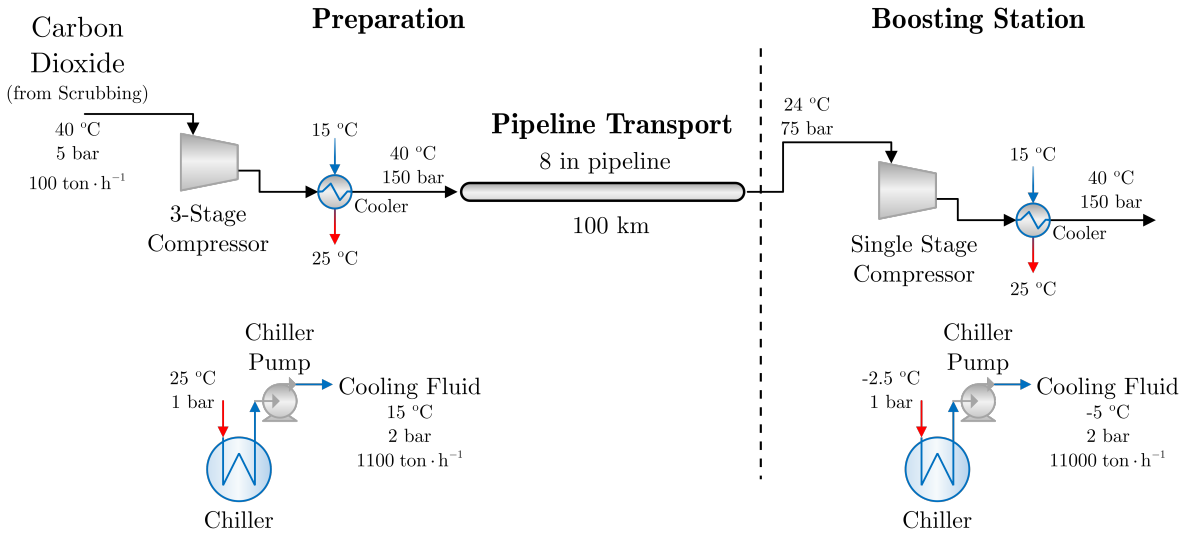



Figure 6.3 – Process diagram for supercritical carbon dioxide preparation and transport.

CAPEX and OPEX of $1.2\,\mathrm{USD}\cdot\mathrm{ton}_{\mathrm{CO_2}}^{-1}$ and $8.5\,\mathrm{USD}\cdot\mathrm{ton}_{\mathrm{CO_2}}^{-1}$, respectively, for the preparation step are obtained, resulting in a total cost of $9.7\,\mathrm{USD}\cdot\mathrm{ton}_{\mathrm{CO_2}}^{-1}$.

Table 6.2 – Equipment costs and energy consumption for the process of Figure 6.3.

| Equipment | Direct Costs (MM USD) | Energy Consumption $\left(\mathrm{kWh}\cdot\mathrm{ton}_{\mathrm{CO_2}}^{-1}\right)$ |
|---|---|---|
| Compressors | 4.5 | 72.2 |
| Pumps | 0.2 | 0.1 |
| Heat Exchangers | 2.6 | - |
| Chiller | 1.1 | 22.4 |
| Total | 8.4 | 94.7 |

The process of transporting supercritical carbon dioxide has the advantage of transporting less amount of material (only carbon dioxide is transported, while in the hydrates case, both water and carbon dioxide are transported). However, the pressure

at which supercritical carbon dioxide is transported is much higher, close to 150 bar (Zhang et al. 2006).

For the transport of $100\,\mathrm{ton}\cdot\mathrm{h}^{-1}$ of carbon dioxide in supercritical conditions, a pipeline of approximately 8 inches (about 0.2 meters) is necessary. This was estimated by considering a pressure drop of 75-80 bar, enough to maintain the $CO_2$ in its supercritical state. The pressure should not be reduced below the threshold pressure of 75 bar, since further decrease would result in the gasification of carbon dioxide. The cost of a pipeline for this purpose is $36.2\,\mathrm{MM\ USD}$. Applying Equation 6.1, the CAPEX costs of the pipeline are $5.2\,\mathrm{USD}\cdot\mathrm{ton}_{\mathrm{CO_2}}^{-1}$. If the boosting station (to raise the pressure again to 150 bar) is added to the previous value, the total CAPEX costs for transportation are $5.8\,\mathrm{USD}\cdot\mathrm{ton}_{\mathrm{CO_2}}^{-1}$. OPEX costs are due to maintenance of the pipeline, and energy consumption of the boosting station, being equal to $2.2\,\mathrm{USD}\cdot\mathrm{ton}_{\mathrm{CO_2}}^{-1}$.

It is important to highlight that due to the highly corrosive nature of water in supercritical carbon dioxide, a dehumidification stage must be performed prior to carbon dioxide compression at the preparation stage. Two different unit operations are typically used to reduce the amount of water in the carbon dioxide stream (Trailblazer 2012): a molecular sieve unit and a TEG dehydration unit. This last unit allows reducing water content from 1000 to 100 ppm (IEAGHG 2014). The maximum water content allowed in supercritical carbon dioxide to avoid prohibitive levels of corrosion is 50 ppm, being required the extra molecular sieve unit. No information regarding operational cost of these two units are available. However, some information regarding capital costs for these units are available (Kemper et al. 2014) and were used in this analysis. It is considered that a unit with a cost of 11 MM USD is required to treat $500\,\mathrm{ton}\cdot\mathrm{h}^{-1}$ of carbon dioxide, resulting in a normalized CAPEX cost of $1.6\,\mathrm{USD}\cdot\mathrm{ton}_{\mathrm{CO_2}}^{-1}$.

The total cost for the preparation and transportation of supercritical $CO_2$, including dehydration units, is $19.3\,\mathrm{USD}\cdot\mathrm{ton}_{CO_2}^{-1}$. This value is larger than the value obtained in Section 6.4, proving that transportation of carbon dioxide as hydrates is competitive. A comparison of the characteristics of both transportation modes is presented in Table 6.3.

Table 6.3 – Comparison of different methods of transporting carbon dioxide: supercritical versus hydrates.

| | SUPERCRITICAL | HYDRATE SLURRY |
|---|---|---|
| PRESSURE | Higher ~ 150 bar | Lower ~ 80 bar |
| | Fracturing | No fracture |
| TEMPERATURE | Extremely low during expansion | Low but constant |
| CORROSION | Dehydration unit | HDPE liner |
| SAFETY | Leakage: high risk | Leakage: controlled risk |
| | Explosion | No explosion |
| | Intensive monitoring | Low monitoring |
| COST $\left(\mathrm{USD}\cdot\mathrm{ton}_{CO_2}^{-1}\right)$ | 19.3 | 18.5 |

Table 6.3 shows that not only the cost of transporting $CO_2$ as hydrates is lower, but also that the inherent transportation risks are less serious than for supercritical carbon dioxide transportation. Also, the corrosion levels are different in both modes, presenting almost one order of magnitude lower corrosion rates in hydrate slurry than in supercritical transport (Sari et al. 2008, Choi and Nešić 2011).

## 6.6 Conclusions

The possibility of producing and transporting carbon dioxide hydrates was assessed regarding its process costs. A simplified strategy to determine the costs using the concepts of CAPEX (capital expenditure) and OPEX (operational expenditure) is used. CAPEX costs were determined based on the equipment costs, while OPEX costs were determined based on the energy requirements of the equipment.

The process is separated in two different steps. In the first step, carbon dioxide is prepared for transport through pipelines. This preparation is done by producing

hydrates from pure carbon dioxide. In the second step, the hydrates slurry is transported through pipeline. The costs of preparation are estimated to be $10.4\,\mathrm{USD}\cdot\mathrm{ton}_{\mathrm{CO_2}}^{-1}$, while the transportation costs for a distance of 100 km's are estimated to be $8.1\,\mathrm{USD}\cdot\mathrm{ton}_{\mathrm{CO_2}}^{-1}$. This results in a total cost of $18.5\,\mathrm{USD}\cdot\mathrm{ton}_{\mathrm{CO_2}}^{-1}$.

A comparison is made with supercritical carbon dioxide transportation through pipeline, the benchmarking technology for carbon dioxide transportation. A similar analysis was applied for this technology. The transport of carbon dioxide using supercritical $\mathrm{CO_2}$ is highly efficient, however, problems regarding corrosion are featured. Therefore, the required use of dehydration units result in a cost increase. The corrosion problem when using hydrates is solved by using HDPE liners in the pipelines. Furthermore, the transportation of carbon dioxide as hydrates presents fewer risks than the transportation of supercritical carbon dioxide. The costs of preparation of supercritical carbon dioxide are estimated to be $11.3\,\mathrm{USD}\cdot\mathrm{ton}_{\mathrm{CO_2}}^{-1}$, while the transportation costs for a distance of 100 km's are estimated to be $8.0\,\mathrm{USD}\cdot\mathrm{ton}_{\mathrm{CO_2}}^{-1}$. This results in a total cost of $19.3\,\mathrm{USD}\cdot\mathrm{ton}_{\mathrm{CO_2}}^{-1}$, which is slightly higher (4%) than the transport of carbon dioxide using hydrates slurry.

Carbon dioxide transport in the form of hydrates have shown to be economically competitive when compared to supercritical carbon dioxide, safer and requires less investment to solve the problem of corrosion. The use of hydrate slurry to transport $\mathrm{CO_2}$ in pipelines is of great interest, and of potential application in a near future.

## 6.7 References

AspenTech, "Reduce Estimating Uncertainty with a Model-Based Approach". *Published online at aspentech.com.* Available at: http://www.aspentech.com/products/economic-evaluation/aspen-capital-cost-estimator/.

Chaczykowski, M., Osiadacz, A.J., **2012**. "Comparative Assesment of Steady-State Pipeline Gas Flow Models / Analiza Porównawcza Modeli Przepływu Gazu w Rurociągu w Stanach Ustalonych". *Archives of Mining Sciences* 57, 23-38.

Chen, B., Cao, S., **2015**. "Key Techniques of Super-Critical $CO_2$ Pipeline Transportation". *International Journal of u- and e- Service, Science and Technology* 8, 285.

Choi, Y.-S., Nešić, S., **2011**. "Determining the Corrosive Potential of $CO_2$ Transport Pipeline in High $pCO_2$–Water Environments". *International Journal of Greenhouse Gas Control* 5, 788-797.

Cussler, E.L., Moggridge, G.D., **2011**. "Chemical Product Design", 2nd ed. Cambridge University Press, New York, NY, USA.

Edwards, J.E., P & I Design Ltd, **2008**. "Design and Rating Shell and Tube Heat Exchangers". Teesside, UK.

EngineeringToolBox, "Ethylene Glycol Heat-Transfer Fluid". *Published online at The Engineering ToolBox*. Available at: http://www.engineeringtoolbox.com/ethylene-glycol-d_146.html.

Fonte, C.M., Leblebici, M.E., Dias, M.M., Lopes, J.C., **2013**. "The NETmix Reactor: Pressure Drop Measurements and 3D CFD Modeling". *Chemical Engineering Research and Design* 91, 2250-2258.

Hall, S., **2012**. Fans, Blowers, and Compressors, in: Hall, S. (Ed.), Branan's Rules of Thumb for Chemical Engineers, 5th ed. Butterworth-Heinemann, Oxford, UK, pp. 118-133.

IEAGHG, International Energy Agency, **2014**. "Evaluation and Analysis of the Performance of Dehydration Units for $CO_2$ Capture". Cheltenham, UK, Doc. No 2014/04.

Kemper, J., Sutherland, L., Watt, J., Santos, S., **2014**. "Evaluation and Analysis of the Performance of Dehydration Units for $CO_2$ Capture". *Energy Procedia* 63, 7568-7584.

Metz, B., Davidson, O., De Coninck, H., Loos, M., Meyer, L., Intergovernmental Panel on Climate Change, **2005**. "IPCC Special Report on Carbon Dioxide Capture and Storage.". New York, NY, USA.

NETL, National Energy Technology Laboratory, **2014**. "FE/NETL $CO_2$ Transport Cost Model: Description and User's Manual". Washington D.C., WA, USA, Doc. No DOE/NETL-2014/1660.

Sari, O., Hu, J., Eicher, S., Egolf, P.W., Homsy, P., **2008**. "Thermo-Physical and Flow Properties of $CO_2$ Hydrate Slurry". Paper presented at: 2008 International Refrigeration and Air Conditioning Conference; Purdue, IN, USA.

Smith, J.M., Van Ness, H., Abbott, M., **2005**. "Introduction to Chemical Engineering Thermodynamics", 7th ed. McGraw-Hill, New York, NY, USA.

Trailblazer, Global CCS Institute, Tenaska, **2012**. "Final Front-End Engineering Design (FEED) Study Report".

UPS, "HDPE Lining". *Published online at United Pipeline Systems*. Available at: http://www.unitedpipeline.com.

Zhang, Z.X., Wang, G.X., Massarotto, P., Rudolph, V., **2006**. "Optimization of Pipeline Transport for $CO_2$ Sequestration". *Energy Conversion and Management* 47, 702-715.

# 7 $N_2/CO_2$ Hydrate-Based Separation Concept

## 7.1 Introduction

Chapter 5 has disclosed some results that are promising regarding the usefulness of the NETmix technology for the design of a process for the continuous production of pure carbon dioxide hydrates. However, the use of this technology can be extended for other applications that require hydrates precipitation. Such applications, as described in Section 2.3.4, include the use of gas hydrates to separate gas mixtures. Separation and purification of gas mixtures, such as flue gas exhausted due to combustion (Kang and Lee 2000, Linga et al. 2008), natural gas (Dabrowski et al. 2009) or even hydrogen (Rice 2006) have been previously proposed.

Flue gas is the gas produced from the combustion of fuels with air, usually from power plants. Flue gas is mostly composed by nitrogen and carbon dioxide, in a concentration of approximately 15-20%, depending on the fuel source. Some water and oxygen may also be present. The purification of exhausted flue gas is one of the major problems that some industries face, and may potentially be solved using hydrates.

The main objective of this chapter is to show how flue gas can be purified using a hydrate-based process. This is done by simulating a multi-stage equilibrium-based process using thermodynamic data from CSMGem (Ballard 2002).

Firstly, the concept of separating a mixture of $N_2/CO_2$ that constitutes the flue gas exhausted from post-combustion power plants is assessed in Section 7.2. The physical model is discussed in Section 7.3, including process considerations and assumptions, equations and thermodynamic modelling strategy. The simulation algorithm is described in Section 7.4, and includes the determination of the initial estimates of the model. The main simulation results are presented and discussed in Section 7.5. Some final considerations regarding the process and experimental procedure using the setup from Chapter 4 is done in Section 7.6. The main conclusions from this chapter are presented in Section 7.7, while the references are presented in Section 7.8.

## 7.2 Separation Concept

The concept of separating flue gas by precipitating hydrates has been previously proposed (Kang and Lee 2000). Dabrowski et al. (2009) has also proposed a process for the purification of methane from natural gas hydrates. Both processes rely on the fact that hydrates have different selectivity for gases, allowing the preferential capture of one of the species.

The hydrates equilibrium pressure curve for the mixed $N_2/CO_2$ system was presented in Figure 2.12, for several concentrations of nitrogen in the flue gas. The pure curves for pure carbon dioxide and pure nitrogen are also presented in Figure 2.12. Both pure gases are capable to produce hydrates on their own. However, while carbon dioxide produces sI hydrates at relatively low pressures (15-30 bar), nitrogen produces sII hydrates at higher pressures (150-200 bar) (Sloan and Koh 2007). The use of a mixture of $N_2/CO_2$ can generate hydrates with the sI or sII structure, depending on the gas composition. For very low concentrations of carbon dioxide in the gas (lower than 15% in mol), sII structured hydrates are formed. If the carbon

dioxide concentration in gas is larger than 15% in mol, then sI hydrates are preferred. The different structures have an impact on the amount of enclathered gas in the framework, since they have different cage structures and sizes.

Nitrogen requires much larger pressures to produce hydrates than carbon dioxide, which may be due to the fact that nitrogen is a much smaller and volatile molecule than carbon dioxide. This means that a process for the separation of flue gas using hydrates is potentially feasible since carbon dioxide may be retained in larger amounts than nitrogen in the solid phase, cleaning the flue gas.

The equilibrium pressure for the mixture to form hydrates is highly dependent on the composition of the gas. Higher content of carbon dioxide results in lower equilibrium pressure, while higher content of nitrogen results in higher equilibrium pressure (Sloan and Koh 2007).

This process is only potentially attractive because the separation of the solid from an aqueous suspension (slurry) is relatively easy, using typical filtration or centrifugation techniques. The carbon dioxide concentration of the separated hydrates should be higher than in the original flue gas. This carbon dioxide can be transported afterwards and stored for CCS. Transport economic viability was discussed in Chapter 6 and was shown to be competitive with the standard technology applied nowadays for carbon dioxide transport.

A potential process to separate carbon dioxide from nitrogen may include the use of several stages. These stages are units where gas and water are put in contact at given temperature and pressure conditions. As in the case of pure carbon dioxide hydrates, these conditions include low temperature (from 0 to 5 $^{o}$C) and high pressures (above 100 bar, due to the presence of nitrogen). These units must be capable to remove the hydration heat that is released due to hydrates crystallization. Studies from Kang et al. (2001) have shown that the dissociation enthalpies are of the same order of magnitude of pure carbon dioxide hydrates, in the order of $60\,\mathrm{kJ}\cdot\mathrm{mol}^{-1}$, assuming that no thermodynamic promoter, namely THF, is introduced in the aqueous phase.

The introduction of THF can significantly reduce the equilibrium pressure (Figure 2.18), but increases the hydration heat (Kang et al. 2001).

The use of several units allows shifting the thermodynamic equilibrium, thus enabling further capture of carbon dioxide through hydrates. However, this is only possible if the mixture at the outlet of each stage in equilibrium is separated. This is done by separating the solids at the outlet of each stage, shifting the thermodynamic equilibrium. In this way, the aqueous phase, which is saturated with gas, is in contact with gas, producing more hydrates.

To increase capture efficiency, the use of a counter-current process is considered. This means that flue gas and water are introduced in the process through opposite stages. The use of such process results in a gas stream at the last stage that has a lower concentration of carbon dioxide than the original flue gas stream. Some nitrogen is lost in the process, since nitrogen is also enclathered in the hydrates cages. The solids obtained are a mixture of hydrates having different compositions. The larger the amount of carbon dioxide in the vapour phase, the larger the carbon dioxide concentration in the hydrate phase. Therefore, since the carbon dioxide concentration in the gas stream is being reduced along the stages, the carbon dioxide concentration in the hydrates are also being reduced through the stages in the opposite direction.

## 7.3 Physical Model

### 7.3.1 Model and Considerations

The physical counter-current model is represented in Figure 7.1. As can be observed, multiple stages are considered. The simulated gas stream (e.g. flue gas) enters the system in the first stage, while a pure water stream enters the system in the last stage. It is assumed that equilibrium is achieved in each stage. The phases present in each stage and the respective compositions are a function of the temperature and pressure. If the thermodynamic conditions are appropriate, $N_2/CO_2$ hydrate precipitation occurs. The solid (hydrate) is suspended in the aqueous-phase, which is

flowing counter-currently to the gas. The gas stream that exits the stage is fed to the next one, while the liquid-hydrate suspension must pass through a separation stage (in practice, the use of a hydro-cyclone, a filter or an equivalent system), where a water-rich stream is obtained and fed to the next stage, and a hydrate-rich stream, the main product of this process is removed.

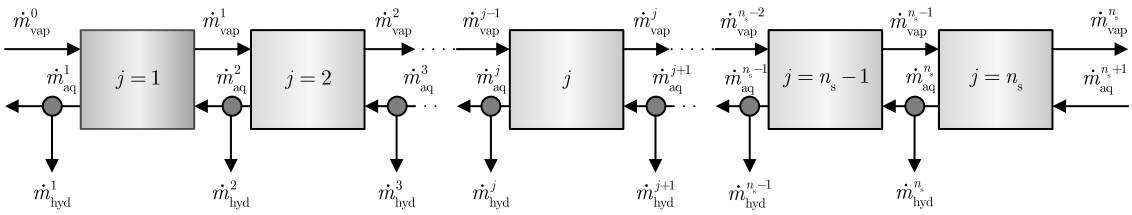



Figure 7.1 – Counter-current process schematic.

To simplify the model, a set of assumptions is considered.

1. Each stage represents a NETmix unit. Each of the NETmix stages is ideally modelled as a stirred tank, with perfect micromixing (i.e., the concentration of each component is uniform in the whole volume);

2. No heat and/or mass transfer limitations are considered in each stage;

3. Thermodynamic phase equilibrium is instantaneous (no kinetic data is considered);

4. The system is isothermal, i.e., the hydrate dissociation heat is completely removed in each stage;

5. The temperature is the same in all stages;

6. Heavier phases (liquid aqueous and solid) are perfectly separated from the vapour phase;

7. The hydrate concentration, $X^{\text{w}}_{\text{hyd}}$, obtained in each stage is set and equal in all stages;

8. The hydrate separation efficiency. $\varsigma_{\text{hyd}}$, is given and equal in all stages;

9. The concentration of the hydrate slurry obtained after separation, $\phi_{\text{slurry}}$, is equal in all stages.

A general stage $j$ is illustrated in Figure 7.2. The stages and streams are numbered in the following manner:

- The stage where the untreated gas enters the system is the first stage, while the stage where fresh water enters the system is the stage $n_{\text{s}}$;
- The outlet streams in equilibrium in each stage have the same number as the stage.

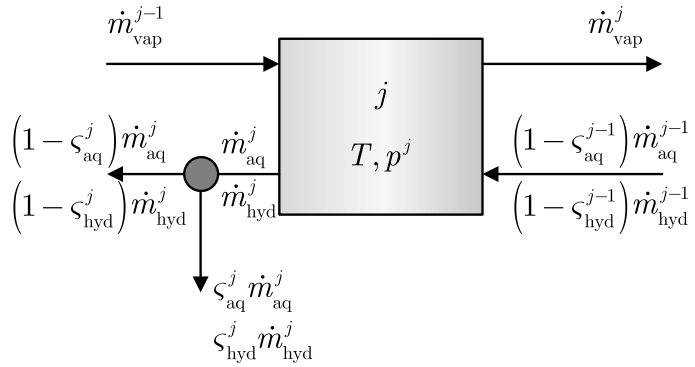



Figure 7.2 – Detailed stage model.

### 7.3.2 Model Equations

To simulate the process, a set of equations per stage needs must be defined. To ease the description, the model is applied stage-by-stage, being then extended to all the stages. However, it is necessary to find a way to define the $j$ index in the variables presented in Figure 7.2 and relate it with the $j$ stage. Every variable that is in equilibrium with the stage $j$ receives the index $j$ for its identification. This is particularly important for variables that are common to two different stages.

Three mass balances are required for each stage: a global mass balance and a component mass balance for two of the three components

$$\dot{m}_{\text{vap}}^{j-1}+\left(1-\varsigma_{\text{aq}}^{j+1}\right)\dot{m}_{\text{aq}}^{j+1}+\left(1-\varsigma_{\text{hyd}}^{j+1}\right)\dot{m}_{\text{hyd}}^{j+1}=\dot{m}_{\text{vap}}^{j}+\dot{m}_{\text{aq}}^{j}+\dot{m}_{\text{hyd}}^{j} \tag{7.1}$$

$$\dot{m}_{\text{vap}}^{j-1}y_{\text{CO}_2}^{\text{w},\,j-1}+\left(1-\varsigma_{\text{aq}}^{j+1}\right)\dot{m}_{\text{aq}}^{j+1}x_{\text{CO}_2}^{\text{w},\,j+1}+\left(1-\varsigma_{\text{hyd}}^{j+1}\right)\dot{m}_{\text{hyd}}^{j+1}\omega_{\text{CO}_2}^{\text{w},\,j+1}=\dot{m}_{\text{vap}}^{j}y_{\text{CO}_2}^{\text{w},\,j}+\dot{m}_{\text{aq}}^{j}x_{\text{CO}_2}^{\text{w},\,j}+\dot{m}_{\text{hyd}}^{j}\omega_{\text{CO}_2}^{\text{w},\,j} \tag{7.2}$$

$$\dot{m}_{\text{vap}}^{j-1} y_{\text{N}_2}^{\text{w},\,j-1} + \left(1-\varsigma_{\text{aq}}^{j+1}\right)\dot{m}_{\text{aq}}^{j+1} x_{\text{N}_2}^{\text{w},\,j+1} + \left(1-\varsigma_{\text{hyd}}^{j+1}\right)\dot{m}_{\text{hyd}}^{j+1}\omega_{\text{N}_2}^{\text{w},\,j+1} = \dot{m}_{\text{vap}}^{j} y_{\text{N}_2}^{\text{w},\,j} + \dot{m}_{\text{aq}}^{j} x_{\text{N}_2}^{\text{w},\,j} + \dot{m}_{\text{hyd}}^{j}\omega_{\text{N}_2}^{\text{w},\,j} \quad (7.3)$$

where $\dot{m}_{\text{vap}}^{j}$, $\dot{m}_{\text{aq}}^{j}$ and $\dot{m}_{\text{hyd}}^{j}$ are the mass flow rate at the outlet of stage $j$ of the vapour, aqueous and hydrates streams, respectively, $y_{\text{CO}_2}^{\text{w},\,j}$ and $y_{\text{N}_2}^{\text{w},\,j}$ are the weight fraction of carbon dioxide and nitrogen respectively in the vapour phase at equilibrium in stage $j$, $x_{\text{CO}_2}^{\text{w},\,j}$ and $x_{\text{N}_2}^{\text{w},\,j}$ are the weight fraction of carbon dioxide and nitrogen respectively in the aqueous phase at equilibrium in stage $j$, $\omega_{\text{CO}_2}^{\text{w},\,j}$ and $\omega_{\text{N}_2}^{\text{w},\,j}$ are the weight fraction of carbon dioxide and nitrogen respectively in the aqueous phase at equilibrium in stage $j$, $\varsigma_{\text{aq}}^{j}$ and $\varsigma_{\text{hyd}}^{j}$ are the separation ratio of aqueous liquid and hydrates, respectively, in stage $j$.

Compositional equations (or component fraction balance equations) are required in all streams. For stage $j$, three outlet streams are in equilibrium, therefore, three equations are required

$$\sum_i y_i^{\text{w},\,j} = 1 \quad (7.4)$$

$$\sum_i x_i^{\text{w},\,j} = 1 \quad (7.5)$$

$$\sum_i \omega_i^{\text{w},\,j} = 1 \quad (7.6)$$

where $i$ is the component (carbon dioxide, nitrogen or water). Four phase equilibrium relationships are required. In theory, nine equations of this type would be required – one equation per stream and per component. However, due to redundancy, five equations are immediately eliminated, since they are not independent from the previous equations. Therefore, only four independent equilibrium equations are considered, and are of the type:

$$y_{\text{CO}_2}^{\text{w},\,j} = f\left(T, p^j, z_{\text{CO}_2}^{\text{w},\,j}, z_{\text{N}_2}^{\text{w},\,j}, z_{\text{H}_2\text{O}}^{\text{w},\,j}\right) \quad (7.7)$$

$$y_{\text{N}_2}^{\text{w},\,j} = f\left(T, p^j, z_{\text{CO}_2}^{\text{w},\,j}, z_{\text{N}_2}^{\text{w},\,j}, z_{\text{H}_2\text{O}}^{\text{w},\,j}\right) \quad (7.8)$$

$$x_{\text{CO}_2}^{\text{w},\,j} = f\left(T, p^j, z_{\text{CO}_2}^{\text{w},\,j}, z_{\text{N}_2}^{\text{w},\,j}, z_{\text{H}_2\text{O}}^{\text{w},\,j}\right) \quad (7.9)$$

$$x_{\text{N}_2}^{\text{w},\,j} = f\left(T, p^j, z_{\text{CO}_2}^{\text{w},\,j}, z_{\text{N}_2}^{\text{w},\,j}, z_{\text{H}_2\text{O}}^{\text{w},\,j}\right) \quad (7.10)$$

where $z_{CO_2}^{w,j}$, $z_{N_2}^{w,j}$ and $z_{H_2O}^{w,j}$ are the global weight fractions of carbon dioxide, nitrogen and water in the stage $j$. Equations 7.7 to 7.10 show that the equilibrium fractions are a function of the thermodynamic properties such as the temperature $T$, pressure of the stage $j$, $p^j$ and the global concentrations of the species.

Two more equations are required to determine the system's composition. Since a three-phase equilibrium is expected at the conditions of the present analysis, only two equations are necessary, since the third is related with the other two and the global stage mass balance

$$\dot{m}_{hyd}^{j} = \alpha_{hyd}^{j}\left[\dot{m}_{vap}^{j-1} + \left(1-\varsigma_{liq}^{j+1}\right)\dot{m}_{aq}^{j+1} + \left(1-\varsigma_{hyd}^{j+1}\right)\dot{m}_{hyd}^{j+1}\right] \tag{7.11}$$

$$\dot{m}_{aq}^{j} = \alpha_{aq}^{j}\left[\dot{m}_{vap}^{j-1} + \left(1-\varsigma_{liq}^{j+1}\right)\dot{m}_{aq}^{j+1} + \left(1-\varsigma_{hyd}^{j+1}\right)\dot{m}_{hyd}^{j+1}\right] \tag{7.12}$$

where $\alpha_{vap}^{j}$ and $\alpha_{aq}^{j}$ are the phase fractions of the vapour and aqueous phases respectively, in equilibrium in stage $j$. The amount of each of the phases is determined using the Gibbs Energy Minimization procedure used by Ballard (2002) and described in Section 5.2.1.1. Since it is already known that in the conditions of the analysis, only three possible phases are present (vapour, aqueous/liquid and hydrate), there is no need to consider more phases. Therefore, applying the considerations described in Section 5.2.1.1 results in the following equations

$$\sum_i \frac{z_i^{w,j}\left(y_i^{w,j}/\omega_i^{w,j}-1\right)}{1+\alpha_{vap}^{j}\left(y_i^{w,j}/\omega_i^{w,j}-1\right)+\alpha_{aq}^{j}\left(x_i^{w,j}/\omega_i^{w,j}-1\right)} = 0 \tag{7.13}$$

$$\sum_i \frac{z_i^{w,j}\left(x_i^{w,j}/\omega_i^{w,j}-1\right)}{1+\alpha_{vap}^{j}\left(y_i^{w,j}/\omega_i^{w,j}-1\right)+\alpha_{aq}^{j}\left(x_i^{w,j}/\omega_i^{w,j}-1\right)} = 0 \tag{7.14}$$

Again, the use of Equations 7.13 and 7.14 in this form is limited to the considered three phases in equilibrium. Therefore, it is extremely important to ensure that the phases present in equilibrium are the expected ones. Imposing a temperature higher than 0 °C eliminates the possibility of precipitation of ice crystals, and the possibility of a different solid phase. The hydrate structure in equilibrium depends on the composition of the gas. Based on experimental results gathered by Herri et al. (2011),

it is possible to say that $N_2/CO_2$ mixed hydrates typically present a sI structure. The sII structure can also be formed for very low concentrations of carbon dioxide. CSMGem only detects sII structure hydrate when the carbon dioxide concentration of the gas is lower than 1% in weight. Therefore, the sII structure is not considered in this work. The sH structure is immediately discarded since $CO_2$ neither $N_2$ form this type of hydrate structure. Therefore, it is possible to say that the only phases to consider in this system are vapour, aqueous and sI hydrate.

It is also required to ensure that the three phases considered are simultaneously present in equilibrium. If one of the phases is not present, Equations 7.13 and 7.14 are not valid. In this system, the presence of the three phases is assured by the following conditions:

- sI hydrate phase will exist if the system pressure is larger than the equilibrium pressure for the gas mixture, and carbon dioxide concentration is higher than 1% in weight;
- Liquid aqueous phase will exist if it is introduced in the system in large excess;
- Vapour phase will exist since $N_2$ is at least ten times less soluble than $CO_2$ in water and is in excess. Therefore, $CO_2$ will be reduced in the gas stream before $N_2$ disappears, ensuring that vapour phase will always exist.

From the conditions presented above, it is possible to conclude that the only condition that is necessary to impose is that the stage pressure is larger than the equilibrium pressure. Also, it is necessary to verify if the carbon dioxide concentration in the vapour phase is higher than 1% in weight.

With Equations 7.1 to 7.14, the system is completely defined if the temperature, pressure and inlet stream conditions are known. It is known that the equilibrium pressure is a very strong function of the global composition, and therefore, to set and maintain a constant pressure in all stages would most likely mean that in some

stages, the pressure would be lower than the minimum required. With the increase of the concentration of nitrogen in the vapour phase, the equilibrium pressure increases as well (see Figure 2.12a). Therefore, the removal of carbon dioxide from the vapour phase results in the increase of the equilibrium pressure. To overcome this problem, two more equations are imposed, which represent restrictions 7 and 9 presented in Section 7.3.1.

- It is assumed that in each stage, the hydrate slurry mass concentration $X^{\mathrm{w}}_{\mathrm{hyd}}$ is known and equal in all stages. Therefore, the equation representing this constraint is

$$\frac{\dot{m}^{j}_{\mathrm{hyd}}}{\dot{m}^{j}_{\mathrm{hyd}} + \dot{m}^{j}_{\mathrm{aq}}} = X^{\mathrm{w}}_{\mathrm{hyd}} \tag{7.15}$$

- It is also imposed that the obtained hydrate paste/slurry has a constant concentration $\phi_{\mathrm{slurry}}$ in the hydrate-rich stream in the separator

$$\frac{\zeta_{\mathrm{hyd}}\dot{m}^{j}_{\mathrm{hyd}}}{\zeta_{\mathrm{hyd}}\dot{m}^{j}_{\mathrm{hyd}} + \zeta^{j}_{\mathrm{liq}}\dot{m}^{j}_{\mathrm{liq}}} = \phi_{\mathrm{slurry}} \tag{7.16}$$

The use of Equation 7.15 is important, since this defines the pressure at which each stage must be operated to produce the amount of hydrates in the desired concentration.

The inclusion of these two last equations results in a system of 16 equations and 16 variables per stage. For a multi-stage process, the number of equations and variables is $16n_{\mathrm{s}}$ non-linear equations.

### 7.3.3 Thermodynamic Modelling

A particularly complex problem in this model is to solve the thermodynamic phase equilibrium of the system in conditions of hydrate precipitation. Experimental and numerical modelling of the thermodynamic behaviour of this system is widely described in the literature (Ballard 2002, Sloan and Koh 2007, Dabrowski et al. 2009, Herri et al. 2011). These are based on the thermodynamic modelling of each of the

phases, in particular, the use of the Van der Waals and Platteeuw model to describe the hydrates phase. However, the solution of these equations in their original form require some computational effort, giving rise of convergence problems in many situations. To overcome this issue, an alternative approach is used.

Thermodynamic equilibrium data is directly extracted from the software package CSMGem as already introduced in Section 5.2.1, which uses the models presented in Appendix B. This data is used to estimate the equilibrium phase compositions that are represented by Equation 7.7 to 7.10.

Due to the complexity of these calculations, this package is not used directly in the model, but a simplified approach is taken. Initially, a database with equilibrium data was created at constant temperature equal to 2 °C. The obtained data comprises component mass fraction in different phases, as well as equilibrium pressure for different global compositions and pressures. The data was then fitted to trend curves, as described in the following sections.

#### *7.3.3.1 Equilibrium Pressure*

To ensure the precipitation of hydrates, each stage pressure must be higher than the equilibrium pressure. For a given global feed composition and temperature, a corresponding equilibrium pressure can be determined using CSMGem. As already mentioned, the equilibrium pressure is a function of the gas composition. However, the amount of water in the system influences the equilibrium pressure as well. It is also a function of the temperature, but since it is kept constant, this variable is not considered here.

A two-variable fitting is required to represent the equilibrium pressure as a function of the components concentration. To make it more significant, the two chosen variables for the fitting were the $N_2/CO_2$ ratio, $z_{N_2}^{w,j} \Big/ z_{CO_2}^{w,j}$, and the feed mass fraction of water $z_{H_2O}^{w,j}$. A two-step fitting procedure was performed. In the first step, the

equilibrium pressure was determined for different values of $z_{H_2O}^{w,j}$, as a function of the $N_2/CO_2$ ratio. The range of $N_2/CO_2$ evaluated is chosen to cover the operational conditions range. Each of the curves was fitted to an equation of the type

$$p_{eq}^{j} = \left( \frac{\varpi k^{*} \left( z_{N_2}^{j} / z_{CO_2}^{j} \right)}{1 + k^{*} \left( z_{N_2}^{j} / z_{CO_2}^{j} \right)} \right)^{n} + \lambda^{n} \tag{7.17}$$

where $\varpi$, $k^{*}$, $\lambda$ and $n$ are fitting parameters. In the second fitting step, the fitting parameters of Equation 7.17 were fitted to a polynomial function as a function of the feed concentration of water $z_{H_2O}^{w,j}$, using an equation of the type

$$\text{Parameter}_{K=\varpi,k^{*},\lambda,n} = \sum_{m=1}^{7} \Phi_{m}^{K} \left( z_{H_2O}^{w,j} \right)^{7-m} \tag{7.18}$$

where $\Phi_{m}^{K}$ is the second-fitting parameter of the parameter K from Equation 7.17, to the $\left(7-m\right)^{th}$ order. Again, the range of water concentration should be enough to describe the full range of operation. These fitting parameters were obtained by the minimization of the least squares method.

The respective fittings and parameters of Equations 7.17 and 7.18 are presented in Appendix E. After two steps, it is possible to obtain an equation that represents reasonably well the equilibrium pressure as a function of the global feed composition for a temperature of 2 °C. The estimations of equilibrium pressure provided by the fitting curves have revealed to be useful during the calculation. A maximum error of 0.4% is obtained when compared to the results from CSMGem. However, it is important to highlight that this value is a guiding value only for the working pressure in each stage. Since it is not involved in the calculation itself, its value determination does not require high accuracy. Also, the solution of Equations 7.13 and 7.14 is not physically possible if the system pressure is lower than the equilibrium pressure (even without calculating it), because the calculation would result in a negative value of $\alpha_{hyd}^{j}$, calculated from

$$\alpha_{\text{vap}}^{j} + \alpha_{\text{aq}}^{j} + \alpha_{\text{hyd}}^{j} = 1 \tag{7.19}$$

The equilibrium pressure values for different global concentrations obtained using CSMGem and the fitting curves from Equation 7.17 and 7.18 are shown in Appendix E. The fitting curves are capable to accurately determine the equilibrium when a three-phase equilibrium system is present, for different global concentrations of carbon dioxide, nitrogen and water.

#### *7.3.3.2 Component Equilibrium Fractions*

It was observed that if the phases that are in equilibrium are known in advance, the mass fraction of each of the components in each phase is only a function of the pressure, for a known and constant temperature in all stages. Therefore, it is possible to describe this behaviour by performing single-variable fittings as a function of pressure.

The equilibrium relationships are obtained using CSMGem. Several values were obtained for different pressures (at constant temperature) and compositions of $CO_2$ and $N_2$ in vapour, aqueous and hydrate phases.

The curves were fitted using polynomial functions, $6^{\text{th}}$ order maximum. The fitting coefficients were determined using the least squares method.

$$\text{Fraction}_{\substack{k=\text{vap, aq, hyd} \\ i=\text{CO}_2,\text{N}_2}} = \sum_{m=1}^{7} A_m^{k,i} p_j^{7-m} \tag{7.20}$$

where $A_m^{k,i}$ is the fitting parameter of $\left(7-m\right)^{\text{th}}$ order for the phase $k$ and component $i$. The fitting curves obtain through this method are accurate, presenting a maximum error of 5%, obtained at high pressure. The pressure range was defined by the pure gas equilibrium pressures at a temperature of 2 °C. The fitting results and parameters for Equation 7.20 are presented in Appendix E.

## 7.4 Algorithm

The general algorithm used for the resolution of Equations 7.1 to 7.16 is presented in Figure 7.3.

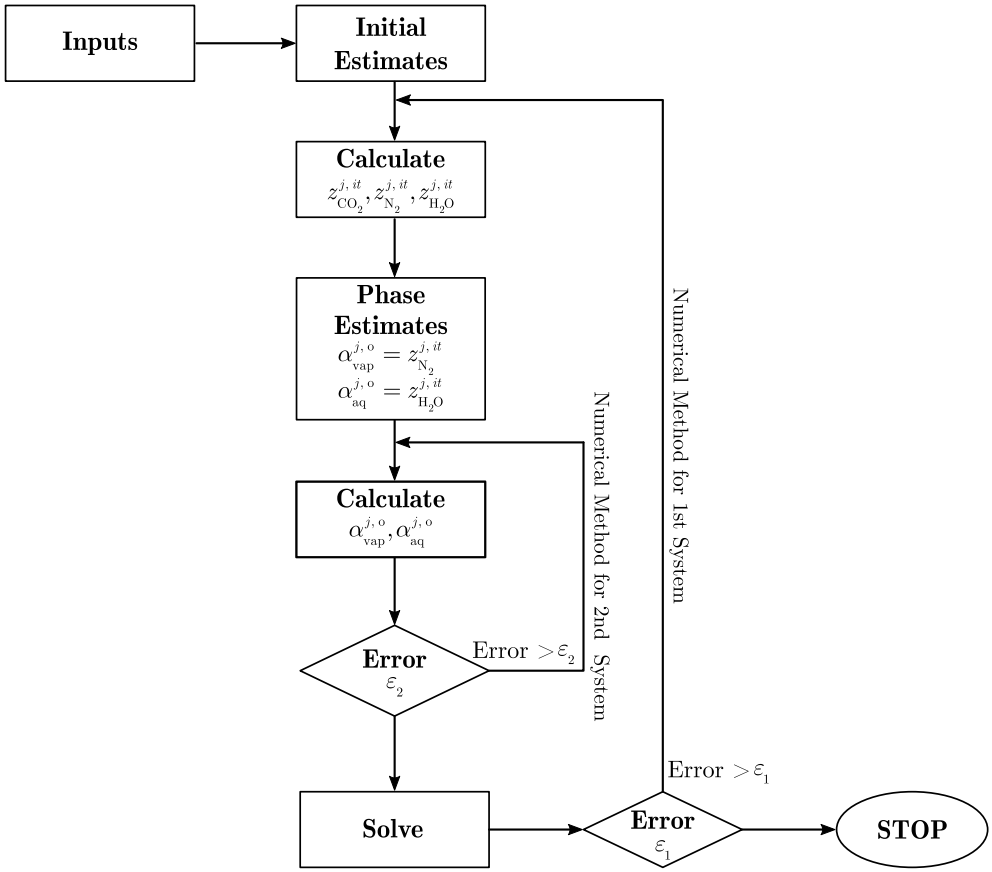



Figure 7.3 – Algorithm for the solution of the physical model.

The calculation procedure comprises two different calculation steps. The determination of equilibrium phase fractions $\alpha_k^j$ from Equations 7.13 and 7.14 is done separately due to the high possibility of convergence to local solutions that are physically irrelevant, or divergence. It was observed that the initial estimative of $\alpha^j_{\text{vap}}$ and $\alpha^j_{\text{aq}}$ are very important for a successful convergence. The resolution of Equations 7.13 and 7.14 together with the remaining equations disallows the possibility of setting the initial estimates of $\alpha^j_{\text{vap}}$ and $\alpha^j_{\text{aq}}$ in each iteration of the main system of equations. This independent control of the estimates of $\alpha^j_{\text{vap}}$ and $\alpha^j_{\text{aq}}$ is extremely helpful for the convergence of the system to the physical meaningful solution. To

bypass this problem, a second system of equations comprising Equations 7.13 and 7.14 is considered, to determine $\alpha^{j}_{\text{vap}}$ and $\alpha^{j}_{\text{aq}}$. This procedure is performed inside the routine to solve the remaining equations. This means that for each iteration of the main system (that comprises all equations but 7.13 and 7.14), the secondary system is solved using initial estimates that are a function of the solution vector obtained from the main system. It was found that, for this system, a good estimative for the phase fractions are $\alpha^{j,\,\text{o}}_{\text{vap}} = z^{j,\,it}_{\text{N}_2}$ and $\alpha^{j,\,\text{o}}_{\text{aq}} = z^{j,\,it}_{\text{H}_2\text{O}}$.

The algorithm presented in Figure 7.3 is described here. Initial guesses are introduced for the main system of equations for $14n_{\text{s}}$ (two equations are solved separately) variables that constitute the solution vector. This information is then introduced to a VBA routine that applies Newton's method for the resolution of a non-linear system of equations. In each iteration, Equations 7.1 to 7.12, 7.15 and 7.16 are solved. However, since Equations 7.11 and 7.12 are a function of the unknown values of $\alpha^{j}_{\text{vap}}$ and $\alpha^{j}_{\text{aq}}$, it is necessary to update these values at each iteration. For that, a second system of equations comprising Equations 7.13 and 7.14 is independently solved. The inputs of this second system are just the feed composition $z^{j}_{\text{CO}_2}$, $z^{j}_{\text{N}_2}$, $z^{j}_{\text{H}_2\text{O}}$ and the stage pressure $p^{j}$. Feed composition is calculated using variables from solution vector of the first system of equations, while the pressure itself is a variable from the same solution vector.

Newton's method is an iterative process that updates the values of the solution vector to get all equations equal to zero. For that, Jacobian matrix with the partial derivatives is required. For the second system, where $\alpha^{j}_{\text{vap}}$ and $\alpha^{j}_{\text{aq}}$ are calculated, the Jacobian matrix is obtained by analytically determining the partial derivatives. The system is assumed to have converged when all equations have a residual error smaller than $10^{-12}$ and maximum variation of the solution vector from consecutive iterations lower than $10^{-12}$. For the main system, the Jacobian matrix was approximated using

centred finite differences. For the resolution of the main system, the residual error was set to $10^{-10}$ while the maximum variation in the solution vector was set to $10^{-8}$.

### 7.4.1 Initial Estimates

To solve the system described above, it is necessary to input initial estimates for all variables of the system. It is important to highlight the importance of having good initial estimates since it can be the difference between converging to the right solution, converging to local minimums, or not converging at all. Therefore, special care is taken when defining the initial estimates, based on the expected dynamics of the system.

The first estimative of $p^j$ is given based on the expected global feed composition and the expected pressure change from stage to stage. Due to the change in the equilibrium pressure when carbon dioxide is captured, the pressure of a given stage $j$ must be higher than the pressure of the previous stage $j-1$ and lower than the following stage $j+1$. The initial estimates for $p^j$ must take this change in consideration, and the use of a constant value of $p^j$ as initial estimate equal for all stages should be avoided. Depending on the amount of liquid entering stage 1 (unknown *a priori*, since the known condition for water is at the $n_s$ stage), it is observed that the equilibrium pressure was about 90-110 bar, since this is the stage where the concentration of carbon dioxide is larger. The following equation is used to determine the initial estimates of the pressure in each stage $p^j$:

$$p^{j,\,o} = p_0 + \Delta p\left(j-1\right) \tag{7.21}$$

where $p_0$ is the pressure at the first stage, and $\Delta p$ represents the pressure increase from stage to stage. Although $\Delta p$ is not constant for all stages, it is assumed constant for the computation of initial estimates. Equation 7.21 assumes that the pressure increases linearly with the stage number.

For a small number of stages (less or equal to three), the values of $p_0 = 100$ bar and $\Delta p = 25$ bar successfully allow the convergence of the system. However, for larger number of stages, these values result in convergence problems. Thus, the values of $p_0 = 60$ bar and $\Delta p = 25$ bar are used when the number of stages is higher than four.

The values of the composition of the $CO_2$ and $N_2$ in the three phases in equilibrium are determined by using the fittings described in Section 7.3.3.2, using the initial pressure estimates. The initial estimates for the mass fraction of water in each of the phases is determined by

$$\begin{cases} y_{H_2O}^{w,j,o} = 1 - y_{CO_2}^{w,j,o} - y_{N_2}^{w,j,o} \\ x_{H_2O}^{w,j,o} = 1 - x_{CO_2}^{w,j,o} - x_{N_2}^{w,j,o} \\ \omega_{H_2O}^{w,j,o} = 1 - \omega_{CO_2}^{w,j,o} - \omega_{N_2}^{w,j,o} \end{cases} \tag{7.22}$$

The initial estimate for the mass flow rate of produced hydrates is assumed to be equal in all stages, and is determined by

$$\dot{m}_{hyd}^{j,o} = \frac{X_{hyd}^{w}\left(1 - X_{hyd}^{w}\right)\dot{m}_{aq}^{n_s+1,o}}{n_s} \tag{7.23}$$

The initial estimates of the amount of gas and liquid in equilibrium in each stage is calculated based on the hydrate production rate, and are determined from

$$\dot{m}_{vap}^{j,o} = \dot{m}_{vap}^{0} - j\left(1 - \omega_{H_2O}^{j,o}\right)\dot{m}_{hyd}^{j,o} \tag{7.24}$$

$$\dot{m}_{aq}^{j,o} = \dot{m}_{vap}^{n_s+1} - \left(n_s - j\right)\omega_{H_2O}^{j,o}\dot{m}_{hyd}^{j,o} \tag{7.25}$$

The initial estimate of the efficiency of separation of water in the separator node from Figure 7.1 is then given by

$$\zeta_{aq}^{j,o} = \frac{\left(1 - \phi_{slurry}\right)\dot{m}_{hyd}^{j,o}}{\phi_{slurry}\dot{m}_{aq}^{j,o}} \tag{7.26}$$

The estimates obtained by the previous equations have shown to be reliable in the range of conditions of the study.

To help convergence, all variables but the pressure are defined in a way that they only vary from 0 to 1. The mass fraction of each component in each of the phases in equilibrium varies from 0 to 1, as does the separation efficiency. Since this is not the case for the mass flow rates, variables $\dot{m}_{\text{vap}}^{j}$, $\dot{m}_{\text{aq}}^{j}$ and $\dot{m}_{\text{hyd}}^{j}$ were normalized by the total flow rate $\dot{m}_{\text{vap}}^{0} + \dot{m}_{\text{aq}}^{n_s+1}$ introduced to the system.

Regarding the second system, due to the poor solubility of $N_2$ in water and due to excess of water in the system, a good estimate of the fractions of vapour and aqueous phase in equilibrium at the first system's iteration $it$ are given by the rearrangement of Equations 7.2 and 7.3

$$\alpha_{\text{vap}}^{j,\text{o}} = z_{\text{N}_2}^{j,it} = \frac{\dot{m}_{\text{vap}}^{j-1,it} y_{\text{N}_2}^{j-1,it} + \left(1-\varsigma_{\text{aq}}^{j+1,it}\right)\dot{m}_{\text{aq}}^{j+1,it} x_{\text{N}_2}^{j+1,it} + \left(1-\varsigma_{\text{hyd}}\right)\dot{m}_{\text{hyd}}^{j+1,it}\omega_{\text{N}_2}^{j+1,it}}{\dot{m}_{\text{vap}}^{j-1,it} + \left(1-\varsigma_{\text{aq}}^{j+1,it}\right)\dot{m}_{\text{aq}}^{j+1,it} + \left(1-\varsigma_{\text{hyd}}\right)\dot{m}_{\text{hyd}}^{j+1,it}} \quad (7.27)$$

$$\alpha_{\text{aq}}^{j,\text{o}} = z_{\text{H}_2\text{O}}^{j,it} = \frac{\dot{m}_{\text{vap}}^{j-1,it} y_{\text{H}_2\text{O}}^{j-1,it} + \left(1-\varsigma_{\text{aq}}^{j+1,it}\right)\dot{m}_{\text{aq}}^{j+1,it} x_{\text{H}_2\text{O}}^{j+1,it} + \left(1-\varsigma_{\text{hyd}}\right)\dot{m}_{\text{hyd}}^{j+1,it}\omega_{\text{H}_2\text{O}}^{j+1,it}}{\dot{m}_{\text{vap}}^{j-1,it} + \left(1-\varsigma_{\text{aq}}^{j+1,it}\right)\dot{m}_{\text{aq}}^{j+1,it} + \left(1-\varsigma_{\text{hyd}}\right)\dot{m}_{\text{hyd}}^{j+1,it}} \quad (7.28)$$

The second system of equations to be solved is very sensitive to the initial estimates. Therefore, any other estimates for $\alpha_{\text{vap}}^{j,\text{o}}$ and $\alpha_{\text{aq}}^{j,\text{o}}$ for any iteration of the first system of equations may result in convergence to physically meaningless solutions. This system is solved separately in each iteration of the main system to ensure that the initial estimate is always correctly defined, and therefore, facilitating the convergence.

## 7.5 Results and Discussion

For the present analysis, it is considered a flow rate of flue gas of $5\,\text{ton}\cdot\text{h}^{-1}$, containing 80% in weight of nitrogen, 15% of carbon dioxide and the remaining 5% of water. The amount of fresh water that enters the process in stage $n_s$ is estimated assuming that a slurry concentration of 30% in weight at the end of the process is obtained. This value is just an estimate and not an imposition. The amount of solids initially estimated assumes that all carbon dioxide from the flue gas is converted to hydrates. For that, the composition of the hydrate at 2 °C and 120 bar are used. The

choice of the pressure of 120 bar is arbitrary. The only requirement is that the value of the used pressure to estimate the amount of water should be between the equilibrium pressure of the first (lower equilibrium pressure) and last stage (higher equilibrium pressure). At these conditions, the hydrate composition is approximately 11.4% in weight in nitrogen and 12.1% in carbon dioxide, according to CSMGem. The amount of water introduced is then determined from

$$\dot{m}_{\mathrm{aq}}^{n_s+1} = \frac{0.7\dot{m}_{\mathrm{vap}}^{0} y_{\mathrm{CO_2}}^{\mathrm{w},0}}{0.3\omega_{\mathrm{CO_2}}^{\mathrm{w},120\ \mathrm{bar}}} \tag{7.29}$$

where $\omega_{\mathrm{CO_2}}^{\mathrm{w},120\ \mathrm{bar}}$ is the carbon dioxide weight fraction in the hydrate phase at 120 bar, and is equal to 0.121. It is initially considered that 70% of the solids that exit stage $j$ are separated in the separation nodes $\left(\varsigma_{\mathrm{hyd}} = 0.7\right)$. The concentration of solids after separation is initially set to 80% in weight $\left(\phi_{\mathrm{slurry}} = 0.8\right)$. Finally, it is imposed that a desired hydrates concentration in the aqueous phase that exits the stage $j$ in equilibrium must be 8% in weight $\left(X_{\mathrm{hyd}}^{\mathrm{w}} = 0.08\right)$.

Using the conditions described above in the simulator, it is possible to study the effect of the increase of the number of stages to the process, as well as to determine its capacity of separation.

The amount of $\mathrm{CO_2}$ recovered from the gas phase and the amount of $\mathrm{N_2}$ lost to the hydrates phase at the outlet of the last stage, as a function of the number of stages is represented in Figure 7.4. The amount of recovered carbon dioxide from the gas stream is determined by

$$\mathrm{Rec}_{\mathrm{CO_2}} = 1 - \frac{\dot{m}_{\mathrm{vap}}^{n_s} y_{\mathrm{CO_2}}^{\mathrm{w},n_s}}{\dot{m}_{\mathrm{vap}}^{0} y_{\mathrm{CO_2}}^{\mathrm{w},0}} \tag{7.30}$$

while the amount of lost nitrogen from the vapour phase is determined by

$$\mathrm{Loss}_{\mathrm{N_2}} = 1 - \frac{\dot{m}_{\mathrm{vap}}^{n_s} y_{\mathrm{N_2}}^{\mathrm{w},n_s}}{\dot{m}_{\mathrm{vap}}^{0} y_{\mathrm{N_2}}^{\mathrm{w},0}} \tag{7.31}$$

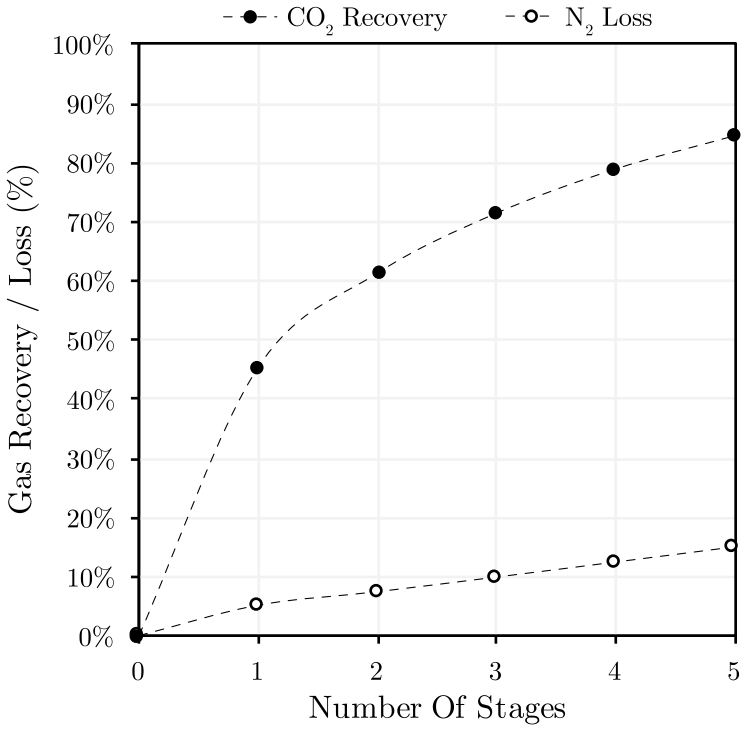



Figure 7.4 – Carbon dioxide recovery and nitrogen loss from the gas stream.

Figure 7.4 shows that, as expected, the amount of carbon dioxide recovered from the vapour phase increases with the increase of the number of stages. The use of a single stage is enough to remove about 50% of the carbon dioxide that is present in the flue gas, being increased to approximately 90% when using 5 stages. At the same time, nitrogen is being lost since nitrogen is also enclathered in the hydrates structure. The final concentration of carbon dioxide in the gas stream at the outlet of the last stage is shown in Figure 7.5.

Figure 7.5 shows that the concentration of carbon dioxide in the gas phase at the outlet can be reduced four times if using a process comprising 5 equilibrium stages. This results in a gas stream that is much cleaner than the original flue gas. It is expected that further increase of the number of stages result in a reduction of the carbon dioxide concentration at the outlet. However, the impact of adding more stages is being gradually attenuated.

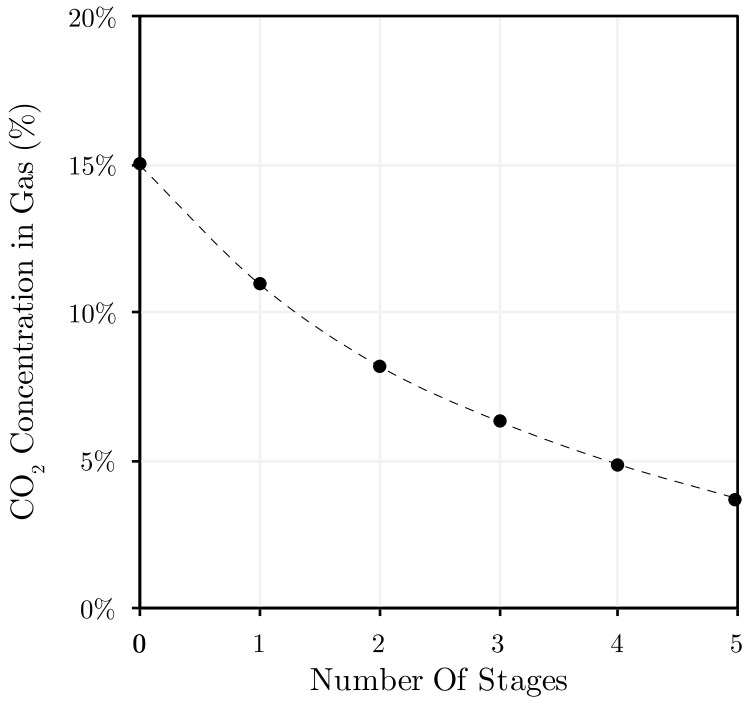



Figure 7.5 – Carbon dioxide concentration in the outlet gas stream.

Thermodynamic data from Appendix E shows that at low pressures, carbon dioxide-rich hydrates are obtained, while for high pressure, nitrogen-rich hydrates are obtained. The pressure of the stage is defined by the equilibrium pressure, which increases with the decrease of the concentration of carbon dioxide in the gas stream. The maximum concentration of carbon dioxide in the gas phase is obtained in the first stage. At this stage, the equilibrium pressure is the lowest, and so the capture of carbon dioxide is preferred over nitrogen. This results in larger recovery of carbon dioxide than nitrogen loss in the gas stream, leading to an increase of the equilibrium pressure. Therefore, the operating pressure of the subsequent stage must be higher than the pressure of the first stage.

With the increase of pressure along each stage, the preference of carbon dioxide to be enclathered in the hydrate cages over nitrogen is being gradually reduced, until a point where the addition of more stages results in the removal of larger amounts of nitrogen than carbon dioxide. Even though this situation still increases the global recovery of the carbon dioxide in the gas stream, it also results in the loss of a large amount of nitrogen that is being transformed into hydrates. This is not desirable, especially if there is the objective of transporting carbon dioxide as hydrates, since

large amounts of nitrogen is also being transported. The actual stage pressure, as well as the equilibrium pressure for the gas mixture in each of the 5 stages is presented in Figure 7.6

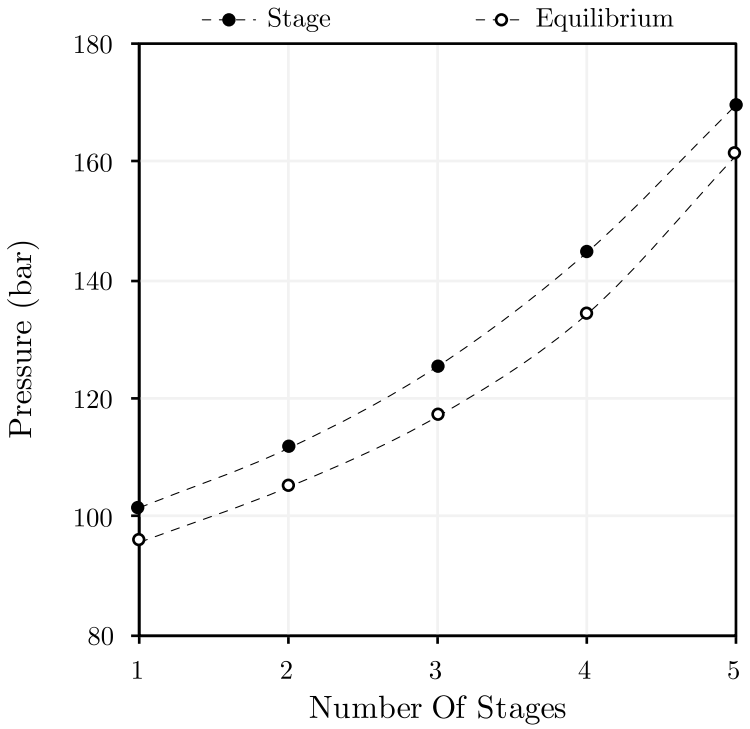



Figure 7.6 – Stage pressure and equilibrium pressure for the 5-stage simulation.

Figure 7.6 shows that, as expected, the pressure of each of the stages must increase relatively to the previous stage, to promote the production of 8% in weight of hydrates in each of the stages. For example, if 5 stages are used, the pressure used in the first stage results in hydrates containing 14.6% in weight of carbon dioxide and 9.6% in weight of nitrogen. On the contrary, the pressure of stage 5 (close to 170 bar) results in the formation of hydrates containing only 5.1% of carbon dioxide and 16.4% of nitrogen, meaning that the gas selectivity changed along the process. In fact, looking closely to the results, it is observed that the selectivity changed from stage 2 to 3. This means that the use of stages 3, 4 and 5 helps to reduce the amount of carbon dioxide, but also results in a higher loss of nitrogen. This also indicates that the efficiency of a process of this type is highly influenced by the carbon dioxide concentration in the original flue gas.

The impact of some parameters such as $X_{\text{hyd}}^{\text{w}}$, $\phi_{\text{slurry}}$ and $\varsigma_{\text{hyd}}$ are also assessed. To do so, one of the parameters was varied while keeping the remaining constant and equal to the values used in the results from Figure 7.4 to Figure 7.6, for a total number of 5 stages. The influence of $X_{\text{hyd}}^{\text{w}}$ is shown in Figure 7.7.

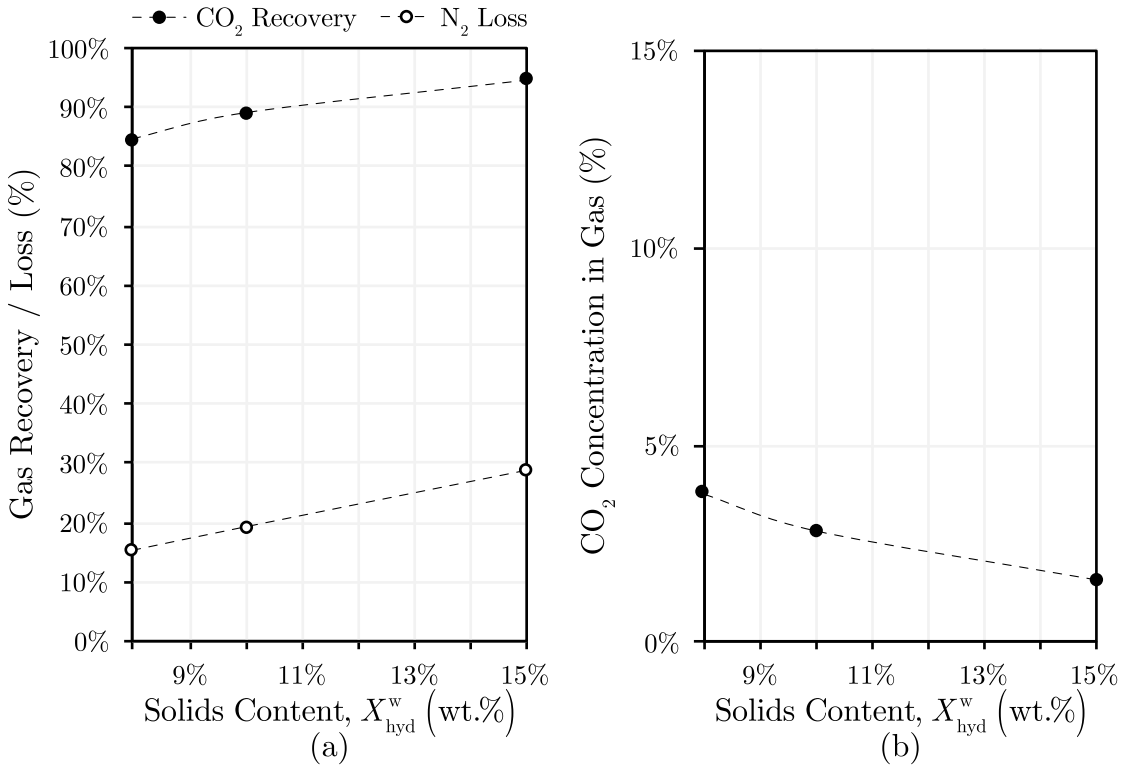



Figure 7.7 – Influence of the solids content $X_{\text{hyd}}^{\text{w}}$ in the process: (a) effect on the carbon dioxide recovery and nitrogen loss; (b) effect on the final carbon dioxide concentration at the outlet.

Figure 7.7 shows that increasing the amount of produced hydrates in each stage, results in the increase of the process efficiency regarding carbon dioxide capture. A capture of more than 90% is obtained if the concentration of solids produced in all stages is 15% in weight in the slurry. A significant increase of the nitrogen loss is also obtained with the increase of $X_{\text{hyd}}^{\text{w}}$. As a result of the increase of the expected $X_{\text{hyd}}^{\text{w}}$, the operational pressure has to increase as well, which, as explained before, leads to a gradually reduction of the hydrates selectivity towards carbon dioxide. This is the main reason why the rate of nitrogen loss with $X_{\text{hyd}}^{\text{w}}$ is higher than the rate of carbon dioxide recovery. However, in the three studied concentrations, carbon dioxide concentration at the outlet of the fifth stage decreased.

The influence of $\phi_{\text{slurry}}$ is shown in Figure 7.8.

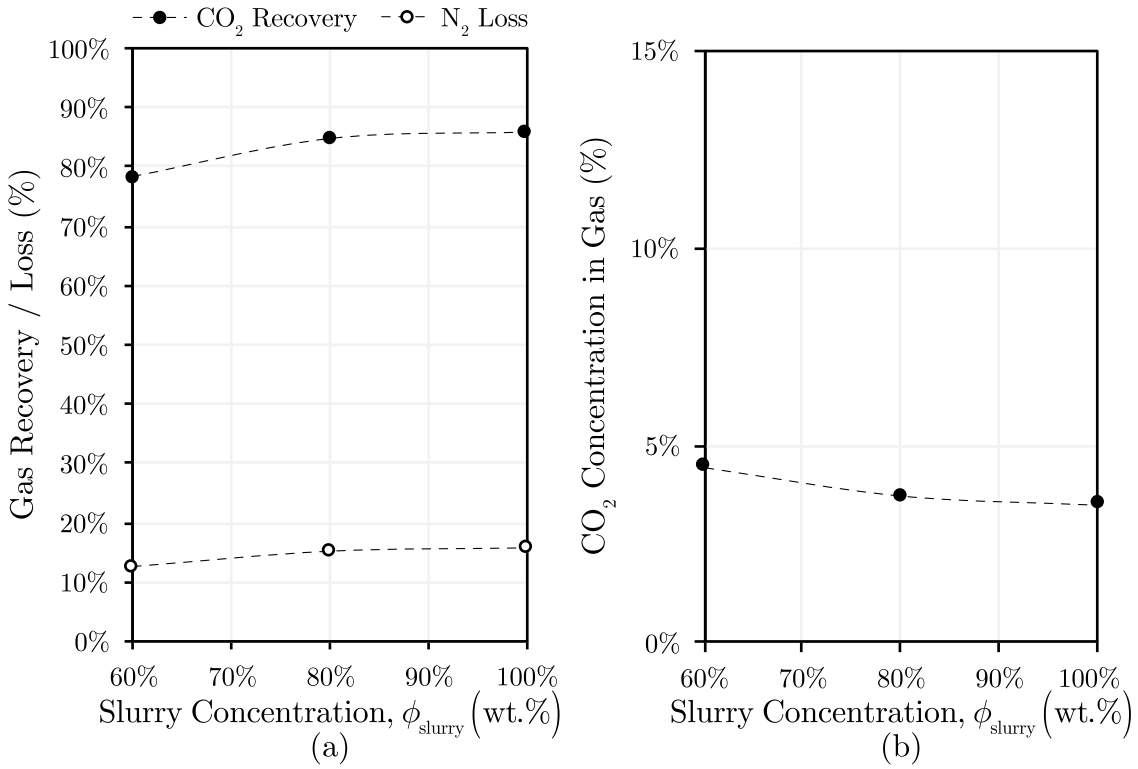



Figure 7.8 – Influence of the concentration of solids after separation $\phi_{\text{slurry}}$ in the process: (a) effect on the carbon dioxide recovery and nitrogen loss; (b) effect on the final carbon dioxide concentration at the outlet.

The increase of $\phi_{\text{slurry}}$ means that for a constant value of $\varsigma_{\text{hyd}}$, the amount of water that is removed from the aqueous phase stream, through the separation nodes is changing. Increasing $\phi_{\text{slurry}}$ results in a lower amount of separated water. As a result, more water is available to produce hydrates in the equilibrium stages, resulting in the increase of the production rate of hydrates. Therefore, the capture rate increases as well. However, the impact of $\phi_{\text{slurry}}$ is less important than the impact of $X_{\text{hyd}}^{\text{w}}$, as can be seen from Figure 7.8. A perfect separation regarding water, i.e., no water is separated in the separation node, leading to pure hydrates in that stream, results in carbon dioxide concentration of about 4% at the outlet of the fifth stage.

The effect of the last parameter $\varsigma_{\text{hyd}}$ is shown in Figure 7.9 Parameter $\varsigma_{\text{hyd}}$ determines the separation efficiency regarding hydrates. Low values of $\varsigma_{\text{hyd}}$ means that large amounts of the produced hydrates are fed to the following stage, while

high values of $\varsigma_{hyd}$ means that most of the hydrates are removed from the system before the next stage. It is important to highlight that a process such as this one relies on the fact that the thermodynamic equilibrium is shifted through the removal of hydrates from the system. If this removal is done at small rates, then the thermodynamic shift is smaller and the production of hydrates is globally lower. On the contrary, if large amounts of hydrates are removed, the shift is larger, resulting in higher precipitation of hydrates. As a result, the global efficiency of the carbon dioxide capture increases. This behaviour is observed in Figure 7.9. As expected, the increase of $\varsigma_{hyd}$ resulted in an increase of both carbon dioxide recovery and nitrogen loss. Also, the carbon dioxide concentration at the outlet of the fifth stage is reduced.

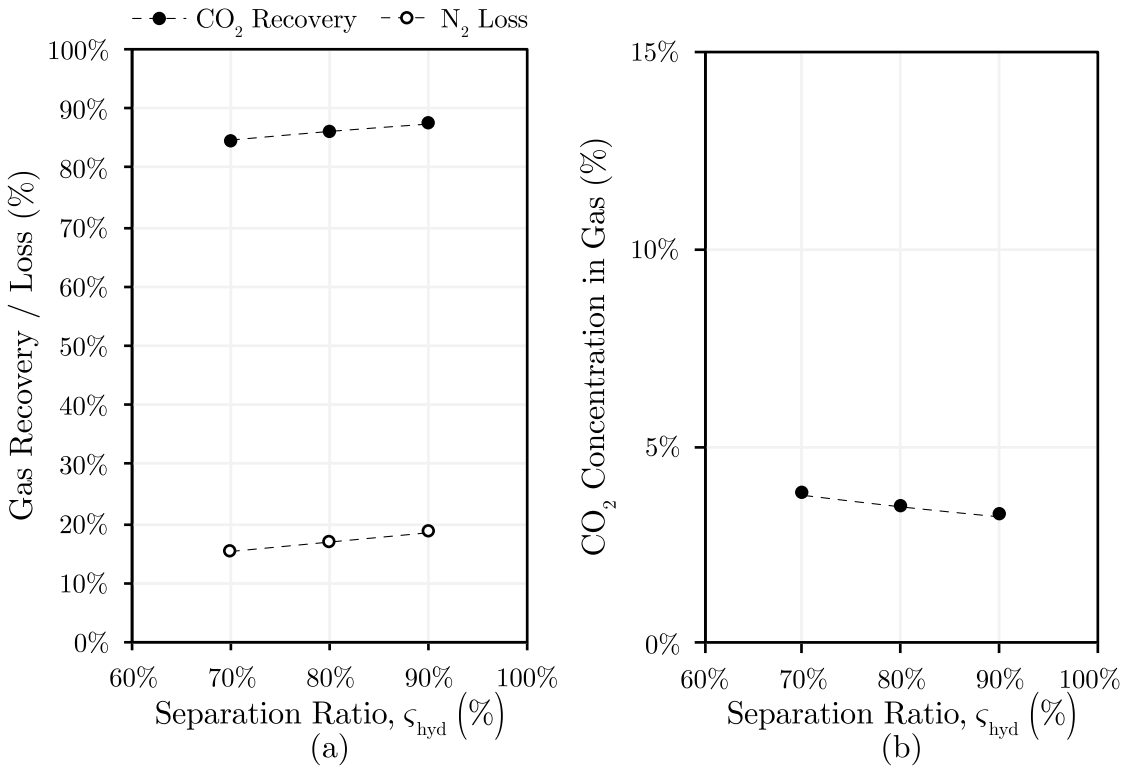



Figure 7.9 – Influence of the solids separation ratio in the separation nodes $\varsigma_{hyd}$ in the process: (a) effect on the carbon dioxide recovery and nitrogen loss; (b) effect on the final carbon dioxide concentration at the outlet.

## 7.6 Final Considerations

The model developed for the simulation of a counter-current process for the capture of $CO_2$ using gas hydrates has shown that it is thermodynamically feasible to reduce

the concentration of carbon dioxide in the flue gas using a hydrate-based technology. Whether it is economically competitive when compared to other technologies, namely amine adsorption, without the inclusion of thermodynamic promoters, is still unclear. The use of thermodynamic promoters has the advantage of reducing the operational pressures (Strobel et al. 2009), however it increases the energy released due to hydration (Kang et al. 2001, Sloan and Koh 2007). Also, promoters action, such as THF, are due to the fact that they are enclathered together with the gases, which can significantly reduce the amount of captured carbon dioxide (Kang et al. 2001).

The present study assumes that each stage operates as ideal equilibrium stages, which may not be the case in reality. Therefore, as future work, it is extremely relevant to use the experimental setup applied throughout the present work, and detailed in Chapter 4, to evaluate the capacity of the NETmix technology to separate carbon dioxide from a flue gas mixture. The setup is already designed to enable the use of a $N_2/CO_2$ mixture to simulate the flue gas. The use of THF is crucial in this experiment, since the setup is not capable to handle with the high pressures required for this mixture, as shown in Figure 7.6. The use of THF can reduce the equilibrium pressure by a factor of 5-6 (Zhang et al. 2014), enabling the use of the experimental setup.

The experiment can be performed by considering the microNETmix unit as an equilibrium stage. The use of the separation vessel E-12 from Figure 4.3 is useful at this point, since it allows the separation of the mixture in equilibrium, composed by gas (with lower concentration in carbon dioxide than the original inlet gas), hydrates and an aqueous phase. The separation, due to gravity, is done in this vessel, allowing the purge of the heavy phases (hydrates and liquid aqueous) from the bottom and the gas phase from the top. The vessel was designed in a way that it minimizes the amount of gas that may be escaped from the bottom and the potential drag of liquid droplets by the gas to the top. At the top of the vessel, a carbon dioxide sensor is installed, which enables the determination of the carbon dioxide concentration at the outlet.

Results from Chapter 5 have shown that hydrates of pure carbon dioxide can be successfully produced using the experimental setup of Chapter 4. Some problems regarding plugging of the gas line were observed, due to ice or hydrate formation in that line. These complications may be transposed for the experiment using $N_2/CO_2$, so ice formation and plugging due to hydrates accumulation are likely to occur. Nevertheless, the application of the technology to promote gas separation is the following natural setup for the maturation of the NETmix as a technology capable to continuously produce gas hydrates.

## 7.7 Conclusions

The present chapter aimed to exhibit a conceptual process that can be applied for the separation of carbon dioxide and nitrogen from flue gas that are exhausted from post-combustion power plants.

A simplified equilibrium model based on thermodynamic data from the simulator CSMGem is developed to simulate the counter-current contact between flue gas in water at low temperatures and pressures, in conditions at which gas hydrates are formed. The fittings used in the model proved to represent reasonably well the equilibrium data within the range of interest of the present study. A constant temperature of 2 °C is assumed for simplification.

Results show that the use of a counter-current process for the separation of gas hydrates is technically feasible. The process relies on the need of removing the solid hydrates at the outlet of each stage, shifting the thermodynamic equilibrium and thus allowing further precipitation of hydrates. Therefore, the capacity to separate the flue gas increases.

Hydrates selectivity depends on the pressure of operation. Low pressures favour the production of carbon dioxide-rich hydrates, while high pressures favour the production of nitrogen-rich hydrates. The need of increasing the pressure from stage to stage due to the change of the gas composition means that the selectivity is

changing with stage. Carbon dioxide selectivity is maximum at the first stage, and minimum in the last stage. Therefore, the use of more stages than required may lead to a large nitrogen depletion from the gas phase.

The use of a single stage allows the recovery of about 45%, while using 5 stages allows the recovery of more than 85% of the total carbon dioxide introduced. This results in a concentration reduction of carbon dioxide from 15% in weight to 11% and 4% in weight, for 1 and 5 stages, respectively.

The influence of other parameters such as the amount of produced hydrates in each stage, solids concentration after separation and separation efficiency were evaluated. Increasing the amount of produced hydrates in each stage $X_{\mathrm{hyd}}^{\mathrm{w}}$ results in an increase of the carbon dioxide recovery and a decrease of its concentration. The same effect is observed when increasing $\phi_{\mathrm{slurry}}$ and $\varsigma_{\mathrm{hyd}}$.

## 7.8 References

Ballard, A.L. **2002**. "A Non-Ideal Hydrate Solid Solution Model For a Multi-Phase Equilibria Program" [*Ph.D Thesis*]. Golden, CO, USA: Department of Chemical and Petroleum-Refining Engineering, Colorado School Of Mines.

Dabrowski, N., Windmeier, C., Oellrich, L.R., **2009**. "Purification of Natural Gases With High $CO_2$ Content Using Gas Hydrates". *Energy & Fuels* 23, 5603-5610.

Herri, J.M., Bouchemoua, A., Kwaterski, M., Fezoua, A., Ouabbas, Y., Cameirao, A., **2011**. "Gas Hydrate Equilibria for $CO_2$–$N_2$ and $CO_2$–$CH_4$ Gas Mixtures—Experimental Studies and Thermodynamic Modelling". *Fluid Phase Equilibria* 301, 171-190.

Kang, S.-P., Lee, H., **2000**. "Recovery of $CO_2$ from Flue Gas Using Gas Hydrate: Thermodynamic Verification through Phase Equilibrium Measurements". *Environmental Science & Technology* 34, 4397-4400.

Kang, S.P., Lee, H., Ryu, B.J., **2001**. "Enthalpies of Dissociation of Clathrate Hydrates of Carbon Dioxide, Nitrogen, (Carbon Dioxide + Nitrogen), and (Carbon Dioxide + Nitrogen+ Tetrahydrofuran)". *The Journal of Chemical Thermodynamics* 33, 513-521.

Linga, P., Adeyemo, A., Englezos, P., **2008**. "Medium-Pressure Clathrate Hydrate/Membrane Hybrid Process for Postcombustion Capture of Carbon Dioxide". *Environmental Science & Technology* 42, 315-320.

Rice, W., **2006**. "Hydrogen Production From Methane Hydrate With Sequestering of Carbon Dioxide". *International Journal of Hydrogen Energy* 31, 1955-1963.

Sloan, E.D., Koh, C., **2007**. "Clathrate Hydrates of Natural Gases", 3rd ed. CRC Press, Boca Raton, FL, USA.

Strobel, T.A., Koh, C.A., Sloan, E.D., **2009**. "Thermodynamic Predictions of Various Tetrahydrofuran and Hydrogen Clathrate Hydrates". *Fluid Phase Equilibria* 280, 61-67.

Zhang, Y., Yang, M., Song, Y., Jiang, L., Li, Y., Cheng, C., **2014**. "Hydrate Phase Equilibrium Measurements for (THF + SDS + $CO_2$ + $N_2$) Aqueous Solution Systems in Porous Media". *Fluid Phase Equilibria* 370, 12-18.

# 8 Final Remarks

This chapter is divided into two sections. The main conclusions of the present work are summarized in Section 8.1. Section 8.2 provides a list of suggestions as future work to enhance the knowledge on the topic.

## 8.1 Conclusions

The present work aims to highlight the impact of the NETmix technology on a system that is highly controlled by the mixing quality, heat and mass transfer. The NETmix technology has been previously shown to be suited for reactions where mixing is of high importance (Silva et al. 2008, Gomes et al. 2009, Laranjeira et al. 2011). Clathrates hydrates are materials where mixing and heat transfer is particularly critical (Sloan and Koh 2007).

Hydrates are icy-like solids that have the capacity to store large amounts of gas in its framework, inside small crystalline cages. This is particularly relevant because it allows the storage of gases such as carbon dioxide or other greenhouse gases that are released to the atmosphere. In times where the global warming is raising several concerns amongst researchers and governmental entities around the world, the

possibility of storing large amounts of greenhouse gases in the form of solid materials is an important achievement. The main problem resides in the development of a process to continuously produce hydrates with large heat transfer rates, one of the central difficulties of producing hydrates.

To firstly evaluate the potential of the technology for the production of gas hydrates, a similar strategy to the one used by Fonte (2013) is applied for the assessment of the heat transfer capacity of the NETmix technology in Chapter 3. A three-dimensional CFD model entitled the NUB (NETmix Unit Block) model, based on the Lab-Scale NETmix 2D, is applied. The results corroborate the observations made by Fonte (2013) regarding the enhancement of heat transfer due to the oscillatory regime that is obtained at Reynolds numbers above the critical. The results from this chapter clearly show that the regime changes that occur inside the mixing chambers are reflected in the heat transfer rates. Even below the critical Reynolds number, regime changes occur which results in an increase of the Nusselt number of the NETmix unit cell.

Chapter 3 has shown that when compared to parallel plates, NETmix can present three to eight times larger Nusselt number. This is observed at larger Reynolds numbers, large enough to promote the appearance of vortices that result in transversal mixing and intense fluid motion in the direction normal to the flow direction, and in a reduction of the thermal boundary layer that is responsible for the convective resistance within the NETmix network.

Chapter 3 also shows the influence of the variation of the ratio of the NETmix channel. The decrease of the ratio $\omega_n / d_c$ leads to an increase of the Nusselt number, being this behaviour well represented by empirical correlations. These correlations allow the determination of the NETmix unit cell Nusselt number assuming a fully developed thermal profile, i.e., there is no influence of the entrance effects, for any dimensions of the NETmix network, for the case of NETmix devices based on geometry presented by the Lab-Scale NETmix 2D.

A comparison of heat transfer capacity between NETmix and other available technologies is also made and presented in Chapter 3. These results show that NETmix can provide two to five times larger heat transfer capacity than typical stirred tanks (with jacket or serpentine), and nearly one order of magnitude larger than microfluidic devices. These preliminary results of heat transfer at the NETmix level are promising for the application of the technology for the continuous production of gas hydrates.

The experimental setup used at laboratorial scale for the application of the NETmix technology to produce carbon dioxide hydrates is described in Chapter 4, as well as its modes of operation. A small NETmix device named microNETmix is used to enhance the removal of heat from the reaction medium.

For a better evaluation of the capacity of the microNETmix device regarding heat transfer, the assessment of the heat transfer at the cooling plates of the reactor is required. The obtained results show that these plates have a similar behaviour to laminar flow between tubes, since the cooling fluid is distributed to cooling channels that absorb heat from the NETmix network from all surfaces.

The microNETmix device possesses global heat transfer coefficients in the range of $1000-2000\ \mathrm{W\cdot m^{-2}\cdot K^{-1}}$, which are of the same order of magnitude of plate heat exchangers. However, unlike plate heat exchangers, NETmix provides a large degree of mixing quality, which is crucial for the dissolution and precipitation of hydrates. Heat transfer is controlled by both convection in the cooling fluid and conduction in the steel between the plates.

The first studies regarding the production of gas hydrates, in particular of carbon dioxide, using the NETmix technology are presented in Chapter 5, more specifically carbon dioxide hydrates. The experimental setup has the capacity to treat about $1\ \mathrm{kg\cdot h^{-1}}$ of carbon dioxide. The influence of several parameters such as pressure, temperature, gas/water ratio and even the presence of thermodynamic promoters are studied. The dynamics of the system regarding temperature and pressure are

thoroughly analysed to understand the physics of the process. The experimental setup disclosed some complications regarding plugging of the gas line, due to ice and/or hydrates formation in the tubes.

From the experimental dynamic thermal data, it is concluded that in general, the change of the process parameters resulted in the expected outcomes. Special attention must be taken with changing the processes' temperature and pressure, which can result in the inhibition of the hydrates production, even if these conditions are within the region of stability of hydrates. Mass transfer limitations can be a potential explanation for this behaviour. Regarding macroscopic morphology, all experiments where hydrates were formed revealed solid materials with similar characteristics.

Gravimetric studies from dissociation tests and chemical analysis of carbon dioxide content show that relatively large amounts of carbon dioxide are captured. The conditions at which depressurization of the solid occurs have a significant impact on the solid gas uptake. Rapid depressurization at ambient temperature results in a more aggressive dissociation that leads to the release of large amounts of carbon dioxide. Therefore, ice may be formed during this process. Under these conditions, the amount of gas stored in the depressurized solid is about 6-8% in weight. On the contrary, if the depressurization is performed at low temperatures, the amount of carbon dioxide stored increases up to 18-19% in weight. This value is slightly different than the theoretical that ranges between 25-30% in weight. Some authors suggest that a thin layer of ice may be formed in these conditions, and this layer is the reason for the metastability of the hydrates (Kuhs et al. 2004). X-ray diffraction together with SEM imaging has shown that both ice and hydrate phases are present in the solid. This raises the question on how to handle hydrates to better characterize them at equilibrium conditions. Gravimetric studies have also showed that the dissociation kinetics can be reduced if the heat transfer rate is controlled.

Carbon dioxide uptake is measured through precipitation of calcium carbonate. The results from Chapter 5 show that the amount of weight that is lost in the first 60 minutes of the dissociation test corresponds to carbon dioxide that is released while

hydrate is dissociating and gradually transformed in ice. The remaining weight loss may be due to water evaporation. This technique has been applied for the first time to determine the amount of carbon dioxide in the solid hydrate. It has the advantage of being easy to implement and straightforward. However, the difficulty on the handling of the solid and the difficulty to avoid release of gas during depressurization is still a problem that this methodology cannot surpass.

Also presented in Chapter 5, is a simplified model based on an equilibrium model developed by Ballard (2002) which is helpful for flash computation and heat balances to units. This model is also used in an economical evaluation that was performed and presented in Chapter 6, that comprises the simulation of a process for the production and transport of carbon dioxide hydrates through pipelines and comparison with the most currently used technology, which is the transport of carbon dioxide in its supercritical state. This evaluation shows that transport of carbon dioxide, as hydrates slurry, is as competitive as in supercritical transport, resulting in a total cost of $18.5\,\mathrm{USD}\cdot\mathrm{ton}_{\mathrm{CO_2}}^{-1}$, which is 4% lower than the cost for transport in supercritical conditions This result highlights not only the potential of hydrates as a way of storing carbon dioxide, since it is economically competitive, but also on the potential impact of a technology such as NETmix to continuously produce hydrates using relatively small reaction times and equipment.

Finally, in Chapter 7, the first steps regarding the separation of flue gas are given. A mathematical model to simulate the flue gas separation in a counter-current process based on thermodynamic equilibrium data is developed. The simulation of the process demonstrates that carbon dioxide can be successfully separated from nitrogen with an efficiency of 85% if a process with 5 stages is used. The use of NETmix units as equilibrium stages can be conceptualized for the design of a new hydrate-based process for carbon dioxide capture.

This work shows that NETmix is a promising technology for the continuous production of gas hydrates at large throughputs. It has the capacity to absorb most

of the heat released during hydration on a device with a residence time of about one second. The technology for gas separation through a hydrate-based process still needs improvements, however, the potential of NETmix in that field has been shown, and its application in an industrial environment is expectable.

## 8.2 Future Work

Some suggestions of future work are presented below:

- Study of the influence of other geometrical parameters in the global heat transfer rate of the reactor, since the only studied parameter is the $\omega_n / d_c$ ratio. The ratio between the channel's width and chambers diameter is also an important parameter, since it may have a significant influence on the mixing scales and intensity.
- Determination of the Nusselt numbers for NETmix operating at turbulent regimes using CFD modelling.
- Assess the gas dissolution rates, namely carbon dioxide, in water on the NETmix device. This can be used by developing a CFD model based on VOF (Volume-of-Fluid) to simulate multiphase flow with interphase mass transfer. The obtainment of correlations to determine the interphase mass transfer coefficient $k_L a$ is extremely useful for a better design of NETmix devices for future applications. Also, investigate the capacity of the NETmix technology to generate high interfacial area between phases is of high interest.
- Modifications of the experimental setup. The use of RTD's instead of thermocouples can be used to increase the accuracy for the determination of the amount of produced hydrates. Also, the accumulation of ice in the gas lines is highly undesirable.
- Reduction of the number of network plates in the experimental setup. By reducing the residence time, it is possible to have an idea of the capacity of the NETmix for interphase mass transfer.

- Determine the amount of hydrates using other inline techniques, such as through density measurements.
- Production of hydrates other than from carbon dioxide, such as methane, ethane, propane and other hydrocarbons, using the NETmix technology.
- Experimentally separate carbon dioxide from nitrogen by precipitating mixed hydrates. Apply the technology in other gas mixtures such as $CH_4/CO_2$.
- Study the impact of other thermodynamic promoters on the equilibrium conditions, as well as the impact of the use of kinetic promoters.
- Extend the range of analysis, namely regarding temperature, of the model of Chapter 7 to simulate the counter-current flue gas separation.
- Development of a detailed economical model to evaluate the potential used of a hydrate-based process to separate carbon dioxide and nitrogen from the flue gas, and comparison with the already existing post-combustion technologies, namely amine-based scrubbing processes.

## 8.3 References

Ballard, A.L. **2002**. "A Non-Ideal Hydrate Solid Solution Model For a Multi-Phase Equilibria Program" [*Ph.D Thesis*]. Golden, CO, USA: Department of Chemical and Petroleum-Refining Engineering, Colorado School Of Mines.

Fonte, C.M. **2013**. "The NETmix Reactor: Application to High Added-Value Products" [*Ph.D Thesis*]. Porto, Portugal: Departamento de Engenharia Química, Universidade do Porto.

Gomes, P.J., Silva, V.M., Quadros, P.A., Dias, M.M., Lopes, J.C., **2009**. "A Highly Reproducible Continuous Process for Hydroxyapatite Nanoparticles Synthesis". *Journal of Nanoscience and Nanotechnology* 9, 3387-3395.

Kuhs, W.F., Genov, G., Staykova, D.K., Hansen, T., **2004**. "Ice Perfection and Onset of Anomalous Preservation of Gas Hydrates". *Physical Chemistry Chemical Physics* 6, 4917-4920.

Laranjeira, P.E., Martins, A.A., Nunes, M.I., Lopes, J.C.B., Dias, M.M., **2011**. "NETmix®, a New Type of Static Mixer: Experimental Characterization and Model Validation". *AIChE Journal* 57, 1020-1032.

Silva, V.M., Quadros, P.A., Laranjeira, P.E., Dias, M.M., Lopes, J.C., **2008**. "A Novel Continuous Industrial Process for Producing Hydroxyapatite Nanoparticles". *Journal of Dispersion Science and Technology* 29, 542-547.

Sloan, E.D., Koh, C., **2007**. "Clathrate Hydrates of Natural Gases", 3rd ed. CRC Press, Boca Raton, FL, USA.

# Appendix A Physical Properties

During the execution of the present work, several physical properties for the different components were used. These properties are presented in this section.

## A.1 Water Properties

Water's physical properties were obtained by fitting experimental data from Lide (1995) to polynomial expressions, in the temperature range of 273-373 K. For simplification, it is assumed that the influence of the pressure in these properties is negligible. The expressions for the density $\rho_{H_2O}$, viscosity $\mu_{H_2O}$, specific heat capacity $c^{w}_{P,H_2O}$ and thermal conductivity $\kappa_{H_2O}$ as a function of the temperature $T$ in K are presented from Equations A.1 to A.4.

$$\rho_{H_2O}\left(\mathrm{kg\cdot m^{-3}}\right) = 3.28\times10^{-5}T^3 - 3.46\times10^{-2}T^2 + 11.5T - 249.5 \tag{A.1}$$

$$\mu_{H_2O}\left(\mathrm{Pa\cdot s}\right) = 9.95\times10^{-12}T^4 - 1.18\times10^{-8}T^3 + 6.60\times10^{-6}T^2 - 1.65\times10^{-3}T + 1.57\times10^{-1} \tag{A.2}$$

$$c^{w}_{P,H_2O}\left(\mathrm{J\cdot kg^{-1}\cdot K^{-1}}\right) = 5.20\times10^{-7}T^4 - 7.84\times10^{-4}T^3 + 0.45T^2 - 116T + 1.53\times10^{4} \tag{A.3}$$

$$\kappa_{H_2O}\left(\mathrm{W\cdot m^{-1}\cdot K^{-1}}\right) = 1.86\times10^{-9}T^3 - 8.08\times10^{-6}T^2 + 5.73\times10^{-3}T + 4.32\times10^{-1} \tag{A.4}$$

## A.2 Ethanol – Water Mixture Properties

The properties of ethanol-water mixture are a function not only of the temperature, but also on the ethanol concentration. The mixture properties are calculated by

weighing the properties of the pure components by their weight concentration, and are determined from

$$M_{\text{mix}} = x^{\text{w}}_{\text{H}_2\text{O}} M_{\text{H}_2\text{O}} + x^{\text{w}}_{\text{EtOH}} M_{\text{EtOH}} \tag{A.5}$$

where $M_{\text{mix}}$, $M_{\text{H}_2\text{O}}$ and $M_{\text{EtOH}}$ represents the physical property (either density, heat capacity or thermal conductivity) of the mixture, pure water and pure ethanol, respectively, and $x^{\text{w}}_{\text{H}_2\text{O}}$ and $x^{\text{w}}_{\text{EtOH}}$ are the weight fraction of water and ethanol in the mixture, respectively. The mixture's viscosity is determined from

$$\ln \mu_{\text{mix}} = x^{\text{mol}}_{\text{H}_2\text{O}} \ln \mu_{\text{H}_2\text{O}} + x^{\text{mol}}_{\text{EtOH}} \ln \mu_{\text{EtOH}} \tag{A.6}$$

where $x^{\text{mol}}_{\text{H}_2\text{O}}$ and $x^{\text{mol}}_{\text{EtOH}}$ are the molar fractions of water and ethanol respectively. The physical properties of pure ethanol were obtained from the extensive database presented by Aspen Plus™, where experimental data from several sources is collected and fitted to several expressions, described in AspenTech (2012), as a function of the temperature $T$ in K (or similar), and represented by Equations A.7 to A.10.

$$\rho_{\text{EtOH}}\left(\text{kg}\cdot\text{m}^{-3}\right) = 2.12\times10^{3}\tau^{3} - 615.2\tau^{2} + 269.6\tau + 624.1\tau^{0.35} + 277.1 \tag{A.7}$$

$$\mu_{\text{EtOH}}\left(\text{Pa}\cdot\text{s}\right) = e^{5.11\times10^{7}T^{-3} - 6.86\times10^{5}T^{-2} + 4.55\times10^{2}T^{-1} - 16.3} \tag{A.8}$$

$$\begin{aligned} c^{\text{w}}_{\text{P, EtOH}}\left(\text{J}\cdot\text{kg}^{-1}\cdot\text{K}^{-1}\right) = {} & -5.74\times10^{-8}T^{4} + 1.08\times10^{-4}T^{3} - \\ & - 2.70\times10^{-2}T^{2} + 1.68T + 1.92\times10^{3} \end{aligned} \tag{A.9}$$

$$\kappa_{\text{EtOH}}\left(\text{W}\cdot\text{m}^{-1}\cdot\text{K}^{-1}\right) = 3.94\times10^{-7}T^{2} - 5.14\times10^{-4}T + 2.86\times10^{-1} \tag{A.10}$$

where $\tau$ is determined by

$$\tau = 1 - \frac{T}{T_{\text{crit}}} \tag{A.11}$$

where $T_{\text{crit}}$ is the critical temperature, and is equal to 514.6 K for ethanol. Again, the effect of the pressure is disregarded.

## A.3 Carbon Dioxide Properties

Regarding carbon dioxide, the properties used in the present work are its specific heat capacity of the gas and the vaporization enthalpy. These are used to perform

the energy balance to the microNETmix unit in Chapter 5. Some other required properties, such as solubility or vapour pressure are presented during Chapter 5.

For simplicity, and since the pressures involved do not pose a significant deviation from the ideal gas behaviour, it is assumed that the specific heat capacity of gaseous carbon dioxide is given by the ideal gas specific heat capacity, and is determined from

$$c_{\mathrm{P,\,CO_2}}^{\mathrm{w,\,ig}}\left(\mathrm{J\cdot kg^{-1}\cdot K^{-1}}\right)=662.6+786.6\left[\frac{1372/T}{\sinh\left(1372/T\right)}\right]^2+575.7\left[\frac{558.5/T}{\cosh\left(558.5/T\right)}\right]^2 \quad \text{(A.12)}$$

The relation from Equation A.12, valid in the range of 50-4500 K, was obtained from Aspen Plus™ database, which is based on experimental data. The vaporization enthalpy of carbon dioxide is also estimated by fitting data obtained from Aspen Plus™, valid in the temperature range of 273 to 293 K, at the vapour pressure at a given temperature. The expression used during this work is

$$\Delta H_{\mathrm{vap,\,CO_2}}^{\mathrm{w}}\left(\mathrm{J\cdot kg^{-1}}\right)=-56.6T^2+2.81\times10^4T-3.23\times10^6 \quad \text{(A.13)}$$

## A.4 Steel Properties

The material used for the construction of the microNETmix unit is stainless steel AISI 316. Due to the lack of information regarding the variation of the physical properties with the temperature, a constant value is used for each of the properties, as shown in Table A.1. Table A.1 also shows the typical ranges of each of the properties. These properties are used for the simulation of heat transfer in the cooling plates of the microNETmix unit (Chapter 4).

Table A.1 – Stainless steel 316 physical properties (AZoM 2017).

| PROPERTY | MINIMUM | MAXIMUM | CONSIDERED |
|---|---|---|---|
| $\rho_{\text{steel}}\left(\mathbf{kg \cdot m^{-3}}\right)$ | 7870 | 8070 | 8000 |
| $c^{\text{w}}_{\text{P, steel}}\left(\mathbf{J \cdot kg^{-1} \cdot K^{-1}}\right)$ | 490 | 530 | 500 |
| $\kappa_{\text{steel}}\left(\mathbf{W \cdot m^{-1} \cdot K^{-1}}\right)$ | 13 | 17 | 16.3 |

## A.5 References

AspenTech, Aspen Technology, Inc., **2012**. "Aspen Physical Property System - Physical Property Models". Burlington, MA, USA.

AZoM, "Stainless Steel - Grade 316". *Published online at Azo Materials*. Available at: http://www.azom.com/properties.aspx?ArticleID=863.

Lide, D.R., **1995**. "CRC Handbook of Chemistry and Physics: A Ready-reference Book of Chemical and Physical Data", 76th ed. CRC Press, Boca Raton, FL, USA.

# Appendix B CSMGem Fugacity Models

Ballard (2002) developed a software (CSMGem) that enables not only the estimation of the equilibrium composition of each of the present phases, but also the estimation of the amount of each phase in equilibrium, at a given temperature and pressure. This is done by minimizing the Gibbs energy of all potential phases, thus determining which of the phases are present at a given set of conditions, as explained in Chapter 5. To determine this, each of the phases has to be modelled. The models of each of the phases used by CSMGem and of interest for this work are presented in this section, and detailed in Ballard (2002).

The fugacity $f_{i,k}$ of any component $i$ in phase $k$ can be expressed as

$$f_{i,k} = f_i^{\mathrm{ig}} e^{\frac{\hat{\mu}_{i,k} - \tilde{g}_i^{\mathrm{mol,ig}}}{R_{\mathrm{gas}} T}} \tag{B.1}$$

where $f_i^{\mathrm{ig}}$ is the ideal gas fugacity of component $i$ at 1 bar, $\hat{\mu}_{i,k}$ is the chemical potential of component $i$ in phase $k$, $\tilde{g}_i^{\mathrm{mol,ig}}$ is the molar Gibbs energy of component $i$ in ideal gas state, calculated using

$$\frac{\tilde{g}_i^{\mathrm{mol,ig}}}{R_{\mathrm{gas}} T} = \frac{\tilde{g}_i^{\mathrm{mol,o}}}{R_{\mathrm{gas}} T^{\mathrm{o}}} - \int_{T^{\mathrm{o}}}^{T} \frac{\tilde{h}_i^{\mathrm{mol,ig}}}{R_{\mathrm{gas}} T^2} dT \tag{B.2}$$

where $\tilde{g}_i^{\mathrm{mol,o}}$ is the molar Gibbs energy of formation at $T^{\mathrm{o}}$ and $p^{\mathrm{o}}$, and $\tilde{h}_i^{\mathrm{mol,ig}}$ is the ideal gas molar enthalpy at $p^{\mathrm{o}}$, and can be calculated from

$$\tilde{h}_i^{\mathrm{mol,ig}} = \tilde{h}_{\mathrm{f},i}^{\mathrm{mol,o}} + \int_{T^{\mathrm{o}}}^{T} c_{\mathrm{P},i}^{\mathrm{mol}} dT \tag{B.3}$$

where $\tilde{h}_{\mathrm{f},\,i}^{\mathrm{mol,\,o}}$ is the molar enthalpy of formation at $T^{\mathrm{o}}$ and $p^{\mathrm{o}}$.

Each of the fugacity models is described in the following sections.

## B.1 Aqueous Phase

The aqueous phase is described by the Shock and Helgeson equation with a coupled Bromley activity model. This model was chosen due to its capacity of handling salts and alcohols. The aqueous phase model accounts for two types of species in the aqueous phase: solutes and water.

The chemical solution of each of the solutes (all components except water) in the aqueous phase is given by

$$\frac{\hat{\mu}_{i,\,\mathrm{aq}}}{R_{\mathrm{gas}}T} = \frac{\overline{g}_{i}^{\mathrm{mol,\,o*}}}{R_{\mathrm{gas}}T^{\mathrm{o}}} - \int_{T^{\mathrm{o}}}^{T} \frac{\overline{h}_{i}^{\mathrm{mol,\,*}}}{R_{\mathrm{gas}}T^{2}}\,dT + \int_{p^{\mathrm{o}}}^{p} \frac{\overline{\nu}_{i}^{\mathrm{mol,\,*}}}{R_{\mathrm{gas}}T}\,dp + \ln a_{i,\,\mathrm{aq}} \tag{B.4}$$

where $\overline{g}_{i_0}^{\mathrm{mol,\,o*}}$, $\overline{h}_{i}^{\mathrm{mol,\,*}}$ and $\overline{\nu}_{i}^{\mathrm{mol,\,*}}$ are the partial molar Gibbs energy of formation, enthalpy and volume of component $i$ in a hypothetical 1 molal solution and at the standard temperature and pressure, respectively, and $a_{i,\,\mathrm{aq}}$ is the activity of component $i$ in the aqueous phase. The partial molar enthalpy is calculated through Equation B.3, where the partial molar heat capacity and volume of solutes in the aqueous phase are determined by

$$\overline{c}_{\mathrm{P},\,i}^{\mathrm{mol,\,*}} = c_1 + \frac{c_2}{\left(T-\Theta\right)^2} - \frac{2T}{\left(T-\Theta\right)^3}\left[c_3\left(p-p^{\mathrm{o}}\right) + c_4 \ln\left(\frac{\Psi+p}{\Psi+p^{\mathrm{o}}}\right)\right] + \omega_{\mathrm{Born}} T X \tag{B.5}$$

$$\overline{\nu}_{i}^{\mathrm{mol,\,*}} = \nu_1 + \frac{\nu_2}{\Psi+p} + \left[\nu_3 + \frac{\nu_4}{\Psi+p}\right]\left(T-\Theta\right)^{-1} - \frac{\omega_{\mathrm{Born}}}{\varepsilon_{\mathrm{elec}}^{2}}\left(\frac{\partial \varepsilon}{\partial p}\right)_{T} \tag{B.6}$$

where $\Theta = 288\ \mathrm{K}$, $\Psi = 2600\ \mathrm{bar}$, $\varepsilon_{\mathrm{elec}}$ is the dielectric constant of water, $\omega_{\mathrm{Born}}$ is the Born coefficient, and $X$ is described as

$$X = \frac{1}{\varepsilon_{\text{elec}}}\left[\left(\frac{\partial^2 \ln \varepsilon_{\text{elec}}}{\partial T^2}\right)_p - \left(\frac{\partial^2 \ln \varepsilon_{\text{elec}}}{\partial T^2}\right)_p^2\right] \tag{B.7}$$

The dielectric constant is given by

$$\varepsilon_{\text{elec}} = \sum_{i=0}^{2}\left(a_{1i} + a_{2i}p + a_{3i}p^2\right)T^i \tag{B.8}$$

The expression for the chemical potential of water in the aqueous phase is

$$\frac{\hat{\mu}_{\text{H}_2\text{O, aq}}}{R_{\text{gas}}T} = \frac{\tilde{g}^{\text{mol}}_{\text{H}_2\text{O}}}{R_{\text{gas}}T^{\text{o}}} - \int_{T^{\text{o}}}^{T}\frac{\tilde{h}^{\text{mol}}_{\text{H}_2\text{O}}}{R_{\text{gas}}T^2}dT + \int_{p^{\text{o}}}^{p}\frac{\tilde{\nu}^{\text{mol}}_{\text{H}_2\text{O}}}{R_{\text{gas}}T}dp + \ln a_{\text{H}_2\text{O, aq}} \tag{B.9}$$

where the properties refer to the pure liquid water phase. This is a simplification, since it determines the potential of water from its pure liquid water. Therefore, it is only valid when the molar water fraction is above 0.65. The volume of water as a function of the temperature and pressure is determined by

$$\nu^{\text{mol}}_{\text{H}_2\text{O}} = \sum_{i=0}^{3}\left(a_{1i} + a_{2i}p + a_{3i}p^2 + a_{4i}p^3\right)T^i \tag{B.10}$$

The Bromley activity model is used to represent the activity of all species in the aqueous phase. This model treats salts as separate ionic species. The fugacity of the salt is determined by

$$f_{\text{salt}} = \left(f_{\text{anion}}\right)^a\left(f_{\text{cation}}\right)^b \tag{B.11}$$

where $a$ is the number of anions in the salt, and $b$ is the number of cations. The activity of each species is determined using

$$a_{j,\text{aq}} = \frac{\tilde{m}_j}{\tilde{m}_j^*}\gamma_{j,\text{aq}} \tag{B.12}$$

where $\tilde{m}_j$ is the molality of component $j$ (which comprises all species except water), expressed in moles of the species per 1 kg of water, $\tilde{m}_j^*$ is the molality at the standard state (1 molal), and $\gamma_{j,\text{aq}}$ is the activity coefficient of species $j$ in the aqueous phase.

For ionic species, the activity coefficients can be determined using the following expression

$$\ln a_{j,\,\mathrm{aq}} = z_j^2 \gamma_{\mathrm{LR}} + \sum_{k=\mathrm{ionic}} \tilde{m}_k \gamma_{\mathrm{SR}_{j,k}} \left( \frac{\left|z_j\right| + \left|z_k\right|}{2} \right)^2 + \\ + 2 \sum_{k=\mathrm{molecular}} \tilde{m}_k \gamma_{\mathrm{P1}_{j,k}} - \frac{z_j^2}{4I^2} \sum_k \sum_n \tilde{m}_k \tilde{m}_n \gamma_{\mathrm{P2}_{k,n}} \tag{B.13}$$

where $z_j$ is the charge of ion $j$ and $I$ is the ionic strength of the solution, expressed as

$$I = \frac{1}{2} \sum_{k=\mathrm{ionic}} z_k^2 \tilde{m}_k \tag{B.14}$$

The Debye-Hückel equation is used to determine the activity coefficient of long-range interactions $\gamma_{\mathrm{LR}}$

$$\gamma_{\mathrm{LR}} = \frac{-A_{\mathrm{DH}} \sqrt{I}}{1 + \sqrt{I}} \tag{B.15}$$

where $A_{\mathrm{DH}}$ is the Debye-Hückel constant and is given by

$$A_{\mathrm{DH}} = \left( \frac{e^2}{\varepsilon_0 \varepsilon_{\mathrm{elec}} R_{\mathrm{gas}} T} \right)^{3/2} \frac{N_{\mathrm{A}}^2}{8\pi} \sqrt{2\rho_{\mathrm{H_2O}}} \tag{B.16}$$

where $e = 1.60218 \times 10^{-19}$ C is the electronic charge, $\varepsilon_0 = 8.85419 \times 10^{-12}\ \mathrm{C^2 \cdot N^{-1} \cdot m^{-2}}$ is the vacuum permittivity and $\varepsilon_{\mathrm{elec}}$ is the dielectric constant determined through Equation B.8.

Short-range interactions are expressed by (applied only for ionic species)

$$\gamma_{\mathrm{SR}_{j,k}} = \frac{\left(0.13816 + 0.6 B_{j,k}\right) \left|z_j z_k\right|}{\left(1 + \dfrac{3I}{2\left|z_j z_k\right|}\right)^2} + B_{j,k} + C_{j,k} I + D_{j,k} I^2 \tag{B.17}$$

where $B_{j,k}$, $C_{j,k}$ and $D_{j,k}$ are interaction parameters. Interactions between ions and molecular species are expressed as

$$\gamma_{\mathrm{P1}_{j,k}} = \beta_{0_{j,k}} + \frac{\beta_{1_{j,k}}}{2I}\left[1-\left(1+2\sqrt{I}\right)e^{-2\sqrt{I}}\right] \tag{B.18}$$

$$\gamma_{\mathrm{P2}_{j,k}} = \beta_{1_{j,k}}\left[1-\left(1+2\sqrt{I}+2I\right)e^{-2\sqrt{I}}\right] \tag{B.19}$$

Equations B.18 and B.19 are applied for the $j$ molecular species.

The activity coefficient of molecular species in aqueous phase is expressed using

$$\ln\gamma_{j,\mathrm{aq}} = 2\sum_{k}\tilde{m}_k\gamma_{\mathrm{P1}_{j,k}} \tag{B.20}$$

The activity of water is explicitly expressed by accounting for contributions from ionic and molecular species

$$\begin{aligned}\ln a_{\mathrm{H_2O,\,aq}} = &\frac{\sum_{c}\sum_{a}\tilde{m}_c\tilde{m}_a z_c^2 z_a^2\gamma_{I_{c,a}}}{\sum_{c}\tilde{m}_c z_c^2\sum_{a}\tilde{m}_a z_a^2} - \\ &- M_{\mathrm{w,\,H_2O}}\left[\sum_{j}\sum_{k}\tilde{m}_j\tilde{m}_k\left(\gamma_{\mathrm{P1}_{j,k}} - \frac{\gamma_{\mathrm{P2}_{j,k}}}{2I}\right) + \sum_{j=\mathrm{molecular}}\tilde{m}_j\right]\end{aligned} \tag{B.21}$$

The sums of the first term are for cations $c$ and anions $a$ only. The total ionic contribution to the water activity $\gamma_{I_{c,a}}$ is expressed as

$$\gamma_{I_{c,a}} = -M_{\mathrm{w,\,H_2O}}\left(\frac{2I}{\left|z_c z_a\right|} + \gamma_{\mathrm{DH}} + \gamma_{B_{c,a}}\right) \tag{B.22}$$

where $\gamma_{\mathrm{DH}}$ accounts for long-range ionic interactions and is expressed as

$$\gamma_{\mathrm{DH}} = 2A_{\mathrm{DH}}\left(\frac{1-\left(1+\sqrt{I}\right)^2}{1+\sqrt{I}} + 2\ln\left(1+\sqrt{I}\right)\right) \tag{B.23}$$

and $\gamma_{B_{c,a}}$ accounts for short-range ionic interactions and is expressed as

$$\gamma_{B_{c,a}} = \frac{\left(0.13816 + 0.6B_{c,a}\right) I \left|z_c z_a\right|}{3/2} \left[ \frac{1 + \frac{3I}{\left|z_c z_a\right|}}{\left(1 + \frac{3I}{2\left|z_c z_a\right|}\right)^2} - \frac{\ln\left(1 + \frac{3I}{2\left|z_c z_a\right|}\right)}{\frac{3I}{2\left|z_c z_a\right|}} \right] + \\ + \frac{2}{\left|z_c z_a\right|} \left( \frac{1}{2} B_{c,a} I^2 + \frac{2}{3} C_{c,a} I^3 + \frac{3}{4} D_{c,a} I^4 \right) \tag{B.24}$$

Note that all Debye-Hückel terms are for the ionic solution and not for the individual ionic interactions.

## B.2 Vapour Phase

A cubic equation of state is needed to model well high-pressure processes. The Soave modification of the Redlich-Kwong EoS (SRK) was chosen to represent both the vapour phase and the liquid hydrocarbons phase. The SRK EoS is expressed as

$$p = \frac{R_{\text{gas}} T}{\tilde{\nu}^{\text{mol}} - b} - \frac{a}{\tilde{\nu}^{\text{mol}} \left(\tilde{\nu}^{\text{mol}} + b\right)} \tag{B.25}$$

where $\tilde{\nu}^{\text{mol}}$ is the specific molar volume, $a$ is the energy constant and $b$ is the volume constant. The energy constant is expressed as

$$a = \sum_{i=1}^{C} \sum_{j=1}^{C} x_i^{\text{mol}} x_j^{\text{mol}} a_{i,j} \tag{B.26}$$

where $a_{i,j}$ represents the attractive forces between components $i$ and $j$, and is expressed as

$$a_{i,j} = \left(1 - k_{i,j}\right) \sqrt{\alpha_i a_i \alpha_j a_j} \tag{B.27}$$

where $k_{i,j}$ is the interaction parameter between components $i$ and $j$, $a_i$ represents the attractive forces between two molecules of component $i$, and is given by

$$a_i = 0.42747 \frac{R_{\text{gas}}^2 T_{\text{crit}_i}^2}{p_{\text{crit}_i}} \tag{B.28}$$

$\alpha_i$ is a corrective term for the vapour pressure of pure component $i$, expressed as

$$\alpha_i = \left[1 + S_{1_i}\left(1 - \sqrt{T_{\text{red}_i}}\right) + S_{2_i}\frac{\left(1 - \sqrt{T_{\text{red}_i}}\right)^2}{\sqrt{T_{\text{red}_i}}}\right] \tag{B.29}$$

where $S_{1_i}$ is expressed in terms of the acentric factor $\omega_{\text{ac},\,i}$ as

$$S_{1_i} = 0.48508 + 1.55171\omega_{\text{ac},\,i} - 0.15613\omega_i^2 \tag{B.30}$$

and $S_{2_i}$ is a constant. The volume constant $b$ from Equation B.25 represents the average hard core volume of the mixture, and is given by

$$b = \sum_{i=1}^{C} x_i^{\text{mol}} b_i \tag{B.31}$$

where $b_i$ is the hard core volume of the component $i$, and is expressed as

$$b_i = 0.08664\frac{R_{\text{gas}}T_{\text{crit}_i}}{p_{\text{crit}_i}} \tag{B.32}$$

The fugacity of any component in the vapour phase using the SRK EoS can be found using the following relationship

$$f_i = x_i^{\text{mol}} p e^{\int_0^p \left(\frac{\bar{v}_i^{\text{mol}}}{R_{\text{gas}}T} - \frac{1}{p}\right)dp} \tag{B.33}$$

Equation B.33 is then integrated from 0 to $p$, using the SRK model to determine the partial molar volume of component $i$.

## B.3 Hydrate Phase

The hydrate phase is modelled using a modified version of the van der Waals and Platteeuw model. The chemical potential of water in the hydrate phase $\hat{\mu}_{\text{H}_2\text{O},\,\text{hyd}}$ is given by

$$\frac{\hat{\mu}_{\text{H}_2\text{O},\,\text{hyd}}}{R_{\text{gas}}T} = \frac{\tilde{g}^{\text{mol}}_{\text{H}_2\text{O},\,\beta}}{R_{\text{gas}}T} + \sum_m \upsilon_m \ln\left(1 - \sum_i \theta_{i,\,m}\right) \tag{B.34}$$

where $\tilde{g}^{\mathrm{mol}}_{\mathrm{H_2O},\,\beta}$ is the specific molar Gibbs energy of water in the standard (empty) hydrate lattice at a given volume, temperature and pressure, $\upsilon_m$ is the number of cages of type $m$ normalized by the number of water molecules in the hydrate lattice, and $\theta_{i,\,m}$ is the fractional occupancy of guest $i$ in hydrate cage $m$. The fractional occupancy is described by a Langmuir-type expression:

$$\theta_{i,\,m} = \frac{C_{i,\,m} f_{i,\,\mathrm{hyd}}}{1 + \sum_j C_{j,\,m} f_{j,\,\mathrm{hyd}}} \tag{B.35}$$

where $f_{i,\,\mathrm{hyd}}$ is the fugacity of component $i$ in the hydrate phase. $C_{i,\,m}$ is the Langmuir constant which describes the potential interaction between encaged molecule $i$ and the water molecules in the hydrate cage $m$ surrounding it. $C_{i,\,m}$ is expressed as

$$C_{i,\,m} = \frac{4\pi}{kT} \int_0^{R_m - a_i} e^{-\frac{\chi_{i,\,m}}{kT}} r^2 \, dr \tag{B.36}$$

where $R_m$ is the radius of the cage $m$ and $\chi_{i,\,m}$ is the potential function. The potential function can be expressed as

$$\chi_{i,\,m} = 2\varepsilon_{\mathrm{p},\,i} z_m \left[ \frac{\sigma_i^{12}}{R_m^{11} r} \left( \delta^{10}_{i,\,m} + \frac{a_i}{R_m} \delta^{11}_{i,\,m} \right) - \frac{\sigma_i^{6}}{R_m^{5} r} \left( \delta^{4}_{i,\,m} + \frac{a_i}{R_m} \delta^{5}_{i,\,m} \right) \right] \tag{B.37}$$

where

$$\delta^N_{i,\,m} = \frac{1}{N} \left[ \left( 1 - \frac{r}{R_m} - \frac{a_i}{R_m} \right)^{-N} - \left( 1 + \frac{r}{R_m} - \frac{a_i}{R_m} \right)^{-N} \right] \tag{B.38}$$

and $z_m$ is the coordination number and $a_i$, $\varepsilon_{\mathrm{p},\,i}$ and $\sigma_i$ are the hard core radius, potential well depth, and soft core radius of guest $i$ in hydrate cage $m$, respectively.

The fugacity of each component in the hydrate phase can be determined by relating the chemical potential of water in the hydrate to that in aqueous phase, which is

done by considering the energy change associated with forming a hydrate and an aqueous phase, both from the empty lattice, as described by

$$\frac{\Delta\hat{\mu}_{\mathrm{H_2O,\,hyd}}}{R_{\mathrm{gas}}T}=\frac{\hat{\mu}_{\mathrm{H_2O,\,hyd}}-\tilde{g}^{\mathrm{mol}}_{\mathrm{H_2O},\,\beta}}{R_{\mathrm{gas}}T}=\sum_m \upsilon_m \ln\left(1-\sum_i \theta_{i,\,m}\right) \tag{B.39}$$

and

$$\begin{aligned}\frac{\Delta\hat{\mu}_{\mathrm{H_2O,\,aq}}}{R_{\mathrm{gas}}T}=\frac{\hat{\mu}_{\mathrm{H_2O,\,aq}}-\tilde{g}^{\mathrm{mol}}_{\mathrm{H_2O},\,\beta}}{R_{\mathrm{gas}}T}=\frac{\Delta\tilde{g}^{\mathrm{mol}}_{\mathrm{H_2O}}}{R_{\mathrm{gas}}T^{\mathrm{o}}}-\int_{T^{\mathrm{o}}}^{T}\frac{\Delta\tilde{h}^{\mathrm{mol}}_{\mathrm{H_2O}}}{R_{\mathrm{gas}}T^2}dT+\\ +\int_{p^{\mathrm{o}}}^{p}\frac{\Delta\tilde{\nu}^{\mathrm{mol}}_{\mathrm{H_2O}}}{R_{\mathrm{gas}}T}dp+\ln a_{\mathrm{H_2O,\,aq}}\end{aligned} \tag{B.40}$$

Equation B.40 can be rewritten as

$$\frac{\Delta\hat{\mu}_{\mathrm{H_2O,\,aq}}}{R_{\mathrm{gas}}T}=\frac{\tilde{g}^{\mathrm{mol}}_{\mathrm{H_2O}}}{R_{\mathrm{gas}}T^{\mathrm{o}}}-\int_{T^{\mathrm{o}}}^{T}\frac{\tilde{h}^{\mathrm{mol}}_{\mathrm{H_2O}}}{R_{\mathrm{gas}}T^2}dT+\int_{p^{\mathrm{o}}}^{p}\frac{\tilde{\nu}^{\mathrm{mol}}_{\mathrm{H_2O}}}{R_{\mathrm{gas}}T}dp+\ln a_{\mathrm{H_2O,\,aq}} \tag{B.41}$$

and

$$\frac{\tilde{g}_{\mathrm{H_2O},\,\beta}}{R_{\mathrm{gas}}T}=\frac{\tilde{g}^{\mathrm{mol,\,o}}_{\mathrm{H_2O},\,\beta}}{R_{\mathrm{gas}}T^{\mathrm{o}}}-\int_{T^{\mathrm{o}}}^{T}\frac{\tilde{h}^{\mathrm{mol}}_{\mathrm{H_2O},\,\beta}}{R_{\mathrm{gas}}T^2}dT+\int_{p^{\mathrm{o}}}^{p}\frac{\tilde{\nu}^{\mathrm{mol}}_{\mathrm{H_2O},\,\beta}}{R_{\mathrm{gas}}T}dp \tag{B.42}$$

The fugacity of water in the hydrate is given by

$$f_{\mathrm{H_2O,\,hyd}}=f_{\mathrm{H_2O,\,aq}}e^{\frac{\Delta\hat{\mu}_{\mathrm{H_2O,\,hyd}}-\Delta\hat{\mu}_{\mathrm{H_2O,\,aq}}}{R_{\mathrm{gas}}T}} \tag{B.43}$$

The drawback of this approach is that an aqueous (or ice) phase has to be present in the equilibrium, which may not be always the case. Ballard (2002) derives a new expression for the calculation of the fugacity that eliminates this constraint. Essentially two modifications to the classical hydrates model were done by Ballard (2002): an activity coefficient which is based on the knowledge of the hydrate volume and a characterization of the standard (empty) hydrate state itself. These modifications allows for a more accurate prediction of the hydrate properties at high-pressures and also allows the determination of the equilibrium when aqueous water (or ice) is present, as already stated. In the first modification, the hydrate volume

calculation takes into account the distortion of the lattice due to guests, which is not considered in the classical theory.

For a thorough description of the modifications to the van der Waals and Platteeuw mode, please refer to Ballard (2002).

## B.4 References

Ballard, A.L. **2002**. "A Non-Ideal Hydrate Solid Solution Model For a Multi-Phase Equilibria Program" [*Ph.D Thesis*]. Golden, CO, USA: Department of Chemical and Petroleum-Refining Engineering, Colorado School Of Mines.

# Appendix C Calcium Carbonate Equilibrium

The species equilibrium for the precipitation of calcium carbonate, used to determine the amount of carbon dioxide from a hydrate (see Chapter 5), is presented in this section.

## C.1 Equilibrium Modelling

When carbon dioxide is in contact with water, carbon dioxide dissolves, forming an aqueous acid solution. For this analysis, it is assumed that the used water is pure, i.e., no ions or dissolved gases are initially present. The dissolution of carbon dioxide in water can be described by the following reaction:

$$\mathrm{CO_2(g)} \rightleftharpoons \mathrm{CO_2(aq)} \tag{C.1}$$

The process represented by Equation C.1 is mathematically described by the Henry's law, as introduced in Section 5.2, using the Henry's constant $K^{\mathrm{mol}}_{\mathrm{H,\,CO_2}}$.

$$p_{\mathrm{CO_2}} = K^{\mathrm{mol}}_{\mathrm{H,\,CO_2}} x^{\mathrm{mol}}_{\mathrm{CO_2}} \tag{C.2}$$

Henry's constant from Equation C.2 can be rewritten so that it is presented as a function of the carbon dioxide concentration in the aqueous phase at equilibrium.

$$p_{\mathrm{CO_2}} = K^{\mathrm{mol},*}_{\mathrm{H,\,CO_2}} \left[\mathrm{CO_2}\right]_{\mathrm{eq}} \tag{C.3}$$

The dissolved carbon dioxide is in equilibrium with carbonic acid, as represented by the following reaction:

$$\mathrm{CO_2(aq)} + \mathrm{H_2O(l)} \rightleftharpoons \mathrm{H_2CO_3(aq)} \tag{C.4}$$

This equilibrium is represented by the equilibrium constant $H^{\text{mol}}_{\text{CO}_2}$.

$$H^{\text{mol}}_{\text{CO}_2} = \frac{\left[\text{H}_2\text{CO}_3\right]_{\text{eq}}}{\left[\text{CO}_2\right]_{\text{eq}}} \tag{C.5}$$

where $\left[\text{H}_2\text{CO}_3\right]_{\text{eq}}$ is the molar concentration of dissolved carbonic acid. Carbonic acid is a diprotic acid, containing two protons that dissociate. Furthermore, carbon acid is considered a weak acid. Therefore, two dissociation constants are required. The first is used for the dissociation into the bicarbonate anion, and the second for the dissociation into the carbonate anion.

$$\text{H}_2\text{CO}_3\left(\text{aq}\right) \rightleftharpoons \text{HCO}_3^-\left(\text{aq}\right) + \text{H}^+\left(\text{aq}\right) \tag{C.6}$$

$$\text{HCO}_3^-\left(\text{aq}\right) \rightleftharpoons \text{CO}_3^{2-}\left(\text{aq}\right) + \text{H}^+\left(\text{aq}\right) \tag{C.7}$$

Reactions represented by Equations C.6 and C.7 are mathematically represented by their dissociation constants $k^{\text{mol}}_{a_1,\,\text{CO}_2}$ and $k^{\text{mol}}_{a_2,\,\text{CO}_2}$.

$$k^{\text{mol}}_{a_1,\,\text{CO}_2} = \frac{\left[\text{HCO}_3^-\right]_{\text{eq}}\left[\text{H}^+\right]_{\text{eq}}}{\left[\text{H}_2\text{CO}_3\right]_{\text{eq}}} \tag{C.8}$$

$$k^{\text{mol}}_{a_2,\,\text{CO}_2} = \frac{\left[\text{CO}_3^{2-}\right]_{\text{eq}}\left[\text{H}^+\right]_{\text{eq}}}{\left[\text{HCO}_3^-\right]_{\text{eq}}} \tag{C.9}$$

The precipitation of calcium carbonate results from the chemical reaction between the carbonate anion and calcium cation. Therefore, a calcium source is required. It is desirable to use a strong base as the calcium source, to guarantee that all calcium is dissociated. The calcium source used in this work is calcium hydroxide.

$$\text{Ca}\left(\text{OH}\right)_2\left(\text{aq}\right) \rightleftharpoons \text{Ca}^{2+}\left(\text{aq}\right) + 2\text{OH}^-\left(\text{aq}\right) \tag{C.10}$$

Calcium carbonate precipitation occurs when the ionic product is larger than the solubility product. The ionic product for calcium carbonate $IP_{\text{CaCO}_3}$ is given by

$$IP_{\text{CaCO}_3} = \left[\text{Ca}^{2+}\right]_{\text{eq}}\left[\text{CO}_3^{2-}\right]_{\text{eq}} > k^{\text{mol}}_{\text{sp},\,\text{CaCO}_3} \tag{C.11}$$

The value of $k_{\mathrm{sp,\,CaCO_3}}^{\mathrm{mol}}$ is extremely low, resulting in a precipitation of calcium carbonate even when small amounts of carbon dioxide is present. Finally, water also possesses its own auto-ionization constant, as a result of the self-dissociation into hydroxide anions and protons.

$$\mathrm{H_2O(l)} \rightleftharpoons \mathrm{H^+(aq)} + \mathrm{OH^-(aq)} \tag{C.12}$$

Equation C.12 is usually written as a function not of the protons but of the hydronium cations.

$$2\mathrm{H_2O(l)} \rightleftharpoons \mathrm{H_3O^+(aq)} + \mathrm{OH^-(aq)} \tag{C.13}$$

For simplification, it is assumed that $\mathrm{H^+}$ and $\mathrm{H_3O^+}$ are interchangeable concepts, and thus the $\mathrm{H^+}$ notation is kept. Equation C.12 (or C.13) is mathematically described by

$$k_{\mathrm{w}}^{\mathrm{mol}} = \left[\mathrm{H^+}\right]_{\mathrm{eq}} \left[\mathrm{OH^-}\right]_{\mathrm{eq}} \tag{C.14}$$

A charge balance equation is required to describe the electrical neutrality of the solution.

$$\left[\mathrm{H^+}\right]_{\mathrm{eq}} + 2\left[\mathrm{Ca^{2+}}\right]_{\mathrm{eq}} = \left[\mathrm{OH^-}\right]_{\mathrm{eq}} + \left[\mathrm{HCO_3^-}\right]_{\mathrm{eq}} + 2\left[\mathrm{HCO_3^{2-}}\right]_{\mathrm{eq}} \tag{C.15}$$

Let's assume that the solution is being contained in a flask with a volume of $V_{\mathrm{flask}}$. Initially there is a solution with a volume of $V_{\mathrm{sol,\,ini}}$ and an initial concentration of calcium hydroxide of $\left[\mathrm{Ca(OH)_2}\right]_{\mathrm{ini}}$. The mass balance for calcium is given by

$$\left[\mathrm{Ca(OH)_2}\right]_{\mathrm{ini}} = \left[\mathrm{Ca^{2+}}\right]_{\mathrm{eq}} + \left[\mathrm{CaCO_3}\right]_{\mathrm{eq}} \tag{C.16}$$

Calcium carbonate is only formed if condition represented through Equation C.11 is reached.

Assuming that equilibrium is reached when in contact with atmospheric air, and that the flask is closed, the mass balance of the carbonate species is given by

$$n_{\mathrm{CO_3}}^{\mathrm{mol,\,tot,\,ini}} = \left(\left[\mathrm{CO_2}\right]_{\mathrm{eq}} + \left[\mathrm{H_2CO_3}\right]_{\mathrm{eq}} + \left[\mathrm{HCO_3^-}\right]_{\mathrm{eq}} + \left[\mathrm{CO_3^{2-}}\right]_{\mathrm{eq}} + \left[\mathrm{CaCO_3}\right]_{\mathrm{eq}}\right) V_{\mathrm{sol,\,ini}} + n_{\mathrm{CO_2}}^{\mathrm{mol,\,vap,\,ini}} \tag{C.17}$$

where $n_{CO_3}^{mol,\,tot,\,ini}$ is the total number of moles of all carbonate species initially in the flask, and $n_{CO_2}^{mol,\,vap,\,ini}$ is the molar amount of carbon dioxide in the vapour phase in equilibrium with the solution. In these conditions, the ideal gas law can be applied to determine $n_{CO_2}^{mol,\,vap,\,ini}$ as follows

$$n_{CO_2}^{mol,\,vap,\,ini} = \frac{p_{CO_2}\left(V_{flask} - V_{sol,\,ini}\right)}{RT} \tag{C.18}$$

Carbon dioxide partial pressure in the air $p_{CO_2}$ is given by

$$p_{CO_2} = y_{CO_2}^{mol} p \tag{C.19}$$

Where $y_{CO_2}^{mol}$ is the molar fraction of carbon dioxide in the air, which is close to 0.035% in moles, and $p$ is the atmospheric pressure, close to 1 atm.

Once hydrate is added to this solution, it dissociates into water and carbon dioxide. The volume of the solution slightly increases due to the presence of water in the hydrate, displacing the equilibrium that was previously achieved. The volume increase is given by

$$V_{sol,\,fin} = V_{sol,\,ini} + \frac{m_{hyd} w_{H_2O}^{w}}{\rho_{H_2O}} \tag{C.20}$$

where $m_{hyd}$ is the mass of the hydrate added to the solution, $w_{H_2O}^{w}$ is the mass fraction of water in the hydrate, and $\rho_{H_2O}$ is the density of water. At these conditions, and assuming that the addition of the hydrate to the solution is so fast that no carbon dioxide from the hydrate is lost, as well as the carbon dioxide initially trapped in the vapour phase inside the flask, the mass balance of the calcium is now given by

$$\left[Ca\left(OH\right)_2\right]_{ini} V_{sol,\,ini} = \left(\left[Ca^{2+}\right]_{eq} + \left[CaCO_3\right]_{eq}\right) V_{sol,\,fin} \tag{C.21}$$

The mass balance of the carbonate species is now given by

$$n_{CO_3}^{mol,\,tot,\,ini} + m_{hyd} w_{CO_2}^{w} = \left(\left[CO_2\right]_{eq} + \left[H_2CO_3\right]_{eq} + \left[HCO_3^{-}\right]_{eq} + \left[HCO_3^{2-}\right]_{eq} + \left[CaCO_3\right]_{eq}\right) V_{sol,\,fin} + n_{CO_2}^{mol,\,vap,\,fin} \tag{C.22}$$

where $n_{CO_2}^{mol,\,vap,\,fin}$ is the amount of carbon dioxide in the vapour phase at the end.

## C.2 Equilibrium Constants

Table C.1 shows the equilibrium constants for the temperature of 25 °C.

Table C.1 – Equilibrium constant values.

| CONSTANT | VALUE | REFERENCE |
|---|---|---|
| $H_{CO_2}^{mol}$ | $1.70\times10^{-3}$ | Greenwood and Earnshaw (1997) |
| $k_{a_1,CO_2}^{mol}\left(mol\right)$ | $2.50\times10^{-4}$ | Greenwood and Earnshaw (1997) |
| $k_{a_2,CO_2}^{mol}\left(mol\right)$ | $4.69\times10^{-11}$ | Greenwood and Earnshaw (1997) |
| $k_{w}^{mol}\left(mol^2\right)$ | $1.00\times10^{-14}$ | Bandura and Lvov (2005) |
| $k_{sp,CaCO_3}^{mol}\left(mol^2\right)$ | $3.80\times10^{-9}$ | SLM (2017) |

## C.3 Procedure Considerations

The solubility product of calcium carbonate is extremely low. This means that even very small amounts of carbon dioxide in the solution may result in precipitation of calcium carbonate. Furthermore, if the solution containing calcium hydroxide is left open to the atmosphere, the precipitation of calcium carbonate due to the dissolution of carbon dioxide from the air, results in the displacement of the chemical equilibrium, which results in further precipitation of calcium carbonate. Therefore, calcium hydroxide aqueous solution must be made avoiding the contact with atmospheric air. If possible, it is desirable that the solution is degassed.

The initial amount of carbon dioxide in the system (from atmospheric air) is dissolved in the aqueous solution of calcium hydroxide. To reduce the influence of the atmospheric air, the free volume inside the flask (volume that is not occupied by the calcium hydroxide solution) should be as low as possible. In this way, calcium carbonate precipitation is avoided in this first stage. The pressure of the vapour phase is reduced due to the amount of carbon dioxide that dissolves in the aqueous phase.

With the addition of extra amounts of carbon dioxide, namely from the hydrate, the equilibrium is again displaced, resulting initially in the accumulation of carbon dioxide in the vapour phase. The pressure of the system increases as a result of this accumulation. Afterwards, while carbon dioxide is being transferred from the vapour phase to the aqueous phase, a pressure reduction occurs, together with precipitation of calcium carbonate.

For simplification, it is assumed that all precipitated calcium carbonate is the result of the presence of carbon dioxide from the hydrate. Also, it is assumed that all carbon dioxide from the hydrate is converted into calcium carbonate. The first assumption means that the amount of carbon dioxide as a result of the hydrate addition may be overestimated. However, due to the gas phase volume that is very low, and the fact that the solution is already saturated (due to a previous equilibrium) prior to the hydrate addition, the assumption is relatively safe to make. The second assumption means that the amount of carbon dioxide is underestimated. Some of the carbon dioxide may be dissolved in water or accumulated in the aqueous phase. Nevertheless, the use of these assumptions to determine the amount of carbon dioxide from the hydrate resulted in a carbon dioxide concentration in the hydrate that is in agreement with the values obtained from the dissociation tests.

## C.4 References

Bandura, A.V., Lvov, S.N., **2005**. "The Ionization Constant of Water over Wide Ranges of Temperature and Density". *Journal of Physical and Chemical Reference Data* 35, 15-30.

Greenwood, N.N., Earnshaw, A., **1997**. "Chemistry of the Elements", 2nd ed. Butterworth-Heinemann, Oxford, UK.

SLM, "Solubility Products of Selected Compounds". *Published online at Salt Lake Metals*. Available at: http://www.saltlakemetals.com/SolubilityProducts.htm.

# Appendix D THF Experimental P-T Profiles

The experimental logs of experiments E-012 and E-013 using the thermodynamic promoter THF are presented in this section. Interpretation of the logs is made in Section 5.5.1.6.

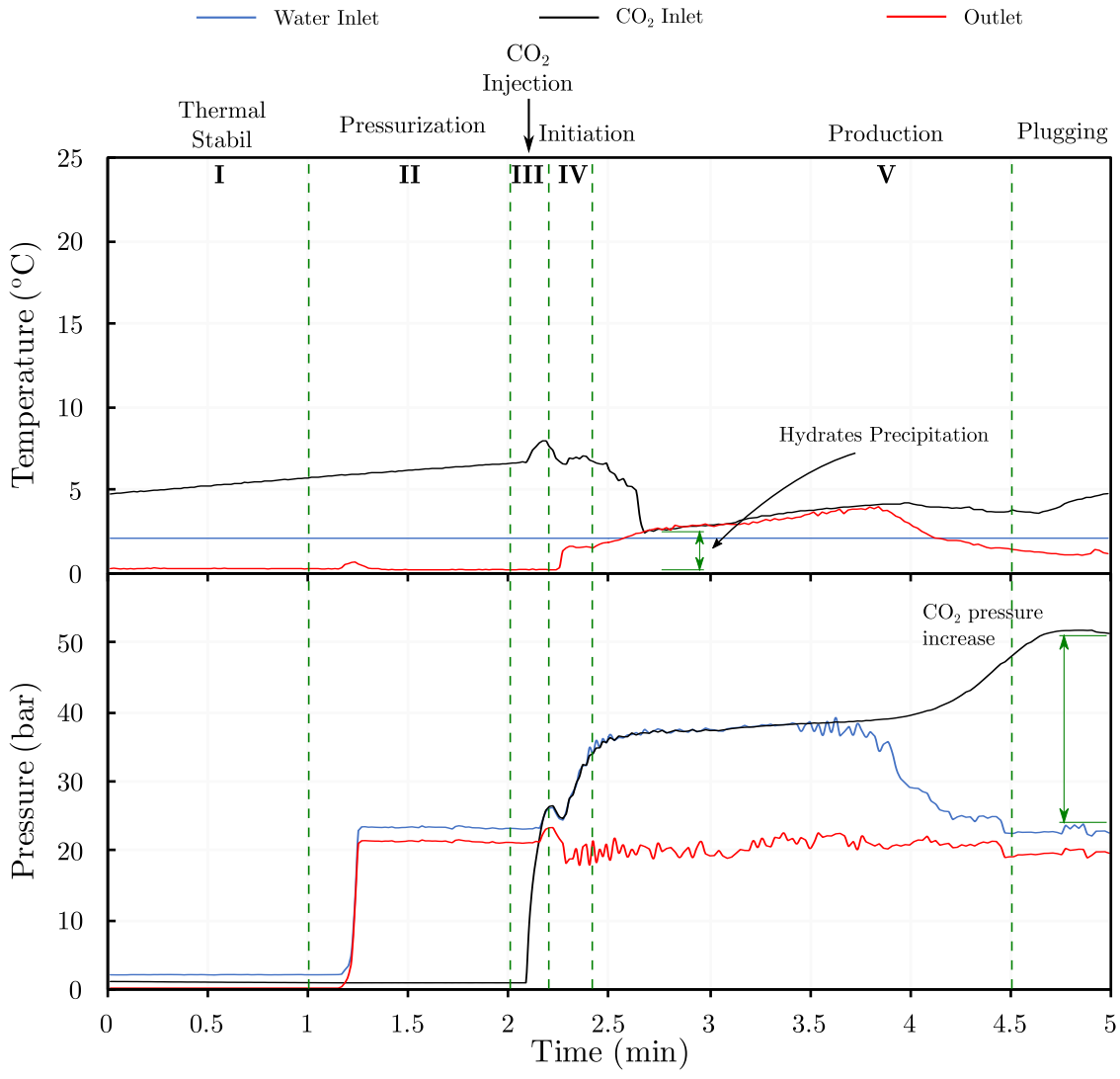



Figure D.1 – Temperature and pressure profiles for experiment E-012.

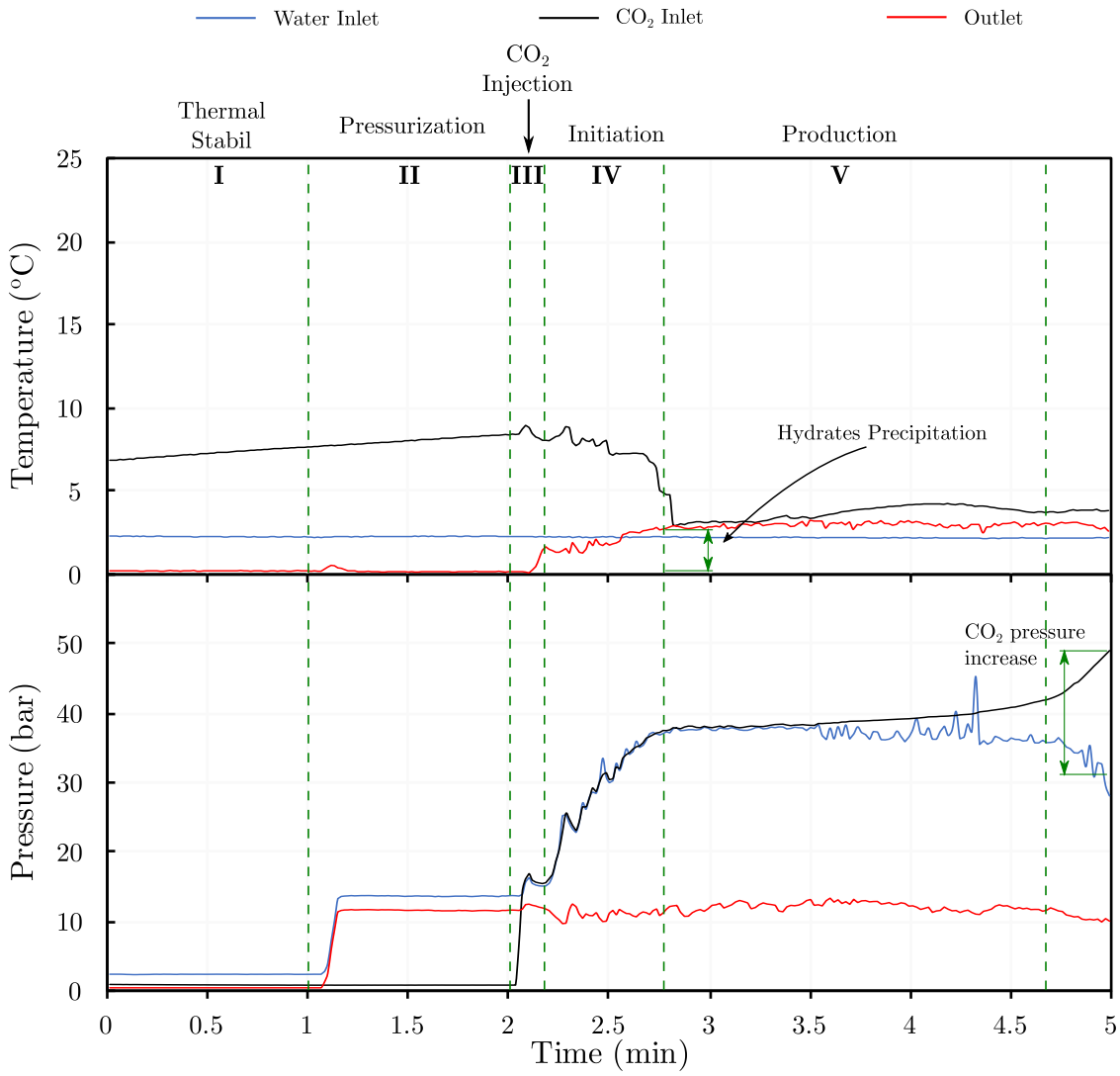



Figure D.2 – Temperature and pressure profiles for experiment E-013.

# Appendix E $N_2/CO_2$ Hydrate Equilibrium Fittings

The fitting curves of the equilibrium data used in Chapter 7 are presented in this section.

## E.1 Equilibrium Pressure

The fitting parameters $\Phi_m^{\mathrm{K}}$ for each of the parameters used to determine the equilibrium pressure of a $N_2/CO_2$ mixture using Equations 7.17 and 7.18 are presented in Table E.1.

Table E.1 – Fitting parameters for Equations 7.17 and 7.18.

| $\Phi_m^{\mathrm{K}}$ | $\varpi$ | $k^*$ | $\lambda$ | $n$ |
|---|---|---|---|---|
| $m=1$ | $8.67\times10^{5}$ | 0 | $1.28\times10^{5}$ | $-2.23\times10^{4}$ |
| $m=2$ | $-3.85\times10^{6}$ | $-4.00\times10^{2}$ | $-5.69\times10^{5}$ | $9.95\times10^{4}$ |
| $m=3$ | $7.10\times10^{6}$ | $1.62\times10^{3}$ | $1.05\times10^{6}$ | $-1.84\times10^{5}$ |
| $m=4$ | $-6.96\times10^{6}$ | $-2.57\times10^{3}$ | $-1.03\times10^{6}$ | $1.81\times10^{5}$ |
| $m=5$ | $3.82\times10^{6}$ | $2.00\times10^{3}$ | $5.70\times10^{5}$ | $-9.97\times10^{4}$ |
| $m=6$ | $-1.11\times10^{6}$ | $-7.68\times10^{2}$ | $-1.67\times10^{5}$ | $2.91\times10^{4}$ |
| $m=7$ | $1.35\times10^{5}$ | $1.16\times10^{2}$ | $2.03\times10^{4}$ | $-3.54\times10^{3}$ |

The fitting curves together with the points extracted from CSMGem are represented as a function of the variables $z^{\mathrm{w}}_{\mathrm{H_2O}}$ and $z^{\mathrm{w}}_{\mathrm{N_2}}/z^{\mathrm{w}}_{\mathrm{CO_2}}$ from Figure E.1 to Figure E.5.

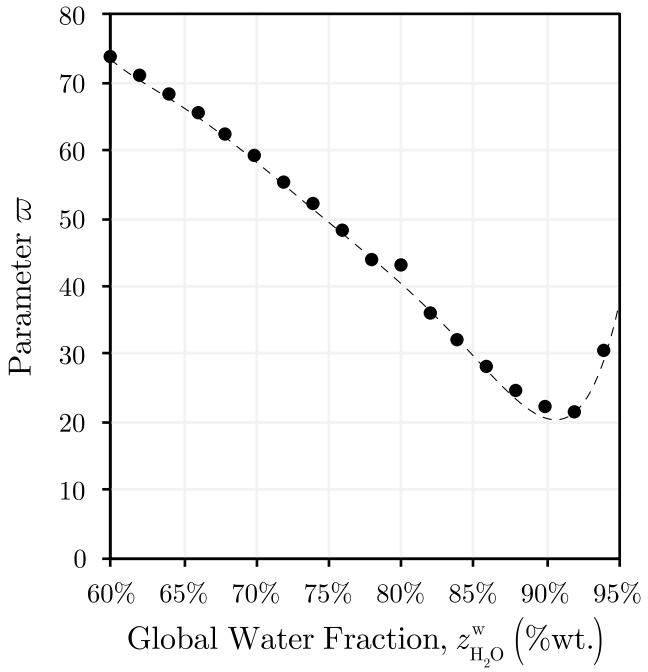



Figure E.1 – CSMGem data (symbols) and fitting curve (dashed line) using values from Table E.1 for the parameter $\varpi$ for the determination of the equilibrium pressure.

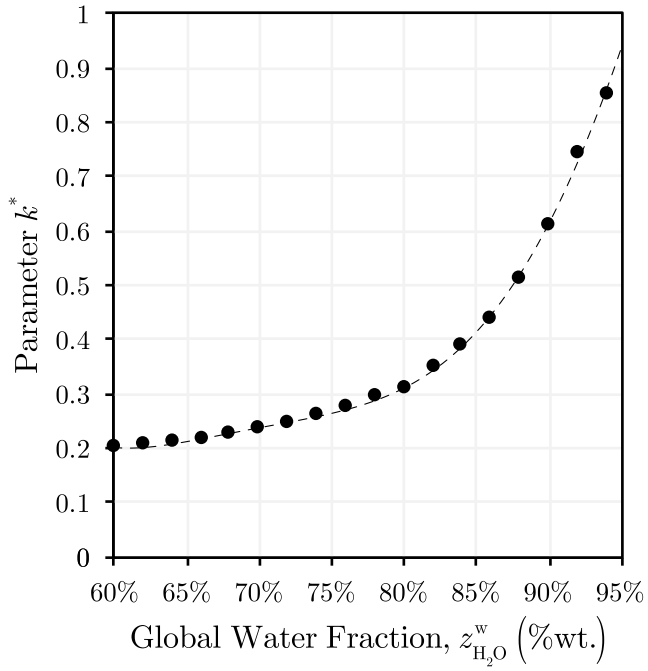



Figure E.2 – CSMGem data (symbols) and fitting curve (dashed line) using values from Table E.1 for the parameter $k^*$ for the determination of the equilibrium pressure.

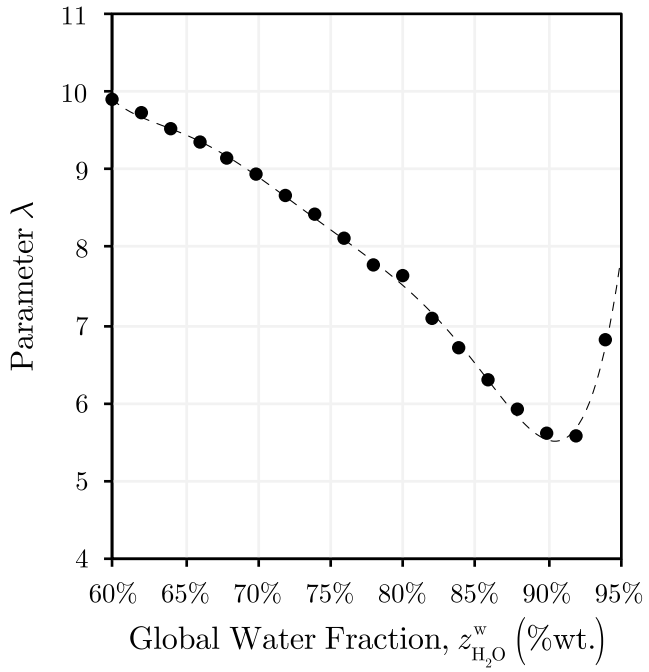



Figure E.3 – CSMGem data (symbols) and fitting curve (dashed line) using values from Table E.1 for the parameter $\lambda$ for the determination of the equilibrium pressure.

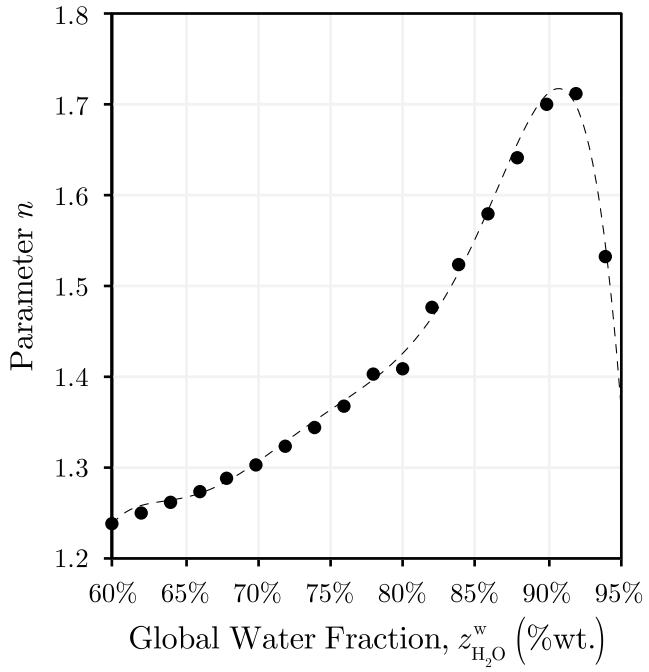



Figure E.4 – CSMGem data (symbols) and fitting curve (dashed line) using values from Table E.1 for the parameter $n$ for the determination of the equilibrium pressure.

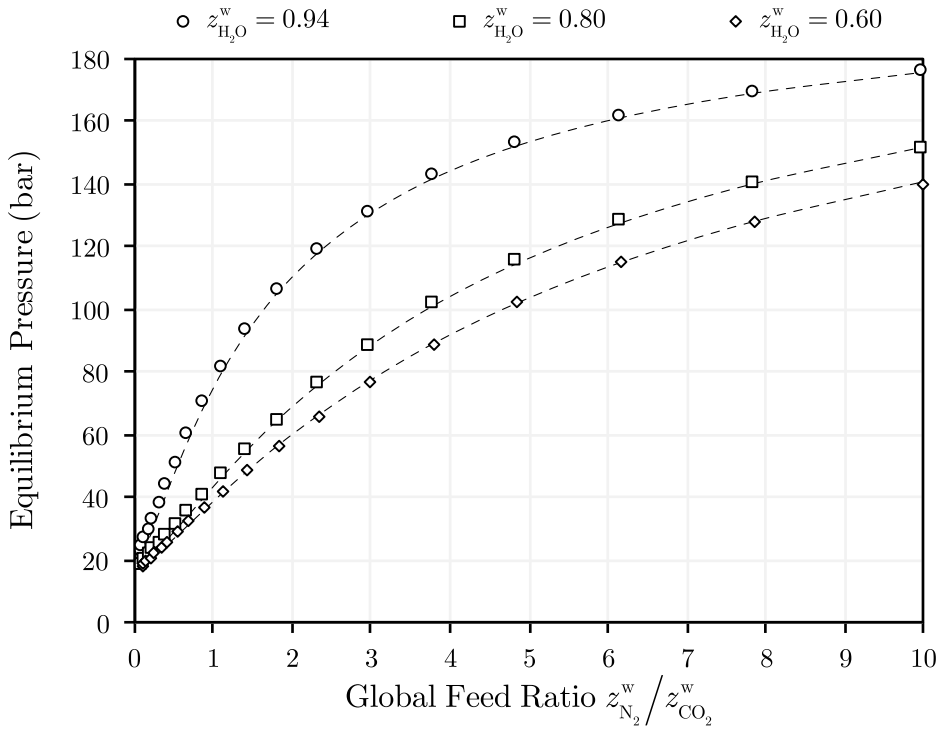



Figure E.5 – Equilibrium pressure from CSMGem (symbols) and from the fitting curves (dashed lines) using the values from Table E.1 and Equation 7.17 and 7.18.

## E.2 Components Equilibrium Fractions

The fitting parameters $A_m^{k,i}$ for the determination of the equilibrium fraction of component $i$ in each of the phases $k$ are presented in Table E.2. These are then applied in Equation 7.20 to determine the component fraction.

Table E.2 – Fitting parameters for the determination of equilibrium component fractions using Equation 7.20.

| | **Vapour Phase** | | **Liquid Phase** | | **Hydrate Phase** | |
|---|---|---|---|---|---|---|
| | $A_m^{\text{vap, N}_2}$ | $A_m^{\text{vap, CO}_2}$ | $A_m^{\text{liq, N}_2}$ | $A_m^{\text{liq, CO}_2}$ | $A_m^{\text{hyd, N}_2}$ | $A_m^{\text{hyd, CO}_2}$ |
| $m = 1$ | $-2.38\times10^{-13}$ | $2.38\times10^{-13}$ | 0 | $8.92\times10^{-16}$ | 0 | 0 |
| $m = 2$ | $1.82\times10^{-10}$ | $-1.82\times10^{-10}$ | 0 | $-6.91\times10^{-13}$ | 0 | 0 |
| $m = 3$ | $-5.71\times10^{-8}$ | $5.71\times10^{-8}$ | 0 | $2.24\times10^{-10}$ | 0 | 0 |
| $m = 4$ | $9.55\times10^{-6}$ | $-9.54\times10^{-6}$ | $5.17\times10^{-11}$ | $-4.00\times10^{-8}$ | $8.01\times10^{-9}$ | $-8.07\times10^{-9}$ |
| $m = 5$ | $-9.16\times10^{-4}$ | $9.16\times10^{-4}$ | $-3.66\times10^{-8}$ | $4.58\times10^{-6}$ | $-2.72\times10^{-6}$ | $2.34\times10^{-6}$ |
| $m = 6$ | $5.12\times10^{-2}$ | $-5.12\times10^{-2}$ | $2.87\times10^{-5}$ | $-5.15\times10^{-4}$ | $-1.30\times10^{-3}$ | $-1.57\times10^{-3}$ |
| $m = 7$ | $-5.35\times10^{-1}$ | 1.53 | $-4.31\times10^{-4}$ | $4.63\times10^{-2}$ | $-1.66\times10^{-2}$ | $2.90\times10^{-1}$ |

The fitting curves together with the points extracted from CSMGem of the components fractions in each of the phases for the temperature of 2 °C are represented as a function of the pressure in Figure E.6.

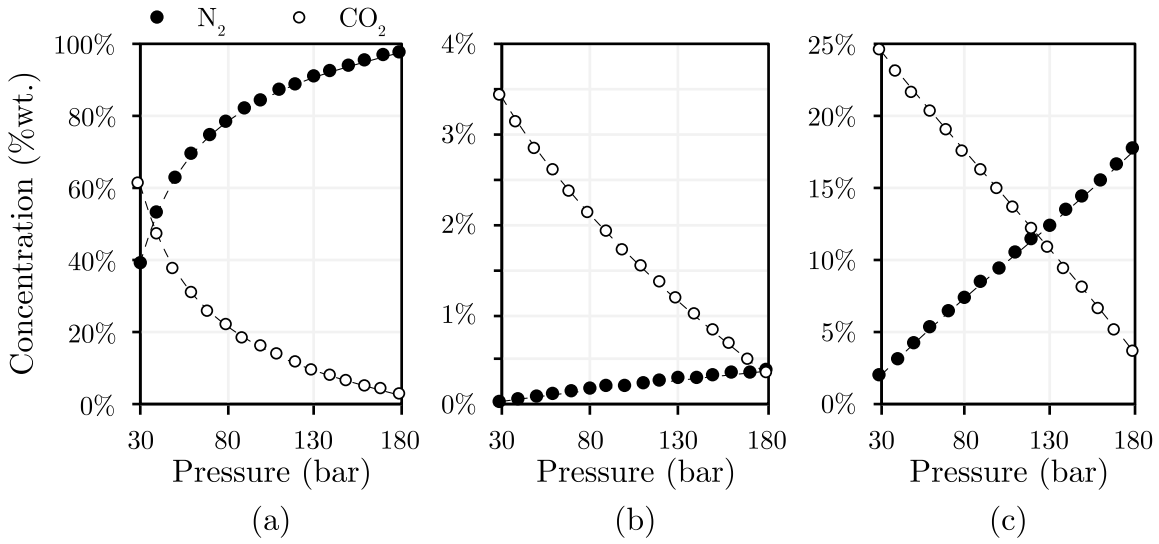



Figure E.6 – Carbon dioxide (full circles) and nitrogen (open circles) and fitting curves (dashed lines) for different phases in equilibrium: (a) vapour phase; (b) liquid phase; (c) hydrate phase.